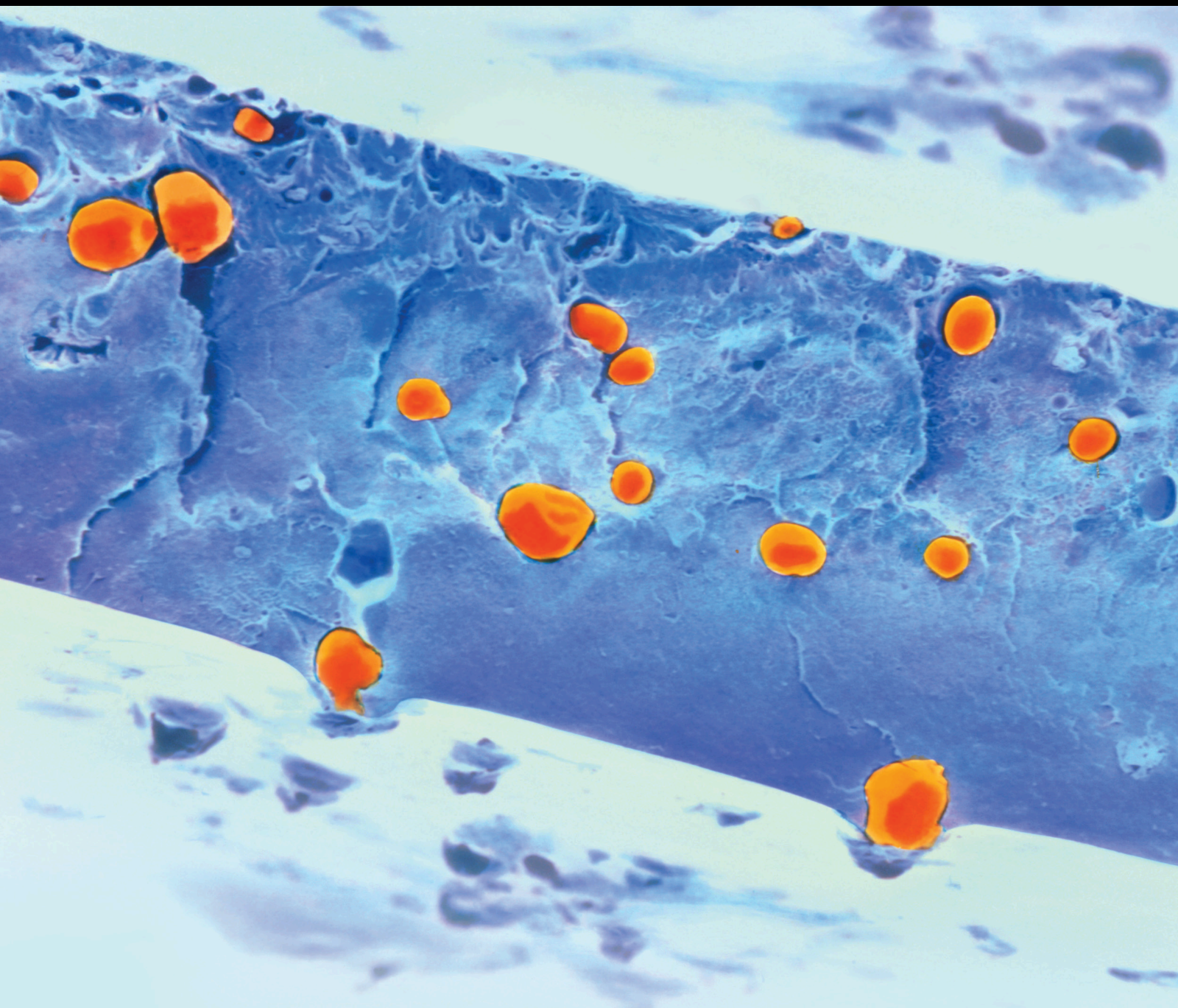# Syntheses and Biomedical Applications of Functional Polymers

Lead Guest Editor: Jianxun Ding
Guest Editors: Di Li, Jing-Xiao Chen, Chao Zhao, and Parisa P. Abadi

Syntheses and Biomedical Applications of Functional Polymers

Syntheses and Biomedical Applications of Functional Polymers

Lead Guest Editor: Jianxun Ding
Guest Editors: Di Li, Jing-Xiao Chen, Chao Zhao, and Parisa P. Abadi

Contents

Contents

Editorial

Synthesis and Biomedical Applications of Functional Polymers

Jianxun Ding ,[1] **Di Li** ,[1] **Jingxiao Chen** ,[2] **Chao Zhao** ,[3]
and Parisa Pour Shahid Saeed Abadi [4]

[1]*Key Laboratory of Polymer Ecomaterials, Changchun Institute of Applied Chemistry, Chinese Academy of Sciences,*
 5625 Renmin Street, Changchun 130022, China
[2]*Department of Pharmaceutics, School of Pharmaceutical Sciences, Jiangnan University, 1800 Pohu Avenue, Wuxi 214122, China*
[3]*Department of Chemical and Biological Engineering, The University of Alabama, 505 Hackberry Lane, Tuscaloosa, AL 35487, USA*
[4]*Department of Mechanical Engineering-Engineering Mechanics, Michigan Technological University, 1400 Townsend Drive,*
 Houghton, MI 49931, USA

Correspondence should be addressed to Jianxun Ding; jxding@ciac.ac.cn

Received 28 July 2021; Accepted 28 July 2021; Published 13 August 2021

In recent years, natural and synthetic biomedical polymers are receiving increasing attention due to their unique and variable chemical, physical, and biological properties. By improving the techniques of polymer synthesis and modification, functional polymers facilely achieve excellent biocompatibility and biodegradability and variable stimuli-responsiveness and bioactivity. Besides, functional polymers can be processed into various device modalities, such as nanoparticles, nanofibers, microspheres, microfibers, hydrogels, membranes, and scaffolds, to meet different practical applications.

Functional polymers have demonstrated promising applications in a wide range of biomedical fields, including disease diagnosis, therapeutic drug delivery, biosensors, tissue engineering, and medical devices. This special issue is aimed at systematically and comprehensively presenting the latest advances in developing preparation approaches and emerging biomedical applications of functional polymer-based materials, providing guidance and reference for future studies.

To meet this aim, the special issue collected sixteen research articles and two review articles. These articles cover the synthesis and biomedical applications of functional polymers.

Twelve research articles focused on polysaccharides and their applications in antitumor, antioxidation, and anti-inflammatory functions. Antitumor activity is a potential property of polysaccharides, and nine different polysaccharides have been reported to exhibit antitumor activity against various tumors. M. Zeng et al. investigated the antitumor effect of *Lycium barbarum* polysaccharide (LBP) on human cutaneous squamous cell carcinoma and demonstrated that LBP induced the apoptosis of human cutaneous squamous cell carcinoma A431 cells by inhibiting autophagy and effectively inhibited tumor growth. Y. Zhang et al. confirmed that *Codonopsis pilosula* polysaccharide effectively inhibited the proliferation and motility of human hepatoma HepG2 cells *in vitro* possibly by inhibiting the β-catenin/TCF4 pathway. Similarly, M. Yao et al. illustrated that *Laminaria japonica* polysaccharide inhibited the survival of non-small-cell lung adenocarcinoma A549 cells through the same pathway. X. Du et al. found that *Radix hedysari* polysaccharide inhibited the growth of glioma U251 cells by cell cycle arrest and regulation of the tumor necrosis factor-α (TNF-α) signaling pathway. X. Xu et al. demonstrated that sulfated polysaccharide from *Undaria pinnatifida* had antitumor activity against human prostate cancer DU145 cells, and the underlying mechanism may be related to inhibiting the migration and proliferation of cancer cells and inducing their apoptosis. W. Zhou et al. studied the effects of *Polygonatum sibiricum* polysaccharide (PSP) on the human esophageal squamous cell carcinoma Eca109 cells. The results showed that PSP significantly inhibited the proliferation, invasion, and migration of Eca109 cells and promoted cell apoptosis, and the underlying mechanism may be related to the inhibition of the nuclear factor-κB (NF-κB) signaling pathway.

Three research articles reported the synergistic antitumor efficacy of polysaccharides and other antitumor drugs. X. Liu et al. demonstrated that lentinan enhanced the cytotoxic effect of cisplatin on tumor cells, and the combined treatment of lentinan and cisplatin showed a satisfactory tumor inhibition effect in multiple tumor models. W. Wu et al. combined macrofungal polysaccharide (MFP) and vemurafenib to treat melanoma. The results showed that MFP significantly enhanced the tumor inhibitory effect of vemurafenib in human melanoma MeWo cell-bearing mice. X. Yang et al. found that *Ganoderma lucidum* polysaccharide (GLP) improved the antitumor effect of 5-fluorouracil against gastric cancer BGC823 and SGC7901 cells by activating the natural killer group 2 member D (NKG2D)/MHC class I-related chain A (MICA) pathway.

Three research articles reported the applications of polysaccharides for treatment of other diseases, such as contrast-induced nephropathy, osteoarthritis, and intervertebral disc degeneration. M. Dai et al. demonstrated that the crude polysaccharide (cSFP-C) extracted from *Sargassum fusiforme* effectively prevented contrast-induced nephropathy due to their excellent antioxidant capacity. G. Lu et al. found that hyaluronic acid and *Astragalus* polysaccharide-capsuled nanoparticle effectively treated osteoarthritis by regulating cytokines and proteinase. Z. Zhai et al. confirmed that *Polygonatum sibiricum* polysaccharide (PSP) effectively reduced the apoptosis, inflammation, and oxidative stress of nucleus pulposus cells in rat with intervertebral disc degeneration, and it was a potential therapeutic drug for intervertebral disc degeneration.

Four original research articles report the synthesis and biomedical applications of other functional polymers. Q. Chen et al. prepared porous chitosan microsphere loaded with platelet-rich plasma and bone marrow-derived mesenchymal stem cells (PCM/PRP/BMSC composite), and they found that PCM/PRP/BMSC composite was beneficial for the repair of tibial defects. D. Patiño-Ruiz et al. synthesized chitosan-alginate nanodisk (Cs-Al ND) using the ionotropic gelation technique and demonstrated that Cs-Al ND was a promising drug delivery system with high encapsulation efficiency and controlled drug release. D. T. Nguyen et al. investigated the effect of microwave irradiation on poly(vinyl alcohol) (PVA) in PVA/Ag$^+$ solution. The results confirmed that the redox reaction of Ag$^+$ with PVA and Ag$^+$ reduced the hydrolysis rate of PVA. A. M. Díaz-Guerrero et al. used a mathematical model to evaluate the acetaminophen release in hydroxypropyl cellulose with polyacrylamide (HPC/PAAm) and confirmed that the proposed mathematical model was reliable.

In addition, two review articles summarized the latest advances in two different functional polymers for biomedical applications. G. Merkininkaitė et al. introduced three-dimensional laser lithography (3DLL) and the main categories of polymers used in 3DLL and then discussed the applications of 3DLL structural polymers in regenerative medicine. Finally, the current challenges and opportunities in this area were highlighted. Y. Yang et al. reviewed the preparation methods of the cellulose nanocrystal and its wide applications in various fields, which provided operable ideas

and techniques for future high-end and ecofriendly functional composites.

In summary, this special issue bridges the synthesis methods, structure-property correlations, and biomedical applications of functional polymers and explores their underlying mechanisms. We hope to provide references for interested authors and inspire relevant researchers.

Conflicts of Interest

The authors declare no conflict of interest regarding the publication of this special issue.

Acknowledgments

Jianxun Ding
Di Li
Jingxiao Chen
Chao Zhao
Parisa Pour Shahid Saeed Abadi

Review Article

Progress on Preparation of pH/Temperature-Sensitive Intelligent Hydrogels and Applications in Target Transport and Controlled Release of Drugs

Lixian Li [iD],[1,2] Yongpeng He,[1] Xiaodong Zheng [iD],[1] Lin Yi,[1] and Weiqi Nian [iD][1]

[1]*Chongqing University Cancer Hospital & Chongqing Cancer Institute & Chongqing Cancer Hospital, Chongqing 400030, China*
[2]*Department of Chemistry, The University of British Columbia, Vancouver, British Columbia, Canada V6T 1Z1*

Correspondence should be addressed to Lixian Li; lilixian2010@yahoo.com, Xiaodong Zheng; zxd052005@sohu.com, and Weiqi Nian; nwqone@126.com

Hydrogels with three-dimensional network structure, hydrophilic, and insoluble in water which are ideal carrier materials for intelligent drug delivery systems. Intelligent hydrogel has become a research frontier and hotspot because of its intelligence, high efficiency, safety, and convenience in drug controlled and prolonged release. It has a broad application prospect in the medicine and biomedicine fields and can lead the medicine fields into a new era of "precise treatment." Based on the latest research progress, the main preparation methods of hydrogel and the development of the drug delivery system are briefly introduced. The most promising three intelligent hydrogels in the human physiological environment, namely, pH responsiveness, temperature responsiveness, and pH/temperature dual responsiveness, are emphatically reviewed. Their release mechanisms, targeting transport, and controlled-prolonged release of drug are also discussed. In addition, some suggestions for the main problems and future development were given.

1. Introduction

Hydrogel is a three-dimensional crosslinked network structure which is formed by hydrophilic polymers through chemical bond, ammonia bond, Van der Waals' force, or physical interaction. In 1960, Wichterle and Lim prepared a polymer network structure by using the crosslinking 2-hydroxyethyl methacrylate (pHEMA) [1]. It is a milestone discovery in the history of hydrogel development. In 1970s, polyethylene glycol (PEG) hydrogel attracted attentions, and it was widely used in controlled delivery vector of drugs due to its good biocompatibility and strong resistance to protein adsorption. Research concerns shift from the relatively simple water-soluble macromolecular network gel into hydrogel systems produced by changes of environmental factors, such as temperature, pH, and biomolecular concentration. Size and shape of hydrogel can be controlled by regulating these environmental factors. Hence, hydrogel is often used as an intelligent material [2]. Among them, temperature sensitive

hydrogel is the environmental sensitive system which has been studied the earliest and used most extensively [3]. The intelligent temperature-sensitive hydrogel is the consequence of equilibrium among different hydrophilic, hydrophobic effects, and Van der Waals' force in the gel system. pH-sensitive hydrogel is the second common environmental sensitive system. Since pH-sensitive hydrogel generally carries weak acid or alkaline groups, the ionization of groups is sensitive to external pH. Internal and external ion concentrations redistribute and reach a new equilibrium upon changes of external pH. Research and development (R&D) of a new drug is time-consuming and requires high cost. The annual expenses for drug R&D in the American pharmaceutical industry exceeded 20 billion of dollars in 1990s, which was further increased to 72 billion of dollars in 2004. Such annual expense was still increasing. The cost for new drug R&D soared up significantly. The average R&D cost of the American pharmaceutical company for each new drug increased from 231 million of dollars in 1987 to 802 million

of dollars in 2000 and even soared up to 1.4 billion of dollars in 2004. The average time consumption for R&D of a new drug is about 14 years. It has been reported by studies that 39% of R&D failures of new drugs are caused by poor dynamic characteristics of drugs in the human body, another 29% of failures are caused by the unsatisfying curative effect, and 21% of failures are attributed to toxicity and side effects of drugs [4].

The drug delivery system (DDS) which achieves rapid development in recent years can transport drugs to the target position according to the desired dosage and action time through the perfect combination of drugs and carrier. In addition, DDS controls drug delivery through the feedback regulation mechanism of the human body, thus realizing the goal of curing diseases. Moreover, this DDS can relieve general toxic and side effects of drugs and improve therapeutic effect of diseases. Controlled releasing of drugs is an extensively studied and perfect technology in DDS. It is a new technology that can control delivery speed and directional release of drugs. On the one hand, hydrogel not only has weak adhesion to cells and proteins but also has excellent biocompatibility with blood, fluid, and tissues of the human body. On the other hand, hydrogel with abundant water has soft texture similar with biological tissues and weak reactivity with antigen of the human body. Hydrogel which is prepared by nontoxic materials can cause small harms to the human body [5]. Under the dual effects of release by hydrogel deformation and self-diffusion, drugs can be released to the target position slowly according to the desired dosage. Hydrogel has advantages of quantitative, directional, and stable delivery of drugs. Therefore, intelligent hydrogel gradually becomes the first chose of carrier of DDS [6, 7]. The second generation DDS of an intelligent drug delivery system which could response to external environmental factors (e.g. pH, temperature, and light) was developed by some polymer materials around 1980. The second generation DDS realized intelligent delivery of drugs and became one of research hotspots in the field of medicines. The third generation DDS of a targeted intelligent drug delivery system was launched in 2010. Different from the second generation DDS, the third generation DDS involves a covalent modification of targeted group by drug carriers. This targeted group has the higher selectivity of tumors and thereby can deliver drugs to the target position of focus actively. This is significantly different from the passive transport depending on enhanced permeation and retention (EPR) of solid tumors. The third generation DDS can not only shorten in vivo circulation of drugs and prevent drug leakage or inactivation but also decrease dosage and side effect of drugs as well as mitigate pains of patients [8]. Intelligent hydrogel which is the drug carrier is the key component of DDS and the primary factor that influences the effect of drugs. At present, applications of intelligent hydrogels in targeted delivery and controlled releasing of drugs have become a research front and hotspot in the field of medicine. Research on applications of intelligent hydrogels in controlled drug releasing has extremely important academic values and promising application prospects in clinics.

2. Hydrogel Preparation Methods

Hydrogel can be hydrolyzed quickly due to the natural super-molecule matrix. Hence, hydrogel often fails to meet the requirements in biomedicine applications [9, 10]. It is of important significance to explore and search new preparation and modification methods or materials. Physical crosslinking and chemical ligation are two common preparation methods of hydrogel. Physical crosslinking is simple and convenient. However, hydrogel prepared by physical crosslinking has some disadvantages, such as insufficient strength and tenacity, instability, and easy hydrolysis. Chemical ligation is relatively complicated and has high requirements on technologies and chemical reactions. Nevertheless, it can improve mechanical properties and structural stability of hydrogel significantly.

2.1. Physical Crosslinking Method. Physical crosslinking among polymers is generally realized by interaction of non-covalent bonds (hydrophobic, ionic and intermolecular hydrogen bonds, subject-object, or various covalent bonds) [9–11]. Due to the strong hydrophobic interaction in aqueous solution, hydrogel can be prepared simply and directly by amphiphilic block polymers. This becomes the most common method of hydrogel preparation based on physical crosslinking.

(1) Stereocomplexation: stereocomplexation, or known as the cocrystallization of two enantiomers, can be used to prepare injectable hydrogel. Enantiomer is mainly used to prepare in situ hydrogel. Hydrogel can be formed by coupling of poly-L-lactide (PLLA) and poly-D-lactide (PDLA) with hydrophilic polymers (e.g., glucan) in aqueous solution. Firstly, protein drugs are dissolved in the solution of gel precursor, through which the protein drug is encapsulated in the hydrogel network [10]. Without any surfactant or chemical ligation agents, Jiang et al. first proposed the unique network structure on the basis of hydrophobic associations of the HMPAM and SDS in the aqueous solution [11]. This micelle cluster is the crosslinking center of the hydrogel network and gives a solid three-dimensional structure of hydrogel. Compared with hydrogel prepared by chemical ligation, HA gel shows unusual swelling-deswelling behaviors in water. Additionally, the existence of micelle cluster increases mechanical properties of HA gel and shows ultra-strong self-healing ability in applications of biomedicine technologies in the future

(2) Polypeptide chain interaction: polypeptide physical hydrogel is mainly prepared by self-assembly of molecules. Due to biodegradation and biocompatibility, polypeptide only produces amino acids during degradation, which may not cause adverse impacts on the living body. Polypeptide will not cause immunoreactions and tissue inflammation after entering into the living body. Besides, polypeptide has multiple configurations, such as spiral, overlapping, and irregular

curling structures. Self-assembly of some polypeptides occurs in the physiological environment. The produced hydrogel can be transported in different environments easily. This type of hydrogels possesses a promising prospect in studies on controlled drug delivery technology and new support for cell therapy as well as tissue engineering

Yang et al. connected peptide chains with the self-assembly ability onto the skeleton composed of the linear hydrophilic compound poly [N-(2-hydroxypropyl) methacrylamide] (HPMA) through covalence bonds, forming the self-assembly peptide chain grafted compounds (Figure 1) [12]. They found that HPMA in the copolymer would not hinder self-assembly of the peptide chain, but the length of the peptide chain, and the peptide chain grafted onto each skeleton affected the formation of self-assembly gel significantly. Kopecek et al. [13] prepared a hybrid hydrogel which was assembled by water-soluble polymers and proteins with a double helix structure. This hybrid hydrogel could be transformed from synergic conformation to a double helix structure upon induction of temperature.

2.2. Chemical Ligation Method. Chemical ligation is one of the most important methods to prepare hydrogel. Firstly, initiator is added for grafting monomers onto groups of raw materials. Secondly, crosslinking agent is added for crosslinking of different polymers, forming a stable three-dimensional network structure. This three-dimensional network structure only swells, but is not dissolved. The mechanical properties of the three-dimensional network structure are stronger than those of a physical crosslinking network. Photopolymerization chemical ligation, native chemical ligation, and click chemistry are highly appreciated by the public due to the simple operation and high transformation rate [10].

2.2.1. Photopolymerization Chemical Ligation. Under the existence of photoactive compounds (or known as photocatalysts), ultraviolet or visible light irradiation can trigger in situ polymerization, thus producing three-dimensional networked hydrogels with intramolecular or intermolecular crosslinking structures. This process is the photopolymerization. The photopolymerization chemical ligation is characteristic of mild conditions, controllable process, few byproducts, and no use of toxic initiator. The mechanism of photopolymerization chemical ligation is introduced as follows: photoinitiator forms free radicals under irradiation of ultraviolet or visible lights, and polymerization of monomers is triggered by these free radicals. This method has some prominent advantages, such as short photocuring (several seconds to several minutes), successful reaction under room temperature or human body temperature, no use of any organic solvents, and temporal-space regulation. For this reason, photopolymerization chemical ligation has been widely applied in biomedicine after it was reported by Hubbell et al. [14]. Liu et al. [15] prepared the pH-sensitive hydrophobic polymethylacrylic acid hydrogel through polymerization of benzoin ethyl ether (photoinitiator), crylic acid-2-ethylhexyl acrylate (hydrophobic monomer), tripropylene

glycol diacrylate (crosslinking agent), and methyacrylic acid under ultraviolet lights. Moreover, they used hydroxyanisole as a model drug and discussed the drug delivery law of polymethacrylic hydrophobic gel.

2.2.2. Native Chemical Ligation. Dawson et al. proposed the native chemical ligation for the first time in 1994. Thioesters and peptide amino acid with an N-end react firstly to produce thioester crosslinked compounds. Subsequently, these thioester crosslinked compounds were rearranged, forming a natural peptide bonds (Figure 2) [16]. The native chemical ligation is widely used in big polypeptide proteins with medium molecular weight and dendritic polymers based on polypeptides.

2.2.3. Click Chemistry. Click chemistry is one type of reaction that synthesizes various structural molecules quickly and effectively through the splicing module. Click chemistry has many advantages: firstly, good spatial orientation and stereoselectivity. Secondly, strong thermomechanical effect: click chemistry often involves reactants with instable thermodynamics or stable products. Thirdly, high reaction rate: water generally causes no negative impacts on click chemistry. In addition, single product: click chemistry generally has no additive reaction of producing by-products or condensation reaction that produces water as the by-product.

In 2006, Hilborn synthesized poval with azide groups, and alkynyl functionalized through "click chemistry" for the first time [17]. Later, he added $CuSO_4$ and vitamin A sodium salt into the system to synthesize the vinol hydrogel. In 2008, he also discovered the formation of oxime, semicarbazone, and tetrahydrothiazole crosslinking points through the reaction between polymer multifunctional crosslinking agents and hyaluronic acids [18]. The multifunctional crosslinking agent based on PVA has good cell compatibility and shows no toxicity after 48 h. It can be shaped quickly under pH = 7.4 and 37°C. The Karl Barry Sharpless research team who won the Nobel Prize in Chemistry in 2014 reported a click chemical reaction based on sexavalence sulfur fluoride exchange (SuFEx) in *Angewandte Chemie*. In the follow-up five years, "click chemistry" between azides and alkyne becomes one of hotspot methods to prepare hydrogel network structures.

3. Drug Delivery System

The drug delivery system (DDS) refers to a new form of drug administration that can release drugs at the fixed time, to the target position, and in the determined dosage by regulating the internal structure of drug carriers. It is characteristic of high efficiency, low toxicity, targeted delivery, few times of drug delivery, and high safety. Specifically, the controlled drug releasing system and targeted controlled drug releasing system based on reversible intelligent hydrogel carrier have attracted wide research attentions in recent years [19, 20].

3.1. Controlled Drug Releasing System. The controlled drug releasing system refers to a drug loading system that can delay the releasing rate of drugs from preparations and release drugs to the acting organ or target tissues and cells
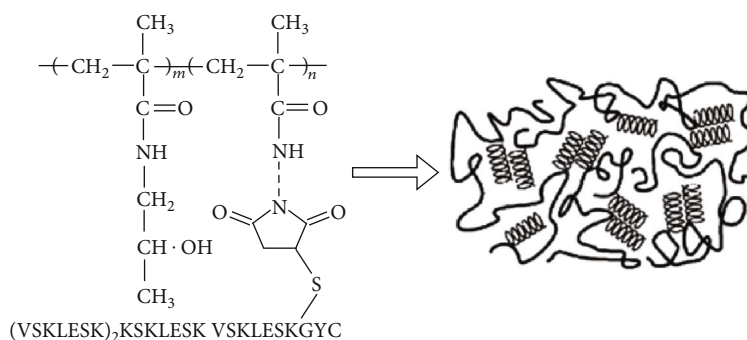
FIGURE 1: Diagram of hydrogel self-assembled from graft copolymer and structure of graft copolymer of HPMA (reproduced from reference [12] with copyright permission from john wiley and sons).
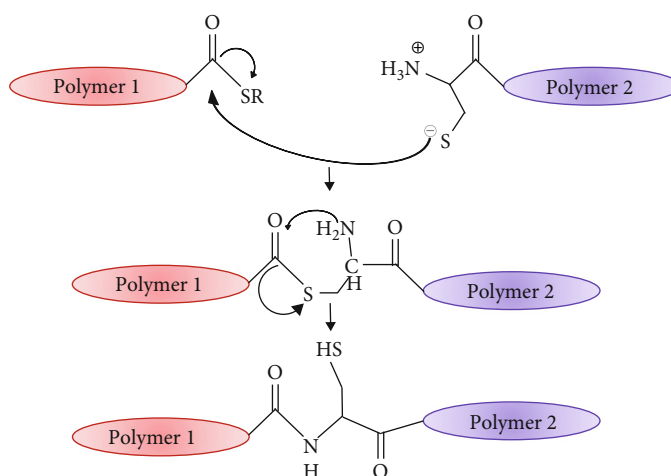
FIGURE 2: Coupling mechanism of native chemical ligation of two polymers (reproduced from reference [16] with copyright permission from ACS Publications).

at a constant speed. It can decrease the drug absorption rate of the human body, delay the action of drugs, eliminate peaks and valleys of drugs, and decrease times of drug administrations, thus realizing better therapeutic effect. The microballoon oral-taking system, osmotic pump tablets oral-taking system, and microballoon injecting system are controlled drug releasing systems.

3.2. Targeted Controlled Drug Releasing System. For some clinical diseases like liver cancer, lung cancer, and solid tumor, large dosage general administration of drugs cannot develop effect of drugs better and cause extremely significant toxic and side effects to normal organ tissues and human body. For example, the ordinary administration mode of drugs generally cannot achieve the satisfying effect of drugs for brain or spinal cord diseases, which is caused by physiological barriers. However, the targeted controlled drug releasing system can concentrate drugs at the target organ tissues or in target cells through local drug delivery based on carriers, ligands or antibodies, or general blood circulation, thus lowering drug concentration in normal positions as much as possible. For instance, directed drug releasing to target tissues and organs through carriers like lipidosome, microcapsule, and microballoon can not only decrease the administration

dosage of drugs but also improve the therapeutic effect and lower toxic and side effects of anticancer drugs [21]. In addition, some antibodies or ligands could be modified onto the carrier surface in accordance to specific diseases, so that the drug carrier can develop immunity or affinity specificity. As a result, the drug carrier is easier to be recognized by tumor tissues or cancer cells and can deliver drugs to the target tissues or cells more efficiently [22]. Due to the strong interaction with cancer cells, folic acid can be used to modify the carrier of anticancer drugs to enhance targeting ability of drugs. Mackiewicz et al. [23] prepared the polyethylene glycol-b-polyglycolic acid (PEG-b-PLA) polymer and then modified it with folic acid and fluorescence needle through click chemistry. On this basis, a nano drug-carrying micelle is self-assembled, which realizes the dual function of targeted drug delivery and cell imaging. Except for folic acid, some carbohydrates also can be used in targeted DDS. Ladmiral et al. [24] modified galactose onto vesicae through the reversible addition-fragmentation transfer (RAFT) polymerization technique for targeted transport of rhodamine B.

Specificity is the most outstanding advantage of the targeted drug releasing system. It overcomes the low target sensitivity of biochemistry. With the continuous innovation of new DDS and continuous updating of new carrier materials,

the connotation and denotation of the drug carrier are updating continuously. For instance, the development of gel, micelle, nanoparticles, and vesicae overcome many disadvantages of anticancer drugs, such as strong toxic and side effects, easy decomposition, and sudden releasing. They can improve efficiency of targeted drug delivery and weaken side effects, thus enabling to achieve better therapeutic effect [8].

4. Application of Intelligent Hydrogels in Controlled Drug Releasing Systems

Compared with ordinary DDS, using intelligent hydrogels with many special performances in the controlled drug releasing system has many evident advantages, such as delaying the drug delivery, prolonging action time of drugs, increasing bioavailability of drugs, stable drug concentration and decrease fluctuation of drug concentration, target transport and controlled releasing of drugs, reducing dosage of drugs, mitigating or preventing toxic and side effects, preventing influences by the "first-pass effect" of gastrointestinal environment and liver as well as the gastrointestinal assimilation resistance, and optimizing therapy and improve compliance of patients.

The drug-carrying and controlled releasing behaviors of xylan P (NIPAM-G-AA) hydrogel network was studied in detail [25]. The NIPAM-G-AA hydrogel network presents a porous structure. The special pores of hydrogel allow drugs wrapped onto hydrogel matrix. The controlled drug releasing rate is determined by the diffusion coefficient of micromolecules or macromolecules in the gel network [25]. It is reported by studies that temperature/pH-sensitive NIPAM-G-AA hydrogel can control drug releasing in gastric fluid and intestinal fluid well.

4.1. Drug Releasing Mechanism of pH-Sensitive Intelligent Hydrogel and Its Applications in Controlled Drug Releasing Systems. There are three major types of pH-sensitive materials, namely, cationic hydrogel, anionic hydrogel, and zwitter-ion hydrogel [26]. The pH-sensitive cationic hydrogels (generally polyacrylamides) mainly include ionizable functional groups of $-NHR$, $-NR_2$, and $-NH_2$. Amino exists as ions in the acid environment. Repulsion among ions increases the distance between hydrogel chains, and more water molecules enter into the hydrogel chain, thus enhancing the swelling ratio. Hydrogen-bond interactions in hydrogel in the alkaline environment further compact the network structure better and thereby decrease the swelling ratio [26]. The pH-sensitive anionic hydrogel (generally acids like polyacrylic acid) mainly exists in $-COO^-$. $-COO^-$ is protonized into $-COOH$ in the acid environment. Due to interaction of groups, the hydrogel network structure is more compacted, which makes it difficult to develop swelling by water absorption. In the alkaline environment, $-COOH$ is changed to $-COO^-$, and the electrostatic repulsion between carboxylic acids further extends the network structure, which is conducive to strengthen water absorption and increase the swelling ratio [26, 27]. Zwitter-ion hydrogel mainly carries acid-based groups. $-COOH$ is ionized, while amino is protonized in the alkaline environment. On the contrary, $-COOH$ is proto-

nized, and amino is ionized in the acid environment. The swelling ratio decreases as approaching to the neutral state. In a word, zwitter-ion hydrogel has ionization of groups in either acid or alkaline environment. Ion strength is the major influencing factor of the swelling ratio of zwitter-ion hydrogel [26]. The phase changes of the swelling performance of all three hydrogels with pH are shown in Figure 3 [27].

The most ideal controlled drug releasing is to control releasing of drugs in accordance with psychological needs at specific positions (target). pH-triggered control is the most attractive target releasing way [28, 29]. pH in gastrointestinal tract of the human body ranges between 1 and 7.5 (1-3 in stomach, 5-6 in saliva, 6.4-7.0 in colon, and 6.6-7.5 in intestines). pH-sensitive intelligent hydrogel can perceive changes of the physiological environment in the human body, thus adjusting the dynamics of drug releasing. The swelling behavior of hydrogel also changes with pH, forming a switching key. Hydrogel has promising application prospects in the field of medicine [16].

The pH-sensitive hydrogel can regulate releasing of drugs in different physiological positions effectively by taking advantages of great differences of pH between the stomach environment (pH ≈ 1.2) and intestinal environment (pH ≈ 7.4) [30]. Cationic hydrogel achieves the minimum swelling ratio under neutral conditions, and only few drugs are released from hydrogel. For example, caffeine which is loaded onto the copolymer hydrogel of polymethyl methacrylate and dimethylamino-ethyl polymethacrylate releases drugs when pH ranges between 3 and 5. Based on this characteristic behavior, it can prevent releasing drugs with poor tastes in the neutral oral environment and thereby improve taste of drugs. The controlled drug releasing in stomach can be realized by the semiinterpenetrating network type of cationic hydrogel. For example, the semi-interpenetrating network hydrogels formed by chitosan and polyethylene glycol have good swelling characteristics in the acid environment (close to pH in stomach). These hydrogels can be used as intelligent hydrogel carriers for targeted releasing of antibiotic drugs in the stomach environment. Some hydrogels which achieves the minimum swelling ratio in the acid environment and maximum swelling ratio in the neutral environment can be used as a potential carrier of intestinal or colon specificity drugs [31].

Xu [32] and Feng et al. [33] synthesized the methacrylic acid-poloxamer copolymer hydrogel and the multilayer sodium alginate tech grade hydrogel for oral DSS, respectively. Releasing and swelling of these hydrogels are inhibited in the acid environment, but they can release drugs quickly in neutral or alkaline environments. Wu et al. [34] prepared pH-sensitive in situ gel for delivery of ophthalmic baicalin by using carbopol P974 as the matrix and macromolecular crosslinked polymer hydroxypropyl methylcellulose hypromellose (HPM C-E4M) as the thickener. This in situ gel achieved the best stability when pH is about 6.0, but the drug releasing rate was increased significantly at pH = 5.8. This in situ gel improved the intraocular comfort of gel and compliance of patients. Due to the unique pH-dependent swelling-deswelling controlled drug releasing characteristics, pH-sensitive hydrogel has been extensively used in the oral
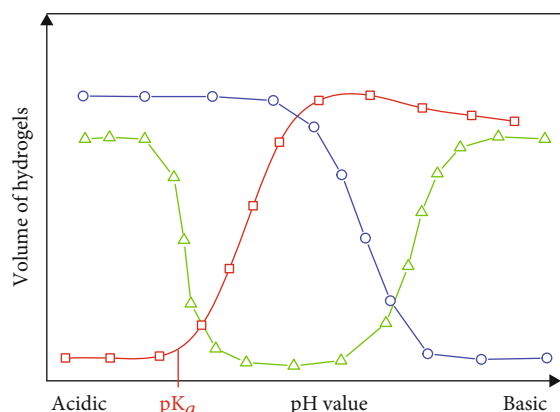
FIGURE 3: Phase transition behavior of different types of pH-sensitive hydrogels. Adapted from [27], acidic hydrogels (red rectangle) are ionised by deprotonation in basic solutions, which have an excess of hydroxyl groups. Basic hydrogels (blue circle) swell in acidic solutions due to the ionisation of their basic groups by protonation. Amphiphilic hydrogels (green triangle) contain both acidic and basic groups. Therefore, they show two phase transitions. (reproduced from reference [27] without permissions that are required for this figure as the original publication is open access).

administration of drugs, traumas, and ophthalmic diseases. However, most associated studies are dealing with experiments. Further, studies on toxic characteristics of carrier materials, encapsulation rate, and selection of polymers are still needed. Moreover, mutual interference of sensitive units in the drug carrier with dual or multiple responses might weaken and even cause disappearance of one response sensitivity.

4.2. Drug Releasing Mechanism of Temperature-Sensitive Intelligent Hydrogel and Its Applications in Controlled Drug Releasing Systems. Temperature-sensitive intelligent hydrogel refers to the gel that swells or contracts of volume upon changes of ambient temperature. This type of hydrogel has hydrophobic monomer and hydrophilic monomer. The interaction between hydrophobic and hydrophilic monomers and hydrogen bonds between molecular chains in hydrogel are influenced by temperature, thus destroying the internal structure of hydrogel and causing volume swelling or contraction [35]. Temperature-sensitive intelligent hydrogel can be divided into low critical solution temperature (LCST) type and upper critical solution temperature (UCST) type. There are three major drug releasing modes and mechanisms of temperature-sensitive intelligent hydrogel [36]:

4.2.1. Squeezing Mode. Squeezing mode releases drugs through the quick contraction of the network structure of hydrogels. Hydrogel adsorbs drugs by swelling behavior under low temperature, but squeezes drugs out of the gel through contraction when the ambient temperature exceeds LCST [37]. This controlled drug releasing path is shown in Figure 4. It has some disadvantages: drugs encapsulated in hydrogel can be released outward slowly through diffusion under the swelling state. However, hydrogel releases drugs

too quickly at contraction after LCST, which fails to realize the goal of long-term drug releasing.

4.2.2. "On-off" Controlling Mode. The "on-off" controlling mode of the hydrogel system can be further divided into the shell "on-off" controlling mode and micropore grafted "on-off" controlling mode. In the shell "on-off" controlling mode, the hydrogel contracts when the ambient temperature exceeds LCST, which induces contraction of the hydration shell on the surface and produces a thin compacted layer keeping water and drugs within hydrogel. This is known as the "off" state. When the ambient temperature is lower than LCST, the compact layer on the hydrogel surface swells, and it is in the "on" state to diffuse drugs from hydrogel freely [38]. This process is shown in Figure 5. The micropore grafted "on-off" controlling mode is formed by grafting hydrogel molecular chains into the matrix of porous material. When the ambient temperature is lower than LCST, the grafted chain of hydrogel can be extended freely to cover micropores in matrix. This is known as the "off" state. When the ambient temperature is higher than LCST, the macromolecular chain grafted onto the hydrogel contracts and micropores on the microballoon surface are showed, turning to the "on" state [39]. Under this circumstance, drugs diffuse outward, and the goal of controlled drug releasing is realized. This process is shown in Figure 6.

4.2.3. Free Diffusion. When the ambient temperature is lower than LCST, hydrophilic drugs in the swelling hydrogel can be released to the external environment through permeation due to the concentration difference between saturated drugs in hydrogel and the external environment. This presents the Fickian releasing mechanism. The diffusion rate is related with swelling degree of hydrogel as well as the drug structure and size [40]. The releasing process is shown in Figure 7.

Temperature-sensitive intelligent hydrogel contains thermosensitive block, which can produce reversible sol-gel phase transition under changes of ambient temperature. Therefore, temperature-sensitive macromolecular materials are extensively used, including cellulose, polyacrylamides, and polysaccharide derivatives.

Although low-temperature swelling and high-temperature contraction N-isopropyl acrylamide (PNIPAM) polymer produce phase transition under LCST (28-32°C) and can make quick responses to temperature changes, its applications in drug delivery are restricted for biotoxicity and nondegradability. For degradation of hydrogel polymer, Jeong et al. [41] synthesized the degradable temperature-sensitive PEO-PLLA-PEG polymer hydrogel. However, UCST of this degradable temperature-sensitive PEO-PLLA-PEG polymer hydrogel was only 45°C, and the polymer solution was easy to form gel to block needle under room temperature. Therefore, this UCST hydrogel is not suitable to be the carrier for drug delivery.

The LCST value of hydrogel can be adjusted by copolymerization of hydrophilic or hydrophobic monomers. Chung et al. [42] prepared gel through copolymerization of hydrophobic butyl methacrylate (BMA) and isopropyl acrylamide, and LCST of this gel could be adjusted. The gel swelled to

FIGURE 4: Extrusion mode of drug delivery from temperature-sensitive hydrogels.
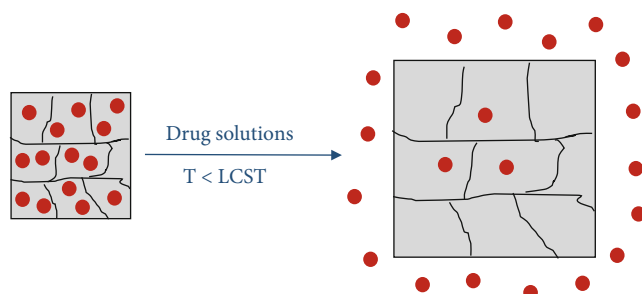
FIGURE 5: Skin layer "on-off" modes of drug delivery.
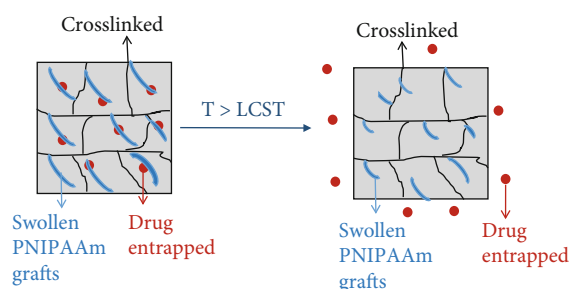
FIGURE 6: Grafted system "on-off" modes of drug delivery.

release drugs at 10°C, but it contracted and stopped drug releasing at 30°C. The surface contraction layer formed by gel copolymerization plays an important role in controlled drug releasing. Liu et al. [43] prepared a pulse drug releasing system based on temperature-sensitive gel with switching functions. When the ambient temperature was higher than LCST, the interaction of lipotropic chains and intermolecular hydrogen bonds form a polymer network to contract the gel and release drugs. When the ambient function was lower than LCST, the gel swelled again and stopped releasing of drugs. Hsiue et al. [44] developed a temperature-sensitive preparation based on PNIPAM to cure glaucoma. Ophthalmic preparation was a solution under room temperature, but it forms gel immediately after applied in eyes, thus releasing drugs continuously and stably. The action time of drugs can be prolonged by 5-7 times than direct administration of drugs.

Targeted thermal chemotherapy guided by temperature-sensitive hydrogel is another hotspot of thermal chemotherapy of tumors. It controls drug releasing by changing local temperature. When the temperature is higher than LCST, drugs carried on the hydrogel carrier are released quickly to the local heating position of tumor, thus producing the thermal targeting effect. It improves the therapeutic effect

through dual advantages of temperature sensitivity and thermal chemotherapy. Chilkoti et al. [45] heated the artificial temperature-sensitive elastin polypeptide which was loaded with ELP-ADR to increase local drug concentration by 2-3 times of that under room temperature.

The temperature response rate can be adjusted by changing the gel network structure [46]. For example, PNIPAM with amine end is prepared by using aminoethyl mercaptan as the chain transfer agent. Next, the macromolecular monomer PNIPAM with polymerizable groups at end could be prepared through condensation reaction of active ester monomers and the end amino. Under the action of crosslinking agents, NIPAM monomer and this macromolecular monomer PNIPAM copolymerize, finally forming the grafted PNIPAM hydrogel. The swelling ratio and swelling rate of the grafted PNIPAM hydrogel are higher than those of ordinary PNIPAM networked hydrogel [47]. This is mainly because the graft chain has higher degree of freedom (DOF) and can move freely and absorb water more. The controlled drug releasing behavior is closely related with the network structure of hydrogel. Therefore, the drug releasing rate and amount can be controlled by adjusting temperature and gel structure [48]. However, monomer and crosslinking agent used in PNIPAM-based hydrogel have no biocompatibility and biodegradability. For example, hydrogel carrying acrylamide will stimulate blood platelet in blood at contact. Therefore, it still needs abundant studies on biotoxicity to realize clinical applications of PNIPAM-based hydrogels. Alternatively, nontoxic hydrogels with biocompatibility and biodegradability which are similar with polyethylene glycol and polylysine shall be developed [49]. The hydrophobic drug delivery process by the temperature-sensitive hydrogel dendritic polymer which is modified by the target ligands and fluorescence needle was researched [50]. When drugs are delivered to the human body, heats in the blood may trigger amphiphilic polymers and target points to produce multifunctional dendrimers, achieving the synergetic enhancement successfully [50].

At present, many studies have applied multiple temperature-sensitive intelligent hydrogels to carry or bond antitumor drugs to treat tumors [28], such as natural polymers (e.g. chitosans, celluloses, and hyaloplasm), polyolefins, polyethers, PEG/polyesters, antitumor drugs (e.g. taxol, adriamycin amycin, and *cis*-platinum), protein drugs (e.g. insulin, interferon, and VEGF), antibiotic drugs, and DNA [51]. PEG-PLGA which is a temperature-sensitive hydrogel that carries taxol has been applied in clinical treatment of tumors. The administration dosage of PEG-PLGA ($0.48 \, mg/m^2/day$) is significantly lower than the traditional administration dosage ($17 \, mg/m^2/day$), but it improves the
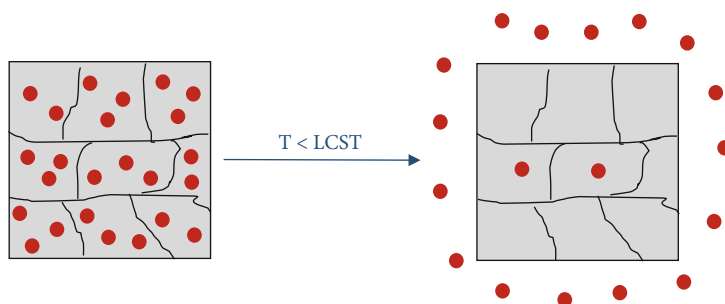
FIGURE 7: Free modes of drug delivery.

therapeutic effect and weakens the general toxic and side effects. The effect of PEG-PLGA can last for 6 weeks, which prevent repeated injection of drugs and mitigate pains of patients. PEG-PLGA is mainly applicable to solid tumor which cannot be excised [52]. Peng et al. [53] performed an injection therapy to liver cancer HCC by using the temperature-sensitive intelligent hydrogel PCL-PEG-PCL with radionuclide (188Re-Tincolloid) and chemotherapeutics (lipidosome adriamycin amycin), which prolonged the action time of 188Re-Tincolloid in HCC. The tumor elimination rate of the combined group reached as high as 80%. Therefore, the combination of the temperature-sensitive intelligent hydrogel carrier and drugs has a promising application prospect. The critical solution temperatures of different temperature-sensitive intelligent hydrogels are shown in Table 1.

4.3. Drug Releasing Mechanism of pH/Temperature-Sensitive Intelligent Hydrogel and Its Applications in Controlled Drug Releasing Systems. Intelligent hydrogel can adapt to external environmental changes (e.g., pH value, temperature, light, electricity, magnetic field, and chemical substance) through volume changes or phase transition. Intelligent hydrogels are used more and more in high-tech fields, such as drug transport, biosensor, and brake [58]. Currently, intelligent response hydrogels generally can be divided into single-response intelligent hydrogels (e.g., pH value, temperature, and magnetic field), dual-response intelligent hydrogels (e.g., temperature-pH response, temperature-magnetic field response, and pH-magnetic field response), and multiresponse intelligent hydrogels (e.g., temperature-pH-magnetic field multi-response and temperature-pH-light multi-response) [57]. Since temperature and pH are not only the most important parameters to maintain normal life activities and the important conditions for survival of bacteria and virus, but also the most common and easiest to be controlled stimuli in the human body and biomedicine [59]. As a result, pH/temperature-sensitive hydrogel is the most popular intelligent hydrogel in the field of targeted controlled drug releasing.

pH/temperature-sensitive hydrogel is mainly synthesized by using monomers sensitive to pH and temperature through graft polymerization, crosslinking, or interpenetrating networks. Substantially, pH/temperature-sensitive hydrogel is the further development of single-sensitivity hydrogel. It can change the response range by adjusting the mixing ratio

of pH and temperature to meet demands of different fields. pH/temperature-sensitive hydrogel can adapt to the complicated physiological environment like human fluid better, because it can perceive dual stimulus responses to pH and temperature. In addition, interaction among multiple materials can not only enhance mechanical strength and biological adhesion of hydrogels but also improve accuracy of controlled drug releasing. It is a kind of promising carrier for controlled drug releasing.

Drug releasing based on pH/temperature-sensitive hydrogel can be divided into follow four steps: Firstly, drugs are dissolved out and enter into surrounding polymers or pores. Secondly, concentration gradient makes drugs passing through the polymer barrier through molecular diffusion. Thirdly, drugs are desorbed from the polymer surface. Finally, drugs are diffused to fluid of the human body or environmental media. The drug releasing is mainly realized by the squeezing effect and dissolution effect [60]. The drug releasing mechanism based on pH/temperature-sensitive hydrogel is shown in Figure 8.

Hydrogel and drugs mainly combine through physical and chemical modes [61]. Physical combination refers to the electric charge effect between ionic polymers and charged drugs. Cationic polymers (e.g., functional groups of amino) can be used to control release of anionic drugs (e.g., benzocaine). Anionic polymers (e.g., hyaluronic acid) can entrap cationic drugs (local anesthetics) and control the drug releasing by taking advantage of the electric charge effect. For uncharged monomer or polymer, anionic polymer can be used to synthesize hydrogel to delayer or strengthen drug releasing by taking the advantages of adsorption to specific drugs. The chemical combination controls the drug releasing through the covalent bonds (hydrolysis or partial hydrolysis) between hydrogels and drugs [61].

Surrounding environmental conditions of tumor are different from normal physiological conditions of the human body. Tumor temperature is about 42°C, which is higher than normal temperature (37°C) of the human body. pH ranges between 7.0 and 7.4 in the surrounding environment of tumor and ranges between 6.9 and 7.0 in tumor cells, which is lower than the normal psychological value of the human body (pH = 7.4). pH/temperature-sensitive hydrogel can control the drug releasing speed and increase bioavailability in addition to targeted drug delivery [62]. It has promising application prospects in the field biomedicine. Therefore, R&D of pH/temperature-sensitive hydrogel

TABLE 1: Critical solution temperature of temperature-sensitive intelligent hydrogel.

Name	Critical solution temperature/°C	References
Poly N-piperidine	5.5	[54]
BMA-PNIPAM	10	[42]
Poly N-methyl-N-PNIPAM	22.3	[54]
Acrylamide-L-proline methylase	24	[54]
Poly N-PNIPAM	30.9	[54]
Poly-N,N-diethyl acrylamide	32	[37]
Chitosan/β-sodium glycerophosphate/gelatin hydrogels	32.6	[55]
Chitosan/gelatin/genipin/β-sodium glycerophosphate hydrogel	37	[3]
Polyvinyl methyl ether	38.0	[54]
PEO-PLLA-PEG polymer hydrogel	45	[41]
Poly N-ethyl methacrylamide	50.0	[54]
Poly N-ethyl acrylamide	72.0	[54]
N-TBA/M,N-dimethylacrylamide copolymer	20-80	[56]
Methacrylic acid 2-(2-methoxy ethoxy) ethyl ester (MEO2MA)-methacrylic acid oligosity (glycol)ester (OEGMA) copolymer hydrogel	26-90	[57]
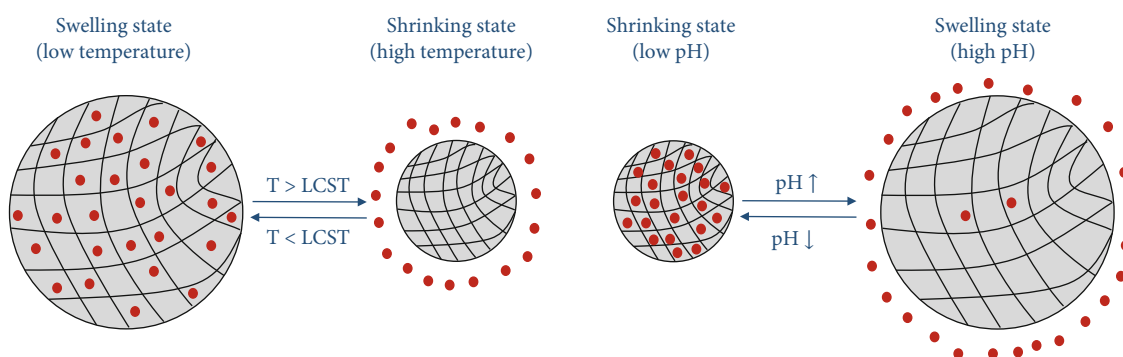
FIGURE 8: Drug release mechanism of hydrogels at different temperatures and pH.

is of important significance to targeted accurate treatment of tumors.

Huynh et al. [62] prepared a four-arm polyethylene glycol-polyurethane pH/temperature-sensitive intelligent hydrogel which was loaded with chlorambucil, which showed excellent hydrophilicity and biocompatibility. It could develop reversible swelling contraction with changes of pH and ambient temperature. This hydrogel can be adsorbed surrounding tissues as a response to pH and temperature of the human body (pH 7.4, 37°C), so that drugs can be released at a constant speed through free diffusion in 14 d and finally dissolved gradually. Huynh et al. [63] prepared pH/temperature-sensitive hydrogel through polymerization of poly β-carbamic acid ester embedded with adriamycin amycin and polyethylene glycol. Under the in vivo psychological conditions (temperature = 37°C and pH = 7.4), gel can be formed quickly to prolong the drug releasing time to five weeks.

Lo et al. [64] prepared the pluronic-polyacrylic acid pH/temperature-sensitive hydrogel loaded with pharmorubicin. This is a type of the ideal degradable drug releasing system. After oral taking of aqueous solution of drugs under room temperature, this pH/temperature-sensitive hydrogel

was changed to gel when body temperature and pH reached 37°C and 6.8, thus enabling to deliver drugs to colon continuously in 12 h. Seo et al. [65] prepared a pH/temperature-sensitive intelligent hydrogel which was loaded with recombinant human granulocyte colony-stimulating factor-macrophage colony stimulating factor (M-CSF) and chitosan of cyclophosphamide. This hydrogel was changed to gel under body temperature and psychological pH (37°C and pH 7.4) to release drugs continuously to tumor tissues in 7 d. Moreover, this hydrogel can be degraded and eliminated gradually and improve the targeted treatment and lethality of tumor cells.

pH/temperature-sensitive hydrogel can be prepared from copolymerization of N-NIPA and monomers containing groups (-COOH or -NH$_2$) which are easy to be hydrolyzed or ionized. Polymerization of ionized pH-sensitive groups in temperature-sensitive hydrogel can affect the swelling behavior of hydrogel. Katime et al. [66] synthesized a pH/temperature-sensitive hydrogel N-PNIPAM-co-2-methylene-succinic acid)P (NIPA-co-MBDA) based on free radical polymerization, finding that LCST (22-37°C) of gels prepared by different mixing ratios of monomers was

TABLE 2: Applications of different hydrogels in controlled drug releasing.

Type of response	Hydrogel polymers	Drugs	Duration	References
pH-sensitive	Hemicellulose grafted polyacrylic acid	Aspirin	12 h	[73]
	Chitosan (CS)-polyvinyl alcohol (PVA)	Dexamethasone/aspirin	7 h	[74]
	Polyacrylic acid	Prednisolone	5 h	[75]
	Chitosan (CS)-polyvinyl pyrrolidone (PVP)	Oral antibiotic	Releasing rate = 73.2% in 3 h (pH = 1.0)	[76]
Temperature-sensitive	Polypropyl caprolactone glutamic acid	TAX	21d	[77]
	Chitosan/sodium glycerophosphate	PYM	18d	[78]
	Polyglycolic acid and polylactic acid	Cytarabine	10d	[79]
	Poly (N-PNIPAM)-carboxymethyl chitosan	cis-Platinum	16d	[80]
	Four-arm polyethylene glycol-polyurethane	Chlorambucil	14d	[62]
pH temperature-sensitve	Pluronic-polyacrylic acid	Pharmorubicin	12 h	[64]
	Poly β-carbamic acid ester/polyethylene glycol	Adriamycin amycin	35 d	[63]
	(N-PNIPAM-cocrylic acid)	Riboflavin (vitamin B2)	Releasing rate = 91.5% in 7 h (pH = 7.0, T = 52°C). Releasing rate = 75% in 3.5 h (pH = 2.0, T = 52°C)	[81]

different. In other words, increasing the content of 2-methylene-succinic acid can increase LCST of the hydrogel, and LCST varies under different pH values. Hoare et al. [67] synthesized the pH/temperature-sensitive functional microgel of NIPAM-inyl stearate (VAc), which could realize ionization in an extremely narrow pH range. In the same time, the volume of the synthesized microgel was swelled by 4 times of that of ordinary hydrogel when psychological temperature reached ionization temperature. However, they also discovered in the temperature-sensitivity process that deswelling behaviors took place at complete protonation of the microgel. In this case, phase transition would not be observed even though the temperature was increased to 70°C. Huang et al. [68] found that P (NIPAM-co-AA) hydrogel loaded with aspirin could release drugs more quickly in the pH 7.4 environment under 37°C compared with that under 25°C. Given the same temperature (37°C), the drug releasing rate at pH 7.4 (>40% in 12 h) was significantly higher than that at pH 1.0 (<20% in 12 h). This reveals that the prepared P(NIPAM-co-AA) hydrogel could realize directional release of most aspirin in intestines.

In addition, pH/temperature-sensitive hydrogel also can be used in controlled release of insulin. Ramkissoon et al. [69] synthesized N-NIPAM- (temperature-sensitive-) BMA-AAc (pH sensitive) trimer hydrogel with different molecular weights by using insulin as the protein model drugs. It found that the release of insulin was closely related with the molecular weight of trimer under 37°C and pH 7.4. Under low molecular weight, the release of insulin was controlled by solubility of the trimer. Under high molecular weight, the hydrogel with low molecular weight can be used

in fast drug releasing in duodenum, while hydrogel with moderate molecular weight can be used in targeted drug releasing in the small intestine and hydrogel with high molecular weight can be used in targeted drug releasing in colon.

Lee et al. [70] prepared injectable pH/temperature-sensitive hydrogel based on oligomerization (β-polyurethane) (OAEU) polymer, which can be transformed into gel through phase transition under psychological conditions (37°C, pH 7.4). This hydrogel could be retained in a living body for at least 2 weeks, and the phase-transition temperature can be regulated by changing the OAEU concentration. Ding [71] synthesized polyethylene oxide (PEO)-polyphenyl ether-polyethylene oxide with end capped by polymer glycol chitosan/benzaldehyde. With high sensitivity to pH and temperature, this PEO-polyphenyl ether-polyethylene oxide is coated with DOX·HCL and prednisolone and formed hydrogels under the body temperature of 37°C. It released drugs continuously when pH decreased to weak acidity (6.5-6.8). Guo et al. [72] prepared a pH/temperature-sensitive intelligent hydrogel based on carboxymethyl chitosan, which showed good reversibility. Under 37°C, the drug releasing rate of coenzyme A in acid buffer solution was 22. 6%, and it reached as high as 89.1% in the intestinal environment of the human body. This indicated that this hydrogel is an excellent carrier for controlled releasing of the drug CoA. Applications of different hydrogels in controlled drug releasing are shown in Table 2.

The multiresponse intelligent DDS (e.g., pH/temperature, pH/glucose, and pH/oxidization/reducing) is significantly superior to single-response DDS. For example, the

temperature-sensitive hydrogel solution is easy to be transformed into gel and block the needle when it is injected to the human body. This problem can be solved effectively by embedding a pH-sensitive segment. The introduction of pH-sensitive functional groups solves and improves the needle blockage and poor water solubility of hydrogel polymers successfully, so that hydrogel can be used in package transport of ionic protein drugs. It provides more selection for the optimal design of hydrogel structures. However, pH/temperature-sensitive hydrogel still faces with some problems [47, 62, 82, 83]: firstly, the package rate of drugs is low, and the preparation technique of hydrogel is complicated. Secondly, some polymers contain cytotoxic groups (e.g., polyacrylic acids), thus resulting in many side effects, such as inflammation and destroying cells or proteins. In addition, it lacks a deep study on the formation mechanism of multiresponse hydrogel and the relationship between degradation rate of hydrogel polymer and controlled drug releasing performance. This influences the optimal design and applications of gel materials.

5. Conclusions and Prospects

With the rapid development of life sciences, pharmaceutics, genomics, intelligent polymer materials, molecular biological technologies, and relevant interdisciplines, intelligent targeted drug delivery is an optimal administration mode of drugs. In 2015, Obama, the present of the United States, proposed a "Precision Medicine Plan", in which he pointed out that the core of precision medicine lies in precision rather than medicine. It fully demonstrates that giving appropriate treatment to appropriate patients at appropriate time can realize precision truly. Precision medicine will surely bring a fresh new era of medicine. An intelligent DDS was established to make targeted transport and controlled release of drugs based on its specific responses to the environment. The targeted quantitative releasing of drugs at appropriate time is an invincible opponent of many refractory diseases.

R&D of pharmaceutic preparations conforms to the principle of "high efficiency, quick efficiency and long-term efficiency," "small toxicity, side effect and dosage," and "conveniences for production, transport, storage, carrying and taking." As the carrier material of pharmaceutic preparation, the intelligent response hydrogel is characteristic of intelligent, efficient, safe, and convenient controlled drug releasing. It has attracted wide research attentions. However, it still has some problems [67, 70, 74, 82–85]: firstly, the response time of temperature-sensitive hydrogel is still long to the drug carrying system. In clinical applications, temperature-sensitive hydrogels have poor hydrophilicity, low relative molecular weight, and initial sudden releasing problems of proteins. Secondly, the controlled releasing of anticancer drugs by chemical gel which can make quick response can only form hydrogel by in vivo chemical reaction. It is difficult to assure effective entrapment of drugs. In addition, this might trigger side reaction of polymers and drugs, thus inactivating drugs. Thirdly, degradation products of some polymers (e.g., PLA and PLGA) can lower the pH value in the injection position, resulting in inflammation, cell damages, or protein problems.

In addition, it is necessary to increase entrapment rate of hydrogel to drugs, improve biocompatibility, biodegradability, and mechanical properties of hydrogel and lower its toxicity. Besides, the in vivo degradation process of hydrogel as well as metabolic products and elimination time shall be interpreted. Cytotoxicity, biotoxicity, and therapeutic effect after drug loading of the hydrogel system have to be verified significantly.

As a new intelligent DDS, pH/temperature-sensitive hydrogel has achieved outstanding progresses. Its applications in targeted drug delivery and controlled drug release have been a research hotspot in the field of medicine. With the continuous development of intelligent polymer materials, genomics, molecular biological technologies, and relevant interdisciplines, the intelligent response hydrogels will achieve more extensive applications in targeted drug delivery and controlled drug releasing and take the leadership in the new era of "Precision Treatment".

Conflicts of Interest

The authors declare that there is no conflict of interest regarding the publication of this paper.

Acknowledgments

References

[1] O. Wichterle and D. Lím, "Hydrophilic gels for biological use," *Nature*, vol. 185, no. 4706, pp. 117-118, 1960.

[2] J. Kopecek, "Hydrogels: from soft contact lenses and implants to self-assembled nanomaterials," *Journal of Polymer Science Part A: Polymer Chemistry*, vol. 47, no. 22, pp. 5929–5946, 2009.

[3] C. Likai, *Research on preparation and performances of temperature-sensitive chitosan hydrogel drug carrier*, Suzhou University, 2015.

[4] B. Wang, T. Siahaan, and R. A. Soltero, *Drug Delivery: Principle and Applications*, pp. 29–51, John Wiley and Sons. Incorporated, New Jersey, 2005.

[5] Z. Yifeng, "Environmental-sensitive intelligent micromolecular organic gel materials," *Progress in Chemistry*, vol. 23, no. 1, pp. 125–135, 2011.

[6] J. F. Almeida, P. Ferreira, A. Lopes, and M. H. Gil, "Photocrosslinkable biodegradable responsive hydrogels as drug delivery systems," *International Journal of Biological Macromolecules*, vol. 49, no. 5, pp. 948–954, 2011.

[7] L. Chao, P (N-MAM-co-DMAA), and P (N-MAM-co-AA), *Research on preparation of intelligent hydrogels and its controlled drug releasing performance*, Xinyang Normal University, 2015.

[8] W. Luo, *Preparation of pH/temperautre-sensitive polymer (PCL-PDMAEMA-PPEGMA)_4 and its controlled drug releasing hydrogels*, South China University of Technology, 2018.

[9] S. J. de Jong, S. C. de Smedt, M. W. C. Wahls, J. Demeester, J. J. Kettenes-van den Bosch, and W. E. Hennink, "Novel self-assembled hydrogels by stereocomplex formation in aqueous solution of enantiomeric lactic acid oligomers grafted to dextran," *Macromolecules*, vol. 33, no. 10, pp. 3680–3686, 2000.

[10] S. R. Van Tomme, G. Storm, and W. E. Hennink, "In situ gelling hydrogels for pharmaceutical and biomedical applications," *International Journal of Pharmaceutics*, vol. 355, no. 1-2, pp. 1–18, 2008.

[11] G. Jiang, C. Liu, X. Liu et al., "Network structure and compositional effects on tensile mechanical properties of hydrophobic association hydrogels with high mechanical strength," *Polymer*, vol. 51, no. 6, pp. 1507–1515, 2010.

[12] J. Yang, C. Xu, P. Kopečková, and J. Kopeček, "Hybrid hydrogels self-assembled from HPMA copolymers containing peptide grafts," *Macromolecular Bioscience*, vol. 6, no. 3, pp. 201–209, 2006.

[13] C. Wang, R. J. Stewart, and J. Ř. KopeČek, "Hybrid hydrogels assembled from synthetic polymers and coiled-coil protein domains," *Nature*, vol. 397, no. 6718, pp. 417–420, 1999.

[14] A. S. Sawhney, C. P. Pathak, and J. A. Hubbell, "Bioerodible hydrogels based on photopolymerized poly(ethylene glycol)-co-poly(.alpha.-hydroxy acid) diacrylate macromers," *Macromolecules*, vol. 26, no. 4, pp. 581–587, 1993.

[15] Y. Y. Liu, W. Q. Liu, W. X. Chen, L. Sun, and G. B. Zhang, "Investigation of swelling and controlled-release behaviors of hydrophobically modified poly(methacrylic acid) hydrogels," *Polymer*, vol. 48, no. 9, pp. 2665–2671, 2007.

[16] T. Vermonden, R. Censi, and W. E. Hennink, "Hydrogels for protein delivery," *Chemical Reviews*, vol. 112, no. 5, pp. 2853–2888, 2012.

[17] D. A. Ossipov and J. Hilborn, "Poly(vinyl alcohol)-based hydrogels formed by "click chemistry"," *Macromolecules*, vol. 39, no. 5, pp. 1709–1718, 2006.

[18] D. A. Ossipov, S. Piskounova, and J.. Hilborn, "Poly(vinyl alcohol) cross-linkers for in vivo injectable hydrogels," *Macromolecules*, vol. 41, no. 11, pp. 3971–3982, 2008.

[19] Z. Dagen, Z. Liu, Q. Zuo, Y. Huang, and W. Xie, "Applications and research progresses of intelligent hydrogels in controlled drug releasing system," *Material Review*, vol. 26, no. 11, pp. 83–88, 2012.

[20] L. He, Q. Zuo, S. Xie, Y. Huang, and W. Xue, "Intelligent hydrogels for drug delivery system," *Recent Patents on Drug Delivery & Formulation*, vol. 5, no. 3, pp. 265–274, 2011.

[21] L. Ma, *Preparation and characterization of pH/temperature-sensitive hydrogel particles/ microspheres and their applications in controlled drug releasing*, Lanzhou University, 2010.

[22] E. R. Gillies and J. M. J. Fréchet, "Dendrimers and dendritic polymers in drug delivery," *Drug Discovery Today*, vol. 10, no. 1, pp. 35–43, 2005.

[23] N. Mackiewicz, J. Nicolas, N. Handké et al., "Precise engineering of multifunctional PEGylated polyester nanoparticles for cancer cell targeting and imaging," *Chemistry of Materials*, vol. 26, no. 5, pp. 1834–1847, 2014.

[24] V. Ladmiral, M. Semsarilar, I. Canton, and S. P. Armes, "Polymerization-induced self-assembly of galactose-functionalized biocompatible diblock copolymers for intracellular delivery," *Journal of the American Chemical Society*, vol. 135, no. 36, pp. 13574–13581, 2013.

[25] C. Gao, J. Ren, C. Zhao et al., "Xylan-based temperature/pH sensitive hydrogels for drug controlled release," *Carbohydrate Polymers*, vol. 151, pp. 189–197, 2016.

[26] M. Ying, *Research on Oral Colon-Targeted Hydrogels as the Controlled Drug Releasing System*, Ji'nan University, 2018.

[27] A. Richter, G. Paschew, S. Klatt, J. Lienig, K. F. Arndt, and H. J. Adler, "Review on hydrogel-based pH sensors and microsensors," *Sensors*, vol. 8, no. 1, pp. 561–581, 2008.

[28] O. Werzer, S. Tumphart, R. Keimel, P. Christian, and A. M. Coclite, "Drug release from thin films encapsulated by a temperature -responsive hydrogel," *Soft Matter*, vol. 15, no. 8, pp. 1853–1859, 2019.

[29] W. Zhang, X. Jin, H. Li, R. R. Zhang, and C. W. Wu, "Injectable and body temperature sensitive hydrogels based on chitosan and hyaluronic acid for pH sensitive drug release," *Carbohydrate Polymers*, vol. 186, pp. 82–90, 2018.

[30] Z. Wang, X. Han, Y. Wang et al., "Facile preparation of low swelling, high strength, self-healing and pH-responsive hydrogels based on the triple-network structure," *Frontiers of Materials Science*, vol. 13, no. 1, pp. 54–63, 2019.

[31] Y. Chen and P. Sun, "pH-sensitive Polyampholyte microgels of poly(acrylic acid-co-Vinylamine) as injectable hydrogel for controlled drug release," *Polymers*, vol. 11, no. 2, p. 285, 2019.

[32] H. Xu, P. Tian, H. Zhao, and J. Zheng, "Diffusion behaviors of drugs in pH-sensitive polymethylacrylic acid-poloxamer hydrogels," *Applied Chemistry*, vol. 18, no. 4, pp. 305–308, 2001.

[33] C. Feng, R. Song, G. Sun et al., "Immobilization of coacervate microcapsules in multilayer sodium alginate beads for efficient oral anticancer drug delivery," *Biomacromolecules*, vol. 15, no. 3, pp. 985–996, 2014.

[34] H. Wu, Z. Liu, L. Li, N. Li, and Q. Guo, "In vitro study on baicalin pH-triggered ophthalmic in situ gel system," *Chinese Journal of New Drugs*, vol. 6, pp. 508–513, 2011.

[35] G. Zhang and X. Jiang, "Temperature responsive nanoparticles based on PEGylated Polyaspartamide derivatives for drug delivery," *Polymers*, vol. 11, no. 2, p. 316, 2019.

[36] J. Yang, *Construction of PLGA Microsphere/P(NIPAAm-Co-AAm) Hydrogel Compound System and Research on Controlled Drug Releasing Performances*, Chongqing University, 2011.

[37] H. G. Schild, "Poly (N-isopropylacrylamide) : experiment, theory and application," *Progress in Polymer Science*, vol. 17, no. 2, pp. 163–249, 1992.

[38] T. Okano, Y. H. Bae, H. Jacobs, and S. W. Kim, "Thermally on-off switching polymers for drug permeation and release," *Journal of Controlled Release*, vol. 11, no. 1-3, pp. 255–265, 1990.

[39] I. Ankareddi and C. S. Brazel, "Synthesis and characterization of grafted thermosensitive hydrogels for heating activated controlled release," *International Journal of Pharmaceutics*, vol. 336, no. 2, pp. 241–247, 2007.

[40] L. Jiang, Y. Feng, L. Sheng, and D. Xu, "Advances in research on drug release mechanisms and modes of themosensitive gel," *China Journal of Chinese Materia Medica*, vol. 33, no. 1, pp. 105–107, 2008.

[41] B. Jeong, Y. H. Bae, D. S. Lee, and S. W. Kim, "Biodegradable block copolymers as injectable drug-delivery systems," *Nature*, vol. 388, no. 6645, pp. 860–862, 1997.

[42] J. E. Chung, M. Yokoyama, M. Yamato, T. Aoyagi, Y. Sakurai, and T. Okano, "Thermo-responsive drug delivery from

polymeric micelles constructed using block copolymers of poly(N -isopropylacrylamide) and poly(butylmethacrylate)," *Journal of Controlled Release*, vol. 62, no. 1–2, pp. 115–127, 1999.

[43] X. M. Liu, B. Yang, Y. L. Wang, and J. Y. Wang, "New nanoscale pulsatile drug delivery system," *Chemistry of Materials*, vol. 17, no. 11, pp. 2792–2795, 2005.

[44] G. H. Hsiue, S. H. Hsu, C. C. Yang, S. H. Lee, and I. K. Yang, "Preparation of controlled release ophthalmic drops, for glaucoma therapy using thermosensitive poly-N-isopropylacrylamide," *Biomaterials*, vol. 23, no. 2, pp. 457–462, 2002.

[45] A. Chilkoti, M. R. Dreher, D. E. Meyer, and D. Raucher, "Targeted drug delivery by thermally responsive polymers," *Advanced Drug Delivery Reviews*, vol. 54, no. 5, pp. 613–630, 2002.

[46] S. Pacelli, P. Paolicelli, M. Avitabile et al., "Design of a tunable nanocomposite double network hydrogel based on gellan gum for drug delivery applications," *European Polymer Journal*, vol. 104, pp. 184–193, 2018.

[47] T. Pan, *Preparation of pH/Temperature-Sensitive Hdyrogels and its Performances in Controlled Drug Releasing*, University of Science and Technology of China, 2011.

[48] A. Allı and B. Hazer, "Poly(N-isopropylacrylamide) thermoresponsive cross-linked conjugates containing polymeric soybean oil and/or polypropylene glycol," *European Polymer Journal*, vol. 44, no. 6, pp. 1701–1713, 2008.

[49] J. L. West and J. A. Hubbell, "Photopolymerized hydrogel materials for drug delivery applications," *Reactive Polymers*, vol. 25, no. 2-3, pp. 139–147, 1995.

[50] P. N. Le, C. K. Huynh, and N. Q. Tran, "Advances in thermosensitive polymer-grafted platforms for biomedical applications," *Materials Science and Engineering: C*, vol. 92, pp. 1016–1030, 2018.

[51] Y. Hongbo, *Preparation of Temperature-Sensitive Hydrogels and Research on its In-Vitro Anti-Tumor Effect of under Co-Loading of VPA and Anti-Tumor Drugs*, Jilin University, 2017.

[52] S. Van Vlierberghe, P. Dubruel, and E. Schacht, "Biopolymer-based hydrogels as scaffolds for tissue engineering applications: a review," *Biomacromolecules*, vol. 12, no. 5, pp. 1387–1408, 2011.

[53] C. L. Peng, Y. H. Shih, K. S. Liang et al., "Development of in situ forming thermosensitive hydrogel for radiotherapy combined with chemotherapy in a mouse model of hepatocellular carcinoma," *Molecular Pharmaceutics*, vol. 10, no. 5, pp. 1854–1864, 2013.

[54] T. Yu, *Preparation of Chitosan-Based Temperature-Sensitive Compound Hydrogels and its Properties*, Changsha University of Science and Technology, 2011.

[55] G. C. Dong, C. Y. Kuan, S. Subramaniam et al., "A potent inhibition of oxidative stress induced gene expression in neural cells by sustained ferulic acid release from chitosan based hydrogel," *Materials Science & Engineering. C, Materials for Biological Applications*, vol. 49, pp. 691–699, 2015.

[56] H. Y. Liu and X. X. Zhu, "Lower critical solution temperatures of N -substituted acrylamide copolymers in aqueous solutions," *Polymer*, vol. 40, no. 25, pp. 6985–6990, 1999.

[57] N. Rasool, T. Yasin, J. Y. Y. Heng, and Z. Akhter, "Synthesis and characterization of novel pH-, ionic strength and temperature- sensitive hydrogel for insulin delivery," *Polymer*, vol. 51, no. 8, pp. 1687–1693, 2010.

[58] M. Ikeda, T. Tanida, T. Yoshii et al., "Installing logic-gate responses to a variety of biological substances in supramolecular hydrogel-enzyme hybrids," *Nature Chemistry*, vol. 6, no. 6, pp. 511–518, 2014.

[59] C. Gao, J. Ren, W. Kong, R. Sun, and Q. Chen, "Comparative study on temperature/pH sensitive xylan-based hydrogels: their properties and drug controlled release," *RSC Advances*, vol. 5, no. 110, pp. 90671–90681, 2015.

[60] G. Yubo, *Controlled Drug Release of pH/Temperature-Sensitive Glycine Ester - Sodium Alginate Hydrogels Based on Poly N-Acroloyl*, Hebei University, 2011.

[61] T. R. Hoare and D. S. Kohane, "Hydrogels in drug delivery: progress and challenges," *Polymer*, vol. 49, no. 8, pp. 1993–2007, 2008.

[62] C. T. Huynh, M. K. Nguyen, D. P. Huynh, S. W. Kim, and D. S. Lee, "pH/temperature-sensitive 4-arm poly(ethylene glycol)-poly(amino urethane) copolymer hydrogels," *Polymer*, vol. 51, no. 17, pp. 3843–3850, 2010.

[63] C. T. Huynh, M. K. Nguyen, J. H. Kim, S. W. Kang, B. S. Kim, and D. S. Lee, "Sustained delivery of doxorubicin using biodegradable pH/temperature-sensitive poly(ethylene glycol)-poly(β-amino ester urethane) multiblock copolymer hydrogels," *Soft Matter*, vol. 7, no. 10, p. 4974, 2011.

[64] Y. L. Lo, C. Y. Hsu, and H. R. Lin, "pH-and thermo-sensitive pluronic/poly(acrylic acid) in situ hydrogels for sustained release of an anticancer drug," *Journal of Drug Targeting*, vol. 21, no. 1, pp. 54–66, 2012.

[65] S. H. Seo, H. D. Han, K. H. Noh, T. W. Kim, and S. W. Son, "Chitosan hydrogel containing GMCSF and a cancer drug exerts synergistic anti-tumor effects via the induction of CD8 + T cell-mediated anti-tumor immunity," *Clinical & Experimental Metastasis*, vol. 26, no. 3, pp. 179–187, 2009.

[66] I. Katime, J. R. Quintana, N. E. Valderruten, and L. C. Cesteros, "Synthesis and properties of pH- and temperature-sensitive poly[(N-isopropylacrylamide)-co-(2-methylenebutane-1,4-dioic acid)] hydrogels," *Macromolecular Chemistry and Physics*, vol. 207, no. 22, pp. 2121–2127, 2006.

[67] T. Hoare and R. Pelton, "Highly pH and temperature responsive microgels functionalized with vinylacetic acid," *Macromolecules*, vol. 37, no. 7, pp. 2544–2550, 2004.

[68] Y. Huang and X. Luo, "Studies on the Controlled release of aspirin in the temperature/pH sensitive hydrogels," *Polymer Materials Science and Engineering*, vol. 14, no. 6, pp. 141–143, 1998.

[69] C. Ramkissoon-Ganorkar, F. Liu, M. Baudyš, and S. W. Kim, "Modulating insulin-release profile from pH/thermosensitive polymeric beads through polymer molecular weight," *Journal of Controlled Release*, vol. 59, no. 3, pp. 287–298, 1999.

[70] C. T. Huynh, M. K. Nguyen, and D. S. Lee, "Biodegradable pH/temperature-sensitive oligo(β-amino ester urethane) hydrogels for controlled release of doxorubicin," *Acta Biomaterialia*, vol. 7, no. 8, pp. 3123–3130, 2011.

[71] C. Ding, L. Zhao, F. Liu et al., "Dually responsive injectable hydrogel prepared by in situ cross-linking of glycol chitosan and benzaldehyde-capped PEO-PPO-PEO," *Biomacromolecules*, vol. 11, no. 4, pp. 1043–1051, 2010.

[72] B. L. Guo and Q. Y. Gao, "Preparation and properties of a pH/temperature-responsive carboxymethyl chitosan/poly(N-isopropylacrylamide)semi-IPN hydrogel for oral delivery of drugs," *Carbohydrate Research*, vol. 342, no. 16, pp. 2416–2422, 2007.

[73] G. Wang and Y. Li, "Preparation of pH-sensitive hydrogels based on hemicellulose and its drug release property," *Modern Chemical Industry*, vol. 32, no. 5, pp. 62–66, 2012.

[74] A. Islam and T. Yasin, "Controlled delivery of drug from pH sensitive chitosan/poly (vinyl alcohol) blend," *Carbohydrate Polymers*, vol. 88, no. 3, pp. 1055–1060, 2012.

[75] A. Bilia, V. Carelli, G. di Colo, and E. Nannipieri, "In vitro evaluation of a pH-sensitive hydrogel for control of GI drug delivery from silicone-based matrices," *International Journal of Pharmaceutics*, vol. 130, no. 1, pp. 83–92, 1996.

[76] M. V. Risbud, A. A. Hardikar, S. V. Bhat, and R. R. Bhonde, "pH-sensitive freeze-dried chitosan-polyvinyl pyrrolidone hydrogels as controlled release system for antibiotic delivery," *Journal of Controlled Release*, vol. 68, no. 1, pp. 23–30, 2000.

[77] Y. Cheng, C. He, J. Ding, C. Xiao, X. Zhuang, and X. Chen, "Thermosensitive hydrogels based on polypeptides for localized and sustained delivery of anticancer drugs," *Biomaterials*, vol. 34, no. 38, pp. 10338–10347, 2013.

[78] F. Chen, S. Song, H. Wang et al., "Injectable chitosan thermogels for sustained and localized delivery of pingyangmycin in vascular malformations," *International Journal of Pharmaceutics*, vol. 476, no. 1-2, pp. 232–240, 2014.

[79] J. Liu, Y. Jiang, Y. Cui, C. Xu, X. Ji, and Y. Luan, "Cytarabine-AOT catanionic vesicle-loaded biodegradable thermosensitive hydrogel as an efficient cytarabine delivery system," *International Journal of Pharmaceutics*, vol. 473, no. 1-2, pp. 560–571, 2014.

[80] C. Cheng, D. Xia, X. Zhang, L. Chen, and Q. Zhang, "Biocompatible poly(N -isopropylacrylamide)-g-carboxymethyl chitosan hydrogels as carriers for sustained release of cisplatin," *Journal of Materials Science*, vol. 50, no. 14, pp. 4914–4925, 2015.

[81] S. Brahima, C. Boztepe, A. Kunkul, and M. Yuceer, "Modeling of drug release behavior of pH and temperature sensitive poly(NIPAAm- co -AAc) IPN hydrogels using response surface methodology and artificial neural networks," *Materials Science and Engineering: C*, vol. 75, pp. 425–432, 2017.

[82] C. Mircioiu, V. Voicu, V. Anuta et al., "Mathematical modeling of release kinetics from supramolecular drug delivery systems," *Pharmaceutics*, vol. 11, no. 3, p. 140, 2019.

[83] T. Irimia, M. Ghica, L. Popa, V. Anuţa, A. L. Arsene, and C. E. Dinu-Pîrvu, "Strategies for improving ocular drug bioavailability and corneal wound healing with Chitosan-based delivery systems," *Polymers*, vol. 10, no. 11, p. 1221, 2018.

[84] H. Badie and H. Abbas, "Novel small self-assembled resveratrol-bearing cubosomes and hexosomes: preparation, charachterization, and ex vivo permeation," *Drug Development and Industrial Pharmacy*, vol. 44, no. 12, pp. 2013–2025, 2018.

[85] M. Qindeel, N. Ahmed, F. Sabir, S. Khan, and A. Ur-Rehman, "Development of novel pH-sensitive nanoparticles loaded hydrogel for transdermal drug delivery," *Drug Development and Industrial Pharmacy*, vol. 45, no. 4, pp. 629–641, 2019.

Research Article

Ionotropic Gelation Synthesis of Chitosan-Alginate Nanodisks for Delivery System and *In Vitro* Assessment of Prostate Cancer Cytotoxicity

David Patiño-Ruiz [iD],[1] **Leandro Marrugo,**[2] **Niradiz Reyes,**[3] **María Acevedo-Morantes,**[1,2] **and Adriana Herrera** [iD][1,2]

[1]*Doctorate in Engineering Program, Nanomaterials and Computer Aided Process Engineering Research Group,*
Universidad de Cartagena, Cartagena, Colombia
[2]*Chemical Engineering Program, Nanomaterials and Computer Aided Process Engineering Research Group,*
Universidad de Cartagena, Cartagena, Colombia
[3]*Medicine Program, Universidad de Cartagena, Cartagena, Colombia*

Correspondence should be addressed to Adriana Herrera; aherrerab2@unicartagena.edu.co

We report on the synthesis of chitosan-alginate nanodisks (Cs-Al NDs) using a simple approach consisting of the ionotropic gelation method. Sodium tripolyphosphate (STPP) was used as crosslinking agent to promote the electrostatic interaction between amine groups the chitosan and hydroxyl and carboxyl groups of alginate. Scanning electron microscopy (SEM) images provided direct evidence of the morphology of the nanodisks where agglomeration was observed due to the electrostatic interaction between the functional groups. Furthermore, dynamic light scattering (DLS) showed that the hydrodynamic size of the Cs-Al NDs was 227 nm and 152 nm in pH 1.2 and pH 7.4, respectively, which is in agreement with the information observed in the SEM images. The chemical structure is presented mainly the amine and carboxyl groups due to the presence of chitosan and alginate in the nanodisks, respectively, which allow the electrostatic interaction through N-H linkages. According to the X-ray diffraction, we found that the Cs-Al NDs exhibited the typical structure of chitosan and alginate, which lead the formation of polyelectrolyte complexes. We also evaluated the encapsulation of amoxicillin in the nanodisk, obtaining a loading efficiency of 74.98%, as well as a maximum *in vitro* release amount of 63.2 and 52.3% at pH 1.2 and 7.4, respectively. Finally, the cytotoxicity effect of the Cs-Al nanodisks was performed in human prostatic epithelial PWR-1E and Caucasian prostate adenocarcinoma PC-3 cell lines, in which the cell viability was above 80% indicating low inhibition and determining the Cs-Al NDs as a promising technology for controlled delivery systems.

1. Introduction

Recently, natural polymers such as polysaccharides have been widely explored for the synthesis of nanomaterials applied to multiple applications, especially in the biomedical and pharmaceutical fields [1, 2]. Polysaccharides such as chitosan and alginate are abundant and can be found easily in the environment and possess excellent physico-chemical and biological properties such as biocompatibility, biodegradability, and low toxicity, which demonstrate

that these biopolymers are suitable for sustained and controlled drug delivery systems [3–5]. These biopolymers are catalogued as Generally Regarded as Safe (GRAS) by the Food and Drug Administration (FDA), allowing their use for drug delivery systems [6].

Chitosan is a linear and cationic biopolymer derived from chitin after a deacetylation process and consisted of β (1-4) linked 2-acetamido-2-deoxy-β-D-glucopyranose and 2-amino-2-deoxy-β-D-glucopyranose structures, offering abundant amine (-NH$_2$) functional groups for better

adsorption capacity and environmental adaptability [1, 7, 8]. On the other hand, alginate is an anionic polymer derived from seaweeds and is chemically structured of (1,4) linked β-D-mannuronic and α-L-guluronic acid moieties, in which the hydroxyl (-OH) and carboxyl (-COOH) functional groups enhance the availability and stability in acidic environments, offering a potential application for encapsulation and controlled release of drugs [9–11].

The amine and carboxyl groups of chitosan and alginate, respectively, can promote through an ionotropic gelation technique a rapid electrostatic interaction leading the formation of a polyelectrolyte complex nanocomposite widely used for wound dressing, tissue engineering, and drug delivery [12–14]. Ionotropic gelation consists of the crosslink of both biopolymers in the presence of polyvalent ion compounds such as sodium tripolyphosphate (STPP); however, the polycationic and polyanionic nature of the biopolymers may form a polyelectrolyte complex in aqueous solution spontaneously [12, 15]. Therefore, the combination of both biopolymers is shown to be more effective than chitosan or alginate separately, improving the binding performance and stability in acidic and basic environments, which enables more controlled delivery and release of drugs according to the external stimuli, and may be also extended to other characteristics of the environment such as temperature and ion strength [16, 17].

We hereby report the synthesis of chitosan-alginate nanodisks (Cs-Al NDs) using the ionotropic gelation technique, in which STPP was used as the highly charged agent to promote the strong electrostatic interaction between the functional groups of both biopolymers. In this study, scanning electron microscopy (SEM), dynamic light scattering (DLS), Fourier-transform infrared spectroscopy (FTIR), and X-ray diffraction (XRD) were performed to obtain morphological and physical information, respectively. We also evaluate the encapsulation efficiency and *in vitro* release capacity of the Cs-Al NDs in acidic and basic environments, using amoxicillin as the model drug. Finally, we assessed the cytotoxicity effects of the Cs-Al NDs on the cell viability of human prostatic epithelial PWR-1E and Caucasian prostate adenocarcinoma PC-3 cell lines.

2. Materials and Methods

2.1. Materials.
Chitosan (85% deacetylation), sodium tripolyphosphate (STPP), and acetic acid were purchased from Alfa Aesar, and sodium alginate was from Danisco. Hydrochloric acid (HCl), potassium phosphate (K_3PO_4), sodium hydroxide (NaOH), and potassium chloride (KCl) were supplied from Panreac. Amoxicillin was acquired from Genfar. Human cell lines PC-3 and PWR-1E were obtained from American Type Culture Collection (ATCC). Fetal bovine serum, penicillin-streptomycin, keratinocyte culture, bovine pituitary extract, and EGF recombinant human protein were supplied from Thermo Fisher Scientific. Phosphate-buffered saline (PBS), trypan blue, phenazine ethosulfate (PES), and (3-(4,5-dimethylthiazol-2-yl)-5-(3-carboxymethoxyphenyl)-2-(4-sulfophenyl)-2H-tetrazolium) MTS were purchased from Sigma-Aldrich. CellTiter 96®

AQueous One Solution Cell Proliferation Kit was acquired from Promega.

2.2. Synthesis of Chitosan-Alginate Nanodisks (Cs-Al NDs).
The Cs-Al NDs were prepared by ionotropic gelation of chitosan and sodium alginate using STPP as a highly charged agent [18]. Chitosan (2.25 mg/mL) was added in acetic acid solution at 1% v/v under magnetic stirring at 700 rpm until the biopolymer was dissolved completely. Then, sodium alginate (0.5 mg/mL) and STPP (1 mg/mL) solutions were prepared in distilled water and mixed to perform the chitosan crosslinking. Gelation was carried out by dropwise addition of the sodium alginate/STPP solution into the chitosan gel following a 3 : 1 v/v ratio under magnetic stirring at 700 rpm for 10 min. Finally, the suspension was centrifuged to precipitate the Cs-Al NDs at 5500 rpm for 15 min, and then the supernatant containing unreacted polymer was removed gently using a pipette. The as-synthesized Cs-Al NDs were washed several times with distilled water and then lyophilized to obtain the final product.

2.3. Characterization.
The surface morphology and shape of the lyophilized Cs-Al NDs were observed using the scanning electron microscopy (SEM) technique in a high-performance JEOL JSM 6490 LV equipment with a high resolution of 3.0 nm and low vacuum mode. The Cs-Al NDs for imaging were drop casted onto gold coat in a sputter coater and left to dry at room temperature. The hydrodynamic size and particle size distribution were determined using a dynamic light scattering (DLS) Horiba LB-550 equipment. Functional groups were determined using a NICOLET 6700 FT-IR (Thermo Scientific) equipment with a wavelength between 400 and 4000 cm^{-1}. X-ray diffraction (XRD) was carried out with the aim to obtain crystalline information using an XPert PANalytical Empyrean Series II with a 2θ range from 5 to 80°. The Cs-Al NDs were dispersed in 2 buffer solutions at pH 1.2 and 7.4 using an ultrasound bath and then analyzed in quintuplicate. UV-Vis spectrophotometry spectra to determine the encapsulation efficiency and release of amoxicillin at pH 1.2 and 7.4 were collected using an UV-2650 spectrometer.

2.4. Encapsulation Efficiency of Amoxicillin.
Amoxicillin was used as a model drug for encapsulation in Cs-Al NDs. Following the process for nanodisk preparation, amoxicillin (0.1 mg/mL) was added to the STPP solution before crosslinking with chitosan. The gelation process was the same as mentioned in a previous step for Cs-Al NDs synthesis. The encapsulation efficiency (EE) of amoxicillin was calculated using the supernatant obtained after centrifugation, in which an UV-2650 UV-Vis spectrophotometer was used to measure the absorbance at 247 nm. Calibration curves allowed to quantify the amount of free amoxicillin in the supernatant and then to determine EE% in triplicate according to

$$EE(\%) = \left(\frac{\text{Total content} - \text{free content}}{\text{Total content}} \right) \times 100. \quad (1)$$

2.5. In Vitro Release of Amoxicillin. A study of amoxicillin releases was performed using PBS solutions at pH 1.2 and 7.4, in order to evaluate the controlled delivery of the drug and the stability of the Cs-Al NDs in acidic and basic mediums, respectively. The PBS at pH 1.2 was prepared using 50 mL of KCl (0.2 M) and 85 mL of HCl (0.2 M) solutions, and in parallel, the PBS at pH 7.4 was obtained mixing 100 mL of K_3PO_4 (0.1 M) and 78.2 mL of NaOH (0.1 M). Then, 30 mg of amoxicillin loaded Cs-Al NDs was dispersed in 120 mL of each PBS solution and placed in an incubator shaker under 150 rpm at 37°C for a total period of 8 h. Aliquots of 5 mL were taken each 0.25 h in the first hour, each 0.5 h in the second hour, and then each hour; subsequently, the same amount was replaced by fresh PBS to keep the total volume constant. Each aliquot was centrifuged at 5500 rpm for 10 min, and its absorbance was collected at 247 nm to calculate the cumulative release (CR) of amoxicillin in Cs-Al NDs according to

$$CR(\%) = \frac{m_{t=0} - m_{t=n}}{m_{t=0}} \times 100, \qquad (2)$$

where $m_{t=0}$ is the amoxicillin amount content in Cs-Al NDs at $t = 0$ (g) and $m_{t=n}$ is the amoxicillin amount contents in Cs-Al NDs at $t = n$ (g).

2.6. In Vitro Cytotoxicity Assessment

2.6.1. Human Cell Line Cultivation. Human prostatic epithelial PWR-1E and Caucasian prostate adenocarcinoma PC-3 cell lines were cultured and incubated in a 96-well plate using Dulbecco's modified Eagle's medium (DMEM) at 37°C and under a 5% CO_2-humidified air atmosphere for 24 h. DMEM was supplemented with 10% fetal bovine serum, 1% penicillin-streptomycin, and keratinocyte cell culture medium. The keratinocyte cell culture medium was previously supplemented with 10% bovine pituitary extract and an EGF recombinant human protein. Cell lines were passaged up to 40 and proliferated until reaching 70-80% of confluency prior cultivation with Cs-Al NDs. After cultivation and incubation, DMEM was removed and replaced by freshly supplemented DMEM containing Cs-Al NDs at 10, 25, and 50 μg/mL using PBS as the culture medium control in which the nanodisks were previously dispersed in the same PBS until reaching 200 μg/mL. Cell lines were cultured and incubated under the same conditions for 48 and 72 h with triplicate.

2.6.2. Trypan Blue and CellTiter 96® AQueous Viability Assays. The viability of PWR-1E and PC-3 cell lines was evaluated through 2 different methods, trypan blue and CellTiter 96® AQueous. After cultivation and incubation, DMEM was removed and cell lines were washed several times with PBS to eliminate the residual Cs-Al NDs. For the first method, fresh DMEM and 10 μL of trypan blue were added to each well following a volume ratio of 10 : 1, respectively. Cell lines were then incubated under the same conditions for 2 h. After incubation, cell lines were placed into a Neubauer chamber for manual cell counting to determine the cell viability (CV) per mL. After

counting the cells that excluded trypan blue, the CV was calculated according to

$$CV(\%) = \frac{\text{Cells that excluded dye}}{\text{Total cells}} \times 100. \qquad (3)$$

The second method consisted in a colorimetry technique using a solution composed of (3-(4,5-dimethylthiazol-2-yl)-5-(3-carboxymethoxyphenyl)-2-(4-sulfophenyl)-2H-tetrazolium) MTS and phenazine ethosulfate (PES) as an electronic coupling agent. This assay was performed using a CellTiter 96® AQueous One Solution Cell Proliferation kit, in which 20 μL of the MTS/PES stable solution was added to the cell line culture wells and then allowed to incubate at 37°C for 2 h. The cell viability was evaluated using Multiskan FC Microplate Photometer by Thermo Fisher Scientific, where the absorbance was measured at 490 nm to determine the total number of viable cells in a culture in which the absorbance value was directly proportional to this total number.

2.7. Statistical Analysis. The statistical analysis was investigated by a one-way analysis of variance (ANOVA) to determine the significance level of $p < 0.05$. GraphPad Prism v6.0 program was used to analyze the experimental data that was performed in triplicate and expressed as the mean ± standard deviation.

3. Results and Discussion

3.1. Characterization of Cs-Al NDs. Scanning electron microscopy (SEM) images shown in Figures 1(a) and 1(b) determine the morphological features of the as-synthesized Cs-Al NDs. Agglomeration can be observed since the nanodisks were lyophilized previously, but the shape of the disks can still be seen clearly as shown in the SEM image in Figure 1(b) [19]. The nanoparticles were successfully synthesized with a more disk shape than the usual spherical or common structures, presenting a regular and smooth surface but a wide size range, which can be attributed to many factors such as the biopolymer concentrations and electrostatic interaction that occurs during ionotropic gelation using sodium tripolyphosphate (STPP) as a highly charged compound [20, 21]. The combination of chitosan and alginate leads the spontaneous aggregation and formation of polyion complexes through the interaction of the carboxyl and amine groups within the structure of both polymers, respectively [22]. Additionally, the electrostatic interaction helps with the formation of polyelectrolyte complexes by using a cross-linking agent such as STPP, which contributes to the cross-linking and orientation of the nanoparticles during the growth [23–25]. Some reports have shown that the variation of several parameters such as the concentration and weight ratio of chitosan and alginate, as well as the pH solution and addition order, can significantly affect the size and shape of the final nanoparticle and even the structure that may be either heterogeneous or homogenous [22]. Wasupalli and Verma found that a balance between pH solution and strong electrostatic interaction leads to the formation of nanofibers, whereas with a weaker interaction it tends to form

(a)

(b)
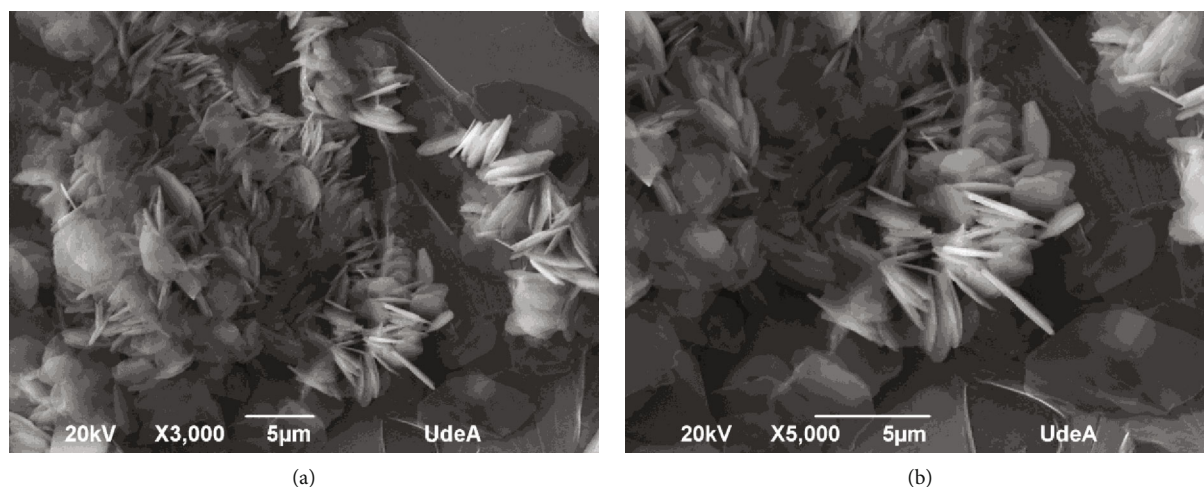
Figure 1: Scanning electron microscopy (SEM) images of the as-synthesized Cs-Al NDs at (a) ×3,000 and (b) ×5,000 magnifications.

nanocolloids [22]. Other reports made by Jeddi and Mahkam and Nalini et al. showed the formation of nanorods using chitosan, alginate, and a highly charged agent, which confirms that a strong electrostatic interaction is working as crosslinking between polymers, which is in agreement with the results obtained in this study [26, 27]. Besides, the presence of dense and agglomerated Cs-Al NDs in Figure 1(a) can be easily related to the availability of amine and carboxylic functional groups that produced strong electrostatic interaction on the surface [28]. This behaviour can be also observed in the size particle distribution as shown in Figure 2.

The chitosan/alginate weight ratio and pH of the solution in which nanodisks are dispersed play an important role in physical properties such as hydrodynamic size, agglomeration, and polydispersity [29]. According to the histograms, the particle size distribution is influenced by the pH of PBS solutions, indicating different responses in acidic and basic mediums. The particle size of Cs-Al NDs increases significantly at pH 1.2 as shown in Figure 2(a), obtaining a hydrodynamic average diameter of 227 ± 100 nm, which can be related to the collapse of the chitosan molecule structure due to deprotonation of amine functional groups on the surface and also to the formation of intermolecular hydrogen bonding during the gelation process [30]. Compared to the hydrodynamic average diameter for Cs-Al NDs in PBS solution at pH 7.4, a decrease up to 152 ± 67 nm is observed in Figure 2(b), indicating good stability at neutral pH. The presence of potassium ions from the STPP appears to be a very important factor in the formation of nanodisk shapes, leading the rapid increase in the agglomeration and particle size produced by a compact membrane of chitosan on the surface of the nanodisks [31, 32]. These results of particle size distribution and hydrodynamic size are consistent with the SEM images reported above and are in agreement with the results reported in the literature about the synthesis of chitosan/alginate nanoparticles by ionotropic gelation [6, 33].

Information related to the chemical structure of the Cs-Al NDs prepared using STTP as ionotropic gelation agent is shown in Figure 3. The spectrum shows the specimens in which vibrations for different functional groups were identified. The broadband between 3370 and 2950 cm^{-1} corresponds to the N-H and O-H stretching vibrations, representing the aliphatic primary amine and alcohol groups, respectively [34, 35]. The peak at 2874 cm^{-1} confirmed the presence of aliphatic C-H stretching [36, 37]. The deformation of N-acetylglucosamine determines the possible interaction between the amine and phosphate groups in the Cs-Al NDs, which can be evidenced by the presence of the peaks around 1592 and 1529 cm^{-1}, as well as the peak at 1407 cm^{-1} indicating an antisymmetric deformation of methyl groups due to the electrostatic interaction with STTP [37–39]. The presence of alginate can be evidenced by the stretching vibration of carboxylic acid at 1382, 1214, and 1027 cm^{-1} [36, 40]. The peak at 1306, 1129, 1065, and 891 cm^{-1} corresponded to the tertiary amide group, C-O-C glycosidic bond, C-O stretching vibration, and C-O-C stretching vibration [36, 37]. The wavenumber range between 790 and 440 cm-1 is attributed to the electrostatic interaction between the functional groups of chitosan and STTP, which can be described as a derivation of linkages with N-H symmetric vibrations [38].

Crystallinity of the as-prepared Cs-Al NDs was evaluated by using the X-ray diffraction (XRD) technique. The diffraction pattern is shown in Figure 4, which evidenced the presence of characteristic peaks corresponding to the chitosan and alginate polymers. Peaks at 9 and 19° confirm the existence of chitosan within the nanodisks' structure and are attributed to the formation of hydrogen bonds between the amine and hydroxyl groups and the dilution of chitosan in acetic acid, respectively [23], whereas peak at 12° and also a broad peak starting at 35° correspond to the presence of alginate [14, 29, 41]. An intense peak was observed at 23° indicating the presence of the Cs-Al NDs, which can be inferred that alginate is influencing the crystalline properties of chitosan through hydrogen bonding, and electrostatic interaction between negative and positive charges, confirming the formation of a polyelectrolyte complex using the ionic gelation method [14, 23, 42]. These results are in agreement with those reported in the literature, allowing to state that the Cs-Al NDs present high crystallinity, strong electrostatic

(a)

(b)
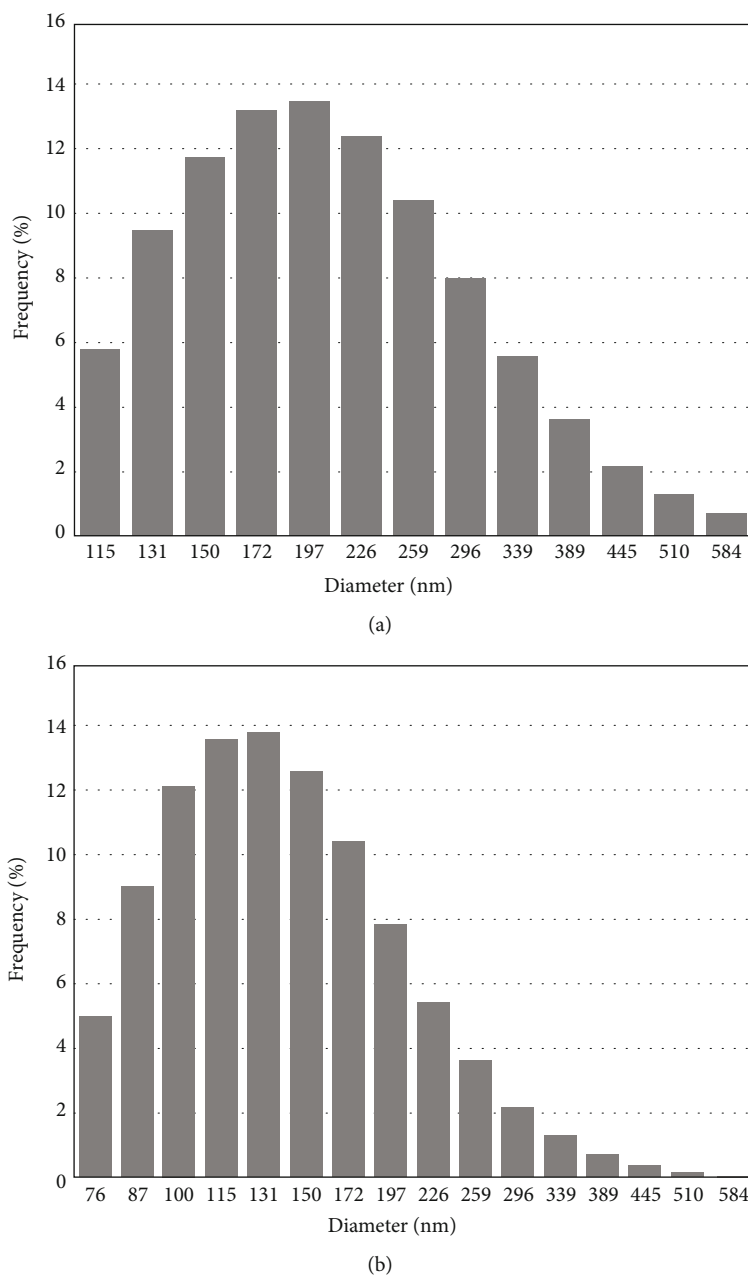
FIGURE 2: Particle size distribution of Cs-Al NDs in PBS at pH (a) 1.2 and (b) 7.4.

interaction, and good order of the crystallites [19]. The crystallite size for the Cs-Al NDs was calculated to be 1.6 nm from the peak with the strongest intensity at 23°, according to the following Debye-Scherrer equation (1):

$$d = \frac{k \times \lambda}{\beta \times \cos \theta}, \qquad (4)$$

where d (nm) is the crystallite size, k (0.94) is the Scherrer constant, λ (Cu − Kα = 0.1541 nm) is the X-ray wavelength, β (FWHM, rad) is the full width at half maximum, and θ (rad) is the Bragg diffraction angle.

3.2. Encapsulation Efficacy and In Vitro Drug Release. The amoxicillin encapsulation efficiency in Cs-Al NDs was calculated from a supernatant by triplicate, giving an efficiency of 74.98% ± 0.23. This result indicates that these nanodisks are a suitable material for a successful loading of amoxicillin and was consistent with the results reported in the literature of other chitosan/alginate nanoparticles [36, 40, 43]. The presence of the STPP crosslinking agent influences the encapsulation efficiency characteristic due to the formation of chitosan/alginate-TPP complex that produces an electrostatic interaction between carboxylic and amine functional groups of chitosan and amoxicillin, increasing the loading of amoxicillin in Cs-Al NDs [44]. However, the encapsulation efficiency is increasing in agglomeration after ionotropic
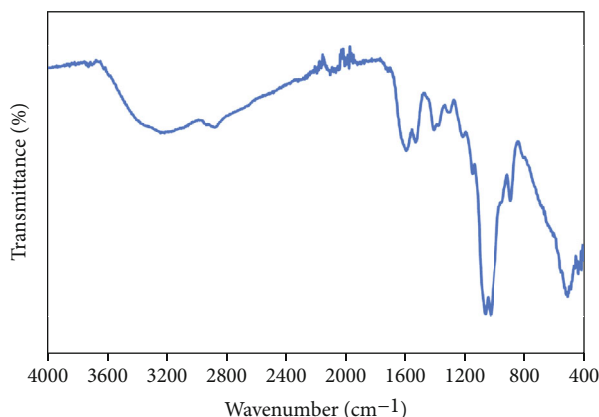
FIGURE 3: Fourier transform infrared (FTIR) spectrum of the as-synthesized Cs-Al NDs.
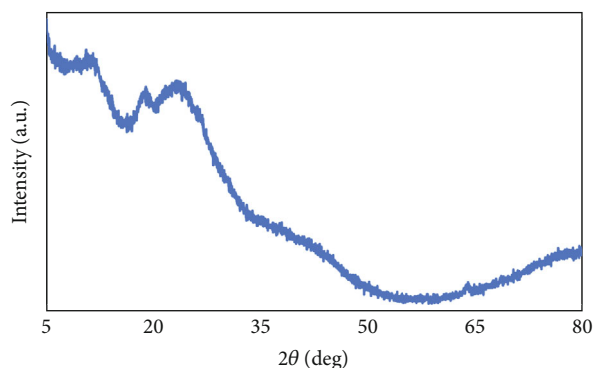
FIGURE 4: X-ray diffraction (XRD) pattern of the as-synthesized Cs-Al NDs.

FIGURE 5: Amoxicillin release from Cs-Al NDs in PBS solutions with pH at 1.2 and 7.4.

gelation as shown in Figure 1, which is expected to decrease the surface area availability of the nanodisks, leading to the saturation of the polymer matrix during the drug loading [36, 45].

The *in vitro* release of amoxicillin from Cs-Al NDs was carried out in PBS solution at pH 1.2 and 7.4 and was monitored as a function of time as shown in Figure 5. According to the curves, the encapsulated drug release showed to be significantly high, which obtained a maximum release amount within 8 h of 63.2 and 52.3% at pH 1.2 and 7.4, respectively. There were two stages in the cumulative amoxicillin release of the Cs-Al NDs in both pH, where initially the release increased rapidly and constantly (burst effect) in the first 2 h due to the limited distribution of the drug onto the surface, and then during the following 6 h, the release slightly decreased and became more stable [46, 47]. Thereby, the release profile of amoxicillin encapsulated in Cs-Al NDs are shown to be sustainable, which is an important factor in reducing the hepatotoxicity effects and damage to healthy cells in anticancer drug delivery systems [27, 48].

Although similar results were observed for both pH condition, Cs-Al NDs at pH 7.4 best released the encapsulated drug within 8 h, suggesting that the Cs-Al NDs can be capable to hold and have controlled release capacity of amoxicillin. Hence, these results can be considered positive, since a

long-term drug delivery system is more suitable for anticancer treatment, due to the low hepatotoxicity for controlled drug concentration, and less doses are required being an economic and therapeutic advantage [49]. This prolonged period and reduced dose at pH 7.4 may be attributed to the electrostatic interaction between functional groups of the chitosan/alginate-STPP complex and the drug, providing good pH sensitivity which improves the controlled release capacity of the Cs-Al NDs [50, 51]. On the contrary, the faster release found at pH 1.2 can be related to a higher solubility and swelling capability of Cs-Al NDs, since there was a change in the complex structure due to a possible protonation of the carboxylic and amine groups weakening the bonding with STPP and thus decreasing the π-π interaction between amoxicillin and the Cs-Al NDs structure [51, 52]. According to the results, a partial release of amoxicillin was observed which may be attributed by the fact that the nanodisks had a low degradation during the test. However, a greater degradation of the polymer framework occurred for the nanodisks exposed to acidic pH, indicating the diffusion of amoxicillin due to the polymer chain relaxation, in which these results were in agreement with those reported in the literature [36, 53].

3.3. In Vitro Cytotoxicity Assessment. Trypan blue and Cell-Titer 96® AQueous tests were performed to evaluate cytotoxicity using different concentrations (10, 25, and 50 μg/mL) of Cs-Al NDs against two cell lines, PWR-1E and PC-3. According to the results from both methods shown in Figures 6(a)–6(d) and 7(a)–7(d), no significant toxicity was observed in the cell lines providing a viability above 80%, which is in agreement with the cytotoxicity requirements for the application of biomaterials in drug delivery systems [50, 51]. Although the viability slightly decreased when the exposure concentration with Cs-Al NDs increases, as was observed mainly in Figures 7(a) and 7(c) for PWR-1E cells, the high percentage corresponds to no-cytotoxic effects indicating that no damage was caused to the cell membrane [2], allowing their normal growth due to the excellent biocompatibility of chitosan and alginate biopolymers [54].

(a)

(b)

(c)

(d)
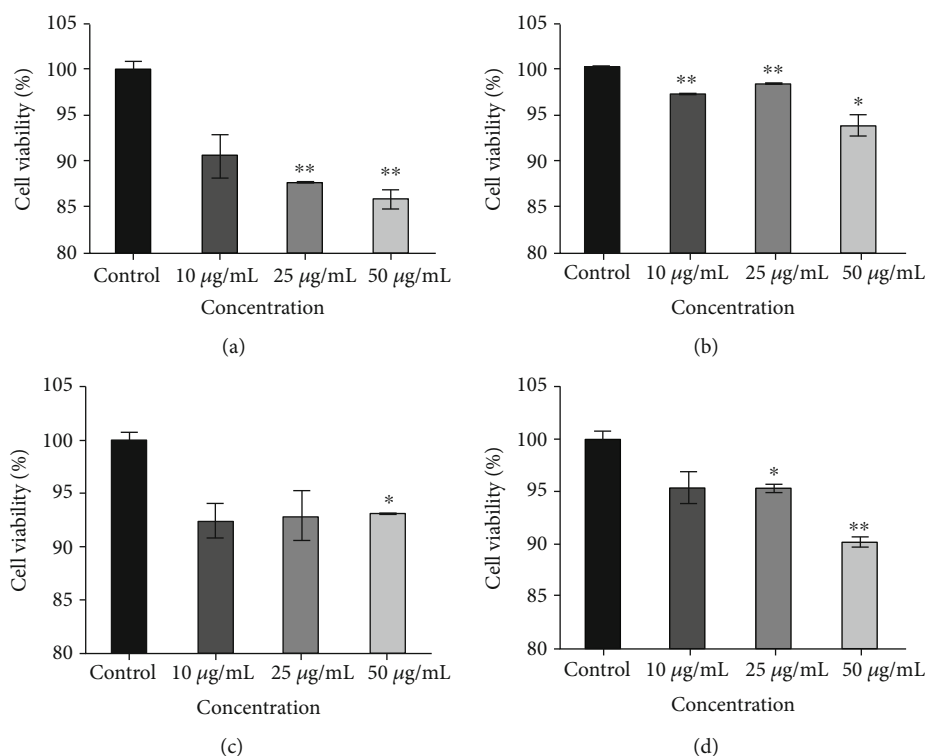
Figure 6: Cell viability using trypan blue technique of PWR-1E line after (a) 48 and (c) 72 h and PC-3 line after (b) 48 and (d) 72 h, exposed to Cs-Al NDs. Significant difference with control: $^*p < 0.05$ and $^{**}p < 0.01$.

(a)

(b)

(c)

(d)
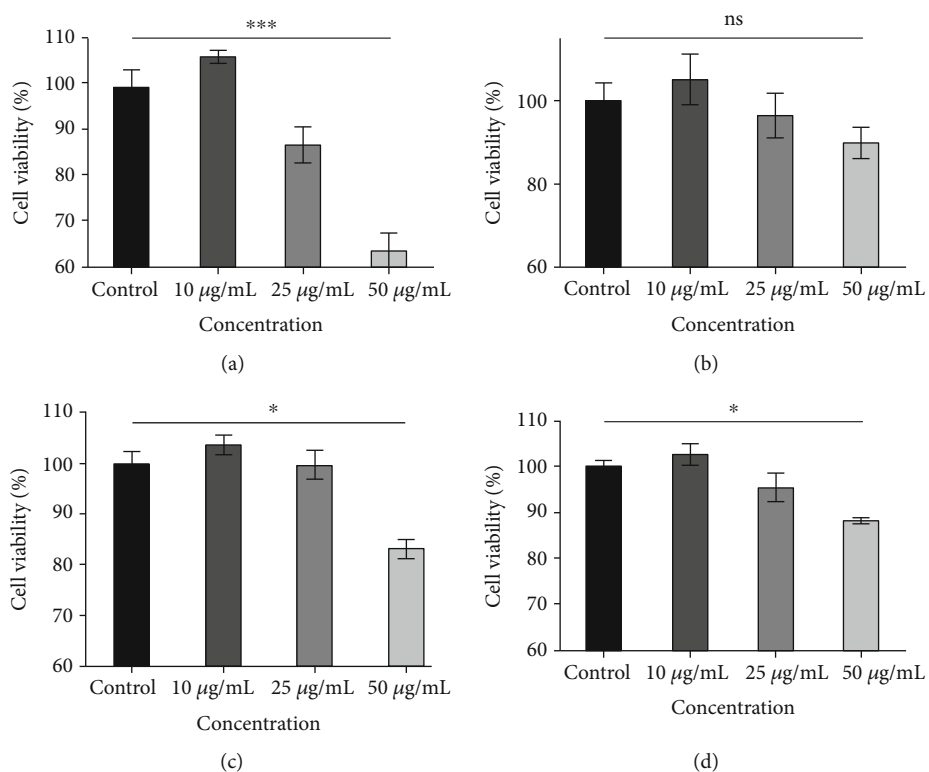
Figure 7: Cell viability using CellTiter 96® AQueous technique of PWR-1E line after (a) 48 and (c) 72 h and PC-3 line after (b) 48 and (d) 72 h, exposed to Cs-Al NDs. Significant difference with control: $^*p < 0.05$, $^{**}p < 0.01$, and $^{***}p < 0.001$. ns = no significant difference.

Differences were observed between the normal cell line and the adenocarcinoma culture as shown in Figures 6 and 7, which can be inferred that the Cs-Al NDs provides better biocompatibility regarding the adenocarcinoma cells, considering them suitable for applications in cancer treatments as nanocarriers for the delivery of drugs. However, the cell viability tends to increase when exposed for 72 h, indicating that eventually cells keep growing due to an improvement in the biocompatibility, promoted as a positive characteristic in terms of prolonged drug delivery [21], which is the opposite for the case of adenocarcinoma cells. From the results, it is also important to take into account that increasing the Cs-Al NDs concentration may affect negatively the cell viability, as was observed for the treatment using 50 μg/mL which resulted in a slight inhabitation of both cell lines due to induced oxidative stress on cells or changes in the cell membrane, as well as inducing damage of the DNA [1, 55, 56]. These results are in quantitative agreement with the results reported in the literature, which obtained low growth inhibition using similar nanomaterials synthesized with chitosan and alginate biopolymers for cytotoxicity assessment [13, 14, 57].

Although the results from trypan blue method indicated high cell viability compared to those obtained by using the CellTiter 96® AQueous method, reports show less accuracy using trypan blue. Accordingly, these results from the CellTiter 96® AQueous method are more reliable and the cytotoxicity pattern observed seems to be in agreement with other reports, in which higher concentration of nanoparticles is the main cause of inducing negative effects on the cell viability [58]. Among these reports, the use of alginate/chitosan and other types of nanocarriers against different cells lines was involved, and the results showed a similar trend in which a variation in the cell viability may be attributed to the selectivity with no discrimination toward the normal and cancerous cells [1, 36, 40, 59].

4. Conclusions

We report a facile strategy to synthesize chitosan-alginate nanodisks (Cs-Al NDs) using ionotropic gelation method and sodium tripolyphosphate (STPP) as a highly charged agent. We observed the interaction between charges of the amine group of chitosan and the carboxyl group of alginate, which was promoted by degradation of some chemical structures and then the electrostatic interaction with phosphates, leading to the formation of the nanodisks as was reported in the SEM images. The characterization results corroborated that the Cs-Al NDs has a high and regular crystalline orientation due to the strong interaction between the polymers. We also found that the hydrodynamic size increases when the nanodisks are exposed to an acidic environment, in which a burst release of drug due to the swelling behaviour in pH 1.2 may occur. Therefore, in a basic environment, the nanodisk presents small hydrodynamic sizes, indicating a better and more controlled release of amoxicillin. These Cs-Al NDs showed high cell viability above 80% when exposed for 48 and 72 h, taking into account that the viability may increase due to the high biocompatibility of the nanodisks, which represent an efficient nanomaterial for medical and pharmaceutical applications, and are also shown to be a new platform for further and deeper studies involving different drugs and cell lines, as well as in vivo tests.

Data Availability

The data used to support the findings of this study are included within the article.

Conflicts of Interest

The authors declare that there is no conflict of interest regarding the publication of this paper.

Acknowledgments

References

[1] M. Bilal, T. Rasheed, H. M. N. Iqbal, C. Li, H. Hu, and X. Zhang, "Development of silver nanoparticles loaded chitosan-alginate constructs with biomedical potentialities," *International Journal of Biological Macromolecules*, vol. 105, Part 1, pp. 393–400, 2017.

[2] D. Aluani, V. Tzankova, M. Kondeva-Burdina et al., "Evaluation of biocompatibility and antioxidant efficiency of chitosan-alginate nanoparticles loaded with quercetin," *International Journal of Biological Macromolecules*, vol. 103, pp. 771–782, 2017.

[3] T. Wu, J. Huang, Y. Jiang et al., "Formation of hydrogels based on chitosan/alginate for the delivery of lysozyme and their antibacterial activity," *Food Chemistry*, vol. 240, pp. 361–369, 2018.

[4] M. Gierszewska, J. Ostrowska-Czubenko, and E. Chrzanowska, "pH-responsive chitosan/alginate polyelectrolyte complex membranes reinforced by tripolyphosphate," *European Polymer Journal*, vol. 101, pp. 282–290, 2018.

[5] M. He, X. Zhang, W. Yao, C. Wang, L. Shi, and P. Zhou, "Construction of alternate layered chitosan/alginate composite hydrogels and their properties," *Materials Letters*, vol. 200, pp. 43–46, 2017.

[6] K. Ling, H. Wu, A. S. Neish, and J. A. Champion, "Alginate/chitosan microparticles for gastric passage and intestinal release of therapeutic protein nanoparticles," *Journal of Controlled Release*, vol. 295, pp. 174–186, 2019.

[7] L. Zakaria, T. W. Wong, N. K. Anuar et al., "Enhancing sustained drug release property of chitosan in spheroids through crosslinking reaction and coacervation," *Powder Technology*, vol. 354, pp. 815–821, 2019.

[8] W. Zhang, H. Wang, X. Hu et al., "Multicavity triethylenetetramine-chitosan/alginate composite beads for enhanced Cr(VI) removal," *Journal of Cleaner Production*, vol. 231, pp. 733–745, 2019.

[9] F. N. Sorasitthiyanukarn, P. Ratnatilaka Na Bhuket, C. Muangnoi, P. Rojsitthisak, and P. Rojsitthisak, "Chitosan/alginate nanoparticles as a promising carrier of novel curcumin diethyl diglutarate," *International Journal of Biological Macromolecules*, vol. 131, pp. 1125–1136, 2019.

[10] M. Halimi, M. Alishahi, M. R. Abbaspour, M. Ghorbanpoor, and M. R. Tabandeh, "Valuable method for production of oral vaccine by using alginate and chitosan against *Lactococcus garvieae/Streptococcus iniae* in rainbow trout (*Oncorhynchus mykiss*)," *Fish & Shellfish Immunology*, vol. 90, pp. 431–439, 2019.

[11] M. A. Khan, C. Yue, Z. Fang et al., "Alginate/chitosan-coated zein nanoparticles for the delivery of resveratrol," *Journal of Food Engineering*, vol. 258, pp. 45–53, 2019.

[12] D. K. Bedade, Y. B. Sutar, and R. S. Singhal, "Chitosan coated calcium alginate beads for covalent immobilization of acrylamidase: process parameters and removal of acrylamide from coffee," *Food Chemistry*, vol. 275, pp. 95–104, 2019.

[13] S. Wichai, P. Chuysinuan, S. Chaiarwut, P. Ekabutr, and P. Supaphol, "Development of bacterial cellulose/alginate/chitosan composites incorporating copper (II) sulfate as an antibacterial wound dressing," *Journal of Drug Delivery Science and Technology*, vol. 51, pp. 662–671, 2019.

[14] J. Venkatesan, J. Y. Lee, D. S. Kang et al., "Antimicrobial and anticancer activities of porous chitosan-alginate biosynthesized silver nanoparticles," *International Journal of Biological Macromolecules*, vol. 98, pp. 515–525, 2017.

[15] A. Da S Pereira, M. M. Diniz, G. De Jong et al., "Chitosan-alginate beads as encapsulating agents for *Yarrowia lipolytica* lipase: Morphological, physico-chemical and kinetic characteristics," *International Journal of Biological Macromolecules*, vol. 139, pp. 621–630, 2019.

[16] F. Maestrelli, M. Jug, M. Cirri, I. Kosalec, and P. Mura, "Characterization and microbiological evaluation of chitosan-alginate microspheres for cefixime vaginal administration," *Carbohydrate Polymers*, vol. 192, pp. 176–183, 2018.

[17] C. Qin, J. Zhou, Z. Zhang, W. Chen, Q. Hu, and Y. Wang, "Convenient one-step approach based on stimuli-responsive sol-gel transition properties to directly build chitosan-alginate core-shell beads," *Food Hydrocolloids*, vol. 87, pp. 253–259, 2019.

[18] A. P. H. Barros, M. T. A. Morantes, M. I. C. Hoyos, and L. J. M. Ospino, "Preparación de nanopartículas de quitosano modificadas con alginato de sodio con potencial para la liberación controlada de medicamentos," *Revista EIA*, vol. 12, no. 57 5, pp. 75–83, 2016.

[19] M. Ji, X. Sun, X. Guo et al., "Green synthesis, characterization and *in vitro* release of cinnamaldehyde/sodium alginate/chitosan nanoparticles," *Food Hydrocolloids*, vol. 90, pp. 515–522, 2019.

[20] A. Bhattacharyya, D. Mukherjee, R. Mishra, and P. P. Kundu, "Preparation of polyurethane-alginate/chitosan core shell nanoparticles for the purpose of oral insulin delivery," *European Polymer Journal*, vol. 92, pp. 294–313, 2017.

[21] K. Yoncheva, M. Merino, A. Shenol et al., "Optimization and in-vitro/in-vivo evaluation of doxorubicin-loaded chitosan-alginate nanoparticles using a melanoma mouse model," *International Journal of Pharmaceutics*, vol. 556, pp. 1–8, 2019.

[22] G. K. Wasupalli and D. Verma, "Molecular interactions in self-assembled nano-structures of chitosan-sodium alginate based polyelectrolyte complexes," *International Journal of Biological Macromolecules*, vol. 114, pp. 10–17, 2018.

[23] H. Wang, X. Gong, Y. Miao et al., "Preparation and characterization of multilayer films composed of chitosan, sodium alginate and carboxymethyl chitosan-ZnO nanoparticles," *Food Chemistry*, vol. 283, pp. 397–403, 2019.

[24] R. Dubey, J. Bajpai, and A. K. Bajpai, "Chitosan-alginate nanoparticles (CANPs) as potential nanosorbent for removal of Hg (II) ions," *Environmental Nanotechnology, Monitoring & Management*, vol. 6, pp. 32–44, 2016.

[25] T. Niaz, H. Nasir, S. Shabbir, A. Rehman, and M. Imran, "Polyionic hybrid nano-engineered systems comprising alginate and chitosan for antihypertensive therapeutics," *International Journal of Biological Macromolecules*, vol. 91, pp. 180–187, 2016.

[26] M. K. Jeddi and M. Mahkam, "Magnetic nano carboxymethyl cellulose-alginate/chitosan hydrogel beads as biodegradable devices for controlled drug delivery," *International Journal of Biological Macromolecules*, vol. 135, pp. 829–838, 2019.

[27] T. Nalini, S. K. Basha, A. M. Mohamed Sadiq, V. S. Kumari, and K. Kaviyarasu, "Development and characterization of alginate / chitosan nanoparticulate system for hydrophobic drug encapsulation," *Journal of Drug Delivery Science and Technology*, vol. 52, pp. 65–72, 2019.

[28] F. M. Goycoolea, G. Lollo, C. Remuñán-López, F. Quaglia, and M. J. Alonso, "Chitosan-alginate blended nanoparticles as carriers for the transmucosal delivery of macromolecules," *Biomacromolecules*, vol. 10, no. 7, pp. 1736–1743, 2009.

[29] S. Maity, P. Mukhopadhyay, P. P. Kundu, and A. S. Chakraborti, "Alginate coated chitosan core-shell nanoparticles for efficient oral delivery of naringenin in diabetic animals—an in vitro and in vivo approach," *Carbohydrate Polymers*, vol. 170, pp. 124–132, 2017.

[30] T. Cerchiara, A. Abruzzo, M. di Cagno et al., "Chitosan based micro- and nanoparticles for colon-targeted delivery of vancomycin prepared by alternative processing methods," *European Journal of Pharmaceutics and Biopharmaceutics*, vol. 92, pp. 112–119, 2015.

[31] S. Abdelghany, M. Alkhawaldeh, and H. S. AlKhatib, "Carrageenan-stabilized chitosan alginate nanoparticles loaded with ethionamide for the treatment of tuberculosis," *Journal of Drug Delivery Science and Technology*, vol. 39, pp. 442–449, 2017.

[32] S. Bhunchu, P. Rojsitthisak, and P. Rojsitthisak, "Effects of preparation parameters on the characteristics of chitosan-alginate nanoparticles containing curcumin diethyl disuccinate," *Journal of Drug Delivery Science and Technology*, vol. 28, pp. 64–72, 2015.

[33] J. Liu, J. Xiao, F. Li, Y. Shi, D. Li, and Q. Huang, "Chitosan-sodium alginate nanoparticle as a delivery system for ε-polylysine: preparation, characterization and antimicrobial activity," *Food Control*, vol. 91, pp. 302–310, 2018.

[34] A. Sharma, K. Sood, J. Kaur, and M. Khatri, "Agrochemical loaded biocompatible chitosan nanoparticles for insect pest management," *Biocatalysis and Agricultural Biotechnology*, vol. 18, p. 101079, 2019.

[35] R. R. Gadkari, S. Suwalka, M. R. Yogi, W. Ali, A. Das, and R. Alagirusamy, "Green synthesis of chitosan-cinnamaldehyde cross-linked nanoparticles: Characterization and antibacterial activity," *Carbohydrate Polymers*, vol. 226, article 115298, 2019.

[36] F. N. Sorasitthiyanukarn, C. Muangnoi, P. Ratnatilaka Na Bhuket, P. Rojsitthisak, and P. Rojsitthisak, "Chitosan/alginate nanoparticles as a promising approach for oral delivery of curcumin diglutaric acid for cancer treatment," *Materials Science and Engineering: C*, vol. 93, pp. 178–190, 2018.

[37] V. S. Gondil, T. Dube, J. J. Panda, R. M. Yennemalli, K. Harjai, and S. Chhibber, "Comprehensive evaluation of chitosan nanoparticle based phage lysin delivery system; a novel approach to counter *S. pneumoniae* infections," *International Journal of Pharmaceutics*, 2019.

[38] S. F. Hosseini, M. R. Soleimani, and M. Nikkhah, "Chitosan/sodium tripolyphosphate nanoparticles as efficient vehicles for antioxidant peptidic fraction from common kilka," *International Journal of Biological Macromolecules*, vol. 111, pp. 730–737, 2018.

[39] Z. Sang, J. Qian, J. Han et al., "Comparison of three water-soluble polyphosphate tripolyphosphate, phytic acid, and sodium hexametaphosphate as crosslinking agents in chitosan nanoparticle formulation," *Carbohydrate Polymers*, vol. 230, p. 115577, 2020.

[40] J. G. Rosch, H. Winter, A. N. DuRoss, G. Sahay, and C. Sun, "Inverse-Micelle Synthesis of Doxorubicin-Loaded Alginate/Chitosan Nanoparticles and *In Vitro* Assessment of Breast Cancer Cytotoxicity," *Colloid and Interface Science Communications*, vol. 28, pp. 69–74, 2019.

[41] P. Mukhopadhyay, S. Maity, S. Mandal, A. S. Chakraborti, A. K. Prajapati, and P. P. Kundu, "Preparation, characterization and *in vivo* evaluation of pH sensitive, safe quercetin-succinylated chitosan-alginate core-shell-corona nanoparticle for diabetes treatment," *Carbohydrate Polymers*, vol. 182, pp. 42–51, 2018.

[42] C. P. Gong, Y. Luo, and Y. Y. Pan, "Novel synthesized zinc oxide nanoparticles loaded alginate-chitosan biofilm to enhanced wound site activity and anti-septic abilities for the management of complicated abdominal wound dehiscence," *Journal of Photochemistry and Photobiology B: Biology*, vol. 192, pp. 124–130, 2019.

[43] S. Arora, S. Gupta, R. K. Narang, and R. D. Budhiraja, "Amoxicillin loaded chitosan-alginate polyelectrolyte complex nanoparticles as mucopenetrating delivery system for *H. pylori*," *Scientia Pharmaceutica*, vol. 79, no. 3, pp. 673–694, 2011.

[44] J. O. Akolade, H. O. B. Oloyede, M. O. Salawu, A. O. Amuzat, A. I. Ganiyu, and P. C. Onyenekwe, "Influence of formulation parameters on encapsulation and release characteristics of curcumin loaded in chitosan-based drug delivery carriers," *Journal of Drug Delivery Science and Technology*, vol. 45, pp. 11–19, 2018.

[45] M. Xie, F. Zhang, H. Peng et al., "Layer-by-layer modification of magnetic graphene oxide by chitosan and sodium alginate with enhanced dispersibility for targeted drug delivery and photothermal therapy," *Colloids and Surfaces B: Biointerfaces*, vol. 176, pp. 462–470, 2019.

[46] F. Shamekhi, E. Tamjid, and K. Khajeh, "Development of chitosan coated calcium-alginate nanocapsules for oral delivery of liraglutide to diabetic patients," *International Journal of Biological Macromolecules*, vol. 120, Part A, pp. 460–467, 2018.

[47] X. Chen, M. Fan, H. Tan et al., "Magnetic and self-healing chitosan-alginate hydrogel encapsulated gelatin microspheres via covalent cross-linking for drug delivery," *Materials Science and Engineering: C*, vol. 101, pp. 619–629, 2019.

[48] J. R. Lakkakula, T. Matshaya, and R. W. M. Krause, "Cationic cyclodextrin/alginate chitosan *nanoflowers* as 5-fluorouracil drug delivery system," *Materials Science and Engineering: C*, vol. 70, Part 1, pp. 169–177, 2017.

[49] J. M. Unagolla and A. C. Jayasuriya, "Drug transport mechanisms and in vitro release kinetics of vancomycin encapsulated chitosan-alginate polyelectrolyte microparticles as a controlled drug delivery system," *European Journal of Pharmaceutical Sciences*, vol. 114, pp. 199–209, 2018.

[50] Y. G. Bi, Z.-t. Lin, and S.-t. Deng, "Fabrication and characterization of hydroxyapatite/sodium alginate/chitosan composite microspheres for drug delivery and bone tissue engineering," *Materials Science and Engineering: C*, vol. 100, pp. 576–583, 2019.

[51] K. Chen, Y. Ling, C. Cao, X. Li, X. Chen, and X. Wang, "Chitosan derivatives/reduced graphene oxide/alginate beads for small-molecule drug delivery," *Materials Science and Engineering: C*, vol. 69, pp. 1222–1228, 2016.

[52] M. Kilicarslan, M. Ilhan, O. Inal, and K. Orhan, "Preparation and evaluation of clindamycin phosphate loaded chitosan/alginate polyelectrolyte complex film as mucoadhesive drug delivery system for periodontal therapy," *European Journal of Pharmaceutical Sciences*, vol. 123, pp. 441–451, 2018.

[53] K. K. Patel, M. Tripathi, N. Pandey et al., "Alginate lyase immobilized chitosan nanoparticles of ciprofloxacin for the improved antimicrobial activity against the biofilm associated mucoid *P. aeruginosa* infection in cystic fibrosis," *International Journal of Pharmaceutics*, vol. 563, pp. 30–42, 2019.

[54] X. Lv, W. Zhang, Y. Liu, Y. Zhao, J. Zhang, and M. Hou, "Hygroscopicity modulation of hydrogels based on carboxymethyl chitosan/Alginate polyelectrolyte complexes and its application as pH- sensitive delivery system," *Carbohydrate Polymers*, vol. 198, pp. 86–93, 2018.

[55] X. Lv, Y. Liu, S. Song et al., "Influence of chitosan oligosaccharide on the gelling and wound healing properties of injectable hydrogels based on carboxymethyl chitosan/alginate polyelectrolyte complexes," *Carbohydrate Polymers*, vol. 205, pp. 312–321, 2019.

[56] J. O. Adeyemi, E. E. Elemike, D. C. Onwudiwe, and M. Singh, "Bio-inspired synthesis and cytotoxic evaluation of silver-gold bimetallic nanoparticles using Kei-Apple (*Dovyalis caffra*) fruits," *Inorg. Chem. Commun.*, vol. 109, article 107569, 2019.

[57] M. Almada, B. H. Leal-Martínez, N. Hassan et al., "Photothermal conversion efficiency and cytotoxic effect of gold nanorods stabilized with chitosan, alginate and poly(vinyl alcohol)," *Materials Science and Engineering: C*, vol. 77, pp. 583–593, 2017.

[58] T. P. Mofokeng, M. J. Moloto, P. M. Shumbula, and P. Tetyana, "Synthesis, characterization and cytotoxicity of alanine-capped CuS nanoparticles using human cervical carcinoma HeLa cells," *Analytical Biochemistry*, vol. 580, pp. 36–41, 2019.

[59] D. K. Chelike, A. Alagumalai, J. Acharya et al., "Functionalized iron oxide nanoparticles conjugate of multi-anchored Schiff's base inorganic heterocyclic pendant groups: Cytotoxicity studies," *Applied Surface Science*, vol. 501, article 143963, 2020.

Research Article

Characterization of Polysaccharides Extracted from *Sargassum fusiforme* and Its Effective Prevention of Contrast-Induced Nephropathy via Enhancing Antioxidant Capacity

Min Dai,[1,2,3] **Ying-Ling Zhou** [1,2] **Tao Jiang,**[3] **Cai-Dong Luo,**[3] **Hu Wang,**[3] **Wei Du,**[3] **and Min Wang**[3]

[1]*The Second School of Clinical Medicine, Southern Medical University, Guangzhou, Guangdong 510515, China*
[2]*Department of Cardiovascular Medicine, Guangdong General Hospital and Guangdong Academy of Medical Sciences, Guangzhou, Guangdong 510080, China*
[3]*Department of Cardiovascular Medicine, Mianyang Central Hospital, Mianyang, Sichuan 621000, China*

Correspondence should be addressed to Ying-Ling Zhou; zylgdh@163.com

Contrast-induced nephropathy (CIN) is a common complication in patients with coronary arteriography, and oxidative stress is involved in the CIN pathogenesis. *Sargassum fusiforme* (SF) is a brown seaweed with medicinal value, and its polysaccharides have good antioxidant activity. In this study, the crude polysaccharides (cSFP-C) were extracted by cold water, precipitated by ethanol, purified by $CaCl_2$, and detected with high contents of sulfate radical and fucose. cSFP-C is composed of glucose, glucuronic acid, xylose, rhamnose, mannose, galactose, and fucose with a molar ratio of $1.0 : 0.4 : 5.6 : 1.2 : 1.7 : 12.3 : 56.1$. The cSFP-C has the typical absorption of polysaccharides. Antioxidation assays *in vitro* showed that cSFP-C exhibited superoxide radical scavenging activity which was better than the hot water-extracted crude polysaccharides (cSFP-H). 20 rats were divided into 4 groups ($n = 5$): sham group; CIN group; CIN+cSFP-C group, and cSFP-C group. The CIN+cSFP-C group and cSFP-C group were pretreated intragastrically with cSFP-C at a dose of 9.45 g/kg twice daily for 5 consecutive days. Then, the CIN group and CIN+cSFP-C group were given indomethacin to develop CIN. The *in vivo* results showed that cSFP-C could decrease blood creatinine and urea nitrogen, inhibiting pathological injury in the renal tissues. The MDA content of renal tissues was decreased, while the activity of SOD was increased. The crude sulfated polysaccharides extracted from *S. fusiforme* have a renoprotective effect on oxidative stress to alleviate the kidney injury in CIN rats.

1. Introduction

With the raised morbidity of coronary atherosclerosis heart diseases, and the marked progress in intravascular interventional radiology, the volume of patients with percutaneous coronary intervention (PCI) has been growing significantly, with the number of PCI centers [1] increasing to 21.2% during 2003~2011. However, among the complications of PCI, the incidence of contrast-induced nephropathy (CIN) ranges from 3% to approximately 30% [2, 3], which has become the third leading cause of hospital-acquired acute kidney injury (AKI) following nephrotoxic drugs and renal perfusion insufficiency [4, 5]. After CIN occurs, the hospital days, the dialysis population, and the late cardiovascular events increase.

So far, there is still lack of therapeutic measures to reverse CIN. Effective prevention and treatment are needed. The commonly used agents are iodine contrasts in PCI, which are mostly unchanged passing through the kidneys into the urine, so as to have a damaging effect on the kidneys. The mechanisms of CIN have not been completely elucidated currently. Previous studies reported that CIN is a complex pathological process related to multiple pathological cascades. Oxidative stress [6, 7], renal ischemia [8], endothelial dysfunction [9], inflammation [10, 11], apoptosis [12–14], and tubular transport dysfunction [15] may be involved

in the pathogenesis of CIN. Increasing studies point out that reactive oxygen species (ROS) play the key role in CIN development [16–18]. In accordance with this, several potent ROS scavenging compounds are proved effective for preventing CIN.

Natural antioxidants extracted from plants may retard renal damage and may be an effective, safe, and economical therapy for organ protection. *Sargassum fusiforme* (SF) is an edible brown seaweed. SF can be used for kidney disease treatment in traditional Chinese medicine (TCM) and is documented in the medical books, such as *Shennong's Classic of Materia Medica*, *Compendium of Materia Medica*, and TCM prescriptions of *Coneha Ostreae Rhizoma Alismatis Powder* invented by Zhang Zhongjing. It was reported to be inhibitive to renal interstitial fibrosis caused by unilateral ureteral obstruction. Sulfated polysaccharides are the most important component of SF, mainly accumulated in the cell wall matrix. The complicated molecular structures of polysaccharides partly contribute to its multiple biological functions [19]. Sulfur-containing groups, such as sulfonate and sulfate, can be part of some natural polysaccharides and provide the polysaccharides more diversity [20, 21]. The sulfated polysaccharides are also called fucoidan from SF, which shows antioxidation, anti-inflammation, antitumor, antiradiation, and anticoagulation effects. It has also been reported that fucoidan extracted from SF increases the activity of antioxidant enzymes such as superoxide dismutase (SOD) and glutathione peroxidase (GPx) *in vivo* [22] and reduces lipid peroxidation products. So far, there is no report for the renal-protective effect of fucoidan from SF in a CIN animal model. This study reports on the preparation of fucoidan from SF, evaluation in antioxidant defense *in vitro*, and the antioxidative effects against CIN *in vivo*.

2. Materials and Methods

2.1. Materials. *Sargassum fusiforme* was collected from Rongcheng in Shandong, China. Reagents and solvents in the study were of analytical purity (AR) grade and purchased from Sinopharm Chemical Reagent Co., Ltd. (Shanghai, China).

2.2. Sample Pretreatment. The parameters of the crude polysaccharide extraction are given in Figure 1. SF was dried at 50°C, ground by a high-speed disintegrator into a powder, and sieved through a 4-mesh screen. 95% methanol was used to remove the fat of the sieved powder (1 : 10 g/ml) by reflowing at 40°C for 24 h. Afterwards, the defatted residue was dried at 40°C for subsequent experiments.

2.3. Extraction of Crude Polysaccharides from SF. The defatted powder was extracted three times with water (1 : 30 g/ml) at room temperature for 3 h. The leaching solutions were filtered and concentrated with a rotary evaporator (Yarong, Shanghai, China) at 40°C under vacuum. 95% ethanol was used to precipitate polysaccharides at room temperature overnight. The residue was collected by filter and reprecipitated in 95% ethanol. After being filtered and lyophilized, the powder was redissolved in calcium chloride solution (4 M) with stirring until no precipitation appeared. Then, repeat the precipitation
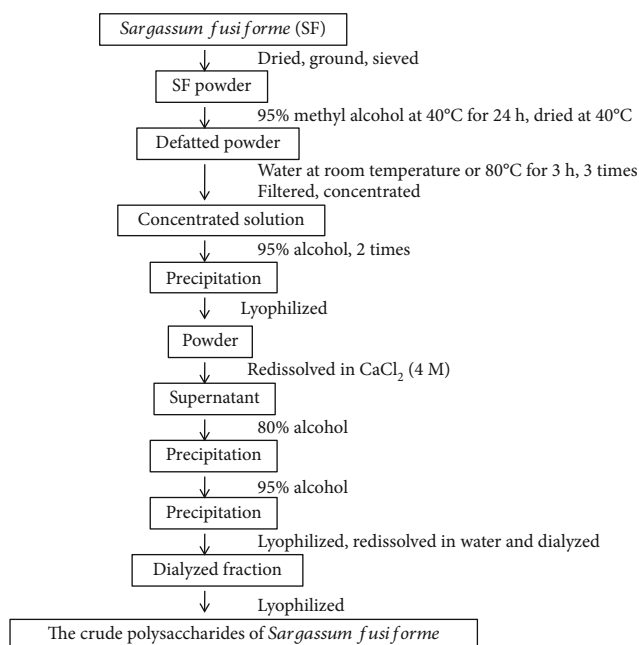
FIGURE 1: The flowchart of the extraction of the crude polysaccharides from *Sargassum fusiforme*.

by using 80% ethanol and 95% ethanol. Finally, the lyophilized powder was redissolved and exhaustively dialyzed (10 kDa molecular weight cutoff) against distilled water for 72 h to remove soluble impurities. By lyophilization, the crude polysaccharides were named as cSFP-C. The hot water-extracted crude polysaccharides, cSFP-H, were extracted three times with water (1 : 30 g/ml) for 3 h at 80°C, but not room temperature. The other steps were the same. The cSFP-C and cSFP-H were weighted and calculated the extraction yield (Y) according to the following equation:

$$Y\,(\%) = \frac{\text{weight of the crude polysaccharides}}{\text{weight of dry } Sargassum\ fusiforme} \times 100. \quad (1)$$

2.4. Determination of Chemical Composition of cSFP-C. The total sugar content in cSFP-C was determined using the phenol-sulfuric acid method. The sulfate radical content was estimated by the barium chloride-gelatin method [23]. The total uronic acid content was tested by the m-phenylphenol method using glucuronic acid as the standard [24]. The protein content was analyzed by Coomassie brilliant blue method with bovine serum albumin as the standard [25].

2.5. Measurement of Monosaccharide Components. 2 mg cSFP-C was mixed with 1 ml trifluoroacetic acid (TFA, 2 M) and then heated at 120°C for 2 h. After being dried with rotary evaporation, 1 ml of methyl alcohol was added to the hydrolyzed product to completely remove TFA, three times. The product and monosaccharide standards were prederivatized with 1-phenyl-3-methyl-5-pyrazolone (PMP). The HPLC system (Waters 1525, Milford, USA) and UV detector (Waters 2487) were used to analyze the monosaccharide components with a wavelength of 254 nm. The monosaccharide

quantification in cSFP-C was analyzed by comparing with the monosaccharide standard curves.

2.6. Fourier-Transform Infrared Spectroscopic Analysis (FT-IR).
The dried cSFP-C was prepared as KBr pellets for the IR spectra measurement in a range of 4000 to 400 cm^{-1} using a Nicolet Nexus FT-IR spectrometer (Thermo Fisher Scientific, Waltham, MA, USA).

2.7. Superoxide Radical Scavenging Activity Measured by PMS-NADH-NBT.
Superoxide anion scavenging activity was detected by the PMS-NADH-NBT method reported by Nishikimi et al. [26] with slight modification. The reaction system contained 0.15 ml NADH (166 μmol/l), 0.45 ml NBT (86 μmol/l), and varying concentrations of cSFP-C (0 mg/ml~2 mg/ml). Then, 0.15 ml PMS (16.2 μmol/l) was used to generate a superoxide radical and start the reaction. The mixture was incubated at room temperature for 5 min, and the absorbance was measured at a wavelength of 560 nm. In the blank control, there was 0 mg/ml cSFP-C in the buffer. The following equation was used to calculate the effect on scavenging superoxide radical:

$$\text{Scavenging effect (\%)} = \frac{A(\text{blank}) - A(\text{cSFP})}{A(\text{blank})} \times 100. \quad (2)$$

2.8. Rat Model of CIN and Treatment.
20 Wistar rats were divided into 4 groups of 5 rats each as follows: (1) sham rats given saline, (2) CIN rats with induced CIN, (3) CIN+cSFP-C rats pretreated with cSFP-C followed by the CIN induction, and 4) cSFP-C rats pretreated with cSFP-C. CIN+cSFP-C and cSFP-C rats were orally administrated 5.67 g/kg cSFP-C twice daily at 7 a.m. and 15 p.m. for 5 days. The dose of cSFP-C in this study was threefold the dose recommended by the Chinese Pharmacopoeia in clinic [27]. Sham and CIN rats were given saline. After pretreatment with cSFP-C or saline, CIN was developed in CIN and CIN+cSFP-C rats on the basis of previously described reports [28]. Briefly, under pentobarbital sodium anesthesia, rats were given 10 mg/kg indomethacin, followed 10 mg/kg NW-nitro-L-arginine methyl ester (L-NAME) 15 min later and 1600 mg iodine/kg of iopromide 30 min later. Sham and cSFP-C rats were given saline at each time point. All rats were sacrificed 24 h after CIN induction. Serum was isolated from the blood for renal biochemical and inflammatory testing. The kidneys were removed for histopathological investigation and oxidative stress detection.

2.9. Biochemical Parameters.
Blood urea nitrogen (BUN) and creatinine were measured using an AU5800 autoanalyzer (Beckman Coulter, USA).

2.10. Histopathological Investigation.
One side of the kidney was fixed in 10% formalin for 24 h and subsequently embedded in paraffin. Then 4 μm thickness sections were stained with hematoxylin and eosin.

2.11. Detection of Oxidative Stress Markers.
One side of the kidney was homogenized using ice-cold saline and then centrifuged. The supernatant was collected and the levels of SOD and MDA were measured using commercial kits (Nanjing Jiancheng, Jiangsu, China).

TABLE 1: Yield and chemical components of cSFP-C.

Yield (%)	Total sugar (%)	Sulfate radical (%)	Uronic acid (%)	Proteins (%)
7.5	85.5	19.3	8.3	0.3

3. Results and Discussion

3.1. Yield and Chemical Compositions of cSFP.
The yields of cSFP-C and cSFP-H from dry SF were 7.5% and 9.1%, respectively. The chemical compositions of cSFP-C (total sugar, sulfate radical, uronic acid, and proteins) are summarized in Table 1. The total sugar was the major constituent of cSFP-C, achieving 85.5%, with small amounts of protein at 0.3%. The contents of sulfate radical and uronic acid were 19.3% and 8.3%, respectively. The fucoidan extraction using cold water combined with calcium-alginate precipitation has not been investigated. Since calcium chloride could precipitate calcium-alginate, the fucoidan purity in cSFP-C can be enhanced [29]. Compared with the previous study by Chen et al. [22], the uronic acid percentage was significantly decreased and the sulfate radical percentage was significantly increased with the procedure for calcium-alginate precipitation.

3.2. Quantitative Analysis of Monosaccharide Components.
To further investigate the monosaccharide composition of extracted cSFP-C, HPLC was run and its retention time was used to quantify the monosaccharide amount normalized to glucose (Figure 2). The quantitative results are summarized specifically in Table 2. Predominantly fucose was found, and abundant galactose was a high component among different monosaccharides. This result was consistent with previous reported findings for components of fucose and galactose, which showed that fucose made up the largest proportion followed by galactose [30–32]. However, glucuronic acid content significantly decreased with 0.4 molar ratio to glucose, which indicated an optimized purity of fucoidan. Glucuronic acid content is much lower than those previous reported findings, perhaps due to the procedure for calcium-alginate precipitation [32, 33]. In addition, it was found that cSFP is composed of glucose, xylose, rhamnose, and mannose.

3.3. FT-IR Analysis.
The FT-IR spectrum provides important information about the conformation and functional groups of cSFP-C in Figure 3. cSFP-C exhibited a strong and broad area of absorption between 3600 and 3200 cm^{-1}, representing O-H stretching vibration. A band was observed at 1635 cm^{-1} for the carboxylate stretching [34]. The absorption peak at 3000~2800 cm^{-1} indicated the presence of the C-H stretching vibration. The signal at 1251 cm^{-1} could be associated with the asymmetric O=S=O stretching vibration of sulfate esters [30]. The absorption peak at 821 cm^{-1} was assigned to the sulfate groups [35].
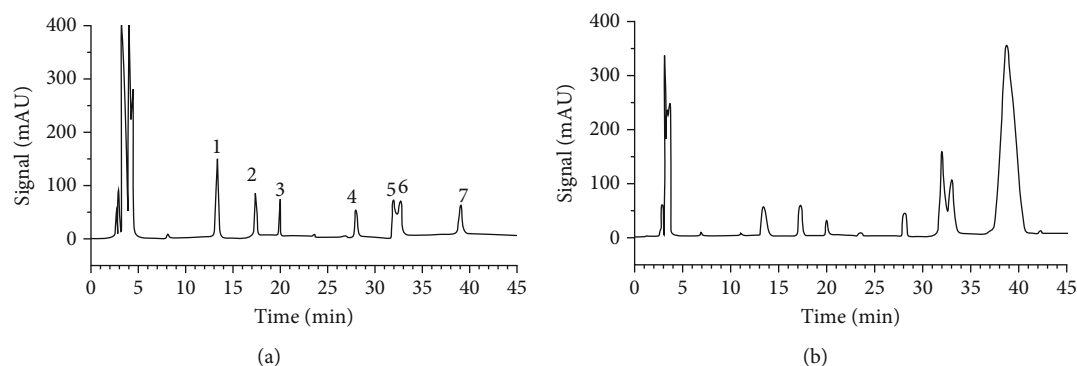
FIGURE 2: HPLC separation of PMP-labeled monosaccharide composition of cSFP-C: (a) monosaccharides standard; (b) cSFP-C. Peaks: 1: mannose; 2: rhamnose; 3: glucuronic acid; 4: glucose; 5: galactose; 6: xylose; 7: fucose.

TABLE 2: Molar ratio of monosaccharide composition in cSFP-C.

Glc	GlcA	Xyl	Rha	Man	Gal	Fuc
1.0	0.4	5.6	1.2	1.7	12.3	56.1

Notes: Glc: glucose; GlcA: glucuronic acid; Xyl: xylose; Rha: rhamnose; Man: mannose; Gal: galactose; Fuc: fucose.
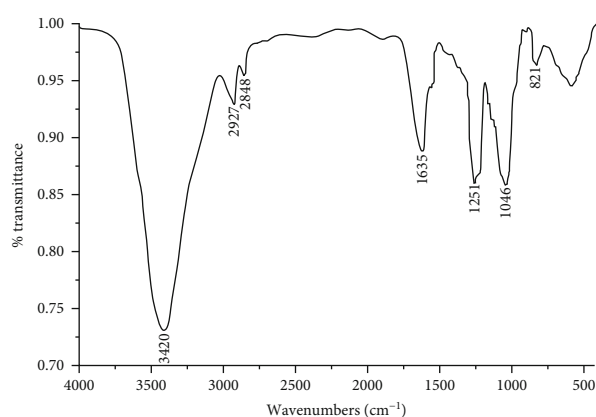
FIGURE 3: FT-IR spectrum of cSFP-C.

FIGURE 4: Scavenging effect on superoxide radicals by cSFP-C and cSFP-H. Values are means ± S.D. ($n = 3$).

3.4. Scavenging Activity of Superoxide Radical by cSFP-C. cSFP-C showed a significant scavenging ability on the superoxide radical in a concentration-dependent manner in Figure 4. Decreased absorbance and increased scavenging effect (%) were present as the cSFP-C concentration increased. All kinds of free radicals are generated in oxidative metabolism, in which the superoxide anion free radical is produced at the earliest [36]. Then, superoxide radical produces other free radicals through disproportionation reaction [37] and also causes lipid peroxidation [38]. Thus, the scavenging for superoxide radical is crucial for the protection of the cells from oxidative damage. As studied previously, hot water extraction, as the traditional procedure, has been widely investigated for the polysaccharide extraction from SF [39, 40]. However, Chen et al. [22] reported that hot water-extracted polysaccharides performed less free radical (superoxide radical) scavenging activity *in vitro* compared to cold water-extracted polysaccharides. In this study, it could be seen that the extracted cSFP-C showed good scavenging ability on the superoxide radical compared to cSFP-H (Figure 4). The result was consistent with the result reported by Chen et al. [22]. It indicated that cSFP-C might have some pharmacological effects according to its antioxidative activity.

3.5. cSFP-C Prevents Iopromide-Induced Renal Dysfunction in CIN Rats. As shown in Figure 5, levels of blood urea nitrogen (BUN) and creatinine of CIN rats were significantly higher than those of sham rats ($P < 0.05$), indicating that iopromide caused renal dysfunction. Compared with CIN rats, CIN+cSFP-C rats significantly reduced BUN and creatinine levels ($P < 0.05$), suggesting that cSFP-C preadministration played a role in renoprotection. Compared with sham rats, cSFP-C rats did not affect BUN and creatinine levels, suggesting that a high dose of cSFP-C had no renal injury. Sulfated polysaccharides, as the major bioactive components of seaweed, have demonstrated various biological effects. Li et al. [41] reported that sulfated polysaccharides from seaweed *Laminaria japonica* markedly decrease BUN and creatinine levels. Chen et al. [42] found that fucoidan from *Sargassum hemiphyllum* inhibits serum creatinine and improves renal function in mice with chronic kidney disease (CKD). Due to the high contents of sulfate radical and fucose, it was speculated that the reduced BUN and creatinine levels in

(a)

(b)
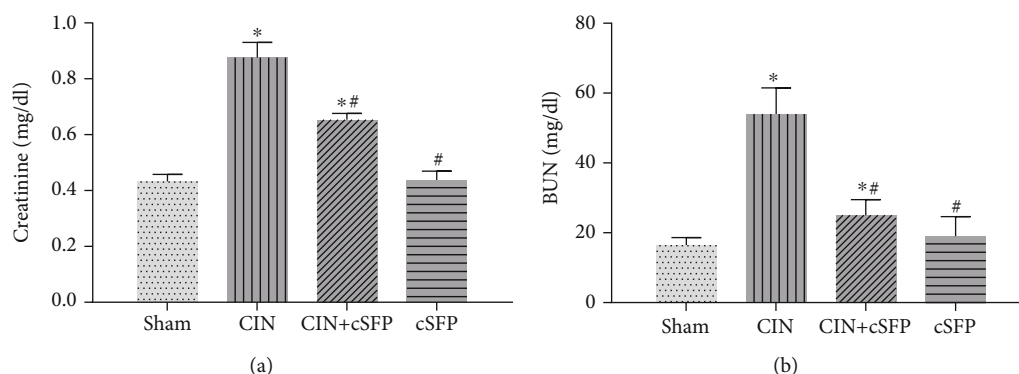
Figure 5: cSFP pretreatment mitigated renal injury against CIN: (a) serum creatinine concentration; (b) serum urea nitrogen concentration. $^*P < 0.05$ versus sham rats; $^\#P < 0.05$ versus CIN rats.

CIN+cSFP-C rats were partially due to the high content of fucoidan in cSFP-C.

3.6. Protective Effect of cSFP on the Kidney. As shown in Figure 6, in the sham group, no significant histological changes were observed, while CIN rats showed severe damage, including lesions of tubular necrosis and inflammatory cell infiltration. In the CIN+cSFP-C group, cSFP-C pretreatment significantly reduced these types of damage, indicating that cSFP-C could protect the kidney of CIN rats from damage. This result was in accordance with the renal biochemical results. It was reported that sulfated polysaccharides reduce renal tubulointerstitial fibrosis in CKD mice [42]. And low molecular weight fucoidan inhibits epithelial mesenchymal transition of human renal proximal tubular cells [43]. These results enlightened us to seek out the underlying mechanism for renoprotection of cSFP-C.

3.7. cSFP Protected the Kidney from Oxidative Stress. In order to evaluate whether cSFP-C protects renal tissue of CIN rats from oxidative stress, SOD activity and MDA content in renal tissue were detected. MDA content of CIN rats was significantly higher than that of sham rats, while SOD activity was significantly reduced ($P < 0.05$). Although the pathological mechanism of CIN has not been clearly elucidated, various studies have investigated that oxidative stress is an important cause of CIN [6, 44]. The direct toxicity of contrast agents leads to the ROS production, while the oxidative stress caused by the increasing free radicals leads to the apoptosis of renal tubules and glomerular cells [45]. These results in Figure 7 showed the deterioration on oxidative stress, suggesting the coincidence with the pathological deterioration. According to the mechanism of ROS-promoted development of CIN, the corresponding removal of ROS has been studied in preclinical and clinical studies. Sodium bicarbonate [46], n-acetylcysteine (NAC) [47], theophylline [48, 49], dopamine [50], furosemide [51], mannitol [52], and ascorbic acid [53] have been studied in the clinical prevention of CIN. In preclinical studies, the protective effects of melatonin [54], tocopherol [55, 56], and L-carnitine [57] have also been studied with regard to CIN. In this study, when cSFP-C was preadministrated, the MDA content was significantly decreased and SOD activity was
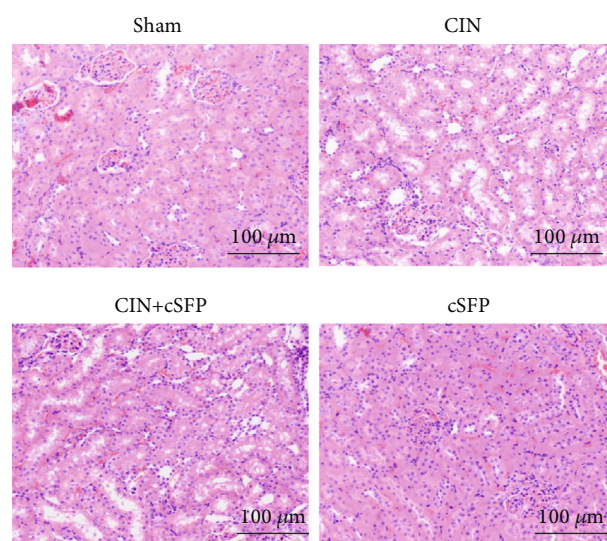
Figure 6: cSFP pretreatment attenuated the renal pathological damage in kidney tissues of CIN rats. Renal histological sections by H&E staining at 24 h CIN induction (100x).

significantly restored ($P < 0.05$). These results showed that preadministration of cSFP-C largely reduces the oxidative stress damage in kidneys of CIN rats and improves the endogenous antioxidative capacity of the kidneys. These results *in vivo* were also in accordance with the scavenging activity of the superoxide radical by cSFP-C *in vitro*. In addition, cSFP-C did not affect SOD activity and MDA content compared with the sham group.

4. Conclusion

In summary, the polysaccharides were purified from *Sargassum fusiforme* (SF) and contained abundant sulfate radical and predominant fucose, which indicated potential bioactivity. Then, the polysaccharides exhibited the scavenging activity for superoxide radical *in vitro*. According to the antioxidative effect, the polysaccharides demonstrated renoprotective properties against CIN *in vivo*. The pretreatment of cSFP-C could effectively improve biochemical indexes and pathological structures and correct the renal dysfunction

(a)   (b)
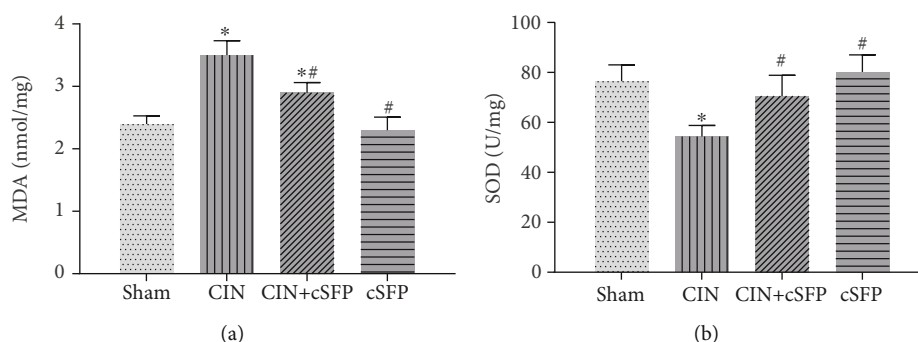
Figure 7: cSFP pretreatment reduced the renal oxidative stress in kidney tissues of CIN rats: (a) renal MDA concentration; (b) renal SOD activity. $^{*}P < 0.05$ versus sham rats; $^{\#}P < 0.05$ versus CIN rats.

and the abnormal levels of MDA and SOD. It can be speculated that the renoprotective effects of cSFP-C might be mediated by inhibition of oxidative stress.

Data Availability

All the data is available in the handwritten notebook documented in our lab.

Conflicts of Interest

The authors declare that there is no conflict of interest regarding the publication of this paper.

Acknowledgments

References

[1] J. R. Langabeer, T. D. Henry, D. J. Kereiakes et al., "Growth in percutaneous coronary intervention capacity relative to population and disease prevalence," *Journal of the American Heart Association*, vol. 2, no. 6, article e000370, 2013.

[2] Y. Yuan, H. Qiu, X. Y. Hu et al., "Relationship between high level of estimated glomerular filtration rate and contrast-induced acute kidney injury in patients who underwent an emergency percutaneous coronary intervention," *Chinese Medical Journal*, vol. 131, no. 17, pp. 2041–2048, 2018.

[3] Y. Liu, Y. H. Liu, J. Y. Chen et al., "Safe contrast volumes for preventing contrast-induced nephropathy in elderly patients with relatively normal renal function during percutaneous coronary intervention," *Medicine*, vol. 94, no. 12, article e615, 2015.

[4] R. Inokuchi, Y. Hara, H. Yasuda, N. Itami, Y. Terada, and K. Doi, "Differences in characteristics and outcomes between community- and hospital-acquired acute kidney injury: a systematic review and meta-analysis," *Clinical Nephrology*, vol. 88, no. 10, pp. 167–182, 2017.

[5] S. Ali-Hasan-Al-Saegh, S. J. Mirhosseini, Z. Ghodratipour et al., "Protective effects of anti-oxidant supplementations on contrast-induced nephropathy after coronary angiography: an updated and comprehensive meta-analysis and systematic review," *Kardiologia Polska*, vol. 74, no. 7, pp. 610–626, 2016.

[6] O. Ozturk, H. A. Eroglu, S. Ustebay, M. Kuzucu, and Y. Adali, "An experimental study on the preventive effects of N-acetyl cysteine and ozone treatment against contrast-induced nephropathy," *Acta Cirúrgica Brasileira*, vol. 33, no. 6, pp. 508–517, 2018.

[7] A. Pisani, E. Riccio, M. Andreucci et al., "Role of reactive oxygen species in pathogenesis of radiocontrast-induced nephropathy," *BioMed Research International*, vol. 2013, Article ID 868321, 6 pages, 2013.

[8] A. Diamantopoulos, I. Kyriazis, K. Geronatsiou et al., "Parstatin prevents renal injury following ischemia/reperfusion and radiocontrast administration," *American Journal of Nephrology*, vol. 36, no. 3, pp. 278–286, 2012.

[9] M. R. Ardalan, A. Rastegar, R. S. Tubbs, and M. M. Shoja, "Contrast-induced nephropathy as an indicator of diffuse endothelial dysfunction: introducing novel therapeutic options for decreasing the long-term mortality," *Medical Hypotheses*, vol. 69, no. 4, pp. 961-962, 2007.

[10] R. Solomon and H. L. Dauerman, "Contrast-induced acute kidney injury," *Circulation*, vol. 122, no. 23, pp. 2451–2455, 2010.

[11] X. F. Guan, Q. J. Chen, X. C. Zuo et al., "Contrast media-induced renal inflammation is mediated through HMGB1 and its receptors in human tubular cells," *DNA and Cell Biology*, vol. 36, no. 1, pp. 67–76, 2017.

[12] X. He, J. Yang, L. Li et al., "Atorvastatin protects against contrast-induced nephropathy via anti-apoptosis by the upregulation of Hsp27 in vivo and in vitro," *Molecular Medicine Reports*, vol. 15, no. 4, pp. 1963–1972, 2017.

[13] J. H. Rundback, D. Nahl, and V. Yoo, "Contrast-induced nephropathy," *Journal of Vascular Surgery*, vol. 54, no. 2, pp. 575–579, 2011.

[14] M. M. Sendeski, "Pathophysiology of renal tissue damage by iodinated contrast media," *Clinical and Experimental Pharmacology & Physiology*, vol. 38, no. 5, pp. 292–299, 2011.

[15] S. N. Heyman, C. Rosenberger, S. Rosen, and M. Khamaisi, "Why is diabetes mellitus a risk factor for contrast-induced nephropathy?," *BioMed Research International*, vol. 2013, Article ID 123589, 8 pages, 2013.

[16] Z. Zhao, G. Liao, Q. Zhou, D. Lv, H. Holthfer, and H. Zou, "Sulforaphane attenuates contrast-induced nephropathy in rats via Nrf2/HO-1 pathway," *Oxidative Medicine and Cellular Longevity*, vol. 2016, Article ID 9825623, 12 pages, 2016.

[17] R. Liang, Q. Zhao, G. Jian et al., "Tanshinone IIA attenuates contrast-induced nephropathy via Nrf2 activation in rats,"

Cellular Physiology and Biochemistry, vol. 46, no. 6, pp. 2616–2623, 2018.

[18] A. Börekçi, M. Gür, C. Türkoğlu et al., "Oxidative stress and paraoxonase 1 activity predict contrast-induced nephropathy in patients with ST-segment elevation myocardial infarction undergoing primary percutaneous coronary intervention," *Angiology*, vol. 66, no. 4, pp. 339–345, 2015.

[19] J. Y. Li, Y. J. Yu, K. Myungwoong et al., "Manipulation of cell adhesion and dynamics using RGD functionalized polymers," *Journal of Materials Chemistry B*, vol. 5, no. 31, pp. 6307–6316, 2017.

[20] Y. Li, T. Yang, Y. Yu et al., "Combinatorial library of chalcogen-containing lipidoids for intracellular delivery of genome-editing proteins," *Biomaterials*, vol. 178, pp. 652–662, 2018.

[21] L. Zhang, Y. Yu, C. Joubert et al., "Differentiation of dental pulp stem cells on Gutta-Percha scaffolds," *Polymers*, vol. 8, no. 5, p. 193, 2016.

[22] P. Chen, D. He, Y. Zhang et al., "*Sargassum fusiforme* polysaccharides activate antioxidant defense by promoting Nrf2-dependent cytoprotection and ameliorate stress insult during aging," *Food & Function*, vol. 7, no. 11, pp. 4576–4588, 2016.

[23] Y. Sun, H. Liang, G. Cai et al., "Sulfated modification of the water-soluble polysaccharides from *Polyporus albicans* mycelia and its potential biological activities," *International Journal of Biological Macromolecules*, vol. 44, no. 1, pp. 14–17, 2009.

[24] T. M. C. C. Filisetti-Cozzi and N. C. Carpita, "Measurement of uronic acids without interference from neutral sugars," *Analytical Biochemistry*, vol. 197, no. 1, pp. 157–162, 1991.

[25] M. M. Bradford, "A rapid and sensitive method for the quantitation of microgram quantities of protein utilizing the principle of protein-dye binding," *Analytical Biochemistry*, vol. 72, no. 1-2, pp. 248–254, 1976.

[26] M. Nishikimi, N. Appaji Rao, and K. Yagi, "The occurrence of superoxide anion in the reaction of reduced phenazine methosulfate and molecular oxygen," *Biochemical and Biophysical Research Communications*, vol. 46, no. 2, pp. 849–854, 1972.

[27] Chinese Pharmacopoeia Commission, *Chinese Pharmacopoeia*, People's Medical Publishing House, 4th ed edition, 2015.

[28] N. Wang, R. B. Wei, Q. P. Li et al., "Renal protective effect of probucol in rats with contrast-induced nephropathy and its underlying mechanism," *Medical Science Monitor*, vol. 21, pp. 2886–2892, 2015.

[29] A. Haug and O. Smidsrød, "Fractionation of alginates by precipitation with calcium and magnesium ions," *Acta Chemica Scandinavica*, vol. 19, pp. 1221–1226, 1965.

[30] L. Chen, P. Chen, J. Liu et al., "*Sargassum fusiforme* polysaccharide SFP-F2 activates the NF-κB signaling pathway via CD14/IKK and P38 axes in RAW264.7 cells," *Marine Drugs*, vol. 16, no. 8, p. 264, 2018.

[31] P. Hu, Z. Li, M. Chen et al., "Structural elucidation and protective role of a polysaccharide from *Sargassum fusiforme* on ameliorating learning and memory deficiencies in mice," *Carbohydrate Polymers*, vol. 139, pp. 150–158, 2016.

[32] B. Li, X. J. Wei, J. L. Sun, and S. Y. Xu, "Structural investigation of a fucoidan containing a fucose-free core from the brown seaweed, *Hizikia fusiforme*," *Carbohydrate Research*, vol. 341, no. 9, pp. 1135–1146, 2006.

[33] Y. Ye, D. Ji, L. You, L. Zhou, Z. Zhao, and C. Brennan, "Structural properties and protective effect of *Sargassum fusiforme* polysaccharides against ultraviolet B radiation in hairless Kun Ming mice," *Journal of Functional Foods*, vol. 43, pp. 8–16, 2018.

[34] T. M. A. Silva, L. G. Alves, K. C. S. de Queiroz et al., "Partial characterization and anticoagulant activity of a heterofucan from the brown seaweed *Padina gymnospora*," *Brazilian Journal of Medical and Biological Research*, vol. 38, no. 4, pp. 523–533, 2005.

[35] S. A. Foley, E. Szegezdi, B. Mulloy, A. Samali, and M. G. Tuohy, "An unfractionated fucoidan from *Ascophyllum nodosum*: extraction, characterization, and apoptotic effects in vitro," *Journal of Natural Products*, vol. 74, no. 9, pp. 1851–1861, 2011.

[36] V. Lobo, A. Patil, A. Phatak, and N. Chandra, "Free radicals, antioxidants and functional foods: impact on human health," *Carbohydrate Research*, vol. 4, no. 8, p. 118, 2010.

[37] B. H. J. Bielski and A. O. Allen, "Mechanism of the disproportionation of superoxide radicals," *The Journal of Physical Chemistry*, vol. 81, no. 11, pp. 1048–1050, 1977.

[38] M. Repetto, J. Semprine, and A. Boveris, "Lipid peroxidation: chemical mechanism, biological implications and analytical determination," in *Lipid Peroxidation*, Angel Catala, Intech Open, 2012.

[39] Y. H. Sun, X. L. Chen, S. Liu et al., "Preparation of low molecular weight *Sargassum fusiforme* polysaccharide and its anticoagulant activity," *Journal of Oceanology and Limnology*, vol. 36, no. 3, pp. 882–891, 2018.

[40] Y. J. Li, X. T. Fu, D. L. Duan, J. C. Xu, and X. Gao, "Comparison study of bioactive substances and nutritional components of brown algae *Sargassum fusiforme* strains with different vesicle shapes," *Journal of Applied Phycology*, vol. 30, no. 6, pp. 3271–3283, 2018.

[41] X. Li, J. Wang, H. Zhang, and Q. Zhang, "Renoprotective effect of low-molecular-weight sulfated polysaccharide from the seaweed *Laminaria japonica* on glycerol-induced acute kidney injury in rats," *International Journal of Biological Macromolecules*, vol. 95, pp. 132–137, 2017.

[42] C. H. Chen, Y. M. Sue, C. Y. Cheng et al., "Oligo-fucoidan prevents renal tubulointerstitial fibrosis by inhibiting the CD44 signal pathway," *Scientific Reports*, vol. 7, no. 1, article 40183, 2017.

[43] X. Li, X. Li, Q. Zhang, and T. Zhao, "Low molecular weight fucoidan and its fractions inhibit renal epithelial mesenchymal transition induced by TGF-β1 or FGF-2," *International Journal of Biological Macromolecules*, vol. 105, Part 2, pp. 1482–1490, 2017.

[44] C. Mamoulakis, K. Tsarouhas, I. Fragkiadoulaki et al., "Contrast-induced nephropathy: basic concepts, pathophysiological implications and prevention strategies," *Pharmacology & Therapeutics*, vol. 180, pp. 99–112, 2017.

[45] S. Detrenis, M. Meschi, S. Musini, and G. Savazzi, "Lights and shadows on the pathogenesis of contrast-induced nephropathy: state of the art," *Nephrology, Dialysis, Transplantation*, vol. 20, no. 8, pp. 1542–1550, 2005.

[46] M. Pakfetrat, L. Malekmakan, Z. Salmanpour, M. H. Nikoo, and P. Izadpanah, "Comparison of normal saline, Ringer's lactate, and sodium bicarbonate for prevention of contrast-induced nephropathy in patients with coronary angiography: a randomized double-blind clinical trial," *Indian Journal of Nephrology*, vol. 29, no. 1, pp. 22–27, 2019.

[47] Y. Feng, X. Huang, L. Li, and Z. Chen, "N-Acetylcysteine versus ascorbic acid or N-acetylcysteine plus ascorbic acid in preventing contrast-induced nephropathy: a meta-analysis," *Nephrology*, vol. 23, no. 6, pp. 530–538, 2018.

[48] M. Arabmomeni, J. Najafian, M. Abdar Esfahani, M. Samadi, and L. Mirbagher, "Comparison between theophylline, N-acetylcysteine, and theophylline plus N-acetylcysteine for the prevention of contrast-induced nephropathy," *ARYA Atherosclerosis*, vol. 11, no. 1, pp. 43–49, 2015.

[49] M. E. M. Bilasy, M. A. Oraby, H. M. Ismail, and F. A. Maklady, "Effectiveness of theophylline in preventing contrast-induced nephropathy after coronary angiographic procedures," *Journal of Interventional Cardiology*, vol. 25, no. 4, pp. 404–410, 2012.

[50] J. Choi, H. Lee, D. Chang et al., "Effect of dopamine on excretory urographic image quality and the prevention of contrast-induced nephropathy in dogs," *The Journal of Veterinary Medical Science*, vol. 63, no. 4, pp. 383–388, 2001.

[51] N. Duan, J. Zhao, Z. Li et al., "Furosemide with saline hydration for prevention of contrast-induced nephropathy in patients undergoing coronary angiography: a meta-analysis of randomized controlled trials," *Medical Science Monitor*, vol. 21, pp. 292–297, 2015.

[52] S. R. Majumdar, C. M. Kjellstrand, W. J. Tymchak, M. Hervas-Malo, D. A. Taylor, and K. K. Teo, "Forced euvolemic diuresis with mannitol and furosemide for prevention of contrast-induced nephropathy in patients with CKD undergoing coronary angiography: a randomized controlled trial," *American Journal of Kidney Diseases*, vol. 54, no. 4, pp. 602–609, 2009.

[53] E. Palli, D. Makris, J. Papanikolaou et al., "The impact of N-acetylcysteine and ascorbic acid in contrast-induced nephropathy in critical care patients: an open-label randomized controlled study," *Critical Care*, vol. 21, no. 1, p. 269, 2017.

[54] D. Onk, O. A. Onk, K. Turkmen et al., "Melatonin attenuates contrast-induced nephropathy in diabetic rats: the role of interleukin-33 and oxidative stress," *Mediators of Inflammation*, vol. 2016, Article ID 9050828, 10 pages, 2016.

[55] M. Monami, A. Cignarelli, S. Pinto et al., "Alpha-tocopherol and contrast-induced nephropathy: a meta-analysis of randomized controlled trials," *International Journal for Vitamin and Nutrition Research*, pp. 1–9, 2019.

[56] S. Kongkham, S. Sriwong, and A. Tasanarong, "Protective effect of alpha tocopherol on contrast-induced nephropathy in rats," *Nefrología*, vol. 33, no. 1, pp. 116–123, 2013.

[57] M. Boyacioglu, H. Turgut, C. Akgullu, U. Eryilmaz, C. Kum, and O. A. Onbasili, "The effect of L-carnitine on oxidative stress responses of experimental contrast-induced nephropathy in rats," *The Journal of Veterinary Medical Science*, vol. 76, no. 1, pp. 1–8, 2014.

Research Article

Effect of Microwave Irradiation on Polyvinyl Alcohol as a Carrier of Silver Nanoparticles in Short Exposure Time

Dat Tan Nguyen [ID]**, Khanh Loan Ly, Nam Minh-Phuong Tran, Minh Hieu Ho, Trang Thi-Phuong Tran, Thi-Hiep Nguyen** [ID]**, Dang Ngọc Thao Nhi, and Van Toi Vo**

Department of Biomedical Engineering, Vietnam National University-Ho Chi Minh City (VNU-HCM)-International University, Ho Chi Minh City 700000, Vietnam

Correspondence should be addressed to Thi-Hiep Nguyen; nthiep1981@gmail.com

Microwave heating of Ag^+ in polyvinyl alcohol (PVA) is an effective method to synthesize silver nanoparticles (AgNPs), a broad-range antibacterial agent. However, the microwave may cause PVA solution to dry out and degrade. This study is aimed at investigating the effect of microwave irradiation on different concentrations of PVA in PVA/Ag^+ solution in short periods of exposure. Fourier-transform infrared (FTIR) spectroscopy was employed to evaluate chemical changes of samples with different exposure times and PVA concentration. The results confirm the redox reaction of Ag^+ with PVA. In addition, Ag^+ reduces the rate of hydrolysis of PVA, and the ether bridges are limited by the spatial structure.

1. Introduction

Antibiotic resistance has become one of the most significant health threats because microbes evolve rapidly against our antibiotics while the development of new antibiotics takes decades. Consequently, the old drugs—including metal and their salts that were used to treat infections before the era of antibiotics dominance—have once again become the research focus [1]. Among metals such as silver, copper, zinc, or gold, silver, whose applications have been widely studied [2, 3], has a broad range of antibacterial properties and has relatively low toxicity. Silver nanoparticles (AgNPs)—whose scale is from 1 to 100 nm—also exhibit good biological interaction. However, many studies proved that inappropriate size and concentration of AgNPs are toxic to mammalian cells [4–6]. Therefore, rather than using pure AgNPs, a carrier or stabilizer to control the size and enhance the surface interaction is generally necessary [7–11].

Polyvinyl alcohol (PVA)—a hydroxy polymer with the idealized formula $[CH_2CH (OH)]_n$—possesses many excellent features such as biocompatibility, biodegradability,

water-solubility, and gel-forming. However, they are thermally unstable. During the heat treatment, two major stages occur: elimination reactions and chain scission and cyclization [12]. Elimination reaction produces reactive carbon atoms along the polymer chain, which makes PVA highly reactive to other chemicals during the thermal process. Taking the advantages of this phenomenon, adding Ag^+ ions in PVA solution will cause a redox reaction between Ag^+, an oxidant, and reactive PVA, a reductant. In previous studies, PVA was proven to be a potential carrier/stabilizer for the synthesis of AgNPs [9]. Moreover, thermal stimulation of PVA could occur without the need of additional catalyst or cross-linker that may induce harmful effects to the body [9].

There are two primary techniques to induce reactions: conventional heating and microwave heating. Compared with conventional heating, microwave heating is a more versatile and economical method with reduced reaction times [13]. Bernal et al. investigated the effect of microwave on PVA with ethylene glycol as the solvent from 4 min to 60 min [12]. However, overexposure of microwave irradiation causes parching and total degradation of PVA. In the

Table 1: List of samples.

Abbreviation	PVA concentration (%)	Exposure time (s)	AgNO₃ added
P8	8	0	No
P8T60	8	60	No
P8T90	8	90	No
P6T60Ag	6	60	Yes
P8T60Ag	8	60	Yes
P10T60Ag	10	60	Yes
P6T90Ag	6	90	Yes
P8T90Ag	8	90	Yes
P10T90Ag	10	90	Yes

(a)

(b)
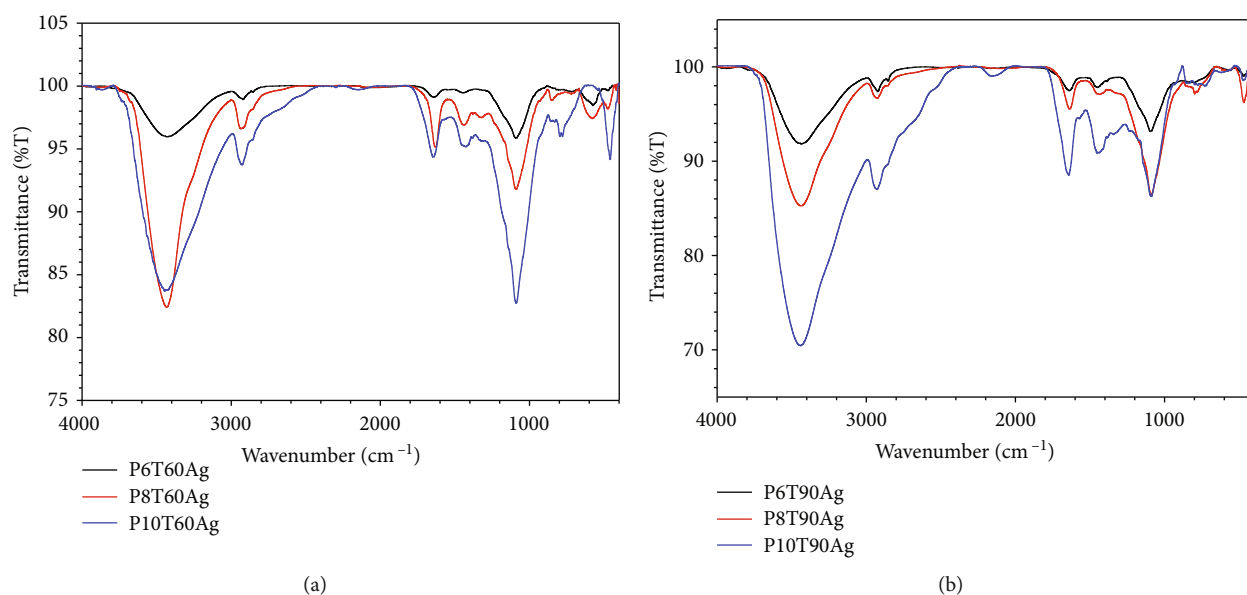
Figure 1: FTIR spectra of (a) P6T60Ag, P8T60Ag, and P10T60Ag and (b) P6T90Ag, P8T90Ag, and P10T90Ag.

application as a carrier of AgNPs, the exposure time of microwave for PVA is a significant factor, and its effects have not been well-understood yet.

In this study, we investigate the effect of microwave irradiation on different concentrations of PVA in PVA/Ag⁺ solution in short periods of exposure.

2. Materials and Methods

2.1. Materials. Polyvinyl alcohol (PVA; hydrolysis degree of 99.0–99.8%) was purchased from Sigma-Aldrich, USA. Silver nitrate ($AgNO_3 \geq 99\%$) was obtained from Guangdong, China. The microwave oven is a magnetron MM250 (Whirlpool Corp., USA).

2.2. Sample Preparation. Typically, aqueous solutions of 6 wt%, 8 wt%, and 10 wt% of fully hydrolyzed PVA were prepared by dissolving PVA in distilled water at 75°C. The 1% silver nitrate solution was added to the PVA solution so that the silver concentration was up to 120 ppm. Subsequently,

the PVA solution was microwaved at 800 W for determined periods. All samples are listed below in Table 1.

2.3. FTIR Measurement. Samples were freeze-dried into powder in order to avoid the interference of the hydrogen bonding of water molecules. Then, their FTIR spectra were obtained using a FTIR analyzer (PerkinElmer Spectrum GX, USA).

3. Results and Discussion

The original PVA was characterized with a broad, strong O-H stretching within the range 3700-3000 cm⁻¹, a medium aliphatic C-H stretching peak within the 2920-2930 cm⁻¹ region, and along with C=O stretch (around 1640 cm⁻¹), C-O stretch (1088 cm⁻¹), and CH_2 and CH_3 bending (1438 cm⁻¹). All the peaks of PVA spectrum reappeared in other samples (Figures 1 and 2), which proved that the effects occurred partially in the PVA structure and PVA can still maintain its properties under microwave in short periods of exposure.

(a)

(b)
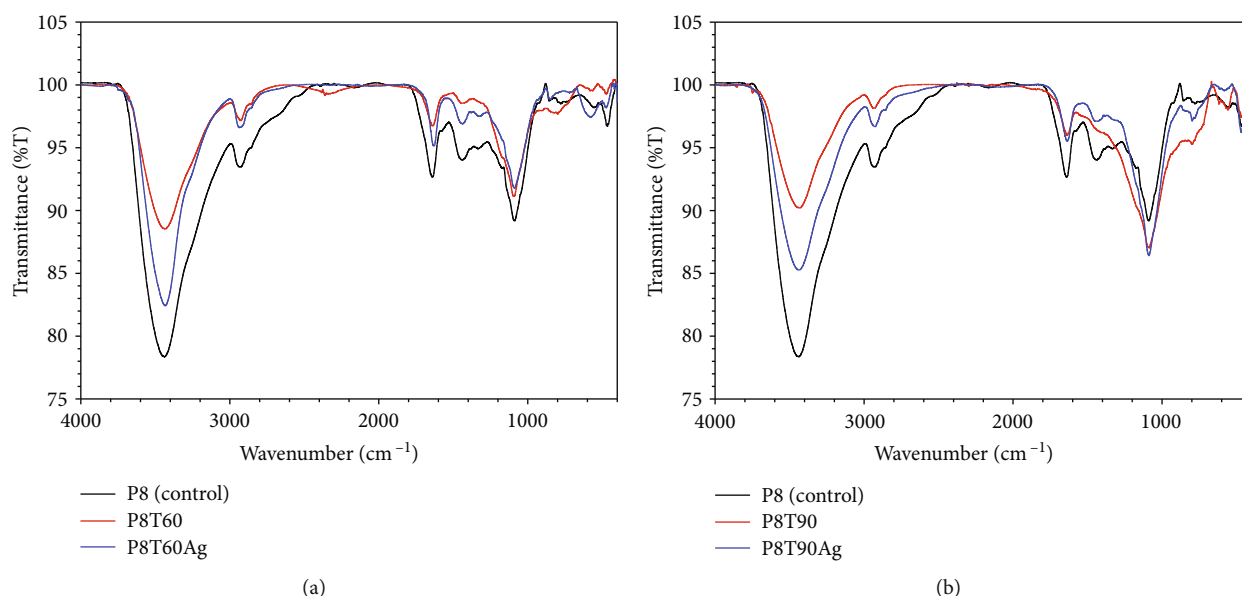
FIGURE 2: FTIR spectra of (a) P8, P8T60, and P8T60Ag and (b) P8, P8T90, and P8T90Ag.

Figure 3 displays the FTIR spectra of microwaved and nonmicrowaved of freeze-dried of 8 wt% PVA solution. As the time of microwave exposure increases, the absorbance of O-H stretch, C-H stretch, and CH_2/CH_3 bend decreases. This reproduces the results in previous reports that PVA molecule undergoes elimination reaction and hydroxyl groups decrease [9, 12]. Subsequently, some C-OH groups theoretically form double bonds C=O causing the reduction of CH_2 and C-H stretch, while some may lead to polymer dehydration with the formation of ether groups between PVA molecules, which is shown by the changes in peak around C-O stretch. Here, C=O stretching of the P8 sample shows the existence of acetate groups. PVA is the product of the hydrolysis process of polyvinyl acetate. This means that the reaction may be incomplete leaving residual acetate groups [12]. Therefore, the changes at this peak may be the replacement of acetate group with ketone or aldehyde group. Notably, the absorbance of C-O stretch does not follow the order of exposure time. This phenomenon expresses the relationship between the reduction of C-OH groups and the formation of C-O groups with respect to time of exposure. To be specific, when PVA is treated with microwave, an increase of C=O groups parallelly reduces C-OH group, thus lowering the absorbance; however, after 90 s of microwave exposure, ether group C-O form and its absorbance of light is higher and enhances the absorbance at peak 1088 cm^{-1}.

Figure 1 depicts the FTIR spectra of freeze-dried PVA/-silver nitrate solution with the concentration of 6 wt%, 8 wt%, and 10 wt% under different periods of microwave irradiation. The intensities of O-H bonds as well as other bonds correlate with the concentration of PVA in the microwaved PVA/silver nitrate solutions, except for C-O peaks after 90 s of microwave exposure. It can be considered that the cross-linking reaction of PVA molecules is limited even when the concentration of PVA increases. As mentioned above, after 90 s of microwave exposure, the ether bridges between PVA molecules form. However, compared between 60 s and 90 s
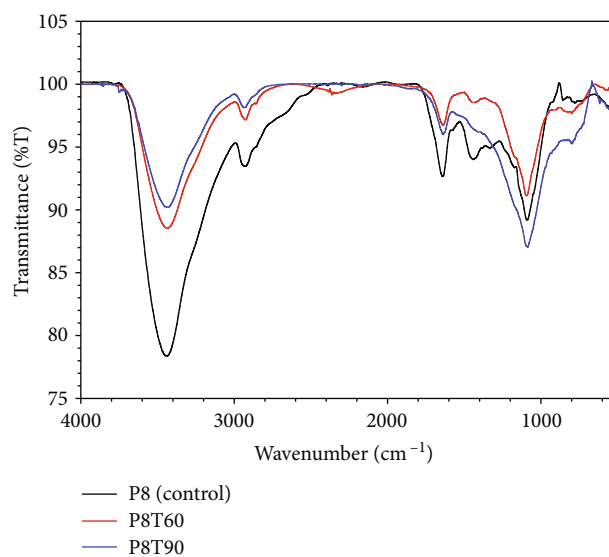
FIGURE 3: FTIR spectra of P8, P8T60, and P8T90.

of microwave exposure, the PVA/Ag$^+$ solution is provided with more energy after being treated with microwave for 90 s; however, C-O peak of P8T90Ag matches that of P10T90Ag. The reason could be that the spatial structure of conjugated PVA prevents themselves from further intermolecular reaction. In other words, the O-H group is continuously broken, but the rate of C-O ether group formation is decreased, causing the equal transmittance at peak 1088 cm^{-1} (as shown in Figure 2).

Figure 2 illustrates the FTIR results of PVA at 8 wt% under microwave irradiation at 60 s and 90 s with or without adding the AgNO$_3$ solution. After 60 s or 90 s of microwave exposure, the transmittances of O-H stretching of samples having Ag$^+$ (P8T60Ag and P8T90Ag) are lower than those

of samples not having Ag (P8T60 and P8T90). This means that at the same time of microwave exposure, Ag^+ in PVA solution prevents the degradation of PVA. It may be caused by the redox reaction of Ag^+ and PVA when part of the energy provided by microwave process may be used for the redox reaction. Moreover, the existence of Ag does not affect the formation of ether bridges as shown in the C-O stretching of those samples.

Stability of nanoparticles is strongly dependent on the viscosity of the gels. When PVA is considered itself, the crosslinking between PVA molecules by ether groups is the only chemical parameter; however, it plays a minor role due to its limitation of spatial complexity. This promotes the combination of PVA with other polymers to crosslink instead of PVA itself.

4. Conclusion

The aim of this work is to investigate the chemical changes in PVA/Ag^+ solution under a short period of microwave irradiation. The results have shown that PVA under microwave is a potential method to synthesize AgNPs. Within a short period of time, PVA still maintains O-H groups, which is the basis of its properties. Ether bridges, intermolecular bonds, are considered minor impacts on PVA crosslinking because of their limitation in spatial structure. The existence of Ag^+ reduces the rate of hydrolysis of PVA.

Data Availability

The data used to support the findings of this study are included within the article.

Conflicts of Interest

The authors declare that there is no conflict of interest regarding the publication of this paper.

Acknowledgments

References

[1] K. Zheng, M. I. Setyawati, D. T. Leong, and J. Xie, "Antimicrobial silver nanomaterials," *Coordination Chemistry Reviews*, vol. 357, pp. 1–17, 2018.

[2] H. Bahadar, F. Maqbool, K. Niaz, and M. Abdollahi, "Toxicity of nanoparticles and an overview of current experimental models," *Iranian Biomedical Journal*, vol. 20, no. 1, pp. 1–11, 2016.

[3] M. Yasuyuki, K. Kunihiro, S. Kurissery, N. Kanavillil, Y. Sato, and Y. Kikuchi, "Antibacterial properties of nine pure metals: a laboratory study using Staphylococcus aureus and Escherichia coli," *Biofouling*, vol. 26, no. 7, pp. 851–858, 2010.

[4] R. Vazquez-Muñoz, B. Borrego, K. Juárez-Moreno et al., "Toxicity of silver nanoparticles in biological systems: does the complexity of biological systems matter?," *Toxicology Letters*, vol. 276, pp. 11–20, 2017.

[5] W. H. De Jong, L. T. M. Van Der Ven, A. Sleijffers et al., "Systemic and immunotoxicity of silver nanoparticles in an intravenous 28 days repeated dose toxicity study in rats," vol. 34, 2013.

[6] M. Akter, M. T. Sikder, M. M. Rahman et al., "A systematic review on silver nanoparticles-induced cytotoxicity: physico-chemical properties and perspectives," *Journal of Advanced Research*, vol. 9, pp. 1–16, 2018.

[7] R. A. Franco, T. H. Nguyen, and B.-T. Lee, "Preparation and characterization of electrospun PCL/PLGA membranes and chitosan/gelatin hydrogels for skin bioengineering applications," *Journal of Materials Science: Materials in Medicine*, vol. 22, no. 10, pp. 2207–2218, 2011.

[8] T.-H. Nguyen, Y.-H. Kim, H.-Y. Song, and B.-T. Lee, "Nano Ag loaded PVA nano-fibrous mats for skin applications," *Journal of Biomedical Materials Research Part B: Applied Biomaterials*, vol. 96B, no. 2, pp. 225–233, 2011.

[9] N. T. Hiep, H. C. Khon, V. V. T. Niem et al., "Microwave-assisted synthesis of chitosan/polyvinyl alcohol silver nanoparticles gel for wound dressing applications," *International Journal of Polymer Science*, vol. 2016, Article ID 1584046, 11 pages, 2016.

[10] T. T. Nhi, H. C. Khon, N. T. T. Hoai et al., "Fabrication of electrospun polycaprolactone coated with chitosan-silver nanoparticles membranes for wound dressing applications," *Journal of Materials Science: Materials in Medicine*, vol. 27, no. 10, pp. 156–156, 2016.

[11] T.-H. Nguyen, K.-H. Lee, and B.-T. Lee, "Fabrication of Ag nanoparticles dispersed in PVA nanowire mats by microwave irradiation and electro-spinning," *Materials Science and Engineering: C*, vol. 30, no. 7, pp. 944–950, 2010.

[12] A. Bernal, I. Kuritka, V. Kasparkova, and P. Saha, "The effect of microwave irradiation on poly(vinyl alcohol) dissolved in ethylene glycol," *Journal of Applied Polymer Science*, vol. 128, no. 1, pp. 175–180, 2013.

[13] J. P. Cook, G. W. Goodall, O. V. Khutoryanskaya, and V. V. Khutoryanskiy, "Microwave-assisted hydrogel synthesis: a new method for crosslinking polymers in aqueous solutions," *Macromolecular Rapid Communications*, vol. 33, no. 4, pp. 332–336, 2012.

Review Article

Polymers for Regenerative Medicine Structures Made via Multiphoton 3D Lithography

Greta Merkininkaitė,[1,2] **Darius Gailevičius,**[1,3] **Simas Šakirzanovas,**[2]
and Linas Jonušauskas [ID][1,3]

[1]*Femtika, Sauletekio Ave. 15, Vilnius LT-10224, Lithuania*
[2]*Faculty of Chemistry and Geoscience, Vilnius University, Naugarduko Str. 24, Vilnius LT-03225, Lithuania*
[3]*Laser Research Center, Physics Faculty, Vilnius University, Sauletekio Ave. 10, Vilnius LT-10223, Lithuania*

Correspondence should be addressed to Linas Jonušauskas; linas@femtika.lt

Multiphoton 3D lithography is becoming a tool of choice in a wide variety of fields. Regenerative medicine is one of them. Its true 3D structuring capabilities beyond diffraction can be exploited to produce structures with diverse functionality. Furthermore, these objects can be produced from unique materials allowing expanded performance. Here, we review current trends in this research area. We pay particular attention to the interplay between the technology and materials used. Thus, we extensively discuss undergoing light-matter interactions and peculiarities of setups needed to induce it. Then, we continue with the most popular resins, photoinitiators, and general material functionalization, with emphasis on their potential usage in regenerative medicine. Furthermore, we provide extensive discussion of current advances in the field as well as prospects showing how the correct choice of the polymer can play a vital role in the structure's functionality. Overall, this review highlights the interplay between the structure's architecture and material choice when trying to achieve the maximum result in the field of regenerative medicine.

1. Introduction

Additive manufacturing-based 3D printing is a revolutionizing field of technology which is gaining a substantial foothold in industry [1]. It offers new possibilities in producing various structures or entire devices in a relatively short time, minimizing the time from the idea to the final physical object. There are numerous different ways to realize the additive manufacturing method [1]; however, multiphoton polymerization-based 3D laser lithography (3DLL) stands out among all other current 3D printing techniques. The idea behind this technology is to sharply focus a laser (in most cases, femtosecond (fs)) beam into a special photoactive material initiating highly localized photomodification *via* multiphoton absorption and/or other related nonlinear light-matter interactions [2]. It combines resolution below the diffraction limit [3, 4], virtually no limitations to the 3D architecture of an object with the structuring process not bound to layer-by-layer printing [5, 6], and a huge variety

of the materials that could be used [7, 8]. Due to this, it was used in numerous fields, which include photonics [9, 10], microoptics [11, 12], micromechanics [13, 14], microfluidics [5, 15], and biomedicine [16, 17].

One of the key attributes in this technology is the vast array of suitable materials [7, 8]. Indeed, the requirements for the materials applicable to 3DLL are rather minimal: they have to be transparent to the laser wavelength and must possess absorption characteristics suitable for multiphoton absorption, which leads to photopolymerization. For this reason, materials such as acrylates [18], epoxies [19], hydrogels [20], hybrids [21], or biopolymers [22] were structured through the years using 3DLL. The correct choice of the material sometimes can be a main issue in a specific application. Thus, when talking about 3DLL and multiphoton polymerization, polymers and their properties should be one of the key aspects which needs to be addressed.

Among other 3DLL applications, regenerative medicine (RM) stands out as one with the most promise and possible

implications for everyday life. RM can be defined as the field which aims to replace, engineer, or regenerate human cells, tissues, or organs to restore or establish their normal functions [23]. However, the combination of achievable resolution, freedom of design, and applicable materials made RM one of the key research areas where 3DLL produced structures are being tested [24–26]. It enables to create objects that could help heal damaged tissue or even replace entire segments of the body. Besides the impressive possibilities, a lot more consideration has to be made in choosing both the geometry of the structure and the suitable polymer. The latter, alongside the two requirements mentioned previously, also have to be biocompatible and/or have properties beneficial for RM. Furthermore, RM research relies on structures with sizes well into the mm scale [16, 27, 28] and statistical testing based on simultaneous examination of multiple structures. This requires high-throughput fabrication. Thus, in RM applications, deep understanding of 3DLL technology and polymers is mandatory.

The main goal of this review is to explore 3DLL structurable polymers in the light of RM application. In order to present the reader with all the necessary information, we start by briefly introducing the basics of 3DLL technology. This includes both a brief discussion of underlying physical phenomena and the engineering required to realize it practically. Then, we proceed to 3DLL materials. Here, we discuss the main categories of polymers used in 3DLL. Photoinitiators (PIs) are also discussed in some detail because the correct choice of substance can lead to some very desirable (for instance, high throughput) or adverse (toxicity) effects. Additionally, the possibilities of polymer functionalization will follow. After that, various biomedical applications are shown with main attention on how in each case the correctly chosen material benefits it. Finally, we conclude by providing an outlook for the perspectives in the field, highlighting some of the challenges and opportunities currently present in this area. Relevant connections to other fields or structuring techniques are presented through the text to reference the usage of 3DLL in RM in the broader, more complete way. Finally, while this review is dedicated to RM, 3DLL was used with huge success in other biology and medicine-related fields, such as microfluidics [29] and in fabricating microneedles [30]. In order to avoid confusion, these areas will not be discussed in detail and only referenced in the context relevant to RM.

2. Multiphoton 3D Lithography

We will begin the review by discussing the fundamentals of 3DLL. These include mechanisms of multiphoton excitation, the kinetics of polymerization reaction, and which practical setups are required to realize it.

2.1. Multiphoton Excitation. In standard UV and stereolithography, the polymerization reaction is induced *via* linear one-photon absorption (Figure 1(a)) and the structure is formed layer by layer [1]. In that case, the photon energy E_p is equal or greater than the bandgap of the material E_g.
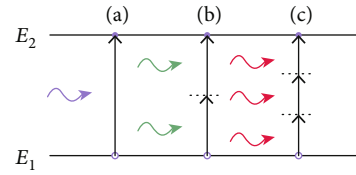
FIGURE 1: Energy level diagrams of one- (a), two- (b), and three- (c) photon absorption. Solid lines represent real arbitrary energy levels E_1 and E_2; dotted lines represent virtual states.

Keeping in mind that $E_p = h\nu = hc/\lambda$, it means that a shorter wavelength (λ) is needed. Here, we also introduced ν—the frequency of laser light. In most cases, UV light sources with $\lambda < 350$ nm are used. The absorption of the photon causes the electron to be exited from an energy state corresponding to the valence band to a state in the conduction band. This might lead to a multitude of outcomes. For instance, an electron might return to the valence band while heating up the material or emitting another photon causing fluorescence. However, it can also alter the chemical bond inducing chemical reaction. In the case of lithography, it is the polymerization reaction that cross-links the material. The exact pathways of such reactions will be discussed later. Light is a potent tool to induce such reactions because it can be done on-demand in localized regions. It is also a contactless method, meaning that there is no contamination to the sample or material by the processing tool.

One photon absorption has some distinct disadvantages. While collimated light can induce polymerization reaction in the relatively big (up to cm) area with high repeatably [31], achieving true 3D shapes is tricky. The standard way used in stereolithography is stacking 2D layers on top of each other. This leads to the necessity to use supports if free-hanging features are made [32]. Another way is using tilted/rotated samples [33]. Then, more geometries become available, yet it is still limited and rather complex process. Also, resins need to be liquid in order to cast a new layer after the previous one is done. Furthermore, if biomaterials are used, UV light might induce damage to the mixed-in living organisms. Therefore, direct bioprinting potential is limited. Finally, due to the nature of such polymerization, relatively significant amounts of unpolymerized resin might remain in the structure. As such resins are very chemically active, they might make manufactured structures toxic [34]. Thus, while one-photon absorption is a powerful tool for manufacturing various structures, including medical ones, there are also some severe limitations.

Linear absorption can be induced even with the low power noncoherent light sources. However, if the light intensity is increased, nonlinear absorption can take place. While such interaction was predicted as early as 1931 [35], it took the creation of the laser to demonstrate nonlinear absorption and subsequent fluorescence [36] experimentally. The absorption during this interaction is induced by the absorption of two or more photons *via* virtual levels (Figure 1(b)). Due to the extremely short lifetime of the virtual levels (~fs [37]), photons have to be absorbed almost simultaneously.

This leads to two important conclusions. First, such interaction is possible only with light intensities that are high enough ($>$GW/cm^2). Second, the probability of multiphoton interaction increases with the decrease in the number of photons involved in the single absorption event. Thus, the two-photon absorption (TPA) can be considered as the most likely process. This is well reflected in the fact that sometimes 3D manufacturing technology discussed in this article is called two-photon polymerization (2PP/TPP). For the sake of simplicity in this article, we will consider only this effect unless otherwise specified.

In TPA case, the number of photons absorbed n_p per time t can be calculated using the following equation:

$$\frac{dn_p}{dt} = \sigma_2 N F^2. \tag{1}$$

Here, σ_2 is the TPA cross-section of a particular material (quantified by Göppert-Mayer units, GM $= 50^{-50}$ cm^4 s), N is the density of the absorbing component, and F is the photon flux which can be defined as $F = I/h\nu$. From Equation (1), we can draw conclusions about what practical considerations should be made when trying to apply TPA for polymerization. First, the photon absorption rate is proportional to I^2, making excessive I one of the main considerations. The N should also be sufficient for the reaction. Finally, the material needs to be reactive enough to have high σ_2. The first requirement is realized using an appropriate processing setup, the second and third by tuning the material properties. The nonlinearity of the process behind 3DLL is the key to achieving fabricated features below the diffraction limit as the threshold I might be well below the size of the laser spot. Due to it, sub-100 nm lines were directly structured using 3DLL [3, 4].

For the final note, it is important to stress that TPA is only one of many light-matter interaction regimes that might appear when matter is exposed to high I. Higher-order absorption can take place [38, 39]. Also, if the pulse duration is long enough, one can expect avalanche ionization to become comparable or even surpass TPA in chemical bond cleavage [2, 40]. Finally, in some cases, thermal effects can start to have an impact on the reaction [41, 42]. Keeping in mind all of this and the fact that there is an active discussion in the field about the nature and impact of some of these processes, one must be careful when naming discussed technology simply as 2PP/TPP. Using multiphoton 3D lithography or just 3DLL terms are a lot more general and correct options. This is especially true if exotic materials or nonstandard laser sources are used.

2.2. Polymerization Mechanisms. Knowing the principles that are important for understanding photoexcitation, we can now proceed to the photopolymerization process itself. The main goal of using light in lithography is to induce photocleavage of the chemical bond and initiation of photochemical reactions. As mentioned before, this is done by the multiphoton process in 3DLL. Depending on the peculiarities of the material, it produces radicals or cations. In turn, polymerization reactions can be divided into radical and cat-

ionic polymerization [43]. Schematics of both processes are shown in Figure 2.

In the case of radicals, after they are formed, they can proceed to interact directly with other species in the material or form secondary radicals *via* hydrogen abstraction. Various chemical bonds can be cleaved this way, including C-C, C=O, C-S, or C-Cl to name a few. In the majority of cases (but not necessarily always), PI is used for this task. Radical generating PIs can be further classified into type I and type II [44]. Type I PIs generate radicals directly after light absorption, while type II requires the presence of some other constitutes in the material like amines or alcohols. Radicals are then generated after these additional constitutes transfer hydrogen atoms to the PI. Hydrogen abstraction involves aromatic ketone which, after light exposure, forms ketyl radical and donor radical. In those cases, the hydrogen donor radical is responsible for initiating polymerization reaction with ketyl radical couples into a growing polymer chain [45]. As the number of radicals increases, the probability of their collision rises accordingly [46]. After such interaction, radicals are deactivated, and the reaction is terminated. The interplay between radicals can take several different paths. Combination of two active chain results in one long chain. Alternatively, an active chain end can interact with an initiator radical, or radical disproportionation can happen, in which two radicals react to form two different non-radical products by transferring hydrogen from one chain end to the another [47]. Furthermore, radicals can interact with quenchers, for instance, stable radicals, easily reduced or oxidized materials, and salts of some metal [48]. Oxygen also can induce the termination of the polymerization reaction which is exploited in modern stereolithography [49].

In the cation case, after photoexcitation, the charge is transferred to the monomer. It then becomes reactive and can interact with other monomers leading to polymerization. Some of the most popular cation PIs include Brønsted acids such as arenediazonium, diaryIodonium, and various sulfonium salts [50]. This is rather problematic in the light of RM as such initiators generate protonic acids that have an adverse impact on cell cultures [51]. In the cationic case, the reaction ends with a combination of an anionic fragment from the counterion with the propagating chain end, as shown in Figure 2.

While in most cases the excitation is discussed in more details, one must not underestimate the importance of termination of polymerization reactions. If polymerization reaction is not properly terminated, it can expand beyond the selectively exposed region, nullifying the intent of spatially selective lithography [52]. On the other hand, smart usage of quenching mechanisms can significantly improve the technology. For instance, first stereolithography machines were based on a resin reservoir with the lowering platform. This required a massive tank of resin to be available at all times, making the whole process less convenient [1]. However, as oxygen is the quencher to most photolithographic materials, in modern 3D printers, structuring is done with only a thin layer of polymer over a transparent, but oxygen access-restricting, window. Then, the printing platform can be raised up out of the resin, and due to quenching, the

	Initiation	Propagation	Termination
Radical:	Type I: $PI + h\nu \longrightarrow R^*_{(1)} + R^*_{(2)}$ Type II: $PI + h\nu \longrightarrow R^* + product$ $R^* + M \longrightarrow MR^*$	$MR^* + nM \longrightarrow M_{n+1}R^*$	$M_{n+1}R^* + M_{n+1}R^* \longrightarrow products$ $M_{n+1}R^* + R^* \longrightarrow products$ $M_{n+1}R^* + Q \longrightarrow products$
Cationic:	$(A\text{-}B)^+ + h\nu \longrightarrow A^{*+} + B^*$ $A^{*+} + RH \longrightarrow AH^+ + R^*$ $AH^+ \longrightarrow A + H^+$ $A^{*+} + M \longrightarrow {}^*A\text{-}M^+$ $H^+ + M \longrightarrow H\text{-}M^+$	${}^*A\text{-}M^+ + nM \longrightarrow {}^*A\text{-}M^+_{n+1}$ $H\text{-}M^+ + nM \longrightarrow H\text{-}M^+_{n+1}$	${}^*A\text{-}M^+_{n+1} + X^- \longrightarrow products$ $H\text{-}M^+_{n+1} + X^- \longrightarrow products$ ${}^*A\text{-}M^+_{n+1} + X^- + Q \longrightarrow products$
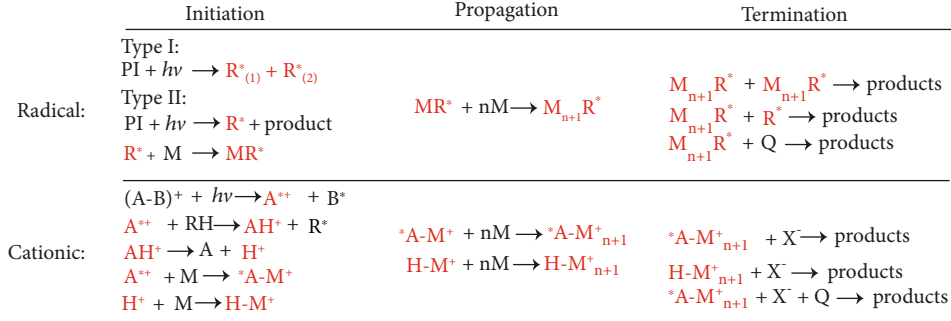
FIGURE 2: Schematics of radical and cation polymerization reactions initiated by one-photon absorption. $h\nu$: absorbed photon; R^* and B^*: free radicals; M: monomer; $M_{n+1}R^*$ and ${}^*A\text{-}M^+_{n+1}$: neutral and cationic macroradicals, respectively; Q: quencher; $(A\text{-}B)^+$: cationic initiator; A^{*+}: cationic radical; AH^+: protonized cation; RH and A: neutral molecules; H^+: proton; $H\text{-}M^+$: protonized monomer; $H\text{-}M^+_{n+1}$: protonized polymer; X^-: counterion. Red markings show the active ingredient that is either causing the reaction or the result of it.

structure does not adhere to the window [49]. For 3DLL, correct control of initiation and quenching is also imperative. Indeed, it can greatly influence the spatial resolution of printing and/or mechanical properties of the final structure [53, 54]. In the light of 3DLL, in RM, the resolution requirements are rather loose. On the other hand, due to the necessity to test exotic materials, correct control of when and where polymerization reaction stops can be very important. Thus, the control of polymerization reaction termination should not be overlooked. However, additional quenching is very rarely used in RM, as it adds additional species to the material that could in some ways compromise biocompatibility. Furthermore, RM structures have, in most cases, features large enough to not require any additional ways to increase printing resolution.

Last, the cross-linking degree must not be overlooked. One of the peculiarities of photopolymerization reaction is the different amounts of photoactive species used, which depends on the exposure parameters. This percent can be somewhere in between ~6% and ~70% depending on the material, excitation, and position in the focal region (decreasing farther from the center) [55]. The last property was employed to generate nanothreads between solid supports. Also, it gives another degree of tunability when considering the concept of the structure [56]. Indeed, refractive index [55], thermal response [13], and mechanical strength [54, 57] depend on it. Consequently, it was exploited in creating various optical and mechanical devices. On the other hand, it means that the characterization of polymers becomes incredibly tricky. Not only must one define what the optical and mechanical properties of the final material are, but also at what conversion degree it was achieved. Therefore, while there will be some characteristic properties of materials listed in this article, one must interpret them with some caution and keep in mind at what exposure parameters it was achieved.

2.3. Fabrication Setup and Strategies. In order to realize TPA, a special workstation is required. In a very generalized case, there are 4 main components in each 3DLL setup: laser source, relay optics, sample positioning, and imaging system (Figure 3). Furthermore, choosing correct writing strategies

are also extremely important, because they can influence both the mechanical properties of the structure and the manufacturing throughput. Thus, when considering the capabilities of 3DLL, the hardware/software part of the technology should not be overlooked.

As discussed previously, TPA is a nonlinear process requiring high light I. On a very general level, one can acquire peak I in the focused Gaussian beam by applying the following:

$$I_0 = \frac{2P}{f\omega_0^2 \pi \tau}. \tag{2}$$

Here, P is the average laser power, f is the laser repetition rate, $\omega_0 = 0.61 NA/\lambda$ is a radius of the beam waist (NA is numerical aperture), and τ is the pulse duration. As we can see, the laser source is responsible for most parameters leading to high I (P, f, and τ). For this reason, ultrafast fs laser with high P (up to a few hundred mW), reasonable f (which rarely exceeds MHz), and very short τ (tens/hundreds of fs range) is the best candidate to induce it [58]. Nevertheless, picosecond (ps) [59], nanosecond (ns) [60], and even continuous wave (cw) [42] lasers were used for 3DLL. However, in these cases, TPA is surpassed by thermal effects and avalanche ionization as a dominant process for inducing polymerization. This resulted in a decrease in the fabrication window and/or necessity to use a substantially lower translation velocity, thus making ultrafast lasers a primary choice for high-efficiency 3DLL setups. It is interesting to point out that both oscillators and amplified fs laser systems can be used. The latter laser systems are also capable of subtractive laser manufacturing, such as ablation or selective glass etching [5, 15, 61]. Thus, a setup with such laser can perform both additive and subtractive laser processing. While at the moment it has limited uses in RM, it was applied for great effect in other medical fields, for instance, producing functional as lab-on-chip (LOC) devices.

The purpose of relay optics is quite straightforward—direct laser light from laser to the sample. However, peculiarities of this operation should not be overlooked. As established
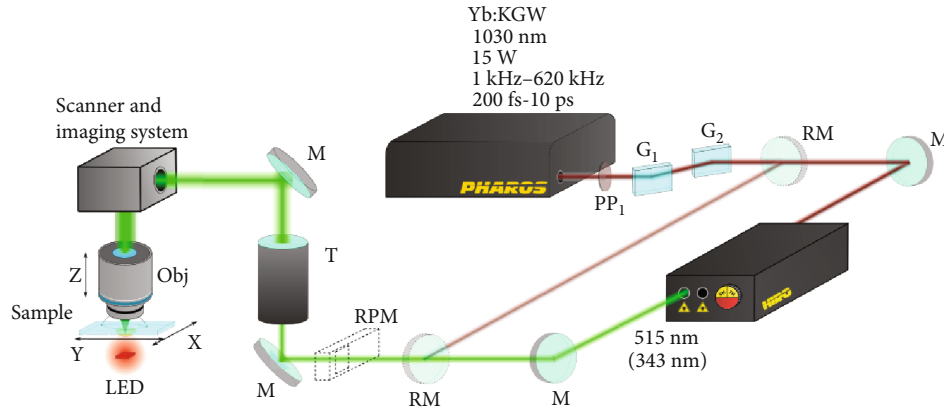
Figure 3: Simplified schematics of a 3DLL fabrication setup employing an amplified fs laser and harmonic generator. PP_1: phase plate; G_1 and G_2: Brewster angle polarizers; M: mirrors; RM: removable mirror; RPM: removable power meter; T: telescope; Obj: objective. Adapted with permission from [6] © The Optical Society.

in the last paragraph, laser should be emitting fs pulses. In the case of oscillators, such pulses can be extremely short (sub-100 fs) and, in turn, have relatively broad spectrum width. Furthermore, several laser harmonics might be used in one 3DLL setup [6]. Therefore, optics in the setup have to be able to sustain all of the relevant harmonics with respective spectral widths. In addition, optics have to assure that there is the minimal temporal pulse broadening due to dechirping of the pulse as it passes various optical elements or it is appropriately controlled for the benefit of printing [62, 63]. Alongside spectrotemporal requirements, the optical chain also has to assure that there are no spatial disturbances to the beam. Indeed, to achieve maximal possible writing accuracy, the laser beam has to be as close to Gaussian as possible [64]. What is more, the beam diameter should match the aperture of focusing optics, introducing the need of a telescope. Finally, appropriate NA objective should be chosen to accommodate the needed feature size/throughput compromise [1]. The light intensity in the focal region of Gaussian beam can be defined as

$$I(r, z) = I_0 \frac{\omega_0^2}{\omega(z)^2} \exp\left(\frac{-2r^2}{\omega(z)^2}\right). \tag{3}$$

Here, r is the distance from the optical axis and z is the distance from the focal plane parallel to the optical axis. Because ω_0 depends on NA, by changing the objective, one can relatively easily tune the size of the modified volume. Indeed, in most cases, RM requires relatively big structures (up to cm) with features in the range up to tens of μm [16, 27, 28]. This is substantially bigger than the hundred nm level features possible with 3DLL. Thus, it is common to use objectives with NA < 1 when fabricating structures for RM.

3DLL is realized by moving a focused laser beam in relation to the sample or the sample in relation to the laser beam. On the onset of the technology, piezoelectric (piezo for simplicity) stages were used [65]. They provide extreme precision down to the sub-nm scale. However, their working area is extremely limited (no more than several hundred μm) and translation velocities are limited. They were also sensitive to physical overloads due to the danger of the piezo-crystals cracking. These problems meant that piezostages were gradually phased out from the fields where high-throughput printing was necessary, including RM. The next two easily applied options were galvanometric scanners and linear stages. Scanners are a superb positioning tool for very high-throughput fabrication due to the minimal inertia [66]. This means that cm/s translation velocities can be achieved even while fabricating very complex shapes. The downside of this approach is the printing area being confined to a working field of an objective which is in the order of several hundred μm. If structure dimensions exceeded the working area of an objective (which is the case for most RM-applicable structures), it had to be divided into segments which were then printed one by one, resulting in stitching between segments [67–70]. Stitches induce optical and mechanical defects which might compromise functionality of the structure. Linear stages do not have this problem and can produce cm-sized structures at high translation velocities (up to cm/s) if the structure is simple and based on straight lines [71–73]. However, due to the high inertia of the stages, distortions might appear in more complex cases also creating a limitation. The solution to these problems is synchronization of galvanometric scanners and linear stages allowing to achieve stitch-free printing with superb quality of complex 3D shapes at high translation velocities [6]. As a result, it was already used in RM-related research [16].

The final component necessary for practical 3DLL setup is the integrated imaging system. In the simplest case, it is needed to assure that the structure is fabricated at an appropriate position of the sample and for real-time observation of the printing process [72]. At the same time, the functionality of the imaging system can be expanded to include additional roles, such as autofocus. In a general sense, autofocus is needed to find the interface between the prepolymer and substrate. It minimizes the workload on the setup operator and enhances repeatability and precision of such an operation. Depending on the desired result, it can be achieved by using existing imaging hardware and additional image post processing [74] or by introducing more components into the setup [75]. It is important to note that implementation

of autofocus is relatively simple in the 3DLL case due to fluorescence of most processable polymers. This sharply contrasts with finding the interface between two nonfluorescent transparent mediums where more advanced solutions are needed [76].

3. Materials for Multiphoton Polymerization

Alongside the fs laser setup, polymeric materials employed are the most important part of the technology. They define both structuring peculiarities and the characteristics of the produced structures. Therefore, the material has to be carefully chosen, especially in biological structures. Thus, in this part of the review, we will discuss some of the most prominent materials that were employed in 3DLL, as well as PI/inhibitors, and finish off with some ways of functionalizing them.

3.1. Common Photopolymers

3.1.1. Acrylates. Acrylates are one of the most common photopolymer families currently in use in 3D printing. This is due to them being extremely photoactive and chemically tunable. Historically, it was the first polymer structured in 2PP fashion [18]. Acrylates are a family of polymers made from acrylate monomers which are esters. The significant feature of acrylates is that vinyl groups are directly bonded to the carbonyl carbon. These monomers are important due to their bifunctionality. The vinyl group is responsive for polymerization [77]. The carboxylate group carries numerous functionalities providing the ability to modify the composition and chemical structure of acrylates. The polymerization chemistry of acrylates is based on the differences between two vinyl carbon atoms. Usually, vinyl groups are electron rich, while carboxyl groups are very polar. Therefore, the carboxyl group in acrylates attracts electrons from the vinyl group that leads to a deficit of electrons in the alpha carbon and an excess in the beta carbon (Figure 4). This behavior results in the high activity of acrylates in the free radical polymerization reactions described previously.

Many acrylates with a variety of properties can be obtained by changing groups connected to the alpha carbon and carboxylate, for instance, methyl, ethyl, or other organic chain having acrylic, methacrylic, and cyanoacrylic esters [78]. There are abundant acrylate monomers and oligomers that are photosensitive, such as hydroxypropyl acrylate, hexanediol diacrylate, polyester tetraacrylate, hexaacrylate, oxazolidone acrylate, pentaerythritol triacrylate, urethane acrylate, some fluorinated acrylates, and methyl methacrylate [79]. Many acrylates have attractive properties depending upon the chemical structure, such as high chemical and heat resistance, stability, toughness, favorable stiffness, flexibility, optical clarity [78, 80], or 3DLL forming possibility.

It is known that, for instance, in polymethyl methacrylates, the softening point, density, and refractive index decrease and the toughness increases as the ester chain increases. In polymethyl methacrylate, by changing the ester group from methyl to isobutyl, the density can be varied from 1.02 to 1.19 g/cm^3, refractive index can be varied from 1.45 to
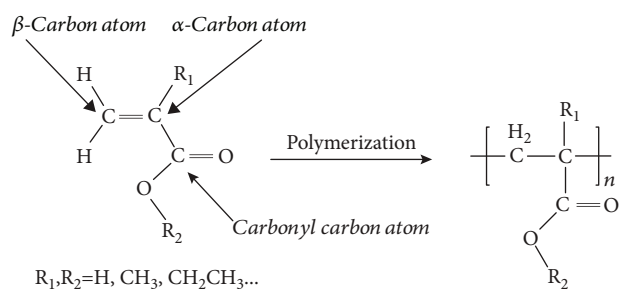
Figure 4: Structural formula of acrylates before and after polymerization. Here R_1 and R_2 are organic substituents and n is the degree of polymerization. Alpha, beta and carbonyl carbon atoms are shown.

1.48, softening point can be varied from 62 to 125°C [78]. On the other hand, if it is necessary to have polymers with special properties, there is a possibility to combine other monomers or modifiers by copolymerization reactions. As a result, the copolymers [78, 81] and blends, also known as acrylic multipolymers [78], are obtained. Some components like ethoxylated trimethylolpropane triacrylate are used in order to reduce shrinkage upon photopolymerization [82]. In order to promote hardness of the polymer, tris(2-hydroxyethyl)isocyanurate should be added [82]. Various modified acrylates were used in 3DLL through the years [83–85]. Overall, acrylate groups play an important role in polymers that will be discussed later, making acrylate chemistry one of the backbones of 3DLL.

3.1.2. SU8. SU8 is a chemically amplified negative photoresin which was introduced commercially in 1996 [86]. It is specially tuned for usage in UV lithography. As a material which was specially designed to be photostructurable, it was natural for it to be applied in 3DLL very early [87, 88]. It is based on the acid-labile groups and the photoacid generator [86]. This results in a rather strict processing protocol. First, it is prebaked to remove the solvent making it hard. It is followed by UV exposure, which generates a strong low concentration acid, for example, hexafluoroantimonic acid from PI decomposes which protonates the epoxides on the oligomer. Such protonated oxonium ions are capable to react with neutral epoxides in cross-linking reactions after irradiation. During this process, the acid also regenerates resulting in a very strong reaction in exposed areas. This reaction is also helped by the fact that in normal circumstances, there are 8 receptive epoxy sites on each monomer (Figure 5). The end result is very well-defined structures that can be relatively big (up to cm) or can have very small features (down to tens of nm [89]).

3DLL processing of SU8 has some interesting features in comparison to the standard UV case. First off, exposure and postbake can be combined into a single processing step [41]. It is possible due to the capability to induce both nonlinear absorption and subsequent heating during the same laser scanning step. The polymerization kinetics are also somewhat different. Raman spectra reveals that when SU8 is exposed to 800 nm, 100 fs, and 1 kHz Ti:saphire, the absorption dynamic is different from the standard UV case. However, the end result is basically the same as SU8 polymerized
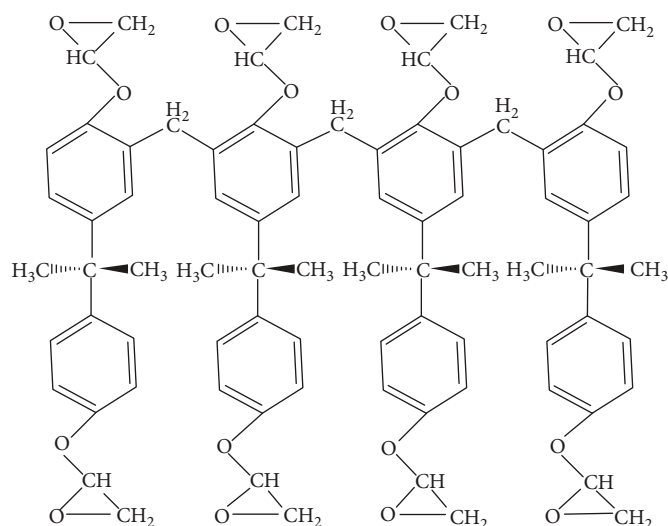
FIGURE 5: Structural formula of SU8, consisting only of the organic matter.

with UV light and TPA has nearly identical Raman spectra [19]. Both subdiffractive structures [88] and mm scale objects [90] were fabricated using 3DLL out of SU8. Due to relatively good adhesion of SU8 to various functional substrates, structures can be printed directly on them. One of the examples is fiber tips [91]. SU8 consists only of the organic matter; therefore, it can also be removed by calcination in ambient atmosphere in rather low temperature of 600°C, making it a good candidate for the template material for other substances that are hard to shape in 3D directly [92]. Interestingly, SU8 usage in medicine is rather sparse, especially in the 3DLL case. This can be explained by the fact that other materials are more customizable, biodegradable, and/or bioinert. However, it is still a potent candidate if structures with well-defined and mechanically strong features are needed.

3.1.3. Hydrogels. Hydrogels can be described as the polymeric networks which have the ability to take and storage an extremely large amount of water in their 3D structures. The reason for this is a chemical structure of material. The hydrogels are formed by hydrophilic groups which are hydrated in an aqueous medium [93, 94]. Generally, hydrogels are insoluble in aqueous solution because of polymeric cross-links. Nevertheless, because of the large quantities of water due to the hydrogen interactions inside the polymer network, these materials exhibit the capability to swell in aqueous solutions [94]. As a result, chemically hydrogels can be defined in two conditions: one of them is the water-insoluble polymeric chain and the other is the hydrophilic functional groups.

The two requirements described above lead to a wide variety of hydrogel precursors. In order to facilitate understanding of hydrogels, they are classified in many aspects. According to the hydrogels origin, they can be classified to the natural or synthetic polymers. Furthermore, the classification based on polymeric composition allows grouping hydrogels into homopolymeric, where a basic structure consists of a monomer, and copolymeric—of two or more differ-

ent monomer species with one hydrophylic component and multipolymeric interpenetrating polymeric hydrogels consisting of two independent cross-linked polymers. Furthermore, hydrogels can be classified according to crystallinity, for example, amorphous, semicrystalline, or crystalline. Also, based on polymeric chains and the electric charge of hydrogels, they can be grouped into nonionic, ionic (that include both cationic and anionic), amphoteric (with acidic and basic groups), and zwitterionic (including both anionic and cationic groups) [94].

However, not all hydrogels can participate in photopolymerization. In 3DLL, precursors of hydrogels are usually liquid and should immediately respond to irradiation of light. Therefore, PIs which accelerate photopolymerization reactions are necessary. Multifunctional cross-linkers, such as acrylic acid or (meth)acrylates, create links between the polymeric chains. Frequently, monofunctional reactive diluters are added in order to adjust the viscosity [26]. Photopolymerizable hydrogel precursors could be HA-MA/acrylamide, modified gelatin, collagen, fibrinogen, fibronectin, concanavalin A, lyophilized BSA (bovine serum albumin), BSA, PEGda/HEMA, and so forth, together with eligible PIs [26]. One of the most used hydrogels for several decades is PEGDA [95, 96]. Its structural formula is depicted in Figure 6. PEGDA consists of polyethylene glycol with two acrylate substituents at the ends of the chain. PEGDA is functionalized by polyacrylic or polymethacrylic acids in order to form cross-linked hydrogels. These compounds have an oxygen atom in a polyethylene glycol part and carboxylic group in an acid part. The hydrogen bond between these groups is formed. This behavior depends on pH, because the reason for hydrogen bond formation is the protonation of the carboxylic group [93]. However, properties of hydrogels can be changed not only by changing pH properties. Various factors, such as temperature, pressure, solvent composition, or ion changes, can control them, including cross-linking density, hydrophobicity, swelling rate, permeability, degradability, and mechanical strenght [26], of gels which are
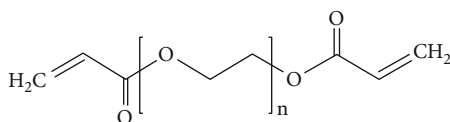
Figure 6: Structural formula of polyethylene glycol diacrylate (PEGDA). Here, n is a degree of polymerization.

important for the 3DLL process and for the applicability of the final product.

Biocompatibility is one of the key properties of hydrogels that make them attractive and promising in RM. The ability to polymerize them with 3DLL further extends their applicability [26]. Indeed, from most of the currently available materials, they offer one of the best analogs for the extracellular matrix. Thus, numerous different structures were created out of hydrogels over the years using 3DLL [20, 72, 97, 98]. Their peculiarities will be discussed in more detail further in this article.

3.1.4. Hybrid Organic-Inorganic Photopolymers.

With the advances of polymer chemistry came the possibility to add a lot of different functional groups to the cross-linkable monomers. One of the key achievements in the field is the possibility to prepare hybrid materials that are cross-linked *via* organic constitutes yet have diverse and significant inorganic part. In most cases, they are prepared by sol-gel technology [99, 100]. The sol-gel synthesis method includes a powerful and adjustable strategy for the preparation of functional organic-inorganic hybrid materials. It provides easy control of the configuration of the materials as well as molecular composition that permits hybrids more applicable to fundamental or applied research and industry. The sol-gel chemistry is based on hydrolysis and polycondensation reactions of suitable molecular precursors such as metal alkoxides M(OR)x [101, 102], where M is the metal or metalloid element, for instance, Si, Sn, Ti, Zr, Hf, Ge, Al, Mo, V, W, and Ce [103], while R is the alkyl chain or any other organic group. The possibility of using metalorganic materials in 3DLL requires one important condition of the alkoxide organic group—one or more organic groups must have a functional group involved in photopolymerization reactions. Therefore, in 3DLL, a silicon-based metalorganic monomer (MAPTMS, TEOS, TMOS [103], or other silane) is used together in the presence or absence of another metal isopropoxide which is usually stabilized by methacrylic acid (Figure 7). The sol-gel method provides the opportunity to synthesize homogeneous materials with the degree of mixing of the organic-inorganic components and a variety of metals that allows a variation of its appealing properties such as molecular homogeneity, transparency, flexibility, and durability [103]. As mentioned above, the hydrolysis and condensation reactions of monomeric metal alkoxides and organyl alkoxides are the two main stages of sol-gel synthesis [104]. In solution, the alkoxides are hydrolyzed and condensed to form polymeric species composed of M-O-M bonds [102, 105]. Both reactions occur by acid- or base-catalyzed bimolecular displacement reactions. The acid-catalyzed mechanisms are carried on protonation of OH or OR sub-

stituents attached to silicon or other metal element, whereas under basic conditions, hydroxyl anions attack metal or the metalloid element directly. Both reactions occur simultaneously and, depending on reaction equilibrium, start to form three-dimensional inorganic molecular networks. The geometry and length of condensation bonds strongly depend on catalysts, steric and inductive effect of the alkyl radical, and solvents [105]. Such hybrids with different composition and diversity of geometry are promising materials for various applications.

Hybrids offer huge tunability in terms of mechanical and optical properties by changing the ratio between the organic and inorganic parts. For this reason, they become extremely popular in 3DLL. Indeed, hybrids with Si [21], Zr [106], Ge [107], and Ti [108] constitutes were tested over the years to name a few. However, they vary heavily in terms of ease of preparing them, shelf life, and general structurability. This led to Si- and Zr-based hybrids becoming the most popular ones. Zr-based hybrids are especially interesting as they were created on purpose for use in 3DLL and offer minimal shrinkage [106]. Zr based initially created with the intent to use it in photonics [106]. Nevertheless, over the years, it was used in basically all research areas where 3DLL can be applied, including photonics [9], microoptics [109], and micromechanics [110]. It was also proven to be exceptionally susceptible to modification, including surface tuning [10] or doping with organic dies [6, 111] or nanoparticles [112]. In RM, the Zr-containing hybrid was employed in the manufacturing standard [16, 73] and shape-shifting scaffolds [113] as well as functional elements such as valves that could be used as implants replacing analogous elements in veins [110]. Biological use of the Zr hybrid is heavily motivated by the superb biocomaptability of the material, proven both *in vitro* [73] and *in vivo*, going as far as preclinical trials [16].

3.1.5. Elastomers.

As the name implies, an elastomer is an elastic polymer. It owns this property to relatively weak intermolecular forces, low Young's modulus (~MPa), and relatively high failure strain. Most of the elastomers are cured using heat, making them very convenient for technologies such as fast replication [114] or microfluidics [115]. While numerous elastomers were created and tested over the years, one of the most popular is the commercially available polydimethylsiloxane (PDMS) (Figure 8), which is sold under the name Sylgard® 184. Furthermore, more monomers were studied by researchers, such as elastomers in photopolymerization. Alongside appropriate monomer reactive, diluents and chain transfer agents [116] are needed too. In the PDMS variant, such a system may consist of MMDS ((mercaptopropyl)methylsiloxane-dimethylsiloxane copolymer) which is oxidized by adding different amounts of the IBDA (iodobenzene diacetate) solution, vinyl-terminated PDMS, PI, and photoabsorber [117]. In other systems, some acrylates may be used as the base monomers. These include aliphatic polyester urethane diacrylate, urethane monacrylate in 20% EHA and aliphatic urethane acrylate oligomer, as reactive diluents such materials as 2-(((butylamino)carbonyl)-oxy)-ethyl acrylate, 2-ethylhexyl acrylate, 2-hydroxyethyl acrylate, and 2-cyanoethyl acrylate. As the chain transfer agents, the

R = OH, OCH$_3$
R$_1$ = OH, OCH(CH$_3$)$_2$
Me = Zr, Ti,Hf...
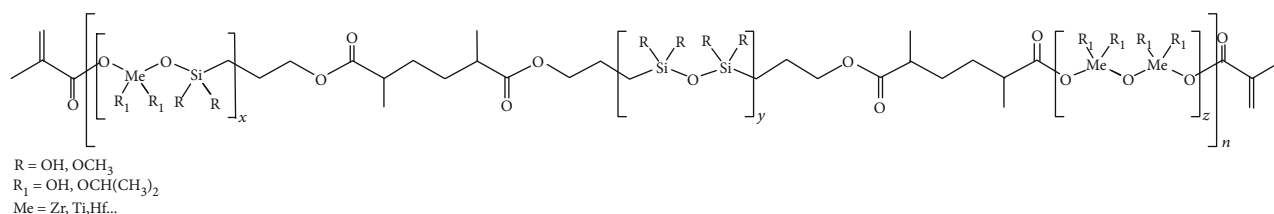
FIGURE 7: Structural formula of hybrid organic-inorganic polymer consisting of MAPTMS and metal isopropoxide. Here x, y, and z are degrees of inorganic polycondensation.

R = H, OH, CH$_3$, CH = CH$_2$...
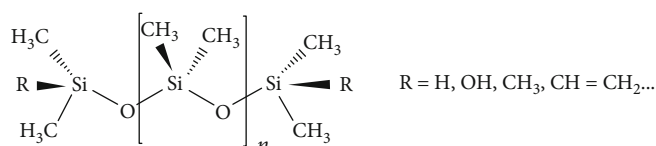
FIGURE 8: Structural formula of polydimethylsiloxane oligomer (PDMS). R is organic substituent at the end of the chain and n is a degree of polycondensation.

pentaerythritol tetrakis(3-mercaptopropionate), and 3,6-dioxa-1,8-octane dithiol are applied [116]. The reagent names indicate that acrylates are the inseparable part of elastomers. However, it should be noted that only a small part of acrylates can exhibit elastomeric properties.

Medical applications are one of the areas where elastomers show huge promise. Here, they excel due to their biocompatibility, capability to pass through gas while retaining liquids and being generally transparent to visible and UV light. One of the areas where it was exploited heavily was LOCs [115]. Cells could live in biological liquids contained in such devices, while also being able to "breath." Transparent nature of elastomers also allows easy assessment of such biological systems. Biooriented scaffolds made out of various elastomers and their composites were also produced for RM applications [118–120].

The importance of 3D nanostructuring of elastomers was recognized very early in 3DLL. However, while 3D structuring of PDMS was achieved, it was done in very slow 100 ms/voxel exposure [121]. In further works, the speed was increased from tens [122] up to thousands [123, 124] μm/s, but the problem of the narrow fabrication window and shrinkage remained. Due to their elasticity and polymerization post-fabrication, the shrinkage remains one of the main problems of 3DLL-compatible elastomers, even if special purpose-built species are used [124]. Thus, while 3DLL structuring is possible and materials are RM compatible, they are not easy and straightforward to use.

3.1.6. Biopolymers. Ever increasing material synthesis capabilities led to the creation of polymers similar to ones found in nature (for instance, synthetic proteins) or based on naturally derived raw materials. Due to these connections, in this review, we will consider both of these types of materials to be biopolymers. Their main attraction is the possibility to extremely closely mimic the biological environment, use readily available natural raw materials, or both.

In a world with dwindling oil resources and ever growing consumption of energy, alternatives for oil-based polymers are highly desired. Naturally derived raw material-based biopolymers are designed to answer this challenge. The polylactic acid (PLA) is one of the first polymers of this kind to be commercialized. Based on corn, it offers an extremely low price (~several dollars for kg) and easy handling [125]. It also shows favourable degradation properties [125, 126]. Both additive [127] and subtractive [128] manufacturing were achieved with PLA. Yet it and other associated biopolymers were rarely used in photolithography due to the difficulties in additive photostructuring. Movement to photolithography requires to tune both monomer formulations and choose the correct PI. It was shown that standard one-photon polymerization might be tricky and hard to use [52]. Interestingly, when moving to TPA, some of these problems are significantly reduced [129]. This might be related to a lot more aggressive and localized energy introduction mechanism in the 3DLL case.

Talking about biomimicking polymers, several kinds were tried over the years, including protein [130, 131], collagen [132], chitosan [22], and gelatin [133]. However, most of these materials are not easy to structure *via* fs lasers. Species with special PIs and even ones without were tried with varying degrees of success. In some cases, deformed, barely standing 3D structures were demonstrated with intent to showcase the possibility of such processing. In other cases, well-defined and usable 3D objects were manufactured. Overall, this area is relatively new, and a lot of advances in further developing biopolymers for 3DLL might be expected.

3.1.7. Positive Photoresins. All photopolymers discussed so far are of the so-called negative tone kind. It means that areas which were exposed to the light are cross-linked and remain after the development. However, the opposite can also be realized by using so-called positive tone resists. In that case, under irradiation, exposed regions of photosensitive material are removed during development. Typically, positive resists consist of a polymer matrix with protected functionalities, small molecular photoactive generator, solvent, and other additives [134, 135]. One of the most

significant requirements of these systems is photosensitivity of the photoactive generator which is basically called a photoacid generator due to its property to produce acid after the light irradiation. The photoactive generators can be divided into two types, first is the ionic, which mostly contains onium salts and upon UV light is able to produce Brønsted acids, while the second type is nonionic that can generate sulfonic, carboxylic, and phosphoric acids. Generally, polymers having tertiary carboxylate, tertiary carbonate, tertiary ether, acetal, hemiacetal ester, or other easily protonizable group are used in positive tone resist systems. In that case, after the photoactivated acid-catalyzed reactions, such polymers are decomposed into poly-carboxylic acids or poly-phenols [134], depending on the initial functional group, and the smaller molecular weight having nonpolymeric compounds. Thereafter, polymers having acidic functional groups can easily dissolve in an alkaline solvent. The described system is called the amplification resins.

But what if the polymer does not have an easily protonizable functional group? The most prevalent type of positive tone photoresist consists of diazonaphthoquinone (DNQ), phenol formaldehyde polymer (Novolac), and propylene glycol monomethyl ether acetate (PGMEA) as the solvent [136–139]. In this way, at normal conditions, the dissolution of the polymer is blocked by the hydroxyl group of Novolac and DNQ interactions. However, after the photoillumination, indenecarboxylic acid is formed via ketenes [136] of the DNQ; as a result, the Novolac polymer becomes soluble [140].

Positive tone resists were applied in 3DLL [141] with the primary focus on the possibility to use them in microfluidics [142]. However, due to their nature, they are relatively chemically unstable with short shelf life and narrow fabrication window. Thus, in recent years, they were used less and less in favour of easier to use and applicable negative tone resists.

3.2. Photoinitiators in Regenerative Medicine. The correct choice of PI or photoexcitation mechanism is imperative for 3DLL. In most cases, a specific PI is used for it. PI's influence to the whole printing process is immense because it determines what laser wavelength should be used and what is the fabrication window. When 3DLL was first used, photopolymers with PIs designed for one UV photon absorption were applied due to being readily available [18, 121]. From the first glance, it might seem that adoption of one-photon PIs for TPA should be pretty straightforward by just making sure that the fs laser wavelength is half of the absorption peak of the PI. However, interestingly enough, it was shown that sometimes PIs with huge one-photon absorption cross-section σ_1 can have very small σ_2 in the range of tens of GM [143]. In comparison, if appropriate chemistry is used, σ_2 can go as high as more than a thousand GM [143]. This proves the necessity to create PIs specially designed for TPA.

TPA-oriented PIs can be realized by applying D-π-D, D-π-A, D-π-A-π-D, and A-π-D-π-A types chemical compounds showing large changes of dipole/quadrupole moments upon excitation, with extended conjugation in molecules [144]. Here, π is a π-conjugated backbone (for example, vinyl groups in ethynylphenyl, ethynylene, or phenyl); D usually represents hydrogen, methoxy, and alkylamino, such as dimethylamino, diphenylamino, and dibutylamino groups which act as electron donors; and A is the acceptors (for instance, various cycloketones, ketones, pyridine, or pyridinium) [144–146]. D-π-D and D-π-A-π-D are two of the most commonly used PI systems in TPA. One of the D-π-D type, commercially available PIs, which is known as Irgacure 2959, could have attractive properties for medicine application as PI, due to its biocompatibility and solubility in water [145]. However, it is only appropriate to the 515 nm wavelength, which may cause the denaturation of proteins, which is critical when processing in the presence of cells [145, 147]. Therefore, D-π-A-π-D system PIs are more attractive in medical applications due to the charge transfer between electron donor (D) and acceptor (A) groups which are responsible for the appearance of low-energy excitations [148], such as 800 nm [146].

If the final structure is expected to be used in RM PI, despite the discussed necessity of low energy excitation, it must match even more requirements. First, it has to be biocompatible. This can be tricky, because PI molecules are purposely designed to be extremely chemically active resulting in possible cytotoxicity [95, 149]. It is known that the cytotoxicity is determined by singlet oxygen quantum yields during photoinitiation. In the case of D-π-A-π-D, cytotoxicity was found to be influenced by the composition of the activator. The smaller number of C atoms in the cycle of cycloketones (at least from C4 to C7) showed the less amount of the singlet oxygen quantum yield [150]. Furthermore, they have to be water dissolvable. This requirement stem from the desire to use water-soluble hydrogels in RM and potentially avoid organic solvents in development process. It was shown that some standard PIs can be biocompatible as long as they are used in inert hard polymer matrices, such as hybrid organic-inorganic photopolymers [16, 73, 113]. Purpose-designed bio-PIs were also developed. In order to achieve water solubility, water-born functional groups can be introduced. These can be, for instance, quaternary ammonium cations or carboxylic sodium salts. Biocompatibility of such water-soluble PIs was proven by both seeding scaffolds with cells and printing structures with whole organisms. It was shown that such bio-PIs can have σ_2 high enough to support printing speeds well over cm/s [151]. Therefore, the selection of PIs suitable for RM is quite big, fully supporting the growth of the technology.

As mentioned above, another important requirement of PIs is the sufficient two-photon absorption cross-section value which is most dependent on the chemical structure, hydrophilicity/-phobicity, and solvent. According to Albota et al., the two photon absorption cross section increases due to the increasing conjugation length of the molecule or the increasing extent of symmetrical charge transfer from the ends of the molecule to the middle or vice versa [152]. Furthermore, with the hydrophilic PI P2CK (Figure 9) under 800 nm excitation in water, the TPA cross-section value was equal to 176 GM, while its hydrophobic analogue (B3FL) in chloroform was 466 GM [153]. The hypothesis of such behavior is interpreted by hydrogen bonding between the solute and solvent and changes in the PI geometry or aggregation [145].
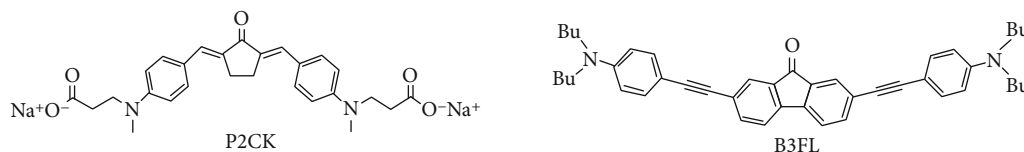
FIGURE 9: Structural formulas of TPA PIs. Here, P2CK is PI-soluble in water, while B3FL is soluble in organic solvents.

While PIs are the primary way to induce cross-linking, it was also shown that in some cases, polymerization reaction can be induced even without PI present [2, 133, 154]. This potentially eliminates the need to use PI and, thus, optimize its printing and biocompatibility-related properties. On the other hand, it reduces the fabrication window, potentially weakens the structure mechanically, and creates additional requirements for the light source [154]. This is due to the change in the undergoing light-matter interaction. It was calculated that if PI is not present, avalanche ionization might become comparable or an even greater contributor to chemical bond cleavage than TPA [40]. However, as the avalanche requires time to achieve its full potential, relatively longer pulses in the range of hundreds of fs are necessary. Another way to achieve PI-less structuring is to specially design the material to have double bonds breakable directly by TPA [133] (Figure 10). Then, the material acts as polymer and PI. PI-free structuring alongside bio-PIs make selection of photosensitization mechanisms very broad which is extremely suitable for such a subtle field as RM.

3.3. Material Functionalization and Modification.
In a lot of cases correct choice of the polymer and PI is sufficient to satisfy the needs of the application. However, in some special cases, further modification of the material might be desired. Due to the extreme flexibility of 3DLL, a lot can be done to the polymers used while retaining the possibility to structure them in 3D fashion.

3.3.1. Organic Modifications.
Polymeric matrix might be enhanced by using organic additives. These might serve several functions. First, these additives might be various biological or curing agents that are released as the biodegradable polymer dissolves in a living tissue or bioliquid [155]. If the scaffold is produced out of such material, it both supports the cell growth and potentially provides cure for the trauma/ disease in its proximity. Second, additional organic dyes can be added [6, 111]. It makes structures easier to see in either ambient lighting or under UV light. This is attractive for medical applications if nondegradable scaffolds need to be observed or removed. However, as with the PIs, care should be taken to make sure that such dyes are not cytotoxic if application is biology oriented. Also, the absorption of the dye needs to be considered and 3D printing performed with laser wavelength for which such material is transparent [6].

3.3.2. Inorganic Modifications.
The problem with organic fluorescent dyes is their bleaching overtime under UV radiation. If long-term emission is needed, inorganic additives are superior. In that case, 3DLL-applicable polymers can be mixed with various inorganic nanoparticles and quantum dots. Indeed, by controlling the shape and size of such nanoobjects, their absorption and emission characteristics can be changed from UV to IR wavelengths [156, 157]. In the 3DLL case, they can be introduced into polymer either after printing [158] or just by mixing them into prepolymer before printing [112, 159, 160]. The second option is extremely attractive due to its simplicity and is always used if possible. Alongside well-controlled absorption/emission characteristics, nanoadditives can also be used in other ways. For instance, they can be used as PIs. With very small concentrations needed ($\sim 10^{-3}$% w.t.) and comparable photoactivation to standard Pi [112], gold nanoparticles are promising in biological applications as a replacement for standard PIs. Finally, enhanced and/or controlled photosensitivity can be realized with other nanoadditives such as ZrO_2 [161] or upconverting lanthanide-doped upconversion materials [162]. Thus, this approach can be considered to be extremely versatile and applicable to multiple materials.

Modifications using inorganic additives extend beyond just a control of photosensitivity. Quantum dots can also be used to modify the mechanical and optical properties of the nanocomposite beyond what could be achieved with only polymer chemistry [159] (Figure 11(a)). Furthermore, magnetic properties can be introduced to the polymer *via* magnetic nanoparticles [163]. Alongside 3DLL-enabled conductive nanocomposites [164], it creates a precedent for the completely controllable electromagnetic properties of the structure. This is extremely relevant for RM as some tissues rely on electric conductivity of the surrounding medium. At the same time, it would enable printing miniaturized active implants such as heart simulators or microrobots. Therefore, nanoadditives and resulting nanocomposites are an extremely important area for development with huge promises to 3DLL overall and with interesting implication to RM in particular.

3.3.3. Postprocessing Solutions.
In its essence, 3DLL is only capable of printing polymeric materials. While polymers can be tuned in extremely diverse ways, there are properties that are nearly unreachable with polymers. Thus, ways to expand additive laser 3D manufacturing beyond polymers exist. Recent works showed that one of the best ways to achieve free-form 3D nanomanufacturing of inorganic materials is combining 3DLL and thermal postprocessing [154, 165–167]. The usage of this methodology can lead to several outcomes. Heat might be used to remove organic polymer completely. Then, it can be used as a mold for a material that could not be directly structured *via* 3DLL, for instance, metal [168]. The end result in such a case is high-quality metallic micro- and nanostructures. In a similar fashion, heat can also be used to directly form inorganic structures. Then, the 3D
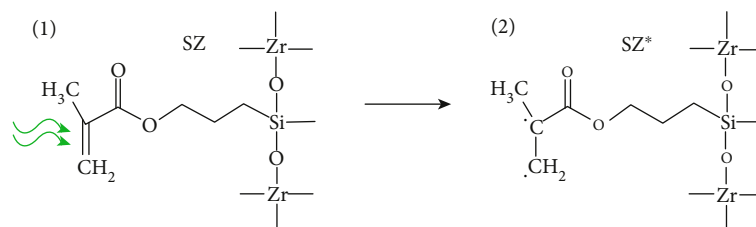
FIGURE 10: Proposed interaction in the acryl group in hybrid organic-inorganic photopolymer SZ2080 (SZ) during PI-free cross-linking. Direct cleavage *via* nonlinear absorption of a double bond in a group results in radicalization and subsequent polymerization. Adopted from [154].

(a)

(b)
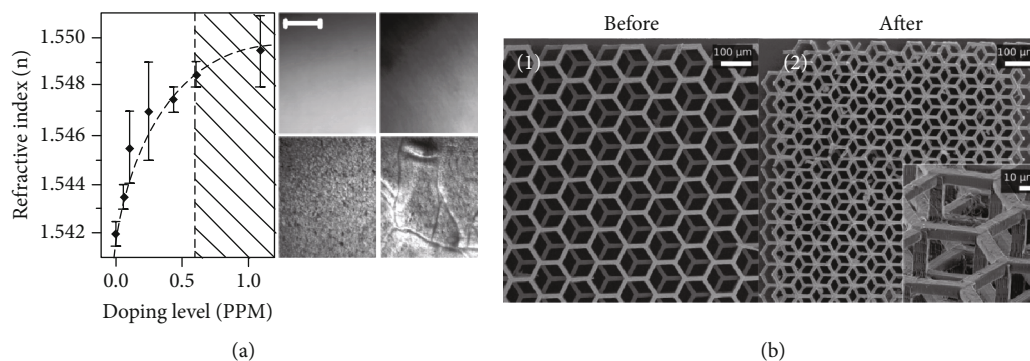
FIGURE 11: (a) Refractive index change and structure topography of material doped with different concentration of PbS quantum dots. Substantial change of both is clearly visible. Scale bar: $50\,\mu m$ (adopted from [159]). (b) Scaffold structure made out of hybrid organic-inorganic photopolymer SZ2080 (1) and then modified into glass-ceramic *via* thermal postprocessing. Clear downscaling while preserving the shape and structural complexity is evident (Adapted with permission from [166] © The Optical Society).

structure is produced by using 3DLL using hybrid organic-inorganic photopolymer or similar mixture. Postprocessing is then used to remove most of the organic constitutes leaving inorganic 3D structure. As an added bonus, during this process, a substantial downscaling of a structure occurs—up to 21% of initial size in the 2D line case [165] and 60% in the 3D case [154]. The shrinkage was observed in both nanolatices [154, 165] and bulk 3D structures [166, 167]. It is also completely isotropic in all directions making it very predictable [166]. Thus, it was used to produce even extremely complex 3D microstructures [166, 167] (Figure 11(b)). A method of this kind was already shown to have huge promise in producing true 3D glass microfluidic systems [169]. While it was not applied in RM, so far, the possibility here would be to produce ceramic implants that could well mimic bone or teeth. Scaffolds of required geometry and overall size were already demonstrated with possible further works in RM direction in the near future.

Finally, surface modifications should not be overlooked. It was shown that correct surface topography and chemistry has immense impact on the functionality of medical implant. Functional groups like carboxylic acid groups, hydroxyl groups and amine groups generally produced by plasma treatment are used to chemically functionalized polymer surfaces. In the case of 3DLL-made structures, such as scaffolds, surfaces can be functionalized by plasma treatment for acrylic acid surface polymerization and further grafted with laminin-1 or gelatin in order to enhance human cardiac pro-

genitor cell (CPC) survival and differentiation potential [170]. Furthermore, surface properties which are significant in medical application, such as adhesion, surface hardening, surface wettability, tribology, blood compatibility, and diffusion barrier, can be obtained by functionalizing polymeric surfaces with organic materials. For example, superhydrophobic materials are obtained by using tetrafluoroethylene or 1H,1H,2H,2H-perfluorooctyl acrylate precursor plasma polymerization. Also, in order to make blood-compatible surfaces, the hexamethyldisiloxane can be used to reduce loss of blood cells through blood contact. For the thermal resistance and electrical properties, a polymer can be functionalized by covering of cyano groups [171]. At the same time, conductive and/or magnetic coating can be selectively deposited on 3DLL-made objects. Then, the metallization process is based on three stages. The first stage is seeding of metal, such as silver, when the 3D structure is immersed in an aqueous solution of silver nitrate ($AgNO_3$), where silver ions connect together with amine moieties, which are only on the polymeric structure's surface, thus forming the initiation of the silver nanoparticles growth. In the second step, metal ions are reduced, in this case, by aqueous solution of sodium borohydride ($NaBH_4$), and silver nanoparticles are formed. The amount of silver plated onto the structures depends on the duration of these stages. Finally, during the plating, the structure is immersed in the reducing agent to form a smooth final layer of metal [10, 172, 173]. The result is a metal layer just only on 3DLL-made structures. This was shown to lead

to conductive 3D structures [172] or plasmonic functionality [10]. Magnetic interaction-based cell transportation was also shown [173]. In medicine, this can be relevant as a way to introduce electricity to various electromechanical implants or simulators.

4. Applications in Regenerative Medicine

In order to achieve the final goal of RM, a lot of different, separate, yet intertwined research topics have to be investigated. Living cell behavior on different materials and geometrical topographies have to be onsidered. These results have to be compared to true living tissues. Novel designs for RM-oriented structures then have to be developed in accordance to obtained results and precise medical needs. Then, overall body response to printed objects have to be known as the final goal of the RM is to have structures and methods that could be used in the human body. All of these directions are being tackled with the help of 3DLL.

One of the key backbones of RM research is scaffolds for cell growth and tissue engineering [174]. They allow both investigating cell behavior in different conditions and being used for curing damaged tissue. When creating scaffolds, a lot of different considerations have to be taken into account. The 3D aspect is especially important here. While a huge array of cell-related research was performed with 2D structures [175–177], the extent of capabilities to mimic living body in 2D environments is limited. Thus, 3D objects are required for any high-level research. Diverse methods were used to fabricate scaffolds. Some of them are considered passive and include phase separation [178], porogen leaching [179], gas foaming [180], freeze-drying [181], and electrospinning [182]. The key advantage of these methods is the capability to create scaffolds for virtually any synthetic or natural material. Furthermore, the feature/pore size in such structures can be tuned to be in the range of what is found in natural ECM. This is extremely important in RM, as ECM influences cell behavior in a variety of different ways, including their proliferation, migration, or mass transportation. However, all of these methods are to some extent random in nature, making predetermined scaffolds with precise architecture nearly impossible. Here, various 3D printing techniques show huge advantage due to structure on-demand capabilities [183]. However, from all of the standard 3D printing techniques available today, only 3DLL have the correct blend of achievable resolution and acceptable throughput [1].

3DLL-made scaffolds were used in a huge variety of ways to investigate the peculiarities of cell and printed structure interaction. Specially designed wells with channel-like structures were applied to investigate the peculiarities of neuron growth and connection, showing that directionality of surrounding structures is extremely important [184]. Also, pore size in the scaffold can have huge implications to cell migration and mass transportation [185] (Figure 12(a)). Even if gaps in the scaffold structure are smaller than the cell itself, the macromolecules can still pass through such barrier [186]. Understanding these mechanics is imperative in creating scaffolds that are custom tuned to allow certain cell migration and, at the same time, unrestricted communication

between cells. Cell adhesion is another important topic. Biochemistry behind the cell-ECM interaction is extremely elaborate. Some materials might have superb cell adhesion while others might repel the cells. The first effect was shown to be extremely useful when controlling cell attachment points in a specially designed scaffold having functionalized points made out of bioactive species on top of the inert scaffold. This can be further expanded to include both repelling and attracting species in a single scaffold [17]. Then, the four-sided supports are printed out of a basic hydrophilic resist, consisting of a mixture of commercially available components: a trifunctional acrylate as the network-forming species (trimethylolpropane ethoxylate triacrylate, TPETA) and a PI (Irgacure369), with a functional photoresist, which has protein- and cell-repellent properties along with a photoreactive component that can be activated by DLW in order to change its properties to attract protein binding; as a result, protein-binding surfaces are obtained on the cross-beams. Such resist is obtained by mixing previously described basic resist (TPETA) and a methacrylate containing either a phenacyl sulfide (PS) or an o-methylbenzaldehyde (photoenol precursor) (PE) part. Finally, the inorganic-organic hybrid photoresist OrmoComp is used as a third resist providing an inherent protein-adhesive surface on the opposite cross-beam ends of the scaffold. Subsequent UV light leads to biotinylation of the functional resist cross-beams, making them either attracting for specific binding of the vitronectin. Due to the passivating properties of both basic and biotinylated resists, fibronectin on laminin only bind to the OrmoComp beams. In this particular case, epithelial (A549) and fibroblast (3T3) cells were chosen: the first kind has good adhesion to OrmoComp-laminin cross-beams and is repealed by the vitronectin, while the second type has completely inverted adhesion-repulsion properties [17]. As expected, cells were shown to attach to a preferential material proving that 3DLL can be employed for complete tissue engineering, starting with the completely freely definable 3D geometry and on-demand chemical functionality all done in the size range that can be smaller, bigger, or the exact cell size.

Having good knowledge about cell-scaffold interaction, scaffolds can be applied directly for treatment purposes. Here 3DLL can be used in a huge variety of ways. For instance, scaffolds might be used as a breeding platform to acquire cells for various cell-based treatments [73] (Figure 12(b)). Then, relatively simple geometry scaffolds with pore sizes optimized for the particular cell type can be made. Such colonies can be up to mm in size, making the entire amount of growth chambers in the range of tens or even hundreds. Furthermore, it can induce the genetic reprogramming of the cell, once again showing the importance of the scaffold shape and subsequent cytoskeletal tension in the cell [187]. While direct cell therapies have huge promise, in some cases, movement of the liquids in the body might destroy new cell colonies. A primary example is the blood flow in the cardiovascular system. Then, more rigid scaffolds can be applied to keep cells in place [71]. Then, the question of biodegradability arises.

Sometimes it would be desired that after cells are self-sufficient, the scaffold would degrade and entirely normal tissue

(a)

(b)

(c)
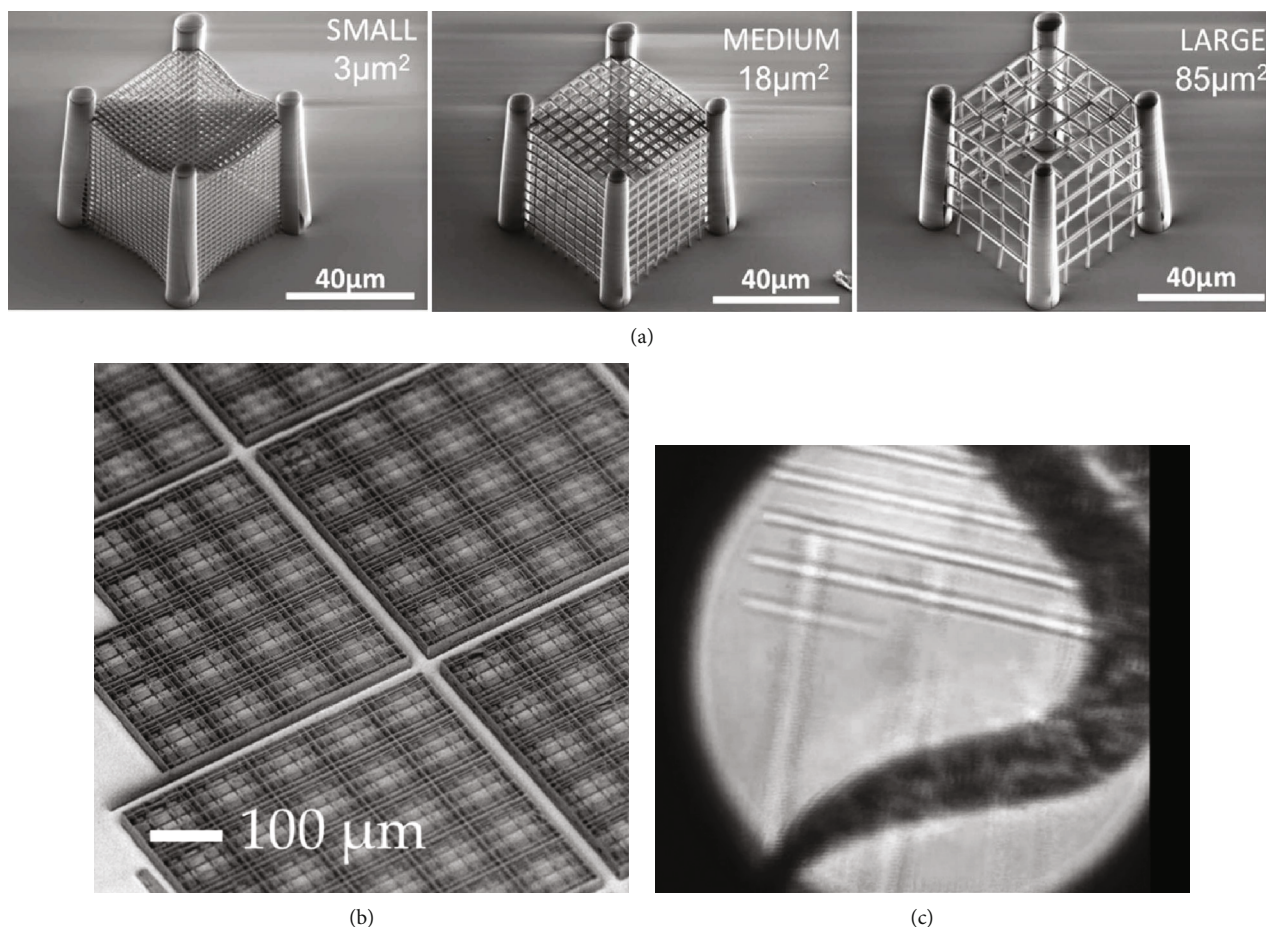
FIGURE 12: (a) SEM images of 3DLL-made structures with varied pore areas used to test cell interaction in scaffolds which might be smaller than the cell itself [186]. (b) Supermatrix of nichoids as a cell culture containing 218 matrices at a distance of 30 μm. Such structures show clear capabilities of 3DLL to be employed at mass production of biological scaffolds [73]. (c) Real-time view *via* setup imaging system depicting the writing of a scaffold in the presence of a living *Caenorhabditis elegans* showcasing that 3DLL combined with a biopolymer can be completely biofriendly and does not have adverse impact on living organisms [72].

would grow [188]. On the other hand, in some cases, nondegradable scaffolds are also acceptable. For instance, they could be employed in bone regeneration where they outperform modern cologne membranes [16, 189]. The middle ground between degradable and stiff scaffolds is shapeshifting structures [113]. 3DLL can be employed to print burr-like structures that could later be seeded with cells. Due to relatively small size and hooks on the outside, such balls can then be applied to the wound as a gel. It then mimics the shape of the wound. The freedom of geometry is a massive enabler in RM, and one could expect only more precisely tuned or nontrivial geometries to be used.

Most of the research conducted so far was performed *in vitro*. Results acquired in this manner are extremely important for the development of the field. However, *in vivo* applications need to follow. So far, several works were done in this area. For example, a 3D structure was printed in hydrogel in the presence of the whole organism [72]. The *Caenorhabditis elegans* used in this work was shown to not only survive in photoactive hydrogel but also live through the printing process (Figure 12(c)). This again shows that the cold nature of fs processing is extremely attractive in

RM. Keeping in mind that 3DLL can be realized through an optical fiber [190] which can also have advanced imaging lenses [12] or manipulation tools attached to it [14], true *in situ* bioprinting inside a living human can be envisioned in the future. Finally, preclinical *in vivo* trials were also performed, showing that hard hybrid polymer 3D scaffolds can outperform standard collagen membranes in healing trauma [16]. The presented results were acquired in the time frame of up to 6 months. It proves that 3DLL made scaffolds can be implanted into living organisms for prolonged amount of times with the positive impact to the healing, which is the final goal of RM.

5. Challenges and Perspectives

The results presented so far show great potential of 3DLL in RM. Nevertheless, a lot more needs to be done before it becomes a widespread solution. Here, we look into some of the newest trends in 3DLL with the emphasis on how these can benefit RM in the future.

Biocompatibility is the key requirement in RM. While a lot of biocompatible materials were tested already [26, 124,

(a)	(b)	(c)
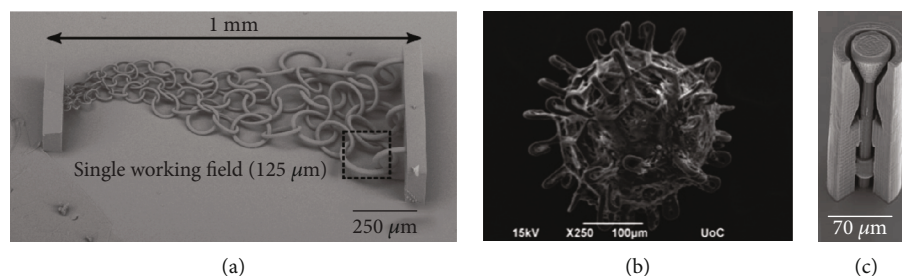
Figure 13: (a) A gradient chainmail-like structure which could be used as a mechanically flexible scaffold while still being made out of hard material. The mm scale size is sufficient for usage in real clinical trials. It is important to note that it was done using a galvo scanner and linear stage synchronization allowing to avoid stitching. It would have been detrimental to the mechanical quality of the structure (Adapted with permission from [6] © The Optical Society.). (b) Burr-like ball seeded with cells. Due to the geometry of the structure and hook-like outer ends, multiples of such objects can join together in the wound forming a shape-replicating structure (Reproduced from [113], with the permission of American Vacuum Society.). (c) Example of a passive microvalve allowing the flow of liquid only in one direction. Enhanced and custom-tuned objects of this kind could potentially be used in the veins to replace worn out biological analogs (adopted from [110]).

188], this area is still relatively active. The key questions here are compromise between effectiveness of PI and fabrication throughput, dissolvability in water, and other appropriate solvents and long-term effects of PI presence in the living body. Indeed, some materials require extensive exposure to fully start the polymerization reaction [52]. Fast-acting PIs are being constantly developed [191]. Thus, one might expect that with the constant increase in fabrication throughput photoexcitation should not become the bottleneck of the 3DLL. What is more, these fast-acting new generation PIs are also being made to be dissolvable in water, allowing them to be used in biodegradable hydrogels [151]. On the other hand, they also have to be biocompatible. Some of the long-term studies showed that in some cases, PI can be completely inert in nondegradable scaffolds even after being in a living organism for up to 6 months [16]. Hydrogel-compatible high-speed PIs also show great promise in this regard [151]. However, more research in this area is needed. Also, one must not forget about the possibility to directly polymerize materials without PI completely forgoing the problem of PI's biocompatibility [133, 154]. This is especially true keeping in mind that PI-free printing was shown to be applicable even at high-speed fabrication.

The next challenge lies in producing deformable scaffolds and structures that could move inside soft tissue after being implanted. Most 3DLL-processable materials are relatively stiff, with Young's modulus well into ~GPa. Therefore, bone tissue replacement is one of the main areas where 3DLL was tested extensively [16, 189]. In order to apply it for soft tissue, several 3DLL-enabled tricks were also employed. A scaffold can have deformable geometry due to being made out of intertwined parts [6] (Figure 13(a)) or having very small features that can deform [13, 14]. Also, shape-shifting scaffolds made out of microballs seeded with cells are also an interesting prospect [113] (Figure 13(b)). However, true 3D nanostructuring of elastomer is desired. Despite this, so far, it was shown to be relatively complicated for several reasons. If standard PDMS is used, translation velocity is limited and/or the fabrication window is narrow (in comparison to standard 3DLL materials) [121, 122]. Shrinkage can also be a problem

[124]. Current progress in the field allows to relatively easily print mm scale scaffolds out of elastic materials [192]. Further downscaling could be expected in near future.

Alongside movement of soft tissue, mechanical flexibility is also relevant for mechanical metamaterials. In short, metamaterials are artificial materials with rationally designed features allowing properties beyond what is normally possible in nature [193], hence the Greek word *meta*, which means "beyond." So far, it was demonstrated that 3DLL is capable of producing objects with negative Poisson index [194], controllable thermal expansion [13], and negative effective static compressibility [195]. The prospect of such special properties on-demand brings the new dimension to RM. First, 3D microprinted stents become a possibility [196]. Then, basically any-sized blood vessel can be accommodated with them. Furthermore, scaffold reacting to the temperature, pressure, or chemical composition of surroundings can be created. Indeed, the polymer has an inherent property to swell or expand in the different liquids [197], meaning that the scaffold can react to this as well, potentially protecting cells from adverse materials in the immediate surrounding or, alternatively, opening more when special healing liquids are present. Overall, combining unlimited 3D geometry and smart architecture has a huge promise in RM, and one can expect this area to be exploited more and more in the near future.

Purpose-driven material development also led to polymers that can be dissolved after manufacturing. Indeed, 3DLL supports multimaterial printing [17, 197–199]. While it is already a powerful tool in RM, the possibility to "erase" some of the components that were 3D printed is an interesting prospect. Thus, polymers based and dissolvable in softer chemical solutions were developed [200]. The implication to RM is scaffolds that can be dissolved in the body at different stages on the treatment. Furthermore, keeping in mind diverse chemistry of the body, such scaffolds might be degraded by the body itself. Also, nondegradable and permanent materials might be combined in one structure. One of the possible applications could be a nondegradable valve [110] (Figure 13(c)) placed in veins with accompanying scaffold for better initial growth. After some time, the

scaffold would degrade leaving a very well-attached permanent valve.

Finally, material development should not overshadow challenges in the hardware and software needed for 3DLL. The key advances here are related to minimized workload to the user and increased throughput. Operator workload is being reduced by employing advanced software, which allows to perform monotonous tasks (for instance, structure placement on substrate) and printing optimization easier [70, 74]. In terms of hardware, additional components can be placed into the optical path enhancing throughout or versatility of the setup. The primary example in this regard is the spatial light modulator (SLM), which might help to increase fabrication throughput [201, 202]. If a cheaper and simpler solution is required, passive light shaping can be done [203, 204] sacrificing flexibility and tunability. Spatiotemporal light shaping is also possible [62, 63]. While it is highly promising for RM due to the capability to print relatively big (up to cm) structures, it has a disadvantage of being relatively complicated. Lastly, hardware solutions for very fast translation velocities are also coming. Current positioning systems based on galvo scanners, linear stages, or their synchronization can go as fast as mm/s–cm/s [6, 72]. However, with the advent of polygon scanners [205] and acoustooptics [206], these translation velocities might exceed m/s or even more. Nevertheless, both of these solutions have some distinct limitations. Polygon scanners cannot easily change the direction of scanning and have limited flexibility. Thus, they are suitable only for mass production of designs that will not change or will change minimally. Acoustooptical deflectors do not have this problem but are bound by limitation in sustaining polarization and possible temporal broadening of a fs pulse due to the severe dispersion. Therefore, a lot of work has to be done in order to apply these solutions to 3DLL technology.

6. Conclusions

RM is an extremely complex and challenging topic. As shown in this review, 3DLL is capable of overcoming these challenges. One of the main reasons is the extremely wide selection of materials and structuring regimes. Indeed, combining free choice of 3D architecture of a structure and usage-specific monomer-PI covers basically any need for RM, starting from hard scaffolds for bone regeneration to EM-imitating multicomponent structures. Keeping in mind that new materials directly tailored for this field are being constantly developed, printing technology improved, and new 3D geometries tested, one might realistically expect widespread adoption of this technology in the near future.

Conflicts of Interest

The authors declare that they have no conflicts of interest.

Authors' Contributions

G.M. prepared information concerning the materials discussed in the article. L.J. contributed parts discussing the technology and trends in the field. D.G. and S.S. provided general insights. All authors contributed to the preparation of the manuscript.

Acknowledgments

References

[1] L. Jonušauskas, S. Juodkazis, and M. Malinauskas, "Optical 3D printing: bridging the gaps in the mesoscale," *Journal of Optics*, vol. 20, article 053001, 2018.

[2] M. Malinauskas, A. Žukauskas, G. Bičkauskaitė, R. Gadonas, and S. Juodkazis, "Mechanisms of three-dimensional structuring of photo-polymers by tightly focussed femtosecond laser pulses," *Optics Express*, vol. 18, pp. 10209–10221, 2010.

[3] W. Haske, V. W. Chen, J. M. Hales et al., "65 nm feature sizes using visible wavelength 3-D multiphoton lithography," *Optics Express*, vol. 15, no. 6, pp. 3426–3436, 2007.

[4] M. Emons, K. Obata, T. Binhammer, A. Ovsianikov, B. N. Chichkov, and U. Morgner, "Two-photon polymerization technique with sub-50 nm resolution by sub-10 fs laser pulses," *Optical Materials Express*, vol. 2, no. 7, pp. 942–947, 2012.

[5] L. Jonušauskas, S. Rekštyte, R. Buividas et al., "Hybrid subtractive-additive-welding microfabrication for lab-on-chip (LOC) applications via single amplified femtosecond laser source," *Optical Engineering*, vol. 56, article 094108, 2017.

[6] L. Jonušauskas, D. Gailevičius, S. Rekštytė, T. Baldacchini, S. Juodkazis, and M. Malinauskas, "Mesoscale laser 3D printing," *Optics Express*, vol. 27, no. 11, pp. 15205–15221, 2019.

[7] M. Farsari, M. Vamvakaki, and B. N. Chichkov, "Multiphoton polymerization of hybrid materials," *Journal of Optics*, vol. 12, no. 12, p. 124001, 2010.

[8] C. Barner-Kowollik, M. Bastmeyer, E. Blasco et al., "3D Laser Micro- and Nanoprinting: Challenges for Chemistry," *Angewandte Chemie, International Edition*, vol. 56, no. 50, pp. 15828–15845, 2017.

[9] L. Maigyte, V. Purlys, J. Trull et al., "Flat lensing in the visible frequency range by woodpile photonic crystals," *Optics Letters*, vol. 38, no. 14, pp. 2376–2378, 2013.

[10] A. I. Aristov, M. Manousidaki, A. Danilov et al., "3D plasmonic crystal metamaterials for ultra-sensitive biosensing," *Scientific Reports*, vol. 6, no. 1, article 25380, 2016.

[11] C. Liberale, G. Cojoc, F. Bragheri et al., "Integrated microfluidic device for single-cell trapping and spectroscopy," *Scientific Reports*, vol. 3, no. 1, p. 1258, 2013.

[12] T. Gissibl, S. Thiele, A. Herkommer, and H. Giessen, "Two-photon direct laser writing of ultracompact multi-lens objectives," *Nature Photonics*, vol. 10, no. 8, pp. 554–560, 2016.

[13] J. Qu, M. Kadic, A. Naber, and M. Wegener, "Micro-structured two-component 3d metamaterials with negative thermal-expansion coefficient from positive constituents," *Scientific Reports*, vol. 7, no. 1, article 40643, 2017.

[14] M. Power, A. J. Thompson, S. Anastasova, and G.-Z. Yang, "A monolithic force-sensitive 3D microgripper fabricated on the tip of an optical fiber using 2-photon polymerization," *Small*, vol. 14, no. 16, article 1703964, 2018.

[15] D. Wu, S. Z. Wu, J. Xu, L. G. Niu, K. Midorikawa, and K. Sugioka, "Hybrid femtosecond laser microfabrication to achieve true 3D glass/polymer composite biochips with multiscale features and high performance: the concept of ship-in-a-bottle biochip," *Laser & Photonics Reviews*, vol. 8, no. 3, pp. 458–467, 2014.

[16] J. Mačiulaitis, M. Deveikytė, S. Rekštytė et al., "Preclinical study of SZ2080 material 3D microstructured scaffolds for cartilage tissue engineering made by femtosecond direct laser writing lithography," *Biofabrication*, vol. 7, no. 1, article 015015, 2015.

[17] B. Richter, V. Hahn, S. Bertels et al., "Guiding cell attachment in 3D microscaffolds selectively functionalized with two distinct adhesion proteins," *Advanced Materials*, vol. 29, no. 5, article 1604342, 2017.

[18] S. Maruo, O. Nakamura, and S. Kawata, "Three-dimensional microfabrication with two-photon-absorbed photopolymerization," *Optics Letters*, vol. 22, no. 2, pp. 132–134, 1997.

[19] Z.-J. Chen, J. Yao, Q.-J. Xu, and Z.-H. Wang, "Two-photon polymerization fabrication and Raman spectroscopy research of SU-8 photoresist using the femtosecond laser," *Optoelectronics Letters*, vol. 13, no. 3, pp. 210–213, 2017.

[20] A. Ovsianikov, M. Gruene, M. Pflaum et al., "Laser printing of cells into 3D scaffolds," *Biofabrication*, vol. 2, no. 1, article 014104, 2010.

[21] J. Serbin, A. Egbert, A. Ostendorf et al., "Femtosecond laser-induced two-photon polymerization of inorganic-organic hybrid materials for applications in photonics," *Optics Letters*, vol. 28, no. 5, pp. 301–303, 2003.

[22] D. S. Correa, P. Tayalia, G. Cosendey et al., "Two-photon polymerization for fabricating structures containing the biopolymer chitosan," *Journal of Nanoscience and Nanotechnology*, vol. 9, no. 10, pp. 5845–5849, 2009.

[23] C. Mason and P. Dunnill, "A brief definition of regenerative medicine," *Regenerative Medicine*, vol. 3, no. 1, pp. 1–5, 2008.

[24] R. J. Narayan, A. Doraiswamy, D. B. Chrisey, and B. N. Chichkov, "Medical prototyping using two photon polymerization," *Materials Today*, vol. 13, no. 12, pp. 42–48, 2010.

[25] M. T. Raimond, S. M. Eaton, M. M. Nava, M. Laganà, G. Cerullo, and R. Osellame, "Two-photon laser polymerization: from fundamentals to biomedical application in tissue engineering and regenerative medicine," *Journal of Applied Biomaterials & Functional Materials*, vol. 10, no. 1, pp. 56–66, 2012.

[26] J. Torgersen, X. H. Qin, Z. Li, A. Ovsianikov, R. Liska, and J. Stampfl, "Hydrogels for Two-Photon Polymerization: A Toolbox for Mimicking the Extracellular Matrix," *Advanced Functional Materials*, vol. 23, no. 36, pp. 4542–4554, 2013.

[27] T. Stichel, B. Hecht, R. Houbertz, and G. Sextl, "Two-photon polymerization as method for the fabrication of large scale biomedical scaffold applications," *Journal of Laser Micro/Nanoengineering*, vol. 5, no. 3, pp. 209–212, 2010.

[28] A. Trautmann, M. Ruth, H.-D. Lemke, T. Walther, and R. Hellmann, "Two-photon polymerization based large scaffolds for adhesion and proliferation studies of human primary fibroblasts," *Optics & Laser Technology*, vol. 106, pp. 474–480, 2018.

[29] B.-B. Xu, Y. L. Zhang, H. Xia, W. F. Dong, H. Ding, and H. B. Sun, "Fabrication and multifunction integration of microfluidic chips by femtosecond laser direct writing," *Lab on a Chip*, vol. 13, no. 9, pp. 1677–1690, 2013.

[30] S. D. Gittard, A. Ovsianikov, B. N. Chichkov, A. Doraiswamy, and R. J. Narayan, "Two-photon polymerization of microneedles for transdermal drug delivery," *Expert Opinion on Drug Delivery*, vol. 7, no. 4, pp. 513–533, 2010.

[31] C.-H. Lin, G.-B. Lee, B.-W. Chang, and G.-L. Chang, "A new fabrication process for ultra-thick microfluidic microstructures utilizing SU-8 photoresist," *Journal of Micromechanics and Microengineering*, vol. 12, no. 5, pp. 590–597, 2002.

[32] D. T. Pham, S. S. Dimov, and R. S. Gault, "Part orientation in stereolithography," *International Journal of Advanced Manufacturing Technology*, vol. 15, no. 9, pp. 674–682, 1999.

[33] M. Han, W. Lee, S.-K. Lee, and S. S. Lee, "3D microfabrication with inclined/rotated UV lithography," *Sensors and Actuators A: Physical*, vol. 111, no. 1, pp. 14–20, 2004.

[34] G. Grigalevičiūtė, D. Baltriukienė, E. Balčiūnas, L. Jonušauskas, and M. Malinauskas, "Fabrication of flexible microporous 3D scaffolds via stereolithography and optimization of their biocompatibility," in *Advanced Fabrication Technologies for Micro/Nano Optics and Photonics XI*, vol. 10544, San Francisco, CA, USA, 2018.

[35] M. Göppert-Mayer, "Über elementarakte mit zwei quantensprüngen," *Annalen der Physik*, vol. 401, pp. 273–294, 1931.

[36] W. Kaiser and C. G. B. Garrett, "Two-photon excitation in CaF$_2$:Eu^{2+}," *Physical Review Letters*, vol. 7, pp. 229–231, 1961.

[37] R. R. Birge and B. M. Pierce, "Semiclassical time-dependent theory of two-photon spectroscopy. The effect of dephasing in the virtual level on the two-photon excitation spectrum of isotachysterol," *International Journal of Quantum Chemistry*, vol. 29, pp. 639–656, 1986.

[38] M. Farsari, G. Filippidis, and C. Fotakis, "Fabrication of three-dimensional structures by three-photon polymerization," *Optics Letters*, vol. 30, no. 23, pp. 3180–3182, 2005.

[39] J. Fischer, J. B. Mueller, J. Kaschke, T. J. A. Wolf, A. N. Unterreiner, and M. Wegener, "Three-dimensional multi-photon direct laser writing with variable repetition rate," *Optics Express*, vol. 21, no. 22, pp. 26244–26260, 2013.

[40] R. Buividas, S. Rekštyte, M. Malinauskas, and S. Juodkazis, "Nano-groove and 3D fabrication by controlled avalanche using femtosecond laser pulses," *Optical Materials Express*, vol. 3, no. 10, pp. 1674–1686, 2013.

[41] K. K. Seet, S. Juodkazis, V. Jarutis, and H. Misawa, "Feature-size reduction of photopolymerized structures by femtosecond optical curing of SU-8," *Applied Physics Letters*, vol. 89, no. 2, article 024106, 2006.

[42] M. Thiel, J. Fischer, G. Freymann, and M. Wegener, "Direct laser writing of three-dimensional submicron structures using a continuous-wave laser at 532 nm," *Applied Physics Letters*, vol. 97, no. 22, article 221102, 2010.

[43] A. I. Ciuciu and P. J. Cywinski, "Two-photon polymerization of hydrogels – versatile solutions to fabricate well-defined 3D structures," *RSC Advances*, vol. 4, no. 85, pp. 45504–45516, 2014.

[44] J. Fouassier, *Photoinitiation Photopolymerization and Photocuring*, Hanser Publishers, 1995.

[45] K. Haraguchi and T. Takehisa, "Nanocomposite hydrogels: a unique organic-inorganic network structure with extraordinary mechanical, optical, and swelling/de-swelling properties," *Advanced Materials*, vol. 14, pp. 1120–1124, 2002.

[46] S. Edmondson and M. Gilbert, "Chapter 2 - the chemical nature of plastics polymerization," in *Brydson's Plastics*

Materials (Eighth Edition), M. Gilbert, Ed., pp. 19–37, Butterworth-Heinemann, 2017.

[47] W.-F. Su, "Radical Chain Polymerization," in *Principles of Polymerization*, pp. 198–349, Springer, Berlin Heidelberg, Berlin, Heidelberg, 2013.

[48] J. Kreutzer and Y. Yagci, "Metal free reversible-deactivation radical polymerizations: advances, challenges, and opportunities," *Polymers*, vol. 10, no. 1, p. 35, 2017.

[49] N. Alharbi, R. Osman, and D. Wismeijer, "Effects of build direction on the mechanical properties of 3D-printed complete coverage interim dental restorations," *The Journal of Prosthetic Dentistry*, vol. 115, no. 6, pp. 760–767, 2016.

[50] J. V. Crivello, *Polymer Science: A Comprehensive Reference, vol. 4*, Elsevier Science, 2012.

[51] K. T. Nguyen and J. L. West, "Photopolymerizable hydrogels for tissue engineering applications," *Biomaterials*, vol. 23, no. 22, pp. 4307–4314, 2002.

[52] E. Skliutas, S. Kašetaite, L. Jonušauskas, J. Ostrauskaite, and M. Malinauskas, "Photosensitive naturally derived resins toward optical 3-D printing," *Optical Engineering*, vol. 57, no. 4, p. 1, 2018.

[53] I. Sakellari, E. Kabouraki, D. Gray et al., "Diffusion-assisted high-resolution direct femtosecond laser writing," *ACS Nano*, vol. 6, no. 3, pp. 2302–2311, 2012.

[54] P. Prabhakaran, Y. Son, C. W. Ha, J. J. Park, S. Jeon, and K. S. Lee, "Optical materials forming tightly polymerized voxels during laser direct writing," *Advanced Engineering Materials*, vol. 20, no. 10, article 1800320, 2018.

[55] A. Žukauskas, I. Matulaitienė, D. Paipulas, G. Niaura, M. Malinauskas, and R. Gadonas, "Tuning the refractive index in 3D direct laser writing lithography: towards GRIN microoptics," *Laser & Photonics Reviews*, vol. 9, no. 6, pp. 706–712, 2015.

[56] M. Malinauskas, G. Bičkauskaitė, M. Rutkauskas, D. Paipulas, V. Purlys, and R. Gadonas, "Self-polymerization of nanofibres and nano-membranes induced by two-photon absorption," *Lithuanian Journal of Physics*, vol. 50, no. 1, pp. 135–140, 2010.

[57] M. Gernhardt, E. Blasco, M. Hippler et al., "Tailoring the mechanical properties of 3d microstructures using visible light post-manufacturing," *Advanced Materials*, vol. 31, article 1901269, 2019.

[58] L. Jonušauskas, D. Mackevičiūtė, G. Kontenis, and V. Purlys, "Femtosecond lasers: the ultimate tool for high-precision 3D manufacturing," *Advanced Optical Technologies*, vol. 8, no. 3-4, pp. 241–251, 2019.

[59] M. Malinauskas, P. Danilevicius, and S. Juodkazis, "Three-dimensional micro-/nano-structuring via direct write polymerization with picosecond laser pulses," *Optics Express*, vol. 19, no. 6, pp. 5602–5610, 2011.

[60] E. Stankevicius, E. Daugnoraite, A. Selskis, S. Juodkazis, and G. Račiukaitis, "Photo-polymerization differences by using nanosecond and picosecond laser pulses," *Optics Express*, vol. 25, no. 5, pp. 4819–4830, 2017.

[61] T. Tičkūnas, M. Perrenoud, S. Butkus et al., "Combination of additive and subtractive laser 3D microprocessing in hybrid glass/polymer microsystems for chemical sensing applications," *Optics Express*, vol. 25, no. 21, pp. 26280–26288, 2017.

[62] F. He, H. Xu, Y. Cheng et al., "Fabrication of microfluidic channels with a circular cross section using spatiotemporally focused femtosecond laser pulses," *Optics Letters*, vol. 35, no. 7, pp. 1106–1108, 2010.

[63] Y. Tan, W. Chu, P. Wang et al., "High-throughput multi-resolution three dimensional laser printing," *Physica Scripta*, vol. 94, no. 1, article 015501, 2018.

[64] J. Hering, E. H. Waller, and G. Von Freymann, "Automated aberration correction of arbitrary laser modes in high numerical aperture systems," *Optics Express*, vol. 24, no. 25, pp. 28500–28508, 2016.

[65] M. Straub and M. Gu, "Near-infrared photonic crystals with higher-order bandgaps generated by two-photon photopolymerization," *Optics Letters*, vol. 27, no. 20, pp. 1824–1826, 2002.

[66] K. Obata, A. El-Tamer, L. Koch, U. Hinze, and B. N. Chichkov, "High-aspect 3D two-photon polymerization structuring with widened objective working range (WOW-2PP)," *Light: Science & Applications*, vol. 2, no. 12, article e116, 2013.

[67] J. S. Oakdale, R. F. Smith, J. B. Forien et al., "*Direct Laser Writing of Low-Density Interdigitated Foams for Plasma Drive Shaping*," *Advanced Functional Materials*, vol. 27, no. 43, article 1702425, 2017.

[68] J. Li, P. Fejes, D. Lorenser et al., "Two-photon polymerisation 3D printed freeform micro-optics for optical coherence tomography fibre probes," *Scientific Reports*, vol. 8, no. 1, p. 14789, 2018.

[69] H. Ni, G. Yuan, L. Sun et al., "Large-scale high-numerical-aperture super-oscillatory lens fabricated by direct laser writing lithography," *RSC Advances*, vol. 8, no. 36, pp. 20117–20123, 2018.

[70] S. Dehaeck, B. Scheid, and P. Lambert, "Adaptive stitching for meso-scale printing with two-photon lithography," *Additive Manufacturing*, vol. 21, pp. 589–597, 2018.

[71] P. Danilevičius, S. Rekštytė, E. Balčiūnas et al., "Direct laser fabrication of polymeric implants for cardiovascular surgery," *Materials Science*, vol. 18, pp. 145–149, 2012.

[72] J. Torgersen, A. Ovsianikov, V. Mironov et al., "Photo-sensitive hydrogels for three-dimensional laser microfabrication in the presence of whole organisms," *Journal of Biomedical Optics*, vol. 17, no. 10, article 105008, 2012.

[73] D. Ricci, M. Nava, T. Zandrini, G. Cerullo, M. Raimondi, and R. Osellame, "Scaling-up techniques for the nanofabrication of cell culture substrates via two-photon polymerization for industrial-scale expansion of stem cells," *Materials*, vol. 10, no. 1, p. 66, 2017.

[74] E. Yulianto, S. Chatterjee, V. Purlys, and V. Mizeikis, "Imaging of latent three-dimensional exposure patterns created by direct laser writing in photoresists," *Applied Surface Science*, vol. 479, pp. 822–827, 2019.

[75] M. Manousidaki, D. G. Papazoglou, M. Farsari, and S. Tzortzakis, "Abruptly autofocusing beams enable advanced multiscale photo-polymerization," *Optica*, vol. 3, no. 5, pp. 525–530, 2016.

[76] Y. Y. Schechner, N. Kiryati, and J. Shamir, "Separation of transparent layers by polarization analysis," *Surfaces*, vol. 8, p. 18, 1999.

[77] C. N. LaFratta and T. Baldacchini, "Two-photon polymerization metrology: characterization methods of mechanisms and microstructures," *Micromachines*, vol. 8, no. 4, p. 101, 2017.

[78] V. R. Sastri, "Chapter 7 - Engineering thermoplastics: acrylics, polycarbonates, polyurethanes, polyacetals, polyesters, and

polyamides," in *Plastics in Medical Devices*, pp. 121–173, William Andrew, 2010.

[79] S. Sarkar, K. B. Visscher, D. K. Hood, and C. J. Wasserman, "National Center for Biotechnology Information," Patent US2016282737, 2014.

[80] U. Ali, K. J. Abd Karim, and N. Buang, "A review of the properties and applications of poly (methyl methacrylate) (pmma)," *Polymer Reviews*, vol. 55, no. 4, pp. 678–705, 2015.

[81] M. Rahmah, N. Razali, A. Ehsan, and S. Shaari, "Characterisation and process optimisation of photosensitive acrylates for photonics applications," *Science and Technology of Advanced Materials*, vol. 6, no. 3-4, pp. 375–382, 2005.

[82] T. Baldacchini, C. N. LaFratta, R. A. Farrer et al., "Acrylic-based resin with favorable properties for three-dimensional two-photon polymerization," *Journal of Applied Physics*, vol. 95, no. 11, pp. 6072–6076, 2004.

[83] M. Farsari, G. Filippidis, K. Sambani, T. S. Drakakis, and C. Fotakis, "Two-photon polymerization of an eosin Y-sensitized acrylate composite," *Journal of Photochemistry and Photobiology A: Chemistry*, vol. 181, no. 1, pp. 132–135, 2006.

[84] R. J. Winfield and S. O'Brien, "Two-photon polymerization of an epoxy-acrylate resin material system," *Applied Surface Science*, vol. 257, no. 12, pp. 5389–5392, 2011.

[85] T. Zandrini, N. Liaros, L. J. Jiang et al., "Effect of the resin viscosity on the writing properties of two-photon polymerization," *Optical Materials Express*, vol. 9, no. 6, pp. 2601–2616, 2019.

[86] A. Campo and C. Greiner, "SU-8: a photoresist for high-aspect-ratio and 3D submicron lithography," *Journal of Micromechanics and Microengineering*, vol. 17, no. 6, pp. R81–R95, 2007.

[87] G. Witzgall, R. Vrijen, E. Yablonovitch, V. Doan, and B. J. Schwartz, "Single-shot two-photon exposure of commercial photoresist for the production of three-dimensional structures," *Optics Letters*, vol. 23, no. 22, pp. 1745–1747, 1998.

[88] W. H. Teh, U. Dürig, G. Salis et al., "SU-8 for real three-dimensional subdiffraction-limit two-photon microfabrication," *Applied Physics Letters*, vol. 84, no. 20, pp. 4095–4097, 2004.

[89] B. Bilenberg, S. Jacobsen, M. S. Schmidt et al., "High resolution 100 kV electron beam lithography in SU-8," *Microelectronic Engineering*, vol. 83, no. 4-9, pp. 1609–1612, 2006.

[90] Y. Liu, D. D. Nolte, and L. J. Pyrak-Nolte, "Large-format fabrication by two-photon polymerization in SU-8," *Applied Physics A: Materials Science & Processing*, vol. 100, no. 1, pp. 181–191, 2010.

[91] H. E. Williams, D. J. Freppon, S. M. Kuebler, R. C. Rumpf, and M. A. Melino, "Fabrication of three-dimensional micro-photonic structures on the tip of optical fibers using SU-8," *Optics Express*, vol. 19, no. 23, pp. 22910–22922, 2011.

[92] J. Serbin, A. Ovsianikov, and B. Chichkov, "Fabrication of woodpile structures by two-photon polymerization and investigation of their optical properties," *Optics Express*, vol. 12, no. 21, pp. 5221–5228, 2004.

[93] M. F. Akhtar, M. Hanif, and N. M. Ranjha, "Methods of synthesis of hydrogels … A review," *Saudi Pharmaceutical Journal*, vol. 24, no. 5, pp. 554–559, 2016.

[94] E. Ahmed and M. Hydrogel, "Hydrogel: Preparation, characterization, and applications: A review," *Journal of Advanced Research*, vol. 6, no. 2, pp. 105–121, 2015.

[95] A. Ovsianikov, M. Malinauskas, S. Schlie et al., "Three-dimensional laser micro- and nano-structuring of acrylated poly(ethylene glycol) materials and evaluation of their cytoxicity for tissue engineering applications," *Acta Biomaterialia*, vol. 7, no. 3, pp. 967–974, 2010.

[96] L. D. V. Lith, *Functionalization of Poly-(Ethylene Glycol)-Diacrylate (PEGda) with Different Molecular Mass using Two-Photon-Polymerisation*, TU Dresden, 2016.

[97] O. Kufelt, A. el-Tamer, C. Sehring, M. Meißner, S. Schlie-Wolter, and B. N. Chichkov, "Water-soluble photopolymerizable chitosan hydrogels for biofabrication via two-photon polymerization," *Acta Biomaterialia*, vol. 18, pp. 186–195, 2015.

[98] J.-F. Xing, M.-L. Zheng, and X.-M. Duan, "Two-photon polymerization microfabrication of hydrogels: an advanced 3D printing technology for tissue engineering and drug delivery," *Chemical Society Reviews*, vol. 44, no. 15, pp. 5031–5039, 2015.

[99] A. Dehghan and J. Ansary, "Sol-gel process applications: a mini-review," *Proceedings of the Nature Research Society*, vol. 2, article 02008, 2018.

[100] J. Livage, "Sol-gel processes," *Current Opinion in Solid State & Materials Science*, vol. 2, no. 2, pp. 132–138, 1997.

[101] R. D. Maggio, S. Dirè, E. Callone, F. Girardi, and G. Kickelbick, "Hybrid organic-inorganic materials using zirconium based NBBs and vinyl trimethoxysilane: Effect of pre-hydrolysis of silane," *Polymer*, vol. 51, no. 4, pp. 832–841, 2010.

[102] F. Osterholtz and E. Pohl, "Kinetics of the hydrolysis and condensation of organofunctional alkoxysilanes: a review," *Journal of Adhesion Science and Technology*, vol. 6, no. 1, pp. 127–149, 1992.

[103] C. Michelina and F. Bollino, "Synthesis and characterization of amorphous and hybrid materials obtained by sol-gel processing for biomedical applications," in *Biomedical Science, Engineering and Technology*, D. N. Ghista, Ed., IntechOpen, 2012.

[104] B. Arkles, J. Steinmetz, J. Zazyczny, and P. Mehta, "Factors contributing to the stability of alkoxysilanes in aqueous solution," *Journal of Adhesion Science and Technology*, vol. 6, no. 1, pp. 193–206, 1992.

[105] C. Brinker, "Hydrolysis and condensation of silicates: effects on structure," *Journal of Non-Crystalline Solids*, vol. 100, no. 1-3, pp. 31–50, 1988.

[106] A. Ovsianikov, J. Viertl, B. Chichkov et al., "Ultra-low shrinkage hybrid photosensitive material for two-photon polymerization microfabrication," *ACS Nano*, vol. 2, no. 11, pp. 2257–2262, 2008.

[107] M. Malinauskas, A. Žukauskas, V. Purlys et al., "3D microoptical elements formed in a photostructurable germanium silicate by direct laser writing," *Optics and Lasers in Engineering*, vol. 50, no. 12, pp. 1785–1788, 2012.

[108] I. Sakellari, A. Gaidukeviciute, A. Giakoumaki et al., "Two-photon polymerization of titanium-containing sol–gel composites for three-dimensional structure fabrication," *Applied Physics A: Materials Science & Processing*, vol. 100, no. 2, pp. 359–364, 2010.

[109] M. Malinauskas, A. Žukauskas, K. Belazaras et al., "Laser fabrication of various polymer microoptical components," *The European Physical Journal Applied Physics*, vol. 58, no. 2, article 20501, 2012.

[110] C. Schizas, V. Melissinaki, A. Gaidukeviciute et al., "On the design and fabrication by two-photon polymerization of a readily assembled micro-valve," *International Journal of Advanced Manufacturing Technology*, vol. 48, no. 5-8, pp. 435–441, 2010.

[111] A. Žukauskas, M. Malinauskas, L. Kontenis et al., "Organic dye doped microstructures for optically active functional devices fabricated via two-photon polymerization technique," *Lithuanian Journal of Physics*, vol. 50, no. 1, pp. 55–61, 2010.

[112] L. Jonušauskas, M. Lau, P. Gruber et al., "Plasmon assisted 3D microstructuring of gold nanoparticle-doped polymers," *Nanotechnology*, vol. 27, no. 15, article 154001, 2016.

[113] P. Danilevicius, R. A. Rezende, F. D. A. S. Pereira et al., "Burr-like, laser-made 3D microscaffolds for tissue spheroid encagement," *Biointerphases*, vol. 10, no. 2, article 021011, 2015.

[114] Y. Xia and G. M. Whitesides, "Soft lithography," *Annual Review of Materials Science*, vol. 28, no. 1, pp. 153–184, 1998.

[115] G. M. Whitesides, "The origins and the future of microfluidics," *Nature*, vol. 442, no. 7101, pp. 368–373, 2006.

[116] S. Baudis, B. Steyrer, T. Pulka et al., "Photopolymerizable elastomers for vascular tissue regeneration," *Macromolecular Symposia*, vol. 296, no. 1, pp. 121–126, 2010.

[117] K. Yu, A. Xin, H. Du, Y. Li, and Q. Wang, "Additive manufacturing of self-healing elastomers," *NPG Asia Materials*, vol. 11, pp. 1–11, 2019.

[118] E. Briganti, D. Spiller, C. Mirtelli et al., "A composite fibrin-based scaffold for controlled delivery of bioactive pro-angiogenetic growth factors," *Journal of Controlled Release*, vol. 142, pp. 14–21, 2010.

[119] A. D. Lantada, H. A. Iniesta, B. P. Sánchez, and J. P. García-Ruíz, "Free-form rapid prototyped porous PDMS scaffolds incorporating growth factors promote chondrogenesis," *Advances in Materials Science and Engineering*, vol. 2014, Article ID 612976, 10 pages, 2014.

[120] D. Martella and C. Parmeggiani, "Advances in cell scaffolds for tissue engineering: the value of liquid crystalline elastomers," *Chemistry - A European Journal*, vol. 24, pp. 12206–12220, 2018.

[121] C. A. Coenjarts and C. K. Ober, "Two-photon three-dimensional microfabrication of poly(dimethylsiloxane) elastomers," *Chemistry of Materials*, vol. 16, no. 26, pp. 5556–5558, 2004.

[122] H. Zeng, D. Martella, P. Wasylczyk et al., "High-Resolution 3D Direct Laser Writing for Liquid-Crystalline Elastomer Microstructures," *Advanced Materials*, vol. 26, no. 15, pp. 2319–2322, 2014.

[123] S. Rekštyte, M. Malinauskas, and S. Juodkazis, "Three-dimensional laser micro-sculpturing of silicone: towards biocompatible scaffolds," *Optics Express*, vol. 21, no. 14, pp. 17028–17041, 2013.

[124] S. Pashneh-Tala, R. Owen, H. Bahmaee, S. Rekštytė, M. Malinauskas, and F. Claeyssens, "Synthesis, characterization and 3D micro-structuring via 2-photon polymerization of poly(glycerol sebacate)-methacrylate - an elastomeric degradable polymer," *Frontiers of Physics*, vol. 6, p. 41, 2018.

[125] T. Ohkita and S.-H. Lee, "Thermal degradation and biodegradability of poly (lactic acid)/corn starch biocomposites," *Journal of Applied Polymer Science*, vol. 100, no. 4, pp. 3009–3017, 2006.

[126] L. Jonušauskas, E. Skliutas, S. Butkus, and M. Malinauskas, "Custom on demand 3D printing of functional microstructures," *Lithuanian Journal of Physics*, vol. 55, no. 3, pp. 227–236, 2015.

[127] J. Torres, J. Cotelo, J. Karl, and A. P. Gordon, "Mechanical property optimization of FDM PLA in shear with multiple objectives," *JOM*, vol. 67, no. 5, pp. 1183–1193, 2015.

[128] E. Garskaite, L. Alinauskas, M. Drienovsky et al., "Fabrication of a composite of nanocrystalline carbonated hydroxyapatite (cHAP) with polylactic acid (PLA) and its surface topographical structuring with direct laser writing (DLW)," *RSC Advances*, vol. 6, no. 76, pp. 72733–72743, 2016.

[129] M. Lebedevaite, J. Ostrauskaite, E. Skliutas, and M. Malinauskas, "Photoinitiator free resins composed of plant-derived monomers for the optical μ-3D printing of thermosets," *Polymers*, vol. 11, p. 116, 2019.

[130] K. Maximova, X. Wang, A. Balčytis, L. Fan, J. Li, and S. Juodkazis, "Silk patterns made by direct femtosecond laser writing," *Biomicrofluidics*, vol. 10, no. 5, article 054101, 2016.

[131] Y.-L. Sun, Q. Li, S. M. Sun et al., "Aqueous multiphoton lithography with multifunctional silk-centred bio-resists," *Nature Communications*, vol. 6, no. 1, pp. 1–10, 2015.

[132] S. J. J. Kwok, I. A. Kuznetsov, M. Kim, M. Choi, G. Scarcelli, and S. H. Yun, "Selective two-photon collagen crosslinking *in situ* measured by Brillouin microscopy," *Optica*, vol. 3, no. 5, pp. 469–472, 2016.

[133] K. Parkatzidis, E. Kabouraki, A. Selimis et al., "Initiator-Free, Multiphoton Polymerization of Gelatin Methacrylamide," *Macromolecular Materials and Engineering*, vol. 303, no. 12, article 1800458, 2018.

[134] M. Shirai and H. Okamura, "UV-curable positive photoresists for screen printing plate," *Polymer International*, vol. 65, no. 4, pp. 362–370, 2016.

[135] X. Zheng, C. Ji, Q. Zeng et al., "Synthesis of novel copolymer based on precipitation polymerization and its application in positive-tone photoresist," *Journal of Polymer Research*, vol. 24, no. 11, article 1370, 2017.

[136] N. Tsutsumi, A. Fukuda, R. Nakamura, K. Kinashi, and W. Sakai, "Fabrication of three-dimensional microstructures in positive photoresist through two-photon direct laser writing," *Applied Physics A*, vol. 123, no. 8, p. 553, 2017.

[137] H.-Z. Cao, M.-L. Zheng, X.-Z. Dong, F. Jin, Z.-S. Zhao, and X.-M. Duan, "Two-photon nanolithography of positive photoresist thin film with ultrafast laser direct writing," *Applied Physics Letters*, vol. 102, no. 20, article 201108, 2013.

[138] O. Wei, F. Hu, and L. Wang, "Formation of nanotunnels inside a resist film in laser interference lithography," *Langmuir*, vol. 31, no. 19, pp. 5464–5468, 2015.

[139] S. Z. Huang and K. Y. Wu, "Health risk assessment of photoresists used in an optoelectronic semiconductor factory," *Risk Analysis*, 2019.

[140] A. Soyano, "Application of polymers to photoresist materials," *International Polymer Science and Technology*, vol. 39, pp. 47–54, 2012.

[141] W. Zhou, S. M. Kuebler, K. L. Braun et al., "An efficient two-photon-generated photoacid applied to positive-tone 3D microfabrication," *Science*, vol. 296, no. 5570, pp. 1106–1109, 2002.

[142] T. Yu, C. K. Ober, S. M. Kuebler, W. Zhou, S. R. Marder, and J. W. Perry, "Chemically amplified positive resists for two-

photon three-dimensional microfabrication," *Advanced Materials*, vol. 15, no. 6, pp. 517–521, 2003.

[143] S. M. Kuebler, K. L. Braun, W. Zhou et al., "Design and application of high-sensitivity two-photon initiators for three-dimensional microfabrication," *Journal of Photochemistry and Photobiology A: Chemistry*, vol. 158, no. 2-3, pp. 163–170, 2003.

[144] B. D. Zhao, G. L. Li, Y. Z. Shi, H. Q. Zhang, and T. Wang, "Synthesis and optical properties of novel d-π-a-π-d type cationic cyclopentadienyliron complexes of arenes," *RSC Advances*, vol. 5, no. 67, pp. 54749–54756, 2015.

[145] Z. Li, J. Torgersen, A. Ajami et al., "Initiation efficiency and cytotoxicity of novel water-soluble two-photon photoinitiators for direct 3d microfabrication of hydrogels," *RSC Advances*, vol. 3, no. 36, 2013.

[146] N. Pucher, A. Rosspeintner, V. Satzinger et al., "Structure−Activity relationship in d-π-a-π-d-based photoinitiators for the two-photon-induced photopolymerization process," *Macromolecules*, vol. 42, no. 17, pp. 6519–6528, 2009.

[147] X. Huang, X. Wang, and Y. Zhao, "Study on a series of water-soluble photoinitiators for fabrication of 3d hydrogels by two-photon polymerization," *Dyes and Pigments*, vol. 141, pp. 413–419, 2017.

[148] F. Terenziani, A. Painelli, C. Katan, M. Charlot, and M. Blanchard-Desce, "Charge instability in quadrupolar chromophores: symmetry breaking and solvatochromism," *Journal of the American Chemical Society*, vol. 128, no. 49, pp. 15742–15755, 2007.

[149] S. J. Bryant, C. R. Nuttelman, and K. S. Anseth, "Cytocompatibility of UV and visible light photoinitiating systems on cultured NIH/3T3 fibroblasts in vitro," *Journal of Biomaterials Science, Polymer Edition*, vol. 11, no. 5, pp. 439–457, 2000.

[150] Q. Zou, Y. Zhao, N. S. Makarov et al., "Effect of alicyclic ring size on the photophysical and photochemical properties of bis(arylidene)cycloalkanone compounds," *Physical Chemistry Chemical Physics*, vol. 14, no. 33, pp. 11743–11752, 2012.

[151] P. E. Petrochenko, J. Torgersen, P. Gruber et al., "Laser 3D printing with sub-microscale resolution of porous elastomeric scaffolds for supporting human bone stem cells," *Advanced Healthcare Materials*, vol. 4, no. 5, pp. 739–747, 2014.

[152] M. Albota, D. Beljonne, J. L. Brédas et al., "Design of organic molecules with large two-photon absorption cross sections," *Science*, vol. 281, no. 5383, pp. 1653–1656, 1998.

[153] L. Markus, O. Dmitri, J. Hilborn et al., "Two-photon degradation of a hyaluronic acid based hydrogel using a two-photon initiator as photosensitizer," *Frontiers in Bioengineering and Biotechnology*, vol. 4, 2016.

[154] L. Jonušauskas, D. Gailevičius, L. Mikoliūnaitė et al., "Optically clear and resilient free-form μ-Optics 3D-printed via ultrafast laser lithography," *Materials*, vol. 10, no. 1, p. 12, 2017.

[155] H. Ceylan, I. C. Yasa, O. Yasa, A. F. Tabak, J. Giltinan, and M. Sitti, "3D-printed biodegradable microswimmer for theranostic cargo delivery and release," *ACS Nano*, vol. 13, no. 3, pp. 3353–3362, 2019.

[156] M. Pelton, J. Aizpurua, and G. Bryant, "Metal-nanoparticle plasmonics," *Laser & Photonics Review*, vol. 2, pp. 136–159, 2008.

[157] M. Moßhammer, K. E. Brodersen, M. Kühl, and K. Koren, "Nanoparticle-and microparticle-based luminescence imaging of chemical species and temperature in aquatic systems: a review," *Microchimica Acta*, vol. 186, no. 2, p. 126, 2019.

[158] A. L. Stepanov, R. Kiyan, A. Ovsianikov et al., "Synthesis and optical properties of silver nanoparticles in ORMOCER," *Applied Physics A: Materials Science & Processing*, vol. 108, no. 2, pp. 375–378, 2012.

[159] M. J. Ventura, C. Bullen, and M. Gu, "Direct laser writing of three-dimensional photonic crystal lattices within a PbS quantum-dot-doped polymer material," *Optics Express*, vol. 15, no. 4, pp. 1817–1822, 2007.

[160] Y. Peng, S. Jradi, X. Yang et al., "3D photoluminescent nanostructures containing quantum dots fabricated by two-photon polymerization: influence of quantum dots on the spatial resolution of laser writing," *Advanced Materials Technologies*, vol. 4, no. 2, article 1800522, 2018.

[161] C. Check, R. Chartoff, and S. Chang, "Effects of nanoparticles on photopolymerization of acrylate monomers in forming nano-composites," *European Polymer Journal*, vol. 70, pp. 166–172, 2015.

[162] V. V. Rocheva, A. V. Koroleva, A. G. Savelyev et al., "High-resolution 3D photopolymerization assisted by upconversion nanoparticles for rapid prototyping applications," *Scientific Reports*, vol. 8, no. 1, p. 3663, 2018.

[163] M. Suter, L. Zhang, E. C. Siringil et al., "Superparamagnetic microrobots: fabrication by two-photon polymerization and biocompatibility," *Biomedical Microdevices*, vol. 15, no. 6, pp. 997–1003, 2013.

[164] E. Blasco, J. Müller, P. Müller et al., "Fabrication of conductive 3D gold-containing microstructures via direct laser writing," *Advanced Materials*, vol. 28, no. 18, pp. 3592–3595, 2016.

[165] J. Li, B. Jia, and M. Gu, "Engineering stop gaps of inorganic-organic polymeric 3D woodpile photonic crystals with post-thermal treatment," *Optics Express*, vol. 16, no. 24, pp. 20073–20080, 2008.

[166] D. Gailevičius, V. Padolskytė, L. Mikoliūnaitė, S. Šakirzanovas, S. Juodkazis, and M. Malinauskas, "Additive-manufacturing of 3D glass-ceramics down to nanoscale resolution," *Nanoscale Horizons*, vol. 4, no. 3, pp. 647–651, 2019.

[167] A. Vyatskikh, S. Delalande, A. Kudo, X. Zhang, C. M. Portela, and J. R. Greer, "Additive manufacturing of 3d nano-architected metals," *Nature Communications*, vol. 9, no. 1, article 593, 2018.

[168] J. K. Gansel, M. Thiel, M. S. Rill et al., "Gold helix photonic metamaterial as broadband circular polarizer," *Science*, vol. 325, no. 5947, pp. 1513–1515, 2009.

[169] F. Kotz, P. Risch, K. Arnold et al., "Fabrication of arbitrary three-dimensional suspended hollow microstructures in transparent fused silica glass," *Nature Communications*, vol. 10, no. 1, pp. 1–7, 2019.

[170] M. Boffito, F. di Meglio, P. Mozetic et al., "Surface functionalization of polyurethane scaffolds mimicking the myocardial microenvironment to support cardiac primitive cells," *PLoS One*, vol. 13, no. 7, article e0199896, 2018.

[171] M. Iqbal, D. K. Dinh, Q. Abbas, M. Imran, H. Sattar, and A. Ul Ahmad, "Controlled surface wettability by plasma polymer surface modification," *Surfaces*, vol. 2, no. 2, pp. 349–371, 2019.

[172] T. Jonavicius, S. Rekštyte, and M. Malinauskas, "Microfabrication of 3D metallic interconnects via direct laser writing and chemical metallization," *Lithuanian Journal of Physics*, vol. 54, no. 3, pp. 162–169, 2014.

[173] S. Kim, F. Qiu, S. Kim et al., "Fabrication and characterization of magnetic microrobots for three-dimensional cell culture and targeted transportation," *Advanced Materials*, vol. 25, no. 41, pp. 5863–5868, 2013.

[174] B. Dhandayuthapani, Y. Yoshida, T. Maekawa, and D. S. Kumar, "Polymeric scaffolds in tissue engineering application: a review," *International Journal of Polymer Science*, vol. 2011, Article ID 290602, 19 pages, 2011.

[175] C. D. Roskelley and M. J. Bissell, "Dynamic reciprocity revisited: a continuous, bidirectional flow of information between cells and the extracellular matrix regulates mammary epithelial cell function," *Biochemistry and Cell Biology*, vol. 73, no. 7-8, pp. 391–397, 1995.

[176] A. Folch and M. Toner, "Microengineering of cellular interactions," *Annual Review of Biomedical Engineering*, vol. 2, no. 1, pp. 227–256, 2000.

[177] J. Fink, M. Théry, A. Azioune et al., "Comparative study and improvement of current cell micro-patterning techniques," *Lab on a Chip*, vol. 7, no. 6, pp. 672–680, 2007.

[178] Y. S. Nam and T. G. Park, "Porous biodegradable polymeric scaffolds prepared by thermally induced phase separation," *Journal of Biomedical Materials Research*, vol. 47, no. 1, pp. 8–17, 1999.

[179] Y. Yang, J. Zhao, Y. Zhao, L. Wen, X. Yuan, and Y. Fan, "Formation of porous PLGA scaffolds by a combining method of thermally induced phase separation and porogen leaching," *Journal of Applied Polymer Science*, vol. 109, no. 2, pp. 1232–1241, 2008.

[180] A. Salerno, M. Oliviero, E. D. Maio, S. Iannace, and P. A. Netti, "Design of porous polymeric scaffolds by gas foaming of heterogeneous blends," *Journal of Materials Science*, vol. 20, no. 10, pp. 2043–2051, 2009.

[181] X. Wu, Y. Liu, X. Li et al., "Preparation of aligned porous gelatin scaffolds by unidirectional freeze- drying method," *Acta Biomaterialia*, vol. 6, no. 3, pp. 1167–1177, 2010.

[182] H. Yoshimoto, Y. Shin, H. Terai, and J. Vacanti, "A biodegradable nanofiber scaffold by electrospinning and its potential for bone tissue engineering," *Biomaterials*, vol. 24, no. 12, pp. 2077–2082, 2003.

[183] A.-V. Do, B. Khorsand, S. M. Geary, and A. K. Salem, "3D printing of scaffolds for tissue regeneration applications," *Advanced Healthcare Materials*, vol. 4, no. 12, pp. 1742–1762, 2015.

[184] S. Turunen, E. Käpylä, M. Lähteenmäki, L. Ylä-Outinen, S. Narkilahti, and M. Kellomäki, "Direct laser writing of microstructures for the growth guidance of human pluripotent stem cell derived neuronal cells," *Optics and Lasers in Engineering*, vol. 55, pp. 197–204, 2014.

[185] P. Danilevicius, L. Georgiadi, C. J. Pateman, F. Claeyssens, M. Chatzinikolaidou, and M. Farsari, "The effect of porosity on cell ingrowth into accurately defined, laser-made, polylactide-based 3D scaffolds," *Applied Surface Science*, vol. 336, pp. 2–10, 2015.

[186] B. Spagnolo, V. Brunetti, G. Leménager et al., "Three-dimensional cage-like microscaffolds for cell invasion studies," *Scientific Reports*, vol. 5, no. 1, article 10531, 2015.

[187] M. M. Nava, A. Piuma, M. Figliuzzi et al., "Two-photon polymerized "nichoid" substrates maintain function of pluripotent stem cells when expanded under feeder-free conditions," *Stem Cell Research & Therapy*, vol. 7, no. 1, p. 132, 2016.

[188] P. Timashev, D. Kuznetsova, A. Koroleva et al., "Novel biodegradable star-shaped polylactide scaffolds for bone regeneration fabricated by two-photon polymerization," *Nanomedicine*, vol. 11, no. 9, pp. 1041–1053, 2016.

[189] A. Marino, C. Filippeschi, G. G. Genchi, V. Mattoli, B. Mazzolai, and G. Ciofani, "The osteoprint: a bioinspired two-photon polymerized 3-D structure for the enhancement of bone-like cell differentiation," *Acta Biomaterialia*, vol. 10, no. 10, pp. 4304–4313, 2014.

[190] E. E. Morales-Delgado, L. Urio, D. B. Conkey, N. Stasio, D. Psaltis, and C. Moser, "Three-dimensional microfabrication through a multimode optical fiber," *Optics Express*, vol. 25, no. 6, pp. 7031–7045, 2017.

[191] R. Whitby, Y. Ben-Tal, R. MacMillan et al., "Photoinitiators for two-photon polymerisation: effect of branching and viscosity on polymerisation thresholds," *RSC Advances*, vol. 7, no. 22, pp. 13232–13239, 2017.

[192] K. Obata, S. Slobin, A. Schonewille et al., "UV laser direct writing of 2D/3D structures using photo-curable polydimethylsiloxane (PDMS)," *Applied Physics A*, vol. 123, no. 7, p. 495, 2017.

[193] A. Q. Liu, W. M. Zhu, D. P. Tsai, and N. I. Zheludev, "Micromachined tunable metamaterials: a review," *Journal of Optics*, vol. 14, no. 11, article 114009, 2012.

[194] T. Bückmann, N. Stenger, M. Kadic et al., "Tailored 3D mechanical metamaterials made by dip-in direct-laser-writing optical lithography," *Advanced Materials*, vol. 24, no. 20, pp. 2710–2714, 2012.

[195] J. Qu, A. Gerber, F. Mayer, M. Kadic, and M. Wegener, "Experiments on metamaterials with negative effective static compressibility," *Physical Review X*, vol. 7, no. 4, article 04106, 2017.

[196] B. Stępak, A. J. Antończak, M. Bartkowiak-Jowsa, J. Filipiak, C. Pezowicz, and K. M. Abramski, "Fabrication of a polymer-based biodegradable stent using a CO_2 laser," *Archives of Civil and Mechanical Engineering*, vol. 14, no. 2, pp. 317–326, 2014.

[197] S. Rekštyte, D. Paipulas, M. Malinauskas, and V. Mizeikis, "Microactuation and sensing using reversible deformations of laser-written polymeric structures," *Nanotechnology*, vol. 28, no. 12, article 124001, 2017.

[198] L. Jonušauskas, S. Rekštyte, and M. Malinauskas, "Augmentation of direct laser writing fabrication throughput for three-dimensional structures by varying focusing conditions," *Optical Engineering*, vol. 53, no. 12, article 125102, 2014.

[199] F. Mayer, S. Richter, J. Westhauser, E. Blasco, C. Barner-Kowollik, and M. Wegener, "Multimaterial 3D laser microprinting using an integrated microfluidic system," *Science Advances*, vol. 5, no. 2, article eaau9160, 2019.

[200] D. Gräfe, A. Wickberg, M. M. Zieger, M. Wegener, E. Blasco, and C. Barner-Kowollik, "Adding chemically selective subtraction to multi-material 3D additive manufacturing," *Nature Communications*, vol. 9, no. 1, p. 2788, 2018.

[201] K. Obata, J. Koch, U. Hinze, and B. N. Chichkov, "Multifocus two-photon polymerization technique based on individually controlled phase modulation," *Optics Express*, vol. 18, no. 16, pp. 17193–17200, 2010.

[202] D. Yang, L. Liu, Q. Gong, and Y. Li, "Rapid Two-Photon Polymerization of an Arbitrary 3D Microstructure with 3D Focal Field Engineering," *Macromolecular Rapid Communications*, vol. 40, no. 8, article 1900041, 2019.

[203] C. F. Phelan, R. J. Winfield, D. P. O'Dwyer, Y. P. Rakovich, J. F. Donegan, and J. G. Lunney, "Two-photon polymerisation of novel shapes using a conically diffracted femtosecond laser beam," *Optics Communication*, vol. 284, no. 14, pp. 3571–3574, 2011.

[204] E. Stankevicius, T. Gertus, M. Rutkauskas et al., "Fabrication of micro-tube arrays in photopolymer SZ2080 by using three different methods of a direct laser polymerization technique," *Journal of Micromechanics and Microengineering*, vol. 22, no. 6, article 065022, 2012.

[205] R. D. Loor, "Polygon scanner system for ultra short pulsed laser micro-machining applications," *Physics Procedia*, vol. 41, pp. 544–551, 2013.

[206] G. R. B. E. Romer and P. Bechtold, "Electro-optic and acousto-optic laser beam scanners," *Physics Procedia*, vol. 56, pp. 29–39, 2014.

Research Article

Ganoderma lucidum Polysaccharide Enhanced the Antitumor Effects of 5-Fluorouracil against Gastric Cancer through Its Upregulation of NKG2D/MICA

Xi Yang,[1] Rui Zhang,[1] Jing Yao,[2] Chen Xi,[1] and Shuzhang Du ![ORCID][1]

[1]*Department of Pharmacy, The First Affiliated Hospital of Zhengzhou University, Zhengzhou, Henan 450000, China*
[2]*Jining Medical University, Jining, Shandong 272067, China*

Correspondence should be addressed to Shuzhang Du; fccdusz@zzu.edu.cn

5-Fluorouracil (5-Fu) is one of the frequently used first-line cytotoxic drugs for chemotherapy against gastric cancer. Chemotherapy and immunotherapy are currently the main methods for treating gastric cancer. Immunotherapy can enhance the antitumor effect of chemotherapy drugs at the same time reducing its toxicity. The combination of these two therapies to treat cancer has become a mainstay and has received increasing attention in clinical practice. *Ganoderma lucidum* polysaccharide (GLP) is isolated from the *Ganoderma lucidum* fruiting body. Studies have shown that GLP has antitumor effects, where GLP does not directly kill tumors, rather exerting its antitumor function by stimulating immune cells including natural killer (NK) cells and T cells. In this study, the antitumor effect of GLP combined with 5-Fu was studied in vivo. At the same time, the associated mechanism of GLP combined with 5-Fu in gastric cancer cell lines BGC823 and SGC7901 was investigated in vitro. The results showed that GLP could stimulate the killing effect of NK-92 cells on gastric cancer cell lines BGC823 and SGC7901 and synergistically enhance the toxic effects of NK-92 cells on gastric cancer cell lines BGC823 and SGC7901. Moreover, GLP could further promote the activity of NK-92 cells by activating the NK cell activating receptor NKG2D and its downstream DAP10/PI3K/ERK signaling pathway.

1. Introduction

Cytotoxic chemotherapy is an effective treatment for cancer. However, the use of cytotoxic drugs tends to be toxic to normal tissues, affecting the body's hematopoietic function and destroying the body's immune suppression system and easily leads to tumor resistance [1, 2]. Recently, an increasing amount of attention has been given to the combination use of chemotherapy and immunotherapy which not surprisingly has also been frequently practiced in clinical settings [3]. Not only sustaining the antitumor effect of chemotherapy drugs, immunotherapy can also reduce the immune damage incurred during chemotherapy [4]. The synergistic effects between chemotherapy and immunotherapy have been confirmed in several clinical trials. For example, gemcitabine combined with interleukin-2 has a significant effect in the treatment of metastatic colorectal cancer. In these studies,

chemotherapy and immunotherapy synergistically enhanced the presentation of tumor antigens by the immune system and made cytotoxic lymphocytes (CTL) and natural killer (NK) cells more sensitive for tumor cells [5–7].

Ganoderma lucidum belongs to the family *Ganoderma lucidum* and is a rarified Chinese herbal medicine [8]. *Ganoderma lucidum* polysaccharides (GLP) are the major active substances of *Ganoderma lucidum* and have various biological functions, including antitumor [9], immunomodulation [8, 10], antioxidation, and hypolipidemic effects [10]. Studies have shown that GLP can inhibit tumor growth in S180 sarcoma-bearing mice and can increase the proportion of CD4 or CD8 T cell subsets in S180 tumor-bearing mice. However, GLP had no cytotoxic effect on S180 cells and PG cells (human lung cancer cells) in vitro. Interestingly, the serum from GLP-treated S180 tumor-bearing mice significantly inhibited the proliferation of S180 cells and PG cells

in vitro. In addition, GLP can also promote the proliferation of spleen lymphocytes induced by concanavalin A (ConA) or lipopolysaccharide (LPS) and enhance the cytotoxic effects of natural killer (NK) cells and increase the rate of neutral red phagocytosis of macrophages as well. These findings suggested that the antitumor activity of GLP may be mainly associated with the host immune response stimulated by NK cells, T cells, and macrophages [11].

5-Fluorouracil (5-Fu) is a commonly used antimetabolic chemical agent that is widely used clinically in cancer treatment. However, application of 5-Fu can inhibit the immune system and cause leukopenia and atrophy of hematopoietic organs [12–14]. At the same time, 5-Fu also has immunomodulatory effects [15]. And clinically, 5-Fu is often used in combination with cytokines to treat cancer. One of a phase II trial for the treatment of pancreatic cancer with the combination of 5-Fu and Interferon (IFN) showed a 5-year overall survival rate of 55% [16].

In this study, we explored the antitumor effects and associated mechanism of 5-Fu combined with GLP in vivo. In vitro, GLP directly stimulated NK-92 cytotoxicity by upregulating the expression of NKG2D and activating the downstream DAP10/PI3K/ERK signaling pathway. As for 5-Fu, it has been shown to increase and maintain the expression of MHC class I-related molecule A (MHC class I-related china A, MICA) a ligand for NKG2D on gastric cancer cell XXX membrane by inhibiting the expression of ADAM10 (A Disintegrin And Metalloprotease 10) on tumor cells. In summary, the synergistic effect of GLP and 5-Fu enhanced the in vitro toxicity of NK-92 cells to gastric cancer cell lines BGC823 and SGC7901. These results suggested that the combination of GLP and 5-Fu may be a potential strategy for future treatment of gastric cancer.

2. Material and Methods

2.1. Material.
The *Ganoderma lucidum* fruiting body was obtained from Changbai Mountain in Jilin Province (Northern elevation $42°35'$, longitude $127°54'$, 731 meters above sea level). DEAE-52 cellulose and Sephadex G-100 were purchased from Sigma (USA). Fetal bovine serum, DMEM medium, 1640 medium, and trypsin were purchased from Gibco (USA). The reagents used in this study were analytical grade. The human natural killer cell line NK-92 and the gastric cancer cell lines BGC823 and SGC7901 were purchased from the Shanghai Institute of Cell Biology. The CytoTox96® nonradioactive cytotoxicity assay was purchased from Promega (USA).

2.2. Extraction and Purification of GLP.
GLP was extracted with a hot water extraction method [17]. The protein in the crude polysaccharide of *Ganoderma lucidum* was removed by following the sevag method [18]. The crude GLP from which the protein was removed were separated using a cellulose column (DEAE-52, $1.6\,cm\,d \times 40\,cm\,h$) to obtain GLP. Distilled water was then used to elute the resulting sample and followed with a gradient of 0.1 M, 0.2 M, 0.3 M, and 0.4 M sodium chloride solution separately. A Sephadex G-100 column ($1.6\,cm\,d \times 60\,cm\,h$) was then used to elute the obtained main component at a flow rate of 0.7 ml/min. Following that the phenol-sulfuric acid method was used to measure the concentration of the polysaccharide at 490 nm. The resulting components were then concentrated, dialyzed, and lyophilized to obtain the purified GLP.

2.3. Cell Culture.
The human natural killer cell line NK-92 was inoculated into α-MEM complete growth medium (DMEM medium was added with 0.2 mM inositol, 0.1 mM 2-mercaptoethanol, 0.02 mM folic acid, 200 U/ml recombinant IL-2, 12.5% horse serum, and 12.5% fetal bovine serum) and cultured in a constant temperature incubator at 37°C with 5% CO_2. Cells in the logarithmic growth phase were selected for subsequent experiments.

The gastric cancer cell lines BGC823 and SGC7901 were inoculated into RPMI-1640 medium supplemented with 10% fetal bovine serum, $100\,\mu g$/ml penicillin, and $100\,\mu g$/ml streptomycin and cultured in a constant temperature incubator at 37°C with 5% CO_2. The growth of tumor cells was monitored under the microscope, and the cells in the logarithmic growth phase were selected for subsequent experiments.

2.4. Measurement of NK Cell Killing Activity.
CytoTox96 nonradioactive cytotoxicity assay was used to detect the killing of NK cells against gastric cancer cells. Specifically, PBS was first used to rinse the tumor cells, and a fresh NK-92 medium was used for cell suspension, and finally, the cell suspension was seeded in 96-well plates with a density of 5×10^3 cells/well. NK-92 cells were then added to 96-well plates at a ratio of 10:1, 5:1, and 1:1, respectively (NK-92 cells to tumor cell). The 96-well plates were cultured for 4 h at 37°C in a 5% CO_2 atmosphere, then the supernatant in each well was collected, and the absorbance was measured at 490 nm. The killing effect of NK cells on target cells was evaluated by the following formula:

$$\%cytotoxicity = \frac{experiment - spontaneous\ effector\ cell - spontaneous\ target\ cell}{maximum\ target\ cell - spontaneous\ target\ cell} \times 100 \qquad (1)$$

2.5. Measurement of Cell Proliferation with Cell Counting Kit-8 (CCK8) Assay.
BGC823 and SGC7901 cell suspensions were seeded in 96-well plates at a density of 5×10^4 cells/ml, $100\,\mu l$ per well. The cells were cultured overnight at 37°C in a 5% CO_2 incubator. Cells were then given different concentrations of 5-Fu (concentration range: 1-50 μg/ml). After

culturing for 24 h, 10 μl of CCK8 solution was added to each well, and incubation was continued for another 4 h. The absorbance value of each well was measured at 450 nm with the microplate reader, and the experiment was repeated 3 times. The survival rate of BGC823 and SGC7901 cells was calculated by the following formula:

$$\%\text{cell survival} = \frac{\text{Mean value of absorbance in the treatment group}}{\text{Mean value of absorbance in the control group}} \times 100 \tag{2}$$

2.6. Establishment and Administration of BGC823 and SGC7901 Tumor-Bearing Mouse Models. BGC823 and SGC7901 cells (0.1 ml, 5×10^6 cells) were subcutaneously transplanted into the right ankle of balb/c nude mice. When the tumor grew to 100 mm^3, the mice were randomly divided into the following 7 groups, 5-6 mice per group: model group: intraperitoneal injection of saline; three different 5-Fu single groups: 6.25, 12.5, and 25 mg/kg (intraperitoneal injection of the corresponding 5-Fu drug); combined treatment group: three 5-Fu drug concentrations (6.25, 12.5, or 25 mg/kg) were combined with 200 mg/kg GLP for intraperitoneal injection [19]. Tumor size was measured every 3 days for 12 days, and data from day 12 was taken for analysis.

2.7. Detection of NKG2D Protein Expression with Fluorescence-Coupled Enzyme-Linked Immunosorbent Assay. NK-92, BGC823, and SGC7901 cell suspensions were seeded in 96-well plates at a density of 5×10^4 cells/ml, 100 μl per well. The cells were cultured overnight at 37°C in a 5% CO_2 incubator. The cells were then given different concentrations of GLP (concentration range: 0-200 μg/ml). After being cultured for 24 h, the disrupted cells were centrifuged to remove the supernatant, and the expression of NKG2D protein in the cells was detected by fluorescence-coupled enzyme-linked immunosorbent assay.

2.8. Western Blot. NK-92 cell suspensions were seeded in 96-well plates at a density of 5×10^4 cells/ml, 100 μl per well. The cells were cultured overnight at 37°C in a 5% CO_2 incubator. The cells were then given different concentrations of GLP (concentration range: 50-200 μg/ml). After being cultured for 24 h, cells were collected and total proteins were extracted with the protein lysate. After quantification, proteins were separated by SDS-PAGE and transferred to a PVDF membrane. After blocking for 2 h at room temperature, 5 different primary antibodies were added and incubated overnight at 4°C. The primary antibodies were then discarded and the corresponding secondary antibodies were added. After incubation at room temperature for 1 h, the images were developed.

2.9. Statistical Analysis. All data were expressed as means ± SEM. ANOVA was used to analyze statistical significance between each experimental group.

3. Results and Discussion

Chemotherapy along with immunotherapy is one of the current research hotspots in the clinical treatment of cancer. The combination of chemotherapy and immunotherapy not only has a synergistic antitumor effect but can also reduce the immune damage caused by chemotherapy [20, 21]. 5-Fu is a widely used chemotherapy drug in clinical settings. Although 5-Fu has immunosuppressive effects, several studies have demonstrated synergistic antitumor effects of 5-Fu when combined with immunomodulators such as IL-12 and IL-15 [21, 22]. The present study investigated the activity and mechanism of GLP combined with 5-Fu for cancer treatment in vitro and in vivo.

3.1. Extraction and Purification of GLP. The deproteinization rate for the crude polysaccharides was 1.5%, and the total sugar content was 27.85%. DEAE-52 cellulose was then used to separate and to obtain two components, DEAE-1 and DEAE-2, with a total sugar content of 58.21% and 18.96%, respectively. The DEAE-1 fraction having a higher polysaccharide content was further purified with a Sephadex G-100 to obtain GLP with a total sugar content of 75.56%.

3.2. GLP Directly Activated the Antitumor Effects of NK-92 Cells. It is well known that NK cells are an important part of the innate immune system and play an important role in combating cancer [23].

The effects of GLP on the activity of NK-92 cells were determined using the CytoTox96 nonradioactive cytotoxicity assay. As shown in Figure 1(a), NK-92 cells were used as effector cells, and BGC823 gastric cancer cells were used as target cells. The results showed that the killing effects of NK-92 cells on BGC823 gastric cancer cells were enhanced after GLP treatment ($p < 0.05$), and the activity of NK-92 cells reached the highest when GLP was at 400 μg/ml, indicating that GLP can directly stimulate the antitumor activity of NK cells in vitro. The results of Figure 1(b) indicated that the 50% inhibitory concentration (IC50) of 5-Fu against BGC823 and SGC7901 gastric cancer cells was about 50 μg/ml at 24 h. Therefore, in the subsequent experiment, 5-Fu was used at a concentration of 20 μg/ml, which was about half of the IC50 value. GLP was used at a concentration of 400 μg/ml.

3.3. GLP and 5-Fu Synergistically Enhanced the Cytotoxic Effects of NK-92 Cells on Tumor Cells. CytoTox96 nonradioactive cytotoxicity assay was used to determine whether GLP combined with 5-Fu can enhance the cytotoxicity of NK-92 cells against BGC823 and SGC7901 cells. NK-92 cells pretreated with GLP (400 μg/ml, 24 h) and BGC823 cells or SGC7901 cells pretreated with 5-Fu (20 μg/ml, 24 h) were cocultured and compared with the normal control group.

(a)

(b)
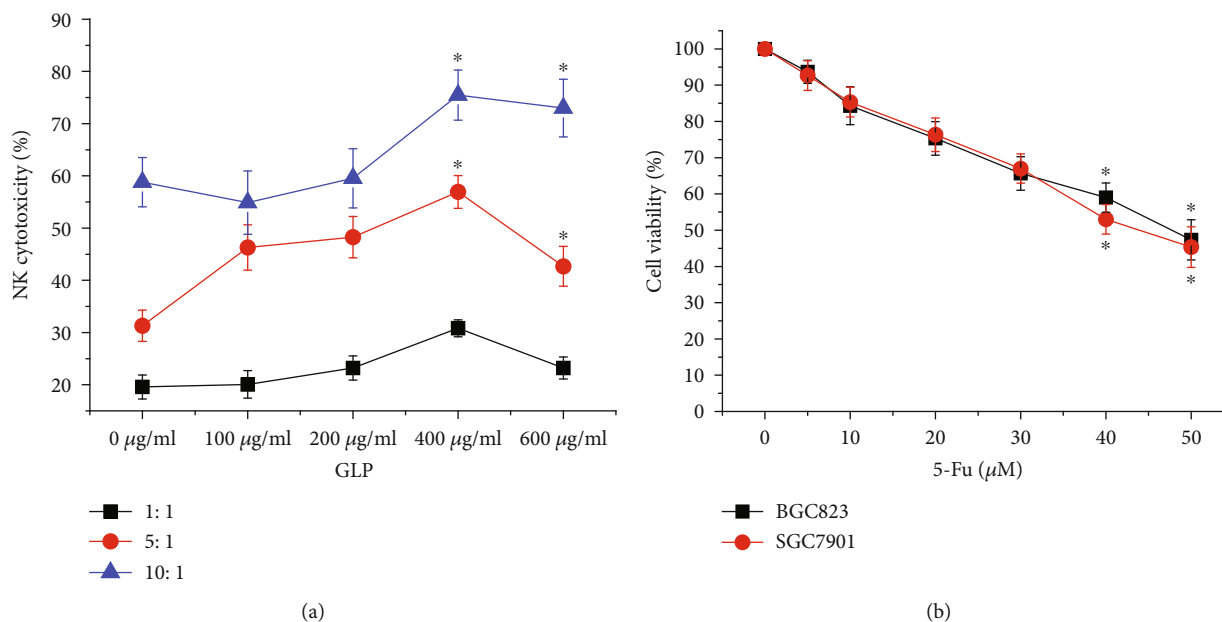
FIGURE 1: GLP directly enhanced the cytotoxicity of NK-92 cells. (a) GLP increased NK-92 cell cytotoxicity against BGC823 gastric cancer cells in a dose- and ratio-dependent manner. (b) CCK8 cell proliferation assay showed that 5-Fu had cytotoxic effects on BGC823 and SGC7901 gastric cancer cells. Data were expressed as means ± SEM, and compared with the normal group, * indicated $p < 0.05$.

(a)

(b)
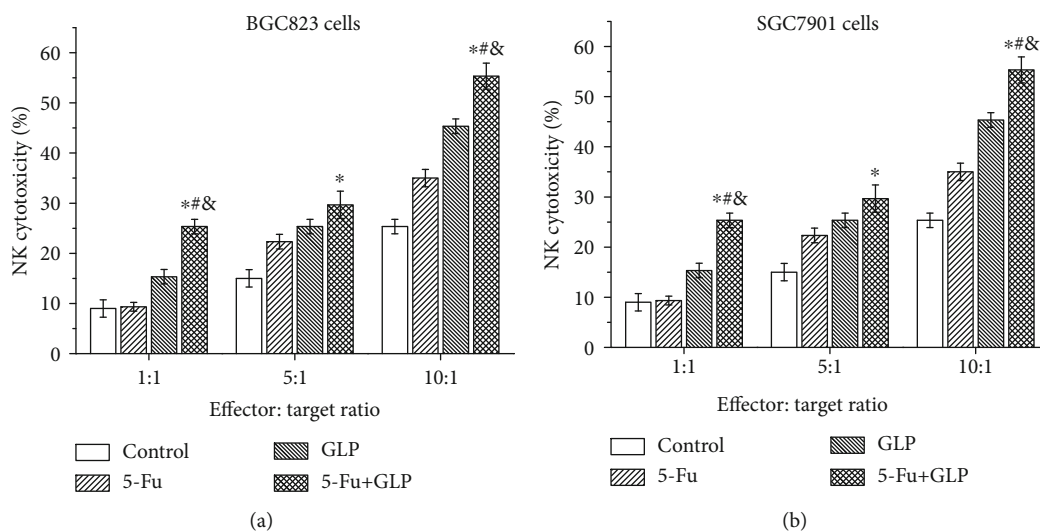
FIGURE 2: GLP and 5-Fu synergistically enhanced the cytotoxic effect of NK-92 cells on BGC823 gastric cancer cells (a) and SGC7901 gastric cancer cells (b). The data were expressed as means ± SEM; compared with the control group, * indicated that $p < 0.05$, ** indicated $p < 0.05$; compared with the 5-Fu group, # indicated $p < 0.05$, ## indicated $p < 0.05$; compared with the GLP group, & indicated $p < 0.05$, && indicated $p < 0.05$.

The results showed that the toxicity of NK cells to both cancer cell lines was significantly enhanced in the cocultured group ($p < 0.05$; Figures 2(a) and 2(b)). When the effector-target ratio (E : T) was at 1 : 1, 5 : 1, and 10 : 1, compared with the 5-Fu group, the toxicity killing rate of NK-92 cells to BGC823 cells in GLP combined with 5-Fu treatment groups increased by 16%, 6.33%, and 20.33%, respectively (Figure 2(a)). As for the SGC7901cells, this increase in killing rate was 16.07%, 7.06%, and 19.73%, respectively (Figure 2(b)).

3.4. GLP Enhanced the Antitumor Activity of 5-Fu in Gastric Cancer Mice. In vitro, GLP and 5-Fu synergistically stimulated the activity of NK cells to kill tumor cells. By establishing BGC823 and SGC7901 tumor-bearing mouse models, we then explored whether GLP combined with 5-Fu can enhance the antitumor effect exerted by 5-Fu. The results showed that GLP combined with 5-Fu significantly inhibited the tumor growth in both models compared to 5-Fu alone ($p < 0.01$; Figures 3(a) and 3(b)). As shown in Figure 3(a), in the BGC823 gastric cancer cell-bearing mouse model, the

(a)

(b)
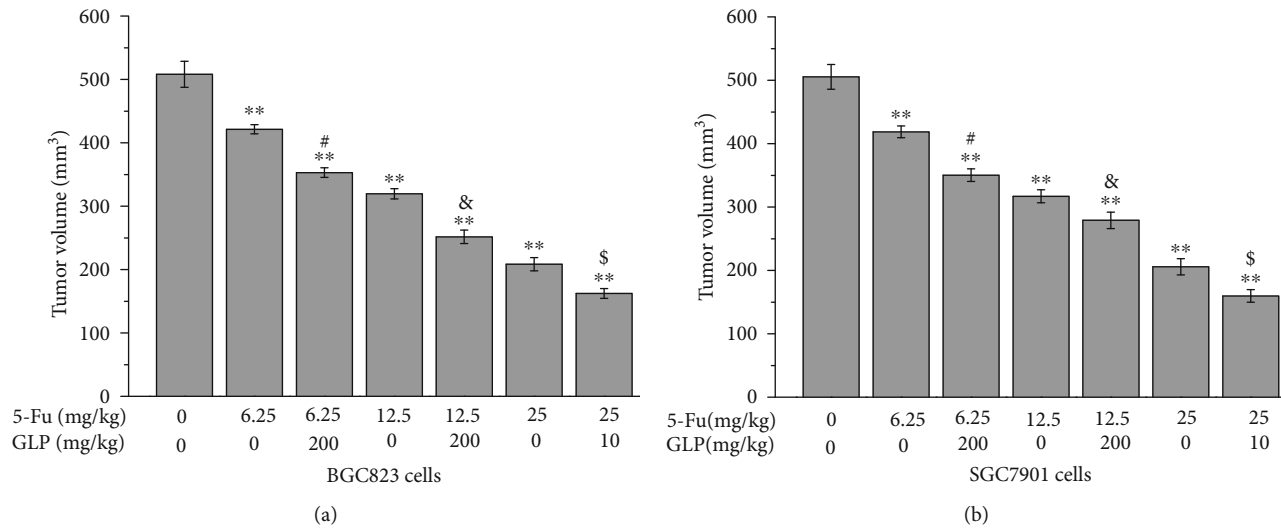
FIGURE 3: GLP increased the antitumor activity of 5-Fu in gastric cancer-bearing mice. (a) During the treatment of BGC823 gastric cancer-bearing mice, GLP enhanced the antitumor activity of 5-Fu at the 12th day of administration. (b) During the treatment of SGC7901 gastric cancer-bearing mice, GLP enhanced the antitumor activity of 5-Fu at the 12th day of administration. Data were expressed as means ± SEM; compared with the control group, * indicated $p < 0.05$, ** indicated $p < 0.05$; compared with the 5-Fu (6.25 mg/kg) group, # indicated $p < 0.05$, ## indicated $p < 0.05$; compared with the 5-Fu (12.5 mg/kg) group, & indicated $p < 0.05$, && indicated $p < 0.05$; compared with the 5-Fu (25 mg/kg) group, $ indicated $p < 0.05$ and $$ indicated $p < 0.05$.

(a)

(b)

(c)
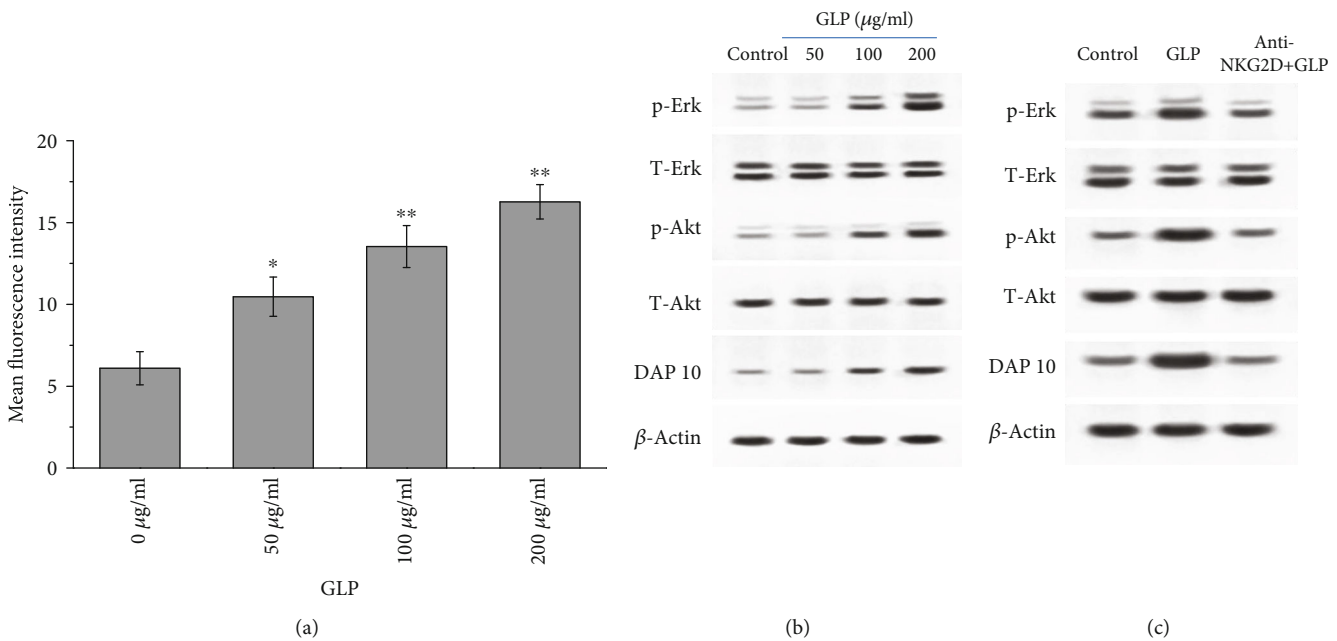
FIGURE 4: GLP activated NK-92 cells via the NKG2D pathway. (a) GLP enhanced the expression of NKG2D on NK-92 cells in a dose-dependent manner. Compared with the untreated group, * indicated $p < 0.05$, ** indicated $p < 0.05$. (b) GLP enhanced the phosphorylation levels of Akt and erk and the expression level of DAP10 protein in NK-92 cells. (c) Enhanced phosphorylation level of Akt and erk and the expression level of DAP10 protein in NK-92 cells by GLP treatment were reduced by silencing NKG2D in NK-92 cells with NKG2D antibody.

tumor volume in the combination treatment group was significantly reduced ($p < 0.05$) at the 12th day of administration in comparison to the 5-Fu treatment alone (6.25 or 12.5 mg/kg: one quarter or half of the highest dose). The tumor inhibition rate reached 68.04% (Figure 3(a)) when 5-Fu (12.5 mg/kg) was combined with GLP (200 mg/kg) as the treatment. Similar results were obtained in SGC7901

tumor-bearing mice. Compared with the 6.25 or 12.5 mg/kg 5-Fu treatment group, the tumor volume decreased significantly on the 12th day in the combination treatment group ($p < 0.05$). When 5-Fu (12.5 mg/kg) was combined with GLP (10 mg/kg) as the treatment, the tumor inhibition rate reached 68.4% (Figure 3(b)). The results showed above indicated that GLP increased the antitumor activity of 5-Fu

during the treatment of BGC823 and SGC7901 gastric cancer-bearing mice.

3.5. GLP Activated NK-92 Cells via the NKG2D Pathway. Studies have shown that on NK cells NKG2D was expressed as a receptor, whereas phosphatidylinositol-3 kinase (PI3K) is a downstream signaling molecule of NKG2D [24]. Moreover, the PI3K-ERK pathway plays an important role in NK cell activation and cytotoxicity [25, 26]. Therefore, the relationship between GLP and NKG2D receptor and its downstream DAP10/PI3K/ERK pathway was verified with ELISA and Western blot.

The results indicated that GLP promoted the expression of NKG2D receptor, as shown in Figure 4(a). The expression of NKG2D was significantly upregulated in NK-92 cells that were treated with GLP compared with the control group ($p < 0.05$). In addition, phosphorylation levels of Akt and erk and expression levels of DAP10 protein were significantly increased in NK-92 cells of the GLP-treated group compared with the control group (Figure 4(b)). After NKG2D was silenced by NKG2D antibody, the phosphorylation levels of Akt and erk and the expression level of DAP10 protein in NK-92 cells of the Anti-NKG2D+GLP group were significantly lower than those treated with GLP alone. And there was no significant difference compared to the control group (Figure 4(c)). These results suggested that GLP may activate the downstream DAP10/PI3K/ERK pathway by upregulating the expression of the NKG2D receptor, resulting in the activation of NK cells.

4. Conclusion

Our study showed that GLP not only inhibited tumor growth in gastric cancer cells and gastric cancer-bearing mice but also promoted NK-mediated cytotoxicity. Moreover, GLP may activate the downstream DAP10/PI3K/ERK pathway by promoting the expression of the NKG2D receptor, thus leading to the activation of NK cells. These results revealed the potential efficacy of GLP combined with 5-Fu in the treatment of cancer and further supported the strategy of combining cytotoxic drugs with immunomodulators for effective cancer treatment.

Data Availability

The data used to support the findings of this study are available from the corresponding author upon request.

Conflicts of Interest

The authors declare that they have no conflicts of interest.

Acknowledgments

References

[1] D. Daniel and J. Crawford, "Myelotoxicity from chemotherapy," *Seminars in Oncology*, vol. 33, no. 1, pp. 74–85, 2006.

[2] V. Tsouris, M. K. Joo, S. H. Kim, I. C. Kwon, and Y. Y. Won, "Nano carriers that enable co-delivery of chemotherapy and RNAi agents for treatment of drug-resistant cancers," *Biotechnology Advances*, vol. 32, no. 5, pp. 1037–1050, 2014.

[3] L. Apetoh, S. Ladoire, G. Coukos, and F. Ghiringhelli, "Combining immunotherapy and anticancer agents: the right path to achieve cancer cure?," *Annals of Oncology*, vol. 26, no. 9, pp. 1813–1823, 2015.

[4] V. K. Anagnostou and J. R. Brahmer, "Cancer immunotherapy: a future paradigm shift in the treatment of non-small cell lung cancer," *Clinical Cancer Research*, vol. 21, no. 5, pp. 976–984, 2015.

[5] L. A. Emens and G. Middleton, "The interplay of immunotherapy and chemotherapy: harnessing potential synergies," *Cancer Immunology Research*, vol. 3, no. 5, pp. 436–443, 2015.

[6] P. Correale, M. G. Cusi, K. Y. Tsang et al., "Chemo-immunotherapy of metastatic colorectal carcinoma with gemcitabine plus FOLFOX 4 followed by subcutaneous granulocyte macrophage colony-stimulating factor and interleukin-2 induces strong immunologic and antitumor activity in metastatic colon cancer patients," *Journal of Clinical Oncology*, vol. 23, no. 35, pp. 8950–8958, 2005.

[7] K. Pan, Q. Jiang, G. Liu, X. Miao, and D. Zhong, "Optimization extraction of *Ganoderma lucidum* polysaccharides and its immunity and antioxidant activities," *International Journal of Biological Macromolecules*, vol. 55, pp. 301–306, 2013.

[8] C. Zhao and Y. He, "Isolation, purification and structural characterization of active polysaccharides from the mycelium of Ganoderma lucidum," *Zhong Yao Cai*, vol. 25, no. 4, pp. 252–254, 2002.

[9] M. Shi, Z. Zhang, and Y. Yang, "Antioxidant and immunoregulatory activity of Ganoderma lucidum polysaccharide (GLP)," *Carbohydrate Polymers*, vol. 95, no. 1, pp. 200–206, 2013.

[10] K. Zhu, S. Nie, C. Li et al., "A newly identified polysaccharide from Ganoderma atrum attenuates hyperglycemia and hyperlipidemia," *International Journal of Biological Macromolecules*, vol. 57, pp. 142–150, 2013.

[11] P. Y. Wang, X. L. Zhu, and Z. B. Lin, "Antitumor and immunomodulatory effects of polysaccharides from broken-spore of Ganoderma lucidum," *Frontiers in Pharmacology*, vol. 3, 2012.

[12] S. Wang, G. Zheng, S. Tian et al., "Echinacoside improves hematopoietic function in 5-FU-induced myelosuppression mice," *Life Sciences*, vol. 123, pp. 86–92, 2015.

[13] S. Kojima, K. Takaba, N. Kimoto et al., "Protective effects of glutathione on 5-fluorouracil-induced myelosuppression in mice," *Archives of Toxicology*, vol. 77, no. 5, pp. 285–290, 2003.

[14] S. Numazawa, K. Sugihara, S. Miyake et al., "Possible involvement of oxidative stress in 5-fluorouracil-mediated myelosuppression in mice," *Basic & Clinical Pharmacology & Toxicology*, vol. 108, no. 1, pp. 40–45, 2011.

[15] Z. Cao, Z. Zhang, Z. Huang et al., "Antitumor and immunomodulatory effects of low-dose 5-FU on hepatoma 22 tumor-bearing mice," *Oncology Letters*, vol. 7, no. 4, pp. 1260–1264, 2014.

[16] V. J. Picozzi, R. A. Kozarek, and L. W. Traverso, "Interferon-based adjuvant chemoradiation therapy after pancreaticoduodenectomy for pancreatic adenocarcinoma," *American Journal of Surgery*, vol. 185, no. 5, pp. 476–480, 2003.

[17] Y. Kan, T. Chen, Y. Wu, J. Wu, and J. Wu, "Antioxidant activity of polysaccharide extracted from Ganoderma lucidum using response surface methodology," *International Journal of Biological Macromolecules*, vol. 72, pp. 151–157, 2015.

[18] M. M. Bradford, "A rapid and sensitive method for the quantitation of microgram quantities of protein utilizing the principle of protein-dye binding," *Analytical Biochemistry*, vol. 72, pp. 248–254, 1976.

[19] L.-F. Li, H.-B. Liu, Q.-W. Zhang et al., "Comprehensive comparison of polysaccharides from *Ganoderma lucidum* and *G. sinense*: chemical, antitumor, immunomodulating and gut-microbiota modulatory properties," *Scientific Reports*, vol. 8, no. 1, p. 6172, 2018.

[20] A. K. Nowak, B. W. Robinson, and R. A. Lake, "Synergy between chemotherapy and immunotherapy in the treatment of established murine solid tumors," *Cancer Research*, vol. 63, no. 15, pp. 4490–4496, 2003.

[21] J. Gołąb, R. Zagożdżon, R. Kamiński et al., "Potentiatied antitumor effectiveness of combined chemo-immunotherapy with Interleukin-12 and 5-fluorouracil of L1210 leukemia *in vivo*," *Leukemia*, vol. 15, no. 4, pp. 613–620, 2001.

[22] S. Cao, A. B. Troutt, and Y. M. Rustum, "Interleukin 15 protects against toxicity and potentiates antitumor activity of 5-fluorouracil alone and in combination with leucovorin in rats bearing colorectal cancer," *Cancer Research*, vol. 58, no. 8, pp. 1695–1699, 1998.

[23] M. Cheng, Y. Chen, W. Xiao, R. Sun, and Z. Tian, "NK cell-based immunotherapy for malignant diseases," *Cellular & Molecular Immunology*, vol. 10, no. 3, pp. 230–252, 2013.

[24] L. L. Lanier, "Up on the tightrope: natural killer cell activation and inhibition," *Nature Immunology*, vol. 9, no. 5, pp. 495–502, 2008.

[25] K. Jiang, B. Zhong, D. L. Gilvary et al., "Pivotal role of phosphoinositide-3 kinase in regulation of cytotoxicity in natural killer cells," *Nature Immunology*, vol. 1, no. 5, pp. 419–425, 2000.

[26] I. Tassi, M. Cella, S. Gilfillan et al., "p110γ and p110δ phosphoinositide 3-kinase signaling pathways synergize to control development and functions of murine NK cells," *Immunity*, vol. 27, no. 2, pp. 214–227, 2007.

Research Article

The Anticancer Activity of *Lycium barbarum* Polysaccharide by Inhibiting Autophagy in Human Skin Squamous Cell Carcinoma Cells In Vitro and In Vivo

Meihua Zeng,[1] Qingtao Kong,[2] Fang Liu,[2] Jun Chen,[2] and Hong Sang [1]

[1]*Jinling Hospital Department of Dermatology, South Medical University, Nanjing 210002, China*
[2]*Jinling Hospital Department of Dermatology, Nanjing 210002, China*

Correspondence should be addressed to Hong Sang; sanghong@nju.edu.cn

Objective. This study is aimed at investigating the effects of *Lycium barbarum* polysaccharide (LBP) on the proliferation and apoptosis of human cutaneous squamous cell carcinoma A431 cells in vitro and in vivo via its regulation on autophagy. *Methods*. In vitro experiment: A431 cells were treated with different concentrations of LBP, and cell viability was measured by the CCK8 method. Flow cytometry was used to detect the cell apoptosis rate. The expression of Ki67, PCNA, cl-caspase-3, Bcl-2, and LC3II and the phosphorylation status of JNK and ERK1/2, as well as the effect of SP600125 cotreatment on the expression of autophagy and apoptosis-associated proteins, were determined via Western blot. In vivo experiment: a transplanted tumor model was established by subcutaneous injection of A431 cells to the nude mice. 50 mg/kg LBP was injected into the mice intraperitoneally; the survival rate of mice, volume, and weight of tumor were determined on the 30th day. The expression of Ki67 and MMP-2 proteins was measured by immunohistochemistry. *Results*. LBP at concentrations of 400 μg/ml and above was significantly cytotoxic to A431 cells, whereas, within the dose range of 50 μg/ml~200 μg/ml, LBP significantly inhibited the expression of Ki67 and PCNA proteins, promoted the expression of cl-caspase-3, inhibited the expression of Bcl-2 protein, downregulated the expression of autophagy marker LC3II, and reduced the phosphorylation of ERK1/2, whereas the level of JNK phosphorylation was upregulated. At the same time, the regulation of Beclin1, LC3II, Bcl-2, and cl-caspase-3 by LBP was effectively reversed by the cotreatment of SP600125. In addition, LBP increased the survival rate of transplanted nude mice, reduced tumor volume and weight, and downregulated the expression of Ki67 and MMP-2. *Conclusion*. LBP can induce apoptosis of A431 cells by inhibiting autophagy and can inhibit tumor growth in vivo.

1. Introduction

Cutaneous squamous cell carcinoma (CSCC) is one the most common skin malignancies, only second to basal cell carcinoma (BCC), which is developed in keratinocytes in epidermal or adnexal structures. It is more common in male patients and preferentially occurs in the elderly. It often happens in the patient's face, head, and parts where light exposure is more frequent; advanced patients are prone to lymph node metastasis, posing a serious threat to their lives [1–3]. At present, surgical resection is the main treatment for early-stage CSCC patients for whom the prognosis is typically good; however, for the middle- and late-stage patients,

they often need to receive a combination of various treatments such as surgery, radiotherapy, and chemotherapy, and the prognosis is usually less desirable. In recent years, targeted therapy for cancer patients has made great progress [4, 5] and finding a suitable drug combined with targeted delivery is one of the approaches for cancer therapy. Along with that, many plant extracts with antitumor activity have begun to be used as an adjunct medication to cancer treatment. Studies have shown that *Lycium barbarum* polysaccharides (LBP), the main bioactive ingredient of Chinese herbal medicines and food supplements, have antioxidation, antiaging, and neuroprotective effects [6]. It is also worth noting that LBP has been shown to exhibit significant

biological activity in inhibiting tumor growth both in vitro and in vivo, including bladder, cervical, colon, liver, and kidney cancers [6–10]. Autophagy is an evolutionarily conserved catabolic process that recycles proteins and damaged organelles and plays an important regulatory role in the balance of cell survival and death. It is also involved in the development of various diseases, including cancer [11, 12]. However, the main focus has been on the mechanism of inhibition of tumor cells by LBP through its effects on cell growth, apoptosis, and autophagy; the relationship between LBP on human CSCC A431 cells and autophagy has not been reported. Therefore, this study preliminarily focuses on the effects of LBP on proliferation and apoptosis of A431 cells in vitro and in vivo and its associated mechanism.

2. Materials and Methods

2.1. Main Materials. Human cutaneous squamous cell carcinoma cell line A431 was purchased from the American model culture pool; DMEM from Sigma; DMSO from Shanghai Biotech; fetal bovine serum, 0.25% trypsin, from Gibco; CCK8 kit from Jiangsu Kaiji Biotechnology Co., Ltd.; Annexin V-FITC/PI Apoptosis Detection Kit from Beijing Solarbio Science & Technology Co., Ltd.; BCA kit from Biyuntian Biotechnology Co., Ltd.; and Ki67 antibody (Cat. No.: ab16667), PCNA antibody (Cat. No.: ab92552), cl-caspase-3 antibody (Cat. No.: ab32042), Bcl-2 antibody (Cat. No.: ab32124), JNK antibody (Cat. No.: ab76125), p-JNK antibody (Cat. No.: ab4821), ERK1/2 antibody (Cat. No.: ab17942), p-ERK1/2 antibody (Cat. No.: ab214362), LC3B antibody (Cat. No.: ab51520), Beclin1 antibody (Cat. No.: ab210498), MMP-2 antibody (Cat. No.: ab92536), and goat anti-rabbit IgG-HRP secondary antibody (Cat. No.: ab6721) from Abcam; the immunohistochemistry kit was purchased from Zhongshan Jinqiao, Beijing. Mannose, glucose, galactose, xylose, rhamnose, and arabinose were purchased from the China National Pharmaceutical Group Co., Ltd. (Sinopharm).

2.2. Methods

2.2.1. Cell Culture. Human CSCC A431 cells were inoculated in DMEM medium containing 10% fetal bovine serum and 1% penicillin-streptomycin and cultured in an incubator with a constant temperature at $37°$ C and concentration of CO_2 at 5%. The microscope was used to observe the growth of cell adherence. When the cell fusion rate reached 80% or more, it was digested and passaged with 0.25% trypsin. Cells in the logarithmic growth phase were selected for subsequent experiments.

2.2.2. Separation and Purification of LBP. The *Lycium barbarum* was dried at room temperature. Then, it was refluxed with 95% ethanol at 75°C for 5 hours and repeated 3 times to remove the lipid and the supernatant in order to extract the dried fruit residue. The dried fruit residue was washed with 10 volumes of distilled water at room temperature for 3 hours each time and repeated 4 times. It was then centrifuged at 5000 rpm for 10 minutes at 20°C, and the supernatant was collected and concentrated 10 times, followed by precipitation with 95% ethanol at a volume ratio

of $1 : 5$ at 4°C for 12 hours. The precipitate was then washed with absolute ethanol, acetone, and ether, through which the crude polysaccharide (CLPB) was obtained. CLBP (100 mg) was dissolved in 0.1 M NaCl (10 mg/ml) solution, and 2 ml of this solution was then placed in a DEAE cellulose-52 column (2.6×30 cm) and then gradually eluted with 0.1, 0.3, and 0.5 M NaCl solutions at a flow rate of 60 ml/h. The eluate (5 ml/tube) was collected automatically, and the carbohydrate was determined by the phenol-sulfuric method using glucose as a standard. These polysaccharides were lyophilized for further study after dehydration and dialysis.

2.2.3. Cell Proliferation Measured with CCK8 Assay. The A431 cell suspension was seeded at a concentration of 2.0×10^5 cells/ml in a 96-well plate at 100 μl per well and randomly divided into 10 groups where LBP solutions of different final concentrations were given to each group (0, 5, 10, 20, 50, 100, 200, 400, 800, and 1000 μg/ml). 6 duplicate wells were set up for each group. After 24 hours of culture, 10 μl of the CCK8 solution was added to each well, and incubation was continued for another 4 h. After that, the absorbance value of each well was measured at 450 nm by a microplate reader, and the experiment was repeated 3 times. The survival rate of human CSCC A431 cells is equal to the average value of absorbance in the treatment group divided by the average value of absorbance in the control group multiplied by 100%.

2.2.4. Apoptosis Detected by Flow Cytometry. A431 cells (density, 1×10^6 cells/well) were seeded on 6-well plates, and cells at 80% confluence were divided into four groups: Ctrl group, LBP (50 μg/ml) group, LBP (100 μg/ml) group, and LBP (200 μg/ml) group, and were incubated with medium containing the final concentrations of LBP for 24 h. Cells from each group were collected and adjusted to a density of 1×10^6 cells/ml. According to kit instructions, 100 μl of cells were added with 5 μl of Annexin V-FITC and 10 μl of PI staining solution and incubated at room temperature in the dark for 15 min for detection.

2.2.5. Autophagy, Apoptosis, and Pathway-Related Protein Expression Measured by Western Blot. The cells cultured for 24 h in each experiment were collected, and the total protein was extracted on an icebox by using the RIPA protein lysate. After centrifugation at 4°C, the supernatant was taken for protein quantification. It was then subjected to SDS-PAGE and transferred to a PVDF membrane. The resulting protein was blocked with 5% skim milk powder for 2 h at room temperature. After that, the primary antibody was added and incubated overnight at 4°C. The primary antibody was then discarded, and the corresponding secondary antibody labeled with horseradish peroxidase was added and incubated for another 1 h at room temperature. The ECL was then added dropwise in the darkroom for exposure development. The GAPDH was used as an internal control.

2.2.6. Preparation of the Transplanted Tumor Model. 6-8-week-old BALB/c nude mice were purchased from Beijing
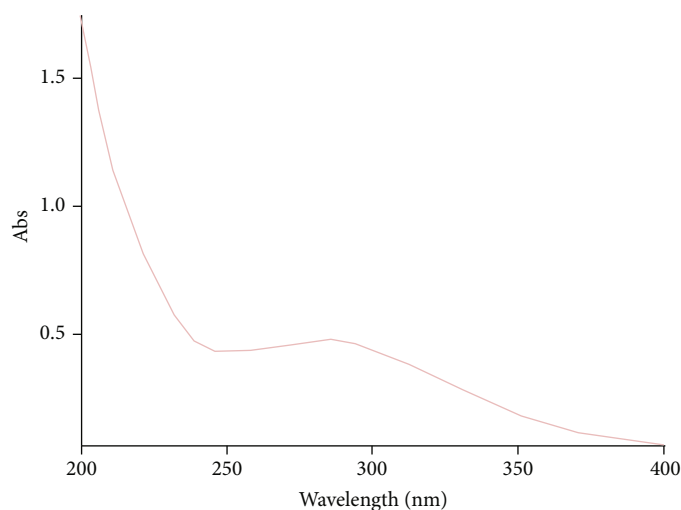
FIGURE 1: UV spectrum for CLBP.

TABLE 1: Polysaccharide content at each elution peak.

Designations	Content	Composition
LBP-1	2.23%	Xylose, glucose, and rhamnose
LBP-2	0.88%	Arabinose, xylose, and glucose
LBP-3	3.11%	Mannose, xylose, and glucose
LBP-4	2.43%	Arabinose, and glucose
LBP-5	83.68%	Arabinose, mannose, xylose, glucose, and rhamnose
LBP-6	5.36%	Xylose, glucose, and rhamnose

Charles River Laboratory Animal Technology Company, and the experiment was carried out after one week of adaptive feeding. A431 cells in the logarithmic growth phase were adjusted to a density of 1×10^7 cells/ml, and 0.2 ml of the cell suspension was injected at the nape subcutaneously. Nude mice were randomly divided into the control group and the LBP (50 mg/kg) group. Animals in the LBP (50 mg/kg) group were given 10 mg/kg of 50 mg/kg LBP solution intraperitoneally, and the control group was given an equal amount of matrix solution. The drug was administered everyday consecutively for a week. The survival data of the mice was recorded, and the tumor volume was measured every 5 days. The mice were sacrificed on the 30th day, and the tumor was separated and weighed. Tumor volume $= 0.5 \times$ length $\times$ width^2.

2.2.7. The Expression of Ki67 and MMP-2 in Tumor Tissues Detected by Immunohistochemistry. The tumor tissue obtained in Section 2.2.4 was routinely prepared and sectioned, and immunohistochemical staining was performed according to instructions. In brief, the sections were immersed in a 3% H_2O_2 solution at 37°C for 30 min, then washed with PBS for 5 min for 3 times. It was then blocked with 10% BSA, after which, the primary antibody was added and incubated overnight at 4°C. It was then rinsed with PBS for 5 min and repeated 3 times. After that, the secondary antibody was added and incubated at 37°C for 1 h, then rinsed with the PBS for 5 min for 3 times. DAB was used to color

it for 10 s and fully rinsed with the running water before being counterstained with hematoxylin for 30 s. After that, it was fully rinsed with the running water again and neutral gum was added after the conventional dehydration and finally covered with a coverslip. The expression of Ki67 and MMP-2 was observed under the microscope.

2.2.8. Statistics. All the obtained data were analyzed with SPSS 17.0. Differences conformed to a normal distribution between groups were tested by one-way ANOVA. The results were denoted as mean ± standard deviation. The difference was considered statistically significant when $P < 0.01$.

3. Results

3.1. Separation and Purification of LBP. In this paper, CLBP was isolated by ethanol precipitation, and the UV spectrum showed no absorption peak at 280 nm, indicating that there was no protein in CLBP, as shown in Figure 1. The content of polysaccharides purified by column chromatography was measured by phenol-sulfuric acid method. Six elution peaks of the polysaccharides were designated as LBP-1, LBP-2, LBP-3, LBP-4, LBP-5, and LBP6 according to the sequence of the elution column. The polysaccharide contents at the six peaks are shown in Table 1. A mixed monosaccharide solution containing mannose, glucose, xylose, rhamnose, and arabinose was used as a control for HPLC detection. By comparing the mixed monosaccharide solution curves, the composition at each peak was different (see Table 1). LBP-5
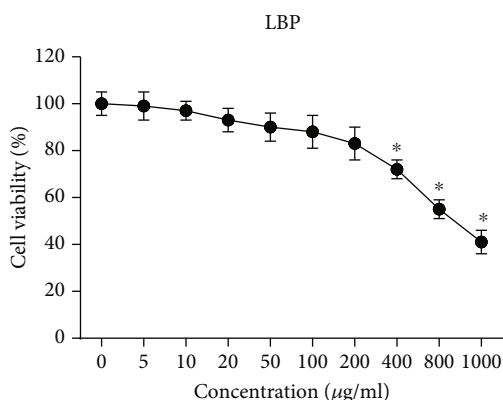
LBP

Figure 2: LBP inhibited the viability of A431 cells ($n = 9$). Compared with the control group, $^*P < 0.01$.

having the highest content of polysaccharides consisted of arabinose, mannose, xylose, glucose, and rhamnose, among which glucose showed much higher content than the other monosaccharides. Therefore, we chose LBP-5 for follow-up experiments and study, which was referred to as LBP in the following experiments.

3.2. The Effects of LBP on the Survival Rate of A431 Cells In Vitro.
The CCK8 method was used to measure the effect of LBP on the survival rate of A431 cells in vitro. The results in Figure 2 showed that the survival rate of A431 cells in each LBP treatment group decreased gradually. Compared with the control group, the survival rate of the LBP-treated group at 400, 800, and 1000 μg/ml decreased significantly ($P < 0.01$), and the half inhibitory concentration of LBP was 873.7 μg/ml. In other words, when the concentration of LBP exceeds 400 μg/ml, it caused significant cytotoxicity to A431 cells in vitro, and the survival rate of A431 cells was less than 80%. Therefore, subsequent experiments were performed using three maximum treatment concentrations of LBP without causing significant cytotoxicity, namely, 50, 100, and 200 μg/ml.

3.3. Effect of LBP on Apoptosis Rate of A431 Cells and the Expression of Proliferation and Apoptosis-Related Proteins in A431 Cells Cultured In Vitro.
The apoptotic rate of A431 cells was detected by flow cytometry, and the results shown in Figure 3(a) indicated that the proportion of apoptotic A431 cells was increased in each LBP-treated group compared with the control group ($P < 0.01$), which was in a LBP dose-dependent manner.

The expression of proliferation and apoptosis-related proteins in A431 cells was determined by Western blot. The results are shown in Figure 3(b). Compared with the control group, the expression levels of proliferation-related proteins (Ki67 and PCNA) in A431 cells treated with LBP of different concentrations were significantly lower than those in the control group ($P < 0.01$). The expression level of apoptosis-related protein cl-caspase-3 was significantly increased ($P < 0.01$), while the expression level of Bcl-2 was significantly decreased ($P < 0.01$). Additionally, the effects of LBP on the expression of these proteins are dose-dependent.

3.4. Effect of LBP on the Expression of Autophagy Markers and Phosphorylation of JNK1/2 and ERK1/2 in Cultured A431 Cells.
Similarly, the expression of LC3II and phosphorylation status of JNK1/2 and ERK1/2 in A431 cells were measured by Western blot. The results are shown in Figure 4. Compared with the control group, the expression of LC3II and p-ERK1/2/ERK1/2 protein in A431 cells of each LBP treatment group was significantly lower ($P < 0.01$), while the expression of p-JNK/JNK protein was significantly upregulated ($P < 0.01$). And these regulations by LBP were all in a dose-dependent manner.

3.5. Effect of LBP on the Expression of Autophagy Marker and Apoptosis Proteins Mediated by the MAPK Pathway in Cultured A431 Cells.
The effect of JNK inhibitor SP600125 on the expression of autophagy markers and apoptotic proteins in A431 cells was determined by Western blot. As shown in Figure 5, compared with the control group, Beclin1, LC3II, and Bcl-2 protein were significantly downregulated in A431 cells after treatment with 50 μg/ml LBP ($P < 0.01$) and the expression of cl-caspase-3 protein was upregulated ($P < 0.01$). When A431 cells were cotreated with LBP (50 μg/ml) and SP600125 (10 μM), compared with LBP (50 μg/ml), the expression of these proteins was reversely regulated ($P < 0.01$).

3.6. Effect of LBP on the Survival of Transplanted Tumor Mice and Their Tumor Growth.
The survival rate of transplanted tumor mice, volume, and weight of the tumor in the two groups are shown in Figures 6(a)–6(c). The survival rate of transplanted tumor mice in LBP treatment groups was significantly higher than that in the control group ($P < 0.001$), and the tumor volume and weight were significantly lower than those in the control group ($P < 0.001$). At the same time, immunohistochemistry performed on the tumor tissues of nude mice demonstrated that the expression levels of Ki67 and MMP-2 were significantly lower in the LBP-treated group than in the control group (see Figure 6(d)) ($P < 0.01$).

4. Discussion

The occurrence and development of human cutaneous squamous cell carcinoma is an extremely complex process, which is controlled by a variety of genes and various factors and is associated with abnormal proliferation, differentiation, and apoptosis of tumor cells. Previous studies have shown that LBP, the main effective component of *Lycium barbarum*, has shown in antitumor studies some efficacy that it can inhibit the growth of a variety of tumor cells and has the advantages of low toxicity, fewer side effects, and availability [6–10]. In recent years, autophagy is emerging as a new strategy for cancer prevention and treatment and has been proven to be closely related to tumor cell growth and proliferation, as well as malignant metastasis [13]. In addition, studies have shown that LBP can protect against cell injury by regulating autophagy and apoptosis [14–19]. The study was aimed at investigating the regulatory effect of LBP on autophagy, and its effect on the proliferation, apoptosis of squamous cells
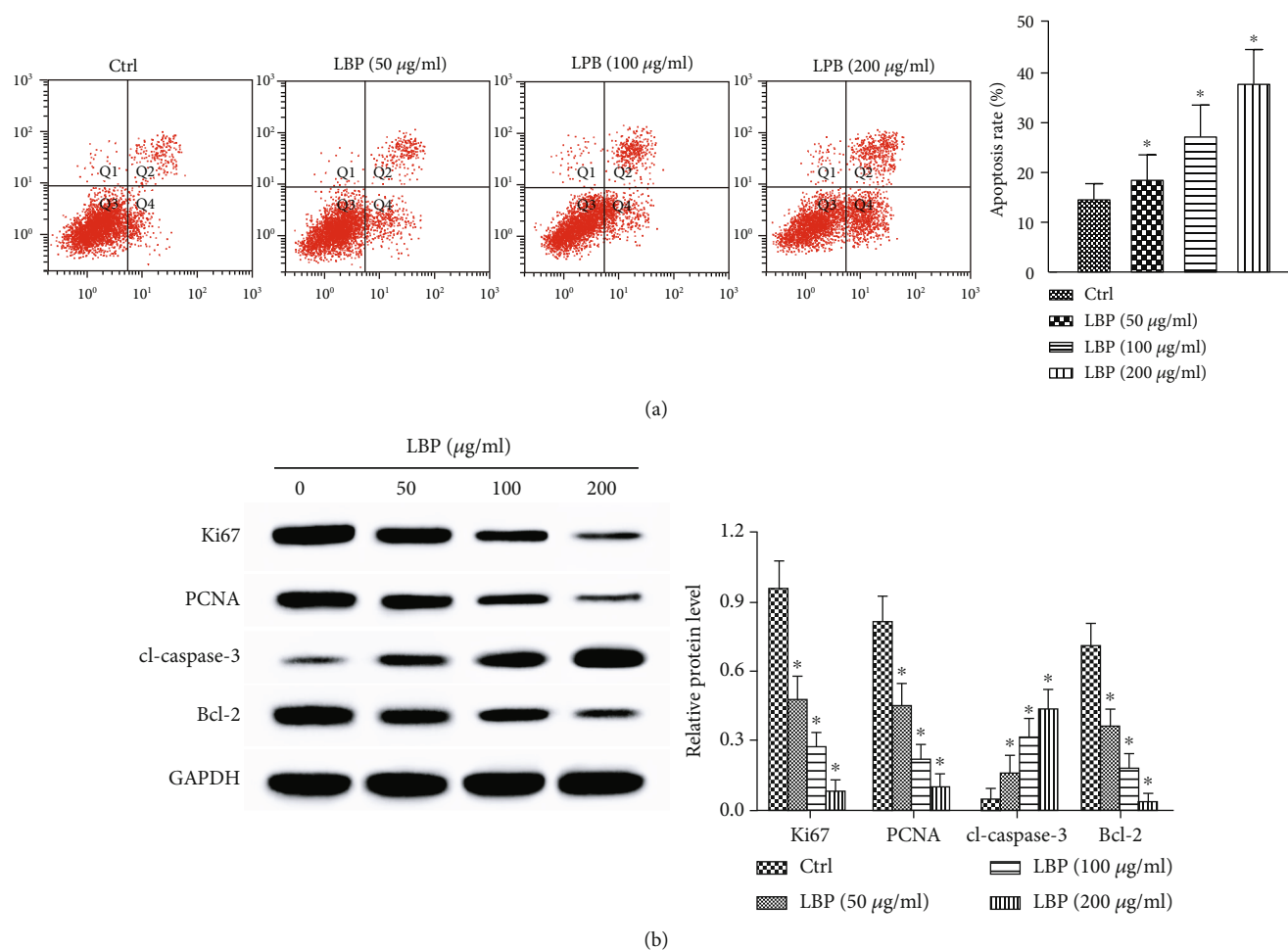
(a)

(b)

FIGURE 3: Effect of LBP on proliferation- and apoptosis-related protein expression in A431 cells. (a) Apoptosis rate of A431 cells was detected by flow cytometry. (b) Expression of apoptosis-related proteins in A431 cells was detected by Western blot. Compared with the control group, $^*P < 0.01$.

developing carcinoma in vitro and in vivo, and survival rate of tumor-xenografted nude mice.

The occurrence of cancer is often associated with abnormal proliferation and apoptosis resistance of tumor cells. Therefore, in this study, human skin cutaneous squamous cell carcinoma A431 cells were first cultured in vitro and treated with LBP at concentrations of 0, 5, 10, 20, 50, 100, 200, 400, 800, and 1000 μg/ml. And the survival rate of A431 cells was determined by the CCK8 method. The results showed that the survival rate of A431 cells in culture was significantly reduced when the LBP concentration reached 400 μg/ml and above. Studies have shown that the proliferative activity of tumor cells is an important prognostic indicator for tumor diagnosis. Ki67 is a widely used proliferation marker, and PCNA is a proliferating cell-specific expression protein, which is also an important participant in DNA replication and repair process [20]. Caspase-3 is the major executive protein for protein degradation during apoptosis; when cells are abnormally stimulated, cytochrome enzyme C together with procaspase-9 forms an apoptosome to activate caspase-9, which further activates caspase-3 to form cl-caspase-3 (cleaved caspase-3), thereby triggering apoptosis

[21], whereas Bcl-2 is a class of anti-apoptotic protein that plays a key role in promoting cell survival [22]. Therefore, the expression levels of proliferating and apoptotic key proteins were measured by Western blot in this study. It was found that LBP treatment induced cl-caspase-3 protein expression in A431 cells in a dose-dependent manner within the concentration range of 50 μg/ml~200 μg/ml. In parallel, inhibition of Ki67, PCNA, and Bcl-2 expression was observed at the same time. The above results indicate that LBP can induce the apoptosis of A431 cells in vitro.

It has been proved that LC3 proteins are autophagy markers, including LC3I (soluble, cytosolic protein) and LC3II (lipid-soluble, membrane protein), and that LC3I transforms to LC3II and localizes to autophagosomal membranes upon autophagy activation; therefore, LC3II expression can reflect the level of autophagy [13]. Western blot showed that LBP upregulated JNK phosphorylation and downregulated ERK1/2 phosphorylation and LC3II protein expression in A431 cells in vitro in a concentration range of 50 μg/ml~200 μg/ml with a dose-dependent manner. Studies have shown that autophagy is different from apoptosis, and autophagy is related to the balance of intracellular
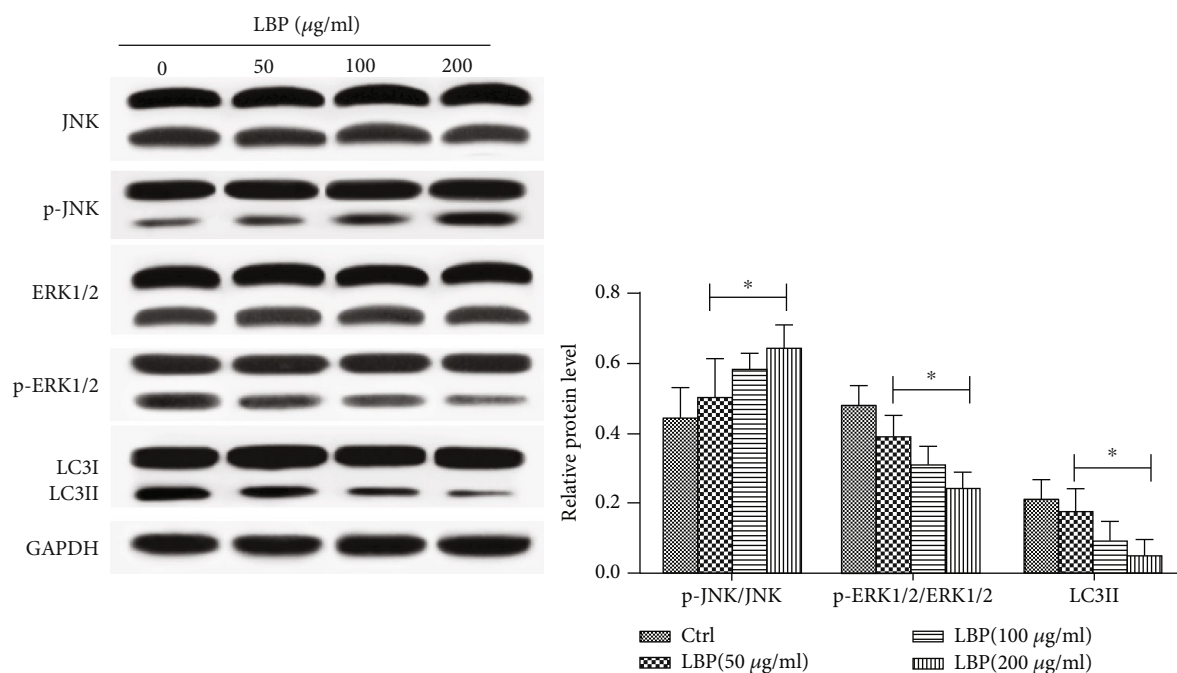
FIGURE 4: Effect of LBP on expression levels of autophagy markers and signaling pathway proteins in A431 cells. Compared with the control group, $^*P < 0.01$.
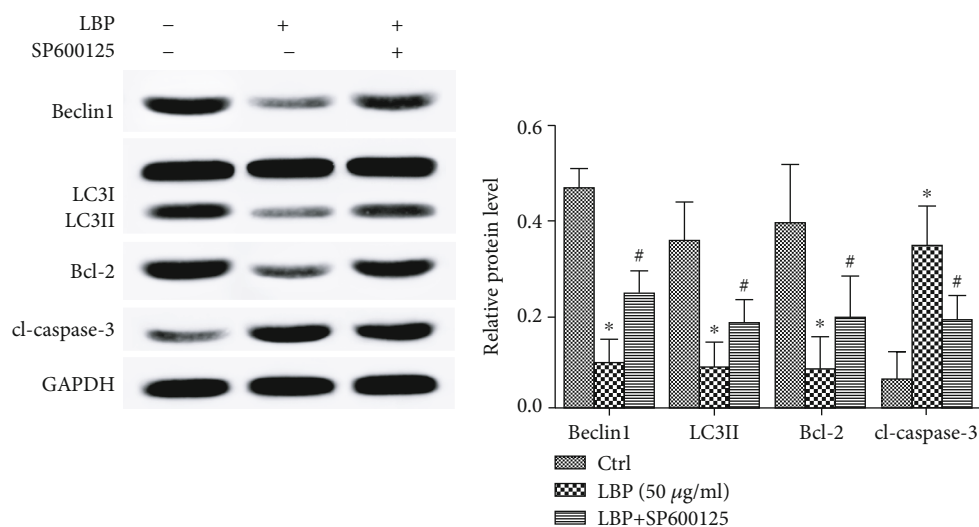
FIGURE 5: LBP induced apoptosis and inhibited autophagy in A431 cells. Compared with the control group, $^*P < 0.01$; compared with the LBP (50 μg/ml) group, $^\#P < 0.01$.

environment and plays an important role in cell survival. In addition, the signaling pathways involved in apoptosis and autophagy actually constitute an interconnected network, including Beclin1 and Bcl-2 [23]. JNK is closely related to autophagy by preventing the phosphorylated Bcl-2 family of proteins from binding to Beclin1, thereby regulating autophagy levels, while activation of the JNK pathway is often caused by MAPK cascades [24]. This study also found that the expression levels of Beclin1, LC3II, and Bcl-2 in A431 cells were upregulated after ANK cells were treated with both JNK inhibitor SP600125 and LBP, while the

expression of apoptosis-executing protein cl-caspase-3 was downregulated. Taken together, the above results indicate that the inhibition of A431 autophagy by LBP is achieved by the JNK pathway.

Finally, we established a nude mouse model of A431 cell xenografts in order to further investigate the effect of LBP on the survival rate of transplanted tumor models, in vivo tumor growth, and proliferation, as well as migration protein expression. The results showed that LBP significantly reduced tumor tissue volume and tumor weight, significantly increased the survival rate of tumor-bearing nude mice, and
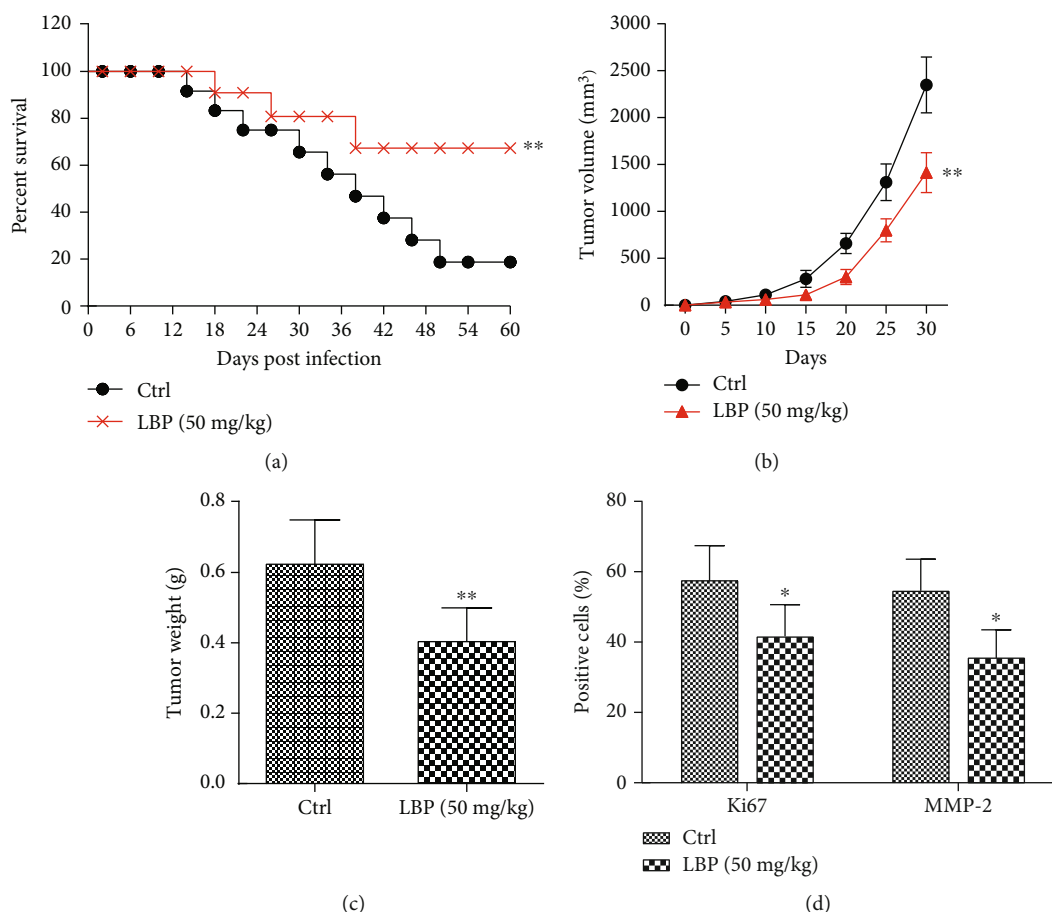
FIGURE 6: Effect of LBP on the growth of A431 cells in vivo ($n = 6$). (a–c) Effects of LBP on the survival rate of transplanted tumor mice, weight, and volume of the tumor. (d) Ki67- and MMP-2-positive cells were detected by immunohistochemistry. Compared with the control group, $^{*}P < 0.01$ and $^{**}P < 0.001$.

significantly downregulated the expression of Ki67 and MMP-2, thereby achieving the in vivo inhibition of A431 cells. Combined with these results, it appears that LBP can inhibit autophagy, induce apoptosis, and inhibit cell proliferation in vitro and in vivo, and its mechanism may be related to the upregulation of JNK and downregulation of ERK1/2 phosphorylation.

In summary, LBP at concentrations of 400 μg/ml and above produced significant cytotoxicity in A431 cells cultured in vitro. When within a concentration range of 50 μg/ml~200 μg/ml, LBP dose-dependently regulated proliferation, apoptosis, and autophagy-related protein expression as well as upregulated the JNK and downregulated the ERK1/2 signaling pathway. Furthermore, the regulation of LBP on autophagy and apoptosis-related proteins was reversely regulated by JNK inhibitor SP600125. And LBP can also inhibit the growth and metastasis ability of A431 cells in vivo. This paper firstly explored the effect of LBP on the proliferation and apoptosis of human cutaneous squamous cell carcinoma A431 by inhibiting autophagy; however, there are still many areas to be explored in the future, such as the effect of LBP on the autophagy of other human skin squamous cell carcinoma cell lines and on other apoptotic signaling pathways.

Data Availability

All data generated or analyzed during this study are included in this published article.

Conflicts of Interest

The authors declare that they have no conflicts of interest.

Acknowledgments

References

[1] A. C. Green and C. M. Olsen, "Cutaneous squamous cell carcinoma: an epidemiological review," *The British Journal of Dermatology*, vol. 177, no. 2, pp. 373–381, 2017.

[2] H. S. Chahal, Y. Lin, K. J. Ransohoff et al., "Genome-wide association study identifies novel susceptibility loci for cutaneous squamous cell carcinoma," *Nature Communications*, vol. 7, article 12048, 2016.

[3] M. Yao, Y. Y. Shang, Z. W. Zhou et al., "The research on lapatinib in autophagy, cell cycle arrest and epithelial to

mesenchymal transition via Wnt/ErK/PI3K-AKT signaling pathway in human cutaneous squamous cell carcinoma," *Journal of Cancer*, vol. 8, no. 2, pp. 220–226, 2017.

[4] J. Chen, J. Ding, W. Xu et al., "Receptor and microenvironment dual-recognizable nanogel for targeted chemotherapy of highly metastatic malignancy," *Nano Letters*, vol. 17, no. 7, pp. 4526–4533, 2017.

[5] S. Li, T. Zhang, W. Xu et al., "Sarcoma-targeting peptide-decorated polypeptide nanogel intracellularly delivers shikonin for upregulated osteosarcoma necroptosis and diminished pulmonary metastasis," *Theranostics*, vol. 8, no. 5, pp. 1361–1375, 2018.

[6] X. J. Zhang, H. Y. Yu, Y. J. Cai, and M. Ke, "Lycium barbarum polysaccharides inhibit proliferation and migration of bladder cancer cell lines BIU87 by suppressing Pi3K/AKT pathway," *Oncotarget*, vol. 8, no. 4, pp. 5936–5942, 2017.

[7] C. P. Zhu and S. H. Zhang, "*Lycium barbarum* polysaccharide inhibits the proliferation of HeLa cells by inducing apoptosis," *Journal of the Science of Food and Agriculture*, vol. 93, no. 1, pp. 149–156, 2013.

[8] W. Wang, M. Liu, Y. Wang et al., "*Lycium barbarum* polysaccharide promotes maturation of dendritic cell via notch signaling and strengthens dendritic cell mediated T lymphocyte cytotoxicity on colon cancer cell CT26-WT," *Evidence-Based Complementary and Alternative Medicine*, vol. 2018, Article ID 2305683, 10 pages, 2018.

[9] Q. Zhang, X. Lv, T. Wu et al., "Composition of *Lycium barbarum* polysaccharides and their apoptosis-inducing effect on human hepatoma SMMC-7721 cells," *Food & Nutrition Research*, vol. 59, no. 1, article 28696, 2017.

[10] S. Chen, L. Liang, Y. Wang et al., "Synergistic immunotherapeutic effects of Lycium barbarum polysaccharide and interferon-α2b on the murine Renca renal cell carcinoma cell line in vitro and in vivo," *Molecular Medicine Reports*, vol. 12, no. 5, pp. 6727–6737, 2015.

[11] C. T. Chen, M. J. Hsieh, Y. H. Hsieh et al., "Sulforaphane suppresses oral cancer cell migration by regulating cathepsin S expression," *Oncotarget*, vol. 9, no. 25, pp. 17564–17575, 2018.

[12] J. M. M. Levy, C. G. Towers, and A. Thorburn, "Targeting autophagy in cancer," *Nature Reviews Cancer*, vol. 17, no. 9, pp. 528–542, 2017.

[13] L. Yao, J. Wang, B. Y. Tian, T. H. Xu, and Z. T. Sheng, "Activation of the Nrf2-ARE signaling pathway prevents hyperphosphatemia-induced vascular calcification by inducing autophagy in renal vascular smooth muscle cells," *Journal of Cellular Biochemistry*, vol. 118, no. 12, pp. 4708–4715, 2017.

[14] Y. Yu, X. Wu, J. Pu et al., "*Lycium barbarum* polysaccharide protects against oxygen glucose deprivation/reoxygenation-induced apoptosis and autophagic cell death via the PI3K/Akt/mTOR signaling pathway in primary cultured hippocampal neurons," *Biochemical and Biophysical Research Communications*, vol. 495, no. 1, pp. 1187–1194, 2018.

[15] M. Bie, Y. Lv, C. Ren et al., "*Lycium barbarum* polysaccharide improves bipolar pulse current-induced microglia cell injury through modulating autophagy," *Cell Transplantation*, vol. 24, no. 3, pp. 419–428, 2015.

[16] S. Y. Liu, L. Chen, X. C. Li, Q. K. Hu, and L. J. He, "*Lycium barbarum* polysaccharide protects diabetic peripheral neuropathy by enhancing autophagy via mTOR/p70S6K inhibition in Streptozotocin-induced diabetic rats," *Journal of Chemical Neuroanatomy*, vol. 89, pp. 37–42, 2018.

[17] G. J. Shi, J. Zheng, X. X. Han et al., "*Lycium barbarum* polysaccharide attenuates diabetic testicular dysfunction via inhibition of the PI3K/Akt pathway-mediated abnormal autophagy in male mice," *Cell and Tissue Research*, vol. 374, no. 3, pp. 653–666, 2018.

[18] J. Xiao, F. Xing, J. Huo et al., "*Lycium barbarum* polysaccharides therapeutically improve hepatic functions in non-alcoholic steatohepatitis rats and cellular steatosis model," *Scientific Reports*, vol. 4, no. 1, pp. 1–12, 2015.

[19] T. Niu, L. Jin, S. Niu, C. Gong, and H. Wang, "Lycium barbarum polysaccharides alleviates oxidative damage induced by H_2O_2 through down-regulating microRNA-194 in PC-12 and SH-SY5Y cells," *Cellular Physiology and Biochemistry*, vol. 50, no. 2, pp. 460–472, 2018.

[20] M. Juríková, Ľ. Danihel, Š. Polák, and I. Varga, "Ki67, PCNA, and MCM proteins: markers of proliferation in the diagnosis of breast cancer," *Acta Histochemica*, vol. 118, no. 5, pp. 544–552, 2016.

[21] K.-H. Huang, W.-L. Fang, A. F.-Y. Li et al., "Caspase-3, a key apoptotic protein, as a prognostic marker in gastric cancer after curative surgery," *International Journal of Surgery*, vol. 52, pp. 258–263, 2018.

[22] A. Ruefli-Brasse and J. C. Reed, "Therapeutics targeting Bcl-2 in hematological malignancies," *The Biochemical Journal*, vol. 474, no. 21, pp. 3643–3657, 2017.

[23] L. Ou, S. Lin, B. Song, J. Liu, R. Lai, and L. Shao, "The mechanisms of graphene-based materials-induced programmed cell death: a review of apoptosis, autophagy, and programmed necrosis," *International Journal of Nanomedicine*, vol. 12, no. 9, pp. 6633–6646, 2017.

[24] Q. Wu, J. Deng, D. Fan et al., "Ginsenoside Rh4 induces apoptosis and autophagic cell death through activation of the ROS/JNK/p53 pathway in colorectal cancer cells," *Biochemical Pharmacology*, vol. 148, pp. 64–74, 2018.

Research Article

Mathematical Modelling of Acetaminophen Release in HPC/PAAm Hydrogel: Synthesis and Application

Abigail M. Díaz-Guerrero [1], **Claudia A. Castillo-Miranda,** [2] **Carlos F. Castro-Guerrero** [3], **Hernán Peraza-Vázquez** [1], **Ana B. Morales-Cepeda** [2], **and Adrián F. Peña-Delgado** [4,5]

[1] *Instituto Politécnico Nacional, Centro de Investigación en Ciencia Aplicada y Tecnología Aplicada (CICATA) Unidad Altamira, Carretera Tampico-Puerto Industrial de Altamira, Km 14.5, Altamira C.P. 89600, Mexico*
[2] *Tecnológico Nacional de México/Instituto Tecnológico de Ciudad Madero, Centro de Investigación en Petroquímica, Parque Industrial Tecnia, Altamira C.P. 89603, Mexico*
[3] *CONACyT-Instituto Nacional de Electricidad y Energías Limpias, Departamento de Sistemas Mecánicos, Reforma 113, Cuernavaca C.P. 62490, Mexico*
[4] *Universidad Politécnica de Altamira, Nuevo Libramiento Altamira KM 3, Altamira/C.P. 89602, Mexico*
[5] *Universidad Tecnológica de Altamira, Boulevard de los Ríos Km. 3+100, Puerto Industrial Altamira, Altamira C.P. 89601, Mexico*

Correspondence should be addressed to Abigail M. Díaz-Guerrero; adiazg1500@alumno.ipn.mx
and Ana B. Morales-Cepeda; abmoralesc@itcm.edu.mx

Received 1 August 2019; Revised 4 October 2019; Accepted 11 October 2019; Published 18 November 2019

Guest Editor: Parisa P. Abadi

Hydrogels are commonly used as Drug Delivery Systems (DDS) as patches due to its ability to store drug molecules within their structures. The release can be activated under certain stimuli, such as temperature and pH. In this paper, the mathematical modelling of acetaminophen release in hydroxypropyl cellulose with polyacrylamide (HPC/PAAm) is reported. The HPC/PAAm gel was synthesized in proportions of 25/75 wt% and was characterized by FTIR, DSC, optical microscopy, SEM, and TGA, with and without acetaminophen. The release tests were performed for hypothermic, normal, and febrile human body conditions, at 35, 37, and 39°C, respectively, on two release media: water and phosphate buffer solution. In order to describe the release of acetaminophen in HPC/PAAm gel, a genetic programming algorithm was used to accomplish Multigene Symbolic Regression (MSR). Characterization results showed that the drug was crystallized on the surface of the HPC/PAAm gel. Release test results showed that several simultaneous processes occurred in the acetaminophen diffusion phenomenon. A unique mathematical model was obtained by MSR. This model was able to describe the release of acetaminophen in HPC/PAAm gel with high values of R^2 and adjusted R^2 and to simulate the drug release at times beyond the end of the experiment. High values of R^2 and low values of Coefficient of Variation (CV), Root-Mean-Square Error (RMSE), and Mean Absolute Error (MAE) were obtained from the comparison between the simulated and the experimental data. This allows to conclude that the mathematical model is reliable to represent and simulate the acetaminophen release in HPC/PAAm gel at 35, 37, and 39°C.

1. Introduction

Drug Delivery Systems (DDS) are those transport mechanisms that allow the drug active substances to be released in the human body. Some well-known examples of DDS are pills, capsules, and injections. Nevertheless, the long-term use of pills or capsules may cause damage in the patient's digestive system. Nowadays, several alternatives have been sought, including the use of DDS as patches. How to use the patches is depicted in Figure 1.
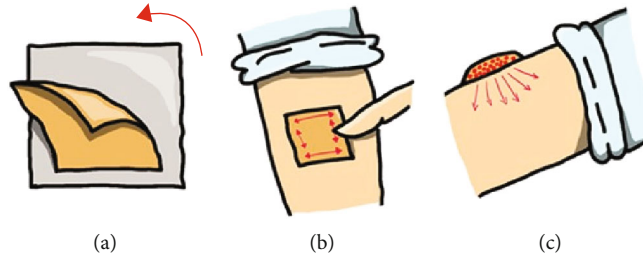
FIGURE 1: Drug Delivery System as patch: (a) the patch is removed from its protective membrane; (b) the patch is placed on the body; (c) phase of drug release, e.g., the release can be activated by stimuli as temperature or pH.

The patches are commonly made of hydrogels, due to its capacity to store drug molecules within their structures and then release them under certain conditions. Hydrogels are hydrophilic polymers that swell in the presence of a liquid, where the swelling continues until the equilibrium between the cohesive forces of the polymeric network and the osmotic forces originated by the entrance of the liquid into it [1]. The highly porous nature of the hydrogels allows the loading and unloading of drug particles, where the porosity can be adjusted by altering the density of the crosslinks of the polymer network. In addition, the release of hydrogel content may be activated due to environmental stimuli, such as pH or temperature [2]. Therefore, it is important to search for hydrogels capable of releasing drugs at pH and temperature values typically reached by the human body, from 7.35 to 7.45 and from 35 to 39°C (in hypothermic, normal, and febrile human body conditions), respectively.

Currently, numerous scientific researches on hydrogels as Drug Delivery Systems have been reported in [3–22]. Hydroxypropyl cellulose with polyacrylamide (HPC/PAAm) is a particularly interesting hydrogel because it is biodegradable. Castillo-Miranda et al. reported in [3] a study on the crystallization of (RS)-2-(4-isobutylphenyl)propionic acid, a drug commonly known as ibuprofen, within a HPC/PAAm gel, as well as the kinetics of drug release in it. The drug release tests were performed at three temperatures (35, 37, and 39°C) and using two different solvents: a buffer solution of water and phosphate with a pH of 7.38 and a (50 : 50) mixture of ethanol with water with pH 7. The drug release was modelled with the zero-order, first order, Higuchi, and Korsmeyer-Peppas models, represented in Equations (1), (2), (3), and (4), respectively. In most cases, the best adjustments were found with the Korsmeyer-Peppas model, meaning that the drug was released as part of a non-Fickian phenomenon, through the viscoelastic relaxation of the polymer.

The drug release modelling has two main objectives: to understand the phenomenon that governs the release of the drug and to facilitate the design of the drug release devices that will be manufactured and distributed on a large scale commercially. The traditional methods of modelling that are currently used allow to reach only the first objective, but not the second. Among these models, the most widely used are the following [23, 24]:

(1) Zero-order equation:

$$\frac{M_t}{M_\infty} = k_0 t + C_0 \qquad (1)$$

(2) First-order equation:

$$\ln\left(1 - \frac{M_t}{M_\infty}\right) = -k_1 t + C_1 \qquad (2)$$

(3) Higuchi equation:

$$\frac{M_t}{M_\infty} = k_H t^{1/2} + C_H \qquad (3)$$

(4) Korsmeyer-Peppas equation:

$$\frac{M_t}{M_\infty} = k_{KP} t^n \qquad (4)$$

where M_t is the mass of water absorbed in time t and M_∞ is the mass of water in the equilibrium; k_0, k_1, k_H, and k_{KP} are the release rate constants which incorporate structural and geometric features of the delivery system; C_0, C_1, and C_H are the intercepts in their equations; and n is an exponent that indicates the mechanism by which drug release occurs.

These models are certainly useful to determine the possible drug release mechanism. Nevertheless, they do not allow the user to make reliable predictions or simulations for drug releasing, e.g., traditional models are not ideal for plotting drug release curves with a limited amount of concentration versus time data.

The present research has two objectives. The first one is to study the incorporation and release of acetaminophen on hydroxypropyl cellulose with polyacrylamide. And the second one is to mathematically model the release of the drug on HPC/PAAm by Multigene Symbolic Regression (MSR). The proposed method can be used to simulate the concentrations of acetaminophen released in HPC/PAAm and to predict the time at which the drug release will be finished.

The rest of this paper is structured as follows: The synthesis of hydroxypropyl cellulose with polyacrylamide as well as

the incorporation of the drug acetaminophen on the HPC/PAAm gel and its characterization are described in the following section. The results of the characterization and the release tests, as well as the details of the mathematical modelling of the acetaminophen release in HPC/PAAm, are reported in Results and Discussion. Finally, the paper closes with a section that summarizes the findings and concludes the paper with a brief discussion on the scope for future work.

2. Materials and Methods

2.1. Materials. For the development of this work the following chemical reagents were used: hydroxypropyl cellulose (HPC), acrylamide (AAm, purity 97%), methylenebisacrylamide (MBAm, purity 99%), tetramethylethylenediamine (TEMED, purity 99%), acetaminophen (PAR), ammonium persulfate (APS, purity 98%), sodium hydroxide (NaOH, purity 97%), and divinyl sulfone (DVS, purity 97%), all of which were purchased from Sigma-Aldrich. Deionized (DI) water and a phosphate buffer solution (PBS) with pH 7.38 were supplied by Hycel.

2.2. Synthesis of HPC/PAAm and Incorporation of Acetaminophen. The HPC/PAAm gel was synthesized according to the method of Castro et al. [25], at a ratio of 25/75 wt%. The reaction was carried out in a four-necked flask with a temperature controlled at $40 \pm 1°C$ and an inert nitrogen atmosphere. The solution consisted of 90% deionized water and 10% reagents in the desired amount to work. At the beginning, 1 g of HPC was diluted in 20 mL of DI water, and the mixture was stirred at room temperature for about 15 hours to achieve a homogeneous solution. Then, the reactor was purged with nitrogen, and 3 g of AAm was added. Thus, 0.06 g of APS was dissolved with 0.003 g of MBAm in a vial containing 8 mL of DI water, while in another vial containing the same amount of water, 0.06 g of TEMED was dissolved; both vials were stirred for 20 minutes. Once well dissolved, the content of the first vial was injected into the reactor, and 0.3 mL of DVS was added; finally, the second vial was injected into the reactor as well. The polymerization was done for one hour at 40°C in an inert atmosphere and with constant stirring at pH 7. After the reaction was finished, the solution was poured in a petri dish, and it was dried at 40°C in an oven in vacuum for one week. Once dried, the resulting films were washed with DI water in order to remove the unreacted substances, and then, they were left to dry again. Acetaminophen was incorporated into the HPC/PAAm gel by swelling, using solutions of 5 mg/mL of drug in ethanol-water at 50-50 proportion in volume.

2.3. Characterization of the Materials. Fourier transform infrared spectroscopy (FTIR) was performed using a PerkinElmer Spectrum 100 in the range 4500-500 cm^{-1}. Differential Scanning Calorimetry (DSC) was performed from 50 to 200°C. The samples were observed in a ZEIZZ microscope model AX10, in polarized mode, using the software Motic Images Plus 3.0. Micrographs of the samples were obtained in a JEOL Scanning Electronic Microscope (SEM),

model JSM-5900, using a size of sample of 1 cm^2; the gels were sputtered with a gold layer. Finally, samples were analyzed with a TA Thermo Gravimetric Analyzer (TGA), model SDT Q600, in the range 30-700°C; data was processed with the software OriginPro 8.6.

2.4. Release Tests. The release tests were performed in deionized water (pH 7) and in a phosphate buffer solution (PBS) with pH 7.38 (in the range of pH values of the human body). Three different temperatures were evaluated: 35, 37, and 39°C (hypothermic, normal, and febrile human body temperatures). Each piece of gel was placed in a container with 5 mL of liquid and remained there for 24 hours subjected to electromagnetic vibrations (80 cycles/minute) and maintaining a constant temperature (35, 37, or 39°C, depending on the case). During the first hour, the PBS was removed and replaced by new liquid at the same temperature every 15 minutes. Subsequently, the PBS was changed once every hour until eight hours is completed. A final change of liquid was also made upon completion of 24 hours of drug release. The drug release was quantified by UV-Vis spectroscopy.

2.5. Mathematical Modelling. The mathematical model that describes the release of acetaminophen in HPC/PAAm was determined by means of the free-access genetic programming tool GPTIPS software in its version 1.0, used to perform Multigene Symbolic Regression in MATLAB [26–28]. The objective of this mathematical modelling was to find a function in the form of Equation (5) to describe the release of acetaminophen over time:

$$y = f(x), \tag{5}$$

where x is the time in minutes and y is the concentration of released acetaminophen in mg/mL.

Experimental measurements of the concentrations of acetaminophen released in mg/mL over time in minutes were used to feed the algorithm. The obtained equation allowed to predict the concentration that would have been released beyond the experiment.

2.5.1. Symbolic Regression. Symbolic regression is an application of genetic programming that finds the best fitting mathematical equation for a data set. This is achieved by generating a random population of mathematical functions in the form of tree structures composed of three parts: a root node, functional nodes, and terminal nodes, as the one shown in Figure 2. The best performing ones are then selected to breeding together in order to generate a new population of functions by means of genetic operators: mutation or crossover, as shown in Figure 3, or direct reproduction (when a tree structure is selected to transfer to the new generation without changes). This process is repeated until the population contains a function that correctly adjusts to the statistical data or until the maximum number of iterations is reached [26–28].

Unlike traditional regression analysis, in which the structure of the model must be specified prior to the fit, SR generates the mathematical function which best fits the available
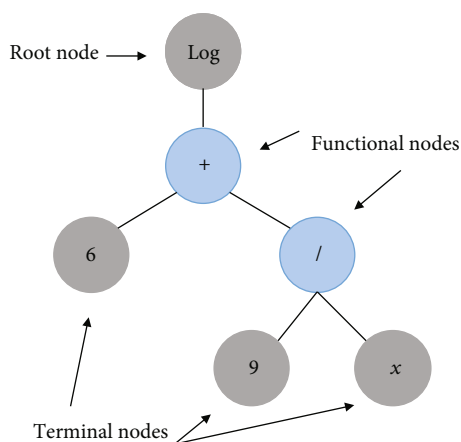
Figure 2: Tree representation of the model $y = \log\left(6 + 9/x\right)$.

data by an evolving tree process. Consequently, the main advantage of SR is the possibility of creating structures that include and combine linear, polynomial, potential, logarithmic, exponential, and sinusoidal functions, among many others [26–28].

2.5.2. Multigene Symbolic Regression. Multigene Symbolic Regression (MSR) is an improvement of SR which enables to generate data structures containing several tree structures within. The most typical equation generated by MSR has the form of

$$y = d_0 + d_1 * f(x) + d_2 * g(x), \tag{6}$$

where $f(x)$ and $g(x)$ are functions generated each one by one tree structure. The complexity of the model is controlled by the number of genes G_{max} and the depth of each gene D_{max}, both defined by the user. Each structure generated in the initial population contains a random number of genes (from 1 to G_{max}). For each model, the linear coefficients d_0, d_1, and d_2 are calculated by least squares methods. The best performing ones are then selected to breeding together in order to generate a new population of functions by crossover. In this process, random crossover points are assigned to each structure to breed, and the genes within these crossover points are exchanged with each other. If, after the exchange, the number of genes in a structure exceeds G_{max}, a random set of genes will be eliminated until it reaches G_{max} [28, 29].

3. Results and Discussion

3.1. Characterization of HPC/PAAm. After swelling, an incorporation of 70.03 grams of acetaminophen was achieved for each gram of HPC/PAAm gel. It is to be noticed that the appearance of the HPC/PAAm gel with the incorporated acetaminophen is whitish.

3.1.1. FTIR. In Figure 4, a comparison between the FTIR spectra of HPC/PAAm gel, acetaminophen, and HPC/PAAm gel with incorporated acetaminophen is shown, represented by the blue, black, and red lines, respectively. Acetaminophen

shows a signal at 3330 cm^{-1} due to the N-H bond of the amide group, followed by a wide and pronounced peak at 3151 cm^{-1}, which is attributable to the O-H bond of the hydroxyl group. There is also an intense band at 1653 cm^{-1} corresponding to the C=O bond of the amide group; the peaks at 1563, 1505, and 1435 cm^{-1} are due to aromatic vibrations, and finally, peaks at 796-859 cm^{-1} are attributable to the substituted benzene ring in the paraposition.

The HPC/PAAm gel with incorporated acetaminophen has an overlap between the N-H bonds of the amide group and the O-H bonds of the hydroxyl group at 3190 cm^{-1}; these two assignments belong to both the HPC/PAAm gel and the acetaminophen; therefore, an increase in its intensity is appreciated in the HPC/PAAm gel with acetaminophen. HPC/PAAm polymers display the stretching bands of N-H and O-H due to both, the cellulose derivative and the polyacrylamide [25, 30, 31]. At 1653 cm^{-1}, the C=O bond of the amide group is observed. At 1563, 1509, and 1454 cm^{-1}, some aromatic vibrations can be seen. Finally, between 800 and 860 cm^{-1}, the substituted benzene ring in the paraposition is observed. These peaks were previously reported in [32].

The differences between the spectra of acetaminophen and the spectra of HPC/PAAm gel with acetaminophen are observed in as far as amide stretching (3329 cm^{-1} for mono- and 3330 cm^{-1} for ortho-), O-H stretching (3182 cm^{-1} for mono- and 3199 cm^{-1} for ortho-), C=O stretching (1649 cm^{-1} for mono- and 1652 cm^{-1} for ortho-), and C-H symmetric stretching (1506 cm^{-1} for mono- and 1504 cm^{-1} for ortho-). The shifting was also observed for skeletal aryl C-C stretching vibrations (1435 cm^{-1} for mono- and 1442 cm^{-1} for ortho-) and C-N stretching mode vibration (1228 cm^{-1} for mono- and 1220 cm^{-1} for ortho-). The peaks observed at 837, 686, and 601 cm^{-1} for mono- and 837, 686, and 601 cm^{-1} for ortho- are due to out of plane C-H bending (aryl-1, 4 disubstituted). Interestingly, the peaks of the spectra of HPC/PAAm gel with acetaminophen in the range 4000-3500 cm^{-1} differ from that showed in the spectra of acetaminophen; this difference is due to the HPC/PAAm polymer peaks. From this FTIR results, it can be inferred that acetaminophen was correctly incorporated into the HPC/PAAm gel.

3.1.2. DSC. In Figure 5, the DSC thermograms of (a) HPC/PAAm gel and (b) HPC/PAAm gel with incorporated acetaminophen are shown. In the thermogram of the pure HPC/PAAm gel, it is observed that the material does not have any T_g peak. On the other hand, in the thermogram of the HPC/PAAm gel with incorporated acetaminophen, a well-defined exothermic peak at 172°C is observed. In [32], a peak of acetaminophen close to 170°C was reported, which allows us to deduce that the peak in Figure 5 corresponds to acetaminophen. According to [33], fully miscible systems of two compounds present a single T_g, even when each compound in the composite has its own T_g. Similarly, Castillo-Miranda et al. [3] reported a single exothermic peak, corresponding to the melting point of the active substance, in a DSC thermogram of HPC/PAAm gel with incorporated

(a)

(b)
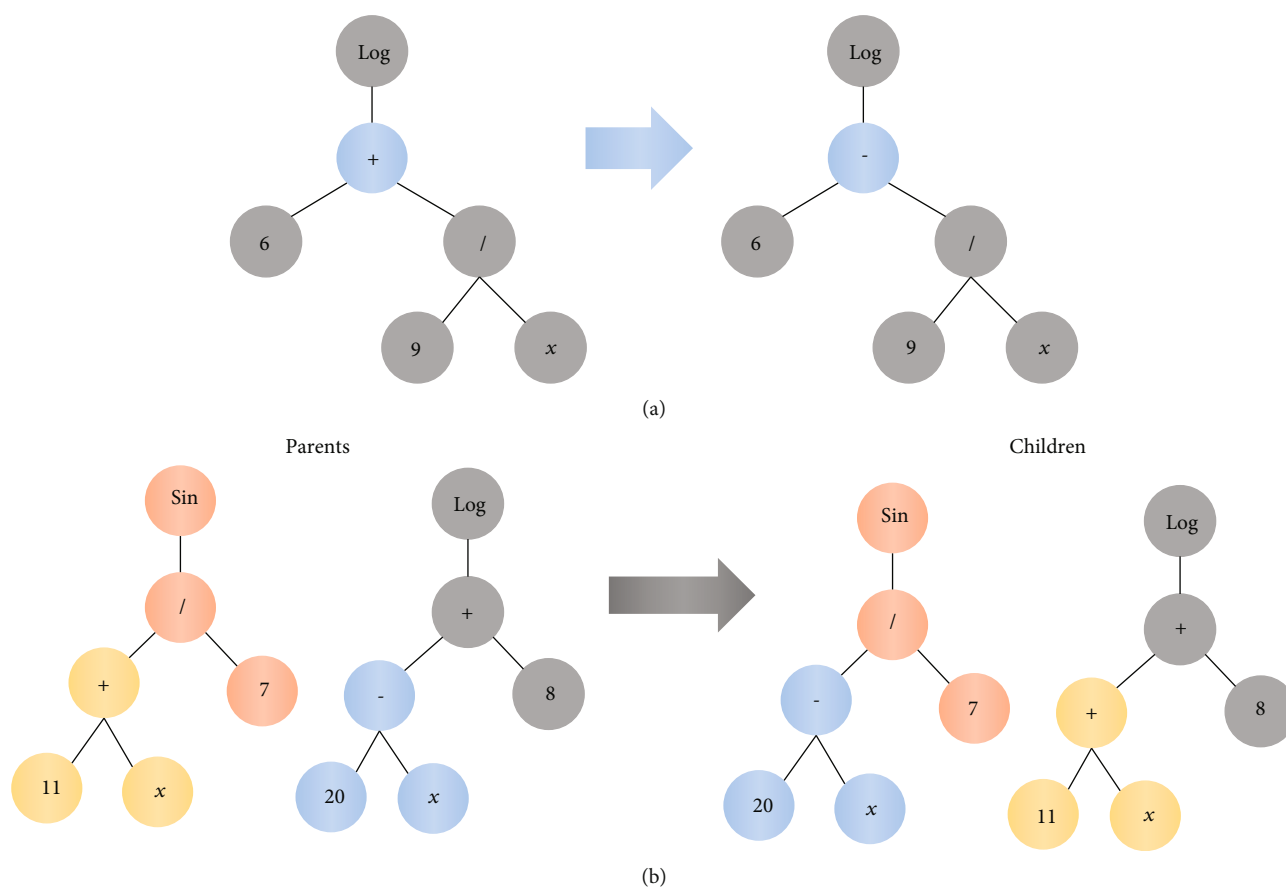
FIGURE 3: Genetic operators: (a) mutation operation; (b) crossover operation.
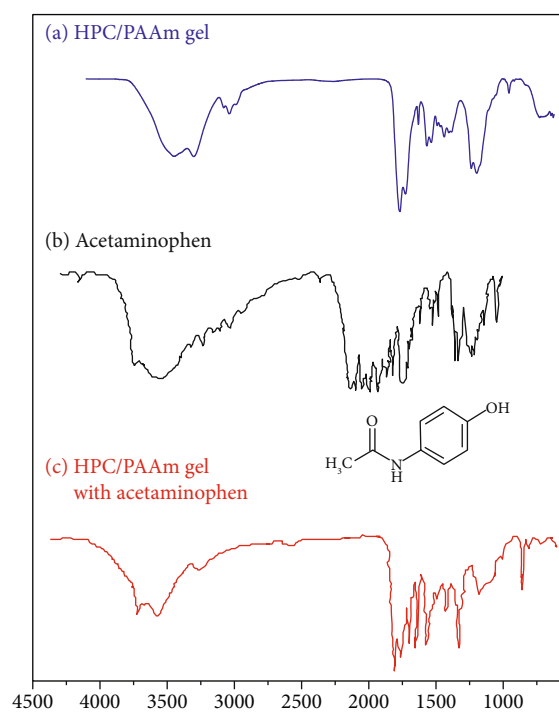
FIGURE 4: FTIR spectra of (a) HPC/PAAm gel, (b) acetaminophen, and (c) HPC/PAAm gel with incorporated acetaminophen.
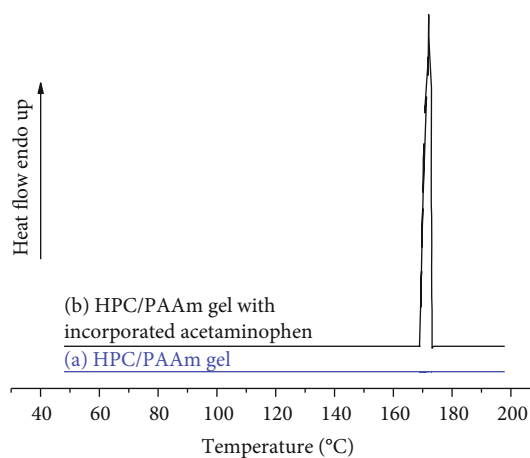
FIGURE 5: Thermograms of (a) HPC/PAAm gel and (b) HPC/PAAm gel with incorporated acetaminophen.

ibuprofen. This supports the statement that acetaminophen was correctly incorporated into the HPC/PAAm gel, previously established based on the FTIR results.

3.1.3. Optical Microscopy. In Figure 6, the optical micrographs of (a) HPC/PAAm gel, (b) HPC/PAAm gel with acetaminophen, and (c) HPC/PAAm gel with acetaminophen after 24 hours of swelling in water can be observed. All three

(a)

(b)

(c)
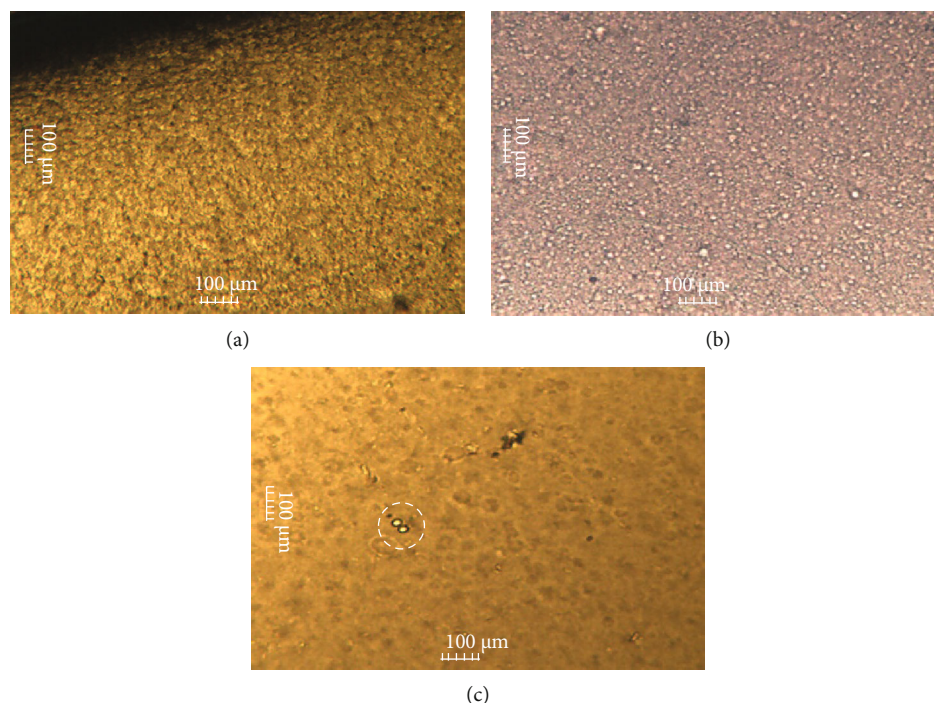
FIGURE 6: Optical micrographs of (a) HPC/PAAm gel, (b) HPC/PAAm gel with acetaminophen, and (c) HPC/PAAm gel with acetaminophen after 24 hours of swelling in water.

micrographs were taken with 5x and 75° prism opening. In Figure 6(a), the absence of acetaminophen particles in the HPC/PAAm gel is observed. On the other hand, Figure 6(b) shows acetaminophen crystals that are mostly between 3.2 and 6.4 μm in size, although there are some few conglomerates whose size reaches over 15 μm. As it is observed, the said crystals are abundant and well dispersed all over the surface of the HPC/PAAm gel. Finally, in Figure 6(c), it is shown that after 24 hours of swelling in water, most of the acetaminophen particles have been released from the HPC/PAAm gel, observing only two remaining conglomerates of approximately 15 μm each that can be observed within the dotted circle.

3.1.4. SEM. The micrographs of the HPC/PAAm gel with incorporated acetaminophen are shown, at different magnifications, in Figure 7. A homogeneous surface is observed, where the crystals are well distributed on the surface of the HPC/PAAm gel.

Two populations of crystals were seen on the micrographs. One of these consists in rectangular prisms with columnar growth in the {001} plane and a size of approximately 4 μm ($2.1 \times 5.2 \times 1.7$ μm average). The other one consists in irregular prims with columnar growth in the planes {110}, {201}, {001}, and {011} and with no agglomerates, which indicates that the acetaminophen was crystallized on the surface of the HPC/PAAm gel and not between its internal chains. Irregular acetaminophen prisms were also reported in [32]. Besides, other polymers have also presented drug crystallization on the surface. Castillo-Miranda et al. [7] reported the formation of acetylsalicylic acid crystals on the surface of hydroxyethyl cellulose/polyacrylamide gel; they

also observed a smooth surface formed by the cellulose derivative. Orthorhombic crystals were also observed on the surface, with larger crystals in the range of 4-10 μm; this morphology is a stable polymorph of acetaminophen at room temperature [34].

Both acetaminophen and the HPC/PAAm gel have atoms that can form hydrogen bonding. Hydrogen bonding between acetaminophen and HPC/PAAm can lead to the formation of not defined crystals, but the formed crystals are stabilized by hydrogen bonding to the polymer surface [35].

3.1.5. TGA. The TGA results are shown in Figure 8. Figure 8(a) shows the weight loss (%) for both the HPC/PAAm gel and the HPC/PAAm gel with incorporated acetaminophen. It can be observed that the thermal behaviour of the drug/polymer system is similar to that of the pure HPC/PAAm gel. The degradation of both materials begins at approximately 225°C, and the final difference between them is approximately 1.4% extra loss of mass when adding acetaminophen to the HPC/PAAm gel. The residual mass was about 18.3% for the pure HPC/PAAm gel and about 16.9% for the HPC/PAAm gel with incorporated acetaminophen. Both curves have also a mass loss of approximately 3% between 175 and 225°C; this loss of mass could be attributed to the decomposition of functional groups on the surface of the HPC/PAAm gel, similarly as explained in [36]. Further, Figure 8(b) shows the derivative thermogravimetric (DTG) curves for both the HPC/PAAm gel and the HPC/PAAm gel with incorporated acetaminophen. It can be observed that the rate of mass loss increased when acetaminophen was added to the HPC/PAAm gel. Also, HPC/PAAm gel peaks moved towards lower temperatures
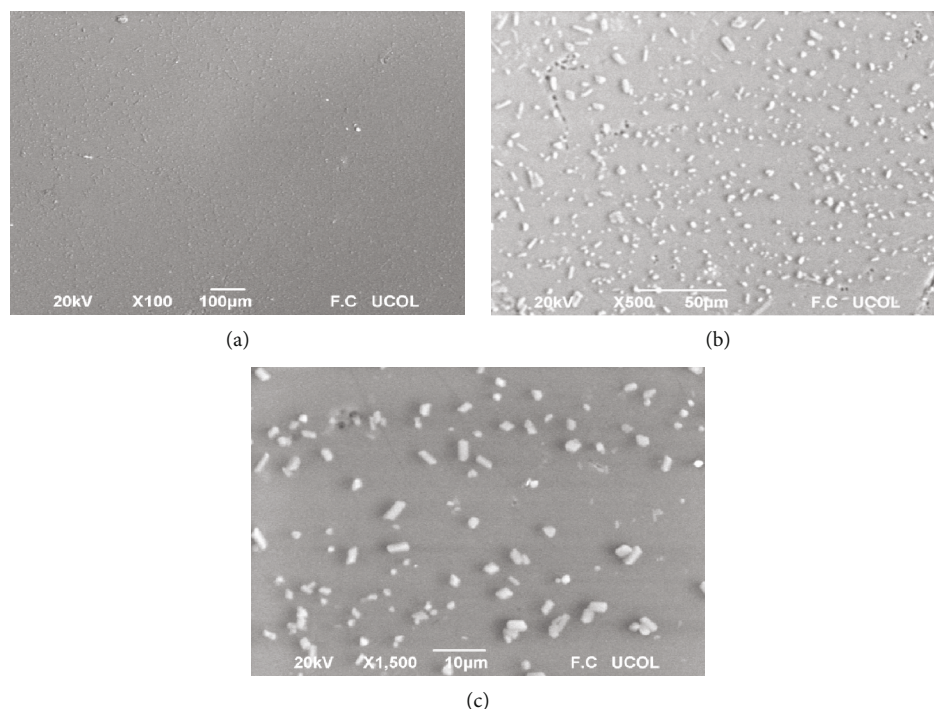
(a)

(b)

(c)

FIGURE 7: Micrographs of the surface of HPC/PAAm gel with incorporated acetaminophen: (a) 100x, (b) 500x, and (c) 1500x.

when acetaminophen was added. This indicates that the HPC/PAAm gel with incorporated acetaminophen has a lower thermal stability than the pure HPC/PAAm gel, as can be inferred from [37].

From Figure 8 can be observed, besides, that the acetaminophen is stable until some point between 200 and 300°C, and after that, its loss of mass increases rapidly. This was also reported in [32]. Additionally, the thermal degradation for the HPC/PAAm gel is similar to that of the hydroxyproyl methyl cellulose/polyacrylamide polymer, with weight losses due to humidity content and the degradation of the cellulosic polymer at 250°C, while the degradation of the polyacrylate was observed in the 350°C range [38, 39].

3.2. Release Tests. Castillo-Miranda et al. [3] modelled ibuprofen release in HPC/PAAm gel by the traditional methods (Equations (1)–(4)), and the best adjustments were obtained with the Korsmeyer-Peppas model, meaning that the release of drug in HPC/PAAm gel occurred through the viscoelastic relaxation of the polymer, as a non-Fickian phenomenon. Therefore, it was decided to model the acetaminophen release in HPC/PAAm gel with the Korsmeyer-Peppas model, assuming that acetaminophen release would also occur through the viscoelastic relaxation of the polymer, since the hydrogel used as DDS was the same.

The values of the constant rate k and exponent n obtained for the release of acetaminophen in water and in buffer (PBS) from the HPC/PAAm gel by the Korsmeyer-Peppas model, at the three proposed temperatures (35, 37, and 39°C), are presented in Table 1.

From Table 1, it is observed that in all the results the values of n are less than 0.5. Therefore, they do not correspond to any of the intervals described in [40]; this indicates the existence of several simultaneous processes in the phenomenon of acetaminophen diffusion from HPC/PAAm, contrary to the assumption based on [3]. This indicates that the drug to be released from a hydrogel has an influence on the release mechanism.

The concentration of acetaminophen released in the HPC/PAAm gel, with water as the release medium, increased proportionally to the temperature; during the second hour of the release test, at 39°C, the maximum concentration was 0.35 mg/mL. This concentration was also achieved by using buffer as the release medium but at 35°C instead, while the values at 37 and 39°C are a little higher; this indicates that, at the same temperature, a higher release of acetaminophen in HPC/PAAm is obtained by using PBS (pH 7.38) instead of water (pH 7) as the release medium. Therefore, as reported in [4, 5], the pH value has an influence on the release of the drug.

3.3. Mathematical Modelling of the Acetaminophen Release in HPC/PAAm. The time versus concentration data sets obtained from the release tests were mathematically modelled by MSR. A unique equation was obtained by modelling the data sets of the acetaminophen release in HPC/PAAm at 35, 37, and 39°C. Therefore, this equation describes the release of the drug at all of the evaluated temperatures. The used data sets were those of the drug release in PBS (pH 7.38), since this release medium proved to be the most optimal in the release tests. The modelling was carried out using the following configuration of parameters: a tree depth of 5 at

(a)

— HPC/PAAm
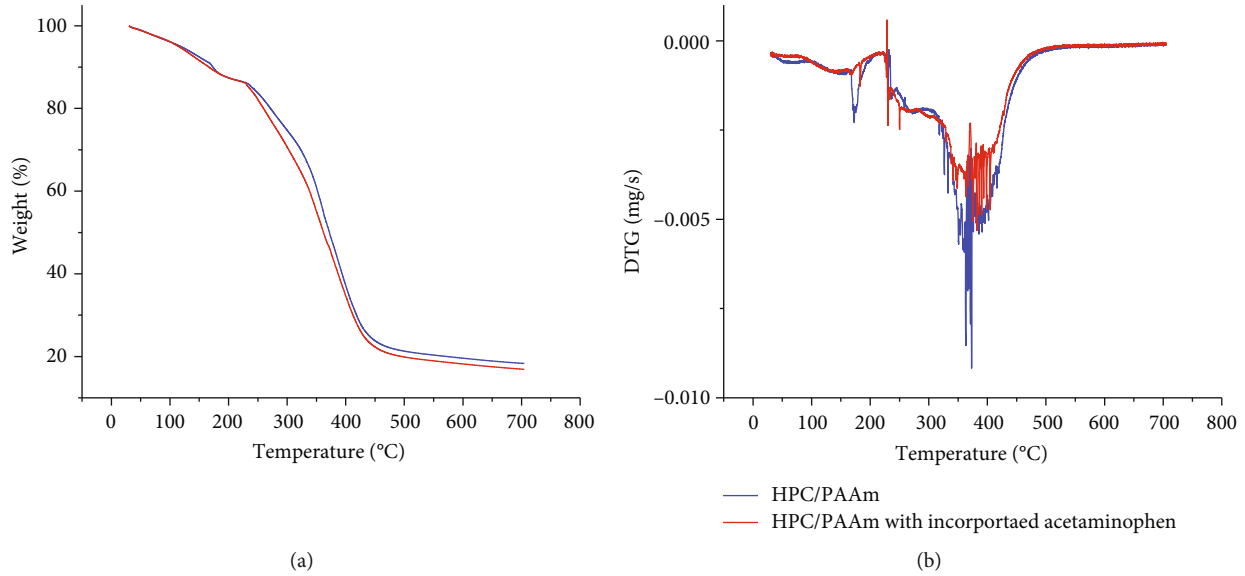— HPC/PAAm with incorportaed acetaminophen

(b)

FIGURE 8: TGA results: (a) TGA curves for HPC/PAAm gel and HPC/PAAm gel with incorporated acetaminophen; (b) DTG curves for HPC/PAAm and HPC/PAAm with incorporated acetaminophen.

TABLE 1: Values of n obtained for the release of acetaminophen in HPC/PAAm.

Solvent	35°C		37°C		39°C	
	n	k	n	k	n	k
Water	0.1282	0.4913	0.1042	0.5607	0.1277	0.4933
PBS	0.1901	0.3699	0.1400	0.4889	0.1471	0.4623

the beginning of the process, a population size of 100 function trees, and a maximum of 200 iterations. The representative mathematical model for the three experimental temperatures can be described by Equation (7). The coefficients of determination R^2 and adjusted R^2 are calculated as 0.98849 and 0.98795, respectively:

$$y = 26.3 * \tanh\left(\frac{0.2784}{x_1^2}\right) - 0.0003271 * x_1 - \frac{1.559}{\ln(|x_1|)} + 0.7194,$$

(7)

where x_1 is the time in minutes and y is the concentration of released acetaminophen in mg/mL.

This mathematical model allows to simulate the concentrations of released acetaminophen even at times beyond the tested and to predict the moment in which the drug release will be finished. Figure 9 shows, in black, the simulation for the release of acetaminophen from HPC/PAAm gel in PBS at any of the three evaluated temperatures, obtained with Equation (7). The red lines in the same figure represent the experimental data at each temperature. As observed, the red curves constructed with experimental data end at about 400 minutes, at which time the experiment finished. However, the mathematical model enabled to predict the release of the drug in times beyond the end of the experiment, allowing to determine that the acetaminophen should be depleted at some point close to 1500 minutes, that is, 25 hours after the start of the release. It is also observed that the simulated data,

obtained with Equation (7), resembles the typical kinetic profile of drug release [41].

The simulated data from the mathematical model was compared with the experimental data collected at each evaluated temperature, and the results are shown in Table 2. The listed measures are the coefficient of determination R^2, the Coefficient of Variation (CV), the Root-Mean-Square Error (RMSE), and the Mean Absolute Error (MAE).

As observed, high R^2 values and low CV, RMSE, and MAE values were obtained for the comparisons between the simulated data and the experimental data obtained at all the three evaluated temperatures. These results corroborate that the mathematical model obtained by MSR is reliable to represent the release of acetaminophen in HPC/PAAm gel in PBS at 35, 37, and 39°C. It is also noticeable that the highest R^2 value and lowest CV, RMSE, and MAE values were obtained when comparing the simulated data with the experimental data collected at 35°C. This explains why, in Figure 9, the experimental data of acetaminophen release at 35°C is the most similar to the curve obtained from the simulation and in consequence the most similar to the typical kinetic profile of drug release [41].

4. Conclusions

The samples of HPC/PAAm gel with acetaminophen were characterized by FTIR, DSC, optical microscopy, SEM, and TGA, finding that the drug was correctly incorporated in the HPC/PAAm gel. The correct incorporation of the acetaminophen into the HPC/PAAm gel demonstrates that this material has the potential to be used as a Drug Delivery System as a patch for this active substance. However, it is still necessary to perform more tests to confirm its suitability, including toxicity studies and stability tests; these studies are contemplated as future work.

(a)

(b)

(c)
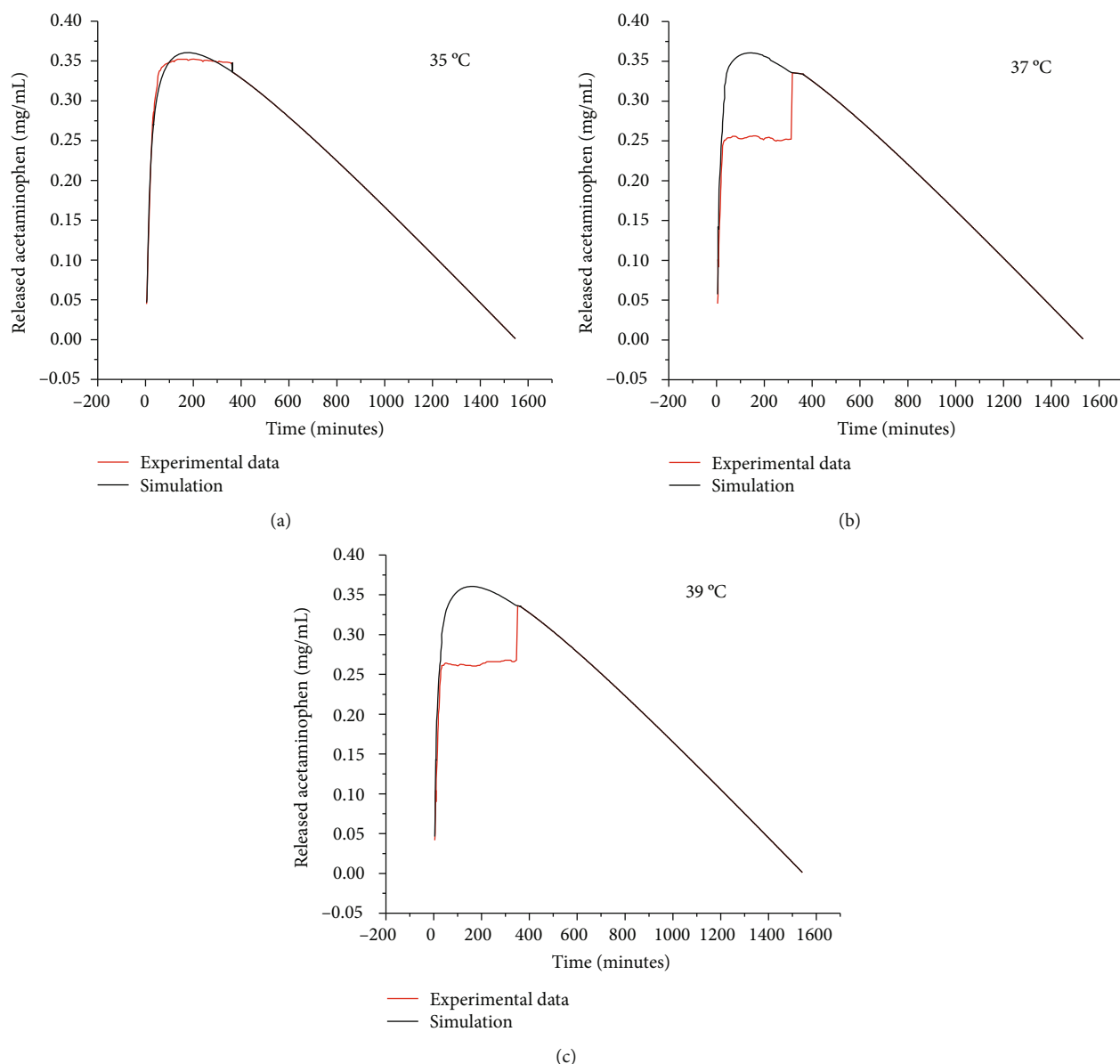
Figure 9: Concentration vs. time curves for the release of acetaminophen from HPC/PAAm gel in PBS at (a) 35, (b) 37, and (c) 39°C.

Release tests were performed in water and in a phosphate buffer solution (PBS) with pH 7.38 at three different temperatures: 35, 37, and 39°C. The release at each temperature was modelled with the Korsmeyer-Peppas model. In all cases, the values of n were less than 0.5, which indicates the existence of several simultaneous processes in the phenomenon of acetaminophen diffusion from HPC/PAAm. Further, the concentration of acetaminophen released in the HPC/PAAm increased proportionally with the pH value of the release medium used.

The results of the release tests were also mathematically modelled by Multigene Symbolic Regression (MSR). The obtained mathematical model achieved R^2 and adjusted R^2 values of 0.98849 and 0.98795, respectively. The equation was used to simulate the concentrations of released acetaminophen in HPC/PAAm at times beyond

Table 2: Simulation statistics for the release of acetaminophen from HPC/PAAm gel in PBS at (a) 35, (b) 37, and (c) 39°C.

Temperature	R^2	CV	RMSE	MAE
35°C	0.99982	0.00625	0.00193	0.00736644
37°C	0.99774	0.01987	0.0063	0.08379797
39°C	0.9845	0.0433	0.01366	0.07457

the tested. It was predicted that drug release would finish 25 hours after its start. The simulated data, obtained with the proposed mathematical model, resembled the typical kinetic profile for drug release. Also, when comparing the simulated data that was generated from the proposed model with the experimental data collected at all the three evaluated temperatures, high values of R^2 and low values of CV, RMSE, and MAE (from 0.9845 to

0.99982, from 0.00625 to 0.0433, from 0.00193 to 0.01366, and from 0.00736644 to 0.08379797, respectively) were obtained. The highest R^2 value and lowest CV, RMSE, and MAE values (0.99982, 0.00625, 0.00193, and 0.00736644, respectively) were obtained when comparing the simulated data with the experimental data collected at 35°C.

This way, it can be concluded that the proposed mathematical model is reliable. Moreover, the mathematical modelling by MSR has proven to be an area of opportunity for pharmacological engineers and researchers who are interested in the study of the release of drugs in hydrogels. However, it is important to note that it is still necessary to evaluate the application of the mathematical model that has been presented in this work to model and simulate drug release by using a different drug-gel combination. This is contemplated as future work.

Data Availability

The data used to support the findings of this study are available from the corresponding author upon request.

Conflicts of Interest

The authors declared no potential conflicts of interest with respect to the research, authorship, and/or publication of this article.

Acknowledgments

References

[1] I. A. Katime, O. Katime, and D. Katime, "Materiales inteligentes: hidrogeles macromoleculares; algunas aplicaciones biomédicas," in *Anales de la Real Sociedad Española de Química*, pp. 35–50, Real Sociedad Española de Química, 2005.

[2] I. Harrison and F. Spada, "Hydrogels for atopic dermatitis and wound management: a superior drug delivery vehicle," *Pharmaceutics*, vol. 10, no. 2, p. 71, 2018.

[3] C. A. Castillo-Miranda, A. Beatriz Morales-Cepeda, C. F. Castro-Guerrero et al., "Deposition of ibuprofen crystals on hydroxypropyl cellulose/polyacrylamide gel: experimental and mathematic modeling releasing," *International Journal of Polymer Science*, vol. 2016, Article ID 2634104, 8 pages, 2016.

[4] S. Xu, H. Li, H. Ding et al., "Allylated chitosan-poly(*N*-isopropylacrylamide) hydrogel based on a functionalized double network for controlled drug release," *Carbohydrate Polymers*, vol. 214, pp. 8–14, 2019.

[5] F. Sabbagh, I. I. Muhamad, Z. Nazari, P. Mobini, and S. B. Taraghdari, "From formulation of acrylamide-based hydro-

[6] A. Gallastegui, M. B. Spesia, I. E. dell'Erba et al., "Controlled release of antibiotics from photopolymerized hydrogels: kinetics and microbiological studies," *Materials Science and Engineering: C*, vol. 102, pp. 896–905, 2019.

[7] C. A. Castillo-Miranda, C. F. Castro-Guerrero, H. A. Velasco-Ocejo et al., "Acetylsalicylic acid (ASA) on hydroxyethylcellulose/polyacrylamide gel (HEC/PAAm) as a proposal for a dermatological compress: mathematical modeling of ASA release kinetics," *International Journal of Polymer Science*, vol. 2019, Article ID 4597641, 10 pages, 2019.

[8] C. A. Garrido, M. Vargas, and J. F. Alvarez-Barreto, "Auto-cross-linking hydrogels of hydrogen peroxide-oxidized pectin and gelatin for applications in controlled drug delivery," *International Journal of Polymer Science*, vol. 2019, Article ID 9423565, 11 pages, 2019.

[9] C. Peng, J. Xu, G. Chen, J. Tian, and M. He, "The preparation of α-chitin nanowhiskers-poly (vinyl alcohol) hydrogels for drug release," *International Journal of Biological Macromolecules*, vol. 131, pp. 336–342, 2019.

[10] D. Hoang Phuc, N. Thi Hiep, D. Ngoc Phuc Chau et al., "Fabrication of hyaluronan-poly(vinylphosphonic acid)-chitosan hydrogel for wound healing application," *International Journal of Polymer Science*, vol. 2016, Article ID 6723716, 9 pages, 2016.

[11] D. Lombardo, M. A. Kiselev, and M. T. Caccamo, "Smart nanoparticles for drug delivery application: development of versatile nanocarrier platforms in biotechnology and nanomedicine," *Journal of Nanomaterials*, vol. 2019, Article ID 3702518, 26 pages, 2019.

[12] E. Szymańska, A. Czajkowska-Kośnik, and K. Winnicka, "Comparison of rheological, drug release, and mucoadhesive characteristics upon storage between hydrogels with unmodified or beta-glycerophosphate-crosslinked chitosan," *International Journal of Polymer Science*, vol. 2018, Article ID 3592843, 12 pages, 2018.

[13] F. Castiglione, M. Casalegno, M. Ferro, F. Rossi, G. Raos, and A. Mele, "Evidence of superdiffusive nanoscale motion in anionic polymeric hydrogels: analysis of PGSE- NMR data and comparison with drug release properties," *Journal of Controlled Release*, vol. 305, pp. 110–119, 2019.

[14] H. Paukkonen, M. Kunnari, P. Laurén et al., "Nanofibrillar cellulose hydrogels and reconstructed hydrogels as matrices for controlled drug release," *International Journal of Pharmaceutics*, vol. 532, no. 1, pp. 269–280, 2017.

[15] J. Duan and J. Jiang, "Structure and properties of hydrophobic aggregation hydrogel with chemical sensitive switch," *International Journal of Polymer Science*, vol. 2017, Article ID 9123248, 5 pages, 2017.

[16] M. Murata, Y. Uchida, T. Takami et al., "Dual drug release from hydrogels covalently containing polymeric micelles that possess different drug release properties," *Colloids and Surfaces B: Biointerfaces*, vol. 153, pp. 19–26, 2017.

[17] R. Zhang, L. Lei, Q. Song, and X. Li, "Calcium ion cross-linking alginate/dexamethasone sodium phosphate hybrid hydrogel for extended drug release," *Colloids and Surfaces B: Biointerfaces*, vol. 175, pp. 569–575, 2019.

[18] S. Khan and N. Anwar, "Highly porous pH-responsive carboxymethyl chitosan-*grafted*-poly (acrylic acid) based smart hydrogels for 5-fluorouracil controlled delivery and colon

targeting," *International Journal of Polymer Science*, vol. 2019, Article ID 6579239, 15 pages, 2019.

[19] S. Sharma, S. Afgan, Deepak, A. Kumar, and R. Kumar, "L-Alanine induced thermally stable self-healing guar gum hydrogel as potential drug vehicle for sustained release of hydrophilic drug," *Materials Science and Engineering: C*, vol. 99, pp. 1384–1391, 2019.

[20] T. N. Barradas, J. P. Senna, S. A. Cardoso, K. G. de Holanda e Silva, and C. R. Elias Mansur, "Formulation characterization and *in vitro* drug release of hydrogel-thickened nanoemulsions for topical delivery of 8-methoxypsoralen," *Materials Science and Engineering: C*, vol. 92, pp. 245–253, 2018.

[21] V. S. Ghorpade, R. J. Dias, K. K. Mali, and S. I. Mulla, "Citric acid crosslinked carboxymethylcellulose-polyvinyl alcohol hydrogel films for extended release of water soluble basic drugs," *Journal of Drug Delivery Science and Technology*, vol. 52, pp. 421–430, 2019.

[22] X.-F. Sun, Y. Feng, X. Shi, and Y. Wang, "Preparation and property of xylan/poly(methacrylic acid) semi-interpenetrating network hydrogel," *International Journal of Polymer Science*, vol. 2016, Article ID 8241078, 8 pages, 2016.

[23] N. Sun, T. Wang, and X. Yan, "Synthesis and investigation of a self-assembled hydrogel based on hydroxyethyl cellulose and its *in vitro* ibuprofen drug release characteristics," *RSC Advances*, vol. 7, no. 16, pp. 9500–9511, 2017.

[24] D. Caccavo, "An overview on the mathematical modeling of hydrogels' behavior for drug delivery systems," *International Journal of Pharmaceutics*, vol. 560, pp. 175–190, 2019.

[25] C. Castro, A. Morales, A. Koschella, and T. Heinze, "Phase behaviour of hydroxypropyl cellulose/ polyacrylamide gels," *Macromolecular Symposia*, vol. 296, no. 1, pp. 429–435, 2010.

[26] D. Searson, M. Willis, and G. Montague, "Co-evolution of non-linear PLS model components," *Journal of Chemometrics*, vol. 21, no. 12, pp. 592–603, 2007.

[27] D. P. Searson, D. E. Leahy, and M. J. Willis, "GPTIPS: an open source genetic programming toolbox for multigene symbolic regression," in *Proceedings of the International MultiConference of Engineers and Computer Scientists 2010 (IMECS 2010)*, pp. 17–19, Hong Kong, March 2010.

[28] D. P. Searson, "GPTIPS 2: an open-source software platform for symbolic data mining," in *Handbook of Genetic Programming Applications*, A. H. Gandomi, A. H. Alavi, and C. Ryan, Eds., Springer, 2015.

[29] S. Soleimani, S. Rajaei, P. Jiao, A. Sabz, and S. Soheilinia, "New prediction models for unconfined compressive strength of geopolymer stabilized soil using multi-gen genetic programming," *Measurement*, vol. 113, pp. 99–107, 2018.

[30] C. Castro-Guerrero, A. Morales-Cepeda, O. Kharissova, A. Koschella, and T. Heinze, "Mesophases in a gel from hydroxypropyl cellulose/polyacrylamide," *Macromolecular Symposia*, vol. 294, no. 2, pp. 58–63, 2010.

[31] S. Chaouf, S. el Barkany, I. Jilal et al., "Anionic reverse microemulsion grafting of acrylamide (AM) on HydroxyEthylCellulose (HEC): synthesis, characterization and application as new ecofriendly low-cost flocculant," *Journal of Water Process Engineering*, vol. 31, 2019.

[32] T. O. Kääriäinen, M. Kemell, M. Vehkamäki et al., "Surface modification of acetaminophen particles by atomic layer deposition," *International Journal of Pharmaceutics*, vol. 525, no. 1, pp. 160–174, 2017.

[33] R. Jayachandra Babu, W. Brostow, I. M. Kalogeras, and S. Sathigari, "Glass transitions in binary drug + polymer systems," *Materials Letters*, vol. 63, no. 30, pp. 2666–2668, 2009.

[34] N. Wahlberg, A. Ø. Madsen, and K. V. Mikkelsen, "Heterogeneous nucleation of polymorphs on polymer surfaces: polymer–molecule interactions using a Coulomb and van der Waals model," *Journal of Molecular Modeling*, vol. 24, no. 7, 2018.

[35] J. V. Parambil, S. K. Poornachary, J. Y. Y. Heng, and R. B. H. Tan, "Template-induced nucleation for controlling crystal polymorphism: from molecular mechanisms to applications in pharmaceutical processing," *CrystEngComm*, vol. 21, no. 28, pp. 4122–4135, 2019.

[36] K. Singh, B. P. Singh, R. Chauhan, and T. Basu, "Fabrication of amperometric bienzymatic glucose biosensor based on MWCNT tube and polypyrrole multilayered nanocomposite," *Journal of Applied Polymer Science*, vol. 125, no. S1, pp. E235–E246, 2012.

[37] T. Zheng, G. Wang, N. Xu et al., "Preparation and properties of highly electroconductive and heat-resistant CMC/buckypaper/epoxy nanocomposites," *Nanomaterials*, vol. 8, no. 12, p. 969, 2018.

[38] B. Zhao, H. Jiang, Z. Lin, S. Xu, J. Xie, and A. Zhang, "Preparation of acrylamide/acrylic acid cellulose hydrogels for the adsorption of heavy metal ions," *Carbohydrate Polymers*, vol. 224, 2019.

[39] R. Das, A. B. Panda, and S. Pal, "Synthesis and characterization of a novel polymeric hydrogel based on hydroxypropyl methyl cellulose grafted with polyacrylamide," *Cellulose*, vol. 19, no. 3, pp. 933–945, 2012.

[40] I. A. Katime, D. Katime, and O. Katime, *Los materiales inteligentes de este milenio. Los hidrogeles macromoleculares: Síntesis, propiedades y aplicaciones*, Servicio Editorial de la Universidad del País Vasco, Bilbao, Spain, 2004.

[41] R. Urso, P. Blardi, and G. Giorgi, "A short introduction to pharmacokinetics," *European Review for Medical and Pharmacological Sciences*, vol. 6, no. 2-3, pp. 33–44, 2002.

Review Article

Preparation and Applications of the Cellulose Nanocrystal

Yong Yang,[1] **Zhou Chen** [ID],[2] **Junxiong Zhang,**[3] **Guanchun Wang,**[4] **Ruiqian Zhang,**[4] **and Dingjie Suo** [ID][5]

[1]*National Engineering Laboratory for Modern Silk, College of Textile and Clothing Engineering, Soochow University, Suzhou 310018, China*
[2]*School of Mechanical and Power Engineering, Nanjing Tech University, Nanjing 211800, China*
[3]*College of Materials Science and Technology, Nanjing University of Aeronautics and Astronautics, Nanjing 210016, China*
[4]*Science and Technology on Reactor Fuel and Materials Laboratory, Nuclear Power Institute of China, Chengdu 610213, China*
[5]*School of Life Sciences, Beijing Institute of Technology, Beijing 100081, China*

Correspondence should be addressed to Zhou Chen; cz6327725@163.com and Dingjie Suo; dingjiesu@gmail.com

Cellulose widely existed in plants and bacteria, which takes important effect on the synthesis of macromolecule polymer material. Because of its great material properties, the cellulose nanocrystal (CNC) showed its necessary prospect in various industrial applications. As a renewable future material, the preparation methods of the CNC were reviewed in this paper. Meanwhile, the important applications of CNC in the field of composites, barrier film, electronics, and energy consumption were also mentioned with brief introductions. The summarized preparations and considerable applications provided operable ideas and methods for the future high-end and eco-friendly functional composites. Suggestions for potential applications were also discussed.

1. Introduction

Cellulose is a macromolecular polysaccharide composed of glucose. It is also the most diverse and widespread group of polysaccharides in nature. As a kind of natural crystalline macromolecular compound, the cellulose nanocrystal (CNC) widely exists in the plant fibers and the capsular polysaccharide of bacteria [1] and possesses a series of characteristics of high crystallization, high strength, large specific surface, low density, biocompatibility, and biodegradability. Therefore, it is usually utilized in the field of construction, foodstuff, electronics, pharmacy, barrier industry, et al. [2–6].

The main methods for preparing CNC at present are the mechanical process, the chemical process of hydrolysis, the biological process of hydrolysis, and the combined method of the above processes. All the above methods mentioned have their own advantages and disadvantages and also different effects on their applications [7, 8]. This paper presents a summary of the research progress of preparations, modifications, and applications of CNC in all aspects.

2. Methods for CNC Preparations

The plant fibers are usually employed in preparing the CNC for its low price and abundance, whose common size is 0.5~3.0 mm for length and 20~40 μm for diameter [9]. Meanwhile, the size of any one dimensionality of cellulose locating in 100 nm is called the CNC [10]. Therefore, the methods for obtaining the CNC are the processes of decreasing the size of natural cellulose, which includes the process of mechanical, the chemical hydrolysis, the biological hydrolysis, and the combined methods.

2.1. Preparation of CNC via the Mechanical Process. The mechanical process is a physical method for getting the CNC and consists of four ways: homogenization under high pressure, microfluidization, fine grinding, and freezing smashing [11].

2.1.1. Homogenization under High Pressure. Homogenization is a one-step process to make a stable suspension by smashing the solid to form ultrafine particles in the solution [12].
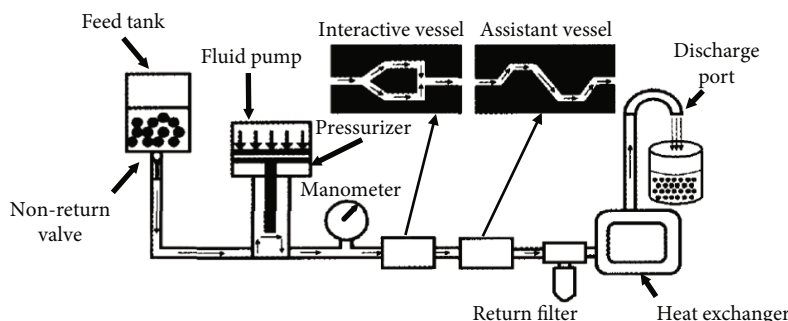
Figure 1: Technological process of the microfluidization [20].

Homogenization under high pressure was usually used to produce the microcrystalline cellulose (MCC), where the process of the homogenization under high pressure usually occurred in the homogeneous valve [13]. The raw material was extruded to the adjustable gap between the rod and the seat of the valve (usually $h = 0.1$ mm) by the outside force to accelerate the solution speed to 200~300 m/s. While leaving the gap, the inner press of the mixed solution fell instantaneously [14]. According to Bernoulli's theory [15], the great change of inner press would create an inner shearing force to produce lots of positive holes and the turbulence, which would break the fibers into ultrafine particles.

The method of homogenization under high pressure was first improved in 1980s [16]. Turbak et al. [17] employed the wood fibers to produce the MCC with this method and obtained the stable MCC gel with high viscosity. And then, a series of studies reported its application for the MCC preparation with varieties of raw materials. Khiari [18] utilized chemistry-treated residue of the Badam to produce cellulose nanofibril (CNF) gel at 600 bars for 10 times, and the resulting CNF was one with a diameter of 3~18 nm. Meanwhile, they also indicated that the parameters of production would be the best by holding the reaction temperature at 70~80°C, and the homogenization under high pressure could be applied in the continuous industry production.

Although the method of the homogenization under high pressure possessed several advantages, its development was also limited by its obvious disadvantages. As an energy-intensive process, the homogenization under high pressure utilizes lots of energy, which meant that its energy waste was huge. Meanwhile, its efficiency was unstable because the valve was easily jammed by the long plant fibers. All the above problems prevented its improvement.

2.1.2. Microfluidization. The microfluidization is called microfluidization under high pressure [19], one of the methods for preparing nanomaterials, and its technological process is shown in Figure 1 [20]. The raw slurry was firstly injected and pressurized to about 4000 bars by the fluid pump. It was then forced into a Y-form interactive vessel, where two squirts of liquid with the speed of 1000 m/s met head-on. This impaction would create a huge shear force as well as the void effect, which results in the manufacture of the nanoparticle. Furthermore, the slurry goes through the assistant vessel with several inner zigzags, which results in

more impaction occurring with the cavity walls and consequently smashing the nanoparticles further to obtain more homogeneous CNC.

Li and Liu [21] employed the high-pressure jet machine to prepare the NFC at 103.4 MPa for 12 times with a diameter of 80 μm of its inner cavity. They indicated that the jet machine with small-bores in its main cavity could improve the relative water content of the prepared MCC. The test result showed that the relative water content of MCC was 1105% prepared by the machine with a diameter of 75 nm of its inner cavity for 10 times. Meanwhile, the MCC size decreased with the homogeneous times increasing and reached 100~200 nm after 5-time microfluidization, when the diameter of the main cavity was 100 nm. Compared to the homogenization under high pressure, the microfluidization had the disadvantage that the cavity was easily jammed by long fibers, and its energy consumption was high. It is not easily applicable in the industry.

2.1.3. Fine Grinding. The method of fine grinding was a novel physical way in preparing the MCC, which was realized by the fine grinder and a commercial grinder as shown in Figure 2. It was obvious that the core components consisted of two discs, the inner and the external, where both discs were covered with grooves with different parameters. The initial step of the process for the MCC preparation was firstly to pour the raw slurry into the gap between two discs, while the external disc remained stationary and the inner disc kept rotating. The relative rotation of the two discs produced the force of crush, shearing, friction, grinding, and tearing to divide the fibers as well as decrease their sizes to obtain the MCC. By controlling the grinding parameters, the MCC with varieties of size levels ended up with low energy consumption; meanwhile, the grinder was easy to clean and maintain. But it was incredibly inefficient, and little application was reported. Li and Liu [21] used the pretreated fibers of the coniferous tree to prepare the MCC by grinding the slurry for 15 times, and the diameter of the obtained MCC was 10~40 nm.

2.1.4. Freezing Smashing. The freezing smashing technique was used in smashing the frozen cellulose fiber with mechanical force to divide the cellulose fibers and produce the CNC. Liquid nitrogen was usually employed as the freezing medium to freeze the cellulose slurry, which could transfer
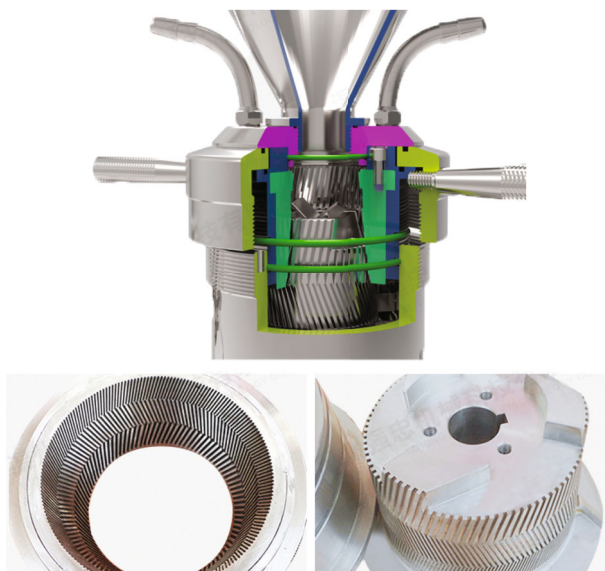
FIGURE 2: A commercial fine grinder.

the fibers from toughness to brittleness under low temperature and subsequently increase its internal stress. The powerful impaction from the mechanical smashing easily broke the structure of the frozen fibers hence dividing it to nanosize [22]. However, its cost was too high while it was also too low to be promoted.

2.2. Preparation of Chemical Process. Although all the above mechanical processes were employed in preparing the CNC, they were not widely applied due to their great energy consumption. Therefore, the chemical process was focused on treating the natural cellulose. As a kind of polysaccharide, the cellulose is made from the glucose molecules, which are connected by the β-1,4-glucosidic bond with each other [23]. Thus, the process of partially breaking glucosidic bonds is the key way to obtaining the CNC, and the chemical hydrolysis offers a case for realizing it [24].

2.2.1. Process of Alkali Hydrolysis. As a kind of natural polymer, the cellulose had the supramolecular structure which made it difficult to be hydrolyzed. However, the alkali had the ability to swell the cellulose as well as break its inner hydrogen bonds [25]. Therefore, the alkali was employed to hydrolyze the cellulose.

Research showed that the crystal form of natural cellulose was transferred from I-form to II-form after treatment with 9 wt% NaOH [26]. Zhang et al. [27] obtained the II-form spherical CNC by treating the cellulose with 5 M NaOH at 80°C and acid solution, successively. Tang et al. [28] used NaClO solution to hydrolyze the microcrystalline cellulose (MCC) to obtain spherical CNC with the diameter of 20~40 nm, and its crystalline was 79.71%. Hagman et al. [29] dissolved the MCC with 2 M NaOH solution and found that the MCC was hydrolyzed to new chains with a lower crystalline degree and kept stable in the solution. Xie et al. [30] investigated the effects of the parameters of the alkali

hydrolysis on the microstructure of the CNC. They showed that the productivity of II-form CNC was 54.50% with an average diameter of 156.9 nm, and its parameter was handling the cellulose with 5 M NaOH solution at 60°C for 2 hours. Although several studies have reported the application of alkali in hydrolyzing cellulose, the alkali was mainly employed in pretreating the cellulose to dissolve the lignin and pectin.

2.2.2. Process of Acid Hydrolysis. The microstructure of the cellulose fiber consisted of discontinuous regions of crystalline cellulose and amorphous cellulose, where the unconfined amorphous region was between two inerratic crystalline regions, and the fiber was made from the repetition of the above structures. Therefore, researches were aimed at how to remove the amorphous regions quickly and keeping the crystalline regions as well.

Liu et al. [31] prepared the CNC from reed pulp with 55 wt% sulfuric acid, using sodium *m*-nitrobenzene sulfonate (SMS) as the cocatalyst. It was indicated that the optimum parameters for the CNC preparation were the reaction at 50°C for 5 hours accompanied with 10 wt% SMS. Compared to the method with two catalysts, sodium dodecyl benzene sulfonate (SDBS) and cupric sulfate simultaneously, the CNC obtained from this process was smaller and more homogeneous, with much higher yield. Wu et al. [32] indicated that the ultrasound-assisted sulfuric acid method could be applied for the preparation of CNC, and its parameters were about 10 nm for diameter and 200~400 nm for length with a crystallinity of 63.3%. Meanwhile, the thermal insulation foam made of the CNC with the freezing-drying method expressed its perfect thermal insulation performance under normal condition.

You et al. [33] used the ultrasonic-assisted method to hydrolyze the MCC with carbon-based phosphotungstic acid as the catalyst. The obtained CNC was rod-like and I-form with a length of 146~862 nm and a diameter of 12~79 nm, whose crystallinity was 76.1%. Sun et al. [34] hydrolyzed the cotton fibers with 63.9% sulfur acid at 50°C and tested its microstructure, solubility in alkali solution, molecular weight, and other characteristics. It was found that the hydrolysis time of 45~55 min was the optimum time range when the CNC yield was 32.2~41.7%, and the 18% NaOH solution was a perfect indicator for the CNC preparation. The process of acid hydrolysis is widely applied all over the world, but the terrible wastes are unavoidable, wasted solution of acid, alkali, water, and residua. And the novel ways for obtaining the CNC have drawn the attentions all the time.

2.2.3. Process of TEMPO Hydrolysis. The TEMPO is a series of reagents used to oxidize the alcohol and ether, including 2,2,6,6-tetramethylepiperridin-1-oxyl and its ramifications with the structure of 1-oxyl, an oxygen radical. Research showed that the function of the TEMPO was its oxidation effect on the alcoholic hydroxyl group [9]. As an efficient and pollution-free reagent, the TEMPO was employed to produce the CNC, and its common reaction system consisted of the TEMPO, the NaBr, and the NaClO [35].
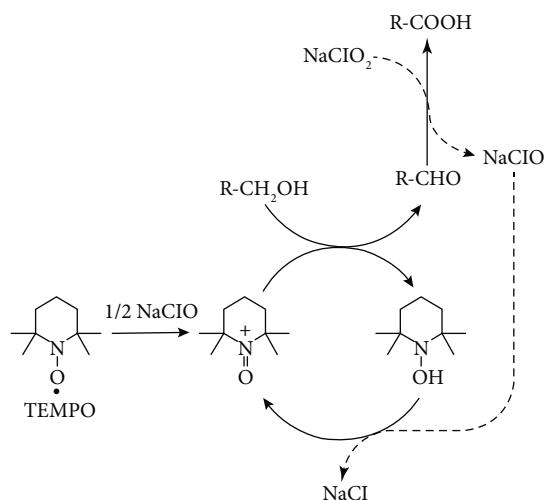
FIGURE 3: Oxidation of primary hydroxyls to carboxyls by the TEMPO/NaClO/NaClO$_2$ system under weak acidic or neutral conditions [37].

2.2.3.1. Development of TEMPO Reaction System. Research indicated that the process of the TEMPO oxidation of the cellulose was a process where the C6-formyl group was transformed to the C6-carboxyl group [36]. As the main oxidation reagent, the NaClO firstly transformed the NaBr into NaBrO, and the produced NaBrO would oxide the TEMPO to be a nitrosonium. Nitrosonium underwent oxidation to transform the alcoholic hydroxyl group and produced an aldehyde or carboxylic acid, where its mechanism was displayed in Figure 3 [37].

However, further study showed that the basicity of alkalinity had great effect on the degree of dissociation of the CNC, which might have led to the decrement of the mechanical properties of the CNC, as the strength and flexibility of the nanofibers [38]. Therefore, the present researches of the reaction systems were mainly focused on the adjustment and controlling of the reaction system [39].

Saito et al. [37] replaced the NaBr in the reaction system of the TEMPO/NaBr/NaClO with the NaClO$_2$ and found the phenomena that the aldehyde groups teemed in the produced CNC surface obtained from the reaction system of the TEMPO/NaBr/NaClO, and it did not occur in the TEMPO/-NaClO/NaClO$_2$ system. This mechanism is shown in Figure 3. Meanwhile, the size of the CNC made from the above reaction system was long for 2 μm and wide for 5 nm; the degree of polymerization was 900, with an optimum reaction pH of 6.8.

Although the system of the TEMPO/NaClO/NaClO$_2$ displayed its advantages, its disadvantages were also unavoidable, such as its terrible reaction rate and relatively low content of the carboxyl in the CNC. Attentions were drawn to improve the efficiency of the TEMPO/NaClO/-NaClO$_2$ system [40]. Iwamoto et al. [41] employed ten kinds of systems consisting of TEMPO ramification, NaBr, NaClO, and NaClO$_2$ to compare their efficiencies in preparing the CNC. It resulted that the 4-acetamido-TEMPO and the 4-methoxy-TEMPO showed their optimum catalytic efficiencies; however, the 4-hydroxyl-TEMPO and 4-oxygen-TEMPO showed the worst efficiencies. In addition, the ultrasonic assistance was usually used in the chemical reaction. Mishra et al. [42] utilized the system of the TEMPO to hydrolyze the cellulose with the ultrasonic assistance, and the productivity of the CNC was raised by about 10%, when the content of the carboxyl was raised by 10~15%. According to the above investigations, it was obvious that the preparations with the system of TEMPO were a pollution-free and efficient way to produce the CNC, which also sketched the contours of its development prospect of the assistance-TEMPO methods.

2.2.3.2. Effect of Treatment on the Dispersion of the CNC. The preparation of the CNC was affected by a series of factors that involved the reaction conditions, the carboxyl content, the homogenization treatment, and other circumstances [43–45], in which the carboxyl content of the CNC controlled the dispersity of the cellulose fiber in water as well as the productivity of the CNC [46].

Hirota et al. [47] indicated that the oxide cellulose fiber obtained with different methods possessed a similar carboxyl concentration of 1.8~2.2 mmol/g on the fiber, which was the maximum content in the undissolved cellulose fibers. On the other hand, low content of the carboxyl in the CNC was against its decentralization in the water. Saito et al. [48] found that the system's viscosity increased quickly with 2~4% solid content; however, the phenomena did not occur while the content was below 1%. In addition, research showed that the CNC solution possessed much more carboxyls and displayed relatively lower viscosity, because of the electrostatic repulsive force among the carboxyls [49, 50]. Okita et al. [43] reported that the TEMPO-CNC dissolved not only in water but also in several organic solvents, and the CNC could also be obtained in the organic solvent just with extremely high energy consumption. The morphology of CNC obtained by four methods is shown in Figure 4 [51].

2.3. Preparation of Biological Fermentation. Usually, the process of chemical hydrolysis is low-cost and convenient for preparing the CNC, but its pollution is terrible since it leaves lots of wasted solutions of acid or alkali, which is difficult to handle and harmful to the environment. Therefore, the noncomplicated, efficient, and pollution-free method for preparing the CNC is focused on in recent years. As a perfect solution, the biological process rises in response to the proper time and conditions, which mainly involves the biological hydrolysis.

The CNC was firstly obtained from some specific bacterial cellulose (BC) in 1886 [52], which was so called bacterial nanocellulose (BNC). Several bacteria were discovered and employed in obtaining the BNC, including the Acetobacter, Azotobacter, Achromobacter, and Aerobacter [53]. In fact, the BC was better than plant cellulose in terms of its higher purity, crystallinity (over 60%), degree of polymerization (between 2000 and 6000), and tensile strength [54, 55]. Therefore, the BC was a perfect resource for the BNC.
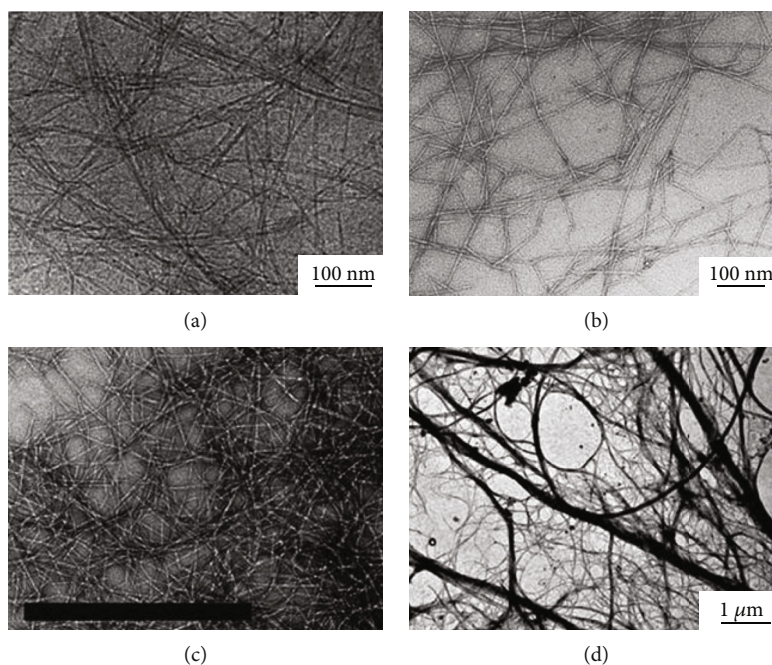
FIGURE 4: TEM of CNCs obtained from wood pulp using different pretreatments, (a) enzymatic, (b) TEMPO-mediated oxidation, and (c) carboxymethylation, and obtained from (d) Opuntia ficus-indica [51].

TABLE 1: Comparison of BNC and cellulose II.

Type	Length (μm)	Width (nm)	Height (nm)	Cross-section	Crystallinity[a] (%)	Iβ (%)
Acetobacter	>1	30-50	6-10	Rectangular	63	3-27
Acetobacter[b]	>1	6-10	6-10	Square	—	53
Cellulose II	Filament	—	—	Cylindrical	27-43	—

Usually, the BNC was extruded through the bacterium cell pores in the form of ribbons. These ribbons started at specific points on the cell surface and became thicker as they built a composite ribbon. Finally, the cellulose nanofibers were with a 2~4 nm diameter and several 100 μm length [51, 56]. However, each bacterium BNC had its own merits according to the difference in the bacterium type as well as its cultured conditions. For instance, the Acetobacter BNC was with an α-crystalline structure and its fiber showed a rectangular section with a parameter in $(6\sim10)$ nm $\times$ $(30\sim50)$ μm. A list of CNC with different characterizations is shown in Table 1 [57].

Although the characterizations of the component ratio of amorphous and crystalline regions and size of the microcellulose are according to the kinds of bacteria, the ways of dividing them from each other by removing the amorphous zones are common, and the cellulase acts as a pair of scissors to do it. Usually, the scissors consisted of several cellulases, 1,4-β-D-glucan glucanohydrolase, 1,4-β-D-glucan cellobiohydrolase, β-1,4-glucosidase, etc. [58]. Because of the heterogeneous catalytic reaction of the cellulase, no cellulase possessed the ability to efficiently catalyze the BC hydrolysis individually, and the biological process was always focused on increasing the hydrolyzed efficiency with the combined actions of kinds of cellulases.

BNCs obtained by catalyzing the pulp with Trichoderma viride G were with great globular characterizations (2.5~10 nm) with optimum conditions of pH 4.8 and temperature of 45°C for 2 h [59]. It was indicated that the BNC produced by Acetobacter xylinum was with a great thermostability ($\leq$330°C) and swelling resistance, while the producing efficiency raised by controlling the fermentation temperature and rotation speeds [60]. On the other hand, researches on the BNC production by sugar derivatives were also focused on long ago, with results showing that the productivity obtained from arabitol and mannitol was 6.2 and 3.8 times, respectively, more than that from the glucose [61]. The MCC obtained from the Cladophora showed an average length of 350 nm with a degree of polymerization of 690 for β-glucan chain [59]. More and more attentions were drawn for its economic efficiency and irreplaceable sustainability.

2.4. Preparation via the Combined Method. In general, all the above solutions could be applied for CNC preparation, but there exists lots of problems that limit the development of those technologies, such as the energy-extensive consumption of the mechanical process, the heavy pollution of the chemical process, and the underactivity of the biological process on raw plant fibers. Therefore, the combination of several methods is an irresistible trend of the CNC preparation. And the normal

combinations are between the process of machinery and chemistry or biology.

By combining chemical pretreatment and mechanical methods, Alemdar and Sain obtained the MFC with a 10~80 nm in diameter and several microns in length [62]. Meanwhile, the MFC from the preoxidized pulp were with average diameters of 5.51 nm by rotation and 4.7 nm by ultrasound [63].

3. Applications of CNC

Owing to lots of perfect properties of strength, light transmission, gas barrier, et al., the applications of the CNC were focused on the optical film, electronics, composite materials, and other fields [64–68].

3.1. CNC Reinforcement Composites. As a prepossessing field, the development of nanocomposites was drawing more and more attentions since the properties of CNC included high strength, low density, great biodegradation, green renewability, crystallinity, porosity, and interphase effects [69].

As a nanofiber from the natural resources, the CNC possessed a mean strength within the ranges of 1.6~3 GPa, which was comparable with those of commercially available multiwalled carbon nanotubes [70]. Therefore, it was available for the reinforcement of the composites with CNC.

It was shown that the CNC-reinforced Polyvinyl Alcohol (PVA) fibrils possessed a tensile modulus of 57 GPa far greater than those of PVA fibrils as well as its storage modulus [71], which was because of uniform dispersion of CNC in the PVA and their hydrogen bonding. Another research employed the use of CNC to modify polyethylene oxide (PEO) and showed that E and S_t of the 20%-CNC/PEO composites improved 2 and 2.5 times comparing to the pure PEO, respectively, [72].

Li et al. [73] obtained the nanocomposites by combining the CNC with the polymerization of phenol, and their thermal stability was much better than the polyphenols. Wang et al. [74] prepared a CNC/soy protein thermoplastics and found that E and S_t of the composite changed from 0.53 to 1.02 GPa and from 16.7 to 31.2 MPa, respectively, by adding 20% CNC. However, it changed from 0.60 to 1.82 GPa and from 20.2 to 59.3 MPa, respectively, with 30% CNC [75].

3.2. Barrier Films. Because of its waterproof and barrier functions, the CNC-modified composites have attracted interest in the applications of barrier films with potential utilizations in filtration and packaging [76]. The investigations were mainly focused on how to prevent water vapor and oxygen from permeation into the envelope.

It was shown that the water vapor permeability decreased with the CNC addition in the envelope. Choi and Simonsen [77] indicated that the CNC composite film possessed great water vapor preventions with a permeability decrease to 11% in thermal treatments. Chinga-Carrasco and Syverud [78] proved that the oxygen permeating speed was 3.0 cm^3·(m^2·24h·0.1 MPa)$^{-1}$ with a 50% relative humidity level by testing the CNC film. The great barrier property was proven by Fukuzumi et al. [79] that the average pore size

of CNC film was about 0.47 nm close to the kinetic diameter of oxygen, and this structure would prevent oxygen from approaching into the envelope.

Meanwhile, applications of CNC in the oxygen permeability of composite film were also investigated. Petersson and Oksman [80] found that the oxygen permeability of the polylactic acid (PLA) was increased by over 3 times compared to pure PLA with 5 wt% MCC addition. In contrast, other researches showed that the oxygen permeability of CNC/PLA film was significantly lowered to 1 mL·m^{-2}·day^{-1}·Pa^{-1} with a film structure of a 0.4 mm TEMPO-NFC film on top of a 25 mm thick PLA film (746 mL·m^{-2}·day^{-1}·Pa^{-1}) [81]. It was interesting that the properties went in the opposite directions with different film structures. Because the barrier properties of envelopes were connected to factors that influence the tortuous path of the diffusion species though the film, the difference between the two studies mentioned above might be affected by several factors, such as orientation, concentration, reinforcement shape, crystallinity, porosity, and interphase effects.

Similarly, it was demonstrated that neat CNC films possessed a relatively low oxygen permeability of 17 mL·m^{-2}·day^{-1} with a thickness of 20~30 mm [82]. However, it was below 10~20 mL·m^{-2}·day^{-1} of the oxygen transmission rate of the atmosphere packaging with this CNC modification [83]. This property demonstrated the potential of neat and/or modified CNC films for oxygen barrier applications.

3.3. Biomaterials. CNC has been widely used in biomedical scaffolds, strain sensor, oil/water separation, drug excipient, wound dressings, and other biological materials for its biodegradability, high biocompatibility, and nontoxicity [84, 85].

Zhang et al. [86] developed an optical probe for the selective and quantitative detection of Cu^{2+} using surface-modified fluorescent CNC. The external surface of fluorescent CNC was modified by the mild EDTAD esterification and amidation with 7-amino-4-methylcumarin, which caused the topological distribution of fluorescent moieties and other functional groups. It is possible that the fluorescent CNC can be widely used for bioimaging and metal ion detection in the coming years. Recently, the CNC-based composite using 3D printing technology has attracted extensive attention in the medical field. Sultan and Mathew [87] prepared porous and 3D printable scaffolds from the hydrogel ink of sodium alginate and gelatin reinforced with CNC. CNC provided nice structural orientation, rheological properties, and mechanical properties during the 3D printing process. The biobased scaffolds with pore size from 80 to 2125 μm and nanoscale pore wall roughness were considered suitable for cell interactions and guided cell growth during tissue regeneration. Though many researches about biocompatibility, long-term toxicology, and security between CNC-based composite and human bodies remain in the exploration stage, lots of results indicate a promising future.

3.4. Other Applications. As a promising material for energy application, the flexible energy storage device was made by using the MWNT nanowire arrays of CNC [88]. The typical structure was based on a single sheet of conductive cellulose

paper (separator) made from room temperature ionic liquid and CNC (electrode). Zhu et al. [89] proved that the CNC nanopapers could be applied as the matrix for light-emitting diode (LED) and also found that LED with CNC matrix are highly transparent in the visible and near-infrared wavelength regions. Meanwhile, the CNC matrix was all flexible enough to be compatible with roll-to-roll processing.

Niu et al. [90] employed the CNC for preparation of the multilayer membrane electrode for the supercapacitor. It indicated that the prepared composite film exhibited great flexibility and elastic resilience for the application prospect. Gao et al. [91] manufactured a conductive paper with a self-assembly of the CNC and reduced graphene oxide (RGO). It indicated that the composite paper possessed an excellent mechanical property, and its transmittance and sheet surface resistance could be designed by controlling the number of layer-by-layer (LbL) assembly. For example, the paper with a 20 LbL shows a sheet resistance of ~2.5 kΩ and a transmittance of 76% (at 550 nm). It revealed a greater prospect in the field of information-transfer than conventional paper.

4. Conclusions

The preparation methods and applications of the CNC were summarized in this paper, and the scarcity of resources urged us to find some renewable resources to effectively contrast this phenomenon. CNC in the form of microfiber or nanofiber had unique properties including high elastic modulus, dimensional stability, outstanding reinforcement potential, and transparency. As a natural resource, efficient obtainment and smart application were still drawing the attentions on environmentally friendly utilization all the time. Since CNC research is still at its booming stage, industrial commercialization has not been arrived at yet. There exists a huge market of CNC, and indications show that the world market of CNC would be 60 billion dollars in 2020. Therefore, a great prospect is displayed for its development. With proof-based investigations, there would be a real improvement in this field to reply all circumstances.

Conflicts of Interest

The authors declare that there is no conflict of interest regarding the publication of this paper.

Acknowledgments

References

[1] Y. Qing, R. Sabo, J. Y. Zhu, U. Agarwal, Z. Cai, and Y. Wu, "A comparative study of cellulose nanofibrils disintegrated via multiple processing approaches," *Carbohydrate Polymers*, vol. 97, no. 1, pp. 226–234, 2013.

[2] J. Han, K. Lu, Y. Yue et al., "Nanocellulose-templated assembly of polyaniline in natural rubber-based hybrid elastomers toward flexible electronic conductors," *Industrial Crops and Products*, vol. 128, pp. 94–107, 2019.

[3] Q. Ding, X. Xu, Y. Yue et al., "Nanocellulose-mediated electroconductive self-healing hydrogels with high strength, plasticity, viscoelasticity, stretchability, and biocompatibility toward multifunctional applications," *ACS Applied Materials & Interfaces*, vol. 10, no. 33, pp. 27987–28002, 2018.

[4] S. Zhou, G. Zhou, S. Jiang, P. Fan, and H. Hou, "Flexible and refractory tantalum carbide-carbon electrospun nanofibers with high modulus and electric conductivity," *Materials Letters*, vol. 200, pp. 97–100, 2017.

[5] S. Gao, G. Tang, D. Hua et al., "Stimuli-responsive bio-based polymeric systems and their applications," *Journal of Materials Chemistry B*, vol. 7, no. 5, pp. 709–729, 2019.

[6] J. Sun, Y. Zhao, Z. Yang et al., "Highly stretchable and ultrathin nanopaper composites for epidermal strain sensors," *Nanotechnology*, vol. 29, no. 35, p. 355304, 2018.

[7] X. Cao, B. Ding, J. Yu, and S. S. al-Deyab, "Cellulose nanowhiskers extracted from TEMPO-oxidized jute fibers," *Carbohydrate Polymers*, vol. 90, no. 2, pp. 1075–1080, 2012.

[8] Q. Wu, X. Li, S. Fu, Q. Li, and S. Wang, "Estimation of aspect ratio of cellulose nanocrystals by viscosity measurement: influence of surface charge density and NaCl concentration," *Cellulose*, vol. 24, no. 8, pp. 3255–3264, 2017.

[9] T. Saito and A. Isogai, "Tempo-mediated oxidation of native cellulose. The effect of oxidation conditions on chemical and crystal structures of the water-insoluble fractions," *Biomacromolecules*, vol. 5, no. 5, pp. 1983–1989, 2004.

[10] G. Chinga-Carrasco, Y. Yu, and O. Diserud, "Quantitative electron microscopy of cellulose nanofibril structures fromEucalyptusandPinus radiataKraft pulp fibers," *Microscopy and Microanalysis*, vol. 17, no. 4, pp. 563–571, 2011.

[11] L. Geng, B. Chen, X. Peng, and T. Kuang, "Strength and modulus improvement of wet-spun cellulose I filaments by sequential physical and chemical cross-linking," *Materials & Design*, vol. 136, pp. 45–53, 2017.

[12] J. Han, Y. Yue, Q. Wu et al., "Effects of nanocellulose on the structure and properties of poly(vinyl alcohol)-borax hybrid foams," *Cellulose*, vol. 24, no. 10, pp. 4433–4448, 2017.

[13] Z. Zhang, "The theoretical analysis and discussion of high pressure homogenizing," *Packaging and Food Machinery*, vol. 1, 2001.

[14] H. U. Yun and J. G. Liu, "Overview on preparation and research projects of nanocellulose," *China Pulp & Paper Industry*, vol. 6, pp. 33–36, 2013.

[15] S. Armstrong and P. Dario, "Elliptic regularity and quantitative homogenization on percolation clusters," *Communications on Pure and Applied Mathematics*, vol. 71, no. 9, pp. 1717–1849, 2018.

[16] F. W. Herrick, R. L. Casebier, J. K. Hamilton, and K. R. Sandberg, "Microfibrillated cellulose: morphology and accessibility," in *Journal of Applied Polymer Science: Applied Polymer Symposium*, vol. 37, pp. 797–813, ITT Rayonier Inc., Shelton, WA, 1983.

[17] A. F. Turbak, F. W. Snyder, and K. R. Sandberg, "Microfibrillated cellulose, a new cellulose product: properties, uses, and commercial potential," in *Journal of Applied Polymer Science:*

Applied Polymer Symposium, vol. 37, pp. 815–827, ITT Rayonier Inc., Shelton, WA, USA, 1983.

[18] R. Khiari, "Valorization of agricultural residues for cellulose nanofibrils production and their use in nanocomposite manufacturing," *International Journal of Polymer Science*, vol. 2017, 10 pages, 2017.

[19] F. Villalobos-Castillejos, V. G. Granillo-Guerrero, D. E. Leyva-Daniel et al., "Fabrication of nanoemulsions by microfluidization," in *Nanoemulsions*, pp. 207–232, Elsevier, 2018.

[20] S. Song, J. Guo, X. Chen et al., "Progress in application of high pressure microfluidization in preparation of nanomedicines," *Chinese Journal of New Drugs*, vol. 22, pp. 2388–2391, 2013.

[21] J. LI and Z.-m. LIU, "Preparation and Hydrophobic Modification of Phyllostachys heterocycla cv. Pubescens NFC/SiO_2 Aerogel," *Journal of Cellulose Science and Technology*, vol. 1, p. 8, 2016.

[22] J. Ma, F. Yu, and J. N. Wang, "Preparation of water-dispersible single-walled carbon nanotubes by freeze-smashing and application as a catalyst support for fuel cells," *Journal of Materials Chemistry*, vol. 20, no. 27, pp. 5742–5747, 2010.

[23] O. Shoseyov, A. Heyman, S. Lapidot, S. Meirovitch, Y. Nevo, and A. Rivkin, *Method for production of cellulose nano crystals from cellulose-containing waste materials*, Yissum Research Development Company Of The Hebrew University Of Jerusalem Ltd., 2012.

[24] K. Löbmann and A. J. Svagan, "Cellulose nanofibers as excipient for the delivery of poorly soluble drugs," *International Journal of Pharmaceutics*, vol. 533, no. 1, pp. 285–297, 2017.

[25] D. Hua, Z. Liu, F. Wang et al., "pH responsive polyurethane (core) and cellulose acetate phthalate (shell) electrospun fibers for intravaginal drug delivery," *Carbohydrate Polymers*, vol. 151, pp. 1240–1244, 2016.

[26] J. Wu, X. Li, J. Ye, L. Zhu, Y. Dou, and J. Hong, "The effects of alkali pretreatment on the properties of cellulose from hempen pulp," *Journal of Nanjing Forestry University*, vol. 34, no. 5, pp. 96–100, 2010.

[27] J. Zhang, T. J. Elder, Y. Pu, and A. J. Ragauskas, "Facile synthesis of spherical cellulose nanoparticles," *Carbohydrate Polymers*, vol. 69, no. 3, pp. 607–611, 2007.

[28] L. R. Tang, B. Huang, D. S. Dai, W. Ou, and X. R. Chen, "Preparation and spectrum properties of cellulose nanoparticles," *Guang pu xue yu guang pu fen xi = Guang pu*, vol. 30, no. 7, pp. 1876–1879, 2010.

[29] J. Hagman, L. Gentile, C. M. Jessen, M. Behrens, K. E. Bergqvist, and U. Olsson, "On the dissolution state of cellulose in cold alkali solutions," *Cellulose*, vol. 24, no. 5, pp. 2003–2015, 2017.

[30] C. Xie, Z. M. Liu, W. U. Peng, G. Z. Fang, and X. Zhao, "Optimization of preparation technology of alkali pretreated reed pulp nano-cellulose," *Chemistry & Industry of Forest Products*, vol. 33, pp. 32–36, 2013.

[31] Z. M. Liu, C. Xie, W. U. Peng, and L. Y. Liu, "Preparation of reed pulp nanocrystalline cellulose by sulfuric acid hydrolysis with sodium m-nitrobenzene sulfonate as cocatalyst," *Biomass Chemical Engineering*, vol. 5, pp. 1–6, 2012.

[32] Q. Wu, S. Chen, and Y. Chen, "Preparation and characterization of nanocellulose crystals from Luffa sponge," *Journal of Northwest A & F University-Natural Science Edition*, vol. 42, pp. 229–234, 2014.

[33] H. You, C. Zeng, Q. Lu, L. Tang, G. Wu, and B. Huang, "Preparation and characterization of nanocrystalline cellulose cata-

lyzed by carbon-based phosphotungstic acid," *Journal of Southwest Forestry University*, vol. 34, pp. 100–103, 2014.

[34] B. Sun, M. Zhang, Q. Hou, R. Liu, T. Wu, and C. Si, "Further characterization of cellulose nanocrystal (CNC) preparation from sulfuric acid hydrolysis of cotton fibers," *Cellulose*, vol. 23, no. 1, pp. 439–450, 2016.

[35] T. Saito, I. Shibata, A. Isogai, N. Suguri, and N. Sumikawa, "Distribution of carboxylate groups introduced into cotton linters by the TEMPO-mediated oxidation," *Carbohydrate Polymers*, vol. 61, no. 4, pp. 414–419, 2005.

[36] T. Saito and A. Isogai, "Introduction of aldehyde groups on surfaces of native cellulose fibers by TEMPO-mediated oxidation," *Colloids and Surfaces A: Physicochemical and Engineering Aspects*, vol. 289, no. 1-3, pp. 219–225, 2006.

[37] T. Saito, M. Hirota, N. Tamura et al., "Individualization of nano-sized plant cellulose fibrils by direct surface carboxylation using TEMPO catalyst under neutral conditions," *Biomacromolecules*, vol. 10, no. 7, pp. 1992–1996, 2009.

[38] A. E. J. de Nooy, A. C. Besemer, H. van Bekkum, J. A. P. P. van Dijk, and J. A. M. Smit, "Tempo-mediated oxidation of pullulan and influence of ionic strength and linear charge density on the dimensions of the obtained polyelectrolyte chains," *Macromolecules*, vol. 29, no. 20, pp. 6541–6547, 1996.

[39] I. Shibata and A. Isogai, "Depolymerization of cellouronic acid during TEMPO-mediated oxidation," *Cellulose*, vol. 10, no. 2, pp. 151–158, 2003.

[40] T. Saito, M. Hirota, N. Tamura, and A. Isogai, "Oxidation of bleached wood pulp by TEMPO/NaClO/NaClO_2 system: effect of the oxidation conditions on carboxylate content and degree of polymerization," *Journal of Wood Science*, vol. 56, no. 3, pp. 227–232, 2010.

[41] S. Iwamoto, W. Kai, T. Isogai, T. Saito, A. Isogai, and T. Iwata, "Comparison study of tempo-analogous compounds on oxidation efficiency of wood cellulose for preparation of cellulose nanofibrils," *Polymer Degradation and Stability*, vol. 95, no. 8, pp. 1394–1398, 2010.

[42] S. P. Mishra, J. Thirree, A. S. Manent, B. Chabot, and C. Daneault, "Ultrasound-catalyzed TEMPO-mediated oxidation of native cellulose for the production of nanocellulose: effect of process variables," *BioResources*, vol. 6, no. 1, pp. 121–143, 2011.

[43] Y. Okita, S. Fujisawa, T. Saito, and A. Isogai, "TEMPO-oxidized cellulose nanofibrils dispersed in organic solvents," *Biomacromolecules*, vol. 12, no. 2, pp. 518–522, 2011.

[44] W. Ma, Z. Guo, J. Zhao et al., "Polyimide/cellulose acetate core/shell electrospun fibrous membranes for oil- water separation," *Separation and Purification Technology*, vol. 177, pp. 71–85, 2017.

[45] A. A. Moud, M. Arjmand, J. Liu, Y. Yang, A. Sanati-Nezhad, and S. H. Hejazi, "Cellulose nanocrystal structure in the presence of salts," *Cellulose*, 2019.

[46] A. Rattaz, S. P. Mishra, B. Chabot, and C. Daneault, "Cellulose nanofibres by sonocatalysed-TEMPO-oxidation," *Cellulose*, vol. 18, no. 3, pp. 585–593, 2011.

[47] M. Hirota, N. Tamura, T. Saito, and A. Isogai, "Cellulose II nanoelements prepared from fully mercerized, partially mercerized and regenerated celluloses by 4-acetamido-TEMPO/NaClO/NaClO_2 oxidation," *Cellulose*, vol. 19, no. 2, pp. 435–442, 2012.

[48] T. Saito, Y. Nishiyama, J.-L. Putaux, M. Vignon, and A. Isogai, "Homogeneous suspensions of individualized microfibrils

from TEMPO-catalyzed oxidation of native cellulose," *Biomacromolecules*, vol. 7, no. 6, pp. 1687–1691, 2006.

[49] I. Besbes, S. Alila, and S. Boufi, "Nanofibrillated cellulose from TEMPO-oxidized eucalyptus fibres: effect of the carboxyl content," *Carbohydrate Polymers*, vol. 84, no. 3, pp. 975–983, 2011.

[50] A. Huang, X. Peng, L. Geng et al., "Electrospun poly (butylene succinate)/cellulose nanocrystals bio-nanocomposite scaffolds for tissue engineering: Preparation, characterization and _in*vitro* evaluation," *Polymer Testing*, vol. 71, pp. 101–109, 2018.

[51] Y. Habibi, "Key advances in the chemical modification of nanocelluloses," *Chemical Society Reviews*, vol. 43, no. 5, pp. 1519–1542, 2014.

[52] A. J. Brown, "XLIII.—On an acetic ferment which forms cellulose," *Journal of the Chemical Society, Transactions*, vol. 49, no. 0, pp. 432–439, 1886.

[53] Z. Shi, G. O. Phillips, and G. Yang, "Nanocellulose electroconductive composites," *Nanoscale*, vol. 5, no. 8, pp. 3194–3201, 2013.

[54] S. Bae, Y. Sugano, and M. Shoda, "Improvement of bacterial cellulose production by addition of agar in a jar fermentor," *Journal of Bioscience and Bioengineering*, vol. 97, no. 1, pp. 33–38, 2004.

[55] S. Bae and M. Shoda, "Statistical optimization of culture conditions for bacterial cellulose production using Box-Behnken design," *Biotechnology and Bioengineering*, vol. 90, no. 1, pp. 20–28, 2005.

[56] C. J. Grande, F. G. Torres, C. M. Gomez, O. P. Troncoso, J. Canet-Ferrer, and J. Martínez-Pastor, "Development of self-assembled bacterial cellulose-starch nanocomposites," *Materials Science and Engineering: C*, vol. 29, no. 4, pp. 1098–1104, 2009.

[57] R. J. Moon, A. Martini, J. Nairn, J. Simonsen, and J. Youngblood, "Cellulose nanomaterials review: structure, properties and nanocomposites," *Chemical Society Reviews*, vol. 40, no. 7, pp. 3941–3994, 2011.

[58] B. Kunasundari, S. Naresh, and N. Z. C. Zakaria, "Isolation and characterization of cellulase producing bacteria from tropical mangrove soil," in *Proceedings of the 2017 International Conference on Biomedical Engineering and Bioinformatics*, pp. 34–37, Bangkok, Thailand, September 14 - 16, 2017.

[59] K. K. Kar, S. Rana, and J. Pandey, *Handbook of Polymer Nanocomposites Processing, Performance and Application*, Springer, Berlin/Heidelberg, Germany, 2015.

[60] M. F. A. K. Tua, "Effects of agitation conditions on bacterial cellulose production by Acetobacter xylinum 0416 in fermentation of matured coconut water medium," *Malaysian Journal of Analytical Sciences*, vol. 21, pp. 261–266, 2017.

[61] R. Jonas and L. F. Farah, "Production and application of microbial cellulose," *Polymer Degradation and Stability*, vol. 59, no. 1-3, pp. 101–106, 1998.

[62] A. Alemdar and M. Sain, "Isolation and characterization of nanofibers from agricultural residues - Wheat straw and soy hulls," *Bioresource Technology*, vol. 99, no. 6, pp. 1664–1671, 2008.

[63] S. P. Mishra, A.-S. Manent, B. Chabot, and C. Daneault, "Production of nanocellulose from native cellulose–various options utilizing ultrasound," *BioResources*, vol. 7, no. 1, pp. 0422–0436, 2011.

[64] Q. Zhu, Y. Jin, G. Sun, K. Yan, and D. Wang, "AQC functionalized CNCs/PVA-co-PE composite nanofibrous membrane with flower-like microstructures for photo-induced multi-functional protective clothing," *Cellulose*, vol. 25, no. 8, pp. 4819–4830, 2018.

[65] P. Daraei, N. Ghaemi, and H. Sadeghi Ghari, "An ultra-antifouling polyethersulfone membrane embedded with cellulose nanocrystals for improved dye and salt removal from water," *Cellulose*, vol. 24, no. 2, pp. 915–929, 2017.

[66] H.-Y. Mi, X. Jing, J. Peng, M. R. Salick, X.-F. Peng, and L.-S. Turng, "Poly(ε-caprolactone) (PCL)/cellulose nano-crystal (CNC) nanocomposites and foams," *Cellulose*, vol. 21, no. 4, pp. 2727–2741, 2014.

[67] J. Sun, J. Zhuang, J. Shi et al., "Highly elastic and ultrathin nanopaper-based nanocomposites with superior electric and thermal characteristics," *Journal of Materials Science*, vol. 54, no. 11, pp. 8436–8449, 2019.

[68] J. Sun, H. Li, Y. Huang et al., "Simple and affordable way to achieve polymeric superhydrophobic surfaces with biomimetic hierarchical roughness," *ACS Omega*, vol. 4, no. 2, pp. 2750–2757, 2019.

[69] I. Siró and D. Plackett, "Microfibrillated cellulose and new nanocomposite materials: a review," *Cellulose*, vol. 17, no. 3, pp. 459–494, 2010.

[70] T. Saito, R. Kuramae, J. Wohlert, L. A. Berglund, and A. Isogai, "An ultrastrong nanofibrillar biomaterial: the strength of single cellulose nanofibrils revealed via sonication-induced fragmentation," *Biomacromolecules*, vol. 14, no. 1, pp. 248–253, 2012.

[71] R. Endo, T. Saito, and A. Isogai, "TEMPO-oxidized cellulose nanofibril/poly(vinyl alcohol) composite drawn fibers," *Polymer*, vol. 54, no. 2, pp. 935–941, 2013.

[72] C. Zhou, R. Chu, R. Wu, and Q. Wu, "Electrospun polyethylene oxide/cellulose nanocrystal composite nanofibrous mats with homogeneous and heterogeneous microstructures," *Biomacromolecules*, vol. 12, no. 7, pp. 2617–2625, 2011.

[73] Z. Li, S. Renneckar, and J. R. Barone, "Nanocomposites prepared by in situ enzymatic polymerization of phenol with tempo-oxidized nanocellulose," *Cellulose*, vol. 17, no. 1, pp. 57–68, 2010.

[74] Y. Wang, X. Cao, and L. Zhang, "Effects of cellulose whiskers on properties of soy protein thermoplastics," *Macromolecular Bioscience*, vol. 6, no. 7, pp. 524–531, 2006.

[75] X. Huang and A. Netravali, "Biodegradable green composites made using bamboo micro/nano-fibrils and chemically modified soy protein resin," *Composites Science and Technology*, vol. 69, no. 7-8, pp. 1009–1015, 2009.

[76] G. Siqueira, J. Bras, and A. Dufresne, "Cellulosic bionanocomposites: a review of preparation, properties and applications," *Polymers*, vol. 2, no. 4, pp. 728–765, 2010.

[77] Y. Choi and J. Simonsen, "Cellulose nanocrystal-filled carboxymethyl cellulose nanocomposites," *Journal of Nanoscience and Nanotechnology*, vol. 6, no. 3, pp. 633–639, 2006.

[78] G. Chinga-Carrasco and K. Syverud, "On the structure and oxygen transmission rate of biodegradable cellulose nanobarriers," *Nanoscale Research Letters*, vol. 7, no. 1, 2012.

[79] H. Fukuzumi, T. Saito, S. Iwamoto et al., "Pore size determination of TEMPO-oxidized cellulose nanofibril films by positron annihilation lifetime spectroscopy," *Biomacromolecules*, vol. 12, no. 11, pp. 4057–4062, 2011.

[80] L. Petersson and K. Oksman, "Biopolymer based nanocomposites: comparing layered silicates and microcrystalline cellulose as nanoreinforcement," *Composites Science and Technology*, vol. 66, no. 13, pp. 2187–2196, 2006.

[81] H. Fukuzumi, T. Saito, T. Iwata, Y. Kumamoto, and A. Isogai, "Transparent and high gas barrier films of cellulose nanofibers prepared by TEMPO-mediated oxidation," *Biomacromolecules*, vol. 10, no. 1, pp. 162–165, 2009.

[82] K. Syverud and P. Stenius, "Strength and barrier properties of MFC films," *Cellulose*, vol. 16, no. 1, pp. 75–85, 2009.

[83] G. Rampinelli, L. Di Landro, and T. Fujii, "Characterization of biomaterials based on microfibrillated cellulose with different modifications," *Journal of Reinforced Plastics and Composites*, vol. 29, no. 12, pp. 1793–1803, 2010.

[84] Q. Li, H. Liu, S. Zhang et al., "Superhydrophobic electrically conductive paper for ultrasensitive strain sensor with excellent anticorrosion and self-cleaning property," *ACS Applied Materials & Interfaces*, vol. 11, no. 24, pp. 21904–21914, 2019.

[85] X. Wang, Y. Pan, X. Liu et al., "Facile fabrication of superhydrophobic and eco-friendly poly(lactic acid) foam for oil–water separation via skin peeling," *ACS Applied Materials & Interfaces*, vol. 11, no. 15, pp. 14362–14367, 2019.

[86] Y.-J. Zhang, X.-Z. Ma, L. Gan, T. Xia, J. Shen, and J. Huang, "Fabrication of fluorescent cellulose nanocrystal via controllable chemical modification towards selective and quantitative detection of cu (II) ion," *Cellulose*, vol. 25, no. 10, pp. 5831–5842, 2018.

[87] S. Sultan and A. P. Mathew, "3D printed scaffolds with gradient porosity based on a cellulose nanocrystal hydrogel," *Nanoscale*, vol. 10, no. 9, pp. 4421–4431, 2018.

[88] V. L. Pushparaj, M. M. Shaijumon, A. Kumar et al., "Flexible energy storage devices based on nanocomposite paper," *Proceedings of the National Academy of Sciences*, vol. 104, no. 34, pp. 13574–13577, 2007.

[89] H. Zhu, Z. Xiao, D. Liu et al., "Biodegradable transparent substrates for flexible organic-light-emitting diodes," *Energy & Environmental Science*, vol. 6, no. 7, pp. 2105–2111, 2013.

[90] Q. Niu, K. Gao, and Z. Shao, "Cellulose nanofiber/single-walled carbon nanotube hybrid non-woven macrofiber mats as novel wearable supercapacitors with excellent stability, tailorability and reliability," *Nanoscale*, vol. 6, no. 8, pp. 4083–4088, 2014.

[91] K. Gao, Z. Shao, X. Wu et al., "Cellulose nanofibers/reduced graphene oxide flexible transparent conductive paper," *Carbohydrate Polymers*, vol. 97, no. 1, pp. 243–251, 2013.

Research Article

Effects of Laminaria Japonica Polysaccharides on the Survival of Non-Small-Cell Lung Cancer A549 Cells

Mengxing Yao [iD],[1] XiaoJun Qian,[2] and Houying Qin[1]

[1]*The Second Hospital of Anhui Medical University, China*
[2]*The Third People's Hospital of Hefei, China*

Correspondence should be addressed to Mengxing Yao; yaomengxing8101@163.com

Objective. To investigate the effect of Laminaria japonica polysaccharides (LJP) on the survival of non-small-cell lung cancer (NSCLC) A549 cells and its mechanism. *Methods*. In vitro: the cells were randomly divided into control group, LJP (5 mg/ml) group, LJP (10 mg/ml) group, and LJP (20 mg/ml) group. After corresponding treatment, the survival rate and the expression of proteins related to proliferation, apoptosis, epithelial-mesenchymal transition (EMT), and signaling pathway were detected by CCK8 assay and Western blot, respectively. In vivo: a xenograft model was established to detect the tumor volume and mass and the expression of the above pathway proteins. *Results*. Compared with the control group, LJP decreased the survival rate of A549 cells ($P < 0.05$), inhibited the protein expression of Ki67 and PCNA ($P < 0.05$), downregulated the expression of Bcl-2 while upregulated the expression of Bax, cl-caspase-3, and cl-caspase-9 ($P < 0.05$), upregulated the expression of E-cadherin, downregulated the expression of vascular endothelial growth factor (VEGF) and N-cadherin ($P < 0.05$), and downregulated β-catenin, transcription factor-4 (TCF4), and c-Myc protein expression levels ($P < 0.05$). In vivo: LJP decreased the volume and mass of the xenograft tumors and downregulated β-catenin, TCF4, and c-Myc protein expression levels compared with the control group ($P < 0.05$). *Conclusion*. LJP can inhibit the survival of non-small-cell lung cancer A549 cells in vitro, and its mechanism is related to the inhibition of activation of β-catenin/TCF4 pathway activation.

1. Introduction

Lung cancer ranks among the leading types of malignant tumors in the world, whose incidence rate ranks the first in male malignant tumors and the second in female in China with its increasing trend year by year. Among them, non-small-cell lung cancer (NSCLC) accounts for about 80% of the total number of lung cancers. Although progression has been made in new technologies for prevention, screening, diagnosis, and treatment, the 5-year survival rate is still very low, imposing a heavy burden on patients and society [1, 2]. At present, the treatment methods for lung cancer are relatively limited, mainly including surgery, radiotherapy, chemotherapy, and targeted drug therapy with poor prognosis commonly seen in patients with lung cancer [3]. Therefore, it is vital to strengthen the research on this disease in medical and medicine field. In recent years, many natural extracts have been widely used in the adjuvant treatment of cancers.

Laminaria japonica polysaccharides (LJP) isolated from Laminaria is a general term for polysaccharides including laminarin, seaweed gel, alginic acid, and fustian. Laminaria japonica polysaccharides show an average degree of polymerization between 26 and 31 with an average chain length between 7 and 10 and 2 to 3 branches to each chain. Figure 1 shows repeated structural units of LJP. Studies have found that Laminaria japonica polysaccharides have a variety of biological activities, including promoting fertility [4], alleviating metabolic syndrome [5], preventing vascular calcification [6], resisting virus [7, 8], immunoregulating [9], and antioxidating [10]. In addition, Laminaria japonica polysaccharides have inhibitory effect on a variety of tumor cells, such as liver cancer cells, nasopharyngeal carcinoma cells, cervical cancer cells, and leukemia cells [11–14], but there are no reports on the effect of Laminaria japonica polysaccharides on human non-small-cell lung cancer A549 cells. In this study, we investigated the effects of Laminaria japonica
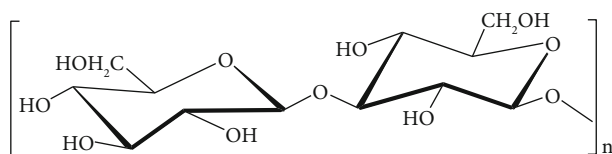
Figure 1: Repeated structural units of LJP.

polysaccharides on the survival of A549 cells in vitro and in vivo and its possible mechanism.

2. Materials and Methods

2.1. Reagents and Instruments. DMEM cell culture solution, 0.25% pancreatin, and fetal bovine serum were all purchased from Gibco Company of the United States. Streptomycin sulfate for injection was purchased from Huabei Pharmaceutical Company. Penicillin sodium for injection was purchased from Shanghai New Pioneer Pharmaceutical Company. Both primary and secondary antibodies were purchased from British Abcam Company. RIPA lysate was purchased from Sigma Company of the United States. BCA kit was purchased from Bi Yun Tian Biotechnology Company.

Carbon dioxide incubator was purchased from Thermo-Forma Company of the United States. Clean bench was purchased from Suzhou Zhongya Purification Equipment Co., Ltd. Electrophoresis apparatus and semidry film transfer apparatus were both purchased from Bio-Rad Laboratories, Inc. of the United States. Gel View 6000 chemiluminescent gel imager was purchased from Guangzhou Yunxing Instrument Co., Ltd. Optical microscope was purchased from Olympus Corporation of Japan. Multifunctional microplate reader was purchased from Bio-Rad Laboratories, Inc. of the United States.

2.2. Cell Culture. Human non-small-cell lung cancer cell line A549 was purchased from FuHeng Cell Center, Shanghai, China. The cells were cultured in a 5% CO_2 incubator at 37°C with DMEM medium containing 10% fetal bovine serum and 1% penicillin-streptomycin. The cell growth was observed daily, and subculture could be carried out when the fusion rate reached 80%. The logarithmic growth phase cells were taken for subsequent experiments.

2.3. Experimental Methods

2.3.1. Preparation of Laminaria Japonica Polysaccharides and Molecular Weight Distribution Analysis. The Laminaria japonica polysaccharides were extracted by acid process. The Laminaria japonica dry powder was mixed with hydrochloric acid solution at $1:20$ (W/V), and the mixed solution was heated at 75°C for 4 hours. After the waste residue was filtered, the filtrate was centrifuged. The precipitate was then dried to obtain Laminaria japonica polysaccharides after acetone washing, TCA precipitating, dialyzing, and centrifuging. Laminaria japonica polysaccharides with compete composition were obtained for subsequent experimental research after the filtrate was precipitated and extracted three times. The molecular weight distribution of Laminaria japonica polysaccharide was detected by high-performance liquid
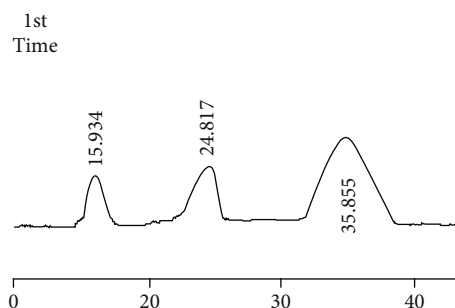

Figure 2: HPLC graph of the LJP.

chromatography (HPLC). The HPLC calibration curve was prepared by using the standard dextran. TSK-GEL G4000PW columns and a refractive index detector (RID) were used for detection (mobile phase: double distilled water, injection volume 20 μl, flow rate 0.15 ml/min at column temperature of 70°C).

2.3.2. Cell Proliferation Detected by CCK 8 Test. Human non-small-cell lung cancer cell line A549 and NCI-H292 cells were seeded into a 96-well plate at 100 μl per well, respectively. After attachment, the cells were randomly divided into 4 groups: the control group, the LJP (5 mg/ml) group, the LJP (10 mg/ml) group, and the LJP (20 mg/ml) group, each group having 5 duplicates and receiving corresponding treatment. After 24 h of culture, 10 μl of CCK-8 solution was added to each well, and incubation was continued for 4 h. The OD value of A549 cells and NCI-H292 cells was detected at 450 nm absorbance by a microplate reader.

2.3.3. Cell Migration Measured by Transwell Assay. The A549 cells were seeded into a 6-well plate with 1×10^6 cells/well. The cells, at 80% confluence, were then grouped in the same way as in Section 2.3.2 and the corresponding final concentration of the solutions was added for treatment for 24 h. The cells in each group were collected, adjusted to a density of 2×10^5 cells, seeded on the upper chamber of a Matrigel-coated Transwell, and cultured in fetal bovine serum-free medium. While normal cell culture medium was added in the lower chamber for another 48 h of incubation. After incubation, the cells underwent crystal violet staining, and five fields of view under the microscope were used to count the stained cells.

2.3.4. Establishment of Transplanted Tumor Models. Five-week-old SCID nude mice were purchased from Beijing Vital River Laboratory Animal Technology Co., Ltd., and the animal quality certificate number was SCXK (Beijing) 2014-0001. Mice were kept in sterile environment at temperature (26-28°C) and humidity (50%-60%) and with free access to food and water. After a week of acclimation, the mice were used for experiments.

The cells were adjusted to a density of 2×10^7/ml, and 0.2 ml of the cell suspension was administered subcutaneously to the mice at the same position in the dorsum of their necks. The next day, the mice were randomly divided into 4 groups: control group, LJP (5 mg/kg) group, LJP (10 mg/kg)
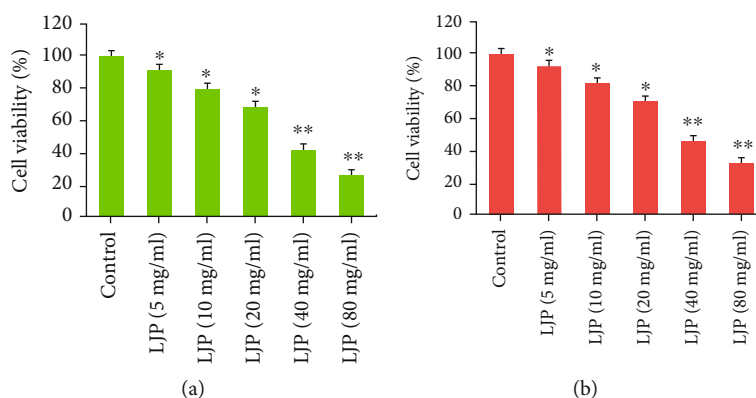
(a)

(b)

FIGURE 3: Proliferation of A549 and NCI-H292 cells. $^{*}P < 0.05$ versus control group. CCK8 assay was used to detect cell viability of A549 (a) and NCI-H292 (b) after treated with different concentrations of LJP for 24 h.
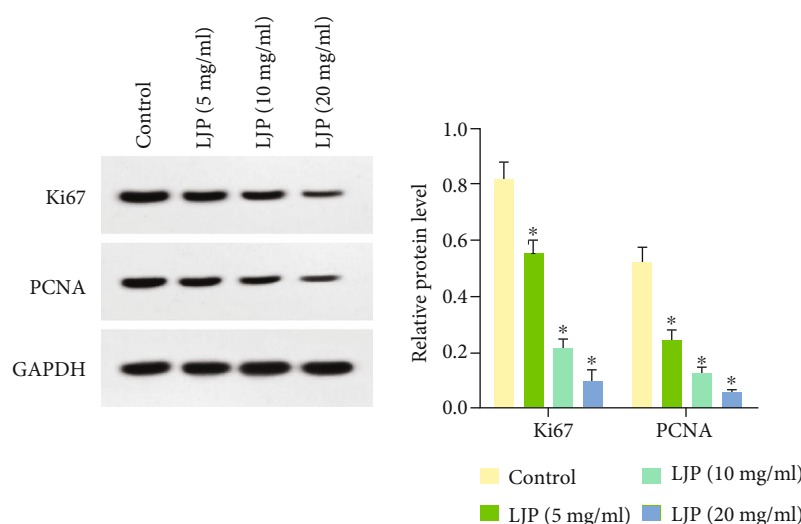

FIGURE 4: Expressions of Ki67 and PCNA. $^{*}P < 0.05$ versus control group. Western blot assay was used to detect expressions of Ki67 and PCNA after treated with different concentrations of LJP for 24 h.

group, and LJP (20 mg/kg) group. Each group was intraperitoneally injected with PBS and 5, 10, and 20 mg/kg LJP drugs, respectively, once a day for 1 week. Tumor volume was measured every 5 days. The mice were sacrificed on the 30th day, and the tumor tissue weight was weighed. Tumor volume: $V = \text{length} \times \text{width}^{2}/2$.

2.3.5. Detection of Expressions of Proliferation, Apoptosis, EMT, and Signaling Pathway-Related Proteins in Lung Cancer A549 Cells Detected by Western Blot. A549 cells were seeded in a 96-well plate. After attachment, the cells were randomly divided into four groups: control group, LJP (5 mg/ml) group, LJP (10 mg/ml) group, and LJP (20 mg/ml) group. Each group had five duplicates and were treated with the corresponding final concentration of solutions for 24 h. The cells washed with PBS were collected after trypsin digestion. The cells of each group or incubated tumor tissues as mentioned in Section 2.3.3 were collected, and the total proteins of each group were extracted using RIPA protein lysate on ice. Then, the protein concentrations of each group were

measured by BCA kit and adjusted. Equal amounts of proteins of each group were separated by 12% SDS-PAGE and were then transferred to PVDF membranes. The membranes were blocked with 5% skim milk at room temperature for 2 h. After the blocking process, the membranes were incubated at 4°C overnight with primary antibodies of Ki67, PCNA, Bax, Bcl-2, cl-caspase-3, cl-caspase-9, VEGF, E-cadherin, N-cadherin, β-catenin, TCF-4, and c-Myc. The primary antibodies were discarded the next day. After being washed with buffer solution, the membranes were added with the corresponding second antibodies, blocked at room temperature for 1 h, and then added with ECL dropwise for exposing and developing in the darkroom. GAPDH was used as an internal reference.

2.4. Statistical Methods. All experimental data were statistically analyzed by statistical software SPSS 20.0. The experimental results were expressed as mean ± standard deviation. Between-group differences conformed to normal distribution were tested by one-way ANOVA. The difference was considered statistically significant when $P < 0.05$.
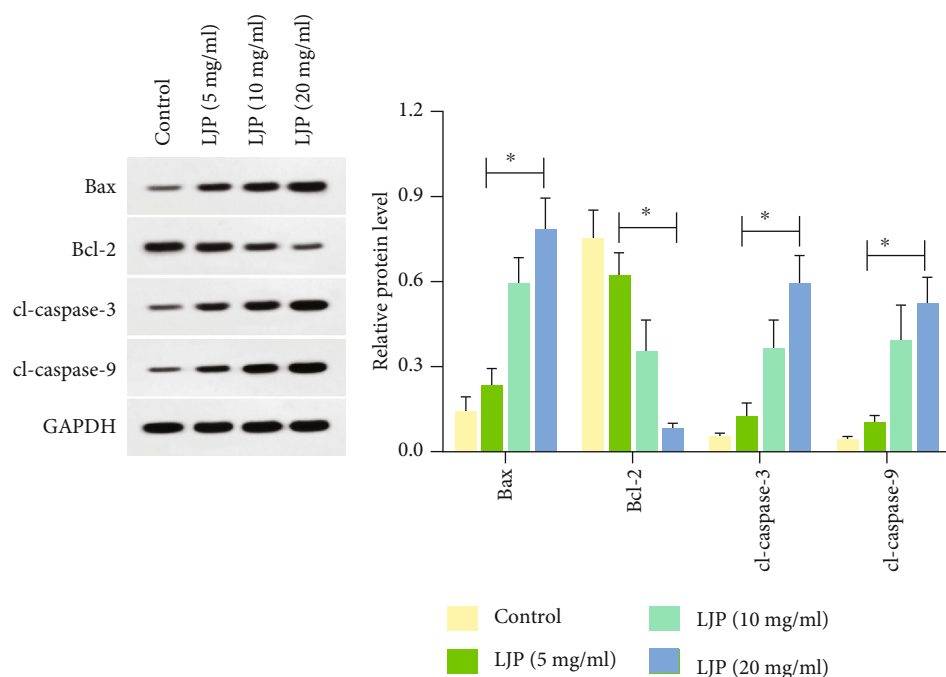
FIGURE 5: Expression of apoptosis-related proteins. $^*P < 0.05$ versus control group. Western blot assay was used to detect expression of apoptosis-related proteins after treated with different concentrations of LJP for 24 h.

3. Results

3.1. Molecular Weight Distribution of LJP Measured by HPLC.
Standard dextran (T-2000, T-500, T-70, T-40, T-10) was prepared for a mixture. A calibration curve ($y = -0.1789x + 9.3810$, $R^2 = 0.994$) was developed based on HPLC detection of elution time (x, min) and the corresponding logarithm of molecular weight (y, lg (MW)). Laminaria japonica polysaccharides extracted by acid process were detected by HPLC to obtain the LJP profile (see Figure 2), which showed three major peaks at 15.934 min, 24.817 min, and 35.855 min, respectively. Calculation by standard curve showed the LJP molecular weight of 3391621, 87345, and 926.

3.2. Effect of Laminaria Japonica Polysaccharides on the Survival Rate of Lung Cancer Cells.
The survival rate of lung cancer cells was detected by a CCK 8 test. As shown in Figure 3, with the increase of LJP administration concentration, the survival rates of A549 and NCI-H292 cells were significantly lower in the LJP treatment group compared with the control group ($P < 0.05$, Figures 3(a) and 3(b)), and the 50% inhibitory concentration (IC50) of LJP on A549 and NCI-H292 cells was 33.21 mg/ml and 39.02 mg/ml, respectively. Therefore, 5, 10, and 20 mg/ml were selected for treatment in subsequent experiments.

3.3. Effect of Laminaria Japonica Polysaccharides on the Expressions of Proliferation-Related Proteins in A549 Cells.
The expressions of proliferation-related proteins were detected by Western blot. As shown in Figure 4, the expression levels of Ki67 and PCNA proteins in the LJP treatment groups were

significantly downregulated with the increase of LJP concentrations as compared with the control group ($P < 0.05$).

3.4. Effect of Laminaria Japonica Polysaccharides on the Expressions of Apoptosis-Related Proteins in A549 Cells.
The expressions of apoptosis-related proteins were detected by Western blot. As shown in Figure 5, the expression levels of Bax, cl-caspase-3, and cl-caspase-9 proteins in the LJP treatment groups were significantly upregulated with the increase of LJP concentrations as compared with the control group ($P < 0.05$, Figure 5), while the expression of Bcl-2 protein was significantly downregulated.

3.5. Effect of Laminaria Japonica Polysaccharides on Invasion and Migration of A549 Cells and on Expressions of EMT-Related Proteins in A549 Cells.
The invasion and migration of A549 cells were detected by Transwell assay, and the expressions of EMT-related proteins in A549 cells were detected by Western blot. As shown in Figure 6, the number of invasive A549 cells was significantly reduced ($P < 0.05$, Figure 6(a)) and the expression levels of VEGF and N-cadherin proteins were significantly downregulated ($P < 0.05$, Figure 6(b)) in the LJP treatment groups as compared with the control group, while the expression of E-cadherin protein was significantly upregulated ($P < 0.05$, Figure 6(b)), which was also associated with LJP concentrations.

3.6. Effect of Laminaria Japonica Polysaccharides on Expression of Signaling Pathway Proteins in A549 Cells.
The expression of signaling pathway proteins in A549 cells cultured in vitro was detected by Western blot, and the results shown in Figure 7 indicated that the expressions of β-catenin, TCF4, and c-Myc proteins were significantly downregulated
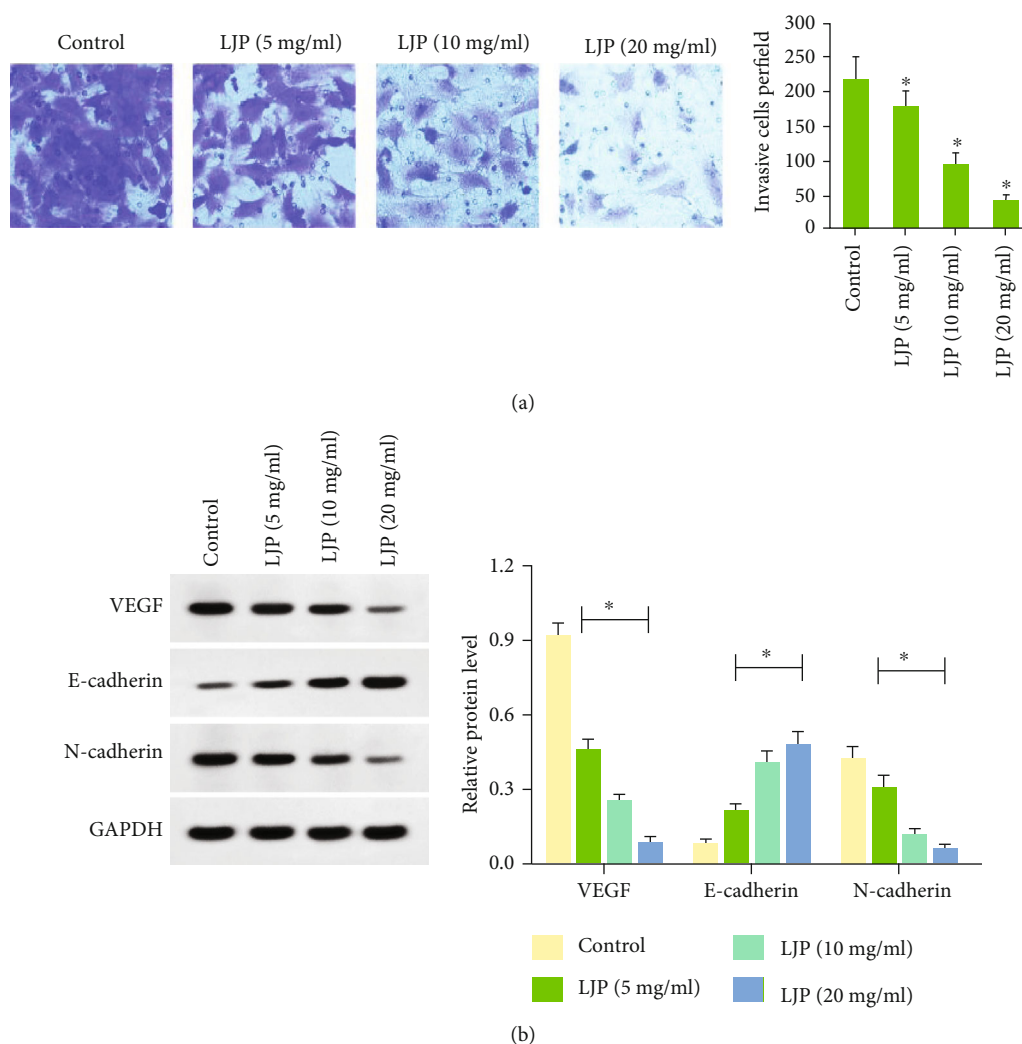
(a)

(b)

Figure 6: Expressions of EMT-related proteins. $^*P < 0.05$ versus control group. Transwell assay was used to detect invasive ability of A549 cells (a) and Western blot was used to detect expressions of EMT-related proteins (b) after treated with different concentrations of LJP for 24 h.

with increasing concentrations of LJP administration in the LJP treatment groups as compared with the control group ($P < 0.05$, Figure 7).

3.7. Effect of Laminaria Japonica Polysaccharides on the Growth and Expression of Signaling Pathway Proteins in Transplanted Tumors. A xenograft model of small-cell lung cancer was established, and the tumor volumes were measured every 5 days. As shown in Figure 8(a), the results showed that the volumes of mice in the LJP group (5 mg/kg), LJP group (10 mg/kg), and LJP group (20 mg/kg) were all significantly decreased ($P < 0.05$) as compared with the control group. The tumor weights were measured at day 30, and the results shown in Figure 8(b) indicated that the tumor weights in the LJP dose groups were significantly lower than those in the control group ($P < 0.05$). The expressions of signaling pathway proteins in transplanted tumors were detected by Western blot, and the results shown in Figure 8(c) suggested that the expressions of β-catenin, TCF4, and c-Myc proteins in each LJP dose group were significantly decreased ($P < 0.05$) as compared with the control group.

4. Discussion

Non-small-cell lung cancer is a common lung cancer. In recent years, investigations have found that its incidence rate is on the rise, and the main causes leading to death are distant metastasis and local infiltration. The occurrence of non-small-cell lung cancer is extremely complicated, involving many factors such as molecules, cytokines, and genes. Signaling pathway is now an important field of research. Recent years have witnessed increasing attention of many plants due to their wide range of biological activities. Polysaccharides from Laminaria japonica have also been shown to possess a variety of biological functions, including antioxidation, antivirus, and tumor growth inhibition [4–14]. Therefore, we studied the human non-small-cell lung cancer A549 cells and discussed the effects of Laminaria japonica polysaccharides on its growth in vivo and vitro and its possible mechanism.

In this study, we found that 5, 10, and 20 mg/ml of Laminaria japonica polysaccharides could effectively reduce the survival rate of human non-small-cell lung cancer A549 cells in vitro through a CCK8 test, and the effect was dose-
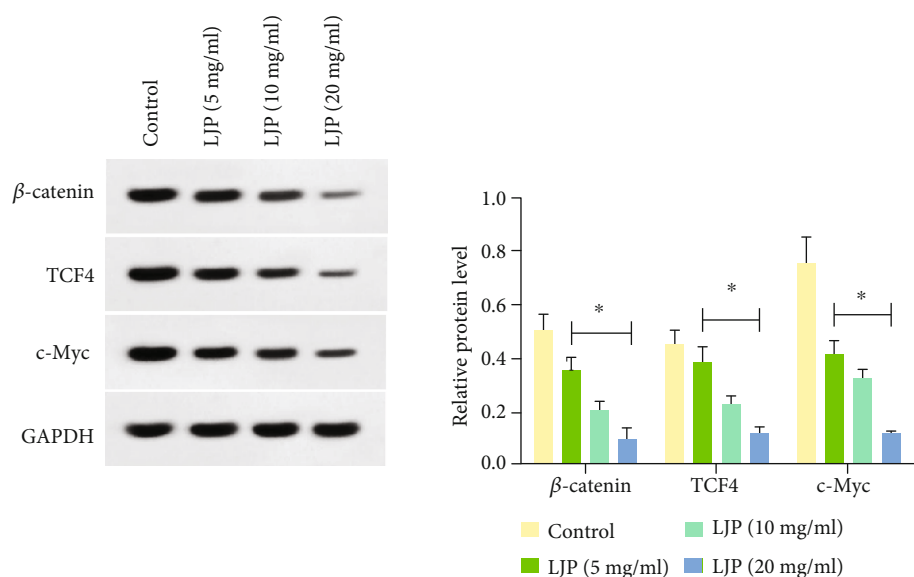
FIGURE 7: Expressions of signaling pathway proteins in A549 cells. $^*P < 0.05$ versus control group. Western blot was used to detect expressions of pathway-related proteins after treated with different concentrations of LJP for 24 h.

dependent (20 mg/ml of Laminaria japonica polysaccharides had the most obvious inhibitory effect on the survival of tumor cells). In order to study the molecular mechanism of Laminaria japonica polysaccharides inhibiting the survival of A549 cells, we detected the expressions of the proliferation marker Ki67 and PCNA in A549 cells cultured in vitro. The results revealed that Laminaria japonica polysaccharides showed a dose-dependent downregulation of the two proteins within the dose range of 5-20 mg/ml, suggesting that Laminaria japonica polysaccharides could inhibit the proliferation of human non-small-cell lung cancer A549 cells in a dose-dependent manner.

As apoptosis inhibition of tumor cells is one of the important mechanisms of tumor development, the upregulation of apoptosis level of tumor cells is also the target of anticancer drugs to inhibit tumor development. It has been shown that the activation of caspase-3 can trigger a series of events leading to apoptosis, and the activation of caspase-9 can induce apoptosis and growth inhibition in tumor tissues of xenograft mice [15, 16]; additionally, the Bcl-2 family proteins consist of members that either promote (like Bcl-2) or inhibit (like Bax) apoptosis [17]. We further demonstrated by Western blot that Laminaria japonica polysaccharides could inhibit the expressions of Bax, caspase-3, and caspase-9 and promote that of Bcl-2 in a dose-dependent manner, thus resulting in the enhancement of apoptosis of human non-small-cell lung cancer A549 cells at molecular level.

Epithelial-mesenchymal transition (EMT) refers to a biological process by which epithelial cells lose polarity and acquire a migratory, mesenchymal phenotype, thus increasing the ability of cell metastasis and invasion [18, 19]. The process is essential in the occurrence, metastasis, and invasion of a variety of tumors. VEGF is a regulator of tumor angiogenesis, mainly secreted by tumor cells. Through binding to VEGF receptor (VEGFR) on the endothelial cells, it increases the permeability of new blood vessels through para-

crine mechanism and promotes the growth of new blood vessels in tumors. Furthermore, VEGF can promote tumor infiltration and metastasis through autocrine mechanism, which may be related to VEGF's regulation of matrix metalloproteinases (MMPs), tumor cytokines, and integrins [20, 21]. Studies have found that the expression level of VEGF has a certain correlation with the prognosis of lung cancer, and its high expression can promote tumor infiltration and metastasis [22]. E-cadherin, an important cell adhesion factor, participates in and mediates adhesion of cells to each other and maintains the adhesion for tissue integrity. It is equivalent to a cancer suppressor and is inextricably linked to invasion and metastasis of various tumors [23]. Its low expression or lack of expression is considered as a key step in epithelial-mesenchymal transformation of tumors. Studies have found that [24] the overexpression of TCF4 in canine renal epithelial cells can increase the invasion ability of cells, thus accelerating the occurrence of tumor EMT, of which the obvious downregulation of epithelial marker protein E-cadherin and the increased expression of interstitial marker protein vimentin can be observed. As for further investigation of Laminaria japonica polysaccharides affecting EMT of A549 cells, we found through experiments that the cells in the LJP treatment group showed high expression of epithelial cell marker protein E-cadherin and low expression of interstitial marker protein N-cadherin and migration marker protein VEGF. The results indicate that Laminaria japonica polysaccharides can inhibit the loss of polarity of non-small-cell lung cancer A549 cultured in vitro, slow down the development of interstitial cells, and reduce the ability of cell invasion and metastasis, thus decreasing the occurrence of EMT in A549 cells.

β-Catenin is a critical component of the Wnt signaling pathway, which is normally inactive. And after being abnormally activated, β-catenin translocates into the nucleus where it binds competitively to TCF4, forming a β-catenin/TCF4 complex which in turn increases the transcription
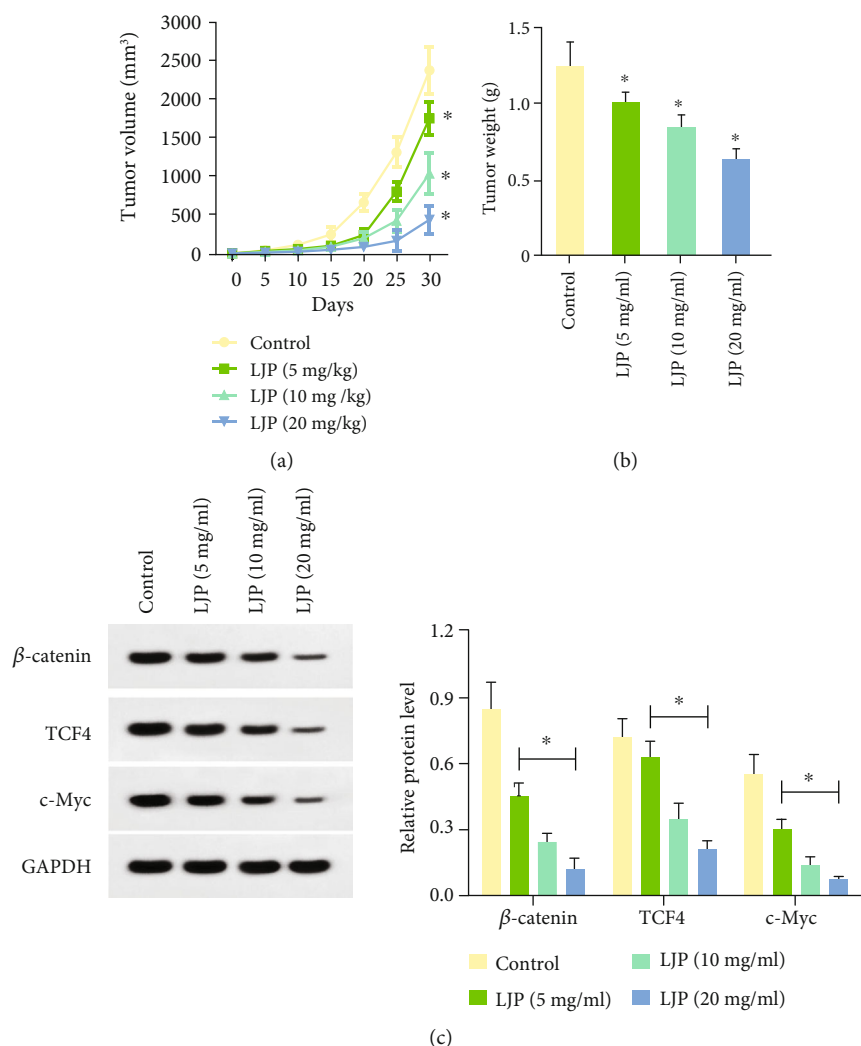
FIGURE 8: Growth and expression of signal pathway protein in transplanted tumor. Mice were randomly divided into 4 groups: control group, LJP (5 mg/kg), LJP (10 mg/kg), and LJP (20 mg/kg) group. Mice were given intraperitoneal injection once a day for a week. Tumor volumes (a) were measured every 5 days, and the mice were sacrificed at the 30th day. Tumor weights (b) and expression of signal pathway proteins (c) in tumors were detected by Western blot. $^*P < 0.05$ versus control group.

of downstream oncogenes, including target genes c-Myc, cyclin D1, E-cadherin, and VEGF, thereby contributing to the promotion of development, invasion, and metastasis of such cancers [25, 26]. For example, long noncoding RNA (ENST0000434223) reduces the proliferation, invasion, and migration of gastric cancer cells by inhibiting this pathway [27]. Yan et al. [28] also found that this pathway plays an important role in the proliferation, invasion, and migration of squamous cell carcinoma of the tongue. However, it is still unknown whether Laminaria japonica polysaccharides can affect human non-small-cell lung cancer A549 cells by regulating the β-catenin/TCF4 signaling pathway. In this study, we found that in A549 cells cultured in vitro, Laminaria japonica polysaccharides inhibited the proliferation, invasion, and migration, promoted the apoptosis, and regulated proliferation, invasion, migration, and apoptosis as well as β-catenin/TCF4 pathway-related protein expression. In order to verify whether Laminaria japonica polysaccharides can play a role in affecting the survival of A549 cells in vivo, we

performed in vivo experiments and found that Laminaria japonica polysaccharides inhibited the in vivo tumorigenesis of A549 cells (reducing tumor volume and mass), while downregulating the expression of β-catenin/TCF4 as well as its downstream C-Myc protein in tumor tissues. As shown in Figure 9, the effect of Laminaria japonica polysaccharides on A549 cell proliferation, apoptosis, invasion, and migration in vitro and tumorigenesis in vivo was closely related to the downregulation of the β-catenin/TCF4 signaling pathway.

In summary, this study explored the role of Laminaria japonica polysaccharides in survival of human non-small-cell lung cancer A549 cells. We found that Laminaria japonica polysaccharides can inhibit the activation of the β-catenin/TCF4 pathway, so as to regulate the expressions of proliferation-, apoptosis-, and migration-related proteins in human non-small-cell lung cancer A549 cells, thus suppressing the survival rate of A549 cells in vivo and vitro. However, future research is warranted on the effect of Laminaria

Laminaria japonica polysaccharides

Extracellular

Intracellular

β-catenin

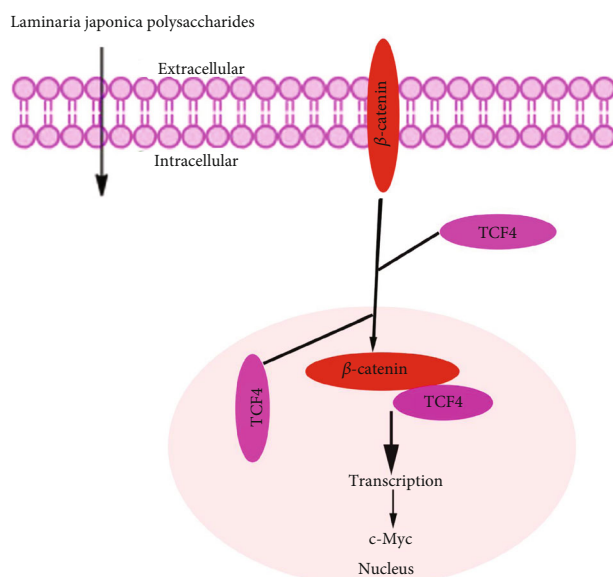TCF4

β-catenin

TCF4

TCF4

Transcription

c-Myc

Nucleus

Figure 9: Schema of LJP regulating β-catenin/TCF4 signaling pathway.

japonica polysaccharides on the regulation of vital pathways pertaining to growth of other tumors.

Data Availability

The data used to support the findings of this study are included within the article.

Conflicts of Interest

The authors confirm that there is no conflict of interest.

Acknowledgments

References

[1] L. A. Torre, F. Bray, R. L. Siegel, J. Ferlay, J. Lortet-Tieulent, and A. Jemal, "Global cancer statistics, 2012," *CA: A Cancer Journal for Clinicians*, vol. 65, no. 2, pp. 87–108, 2015.

[2] F. Zou, Z. H. Zhang, Y. T. Zhang et al., "Cancer-associated-fibroblasts regulate the chemoresistance of lung cancer cell line A549 via SDF-1 secretion," *Zhonghua Zhong Liu Za Zhi*, vol. 39, no. 5, pp. 339–343, 2017.

[3] S. C. Tripathi, J. F. Fahrmann, M. Celiktas et al., "MCAM mediates chemoresistance in small-cell lung cancer via the PI3K/AKT/SOX2 signaling pathway," *Cancer Research*, vol. 77, no. 16, pp. 4414–4425, 2017.

[4] F. Ren, Q. Fang, T. Feng et al., "*Lycium barbarum* and *Laminaria japonica* polysaccharides improve Cashmere goat sperm quality and fertility rate after cryopreservation," *Theriogenology*, vol. 129, no. 4, pp. 29–36, 2019.

[5] M. Duan, X. Sun, N. Ma et al., "Polysaccharides from *Laminaria japonica* alleviated metabolic syndrome in BALB/c mice by normalizing the gut microbiota," *International Journal of Biological Macromolecules*, vol. 121, no. 1, pp. 996–1004, 2019.

[6] X. Y. Li, Q. M. Li, Q. Fang, X. Q. Zha, L. H. Pan, and J. P. Luo, "*Laminaria japonica* polysaccharide inhibits vascular calcification via preventing osteoblastic differentiation of vascular smooth muscle cells," *Journal of Agricultural and Food Chemistry*, vol. 66, no. 8, pp. 1821–1827, 2018.

[7] Y. Yue, Z. Li, P. Li et al., "Antiviral activity of a polysaccharide from *Laminaria japonica* against enterovirus 71," *Biomedicine & Pharmacotherapy*, vol. 96, no. 12, pp. 256–262, 2017.

[8] Y. G. Cao, Y. Hao, Z. H. Li, S. T. Liu, and L. X. Wang, "Antiviral activity of polysaccharide extract from *Laminaria japonica* against respiratory syncytial virus," *Biomedicine & Pharmacotherapy*, vol. 84, no. 12, pp. 1705–1710, 2016.

[9] L. Geng, W. Hu, Y. Liu, J. Wang, and Q. Zhang, "A heteropolysaccharide from *Saccharina japonica* with immunomodulatory effect on RAW 264.7 cells," *Carbohydrate Polymers*, vol. 201, no. 1, pp. 557–565, 2018.

[10] M. Garcia-Vaquero, G. Rajauria, B. Tiwari, T. Sweeney, and J. O'Doherty, "Extraction and yield optimisation of fucose, glucans and associated antioxidant activities from *Laminaria digitata* by applying response surface methodology to high intensity ultrasound-assisted extraction," *Marine Drugs*, vol. 16, no. 8, p. 257, 2018.

[11] Q. Zhu, J. Chen, Q. Li, T. Wang, and H. Li, "Antitumor activity of polysaccharide from *Laminaria japonica* on mice bearing H22 liver cancer," *International Journal of Biological Macromolecules*, vol. 92, no. 11, pp. 156–158, 2016.

[12] M. Zeng, X. Wu, F. Li et al., "Laminaria japonica polysaccharides effectively inhibited the growth of nasopharyngeal carcinoma cells in vivo and in vitro study," *Experimental and Toxicologic Pathology*, vol. 69, no. 7, pp. 527–532, 2017.

[13] Q. Zhai, X. Li, Y. Yang, L. Yu, and Y. Yao, "Antitumor activity of a polysaccharide fraction from *Laminaria japonica* on U14 cervical carcinoma-bearing mice," *Tumour Biology*, vol. 35, no. 1, pp. 117–122, 2014.

[14] H. S. Shang, Y. L. Shih, C. P. Chen et al., "Laminarin promotes immune responses and normalizes glutamic oxaloacetic transaminase and glutamic pyruvic transaminase levels in leukemic Mice *In vivo*," *In Vivo*, vol. 32, no. 4, pp. 783–790, 2018.

[15] I. M. Cartwright, X. Liu, M. Zhou, F. Li, and C. Y. Li, "Essential roles of caspase-3 in facilitating Myc-induced genetic instability and carcinogenesis," *eLife*, vol. 6, no. 10, article e26371, 2017.

[16] P. Garg, S. Pandey, S. Hoon et al., "JNK2 silencing and caspase-9 activation by hyperosmotic polymer inhibits tumor progression," *International Journal of Biological Macromolecules*, vol. 120, Part B, pp. 2215–2224, 2018.

[17] Q. Kang, H. Zou, X. Yang et al., "Characterization and prognostic significance of mortalin, Bcl-2 and Bax in intrahepatic cholangiocarcinoma," *Oncology Letters*, vol. 15, no. 2, pp. 2161–2168, 2018.

[18] J. P. Thiery and J. P. Sleeman, "Complex networks orchestrate epithelial-mesenchymal transitions," *Nature Reviews Molecular Cell Biology*, vol. 7, no. 2, pp. 131–142, 2006.

[19] L. Przybyal, J. M. Muncie, and V. M. Weaver, "Mechanical control of epithelial-to-mesenchymal transitions in development and cancer," *Annual Review of Cell Biology*, vol. 32, no. 1, pp. 527–554, 2016.

[20] K. Wang, F. Wu, B. R. Seo et al., "Breast cancer cells alter the dynamics of stromal fibronectin-collagen interactions," *Matrix Biology*, vol. 60-61, no. 7, pp. 86–95, 2017.

[21] M. Z. Wojtukiewicz, E. Sierko, and P. Skalij, "Granulocyte-colony stimulating factor receptor, tissue factor, and VEGF-R bound VEGF in human breast cancer in loco," *Advances in Clinical and Experimental Medicine*, vol. 25, no. 3, pp. 505–511, 2016.

[22] L. Jiang, Y. Luan, X. Miao et al., "Platelet releasate promotes breast cancer growth and angiogenesis via VEGF- integrin cooperative signalling," *British Journal of Cancer*, vol. 117, no. 5, pp. 695–703, 2017.

[23] C. Xiangming, S. Hokita, K. Nuruki et al., "The expression of cadherin-catenin complex in association with the clinicopathologic features of early gastric cancer," *Surgery Today*, vol. 28, no. 6, pp. 587–594, 1998.

[24] V. R. Sobrado, G. Moreno-Bueno, E. Cubillo et al., "The class I bHLH factors E2-2A and E2-2B regulate EMT," *Journal of Cell Science*, vol. 122, no. 7, pp. 1014–1024, 2009.

[25] Z. Yang, K. Li, Q. Liang et al., "Elevated hydrostatic pressure promotes ameloblastoma cell invasion through upregulation of MMP-2 and MMP-9 expression via Wnt/β-catenin signalling," *Journal of Oral Pathology & Medicine*, vol. 47, no. 9, pp. 836–846, 2018.

[26] S. H. Shin, D. Y. Lim, K. Reddy et al., "A Small Molecule Inhibitor of the β-Catenin-TCF4 Interaction Suppresses Colorectal Cancer Growth *In Vitro* and *In Vivo*," *eBioMedicine*, vol. 25, no. 11, pp. 22–31, 2017.

[27] Y. X. Zhao, J. F. Liu, W. J. Sun, R. F. Zeng, T. Li, and R. M. Ma, "Long non-coding RNA-ENST00000434223 suppresses tumor progression in gastric cancer cells through the Wnt/β-catenin signaling pathway," *International Journal of Biological Macromolecules*, vol. 120, no. Part A, pp. 491–501, 2018.

[28] G. Yan, R. Zou, Z. Chen et al., "Silencing RhoA inhibits migration and invasion through Wnt/β-catenin pathway and growth through cell cycle regulation in human tongue cancer," *Acta Biochimica et Biophysica Sinica*, vol. 46, no. 8, pp. 682–690, 2014.

Research Article

Effects of *Polygonatum sibiricum* Polysaccharides (PSP) on Human Esophageal Squamous Cell Carcinoma (ESCC) via NF-κB Signaling Pathway

Weizheng Zhou, Jiang Hong, Ji Zhu, and Xiaowei Wang 🄳

Department of Thoracic Surgery, Changhai Hospital, Shanghai 200435, China

Correspondence should be addressed to Xiaowei Wang; xiaoweiwang@genopub.com

Objective. To explore the effects of different concentrations of *Polygonatum sibiricum* polysaccharides (PSP) on human esophageal squamous cell carcinoma (ESCC) cell line Eca109 and explore the new approach for the treatment of ESCC. *Methods.* Eca109 cells were divided into 5 groups, including one control group and 4 experimental groups where the concentrations of PSP used were 50, 100, 200, and 400 μg/mL. The proliferation rate of Eca109 cells in each group was measured with the CCK8 assay, and the apoptosis rate in each group was analyzed by flow cytometry; the in vitro scratch assay was used to determine the migration ability of Eca109 cells after PSP treatment; the expression levels of IL-1, IL-6, IL-10, TNF-α, and TGF-β were measured by RT-PCR, and the expression levels of TLR4 and proteins that are related to NF-κB signaling pathways were determined by Western blot. *Results.* PSP significantly inhibited the proliferation of Eca109 cells ($p < 0.05$) on a time- and dose-dependent manner; the apoptosis rates of Eca109 cells in experimental groups were significantly increased after 48 h of culture ($p < 0.05$); PSP significantly reduced the migration and invasion ability of Eca109 cells ($p < 0.05$); RT-PCR results showed that the expression of IL-10 in Eca109 cells increased significantly after treatment with PSP ($p < 0.05$), while the expression of IL-1, IL-6, TNF-α, and TGF-β decreased significantly ($p < 0.05$). Compared with the control group, the expression level of TLR4, NF-κB/p50, and NF-κB/p65 protein in each experimental group was significantly lower than that in the control group ($p < 0.05$). *Conclusions.* PSP significantly inhibited the proliferation, invasion, and migration of Eca109 cells and promoted cell apoptosis. These observed effects were probably due to the PSP's inhibition on the NF-κB signaling pathway in Eca109 cells via the regulation of the TLR4 expression.

1. Introduction

Esophageal squamous cell carcinoma (ESCC) is one of the most common malignant tumors in the world, accounting for 80% of esophageal cancer (EC) in China [1]. ESCC is characterized by strong invasiveness, poor prognosis, and rapid clinical progression, is often accompanied by lymph node metastasis, and is also highly prone to recurrence. Although the diagnostic and therapeutic techniques have been greatly advanced, the pathological mechanism of ESCC is still poorly understood, and the current five-year survival rate of ESCC is only 20-30% [2]. Therefore, the exploration of the mechanism for the occurrence, invasion, and metasta-

sis of ESCC has become one of the topical issues in the current research field.

The NF-κB signaling pathway is involved in the regulation of gene expression related to immune response, inflammatory response, and apoptosis and is an important signaling pathway affecting tumorigenesis and tumor development. It is also of great significance in cell stress response. The most common form of NF-κB is a heterodimer consisting of p50 and p65, where p50 is the site for DNA binding and p65 is involved in transcriptional regulation of genes and promotes p50 binding to DNA [3]. In quiescent cells, NF-κB typically binds to repressor IkBα and is present in the cytoplasm in an inactive form. This inactive form can be degraded by a

number of stimuli via phosphorylation of IkBα, allowing dissociated NF-κB to enter the nucleus and expose its nuclear recognition site, thereby promoting transcription of the target gene. Toll-like receptors (TLRs) are a class of transmembrane receptors expressed on the surface of immune cells, which are involved in innate immunity and indirect activation of acquired immunity [4]; it can also activate transcription factor NF-κB by recognizing invading pathogens and mediate the massive release of inflammatory cytokines and chemokines. Studies have shown that the TLR/NF-κB signaling pathway is involved in the development of various malignant tumors including prostate cancer, non-small cell carcinoma, and colorectal cancer and is also associated with tumor proliferation, apoptosis resistance, invasion, and metastasis [5–7]. At present, there are few reports on the connections between TLR/NF-κB and ESCC.

As a traditional Chinese medicinal material, *Polygonatum sibiricum* has been intensively researched in recent years. *Polygonatum sibiricum* polysaccharides (PSP) are the main active ingredient extracted from *Polygonatum*. Because of its low toxicity, it can be used for clinical practice in the long term. Studies have shown that PSP plays various important roles including antioxidation, antiaging, neuroprotection, immune regulation, and antitumor [8]. Especially in human breast cancer cells (MCF-27), colorectal cancer cells (HCT-8), and gastric cancer cells (HGC-27), PSP can significantly inhibit tumor growth and promote tumor cell apoptosis [9]. Han et al. found that PSP can inhibit the proliferation of cancer-associated fibroblasts (CAFs) in prostate cancer cells but had no effect on the proliferation of normal fibroblasts [10]. At present, the therapeutic effects of PSP on human esophageal squamous cell carcinoma have not been reported, and the associated mechanism is still unclear. Therefore, it is of clinical significance to study the effect of PSP on esophageal squamous cell carcinoma. In this study, we investigated the effects of PSP on the proliferation, apoptosis, migration, and TLR4/NF-κB signaling pathway-related proteins in human ESCC cell line Eca109 and explored the modes of action of PSP on ESCC, hoping to explore new approaches for the treatment of human ESCC.

2. Material and Methods

2.1. PSP Extraction and HPLC Analysis. The hot water leaching method was used to extract the PSP. The *Polygonatum sibiricum* pieces (purchased from Golden Leaf Pharmaceutical Co., Ltd., China) were mixed with water at the volume ratio of 1 : 8, which was then boiled for 2 h and repeated 3 times. After that, the aqueous extract was precipitated with 80% ethanol (Sinopharm Group, China) to remove the bioactive protein substance. PSP was obtained after precipitation and evaporation of ethanol. 0.25 g of PSP was then mixed with 0.1 L of 2 mol/L TFA (Sinopharm Group, China) solution before drying in a DHG-9070A oven (Yiheng Technology, China) at 100°C. 0.1 L of methanol (Sinopharm Group, China) was then added to remove TFA. After being repeated for 3 times, the resulting product was subjected to (1-phenyl-3-methyl-5-pyrazolone) PMP for derivatization. The product was then mixed with 0.1 L of 0.3 mol/L NaOH

(Sinopharm Group, China), and together with 0.12 L of 0.5 mol/L methanol solution, the mixed solution was then incubated in a 70°C water bath for 30 min. After incubation, 0.1 L of 0.3 mol/L HCL (Sinopharm Group, China) was added and the solution was then extracted by an equal volume of chloroform to obtain an aqueous layer. And the aqueous layer was dried afterward. Finally, this extracted product was dissolved with 0.2 L of methanol and the filtrate was taken for the test. The mixed monosaccharide (consisting of mannose, glucose, galactose, glucuronic acid, galacturonic acid, and trehalose purchased from Sinopharm Group, China) solution was used as a reference for HPLC analysis.

2.2. Cell Culture and Treatment Grouping. The human ESCC cell line Eca109 (purchased from China Center for Type Culture Collection) was cultured in RPMI 1640 (Gibco, USA) medium containing 10% fetal bovine serum (FBS), 100 U/mL penicillin, and 100 U/mL streptomycin at 37°C with 5% CO_2. A blank control group and 4 PSP experimental groups with final concentrations of 50, 100, 200, and 400 μg/mL were set up in this study.

2.3. Cell Proliferation Measured with CCK8 Assay. Cell counting kit-8 (CCK8) (Dojindo, Japan) was used to determine the proliferation of human ESCC cells. Eca109 cells in the logarithmic growth phase were seeded in 96-well plates at a concentration of 1×10^4 cells/well. The culture was grouped as described above, and 4 replicate wells were set for each group. After being cultured for 0, 24, 48, and 72 h in an incubator at 37°C, with 5% CO_2, 10 μL of CCK8 working solution was added to each well, and incubation was continued at 37°C for another 2 h. The optical density (OD) was measured at 450 nm afterward.

2.4. Apoptosis Determined with Flow Cytometry. Annexin V-FITC (Sigma-Aldrich, USA) was used to measure the apoptosis of Eca109 cells with flow cytometry. After 48 h of culture, cell suspensions of the control group and the experimental group were collected and centrifuged at 1000 rpm for 5 min. Following that, the cells within the supernatant were washed with PBS buffer. Centrifuge again at 1000 rpm for 5 min, and a 500 μL of annexin binding buffer was added to the pellet and mixed by pipetting. Then, 5 μL of Annexin V-FITC reagent was added, and the solution was kept at room temperature for 10 min in the dark. 10 μL of PI reagent was added as well, and the solution was incubated at room temperature in the dark for another 5 min before the apoptosis rate of cells in each group was analyzed using a flow cytometer.

2.5. Cell Migration and Invasion Measured by In Vitro Scratch Assay. Eca109 cells in a logarithmic growth phase were taken to prepare a cell suspension with a density of 2×10^5 cell/mL. 2 mL of cell suspension was inoculated into a 6-well plate and cultured for 12 h. Then, a 200 μL micropipette tip was used to draw a straight line along the diameter of the tip's hole for the control group and experimental group, and the scratches were recorded under the microscope at 0 h and 48 h after scratching. PS software was used to calculate the relative ratio of cell scratching space between the

TABLE 1: The primers used in this study.

Gene	Primers
IL-1	F: 5′-CCACAGACCTTCCAGGAG-3′
	R: 5′-GCGTGCAGTTCAGTGATC-3′
IL-6	F: 5′-CCTCCAGAACAGATTTGAG-3′
	R: 5′-ATTTGTGGTTGGGTCAGG-3′
IL-10	F: 5′-AGTGTCTCGGAGGGGATTC-3′
	R: 5′-TTCACCATGTTGACCAGG-3′
TNF-α	F: 5′-TCTGCCTGCTGCACTTTG-3′
	R: 5′-AACATGGGCTACAGGCTT-3′
TGF-β	F: 5′-AGAGCTGCGTCTGCTGAG-3′
	R: 5′-ACCACTGCCGCACAACTC-3′
β-Actin	F: 5′-GCAAATGCTTCTAGGCGGAC-3′
	R: 5′-GCTGTCACCTTCACCGTTCC-3′

control group and the experimental group. The experiment was repeated 3 times and averaged. The scratch recovery rate was calculated with the following formula: (width at 0 h – width at 48 h)/width at 0 h.

2.6. Cytokine Expression Detected with RT-PCR. The mRNA expression level of IL-1, IL-6, IL-10, TNF-α, and TGF-β was measured with RT-PCR, and the β-actin was used as the reference gene. Eca109 cells cultured for 48 h were collected, and the total RNA was extracted according to the instructions of TRIzol (Invitrogen, USA). The concentration of RNA was quantified based on the O.D. value and subsequently subjected to reverse transcription with the help of the PrimeScipt™ RT Master (Takara, Japan) kit. The resulting cDNA was stored at -20°C. RT-PCR experiments were then performed using cDNA as a template according to the instructions of the SYBR Green Realtime PCR Master Mix (Toyobo, Japan). $2^{-\Delta\Delta ct}$ was used for quantitative analysis. The primers used in this are shown in Table 1.

2.7. Expression of TLR4 and Proteins Involved in the NF-κB Signaling Pathway Determined with Western Blot. Total protein was extracted from the control group and each experimental group after 48 h of culture. The protein concentration was determined by BCA kit (Beyotime, China). After protein quantification, an appropriate amount of protein was taken for electrophoresis and to ensure that the total amount of protein added to each well is approximately the same. Protein was separated by 12% polyacrylamide gel electrophoresis and then transferred to the PVDF membrane. 5% BSA was then used for blocking for 1 h, followed by addition of primary antibodies (rabbit anti-human TLR4 polyclonal antibody (Boster, China 1 : 50), rabbit anti-human NF-κB/p50 monoclonal antibody (Santa Cruz, USA 1 : 100), NF-κB/p65 polyclonal antibody (Santa Cruz, USA 1 : 100), and β-actin, after which it was then incubated overnight at 4°C. The next day, the second antibody was added

and incubated for 2 h at room temperature. The PVDF membrane was then washed with TBST 3 times, and Image Lab 3.0 was used for imaging. ImageJ software was used to quantitatively analyze the differential expression of proteins in each group, and β-actin was used as an internal reference for the relative quantification.

2.7.1. Statistical Analysis. The data were collated and analyzed using Origin 8.0. The results for each group were expressed as mean ± SEM, and one-way ANOVA was used for comparison between groups. $p < 0.05$ represents a statistical difference.

3. Results

3.1. PSP Extraction Analysis by HPLC. In order to detect the monosaccharide component in the PSP extract, the PSP extract (test sample) and the mixed monosaccharide solution (control) were separately subjected to HPLC separation. As shown in Figure 1, monosaccharide mixture control was well separated, with each monosaccharide showing a single peak, and there were 4 single peaks in the test sample. Compared with the control curve, the monosaccharides with higher content in the PSP extract were mannose, glucose, galactose, and trehalose, among which the glucose is the major component of PSP.

3.2. Effect of PSP on the Proliferation of Human ESCC. PSP of 50, 100, 200, and 400 μg/mL were added to Eca109 cells and cultured for 48 h. CCK8 was then used to measure the effects of different concentrations of PSP on the proliferation of human ESCC. As shown in Figure 2(a), after 48 h of culture, compared with the control group, the cell survival rate of Eca109 in each experimental group decreased significantly, and the proliferation ability of Eca109 cells was significantly inhibited ($p < 0.05$). The half-inhibitory concentration (IC50) of PSP against Eca109 cells was 262 μg/mL. The cell viability of Eca109 after 0, 24, 48, and 72 h of PSP culture at 200 μg/mL was further explored as well. The results showed that the viability of Eca109 cells decreased significantly with time (Figure 2(b)), and the difference was statistically significant ($p < 0.05$). Thus, these results indicated that PSP significantly inhibited the proliferation of Eca109 cells in a dose- and time-dependent manner.

3.3. Effect of PSP on Apoptosis of Human ESCC. Flow cytometry was used to detect the apoptosis of Eca109 cells in the control group and the experimental group 48 h after culture. The results showed that the apoptosis rates of Eca109 cells cultured at 50, 100, 200, and 400 μg/mL PSP were 23.07%, 33.09%, 41.20%, 63.15%, and 69.18%, respectively (Figure 3). Compared with the control group, the apoptosis rate of Eca109 was significantly higher in the experimental group, and the difference was statistically significant ($p < 0.05$), which indicates the apoptosis-promoting effect of PSP on Eca109 cells.

3.4. Effect of PSP on Migration and Invasion of Human ESCC. After 48 h of Eca109 cells cultured with different concentrations of PSP, the cell migration and invasion ability was
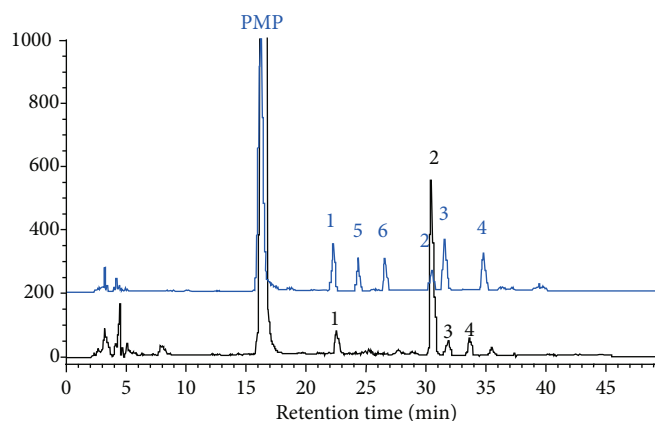
FIGURE 1: PSP component analysis by HPLC. 1: mannose; 2: glucose; 3: galactose; 4: trehalose; 5: glucuronic acid; 6: galacturonic acid.
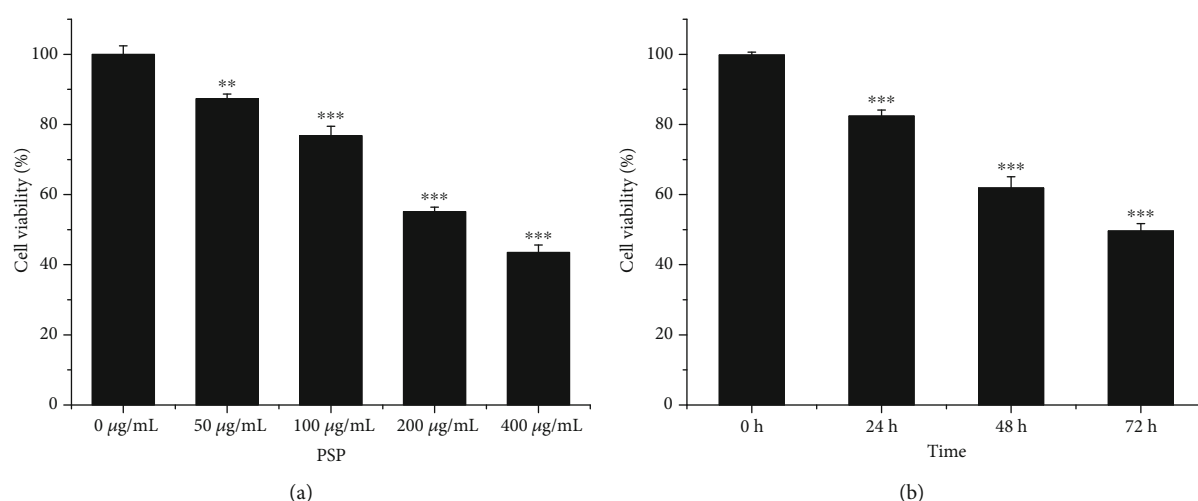

(a)

(b)

FIGURE 2: The proliferation of esophageal squamous cell carcinoma Eca109 cells was inhibited by PSP. (a) The toxicity of different concentrations of PSP on Eca109 cells (culture for 48 h) measured with CCK8, compared with the control group, $^{**}p < 0.01$; $^{***}p < 0.001$. (b) The toxicity of PSP on Eca109 cells after different durations (200 μg/mL PSP) measured with CCK8, compared with the control group; $^{***}p < 0.001$. The proliferation of Eca109 cells in each group measured by CCK8 assay. Compared with the control group: $^{**}p < 0.01$ and $^{***}p < 0.001$.

detected by in vitro scratch assay. The results showed that the cell scratch recovery rate of the experimental group was significantly lower than that of the control group (Figure 4, $p < 0.05$). Specifically, the recovery rates of the control group and the experimental group were 80.37%, 76.63%, 68.77%, 50.47%, and 43.63%, respectively, which indicated that PSP decreased the ability of Eca109 cells to migrate and invade.

3.5. Effect of PSP on Cytokine in Human ESCC. Furthermore, the expression of various cytokines (IL-1, IL-6, IL-10, TNF-α, and TGF-β) affected by PSP in Eca109 cells was measured by RT-PCR. As shown in Figure 5, the mRNA expression levels of IL-I and IL-6 in Eca109 cells were significantly downregulated compared with those in the control group after 48 h of culture with PSP at 200 μg/mL ($p < 0.05$). This decreasing trend was heightened with the increasing concentration of PSP. However, as the concentration of PSP increased, the expression level of IL-10 was significantly upregulated ($p < 0.05$) while there was a significant decrease in the expression level of TNF-α and TGF-β ($p < 0.05$).

3.6. Effect of PSP on the Expression of TLR4 and Proteins Involved in the NF-κB Signaling Pathway in Human ESCC. The expression of TLR4 and proteins involved in the NF-κB signaling pathway in Eca109 cells was determined after 48 h of cell culture (Figure 6). Compared with the control group, the expression of TLR4 showed a significant decrease with the increase of PSP concentration, and the difference was statistically significant (Figure 6(b), $p < 0.05$); the expression levels of proteins related to the NF-κB signaling pathway (NF-κB/p50 and NF-κB/p65) were also significantly downregulated (Figure 6(c), $p < 0.05$). This result indicated that in Eca109 cells, PSP may decrease the expression of NF-κB signaling pathway-related proteins by inhibiting the TLR4 protein expression.

4. Discussion

In China, the majority of esophageal cancers are squamous cell carcinoma and the incidence of ESCC ranks fifth in all malignant tumor types [11]. At present, the research on
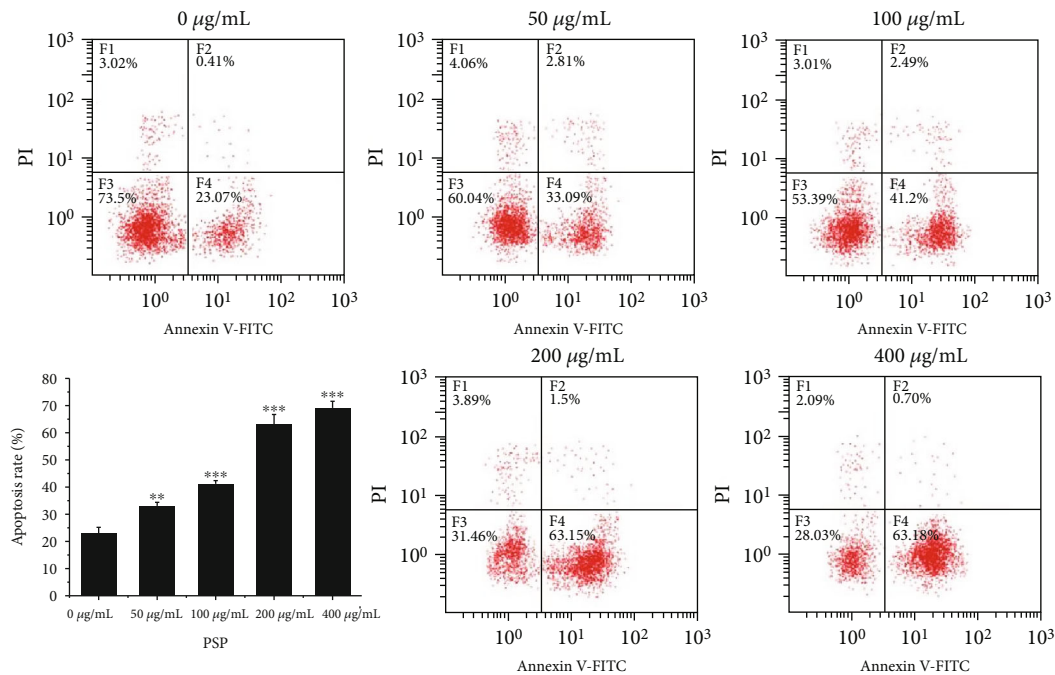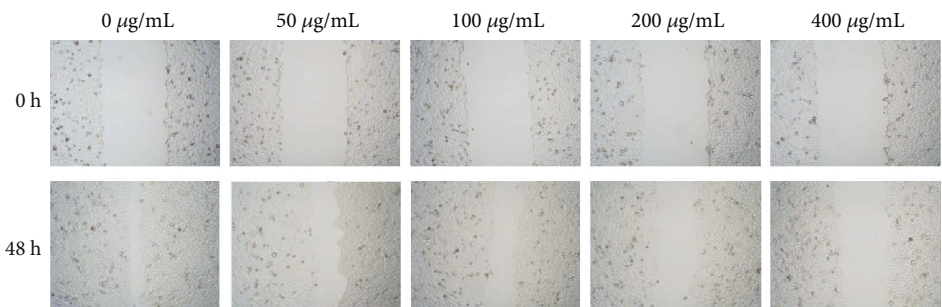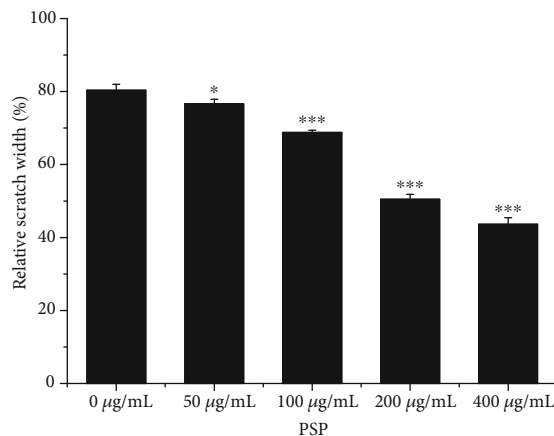
FIGURE 3: Flow cytometry used to detect apoptosis of Eca109 cells. Compared with the control group, $^*p < 0.05$, $^{**}p < 0.01$, and $^{***}p < 0.001$.

(a)

(b)

FIGURE 4: PSP inhibited migration and invasion of Eca109 cells. (a) The migration and invasion of Eca109 cells in each group determined by in vitro scratch assay. (b) Quantitative results of (a), compared with the control group, $^*p < 0.05$ and $^{***}p < 0.001$.

ESCC mainly focuses on the excessive activation of key signaling pathways involved in disease occurrence and the abnormal expression of some proteins and cellular inflam- matory factors. Although the survival of ESCC patients has been effectively prolonged with the progress of various treat- ments such as early diagnosis, surgery, and chemotherapy
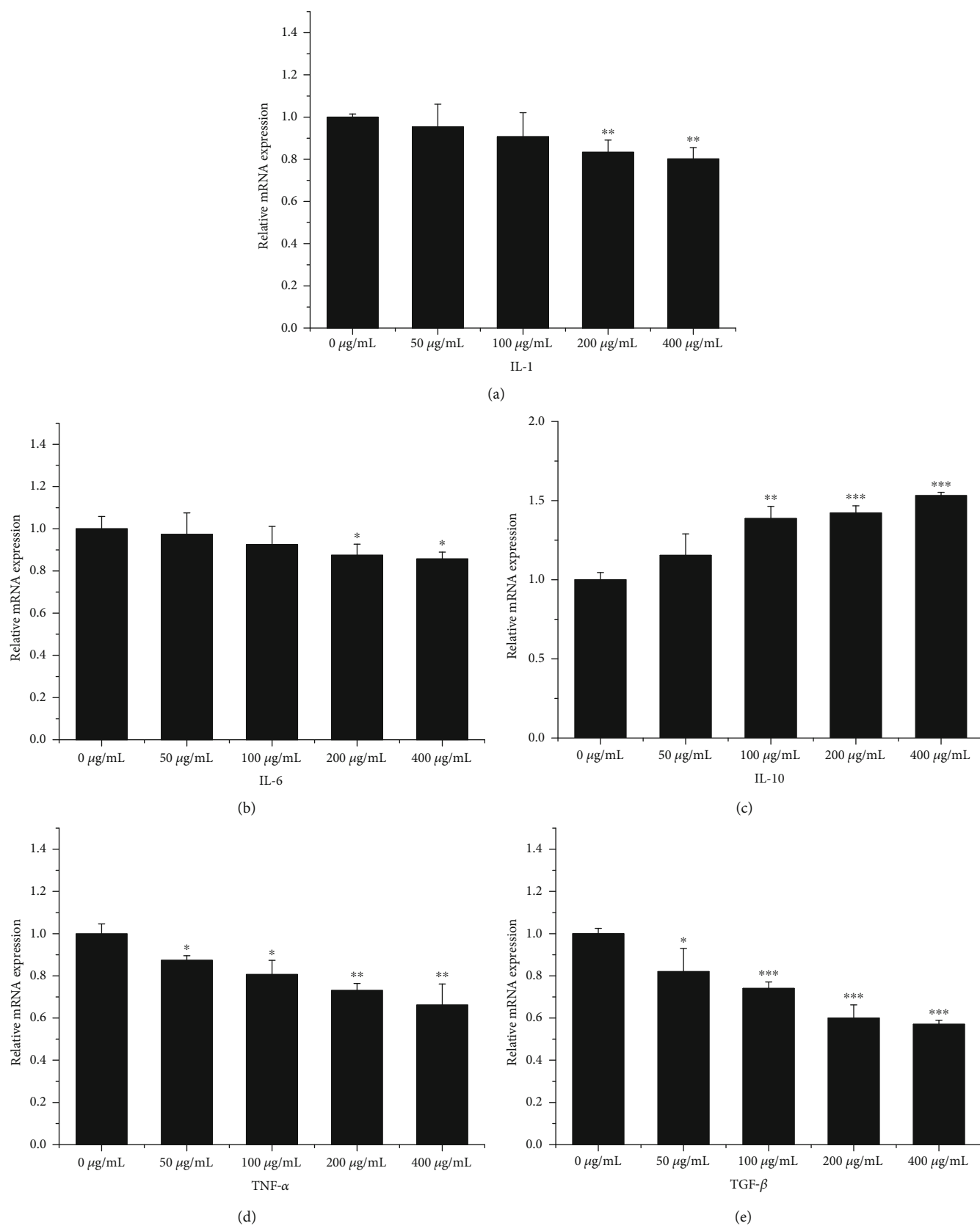
Figure 5: RT-PCR was used to detect the expression of cytokines in Eca109 cells: (a) IL-1; (b) IL-6; (c) IL-10; (d) TNF-α; (e) TGF-β. Compared with the control group, $^{*}p < 0.05$, $^{**}p < 0.01$, and $^{***}p < 0.001$.
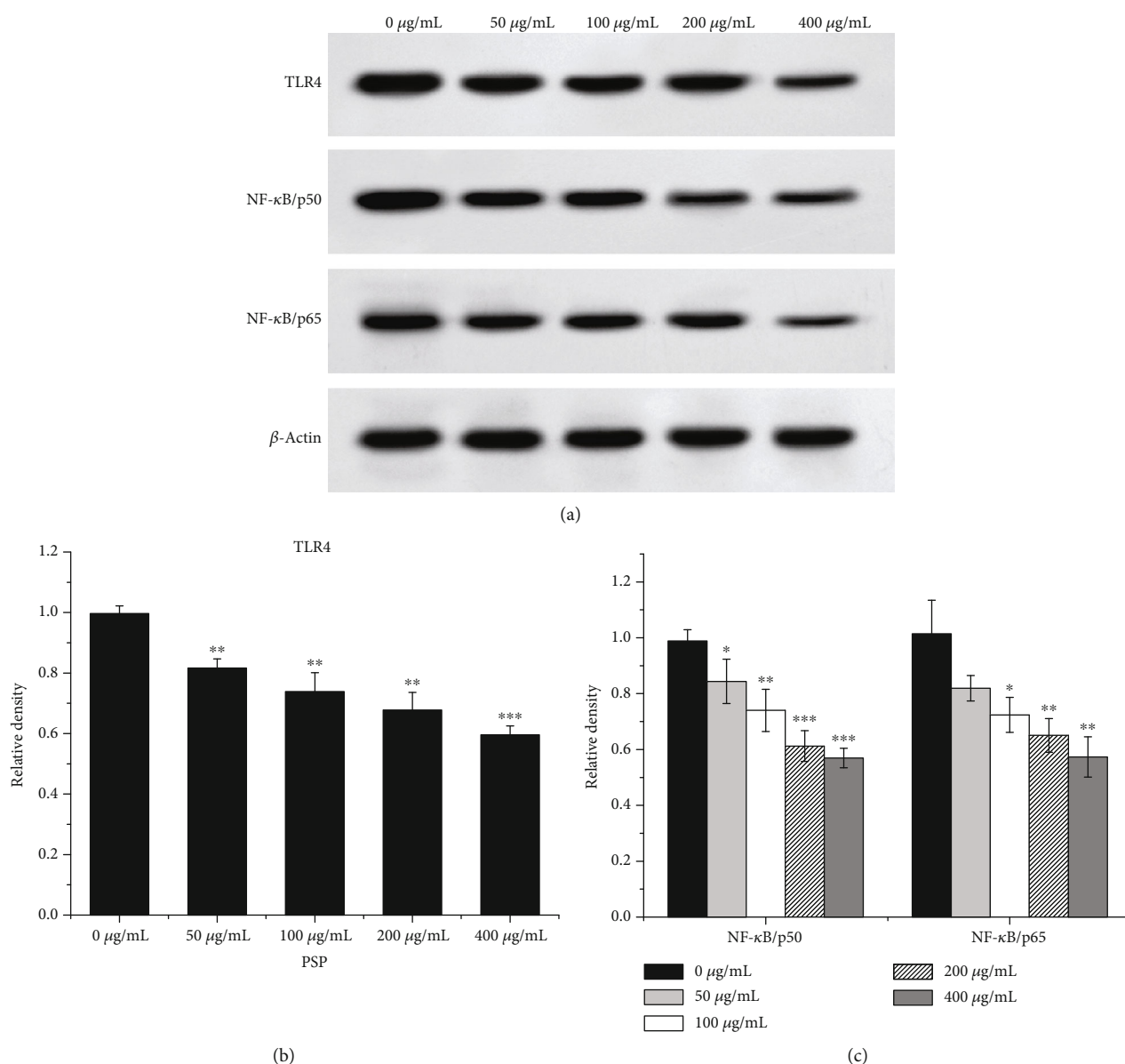
Figure 6: Expression of TLR4/NF-κB signaling pathway protein in Eca109 cells. (a) Western blot analysis of TLR4, NF-κB/p50, and NF-κB/p65 protein expression in Eca109 cells. (b) Quantitative results of (a), compared with the control group, $^*p < 0.05$, $^{**}p < 0.01$, and $^{***}p < 0.001$.

drugs, the efficacy of ESCC treatment is still not ideal due to the characteristics of ESCC being easy to relapse and easy to metastasize. Therefore, investigating the pathogenesis, invasion, and metastasis of ESCC and developing more effective therapeutic drugs are of great significance for the treatment of ESCC.

Studies have found the abnormal activation of NF-κB in a variety of malignant tumors, which suggests a certain correlation with tumor proliferation, invasion, and migration [12]. For example, Sovak et al. have reported that NF-κB was in a state of constant activation in ER-negative breast cancer cells and it was associated with poorly differentiated, highly metastatic cancer cells [13]. In this study, we showed that PSP significantly inhibited the proliferation of Eca109 cells and enhanced the apoptosis of Eca109 cells in vitro; in

addition, PSP also showed inhibitory effects on the migration and invasion of Eca109 cells. PSP is a class of polysaccharide that is extracted from a traditional Chinese medicine *Polygonatum sibiricum*. In recent years, research has suggested that PSP has certain antitumor and immune-enhancing functions. In this study, we found that the proliferation and migration ability of Eca109 cells were decreased significantly with the increase of PSP concentration and the inhibitory effect of PSP on the proliferation of human ESCC was dose- and time-dependent. Furthermore, we found that PSP significantly increased the apoptosis rate of human ESCC and inhibited the migration ability of ESCC in this study. These results indicated that PSP has a certain antitumor effect on ESCC in vitro. After cultured with various concentrations of PSP, on the one hand, the expression levels of IL-1 and

IL-6 in Eca109 cells showed a decreasing trend, and when the concentration of PSP was 200 μg/mL, the expression levels of IL-1 and IL-6 were significantly reduced. IL-1 is a proinflammatory cytokine whose biological properties are mainly involved in mediating inflammatory responses and regulating immune responses. In the cancer cell development, IL-1 not only provides cancer cells with inflammatory signals, stimulates the production of other proinflammatory cytokines, and mediates changes in the tumor microenvironment, but also directly participates in cancer-related signaling pathways and promotes the occurrence and development of cancer [14]. In fact, one study has found that the level of IL-6 in the serum of patients with gastric cancer is significantly higher than that of the normal control group [15]. To actively play the biological role, IL-6 needs to bind to its specific receptor IL-6R, which subsequently induces proliferation and differentiation of immune cells, regulates immunity, and promotes differentiation and maturation of hematopoietic stem cells. These functions are realized through a complex and delicate regulation within the body. Thus, when the timely and correct regulation of differentiation, proliferation, apoptosis, etc. is out of order, they may cause and promote tumors. On the other hand, the expression of TNF-α and TGF-β in Eca109 cells decreased significantly, whereas the expression of IL-10 significantly increased. TNF-α is one of the key cytokines involved in inflammatory and immune responses, which accelerates tumorigenesis by promoting tumor proliferation and metastasis [16] whereas TGF-β can promote tumorigenesis by inhibiting T cell immune response [17]. As for IL-10, it is a multifunctional cytokine. In melanoma, researchers have found that IL-10 has certain antitumor functions [18]. Not surprisingly, our research has some similarities with those reported in the literature. The effects of PSP on cytokines such as IL-1, IL-6, TNF-α, TGF-β, and IL-10 indicate that in human ESCC, PSP probably exerted a certain immunomodulatory effect and inhibited the development of tumor cells, which is consistent with the effect of PSP in other tumor cells. Our results showed that PSP specifically downregulated the expression of TLR4 protein, thereby inhibiting the expression of NF-κB/p50 and NF-κB/p65 proteins in the NF-κB signaling pathway. Inhibition of p50 and p65 protein expression indicates that PSP may inhibit the NF-κB signaling pathway by regulating the TLR4 protein, thereby exerting immunoregulatory and anticancer effects, and hindering the proliferation, occurrence, and development of ESCC cells. PSP has shown broad promise as an antitumor drug, which also provides perspectives for further research on ESCC.

Data Availability

The data used to support the findings of this study are included within the article.

Conflicts of Interest

The authors declare that they have no competing interests.

Authors' Contributions

Weizheng Zhou and Jiang Hong contributed equally to this study.

Acknowledgments

References

[1] L. A. Torre, F. Bray, R. L. Siegel, J. Ferlay, J. Lortet-Tieulent, and A. Jemal, "Global cancer statistics, 2012," *CA: A Cancer Journal for Clinicians*, vol. 65, no. 2, pp. 87–108, 2015.

[2] F. Kamangar, G. M. Dores, and W. F. Anderson, "Patterns of cancer incidence, mortality, and prevalence across five continents: defining priorities to reduce cancer disparities in different geographic regions of the world," *Journal of Clinical Oncology*, vol. 24, no. 14, pp. 2137–2150, 2006.

[3] A. S. Baldwin Jr., "The NF-κB and IκB proteins: new discoveries and insights," *Annual Review of Immunology*, vol. 14, no. 1, pp. 649–681, 1996.

[4] A. Aderem and R. J. Ulevitch, "Toll-like receptors in the induction of the innate immune response," *Nature*, vol. 406, no. 6797, pp. 782–787, 2000.

[5] Y. Zhang, Y. Wang, J. Yuan et al., "Toll-like receptor 4 ligation confers chemoresistance to docetaxel on PC-3 human prostate cancer cells," *Cell Biology and Toxicology*, vol. 28, no. 4, pp. 269–277, 2012.

[6] W. He, Q. Liu, L. Wang, W. Chen, N. Li, and X. Cao, "TLR4 signaling promotes immune escape of human lung cancer cells by inducing immunosuppressive cytokines and apoptosis resistance," *Molecular Immunology*, vol. 44, no. 11, pp. 2850–2859, 2007.

[7] R. Y. C. Hsu, C. H. F. Chan, J. D. Spicer et al., "LPS-induced TLR4 signaling in human colorectal cancer cells increases β1 integrin-mediated cell adhesion and liver metastasis," *Cancer Research*, vol. 71, no. 5, pp. 1989–1998, 2011.

[8] X. Cui, S. Wang, H. Cao et al., "A review: the bioactivities and pharmacological applications of *Polygonatum sibiricum* polysaccharides," *Molecules*, vol. 23, no. 5, article 1170, 2018.

[9] L. Li, L. N. Tian, Z. X. Ren, and Z-J. Long, "Research progress on the structural analysis and functional activity of polysaccharides," *Chinese Journal of Experimental Traditional Medical Formulae*, vol. 21, pp. 231–234, 2015.

[10] S. Y. Han, M. H. Hu, G. Y. Qi et al., "Polysaccharides from Polygonatum inhibit the proliferation of prostate cancer-associated fibroblasts," *Asian Pacific Journal of Cancer Prevention*, vol. 17, no. 8, pp. 3829–3833, 2016.

[11] W. Chen, R. Zheng, P. D. Baade et al., "Cancer statistics in China, 2015," *CA: A Cancer Journal for Clinicians*, vol. 66, no. 2, pp. 115–132, 2016.

[12] F. Jiang, N. P. Caraway, R. Li, and R. L. Katz, "RNA silencing of S-phase kinase-interacting protein 2 inhibits proliferation and centrosome amplification in lung cancer cells," *Oncogene*, vol. 24, no. 21, pp. 3409–3418, 2005.

[13] M. A. Sovak, R. E. Bellas, D. W. Kim et al., "Aberrant nuclear factor-kappaB/Rel expression and the pathogenesis of breast

cancer," *The Journal of Clinical Investigation*, vol. 100, no. 12, pp. 2952–2960, 1997.

[14] R. N. Apte, S. Dotan, M. Elkabets et al., "The involvement of IL-1 in tumorigenesis, tumor invasiveness, metastasis and tumor-host interactions," *Cancer Metastasis Reviews*, vol. 25, no. 3, pp. 387–408, 2006.

[15] J. S. Jang, S. R. Choi, S. Y. Han et al., "Predictive significance of serum IL-6, VEGF, and CRP in gastric adenoma and mucosal carcinoma before endoscopic submucosal dissection," *The Korean Journal of Gastroenterology*, vol. 54, no. 2, pp. 99–107, 2009.

[16] F. Balkwill, "Tumour necrosis factor and cancer," *Nature Reviews Cancer*, vol. 9, no. 5, pp. 361–371, 2009.

[17] M. O. Li, S. Sanjabi, and R. A. Flavell, "Transforming growth factor-β controls development, homeostasis, and tolerance of T cells by regulatory T cell-dependent and -independent mechanisms," *Immunity*, vol. 25, no. 3, pp. 455–471, 2006.

[18] S. Huang, K. Xie, C. D. Bucana, S. E. Ullrich, and M. Bar-Eli, "Interleukin 10 suppresses tumor growth and metastasis of human melanoma cells: potential inhibition of angiogenesis," *Clinical Cancer Research*, vol. 2, no. 12, pp. 1969–1979, 1996.

Research Article

Combined Effect of Lentinan and Cisplatin on Cytokines IL-6, TNF-α, and TGF-β in Tumor Therapy

Xu-dong Liu, Min Li, Wan-xiang Li, Qing-yu Wang, and Hong-xia Zhang

Clinical Laboratory of Wei Fang People's Hospital, 261041, China

Correspondence should be addressed to Hong-xia Zhang; zhanghx1122@126.com

Lentinan is a biologically active ingredient isolated from the fruiting body of Lentinula edodes (shiitake) and has antitumor properties. Cytokines, at the same time, are a key factor in regulating immune responses in physiological and pathological states. Many cytokines have shown positive effect on different malignancies in clinical trials. Studies have shown that such cytokines as IL6, TNF-α, and TGF-β play a quite important role in the formation of tumor microenvironment. In this study, we investigated the antitumor effect of combined medication of lentinan and cisplatin, another antitumor drug, and its impact on cytokines IL-6, TNF-α, and TGF-β in the treatment of tumor. The results showed that lentinan enhanced the cytotoxic effect of cisplatin on tumor cells. Furthermore, it was proved that the combined treatment of lentinan and cisplatin enhanced the inhibitory effect of cisplatin on the expression of IL-6, TNF- α, TGF-β and tumor growth in mice bearing human ovarian cancer xenograft, human prostate tumor xenograft, and human non-small cell lung cancer xenograft.

1. Introduction

Lentinan (LNT) is a structural component of the mushroom cell wall which contains two main polymers, namely, chitin and β-glucans. The single strands of both molecules are linked to a hydrogen bridge bond to form a covalent bond between the two polymers. This process leads to the formation of a strong cell wall in which chitin fibers are linked to glucans to form a network of matrix [1]. The cell wall structure of Lentinus edodes can be divided into three layers. The outer layer is heteropolysaccharide and β-(1→3)-glucans with a β-(1→6) branch, which can be extracted with water and dilute alkali solution. The middle layer is mainly β-(1→6)-glucans containing a few β-(1→3)-branched chains, which are insoluble in water and can be extracted with strong alkali solution. The inner layer is a compound of chitin, β-glucans, and a small amount of acidic polymers [2].

The extraction method of polysaccharides varies with its structure and water solubility. The basic rule is to destroy the cell wall from the outer layer to the inner layer under mild conditions. The extracted polysaccharides can be further purified by a series of combinatorial techniques. Acid solution, alkali solution, and water are the three basic extraction solvents, in which water extraction is the most commonly seen. At present, several polysaccharides have been identified through different extraction methods and purification processes. The extraction method varies depending on the chemical structure of the polysaccharides from different parts of Lentinus edodes. Lentinan is insoluble in cold water and slightly soluble in hot water [3]. Another study showed that lentinan is β-d-(1,3)-d-glucopyranose with a branched chain of β-d-(1,6)-monosaccharide, which is water soluble and has the property of $[\alpha] \, d = +20o-+22o$ (NaOH) [4]. The structures of the side chains together with their physical properties are slightly different.

Based on the fact that lentinan is harmless and does not impose additional stress on the human body, lentinan is also considered as biological response modifiers (BRMS). It has been shown that lentinan has antitumor properties and its antitumor mechanism includes prevention of tumorigenesis (cancer prevention activities, enhancement of human immunomodulatory activity, and direct antitumor activity by

inducing apoptosis of tumor cells (direct tumor suppressor activity) [5].

Lentinan also has an effect of preventing cancer, which was discovered in farmers who were engaged in the cultivation of mushrooms. The study showed that the cancer mortality rate of these farmers was remarkably 40% lower than that of the common people [6]. It was proved that cytochrome P450s (CYP) is involved in the cancer prevention of lentinan. CYP is a kind of exogenous digestive enzyme mainly expressed in the liver. The study showed that inhibition of CYP activity helps to enhance the cancer prevention of lentinan, because the CYP1A subfamily induced by exogenous substances such as polycyclic aromatic hydrocarbon can metabolize carcinogens [7]. In Hashimoto's study, the female BALB/C mice were intraperitoneally injected with lentinan and it was observed that lentinan downregulated the expression of CYP and the activity and level of CYP1A induced by 3-methylcholanthrene. In addition, it was accompanied by the inhibition of the production of tumor necrosis factor-α (TNF-α) and the DNA-binding activity of aryl hydrocarbon receptor as well as the enhancement of the DNA-binding activity of nuclear factor-κB [7, 8]. These results suggested that mushroom polysaccharides, such as lentinan, had anticancer activity, as downregulation of CYP1A was considered to prevent metabolic activation of protocancer cells [7, 8]. In addition, the cancer prevention of lentinan may also be related to the fact that lentinan can inhibit the activity of telomerase [9]. Lentinan not only has anticancer activity but also can be used as an immunopotentiator to treat tumors in combination with anticancer drugs.

Since lentinan requires a functional T cell to exert its antitumor activity, it is also considered as a T cell-directed immunopotentiator. It has also been shown that the enhancement of the host immune system by β-(1→3)-glucans is mainly manifested in three aspects—an increase in the number of T helper cells (Th), enhancement of macrophage activation, and nonimmunological activity, where proliferation of macrophage and peripheral monocyte and the activation of lymphocyte and complement system are successively affected by stimulating the host defense mechanisms and colony-stimulating factor (CSF) of acute phase proteins [10, 11].

Cytokines are key factors in regulating immune responses under physiological and pathological conditions. Many cytokines have had a positive clinical effect on different malignancies in clinical trials [12]. It was shown that the cytokines IL6, TNF-α, and TGF-β play a very important role in the formation of tumor microenvironment [13].

Interleukin-6 (IL-6) is an essential cytokine involved in innate immunity. In a series of animal cancer models, IL-6 secreted by malignant tumor cells and mesenchymal stem cells has been proved to promote tumor growth [14]. Meanwhile, IL-6 also acts as a downstream effector of the oncogene ras [15] and is considered to be an important component of certain cancer cytokine networks, such as ovarian serous and clear cell carcinoma [16], multiple myeloma [17], ricin poisoning [18], and hepatocellular carcinoma [19].

There is preclinical evidence that IL-6 can increase the survival rate of ovarian cancer cells and enhance the resistance to chemotherapy by JAK/STAT signaling in tumor cells and translocation of IL-6 receptor alpha on tumor endothelial cells. In addition, IL-6 also has angiogenic properties and regulates immune cell infiltration, matrix response, and tumorigenic effects of Th17 lymphocytes [20, 21].

Many studies have confirmed that tumor necrosis factor-α (TNF-α) is a cytokine produced by activated macrophages and has multiple biological effects. TNF-α has been shown to inhibit the growth of both tumor cells and tumor-bearing mice in some vitro experiments, but clinical trials, taking it as an antitumor agent, have not achieved positive clinical results [22]. What is more, TNF-α has also been shown to be a key cytokine that promotes tumor cell proliferation and invasion in tumor microenvironment. After treatment with anti-TNF-α antibody in mice with in situ pancreatic tumors, the tumor growth and migration ability of mice were inhibited [23]. TNF-α has been proved to be closely associated with tumor cell growth and metastasis in studies of thoracic tumors, skin tumors, and gastrointestinal cancers [24]. The level of TNF-α has a certain correlation with the extent, recurrence, metastasis, and prognosis of malignant tumors in patients with prostate cancers [25]. Meanwhile, TNF-α has also been shown to enhance the invasive ability of pancreatic cancer cell lines in vitro [26].

The specific mechanism of TNF-α promoting malignant tumor progression has not been elucidated. Certain studies have found that TNF-α promotes the inflammatory response of various cytokines and chemokines, thereby affecting the formation and development of tumor vessels and promoting tumor invasion and metastasis [27]. TNF-α may also affect the activity of tumor cells and promote tumor cell proliferation by activating transcription factors and related gene cell signaling pathways [28]. TNF-α has also been proved to directly cause genetic damages, mutations, and DNA amplification, and thereby influence tumor development [29, 30]. Besides, TNF-α can also alter the function of immune cells and promote tumor progression [30].

Transforming growth factor-β (TGF-β) is a necessary cytokine for activating tumor stroma. TGF-β plays a vital role in tumor microenvironment, promotes the recruitment of immune cells, inhibits the antitumor immune response, and affects the differentiation of epithelial cells and endothelial cells. The signaling pathway of TGF-β could be simplified as the binding of TGF-β to its TGF-β receptor II (TβRII), which promoted the activation of TβRI molecules, and phosphorylated the sites of TβRI serine and threonine, thus activated the catalytic activity of TβRI and generated the trimeric complexes of TGF-β/TβRII/TβRI proteins. The complexes could be activated by autophosphorylation and activated the TGF-β/Smad pathway through a series of signal activations, thereby inducing or inhibiting gene expression [31].

The study was to investigate the antitumor effect of the combined use of lentinan and antitumor drug cisplatin and its effect on cytokines IL-6, TNF-α and TGF-β in tumor therapy. Its specific mechanism, however, remains to be discovered in further studies. In general, the study provides a potential therapeutic method and research protocol for cancer treatment.
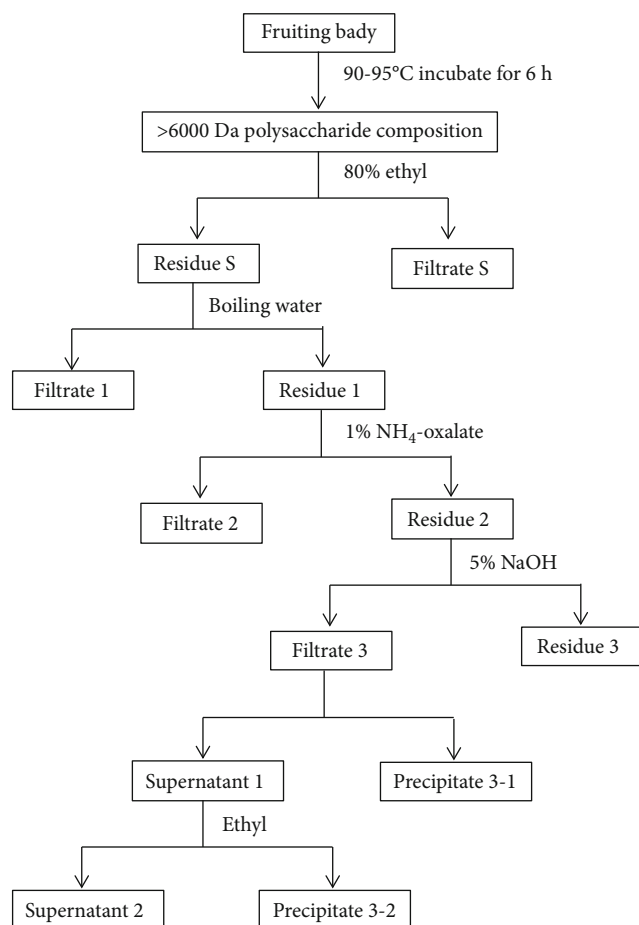
Fruiting body

90-95°C incubate for 6 h

>6000 Da polysaccharide composition

80% ethyl

Residue S

Filtrate S

Boiling water

Filtrate 1

Residue 1

1% NH$_4$-oxalate

Filtrate 2

Residue 2

5% NaOH

Filtrate 3

Residue 3

Supernatant 1

Precipitate 3-1

Ethyl

Supernatant 2

Precipitate 3-2

FIGURE 1: Extraction of lentinan from the shiitake.

2. Materials and Methods

2.1. Experimental Materials. Hey ovarian carcinoma cells, prostate cancer LNCaP cells, and non-small cell lung cancer A549 cells were all purchased from Shanghai Cell Bank of the Chinese Academy of Sciences. Fetal bovine serum (FBS), RPMI-1640 medium, EDTA trypsin, penicillin, and streptomycin were purchased from Gibco Life Technologies. The CCK-8 kit was obtained from Dojindo (Japan). IL-6 ELISA kit and TNF-α ELISA kit were purchased from Xinbosheng Biotechnology Co., Ltd. RNAiso Reagent (total RNA extraction reagent) and SYBR® Premix Ex TaqTM II Reagent and PrimeScript™ RT Master Mix (reverse transcription kit) were purchased from Takara. Ethanol, chloroform, and methanol were purchased from Sinopharm Chemical Reagent Co., Ltd. Diethyl pyrocarbonate (DEPC) was purchased from Beyotime Biotechnology. SPF male BALB/C/nu nude mice weighing 18 ± 2 g were purchased from Shanghai Slack Laboratory Animal Co., Ltd.

2.2. Preparation of Lentinan (LNT). Lentinula edodes powder dissolved in water was incubated at 90-95°C for 6 hours. The ultrafiltration membrane was used to filter components having a molecular mass greater than 6000 Da, and only Lentinula edodes extract with molecular weight less than 6000 Da was collected. The shiitake material, from which

low molecular weight substances were removed using 80% ethanol, was then extracted three times with water (100°C, 3 h), 2% ammonium oxalate (100°C, 6 h), and 5% sodium hydroxide (80°C, 6 h). The polysaccharides obtained in the first time were water soluble, while those in the other two times were water insoluble. The extracted polysaccharides were further purified by different concentrations of ethanol and other technologies. Firstly, neutral and acidic polysaccharides were separated by DEAE cellulose column in ion-exchange chromatography. The neutral polysaccharides were further classified into α-glucan (adsorbed fraction) and β-glucan (nonabsorbed fraction) by gel filtration and affinity chromatography. Purified polysaccharides were obtained by the elution of acidic polysaccharides with 1 M sodium chloride [5], as shown in Figure 1.

2.3. Cell Culture. Hey ovarian carcinoma cells, prostate cancer LNCaP cells, and non-small cell lung cancer A549 cells were cultured in RPMI-1640 medium containing 10% fetal bovine serum, penicillin (100 U/ml), and streptomycin (100 mg/ml) in a humidified atmosphere of 5% CO_2 at 37°C. Cells in exponential growth phase were collected for the investigation of antitumor effect.

2.4. Detection of Cytotoxic Activity of Cells by CCK8 Assay. Cell suspension (100 μL) was inoculated in a 96-well plate. The plate was then precultured at 37°C in an incubator supplied with 5% CO_2. Thereafter, 10 μL of CCK8 solution was added to each well, and the plate was incubated for 2 hours, followed by the measurement of absorbance at 450 nm.

Viability calculation : cell viability $*$ (%) = [A(dosing) − A(blank)] × 100/[A(0 dosing) − A(blank)], where A (dosing) is the absorbance of a well containing cells, CCK8 solution, and drug solution; A (blank) is the absorbance of a well having a medium and CCK8 solution but no cells; A (0 dosing) is the absorbance of a well having cells and CCK8 solution but no drug solution; and $*$ is the cell viability (cell proliferation or cytotoxic activity).

2.5. Establishment of Tumor-Bearing Mice Models

2.5.1. Mice Bearing Human Ovarian Cancer Xenograft. Hey cells in logarithmic growth phase were prepared into single cell suspension. The 0.2 ml of cell suspension (containing about 1×10^5 Hey cells) was taken and inoculated subcutaneously into the right axilla of BALB/c/nu nude mice. After the tumor grew to about 50 mm^3, the tumor-bearing mice were divided into 3 groups for drug treatment: the normal group, treated with intraperitoneal injection of the same amount of normal saline for 30 days; the cisplatin group, given intraperitoneal injection of 0.2 ml (2 mg kg^{-1}) cisplatin solution once a day for 30 days; the cisplatin-lentinan group, treated with intraperitoneal injection of 0.2 ml (cisplatin: 7 mg kg^{-1}; lentinan: 25 mg kg^{-1}) cisplatin and lentinan solution once a day for 30 days. The size and weight of tumor were measured every 3 days for generating a tumor growth curve.

2.5.2. Mice Bearing Human Prostate Tumor Xenograft. LNCaP cells in logarithmic growth phase were prepared into single cell suspension. 0.2 ml of the cell suspension (containing about

1×10^6 LNCaP cells) was taken and inoculated subcutaneously into the right axilla of BALB/C/nu nude mice. As the tumor grew to about 50 mm^3, the tumor-bearing mice were divided into 3 groups for drug treatment: the normal group, treated with intraperitoneal injection of the same amount of normal saline for 30 days; the cisplatin group, given intraperitoneal injection of 0.2 ml (7 mg kg^{-1}) cisplatin solution once a day for 30 days; and the cisplatin-lentinan group, treated with intraperitoneal injection of 0.2 ml (cisplatin: 7 mg kg^{-1}; lentinan: 25 mg kg^{-1}) cisplatin and lentinan solution once a day for 30 days. The size and weight of tumor were measured every 3 days for generating a tumor growth curve.

2.5.3. Mice Bearing Human Non-Small Cell Lung Cancer Xenograft. A549 cells in logarithmic growth phase were prepared into single cell suspension. 0.2 ml of the cell suspension (containing about 1×10^7 A549 cells) was taken and inoculated subcutaneously into the right axilla of BALB/c/nu nude mice. When the tumor size was up to 50 mm^3, the tumor-bearing mice were divided into 3 groups for drug treatment: the normal group, treated with intraperitoneal injection of the same amount of normal saline for 30 days; the cisplatin group, given intraperitoneal injection of 0.2 ml (7 mg kg^{-1}) cisplatin solution once a day for 30 days; and the cisplatin-lentinan group, treated with intraperitoneal injection of 0.2 ml (containing cisplatin: 7 mg kg^{-1}; lentinan: 25 mg kg^{-1}) cisplatin and lentinan solution once a day for 30 days. The size and weight of tumor were measured every 3 days for generating a tumor growth curve.

2.6. ELISA Test. Serum was prepared from the orbit blood sampling. 100 μl per well of serum was then added to the enzyme label plate coated with monoclonal antibody and mixed gently. After incubation for 90 min at 37°C, the supernatant liquid was discarded, and the secondary antibody was added for further incubation at 37°C for 1 h. Working solutions of the enzyme conjugate was then added, followed by incubation at 37°C for 30 min. Afterwards, the supernatant was discarded, and the substrate solution was added for further incubation in the dark for 20 min. Finally, the termination solution was added to stop the reaction. The value of optical density of each well was measured at a wavelength of 450 nm. Finally, the content of IL-6, TNF-α, and TGF-β in serum was calculated according to the standard curve.

2.7. Flow Cytometry Assessment. We investigated the expression of cluster of determinant (CD) of cell surface molecules targeting immunophenotyping of cells. Single-cell suspension was extracted from tumor-bearing mice, and the mice were cultured with monoclonal antibodies, CD3-PERCP, CD4-FITC, FOXP3-PE, and IL-17-APC. After incubation at 4°C for 3 hours, the expressing cell population was analyzed by flow cytometer (Becton Dickinson and Company).

2.8. Statistical Analysis. The experimental data were expressed as mean ± S.E.M and were analyzed by oringe 8.0 software. Significant difference was measured by SPSS 19.0 one-way analysis of variance (ANOVA). $^*P < 0.05$ and $^{**}P < 0.01$ were considered significant statistically.

3. Results

3.1. Enhanced Cytotoxic Effect of Cisplatin on Tumor Cells by Lentinan. To explore the antitumor effect of lentinan, the cytotoxic effect of lentinan, cisplatin, or the combined use of both on Hey human ovarian carcinoma cells, LNCaP human prostate cancer cells and human non-small cell lung cancer A549 cells were evaluated by CCK-8 assay. The results showed that the IC50 of lentinan for killing Hey cells, LNCap cells, and A549 cells was 800 μM, and the IC50 of cisplatin for killing the cells was 30 μM. The combined use of lentinan (800 μM) and cisplatin reduced the proliferation of Hey cells, LNCap cells, and A549 cells in a dose-dependent manner (Figures 2(a) and 2(b)). In the meantime, the combined treatment of lentinan and cisplatin significantly increased the killing effect of cisplatin on the tumor cells ($P < 0.05$, as shown in Figures 2(c), 2(d), and 2(e)).

3.2. Enhanced Inhibitory Effect of Cisplatin on Expressions of IL-6, TNF-α, TGF-β, and Tumor Growth in Mice Bearing Human Ovarian Cancer Xenograft by Combined Treatment of Lentinan and Cisplatin. To explore the effect of the combined use of lentinan and cisplatin on the cytokines IL-6, TNF-α, and TGF-β in tumor therapy, the expressions of IL-6, TNF-α, and TGF-β in mice bearing human ovarian cancer xenograft after the combination therapy were detected by ELISA and qPCR. The experimental results are shown in Figure 3. The expressions of IL-6, TNF-α, and TGF-β proteins in serum of tumor-bearing mice in the normal saline group were 95.40333 ± 2.69563 pg/ml, 1536.84333 ± 41.83909 pg/ml, and 194 ± 2.5 pg/ml, respectively. The expressions of IL-6, TNF-α, and TGF-β proteins in serum of tumor-bearing mice in cisplatin group were 53.02667 ± 3.09189 pg/ml, 1270.97 ± 26.21165 pg/ml, and 153 ± 3.84 pg/ml, respectively. The expressions of IL-6, TNF-α, and TGF-β proteins in serum of tumor-bearing mice in lentinan-cisplatin group were 43.74333 ± 2.31067 pg/ml, 966.98333 ± 34.28658 pg/ml, and 137 ± 2.51 pg/ml, respectively. The expressions of IL-6, TNF-α, and TGF-β in serum of mice were significantly decreased in both the cisplatin group and lentinan-cisplatin group ($P < 0.01$) compared with the normal saline group. The expressions of IL-6, TNF-α, and TGF-β were significantly decreased in the lentinan-cisplatin group ($P < 0.05$) compared with the cisplatin group. The results indicated that the combined use of lentinan and cisplatin significantly enhanced the inhibitory effect of cisplatin on the expressions of IL-6, TNF-α, and TGF-β in the serum of mice bearing human ovarian cancer xenograft (Figures 3(a), 3(b), and 3(c)). Meanwhile, the combination enhanced the inhibitory effect of cisplatin on tumor growth of mice bearing human ovarian cancer xenograft as well (Figure 3(d)).

3.3. Enhanced Inhibitory Effect of Cisplatin on Expressions of IL-6, TNF-α, and TGF-β and Tumor Growth in Mice Bearing Human Prostate Tumor Xenograft by Combination Therapy of Lentinan and Cisplatin. To explore the effect of combined use of lentinan and cisplatin on the cytokines IL-6, TNF-α, and TGF-β in tumor therapy, the expressions of IL-6, TNF-
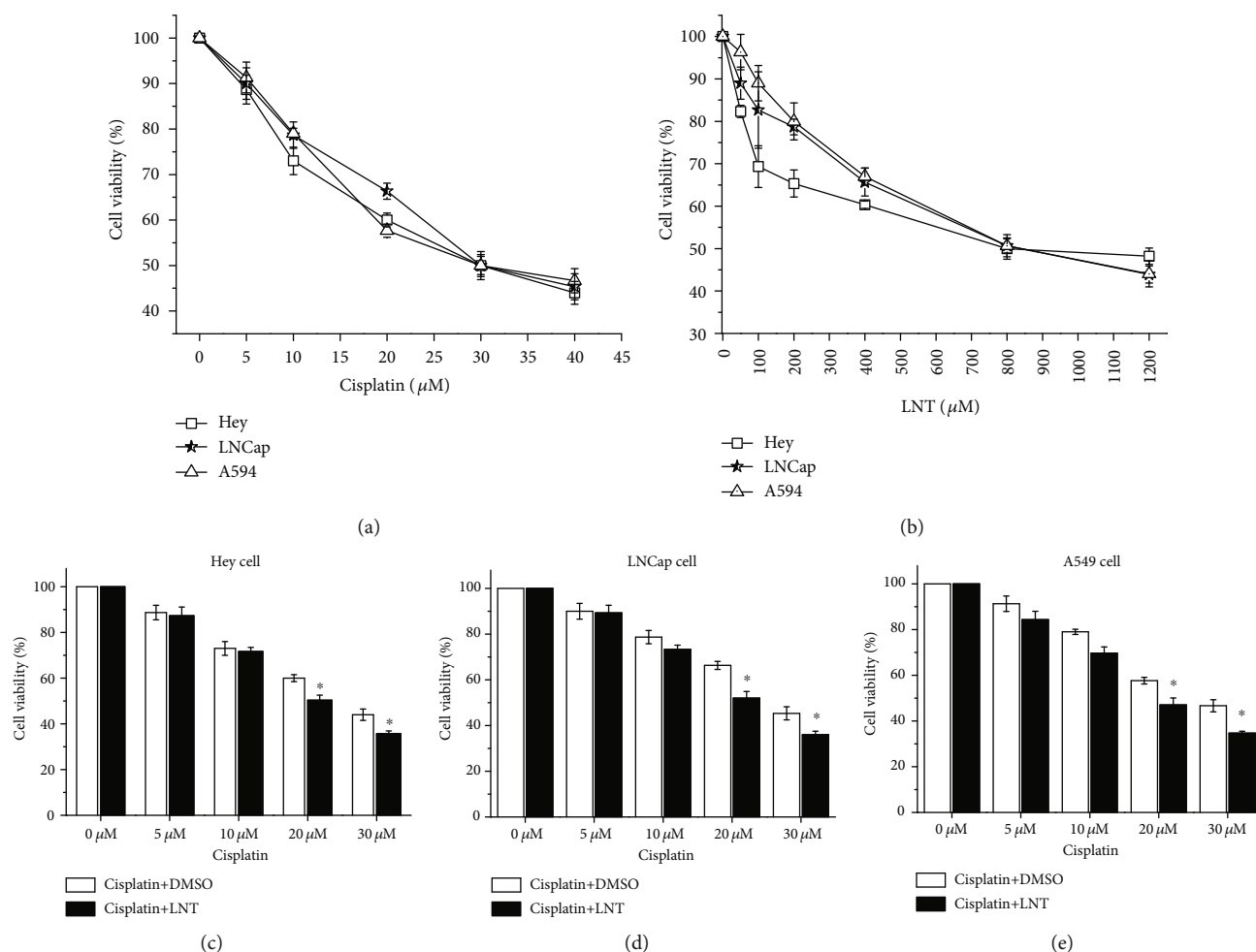
FIGURE 2: Cytotoxic effect of cisplatin on tumor cells enhanced by lentinan. (a) The cytolytic activity of cisplatin on different doses to Hey cells, LNCap cells, and A594 cells. (b) The cytolytic activity of LNT on different doses to Hey cells, LNCap cells, and A594 cells. (c–e) The cytolytic activity of the combination of LNT (800 μM) and cisplatin to Hey cells (c), LNCap cells (d), and A594 cells (e). $^{*}P < 0.05$, $^{**}P < 0.01$, significantly different from the cisplatin+DMSO group.

α, and TGF-β in mice bearing human prostate tumor xenograft after the combination therapy were detected by ELISA and qPCR. The experimental results are shown in Figure 4. The expressions of IL-6, TNF-α, and TGF-β proteins in serum of tumor-bearing mice in the normal saline group were 95.40667 ± 2.83179 pg/ml, 1542.17667 ± 18.39545 pg/ml, and 1661 ± 15.37 pg/ml, respectively. The expressions of IL-6, TNF-α, and TGF-β proteins in serum of tumor-bearing mice in the cisplatin group were 52.97 ± 2.29613 pg/ml, 1264.63667 ± 32.63896 pg/ml, and 126.331 ± 8.298 pg/ml, respectively. The expressions of IL-6, TNF-α, and TGF-β proteins in serum of tumor-bearing mice in the lentinan-cisplatin group were 44 ± 1.45039 pg/ml, 965.31667 ± 44.84394 pg/ml, and 107 ± 3.79 pg/ml, respectively. The expressions of IL-6, TNF-α, and TGF-β in serum of mice were significantly decreased in both the cisplatin group and lentinan-cisplatin group ($P < 0.01$) compared with the normal saline group. The expressions of IL-6, TNF-α, and TGF-β were significantly decreased in the lentinan-cisplatin group ($P < 0.05$) compared with the cisplatin group. The results suggested that the combined use of lentinan and cisplatin significantly

enhanced the inhibitory effect of cisplatin on the expressions of IL-6, TNF-α, and TGF-β in the serum of mice bearing human prostate tumor xenograft (Figures 4(a), 4(b), and 4(c)). Meanwhile, the combination enhanced the inhibitory effect of cisplatin on tumor growth of mice bearing human prostate tumor xenograft as well (Figure 4(d)).

3.4. Enhanced Inhibitory Effect of Cisplatin on Expressions of IL-6, TNF-α, and TGF-β and Tumor Growth in Mice Bearing Human Non-Small Cell Lung Cancer Xenograft by Combination Therapy of Lentinan and Cisplatin. To explore the effect of combined use of lentinan and cisplatin on the cytokines IL-6, TNF-α, and TGF-β in tumor therapy, the expressions of IL-6, TNF-α, and TGF-β in mice bearing human non-small cell lung cancer xenograft after the combination therapy were detected by ELISA and qPCR. The experimental results are shown in Figure 5. The expressions of IL-6, TNF-α, and TGF-β proteins in serum of tumor-bearing mice in the normal saline group were 96.53 ± 2.97073 pg/ml, 1548.63 ± 10.38419 pg/ml, and 194.67 ± 3.84 pg/ml, respectively. The expressions of IL-6, TNF-α,
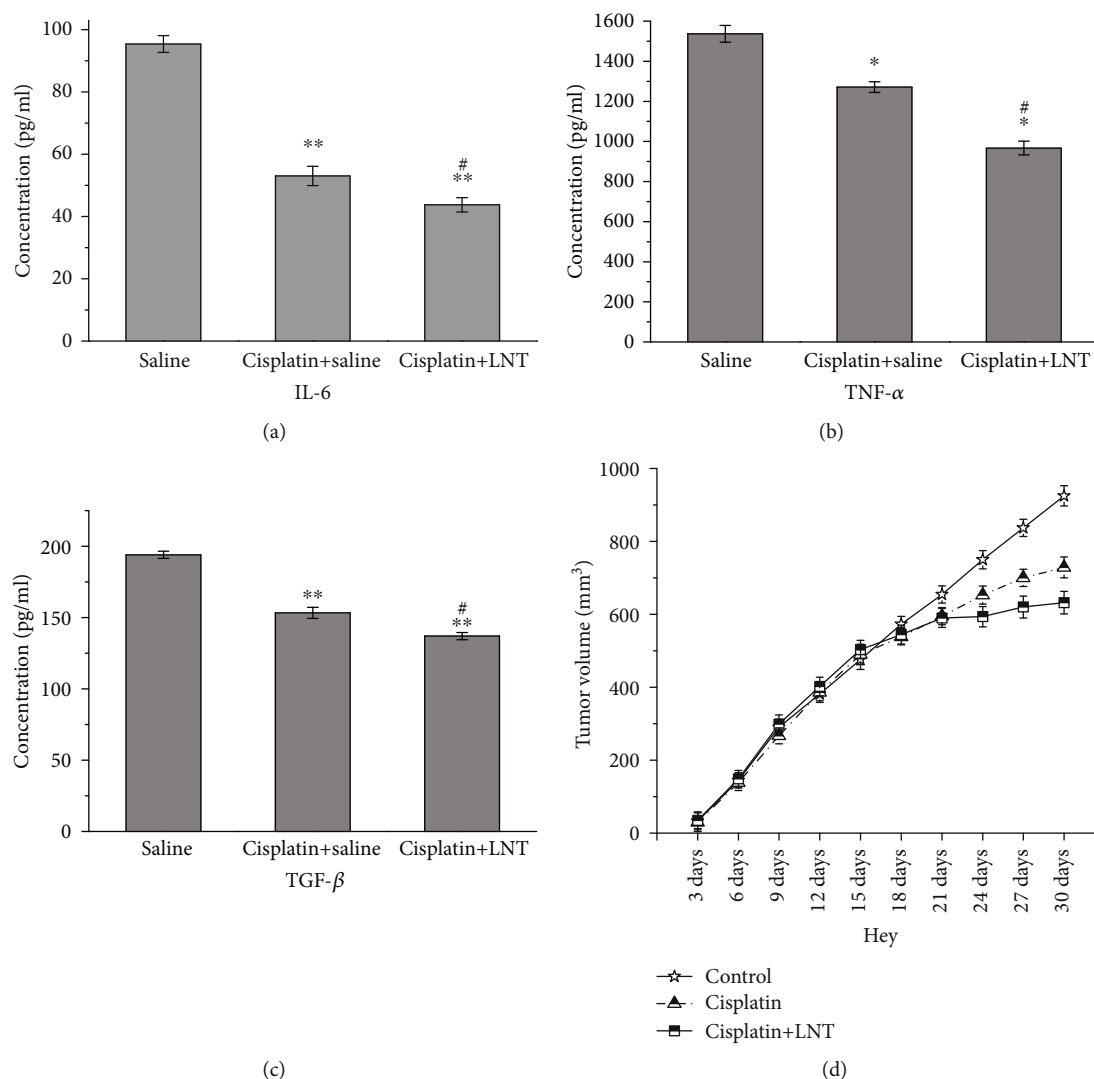
(a)

(b)

(c)

(d)

FIGURE 3: Enhanced inhibitory effect of cisplatin on expressions of IL-6, TNF-α, and TGF-β and tumor growth in mice bearing human ovarian cancer xenograft by combination therapy of lentinan and cisplatin. (a–c) It is enhanced by the combined treatment of lentinan and cisplatin that the expression of IL-6 (a), TNF-α (b), and TGF-β (c) on the serum of mice bearing ovarian cancer induced by cisplatin. (d) It is enhanced by the combined treatment of lentinan and cisplatin that the inhibition of tumor growth of mice bearing ovarian cancer by cisplatin. $^{*}P < 0.05$, $^{**}P < 0.01$, significantly different from the saline group. $^{\#}P < 0.05$, $^{\#\#}P < 0.01$, significantly different from the cisplatin+saline group.

and TGF-β proteins in serum of tumor-bearing mice in cisplatin group were 54.03333 ± 1.92365 pg/ml, 1259.42333 ± 49.99775 pg/ml, and 140.33 ± 8.089778 pg/ml, respectively. The expressions of IL-6, TNF-α, and TGF-β proteins in serum of tumor-bearing mice in the lentinan-cisplatin group were 45.37667 ± 0.69528 pg/ml, 964.77 ± 56.22525 pg/ml, and 107.1 ± 4.37 pg/ml, respectively. The expressions of IL-6, TNF-α, TGF-β in serum of mice were significantly decreased in both the cisplatin group and lentinan-cisplatin group ($P < 0.01$) compared with the normal saline group. The expressions of IL-6, TNF-α, and TGF-β were significantly decreased in the lentinan-cisplatin group ($P < 0.05$) compared with the cisplatin group. The results indicated that the combined use of lentinan and cisplatin significantly enhanced the inhibitory effect of cisplatin on the expressions of IL-6, TNF-α, and TGF-β in the serum of mice bearing

human non-small cell lung cancer xenograft (Figures 5(a), 5(b), and 5(c)). Meanwhile, the combination enhanced the inhibitory effect of cisplatin on tumor growth of mice bearing human non-small cell lung cancer xenograft as well (Figure 5(d)).

3.5. Enhanced Antitumor Effect of Cisplatin in Tumor Microenvironment in Mice Bearing Human Non-Small Cell Lung Cancer Xenograft by Combination Therapy of Lentinan and Cisplatin. To further investigate the anticancer mechanism of the combined use of lentinan and cisplatin, we detected the expressions of cytokines IL-6, TNF-α, TGF-β, regulatory T cells (Tregs), and T helper cell 17 (Th17) in tumor-infiltrating cells of non-small cell lung cancer-bearing mice. Tregs play an important role in the maintenance of immunological self-tolerance and immune homeostasis.
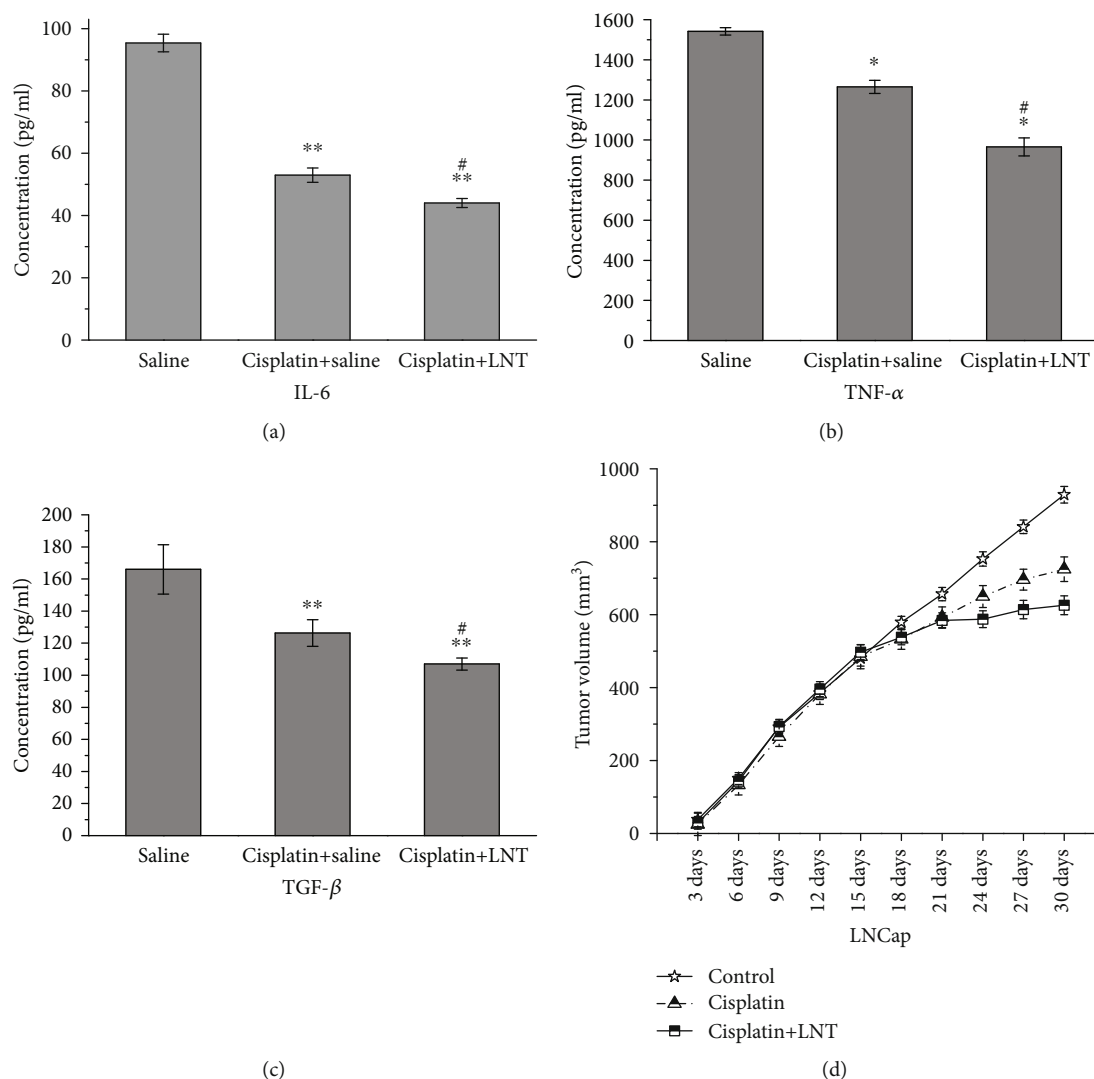
(a)

(b)

(c)

(d)

FIGURE 4: Enhanced inhibitory effect of cisplatin on expressions of IL-6, TNF-α, and TGF-β and tumor growth in mice bearing human prostate tumor xenograft by combination therapy of lentinan and cisplatin. (a–c) It is enhanced by the combined treatment of lentinan and cisplatin that the expression of IL-6 (a), TNF-α, and TGF-β enhanced by the combined treatment for prostate cancer induced by cisplatin. (d) It is enhanced by the combined treatment of lentinan and cisplatin that the inhibition of tumor growth of mice bearing prostate cancer by cisplatin. $^{*}P < 0.05$, $^{**}P < 0.01$, significantly different from the saline group. $^{#}P < 0.05$, $^{##}P < 0.01$, significantly different from the cisplatin+saline group.

Th17 as a newly discovered T cell subpopulation capable of secreting interleukin 17(IL-17) is of great significance in the body's defense response. Transforming growth factor b (TGF-β), IL-6, IL-23, and IL-21 promote the differentiation and formation of Th17. Studies have shown that the Th17/Treg balance regulation is the focus of current studies, and Th17/Treg immune imbalance has been linked to the tumorigenesis [6].

The results of our study showed that the expressions of IL-6, TNF-α, and TGF-β in the supernatant of single-cell suspension of human non-small cell lung cancer tumor-bearing mice were significantly decreased in lentinan-cisplatin group (Figure 6) compared with the cisplatin group, which is consistent with the expressions in serum of the tumor-bearing mice.

Tregs are characterized by the expression of transcription factor FoxP3, and Th17 cells are characterized by that of IL-17. Therefore, in this study, Tregs and Th17 cells were labeled with FoxP3 antibody and IL-17 antibody, respectively. The results indicated that compared with the cisplatin group, the lentinan-cisplatin group showed significantly decreased Tregs but increased Th17 in the single-cell suspension of mice bearing human non-small cell lung cancer xenograft (Figure 7).

4. Discussion

The results of this study demonstrated that lentinan enhanced the cytotoxic effect cisplatin on tumor cells and that the combined treatment of lentinan and cisplatin
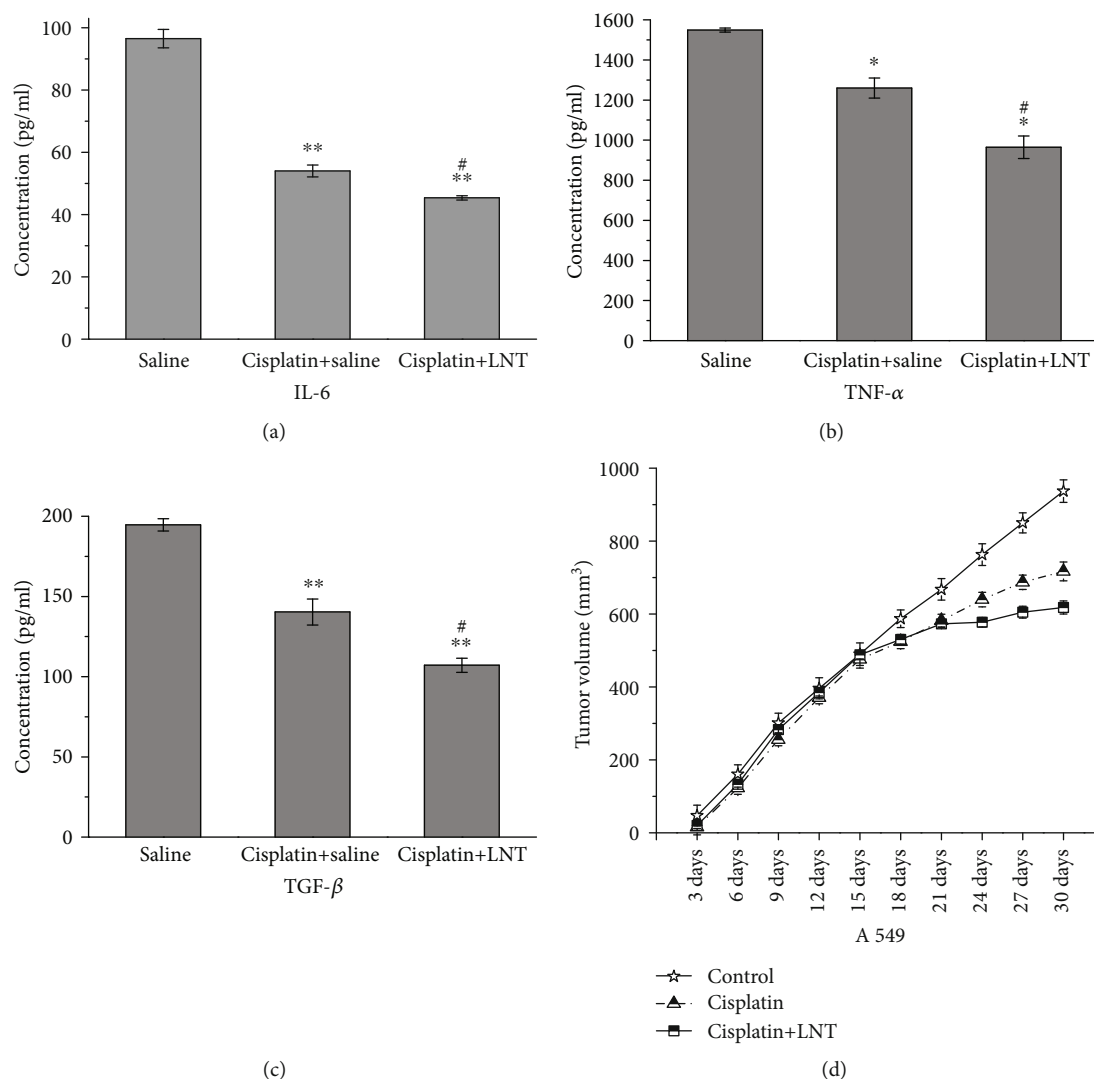
(a)

(b)

(c)

(d)

FIGURE 5: Enhanced inhibitory effect of cisplatin on expressions of IL-6, TNF-α, and TGF-β and tumor growth in mice bearing human non-small cell lung cancer xenograft by combination therapy of lentinan and cisplatin. (a–c) It is enhanced by the combined treatment of lentinan and cisplatin that the expression of IL-6 (a), TNF-α (b), and TGF-β (c) on the serum of mice bearing non-small cell lung cancer induced by cisplatin. (d) It is enhanced by the combined treatment of lentinan and cisplatin that the inhibition of tumor growth of mice bearing non-small cell lung cancer by cisplatin. $^{*}P < 0.05$, $^{**}P < 0.01$, significantly different from the saline group. $^{\#}P < 0.05$, $^{\#\#}P < 0.01$, significantly different from the cisplatin+saline group.
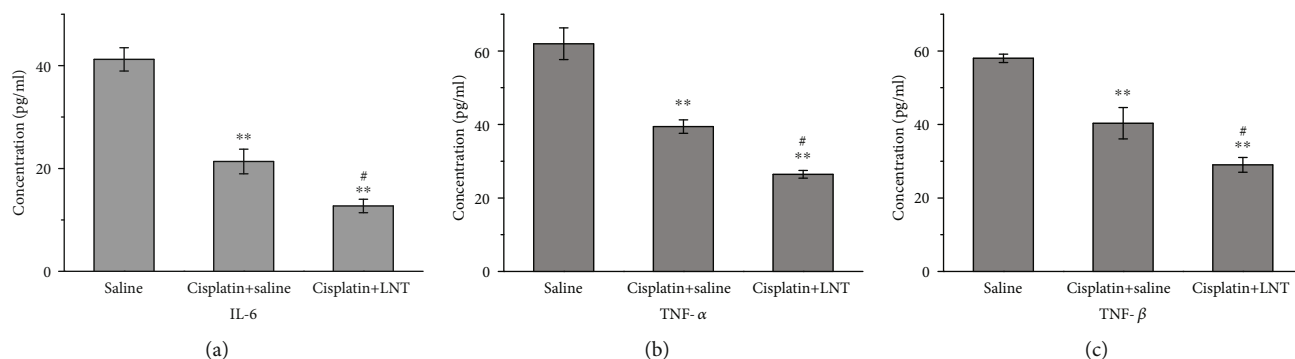

(a)

(b)

(c)

FIGURE 6: The expression of IL-6, TNF-α, and TGF-β on the tumor of tumor-bearing mice with non-small cell lung cancer. (a–c) The expression of IL-6 (a), TNF-α (b), and TGF-β (c) on the tumor cell suspension supernatant of tumor-bearing mice with non-small cell lung cancer after the combined treatment of lentinan and cisplatin. $^{*}P < 0.05$, $^{**}P < 0.01$, significantly different from the saline group. $^{\#}P < 0.05$, $^{\#\#}P < 0.01$, significantly different from the cisplatin+saline group.
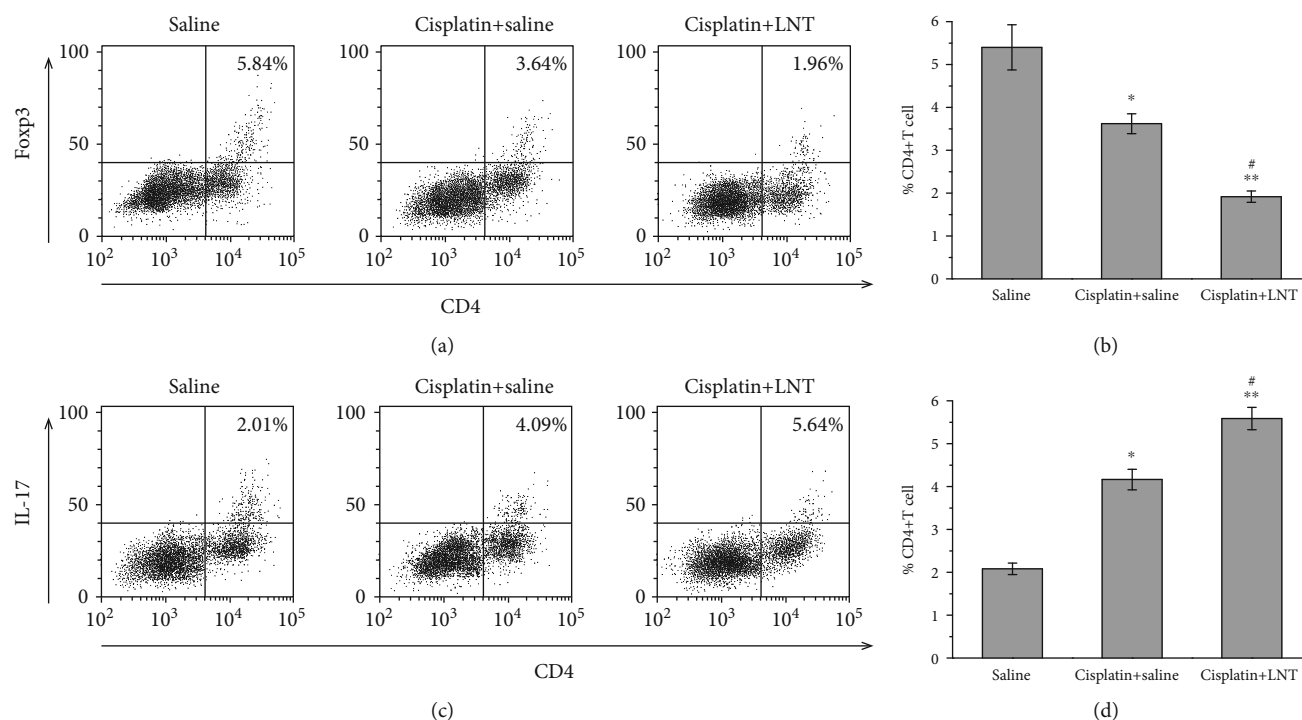
FIGURE 7: Change of Treg and Th17 cells in tumor tissues of human non-small cell lung cancer-bearing mice. (a, b) Tregs in mouse tumors were significantly reduced after the combined treatment of lentinan and cisplatin. (c, d) Th17 cells in mouse tumors were significantly increased after the combined treatment of lentinan and cisplatin.

enhanced the inhibitory effect of cisplatin on the expression of IL-6, TNF-α, and TGF-β and tumor growth in mice bearing human ovarian cancer xenograft, human prostate tumor xenograft, and human non-small cell lung cancer xenograft.

Cytokines are key factors in regulating immune responses under physiological and pathological conditions. Many cytokines have shown positive effect on different malignancies in clinical trials [12]. Tumor microenvironment is the result of the interaction of many factors, including natural immune cells such as macrophages, neutrophils, mast cells, myeloid-derived suppressor cells, dendritic cells, natural killer cells, and adaptive immune cells such as T lymphocytes and B lymphocytes, vascular and lymphatic networks, interstitial fibroblasts, and growth factors, inflammatory factors, chemokines, and the like generated by autocrine or paracrine of cells. Cytokines IL6, TNF-α, and TGF-β play a quite important role in the formation of tumor microenvironment [13].

High levels of IL-6 have been found in both plasma and malignant ascites [32] in patients with advanced ovarian cancer, which has been proved to be associated with poor prognosis of the cancer [33]. Some ovarian cancer cells constitutively secrete IL-6. When these cells are cocultured with other cells from ovarian cancer microenvironment [34, 35], the expression level of IL-6 can be found to be increased. We found that IL-6 is part of the autocrine cytokine network of malignant ovarian tumor cells [35]. The network was involved in the regulation of the cytokines TNF-α and IL-1β, CCl2, CXCL12, and VEGF and could affect angiogenesis in tumor microenvironment by a paracrine manner.

Th17 cell-mediated immunity plays a critical role in maintaining the balance of the mucosa and hematopoietic system. Meanwhile, Th17 cell response, if too intense, can induce autoimmune diseases. It was shown that Th17 cell-induced excessive inflammation and Treg-induced overimmunosuppression (i.e., imbalance of Th17/Tregs) may result in carcinogenesis [7]. In this study, we found that Tregs were significantly reduced and Th17 cells were obviously increased in single-cell suspension of mice bearing human non-small cell lung cancer xenograft in lentinan-cisplatin group as compared with the cisplatin group. And the expressions of IL-6, TNF-α, and TGF-β in the supernatant of single-cell suspension were significantly reduced. The above results suggested that lentinan may regulate the balance of Th17/Tregs by decreasing the expressions of IL-6, TNF-α, and TGF-β, thereby enhancing the antitumor effect of cisplatin.

Our study on the combination therapy of lentinan and cisplatin against tumors provides a potential solution for future cancer treatment.

Data Availability

The data used to support the findings of this study are included within the article.

Conflicts of Interest

The authors declare that they have no conflicts of interest.

Acknowledgments

References

[1] O. Rop, J. Mlcek, and T. Jurikova, "Beta-glucans in higher fungi and their health effects," *Nutrition Reviews*, vol. 67, no. 11, pp. 624–631, 2009.

[2] M. Shida, Y. Ushioda, T. Nakajima, and K. Matsuda, "Structure of the alkali-insoluble skeletal glucan of Lentinus edodes," *Journal of Biochemistry*, vol. 90, no. 4, pp. 1093–1100, 1981.

[3] G. Chihara, J. Hamuro, Y. Maeda, Y. Arai, and F. Fukuoka, "Fractionation and purification of the polysaccharides with marked antitumor activity, especially lentinan, from Lentinus edodes (Berk.) Sing. (an edible mushroom)," *Cancer Research*, vol. 30, no. 11, pp. 2776–2781, 1970.

[4] B. Z. Zaidman, M. Yassin, J. Mahajna, and S. P. Wasser, "Medicinal mushroom modulators of molecular targets as cancer therapeutics," *Applied Microbiology and Biotechnology*, vol. 67, no. 4, pp. 453–468, 2005.

[5] S. P. Wasser, "Medicinal mushrooms as a source of antitumor and immunomodulating polysaccharides," *Applied Microbiology and Biotechnology*, vol. 60, no. 3, pp. 258–274, 2002.

[6] T. Ikekawa, "Beneficial effects of edible and medicinal mushrooms on health care," *International Journal of Medicinal Mushrooms*, vol. 3, no. 4, p. 2, 2001.

[7] T. Hashimoto, Y. Nonaka, K.-i. Minato et al., "Suppressive effect of polysaccharides from the edible and medicinal Mushrooms,Lentinus edodesandAgaricus blazei, on the expression of cytochrome P450s in mice," *Bioscience, Biotechnology, and Biochemistry*, vol. 66, no. 7, pp. 1610–1614, 2002.

[8] A. T. Yap and M. L. Ng, "An improved method for the isolation of lentinan from the edible and medicinal shiitake mushroom, Lentinus edodes (Berk.) Sing. (Agaricomycetideae)," *International Journal of Medicinal Mushrooms*, vol. 3, no. 1, p. 11, 2001.

[9] K. Sreenivasulu, M. Vijayalakshmi, and K. R. S. S. Rao, "hTERT gene inhibition studies in cancer cells by using polysaccharide lentina," *Journal of Medical Genetics & Genomics*, vol. 3, no. 1, pp. 7–12, 2011.

[10] S. P. Wasser, "Medicinal mushroom science: current perspectives, advances, evidences, and challenges," *Biomedical Journal*, vol. 37, no. 6, pp. 345–356, 2014.

[11] X. Xu, H. Yan, J. Tang, J. Chen, and X. Zhang, "Polysaccharides inLentinus edodes: isolation, structure, immunomodulating activity and future prospective," *Critical Reviews in Food Science and Nutrition*, vol. 54, no. 4, pp. 474–487, 2014.

[12] Z. Valedkarimi, H. Nasiri, L. Aghebati-Maleki, and J. Majidi, "Antibody-cytokine fusion proteins for improving efficacy and safety of cancer therapy," *Biomedicine & Pharmacotherapy*, vol. 95, pp. 731–742, 2017.

[13] B. Burkholder, R. Y. Huang, R. Burgess et al., "Tumor-induced perturbations of cytokines and immune cell networks," *Biochimica et Biophysica Acta*, vol. 1845, no. 2, pp. 182–201, 2014.

[14] S. Grivennikov and M. Karin, "Autocrine IL-6 signaling: a key event in tumorigenesis?," *Cancer Cell*, vol. 13, no. 1, pp. 7–9, 2008.

[15] B. Ancrile, K. H. Lim, and C. M. Counter, "Oncogenic Ras-induced secretion of IL6 is required for tumorigenesis," *Genes & Development*, vol. 21, no. 14, pp. 1714–1719, 2007.

[16] M. S. Anglesio, J. George, H. Kulbe et al., "IL6-STAT3-HIF signaling and therapeutic response to the angiogenesis inhibitor sunitinib in ovarian clear cell cancer," *Clinical Cancer Research*, vol. 17, no. 8, pp. 2538–2548, 2011.

[17] K. H. Shain, D. N. Yarde, M. B. Meads et al., "Beta1 integrin adhesion enhances IL-6-mediated STAT3 signaling in myeloma cells: implications for microenvironment influence on tumor survival and proliferation," *Cancer Research*, vol. 69, no. 3, pp. 1009–1015, 2009.

[18] N. Nishimoto, Y. Kanakura, K. Aozasa et al., "Humanized anti-interleukin-6 receptor antibody treatment of multicentric Castleman disease," *Blood*, vol. 106, no. 8, pp. 2627–2632, 2005.

[19] W. E. Naugler, T. Sakurai, S. Kim et al., "Gender disparity in liver cancer due to sex differences in MyD88-dependent IL-6 production," *Science*, vol. 317, no. 5834, pp. 121–124, 2007.

[20] C. W. Lo, M. W. Chen, M. Hsiao et al., "IL-6 trans-signaling in formation and progression of malignant ascites in ovarian cancer," *Cancer Research*, vol. 71, no. 2, pp. 424–434, 2011.

[21] Y. Miyahara, K. Odunsi, W. Chen, G. Peng, J. Matsuzaki, and R. F. Wang, "Generation and regulation of human CD4+ IL-17-producing T cells in ovarian cancer," *Proceedings of the National Academy of Sciences of the United States of America*, vol. 105, no. 40, pp. 15505–15510, 2008.

[22] N. J. Roberts, S. Zhou, Diaz la Jr, and M. Holdhoff, "Systemic use of tumor necrosis factor alpha as an anticancer agent," *Oncotarget*, vol. 2, no. 10, pp. 739–751, 2011.

[23] J. H. Egberts, V. Cloosters, A. Noack et al., "Anti-tumor necrosis factor therapy inhibits pancreatic tumor growth and metastasis," *Cancer Research*, vol. 68, no. 5, pp. 1443–1450, 2008.

[24] K. Zins, D. Abraham, M. Sioud, and S. Aharinejad, "Colon cancer cell-derived tumor necrosis factor-alpha mediates the tumor growth-promoting response in macrophages by up-regulating the colony-stimulating factor-1 pathway," *Cancer Research*, vol. 67, no. 3, pp. 1038–1045, 2007.

[25] M. Ohori, T. M. Wheeler, and P. T. Scardino, "The new American joint committee on Cancer and International Union against Cancer TNM classification of prostate cancer. Clinicopathologic correlations," *Cancer*, vol. 74, no. 1, pp. 104–114, 1994.

[26] P. Radhakrishnan, V. Chachadi, M. F. Lin, R. Singh, R. Kannagi, and P. W. Cheng, "TNFα enhances the motility and invasiveness of prostatic cancer cells by stimulating the expression of selective glycosyl- and sulfotransferase genes involved in the synthesis of selectin ligands," *Biochemical and Biophysical Research Communications*, vol. 409, no. 3, pp. 436–441, 2011.

[27] H. Kulbe, R. Thompson, J. L. Wilson et al., "The inflammatory cytokine tumor necrosis factor-alpha generates an autocrine tumor-promoting network in epithelial ovarian cancer cells," *Cancer Research*, vol. 67, no. 2, pp. 585–592, 2007.

[28] M. Akiyama, T. Hideshima, T. Hayashi et al., "Nuclear factor-kappaB p65 mediates tumor necrosis factor alpha-induced nuclear translocation of telomerase reverse transcriptase protein," *Cancer Research*, vol. 63, no. 1, pp. 18–21, 2003.

[29] J. Li, D. P. Sejas, X. Zhang et al., "TNF-alpha induces leukemic clonal evolution ex vivo in Fanconi anemia group C murine

stem cells," *The Journal of Clinical Investigation*, vol. 117, no. 11, pp. 3283–3295, 2007.

[30] B. Li, A. Vincent, J. Cates, D. M. Brantley-Sieders, D. B. Polk, and P. P. Young, "Low levels of tumor necrosis factor alpha increase tumor growth by inducing an endothelial phenotype of monocytes recruited to the tumor site," *Cancer Research*, vol. 69, no. 1, pp. 338–348, 2009.

[31] L. Caja, F. Dituri, S. Mancarella et al., "TGF-β and the tissue microenvironment: relevance in fibrosis and cancer," *International Journal of Molecular Sciences*, vol. 19, no. 5, article ijms19051294, p. 1294, 2018.

[32] S. K. Lutgendorf, A. Z. Weinrib, F. Penedo et al., "Interleukin-6, cortisol, and depressive symptoms in ovarian cancer patients," *Journal of Clinical Oncology*, vol. 26, no. 29, pp. 4820–4827, 2008.

[33] G. Scambia, U. Testa, P. Benedetti Panici et al., "Prognostic significance of interleukin 6 serum levels in patients with ovarian cancer," *British Journal of Cancer*, vol. 71, no. 2, pp. 354–356, 1995.

[34] S. B. Coffelt, F. C. Marini, K. Watson et al., "The proinflammatory peptide LL-37 promotes ovarian tumor progression through recruitment of multipotent mesenchymal stromal cells," *Proceedings of the National Academy of Sciences of the United States of America*, vol. 106, no. 10, pp. 3806–3811, 2009.

[35] H. Kulbe, P. Chakravarty, D. A. Leinster et al., "A dynamic inflammatory cytokine network in the human ovarian cancer microenvironment," *Cancer Research*, vol. 72, no. 1, pp. 66–75, 2012.

Research Article

Effects of Macrofungal Polysaccharides Combined with Vemurafenib on Melanoma and Its Associated Mechanism

Wenya Wu,[1] Zhigang Su,[2] and Shasha Fan [3]

[1]*Department of Dermatology, The Second Affiliated Hospital of Soochow University, Suzhou, China*
[2]*Department of Urology, The Second Affiliated Hospital of Soochow University, Suzhou, China*
[3]*Department of Dermatology, Zhejiang Provincial People's Hospital, People's Hospital of Hangzhou Medical College, Hang Zhou, China*

Correspondence should be addressed to Shasha Fan; fanshasha@hmc.edu.cn

Fungal polysaccharides have demonstrated various biological functions such as antitumor, immune regulation, and antioxidant activities. It has also been reported to be beneficial in reshaping the immune system's surveillance on tumor cells and in helping the immune system kill tumor cells. In this study, a melanoma mouse model was constructed, and a macrofungal polysaccharide (MFPS) extracted from Pleurotus ostreatus combined with Vemurafenib monoclonal antibody was used to study their effects against melanoma and its antitumor mechanism by using the lactate dehydrogenase release assay, enzyme-linked immunosorbent assay, and flow typing assay. Results indicated that MFPS enhanced the inhibitory effect of Vemurafenib on tumor growth in melanoma-bearing mice and the secretion of cytokines IFN-γ and IL-12 in PBMCs of melanoma-bearing mice. In addition, the combination of MFPS1 and Vemurafenib can enhance the immunomodulatory activity of melanoma-bearing mice as well as elicit the activation and proliferation of B cells and T cells.

1. Introduction

Traditional chemotherapy targets tumors, but it is often accompanied with obvious side effects including causing toxic effects in healthy organs. In recent years, with the continuous advancement in research related to cancer treatment, the combination of immunotherapy and chemotherapy has received more and more attention. Some clinical trials with combined immunotherapy and chemotherapy have shown that patients who received chemotherapy with subsequent reception of immunotherapy had better clinical outcomes than patients who only received chemotherapy [1, 2]. Other preclinical and clinical studies have also shown that chemotherapy can improve the efficacy of immunotherapy through various mechanisms [3]. Chemotherapy can not only overcome partial immunosuppression but also heighten the cross-expression of tumor antigens and enhance the infiltration of immune cells into the tumor tissue.

Fungal polysaccharides are a class of polysaccharides that have received an increasing amount of attention in recent years. Fungal polysaccharides have been shown to have a variety of biological activities such as antitumor, immune regulation, and antioxidant [4, 5]. Its biological activity depends on the structure, molecular weight, monosaccharide unit, and type of links in the polysaccharide. Fungal polysaccharides consist of different types of polysaccharides found in fungal cells, from high molecular weight to low molecular weight and from homopolysaccharides to heteropolysaccharides with different linkage types [6, 7].

In the advanced stages of cancer, tumor cells usually enter the blood circulation and begin to metastasize. At this stage, tumor cells can circulate into various organs and cells of the body through the blood. The blood circulation system contains certain components of the immune system, and these components typically can play an immune surveillance role in the early stages of cancer; however, with an advanced
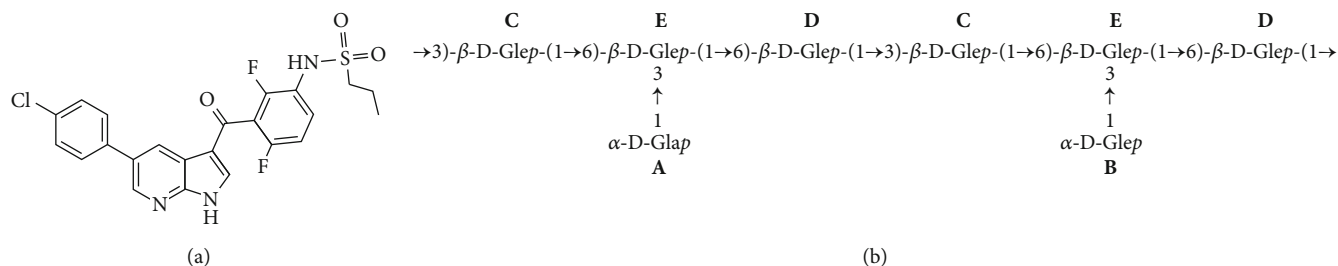
FIGURE 1: The molecular formula of Vemurafenib and the water-soluble component of macrofungal heteropolysaccharide (MFPS1): (a) Vemurafenib; (b) MFPS1.

stage of cancer, the immune system has been proved to have lost the role of immune surveillance and unable to recognize cancer cells [8]. Therefore, remodeling the immune system's surveillance of tumor cells plays a key role in the treatment of cancer. Studies have demonstrated that fungal polysaccharides can be beneficial in the reshaping of the immune system to monitor tumor cells and in helping the immune system kill tumor cells [9–11].

Vemurafenib is a mutant-selective serine/threonine kinase inhibitor specifically designed to inhibit V-RAF mutations of the murine sarcoma viral oncogene homolog B1 (BRAF) gene in the mitogen-activated protein kinase/extracellular signal-regulated kinase signaling pathway (MAPK/ERK) that is often associated with cancer development. BRAF mutations are typically found in melanoma, colorectal cancer, papilloma, thyroid cancer, non-small-cell lung cancer, and ovarian cancer [12]. Studies have shown that almost 50% of patients with malignant melanoma contain BRAF mutations [13]. With that, Vemurafenib was approved in 2011 for the treatment of advanced malignant melanoma with BRAF mutations [14]. The structure for Vemurafenib is shown in Figure 1(a).

The clinical trial of Vemurafenib began in 2006. In a phase I trial, 32 patients reported an objective response rate of 81% after being treated with Vemurafenib. The next phase III trial showed that patients treated with Vemurafenib had a significant improvement in the survival rate compared with patients receiving dacarbazine, and the risk of death was reduced by 63% [15].

In this study, we focus on the combined effects of macrofungal polysaccharides (MFPS) extracted from Pleurotus ostreatus and Vemurafenib monoclonal antibody on melanoma and its antitumor mechanism. We also attempted to uncover the antimelanoma-associated immune pathway affected by the combination use of MFPS and Vemurafenib.

2. Materials and Methods

2.1. Experimental Materials. Human melanoma MeWo cell lines were purchased from the Shanghai Cell Bank of the Chinese Academy of Sciences. Fetal bovine serum (FBS), RPMI-1640 medium, and EDTA were purchased from Gibco. The lymphocyte separation solution and lactate dehydrogenase release assay (LDH) kit were purchased

from Japan Tongren Co. Ltd. The enzyme-linked immunosorbent assay kit for measurement of IL-12 and INF-γ was purchased from Xinbosheng Biotechnology Co. Ltd. SPF male BALB/c/nu nude mice with body weight 18 ± 2 g were purchased from Shanghai Slack Laboratory Animal Center. CD45-percp, CD4-fitc, CD19-apc, CD34-fitc, and CD335-apc antibodies were all purchased from BD Biotechnology Co. Ltd. Other biochemical reagents were purchased from Sinopharm Group.

2.2. Isolation and Purification of Macrofungal Polysaccharide. The mushroom fruiting bodies were washed with sterilized double distilled water, pulverized, and then soaked at 90°C, with 4% NaOH for 6h. The extract was filtered with Whatman No. 1 filter paper, and the filtrate was mixed with 80% ethanol at a volume ratio of 1:5 and then allowed to stand at 4°C overnight to precipitate polysaccharide. The precipitated crude polysaccharide was centrifuged at 4°C, 8000 rpm for 40 minutes, and then washed with 80% and 90% ethanol and acetone, respectively, followed by the collection of high alkaline crude polysaccharide solution having a pH of 11. The solution was then dialyzed in the double distilled water against a membrane with a molecular weight of 10000 g/mol at 4°C for 3 days to remove compounds of low molecular weight and excess NaOH. During the dialysis, the alkali-soluble fraction precipitates and the water-soluble components remain in the solution. The macrofungal heteropolysaccharide (MFPS1) was obtained after centrifugation and then lyophilized and stored [16]. The molecular formula of MFPS1 obtained in this way is shown in Figure 1(b).

2.3. Construction of Human Melanoma MeWo Cell-Bearing Mice. BALB/c nude mice of 6 to 12 weeks old were used to construct human melanoma tumor-bearing mice. 3×10^6 human melanoma MeWo cells in a logarithmic growth phase were injected subcutaneously into the right ankle of nude mice. When the tumor grows to at least 100-300 mm^3, the mice were used for in vivo experiments [17].

2.4. Drug Treatment for Human Melanoma Tumor-Bearing Mice. When the tumor of human melanoma-bearing mice grows to at least 100-300 mm^3, the tumor-bearing mice were divided into the following 4 groups (6 in each group) for drug treatment: (1) control group: normal diet for 12 days;

(2) Vemurafenib group: Vemurafenib and MFPS1 were dissolved in DMSO and saline solution, respectively, and then orally administered at 50 mg/kg/day for 12 days [18]; (3) low-dose MFPS1+Vemurafenib group: Vemurafenib was orally administered at 50 mg/kg/day, and the MFPS1 was also administered at 100 mg/kg/day at the same time for 12 days; (4) high-dose MFPS1+Vemurafenib group: Vemurafenib was orally administered at 50 mg/kg/day, and the MFPS1 was also administered at 150 mg/kg/day at the same time for 12 days. The control group was given the same amount of saline or DMSO solution per day as in the experimental group. The tumor size was measured every 3 days and weighed; the tumor growth curve was drawn afterward.

2.5. Isolation of Mouse Peripheral Blood Mononuclear Cells (PBMCs).
Human melanoma-bearing mice were anesthetized with an appropriate amount of pentobarbital sodium anesthetic. Blood was then taken from the eyelids, 1 ml/mouse, and was collected into an EDTA anticoagulant tube, and then, the PBMCs were isolated by the Ficoll method. The isolated PBMCs were used for the lactate dehydrogenase (LDH) release assay and flow cytometry.

2.6. LDH Experiment.
The PBMCs of 4 groups of melanoma-bearing mice were separately prestimulated by adding corresponding drugs; that is, DMSO was added to PBMCs from normal mice as a control, Vemurafenib ($2 \mu g/ml$) was added to PBMCs from Vemurafenib mice, Vemurafenib ($2 \mu g/ml$) and MFPS1 ($4 \mu g/ml$) were added to PBMCs from low-dose MFPS1 combined with Vemurafenib mice, and Vemurafenib ($2 \mu g/ml$) and MFPS1 ($8 \mu g/ml$) were added to PBMCs from high-dose MFPS1 combined with Vemurafenib mice. After 24 hours of incubation, PBMCs and human melanoma MeWo cells were subjected to LDH experiments at 1:1, 5:1, and 10:1 effective target ratios, respectively.

2.7. Enzyme-Linked Immunosorbent Assay (ELISA).
The PBMCs of 4 groups of melanoma-bearing mice were prestimulated according to the method of LDH experiment, the supernatant was collected after 24 hours of incubation, and ELISA was performed to detect cytokines IFN-γ and IL-12 and IL-6 and TNF-α.

2.8. Immunophenotyping.
The PBMCs of 4 groups of melanoma-bearing mice were prestimulated according to the method of LDH experiment, and after 24 hours of incubation, the cells were collected in precooled PBS and cultured with monoclonal antibodies: CD45-percp, CD4-fitc, CD19-apc, CD34-fitc, and CD335-apc. After incubation at 4°C for 3 h, the expression-dependent cell population was analyzed by flow cytometry.

2.9. Data Analysis.
Data were expressed as the mean ± standard deviation. Software Origin8.5 was used for one-way variance analysis, and statistical significance was observed when $p < 0.05$.

3. Results

3.1. MFPS1 Enhanced the Inhibitory Effect of Vemurafenib on Tumor Growth in Melanoma-Bearing Mice.
The combined effects of MFPS1 and Vemurafenib on the tumor growth of melanoma-bearing mice were studied in the human melanoma MeWo cell-bearing mice. The results showed that both low-dose and high-dose MFPS1 enhanced the inhibitory effect of Vemurafenib on tumor growth in melanoma-bearing mice (Figure 2(a)). On the 12th day after drug administration, the tumor volumes of the tumor-bearing mice in the normal group, the Vemurafenib group, the low-dose MFPS1+Vemurafenib group, and the high-dose MFPS1+Vemurafenib group were $515.23 \pm 19.14 \, mm^3$, $411.9 \pm 20.14 \, mm^3$, $387.02 \pm 17.14 \, mm^3$, and $362.02 \pm 19.83 \, mm^3$, respectively. Compared with the normal group, the tumor volumes of the tumor-bearing mice in the Vemurafenib group, in the low-dose MFPS1+Vemurafenib group, and the high-dose MFPS1+Vemurafenib group were significantly reduced ($p < 0.05$). Moreover, compared with the Vemurafenib group, the tumor volumes in the low-dose MFPS1+Vemurafenib group and in the high-dose MFPS1+Vemurafenib group were both significantly smaller ($p < 0.05$), and the high-dose MFPS1 group was superior to the low-dose MFPS1 group in this regard as shown in Figure 2(b).

3.2. In Vivo Experiments, MFPS1 Enhanced the Killing Effect of Vemurafenib on Human Melanoma MeWo Cells.
The PBMCs of each group of melanoma-bearing mice were isolated and then prestimulated by the corresponding drugs; after that, the lactate dehydrogenase release assay (LDH) was then conducted for the in vivo experiment. The results from in vivo experiments indicated that MFPS1 enhanced the killing effect of Vemurafenib on human melanoma MeWo cells (Figure 3(a)).

When the ratio of immune cells and tumor cells (target ratio) was 5:1, in the normal group, the Vemurafenib group, the low-dose MFPS1+Vemurafenib group, and the high-dose MFPS1+Vemurafenib, the killing rates of MeWo cells were 21.56 ± 0.21, 62.98 ± 2.21, 67.1 ± 3.81, and 69.66 ± 3.31, respectively. Compared with the normal group, the killing effects on the human melanoma MeWo cells in the Vemurafenib group, in the low-dose MFPS1+Vemurafenib group, and in the high-dose MFPS1+Vemurafenib group were significantly higher ($p < 0.01$). Compared with the Vemurafenib group, the killing effects on the human melanoma MeWo cells in the low-dose MFPS1+Vemurafenib group and in the high-dose MFPS1+Vemurafenib group were significantly heightened ($p < 0.05$), and the high-dose MFPS1 group was superior to the low-dose MFPS1 group as suggested in Figure 3(b).

When the ratio of immune cells and tumor cells (target ratio) was 10:1, in the normal group, the Vemurafenib group, the low-dose MFPS1+Vemurafenib group, and the high-dose MFPS1+Vemurafenib, the killing rates of MeWo cells were 20.35 ± 0.98, 85.75 ± 3.98, 93 ± 3.72, and 96.66 ± 3.966, respectively. And compared with the normal group, the killing effects on the human melanoma MeWo cells in
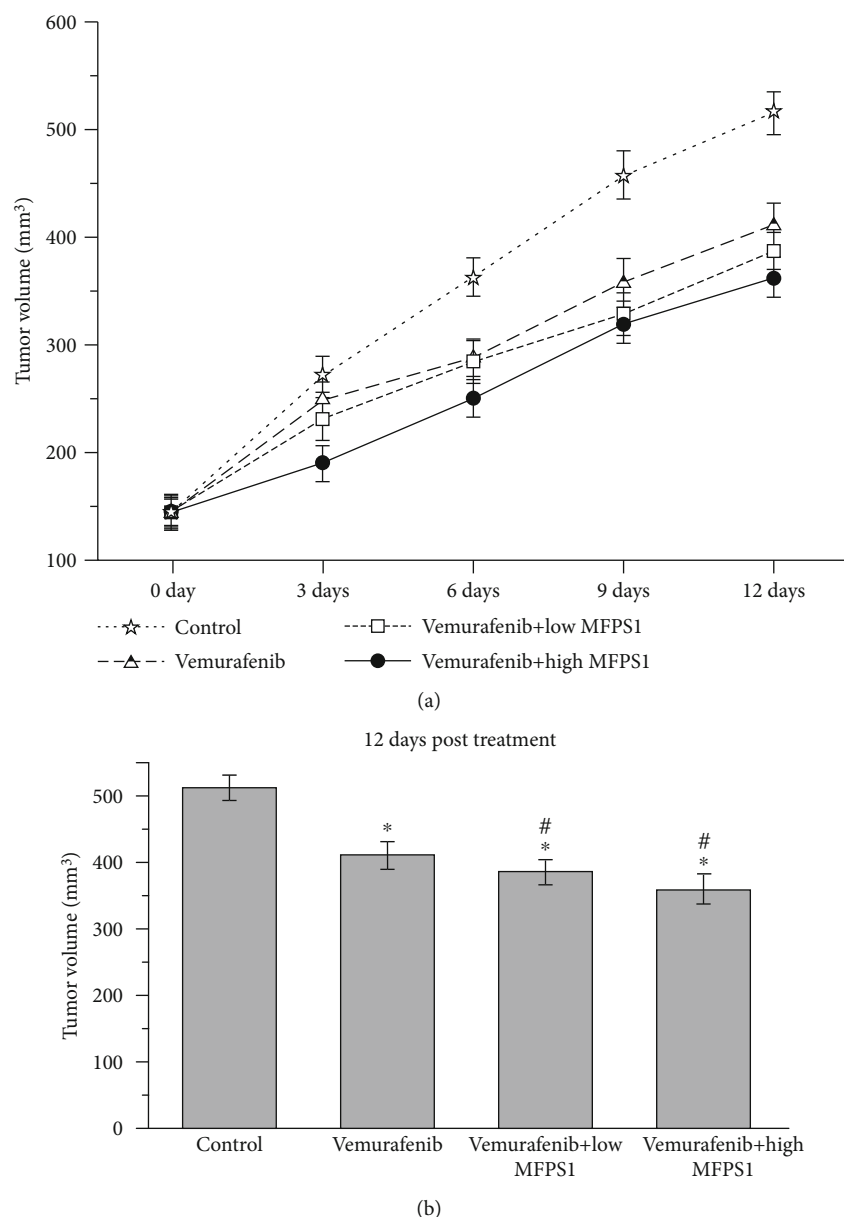
(a)

(b)

FIGURE 2: MFPS1 enhanced the inhibitory effect of Vemurafenib on tumor growth in melanoma-bearing mice: (a) tumor growth curve of human melanoma MeWo cell-bearing mice 12 days after drug treatment; (b) tumor size of human melanoma MeWo cell-bearing mice at 12 days of drug treatment. ∗ represents the normal group as the control: $^*p < 0.05$ and $^{**}p < 0.01$; # represents the Vemurafenib group as the control: $^\#p < 0.05$ and $^{\#\#}p < 0.01$.

the Vemurafenib group, in the low-dose MFPS1+Vemurafenib group, and in the high-dose MFPS1+Vemurafenib group were significantly higher ($p < 0.01$). When compared with the Vemurafenib group, the killing effects on the human melanoma MeWo cells in the low-dose MFPS1+Vemurafenib group and in the high-dose MFPS1+Vemurafenib group were significantly increased ($p < 0.05$), and the high-dose MFPS1 group was superior to the low-dose MFPS1 group (Figure 3(c)), which is similar to what was observed when the target ratio was 5 : 1.

3.3. In Vivo Experiments, MFPS1 Enhanced the Cytokine-Secreting Effect of Vemurafenib on PBMCs in Melanoma-Bearing Mice. To study the mechanism against melanoma

by the combination of MFPS1 and Vemurafenib, the supernatant of PBMCs was collected after the tumor-bearing mice were prestimulated as described above, and the levels of cytokines interleukin-12 (IL-12) and interferon-γ (IFN-γ) in the supernatant were measured. The results showed that the levels of IFN-γ and IL-12 were both increased in the MFPS1-treated PBMCs (Figure 4).

The levels of IL-12 in PBMCs for the normal group, Vemurafenib group, low-dose MFPS+Vemurafenib group, and high-dose MFPS+Vemurafenib group were 391.5 ± 2.97, 449 ± 1.92, 490.35 ± 24.5, and 491 ± 19, respectively. Compared with the normal group, the levels of IL-12 in PBMCs in the Vemurafenib group, in the low-dose MFPS1 +Vemurafenib group, and in the high-dose MFPS1
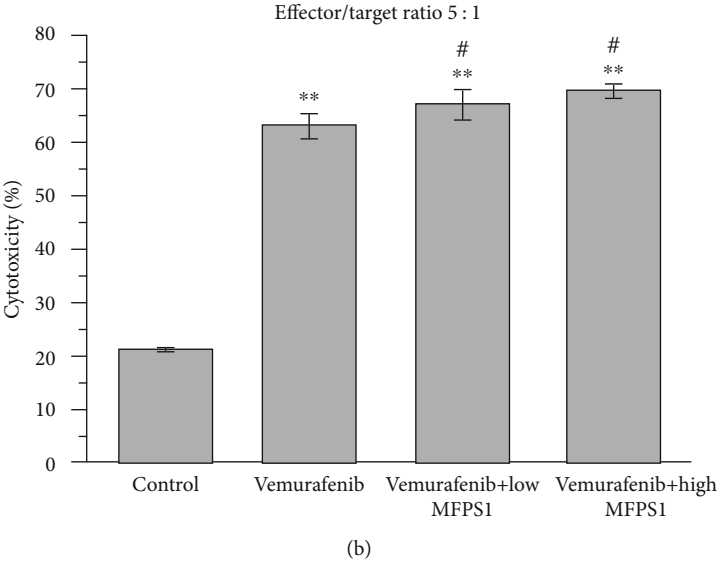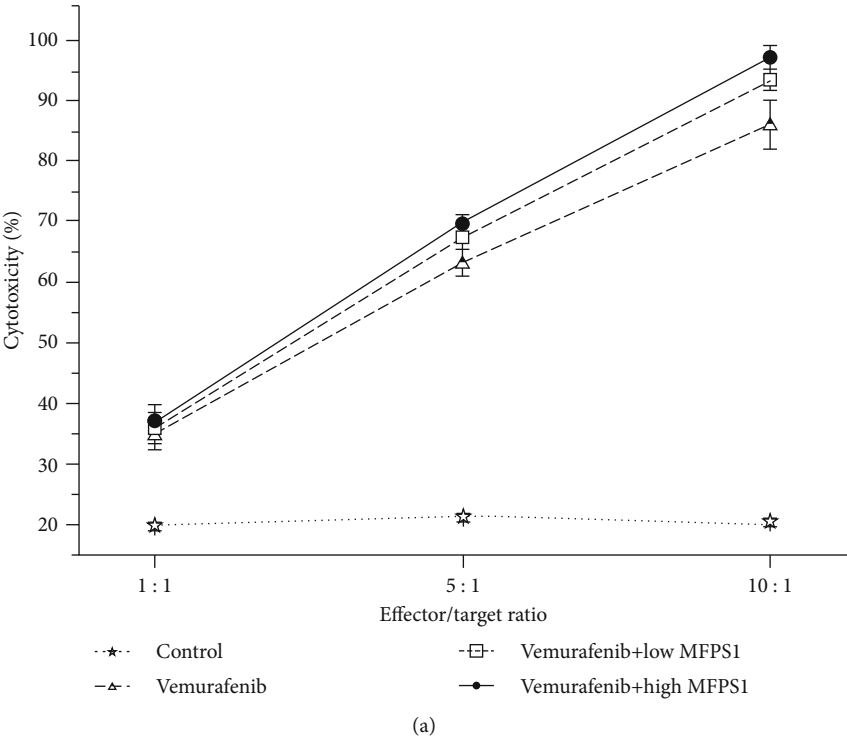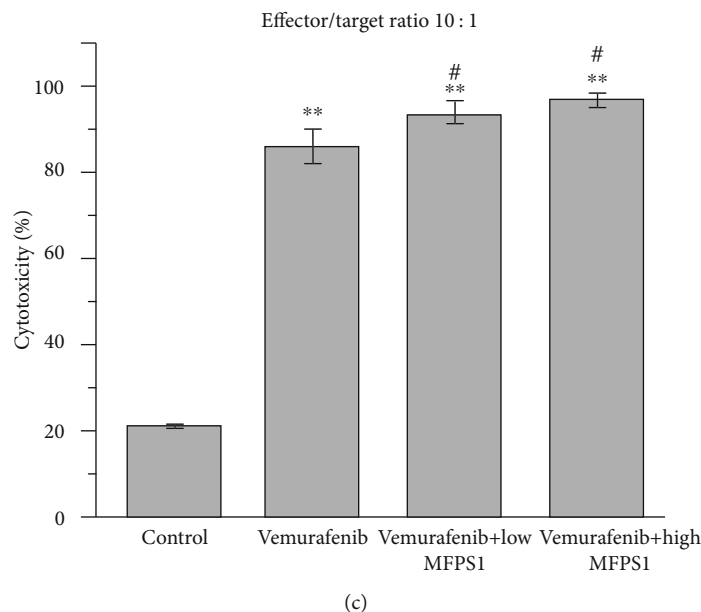
(a)

(b)

Figure 3: Continued.

(c)

Figure 3: In vivo experiments, MFPS1 enhance the killing effect of Vemurafenib on human melanoma MeWo cells. (a) Killing effects on the human melanoma MeWo cells at target ratios of $1:1$, $5:1$, and $10:1$ after drug treatment; (b) killing effects on the human melanoma MeWo cells at target ratio of $5:1$ after drug treatment; (c) killing effects on the human melanoma MeWo cells at a target ratio of $10:1$ after drug treatment. ∗ represents the normal group as the control: $^{*}p < 0.05$ and $^{**}p < 0.01$; # represents the Vemurafenib group as the control: $^{#}p < 0.05$ and $^{##}p < 0.01$.

+Vemurafenib group were significantly increased ($p < 0.01$). Compared with the Vemurafenib group, the levels of IL-12 in PBMCs in the low-dose MFPS1+Vemurafenib group and in the high-dose MFPS1+Vemurafenib group were significantly higher ($p < 0.05$) (Figure 4(a)).

The contents of INF-γ in PBMCs for the normal group, Vemurafenib group, low-dose MFPS+Vemurafenib group, and high-dose MFPS+Vemurafenib group were 60.27 ± 2.25, 81.06 ± 2.44, 90.41 ± 2.48, and 91.333 ± 1.86, respectively. Compared with the normal group, the contents of INF-γ in PBMCs in the Vemurafenib group, in the low-dose MFPS1+Vemurafenib group, and in the high-dose MFPS1+Vemurafenib group were significantly increased ($p < 0.01$). Compared with the Vemurafenib group, the contents of INF-γ in PBMCs in the low-dose MFPS1+Vemurafenib group and in the high-dose MFPS1+Vemurafenib group were significantly higher ($p < 0.05$) (Figure 4(b)).

3.4. Effect of MFPS1 Combined with Vemurafenib on Immunomodulatory Activity in Melanoma-Bearing Mice. The activation of the immune system plays a very important role in tumor therapy. To further explore the antitumor mechanisms of MFPS1 in combination with Vemurafenib, we investigated the expression of immune cell-specific markers in PBMC cells. The results showed that the combination of MFPS1 and Vemurafenib enhanced the immunomodulatory effects of Vemurafenib on melanoma-bearing mice.

The lymphocyte contents in PBMCs for the normal group, Vemurafenib group, low-dose MFPS1+Vemurafenib group, and high-dose MFPS1+Vemurafenib group were 29.2 ± 1.34, 37.87 ± 2.85, 45.28 ± 1.33, and 49.4 ± 2.93, respectively. Compared with the normal group, the lymphocyte contents in PBMCs in the Vemurafenib group, in the low-dose MFPS1+Vemurafenib group, and in the high-dose MFPS1+Vemurafenib group were significantly increased ($p < 0.01$). Compared with the Vemurafenib group, the lymphocyte contents in PBMCs in the low-dose MFPS1+Vemurafenib group and in the high-dose MFPS1+Vemurafenib group were significantly higher ($p < 0.05$) as indicated in Figure 5(a).

As shown in Figures 5(c) and 5(d), the content of mature B cells in PBMCs was increased after the combined treatment of MFPS1 and Vemurafenib, whereas the content of immature B cells was decreased. A similar trend was also observed for the T cell content (Figures 5(e) and 5(f)). Additionally, CD335+ cells were also found to increase after the combined treatment of MFPS1 and Vemurafenib (Figure 5(b)). Since CD335 is a cytotoxic activating receptor expressed in activated NK cells, the results above thus suggested that NK cells were also activated in PBMCs of MFPS1 and Vemurafenib-treated mice.

4. Discussion

Results in this study demonstrated that MFPS1 enhanced the inhibitory effect of Vemurafenib on tumor growth in melanoma-bearing mice and the secretion of cytokines IFN-γ and IL-12 in PBMCs of melanoma-bearing mice. Moreover, the combination of MFPS1 and Vemurafenib can enhance the immunomodulatory activity of melanoma-bearing mice.
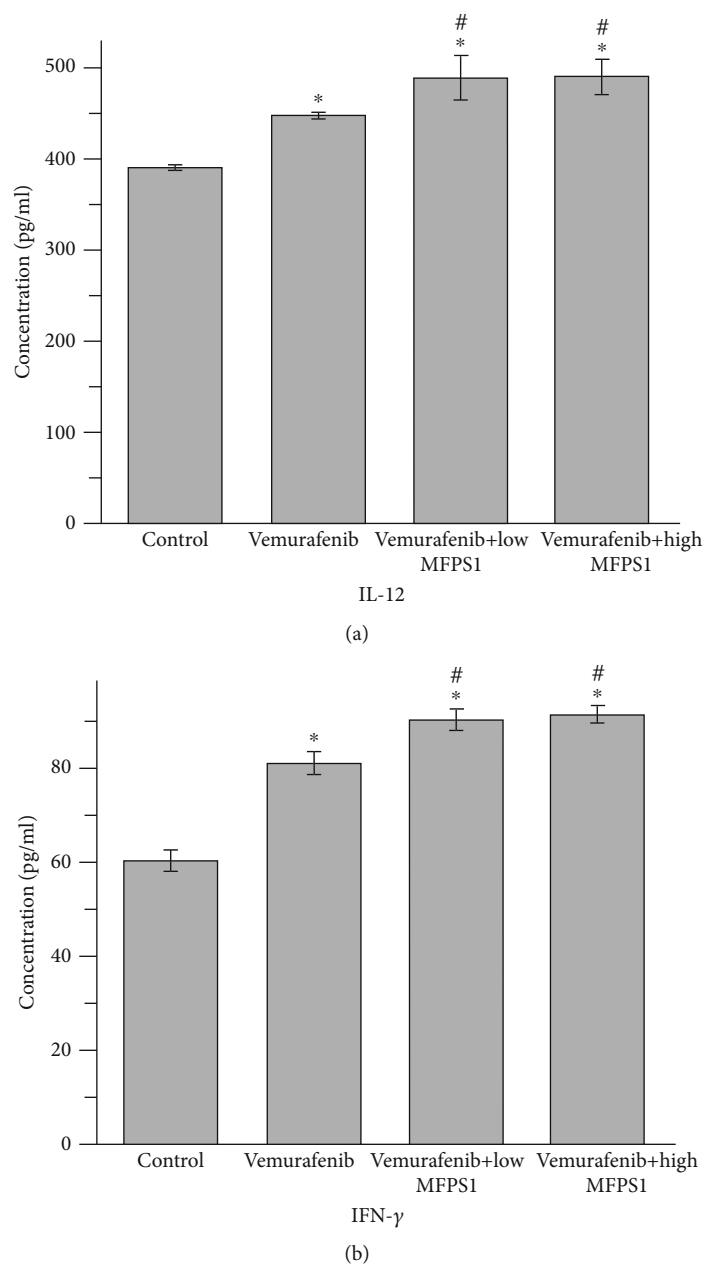
(a)

(b)

FIGURE 4: In vivo experiments, MFPS1 enhanced the secretion of cytokines IL-12 and INF-γ induced by Vemurafenib in PBMCs of melanoma-bearing mice. (a) The concentration of cytokine IL-12 in PBMCs of melanoma-bearing mice after drug treatment; (b) the concentration of cytokine INF-γ in PBMCs of melanoma-bearing mice after drug treatment. ∗ represents the normal group as the control: $^*p < 0.05$ and $^{**}p < 0.01$; # represents the Vemurafenib group as the control: $^\#p < 0.05$ and $^{\#\#}p < 0.01$.

It has been reported that Th1 (T helper cells) lymphocytes and M1 macrophages play a crucial role in antitumor immune surveillance and cytotoxicity [19]. We observed the increased expression of IFN-γ and IL-12 in PBMC cells after the combined treatment of MFPS1 and Vemurafenib. On the one hand, IFN-γ secreted by Th1 cells plays a role in maintaining the macrophage M1 phenotype, and on the other hand, M1 macrophages release IL-12 to maintain the Th1 phenotype [19]. Therefore, the overexpression of these two cytokines observed in this study suggests that the combination of MFPS1 and Vemurafenib can initiate proinflammatory antitumor immune surveillance via m1Φ.

An increase in CD335+ NK cells was also found in PBMCs treated with MFPS1 and Vemurafenib. It has also been reported that the overexpression of TNF-α can activate NK cells against tumor cells [20, 21]. In this study, we also showed that the combination of MFPS1 and Vemurafenib can trigger the activation and proliferation of B cells and T cells.
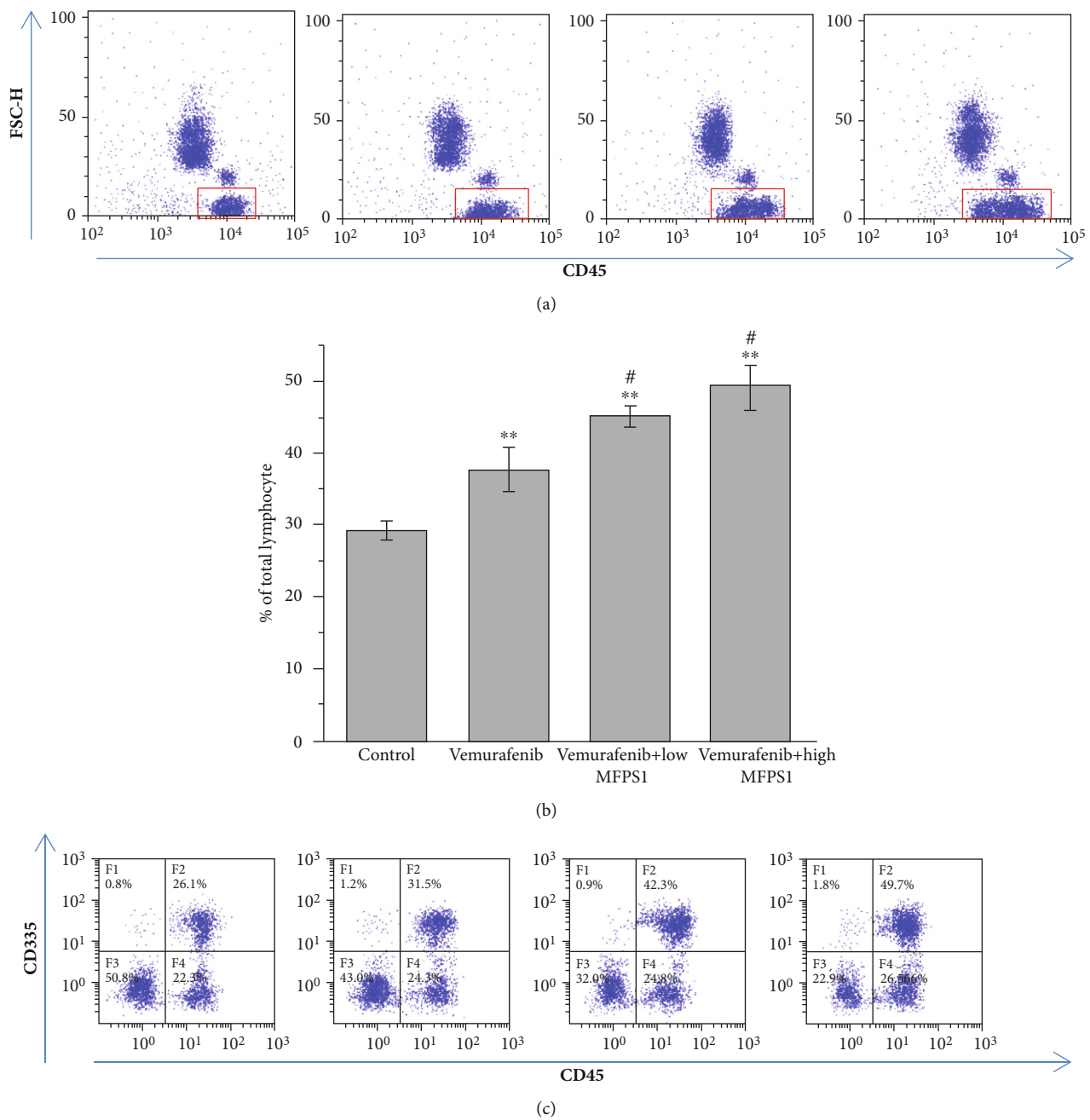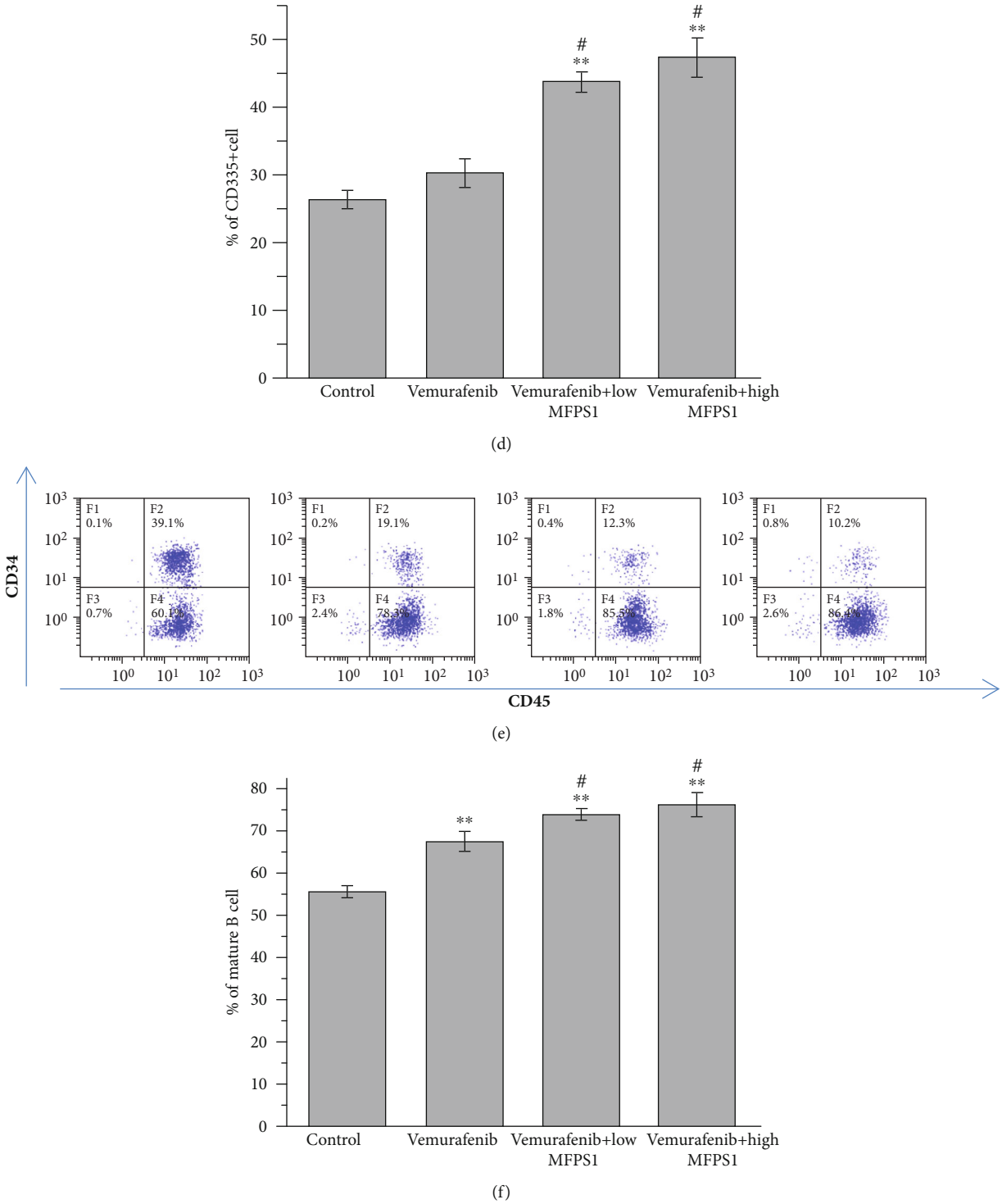
(a)

(b)

(c)

FIGURE 5: Continued.

(d)
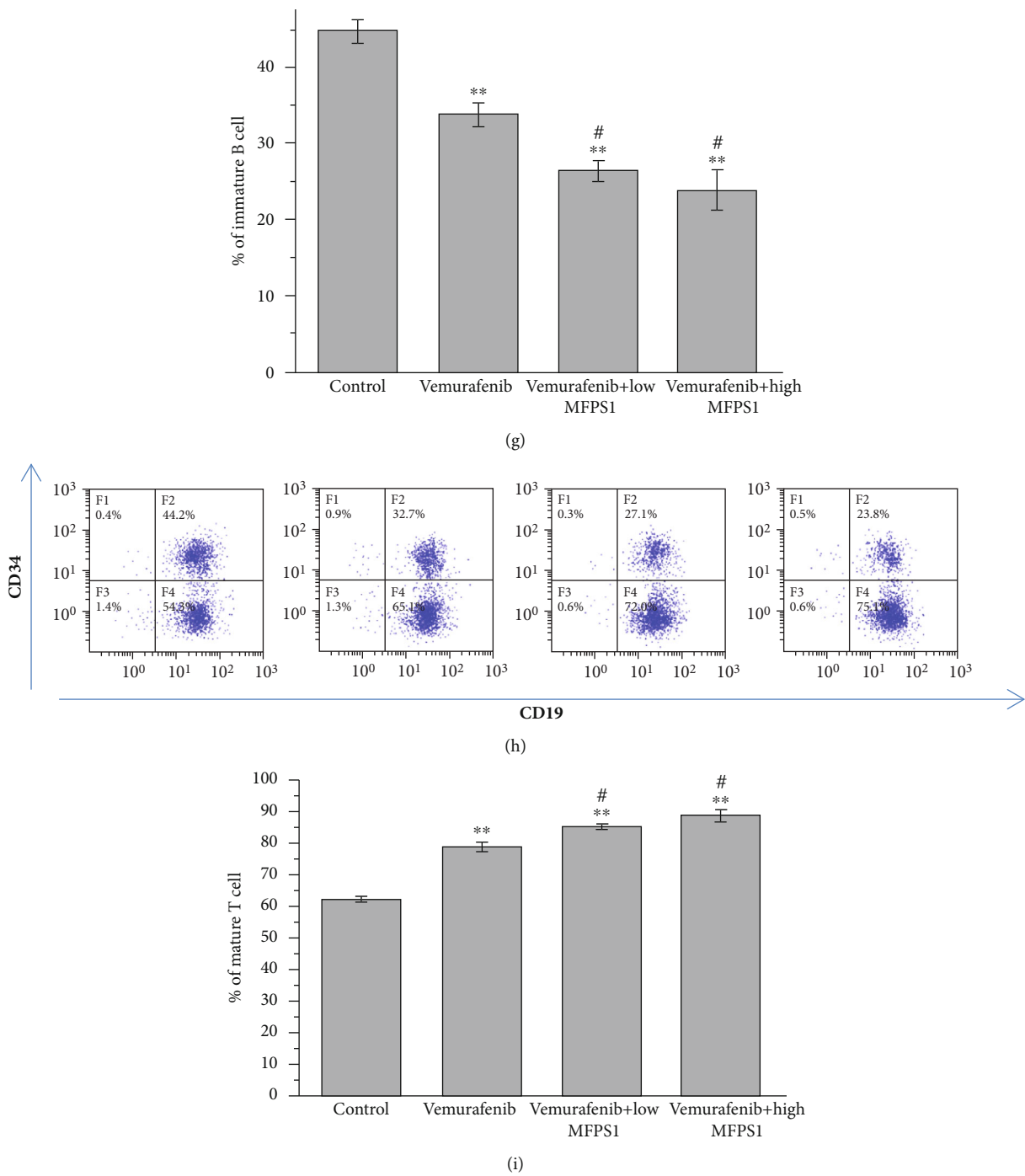

(e)

(f)

FIGURE 5: Continued.
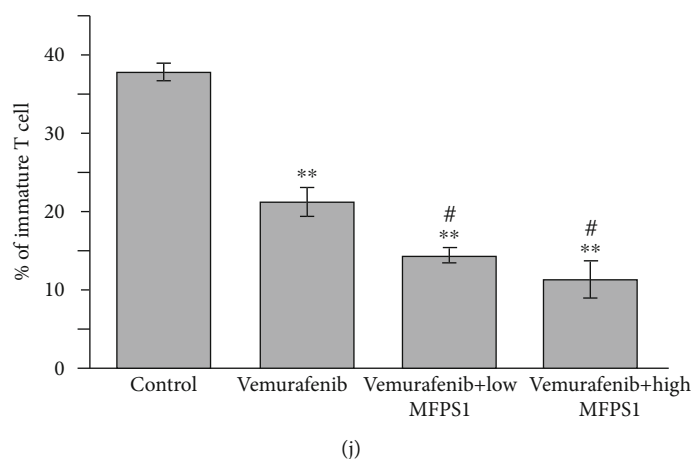
(g)

(h)

(i)

Figure 5: Continued.

(j)

FIGURE 5: Effect of MFPS1 combined with Vemurafenib on immunomodulatory activity in melanoma-bearing mice. Results of immunophenotypic flow cytometry for a single mouse (a, c, e, h); (a, b) lymphocyte content in PBMCs of melanoma-bearing mice after drug treatment; (c, d) CD335-positive NK cell content in PBMCs of melanoma-bearing mice; (e, f) the content of mature B cells in PBMCs of melanoma-bearing mice (upper right corner in (e)); (e, g) the content of immature B cells in PBMCs of melanoma-bearing mice (lower right corner in (e)); (h, i) the content of mature T cells in PBMCs of melanoma-bearing mice (upper right corner in (h)); (h, j) the content of immature T cells in PBMCs of melanoma-bearing mice (lower right corner in (h)). $*$ represents the normal group as the control: $^*p < 0.05$ and $^{**}p < 0.01$; # represents the Vemurafenib group as the control: $^\#p < 0.05$ and $^{\#\#}p < 0.01$.
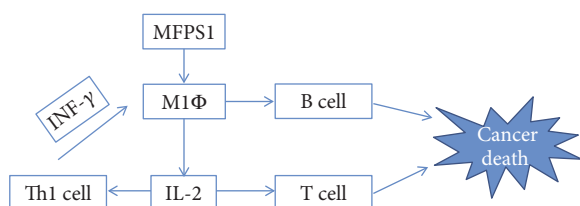

FIGURE 6: The speculated antitumor mechanism for the combination use of MFPS1 with Vemurafenib.

5. Conclusion

Taken together, the combination of MFPS1 and Vemurafenib may initiate proinflammatory antitumor immune surveillance via m1Φ, triggering the activation and proliferation of B cells and T cells and enhancing the immunomodulatory activity of melanoma-bearing mice (Figure 6).

Data Availability

The data used to support the findings of this study are available from the corresponding author upon request.

Conflicts of Interest

The authors declare that there is no conflict of interest regarding the publication of this paper.

Acknowledgments

References

[1] J. Schlom, P. M. Arlen, and J. L. Gulley, "Cancer vaccines: moving beyond current paradigms," *Clinical Cancer Research*, vol. 13, no. 13, pp. 3776–3782, 2007.

[2] C. J. Wheeler, A. Das, G. Liu, J. S. Yu, and K. L. Black, "Clinical responsiveness of glioblastoma multiforme to chemotherapy after vaccination," *Clinical Cancer Research*, vol. 10, no. 16, pp. 5316–5326, 2004.

[3] L. Apetoh, S. Ladoire, G. Coukos, and F. Ghiringhelli, "Combining immunotherapy and anticancer agents: the right path to achieve cancer cure?," *Annals of Oncology*, vol. 26, no. 9, pp. 1813–1823, 2015.

[4] M. Lemieszek and W. Rzeski, "Anticancer properties of polysaccharides isolated from fungi of the Basidiomycetes class," *Contemporary Oncology*, vol. 16, no. 4, pp. 285–289, 2012.

[5] C. Sanchez, "Reactive oxygen species and antioxidant properties from mushrooms," *Synthetic and Systems Biotechnology*, vol. 2, no. 1, pp. 13–22, 2017.

[6] X. Huang and S. Nie, "The structure of mushroom polysaccharides and their beneficial role in health," *Food & Function*, vol. 6, no. 10, pp. 3205–3217, 2015.

[7] X. Meng, H. Liang, and L. Luo, "Antitumor polysaccharides from mushrooms: a review on the structural characteristics, antitumor mechanisms, and immunomodulating activities," *Carbohydrate Research*, vol. 424, pp. 30–41, 2016.

[8] S. I. Grivennikov, F. R. Greten, and M. Karin, "Immunity, inflammation, and cancer," *Cell*, vol. 140, no. 6, pp. 883–899, 2010.

[9] S. Wasser, "Medicinal mushrooms as a source of antitumor and immunomodulating polysaccharides," *Applied Microbiology and Biotechnology*, vol. 60, no. 3, pp. 258–274, 2002.

[10] D. Li, W. Xu, P. Li et al., "Self-targeted polysaccharide prodrug suppresses orthotopic hepatoma," *Molecular Pharmaceutics*, vol. 13, no. 12, pp. 4231–4235, 2016.

[11] M. F. Moradali, H. Mostafavi, S. Ghods, and G. A. Hedjaroude, "Immunomodulating and anticancer agents in the realm of macromycetes fungi (macrofungi)," *International Immunopharmacology*, vol. 7, no. 6, pp. 701–724, 2007.

[12] C. Garbe and T. K. Eigentler, "Vemurafenib," *Recent Results in Cancer Research*, vol. 211, pp. 77–89, 2018.

[13] L. D. Gutierrez-Castaneda, J. A. Nova, and J. D. Tovar-Parra, "Frequency of mutations in BRAF, NRAS, and KIT in different populations and histological subtypes of melanoma: a systemic review," *Melanoma Research*, p. 1, 2019.

[14] G. Kim, A. E. McKee, Y. M. Ning et al., "FDA approval summary: vemurafenib for treatment of unresectable or metastatic melanoma with the BRAFV600E mutation," *Clinical Cancer Research*, vol. 20, no. 19, pp. 4994–5000, 2014.

[15] G. Bollag, J. Tsai, J. Zhang et al., "Vemurafenib: the first drug approved for BRAF-mutant cancer," *Nature Reviews. Drug Discovery*, vol. 11, no. 11, pp. 873–886, 2012.

[16] K. K. Maity, S. Patra, B. Dey et al., "A heteropolysaccharide from aqueous extract of an edible mushroom, Pleurotus ostreatus cultivar: structural and biological studies," *Carbohydrate Research*, vol. 346, no. 2, pp. 366–372, 2011.

[17] P. Slobbe, A. D. Windhorst, K. Adamzek et al., "Development of [^{11}C]vemurafenib employing a carbon-11 carbonylative Stille coupling and preliminary evaluation in mice bearing melanoma tumor xenografts," *Oncotarget*, vol. 8, no. 24, pp. 38337–38350, 2017.

[18] A. K. MacLeod, L. A. McLaughlin, C. J. Henderson, and C. R. Wolf, "Activation status of the pregnane X receptor influences vemurafenib availability in humanized mouse models," *Cancer Research*, vol. 75, no. 21, pp. 4573–4581, 2015.

[19] O. A. W. Haabeth, B. Bogen, and A. Corthay, "A model for cancer-suppressive inflammation," *OncoImmunology*, vol. 1, no. 7, pp. 1146–1155, 2014.

[20] B. Burkholder, R. Y. Huang, R. Burgess et al., "Tumor-induced perturbations of cytokines and immune cell networks," *Biochimica et Biophysica Acta (BBA) - Reviews on Cancer*, vol. 1845, no. 2, pp. 182–201, 2014.

[21] E. Vivier, S. Ugolini, D. Blaise, C. Chabannon, and L. Brossay, "Targeting natural killer cells and natural killer T cells in cancer," *Nature Reviews. Immunology*, vol. 12, no. 4, pp. 239–252, 2012.

Research Article

Effect of Sulfated Polysaccharide from Undaria pinnatifida (SPUP) on Proliferation, Migration, and Apoptosis of Human Prostatic Cancer

Xiaolin Xu, Xin Zhu, Wenglong Lu, Yandong He, Yihan Wang, and Feng Liu [ID]

Department of Urology, Shanghai Fengxian District Central Hospital, China

Correspondence should be addressed to Feng Liu; liufeng198602@sina.com

Objective. To observe the effect of sulfated polysaccharide from Undaria pinnatifida (SPUP) on proliferation, migration, and apoptosis of human prostatic cancer. *Methods*. DU145 human prostate cancer cells were cultured in vitro, and the proliferation activity both in the control group and the SPUP treatment groups (25, 50, 100, 200 μg/ml) was measured by CCK-8 assay. The wound healing assay was conducted to detect the cell migration. Cell apoptosis was measured by flow cytometry. The protein and mRNA expressions of matrix metalloproteinase-9 (MMP-9) and apoptosis-related factor Bax were detected by qRT-PCR and Western blot. The expressions of cleaved caspase-3 and cleaved caspase-9 were also determined by Western blot. *Results*. (1) CCK-8 results showed that the proliferative activity of DU145 cells was significantly decreased with the increase of SPUP treatment concentration ($P < 0.05$) in a dose-dependent manner and that the inhibitory effect of SPUP was most significant at 72 h ($P < 0.05$) as compared with the control group; (2) the migration rate of SPUP-treated cells was significantly decreased ($P < 0.05$) as compared with the control group. And the results of qRT-PCR and Western blot assays showed that SPUP inhibited the expression of MMP-9 in DU145 cells; (3) compared with the control group, the SPUP-treated groups had increased apoptosis of the cells. The expressions of apoptosis-related factors cleaved caspase-3, cleaved caspase-9, and Bax were upregulated ($P < 0.05$), and the mRNA expression of Bax was increased ($P < 0.05$). *Conclusion*. SPUP showed an antitumor activity in prostatic cancer, and the underlying mechanism may be pertaining to inhibition of migration, proliferation, and induction of apoptosis of cancer cells.

1. Introduction

Prostate cancer, one of the most common malignancies in men, is the third leading cause of cancer-related deaths in men worldwide [1]. As prostate cancer cells are prone to malignant invasion and metastasis, current treatment for the disease is still facing difficulties [2]. Despite great advances in cancer treatment over the past decades, patients with advanced prostate cancer still suffer from the lack of effective treatments [3]. Early prostate cancer and local lesions can be treated by surgical resection or radiation [4]; however, the mortality rate of prostate cancer with distant metastasis and castration-resistant prostate cancer remains high. Therefore, the discovery of promising and effective treatments for prostate cancer is of great clinical significance.

Recent years have seen increasing attention from cancer experts and scholars to natural antitumor polysaccharides demonstrating significant anticancer activity as well as low toxic and side effects [5]. More and more researchers believe that polysaccharides can inhibit the proliferation of tumor cells; moreover, they can directly induce apoptosis or enhance immune activity in combination with chemotherapy [6]. Undaria pinnatifida, widely distributed in China and the rest of the world, is rich in protein, polysaccharides, and minerals. It has been used as medication and food for centuries [7]. Studies have reported that as Undaria pinnatifida has various biological functions including immunomodulation, anticancer, and antiviral activities [8], it has become one of the most popular food for cancer prevention, for instance, breast cancer [9]. Fucoidan extracted from Undaria
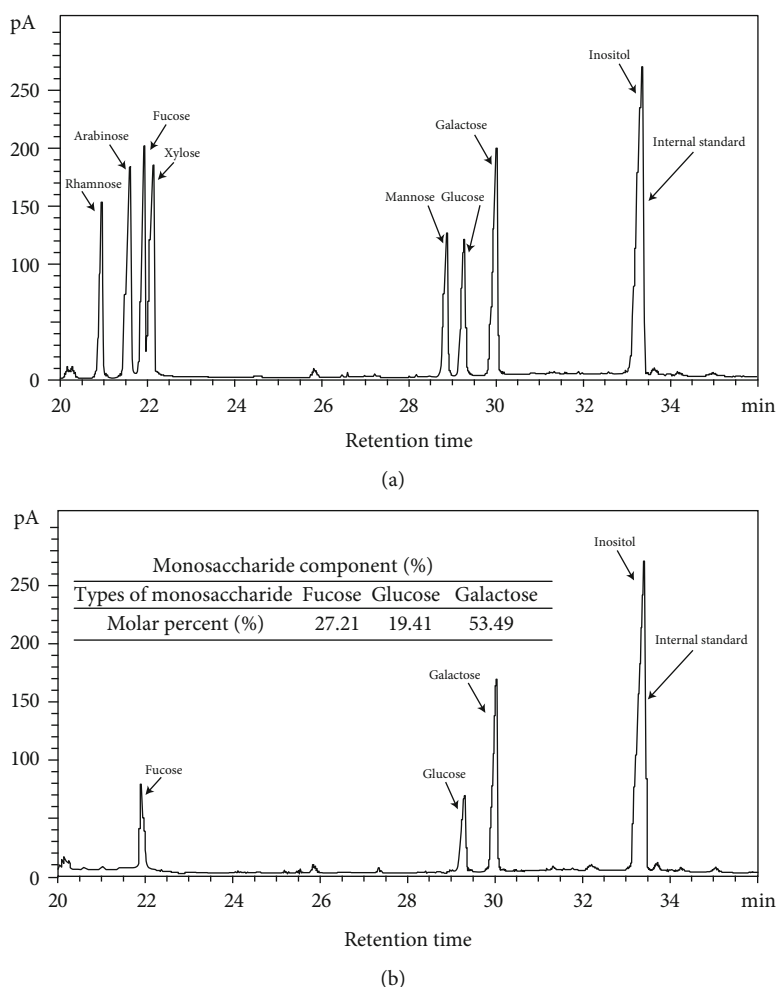
(a)

(b)

Figure 1: Gas chromatograms of monosaccharide standards (a) and SPUP hydrolysates (b).

pinnatifida has been proven to have antitumor activity in prostate cancer cell PC-3, cervical cancer cell A549, and hepatoma cell HepG2 [10]. In addition, it has been found that sulfated polysaccharide from Undaria pinnatifida (SPUP) inhibits the proliferation and migration activity while promoting apoptosis [11]. However, no study has reported the therapeutic efficacy of SPUP on prostate cancer. Therefore, our study will investigate the effect of SPUP on migration, proliferation, and apoptosis of prostate cancer cell (DU145) to elucidate its anticancer mechanism.

2. Materials and Methods

2.1. Materials and Reagents. The preparation of SPUP was described in the publication by Han et al. [12]. The composition of SPUP was identified by gas chromatography (see Figure 1). The contents of total sugar, ursolic acid, protein, and sulfate in SPUP were 80.32%, 3.19%, 7.07%, and 29.17%, respectively. In addition, SPUP was composed of fucose, glucose, and galactose with a molar ratio of 27.21 : 19.41 : 53.49 and a molecular weight of 97.9 kDa. Cell Counting Kit-8 (CCK-8) was purchased from Dojindo Molecular Technologies Inc. (Shanghai, China), and Annexin V-FITC/PI Apoptosis Detection Kit was purchased from

Sigma-Aldrich Corporation (USA). TRIzol™ LS Reagent, RPMI 1640 medium, and fetal bovine serum were purchased from Thermo Fisher Scientific (USA). Cleaved caspase-3, cleaved caspase-9, Bax, and MMP-9 antibodies were all purchased from Abcam Trading Co., Ltd. (Shanghai, China). PrimeScript RT Master Mix and SYBR-Green Premix were all purchased from Takara Bio Inc. (Japan).

2.2. Cell Culture. DU145 human prostate cancer cells purchased from FuHeng Cell Center, Shanghai, China, were cultured in a RPMI 1640 medium containing 10% fetal bovine serum, 10 mg/ml of streptomycin, and 100 U/ml of penicillin at 37°C, 5% CO_2.

2.3. Cell Viability Detected by CCK-8 Assay. DU145 cells in a logarithmic growth phase were seeded in 96-well plates at a density of 5000/well and divided into the control group and the SPUP experimental groups. When cells adhered to the wells after 24 hours of growth, a RPMI 1640 medium with different concentrations of SPUP (25, 50, 100, and 200 μg/ml) was added into each well, respectively, and the same volume of medium was added into a well as the control group. According to the instruction of the kit, the cell viability of

each well was measured after 0, 12, 24, 36, 48, and 72 h of incubation, respectively.

2.4. Cell Migration Detected by Wound Healing Assay.

Cells were seeded in 6-well plates at a density of $1 * 10^5$/well and cultured for 48 h. Two 1 mm wide horizontal lines were drawn across the confluent monolayer of cells in each well using a pipette tip over ruler. The cells washed 3 times with PBS were added with a medium as the control group. And the experimental groups were treated with different concentrations of SPUP (25, 50, 100, and 200 μg/ml). Then, the scratch area was photographed at 0, 48, and 72 h after treatment, respectively, and the scratch width was measured using image analysis software (cell mobility = $(L_{0h} - L_{nh})/L_{0h} *$ 100%; $n = 48, 72$ h).

2.5. Cell Apoptosis Detected by Flow Cytometry.

DU145 cells were seeded in 6-well plates at a density of $1 * 10^5$/well and cultured for 24 h. After adherence, the control group was added with SPUP-free medium, while the experimental groups were treated with different concentrations of SPUP (25, 50, 100, and 200 μg/ml) for 72 h. Then, the cells were digested with EDTA-free trypsin digestion solution, collected to the centrifuge tubes, washed with precooled PBS, and centrifuged for three times. The cells were resuspended with 100 μl of binding buffer (1 : 1 ratio). Then, each tube of cells was added with 5 μl of Annexin V-FITC staining solution and 10 μl of PI staining solution and incubated in the dark for 15 min at room temperature. Afterwards, the cells were added with 400 μl of binding solution (1 : 1 ratio), mixed well, and placed on ice. Samples would be tested on the machine within 1 h.

2.6. Protein Expression Detected by Western Blot.

DU145 cells were seeded in 6-well plates at a density of $1 * 10^5$/well and cultured for 24 h. After adherence, cells were added into SPUP-free medium as control and treated with different concentrations of SPUP (25, 50, 100, and 200 μg/ml) for 72 h. After that, the whole cell protein was extracted with RIPA whole cell lysate according to the instruction, followed by protein electrophoresis, PVDF membrane transfer, incubation combined with specific primary and secondary antibodies, and ECL fluorescence imaging.

2.7. mRNA Expression Detected by qRT-PCR.

The cells were lysed by a TRIzol method to extract total cellular mRNA. Reverse transcription of mRNA into cDNA was then performed according to the instruction of the kit for quantitative fluorescence amplification. $β$-Actin was used as a housekeeping gene to calculate the relative expression level of the target gene. The primer sequences were as follows: MMP-9 forward primer: 5′-TCCAACCACCACCACCGC-3′, reverse primer: 5′-CAGAGAATCGCCAGTACTT-3′; Bax forward primer: 5′-CCCGAGAGGTCTTTTCCGAG-3′, reverse primer: 5′-CCAGCCCATGATGGTTCTGAT-3′; and $β$-actin forward primer: 5′-GGCTCCGGCATGTGCAAG-3′, reverse primer: 5′-CCTCGGTCAGCAGCACGG-3′.
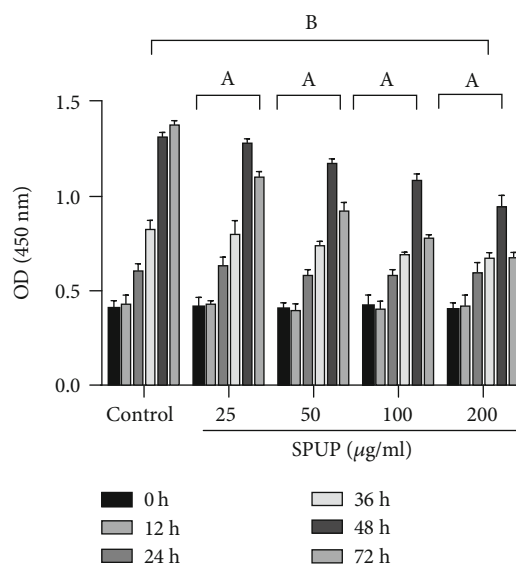

FIGURE 2: Effect of SPUP on the proliferative activity of DU145 cells. Compared with the control group, A: <0.05; within-group comparison of different time points at the same concentration, B: <0.05.

2.8. Statistical Analysis.

All measured data represent as $\bar{x} \pm$ SD, and each experiment was independently repeated at least three times. Data were analyzed using SPSS 20.0 statistical software (USA). Between-group comparison and within-group comparison at different times were performed with one-way analysis of variance, and P values < 0.05 were considered statistically significant.

3. Results

3.1. SPUP Inhibited the Proliferative Activity of DU145 Cells.

As shown in Figure 2, with increasing dose, the proliferative activity of cells was significantly decreased ($P < 0.05$), which indicated that the inhibitory effect was dose dependent; the effect was most significant at 72 h ($P < 0.05$). Therefore, we took 48 h and 72 h as treatment time points in subsequent tests.

3.2. SPUP Inhibited the Migratory Activity of DU145 Cells.

As shown in Figure 3, we found that SPUP inhibited the closure of DU145 cell scratch wound in a time- and dose-dependent manner. The migration rates of all SPUP-treated cells were significantly smaller than those of the control group ($P < 0.05$). The above results showed that SPUP inhibited the migration of DU145 cells in a dose-dependent manner, which revealed that SPUP can inhibit the migration of prostate cancer cells.

3.3. SPUP Downregulated the mRNA and Protein Expression of MMP-9: A Protein Involved in Cell Migration.

As shown in Figure 4, compared with the control group, when the concentration of SPUP was 25 μg/ml, no significant change was observed in MMP-9 protein expression ($P < 0.05$). The expression level of MMP-9 was gradually decreased ($P < 0.05$) with the increase of SPUP concentration (50,
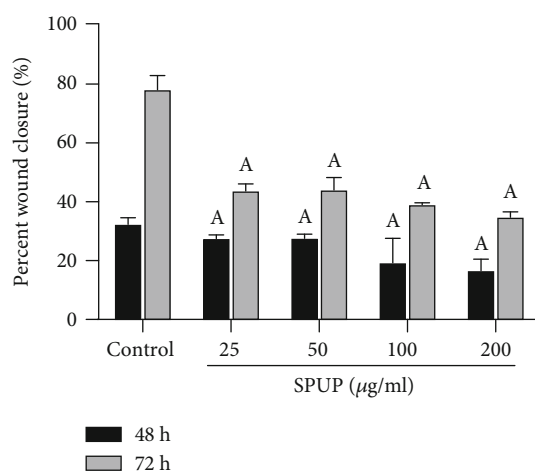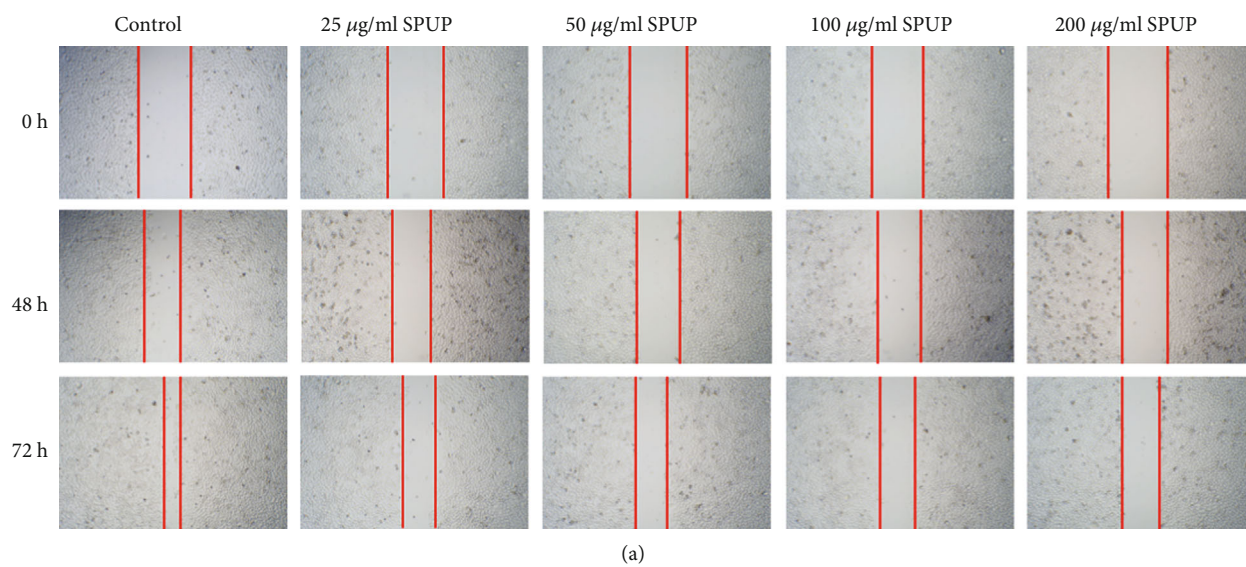
(a)

(b)

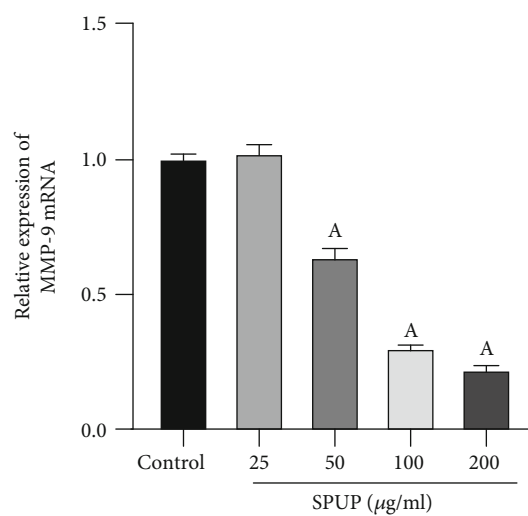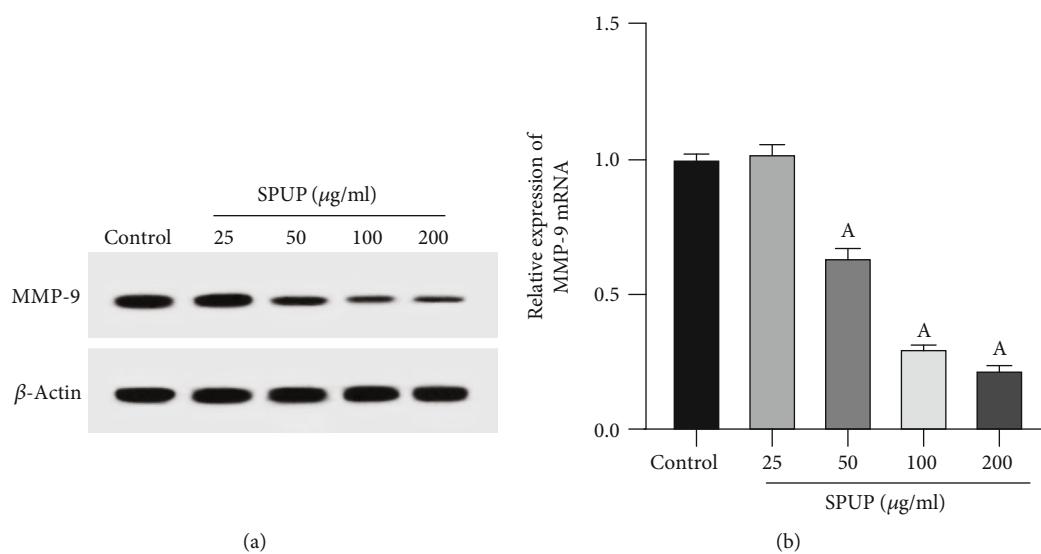FIGURE 3: Effect of SPUP on the migration of DU145 cells. Compared with the control group, A: <0.05.

(a)

(b)

FIGURE 4: SPUP reduced both the expression of DU145 cells and that of migration-related protein MMP-9. Compared with the control group, A: <0.05.
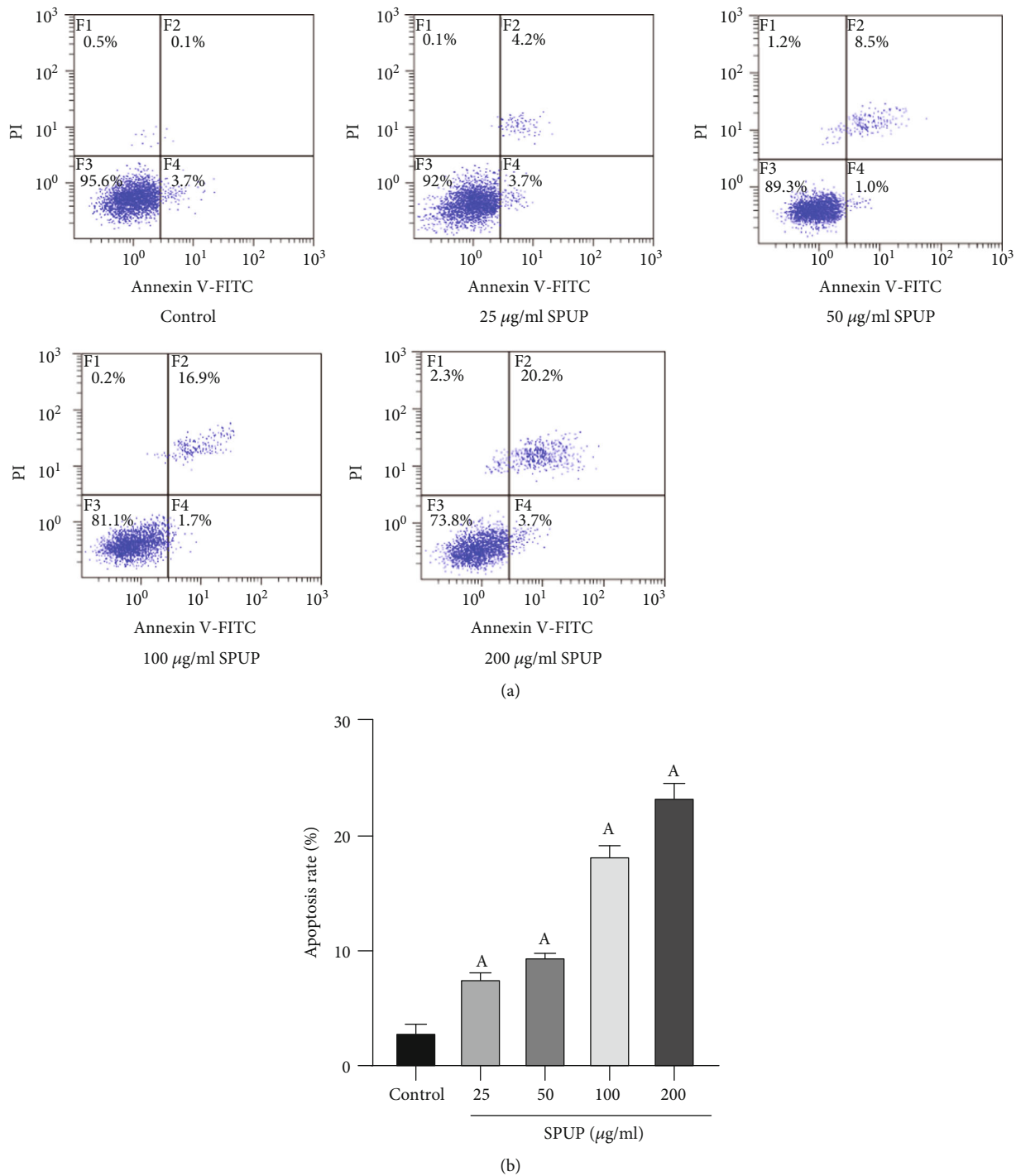
(a)

(b)

FIGURE 5: Effect of SPUP on the apoptosis of DU145 cells. Compared with the control group, A: <0.05.

100, and 200 μg/ml), revealing that SPUP inhibited the expression of migration-related protein MMP-9 at a certain concentration and the mRNA expression was consistent with its protein expression.

3.4. SPUP Induced the Apoptosis of DU145 Cells. As shown in Figure 5, after cells were treated with different concentrations of SPUP for 72 h, various degrees of apoptosis were observed in all groups of DU145 cells. Compared with the control

group, the apoptosis rates of all SPUP groups were significantly increased ($P < 0.05$).

3.5. SPUP Upregulated the Expressions of Apoptosis-Related Proteins Cleaved Caspase-3, Cleaved Caspase-9, and Bax. As shown in Figure 6, compared with the control group, the expressions of cleaved caspase-3, cleaved caspase-9, and Bax were significantly increased ($P < 0.05$) in high-dose groups after SPUP treatment (25, 50, 100, and 200 μg/ml)
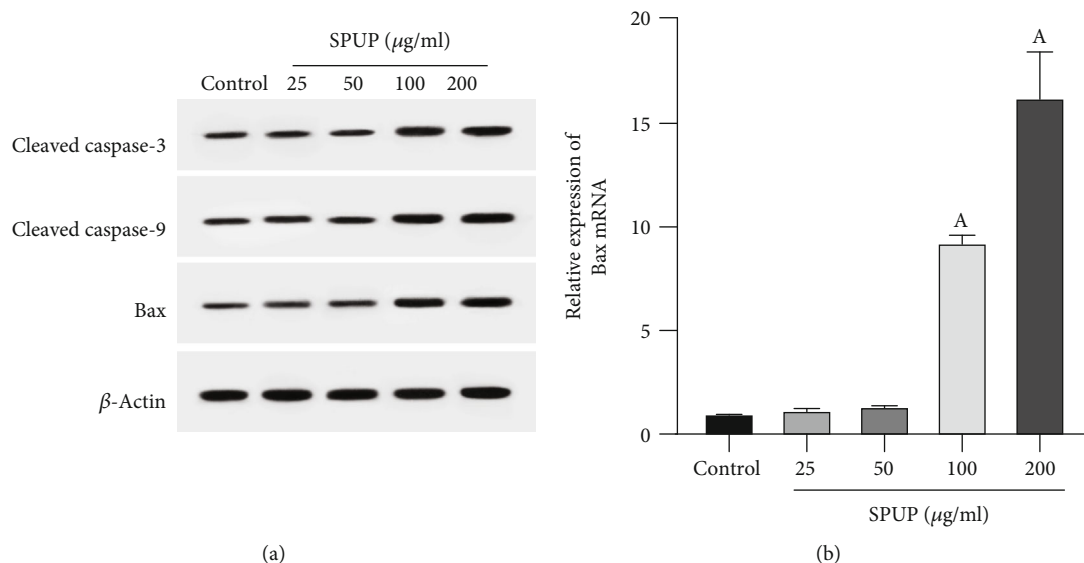
(a)

(b)

FIGURE 6: Expression of apoptosis-related protein and mRNA in DU145 cells treated with SPUP. Compared with the control group, A: <0.05.

for 72 h. The mRNA expression of Bax measured by qRT-PCR was consistent with its protein expression ($P < 0.05$).

4. Discussion

In recent years, patients with prostate cancer have suffered from increasingly higher odds of recurrence and limited life expectancy [13]. At present, surgical resection, radiation therapy, and hormone therapy are mainly used for the treatment of prostate cancer. However, for patients terminally ill with metastasis, there is still a lack of effective treatment measures, which can reduce the harm to their body and improve their quality of life. As such, it is urgent to develop new antitumor drugs.

In the study, sulfated polysaccharides isolated from Undaria pinnatifida and purified were studied for inhibitory effects on the growth of prostate cancer cells cultured in vitro. The inhibitory effect of SPUP on the proliferation of DU145 cells was detected by CCK-8 assay. It was found that when DU145 cells were treated with different concentrations of SPUP, the inhibition of proliferation was positively correlated with the SPUP concentration. DU145 cells treated with 200 μg/ml of SPUP for 72 h could show significantly downregulated proliferative activity as compared with the control group. To further understand the role of SPUP in prostate cancer progression, we also performed studies on cell migration and apoptosis, respectively. In the scratch assay, we chose 72 h as treatment time when cell proliferation was significantly inhibited in CCK-8. After treating the cells with different concentrations of SPUP, we found that the degree of closure of the scratches in all SPUP-treated cells was significantly smaller than that in the control group. Furthermore, we found that the effect of SPUP on the scratch closure of DU145 cells was significantly dose dependent, suggesting that SPUP inhibits the migration of prostate cancer cells. Matrix metalloproteinases (MMPs), including MMP2 and MMP9, facilitate the invasiveness and metastasis of a variety of cancer cells by degrading extracellular matrix and other

barriers [14]. MMPs have been shown to be important targets for treating metastatic prostate cancer. For example, Larsson et al. found that MMP9 can increase the aggressiveness of metastatic cancer and promote the growth of metastatic tumors by interacting with other factors [15]. Li et al. found that reducing the expression of MMP-9 in prostate cancer cells was accompanied by a decrease in cell invasion and migration [16]. Since we found that SPUP-treated cells inhibit the migration of prostate cancer, we hypothesized that SPUP exerts the effect through cancer cell invasion and metastasis-promoting factor MMP-9 [17] and then found that the higher the concentration of SPUP, the lower the expression of MMP-9, indicating that SPUP may suppress cell migration by inhibiting the expression of MMP-9 protein. In terms of induction of apoptosis, DU145 cells were treated with different SPUP concentrations (25, 50, 100, and 200 μg/ml) for 72 h, and the results indicated that SPUP can induce apoptosis in a dose-dependent manner in DU145 cells. By detecting the expression of apoptosis-related proteins cleaved caspase-3, cleaved caspase-9, and Bax as well as mRNA expression of Bax, we found that the expression level of apoptosis-related proteins significantly increased after treatment of SPUP as compared with the control group, suggesting that SPUP may promote apoptosis in DU145 cells by upregulating the expression of the above induction-related factors; yet, the specific mechanism of pathway needs further study.

The above results showed that SPUP can inhibit the proliferation and migration of DU145 cells and promote apoptotic response, and further study based on the results can underlie necessary data to support the therapeutic effect of SPUP against prostate cancer, making SPUP a promising drug for the treatment of prostate cancer.

5. Conclusion

In the study, sulfated polysaccharide isolated from Undaria pinnatifida and purified was investigated for its mechanism and effect on DU145 human prostate cancer cells cultured

in vitro, expecting to find a newly effective drug with low toxicity against prostate cancer. The experimental results confirmed that SPUP can inhibit DU145 cell proliferation, suppress cell migration by downregulating the expression of MMP-9 protein, and promote apoptotic response by upregulating the expression of apoptosis-related proteins cleaved caspase-3, cleaved caspase-9, and Bax. Thus, it can be seen that SPUP has great potential in treating prostate cancer, while we still need to conduct more in-depth experimental studies on its mechanism and large-scale population-based studies to clarify its therapeutic effect.

Data Availability

The datasets used and/or analyzed during the current study are available from the corresponding author on reasonable request.

Conflicts of Interest

The authors declare that they have no competing interests.

Acknowledgments

References

[1] R. L. Siegel, K. D. Miller, and A. Jemal, "Cancer statistics, 2015," *CA: A Cancer Journal for Clinicians*, vol. 65, no. 1, pp. 5–29, 2015.

[2] C. Hanna and R. J. Jones, "Emerging treatments for recurrent prostate cancer," *Future Oncology*, vol. 11, no. 21, pp. 2873–2880, 2015.

[3] M. P. Edlind and A. C. Hsieh, "PI3K-AKT-mTOR signaling in prostate cancer progression and androgen deprivation therapy resistance," *Asian Journal of Andrology*, vol. 16, no. 3, pp. 378–386, 2014.

[4] C. P. Filson, L. S. Marks, and M. S. Litwin, "Expectant management for men with early stage prostate cancer," *CA: A Cancer Journal for Clinicians*, vol. 65, no. 4, pp. 265–282, 2015.

[5] A. Zong, Y. Liu, Y. Zhang et al., "Anti-tumor activity and the mechanism of SIP-S: a sulfated polysaccharide with antimetastatic effect," *Carbohydrate Polymers*, vol. 129, no. 50, pp. 50–54, 2015.

[6] A. Zong, H. Cao, and F. Wang, "Anticancer polysaccharides from natural resources: a review of recent research," *Carbohydrate Polymers*, vol. 90, no. 4, pp. 1395–1410, 2012.

[7] A. Y. Zhou, J. Robertson, N. Hamid, Q. Ma, and J. Lu, "Changes in total nitrogen and amino acid composition of New Zealand *Undaria pinnatifida* with growth, location and plant parts," *Food Chemistry*, vol. 186, pp. 319–325, 2015.

[8] W. A. J. P. Wijesinghe and Y.-J. Jeon, "Biological activities and potential industrial applications of fucose rich sulfated polysaccharides and fucoidans isolated from brown seaweeds: a review," *Carbohydrate Polymers*, vol. 88, no. 1, pp. 13–20, 2012.

[9] S. Fukuda, H. Saito, S. Nakaji et al., "Pattern of dietary fiber intake among the Japanese general population," *European Journal of Clinical Nutrition*, vol. 61, no. 1, pp. 99–103, 2007.

[10] O. S. Vishchuk, S. P. Ermakova, and T. N. Zvyagintseva, "The fucoidans from brown algae of Far-Eastern seas: anti-tumor activity and structure–function relationship," *Food Chemistry*, vol. 141, no. 2, pp. 1211–1217, 2013.

[11] J. Wu, H. Li, X. Wang et al., "Effect of polysaccharide from *Undaria pinnatifida* on proliferation, migration and apoptosis of breast cancer cell MCF7," *International Journal of Biological Macromolecules*, vol. 121, pp. 734–742, 2019.

[12] Y. Han, J. Wu, T. Liu et al., "Separation, characterization and anticancer activities of a sulfated polysaccharide from *Undaria pinnatifida*," *International Journal of Biological Macromolecules*, vol. 83, pp. 42–49, 2016.

[13] I. Ahmad, L. B. Singh, Z. H. Yang et al., "Mir143 expression inversely correlates with nuclear ERK5 immunoreactivity in clinical prostate cancer," *British Journal of Cancer*, vol. 108, no. 1, pp. 149–154, 2013.

[14] M. I. Cockett, G. Murphy, M. L. Birch et al., "Matrix metalloproteinases and metastatic cancer," *Biochemical Society Symposium*, vol. 63, pp. 295–313, 1998.

[15] P. Larsson, A. S. Syed Khaja, J. Semenas et al., "The functional interlink between AR and MMP9/VEGF signaling axis is mediated through PIP5K1α/pAKT in prostate cancer," *International Journal of Cancer*, 2019.

[16] W. Li, K. Qi, Z. Wang et al., "Golgi phosphoprotein 3 regulates metastasis of prostate cancer via matrix metalloproteinase 9," *International Journal of Clinical and Experimental Pathology*, vol. 8, no. 4, pp. 3691–3700, 2015.

[17] M. W. Roomi, T. Kalinovsky, A. Niedzwiecki, and M. Rath, "Modulation of MMP-2 and -9 secretion by cytokines, inducers and inhibitors in human melanoma A-2058 cells," *Oncology Reports*, vol. 37, no. 6, pp. 3681–3687, 2017.

Research Article

Protective Effect of Polygonatum sibiricum Polysaccharides on Apoptosis, Inflammation, and Oxidative Stress in Nucleus Pulposus Cells of Rats with the Degeneration of the Intervertebral Disc

Zhaohui Zhai [ID],[1] Zhaoxin Li,[2] Zhonglei Ji [ID],[3] and Xiaosheng Lu [ID][4]

[1]*Department of Plastic Surgery, Plastic Surgery Hospital of Weifang Medical University, Weifang, Shandong 261042, China*
[2]*Emergency Department of Weifang Traditional Medicine Hospital, Shandong Province 261041, China*
[3]*Rehabilitation Medicine Department, Affiliated Hospital of Weifang Medical University, 261031, China*
[4]*Plastic Surgery Department, Affiliated Hospital of Weifang Medical University, 261031, China*

Correspondence should be addressed to Zhonglei Ji; wyfyjzl@163.com and Xiaosheng Lu; luxiaosheng2006@163.com

Objective. Polygonatum sibiricum polysaccharide (PSP) has antioxidant activity, immune enhancement, and other biological properties. However, the effect of PSP on intervertebral disc degeneration has not been reported. In this study, we mainly investigated the effect of PSP on the apoptosis, inflammation, and oxidative stress of nucleus pulposus cells (NPCs) during the process of intervertebral disc degeneration. *Methods*. A rat NPC model induced by H_2O_2 was constructed. The CCK8 method was used to measure the effects of PSP on the apoptosis of rat NPCs induced by H_2O_2. The effects on the activity of SOD and content of MDA were also determined. The rat model of intervertebral disc degeneration was treated with PSP for 1 month, and the mRNA expression levels of IL-1β, COX2, iNOS, Col2α1, Col10α1, and MMP3 were measured by qPCR in the tissue of intervertebral disc. NPCs from the degenerated intervertebral discs were separated, and the cell viability was measured by the CCK8 method. The contents of SOD and MDA in NPCs were determined as well. *Results*. PSP significantly reduced the apoptosis of NPCs induced by H_2O_2, significantly increased the SOD content, and decreased the content of MDA in H_2O_2-induced NPCs. The expression level of IL-1β, COX2, and iNOS in the rat model with intervertebral disc degeneration was significantly downregulated after 1 month of PSP treatment. PSP treatment increased the expression of Col2α1 type and significantly decreased the expression of Col10α1 type collagen and MMP3 in rats with disc degeneration. PSP treatment significantly reduced NPC apoptosis and increased its SOD content and reduced MDA content, which is consistent with the results from cell-level experiments. *Conclusion*. PSP can effectively reduce the apoptosis, inflammation, and oxidative stress of H_2O_2-induced NPCs in rats with intervertebral disc degeneration and mitigate the progression of intervertebral disc degeneration, which has the potential to be developed as new drugs for the treatment of intervertebral disc degeneration.

1. Introduction

Polygonatum kingianum Coll.et Hemsl is widely and abundantly distributed in China. Polygonatum sibiricum is the dry rhizome of Polygonatum kingianum Coll.et Hemsl which is a well-known traditional Chinese herbal medicine and functional food [1, 2]. The major extract from Polygonatum sibiricum is Polygonatum sibiricum polysaccharides (PSP) mainly consisting of mannose, galactose, glucose, and xylose,

which is also rich in various bioactive components such as alkaloids, steroidal saponins, flavonoids, and lignin [3, 4]. In recent years, PSP has been reported to have many pharmacological applications and biological activities, such as antioxidant, antiaging, antiosteoporosis, antidiabetes, anticancer, and antifatigue, as well as immune enhancement, neuroprotection [5, 6].

Low back pain is a common disease that places a huge burden on public health and the economy. There are lots of

reason for causing the low back pain, of which disc degeneration is one of the most important pathological changes; nevertheless, the molecular mechanism of the pathogenesis in intervertebral disc degeneration remains unclear [7]. There is increasing evidence that the role of nucleus pulposus cells (NPCs) in producing extracellular matrix components and secreting cytokines is critical to maintaining disc integrity. Importantly, apoptosis of NPCs, inflammation, and oxidative stress is involved in the development of intervertebral disc degeneration [8]. However, whether PSP with a variety of bioactivity can effectively treat intervertebral disc degeneration has not been reported yet.

2. Methods

2.1. PSP Extraction and HPLC Detection. The hot water leaching method was used to extract the PSP. The Polygonatum sibiricum pieces (Golden Leaf Pharmaceutical Co. Ltd., China) were mixed with water at the volume ratio of $1:8$, which was then boiled for 2 h and repeated three times, and the aqueous extract was precipitated by ethanol (80%) (Sinopharm Group, China) to remove the bioactive protein substance. PSP was obtained after precipitation and evaporation of ethanol [4]. The PSP was then subjected to acid hydrolysis; specifically, PSP (0.25 g) was mixed with 0.1 L of 2 mol/L TFA (Sinopharm Group, China) solution and dried in DHG-9070A oven (Shamghai Bluepard Instruments Co. Ltd) at 100°C, and 0.1 L methanol (Sinopharm Group, China) was added afterward to remove the TFA. After 3 times of repeated acid hydrolysis, the product was subjected to PMP (1-phenyl-3-methyl-5-pyrazolone) derivatization to obtain an HPLC test solution. In detail, the acid hydrolyzate was mixed with 0.1 L of 0.3 mol/L NaOH (Sinopharm Group, China), and 0.12 L of 0.5 mol/L methanol solution was added after that, the mixer was then incubated at 70°C in a water bath for 30 min. After that, 0.1 L of 0.3 mol/L HCl (Sinopharm Group, China) was added and an equal volume of chloroform was used for extraction. The aqueous solution was taken for drying, and the extracted product is dissolved in 0.2 L of methanol to obtain an HPLC test solution. HPLC detection was then carried out using a mixed monosaccharide solution as a control; mannose, glucose, galactose, xylose, glucuronic acid, rhamnose, galacturonic acid, arabinose, and trehalose were all purchased from Sinopharm Group, China.

2.2. CCK8 Assay. NPCs were seeded at a density of 5000 cells per well in 96-well plates. The cells were washed with phosphate-buffered saline (PBS) for 3 times after H_2O_2 or PSP treatment. The CCK8 test was performed according to the kit manual, and the absorbance at 450 nm was measured with a spectrophotometer to calculate the cell survival rate.

2.3. Apoptosis Detected with Flow Cytometry. The cells were collected and fixed using absolute ethanol precooled at -20°C. The fixed cells were slowly and fully resuspended with RNase A solution (Beijing Solabao Technology Co. Ltd., China) to digest the RNA in the cells. 400 μL of a Propidium Iodide solution (PI, 50 μg/mL) was added to each cell sample

to stain the nuclei for 10 min in the dark. Flow cytometry detection was completed within 24 hours after dyeing was completed. The red fluorescence was detected at an excitation wavelength of 488 nm through the BD flow cytometer channel FL2, and the light scattering was detected at the same time.

2.4. Detection of SOD and MDA. The amount of SOD reflecting the content of reducing substances in the cells was quantitatively measured by the formazan dye, which indicates the state of the antioxidant substances in the cells. The formazan dye is a substance that can be removed by SOD. In this study, we used the SOD test kit (Dojindo, Japan) to quantify the amount of formazan dye in turn to study SOD activity. According to the instructions, the OD value of the test sample and the standard at 450 nm were measured, and the SOD activity was calculated based on the formazan dye content.

The level of malondialdehyde (MDA) reflecting the level of oxidation in the cells was determined by the thiobarbituric acid (TBA) method. The OD value of the test sample and the standard at 530 nm were measured according to the instruction, and the content of MDA in the sample was calculated accordingly.

2.5. qPCR. NPCs were collected and total RNA was extracted with the RNeasy Protect Mini kit (74104, QIAGEN, Germany). The absorbance at 260 nm and 280 nm of the total RNA was determined by a spectrophotometer. And the RNA was reversely transcribed into cDNA if the OD_{260}/OD_{280} is between 1.6 and 2.0. The qPCR assay was performed according to the protocol, and the reaction was conducted in the ABI PRISM 7700 Sequence Detection System with the ABI PRISM 7700 Sequence Detection Software 1.9.1. GAPDH was used as an internal reference gene. The relative expression level of each gene of interest was represented by $2^{-\Delta\Delta Ct}$.

2.6. NPC Separation. All experiments in this study were approved by the Animal Experimental Ethics Committee. NPCs were isolated from the intervertebral discs of 180 g-200 g SD rats. The cells were first treated with PBS containing 10% penicillin at 37°C for 10 minutes and then cultured at 37°C for 18 h in DMEM-F12 containing 10% fetal bovine serum, 0.05 mg/ml ascorbic acid, 1% penicillin, and 0.2% collagenase. NPCs were collected afterward and continued to be cultured in a DMEM-F12 medium, and the medium was changed every 3 days.

2.7. Animal Model. Male SD rats were randomly divided into the following 3 groups (6 in each group): control group, model group, and PSP treatment group. Rats in the control group did not receive any treatment and were kept in an ordinary cage. The forelimbs of the rats in the model the PSP treatment group were excised from the shoulder joint. Specifically, after shaving the front limbs of the rats, the upper limb skin was disinfected with iodophor. The skin was cut at the proximal end of the forearm, fascia and muscles were then removed, the vascular nerve bundle under the deltoid muscle were ligatured, and the humerus was clamped at the distal
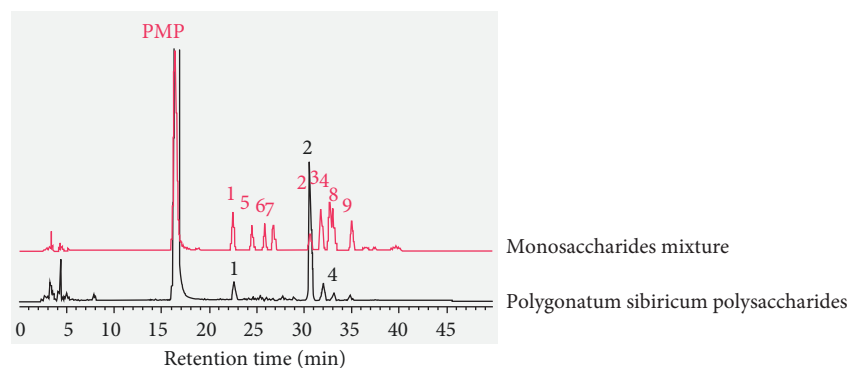
Figure 1: Chromatography of Polygonatum sibiricum polysaccharide (PSP) derivatization. 1: mannose; 2: glucose; 3: galactose; 4: xylose; 5: glucuronic acid; 6: rhamnose; 7: galacturonic acid; 8: arabinose; 9: fucose.

end of the ligation. After muscles, blood vessels, nerves, and skin were cut, the gentamicin hydrochloride was distilled into the incision; the muscles, fascia, and skin were then sutured layer by layer. The postoperative rat was forced to maintain an upright posture for seven months in a specially designed cage. Rats in the PSP treatment group was given PSP (600 mg/(kg∗d)) treatment 6 months after their operation for 30 days. The rats were then sacrificed, and the lumbar spine was analyzed.

2.8. Data Analysis. Data were analyzed using SPSS 21.0. The results for each group are expressed as mean ± standard deviation ($\bar{x} \pm s$). For the comparison between two groups, independent sample t-tests were used when the variance was uniform and the Satterthwaite approximate t-test was used when the variance was not uniform. $P < 0.05$ indicates that the difference was statistically significant.

3. Results

3.1. HPLC Detection of PSP Extract. As shown in Figure 1, compared with the control curve of the monosaccharide mixture, a variety of monosaccharides were well separated in PSP extract. Four peaks were observed from the test curve. Compared with the control curve, the majority of monosaccharides in the test sample were mannose, glucose, galactose, and xylose and the glucose content was much higher than the other three monosaccharides.

3.2. Protective Effect of PSP on Apoptosis of Rat NPCs Induced by H_2O_2. The cytotoxicity of PSP on NPCs at different concentrations (0.625 mg/L, 1.250 mg/L, 2.5 mg/L, and 5 mg/L) was determined by CCK8 assay. The results shown in Figure 2(a) indicated that PSP from 0.625 mg/L to 5 mg/L had no significant cytotoxic effect on NPCs ($P > 0.05$). We further explored the optimal concentration of H_2O_2 for the induction of apoptosis in NPCs. The cell viability of NPCs treated with 100 μM, 200 μM, and 400 μM H_2O_2 was determined by CCK8, respectively. The result showed that the three concentration gradients of H_2O_2 inhibited the viability of NPCs to various degrees and H_2O_2 at a concentration of 200 μM reached a 55% inhibition rate ($P < 0.05$) after 6 h of treatment as shown in Figure 2(b). To investigate whether

PSP has a protective effect on H_2O_2-induced apoptosis in rat NPCs, NPCs were treated with PSP at concentrations of 0.625 mg/L, 1.250 mg/L, 2.5 mg/L, and 5 mg/L separately for 48 h before the induction of apoptosis in NPCs with 200 μM H_2O_2. The control group was treated only with 200 μM H_2O_2, and finally, the cell viability of NPCs was determined using CCK8. The results are shown in Figure 2(c). Compared with the control group, the PSP group with 0.625 mg/L to 5 mg/L concentration had a significant protective effect on H_2O_2-induced apoptosis in NPCs ($P < 0.05$), and the cell viability was similar under the treatment of PSP at 1.250 mg/L, 2.5 mg/L, and 5 mg/L, respectively ($P > 0.05$). Therefore, the smallest dose of 1.250 mg/L was selected in the subsequent experiments. To further verify that the PSP had a significant protective effect on H_2O_2-induced apoptosis in NPCs, we used flow cytometry to detect the apoptosis rate of H_2O_2-induced NPCs that were treated with PSP from 0.625 mg/L to 5 mg/L. As shown in Figure 3, compared with the apoptosis rate of 30.4% in the control group, the apoptosis rate of H_2O_2-induced NPCs was significantly decreased by PSP (0.625 mg/L to 5 mg/L) to 24.6%, 16.2%, 15.4%, and 15.6% separately ($P < 0.05$).

3.3. Protective Effect of PSP on H_2O_2-Induced Oxidative Stress in Rat NPCs. The amount of SOD reflecting the content of reducing substances in the cells was quantitatively determined by the formazan dye method. The results showed that the level of SOD in rat NPCs induced by H_2O_2 was significantly lower than that in the blank group ($P < 0.05$). Whereas after pretreatment with PSP for 48 hours, the level of SOD in NPCs induced with H_2O_2 was significantly higher than that in the model group ($P < 0.05$) as indicated in Figure 4(a).

The level of malondialdehyde (MDA) reflecting the level of oxidation in the cells was determined by the thiobarbituric acid (TBA) method. As shown in Figure 4(b), the MDA level in rat NPCs induced with H_2O_2 was significantly higher than that of the blank group ($P < 0.05$). However, after pretreatment with PSP for 48 hours, the MDA level was significantly reduced compared to the model group ($P < 0.05$).

3.4. Protective Effect of PSP on Inflammation of Rats with Degeneration of the Intervertebral Disc. The rat model with intervertebral disc degeneration was constructed, and qPCR
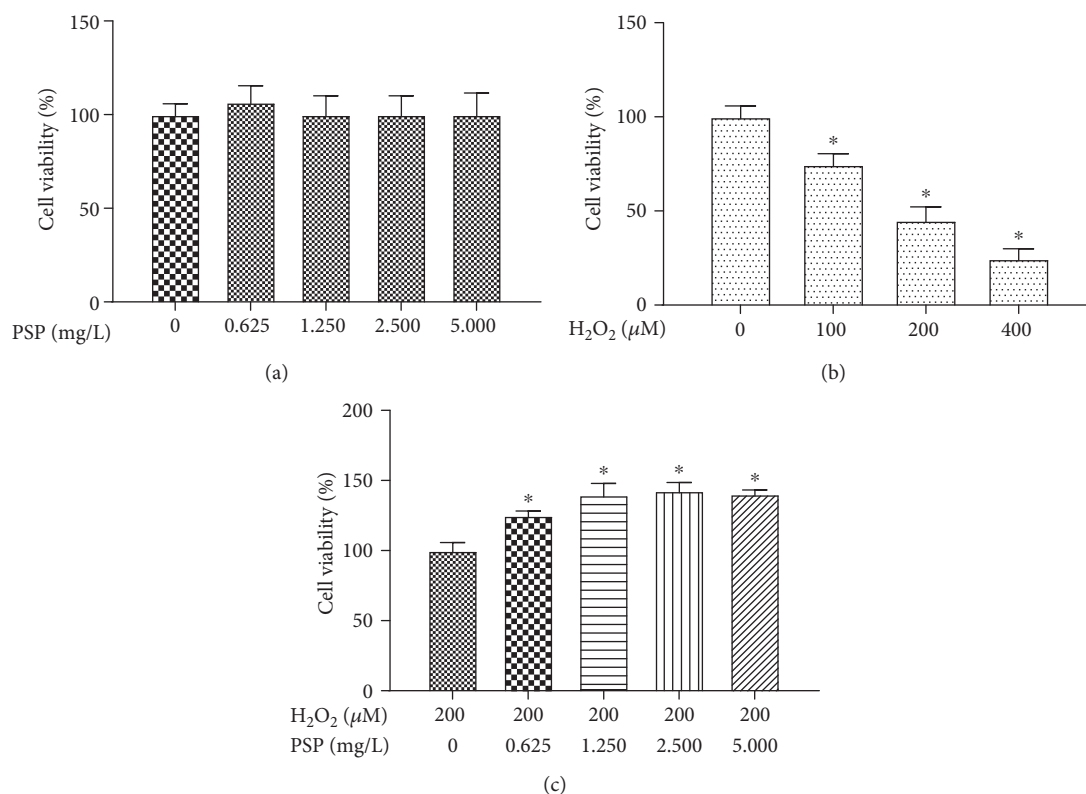
(a)

(b)

(c)

FIGURE 2: PSP inhibits H_2O_2-induced apoptosis in NPCs. (a) The toxicity of different concentrations of PSP on NPCs. $^*P < 0.05$, compared with the blank group. (b) The effects on cell viability by different concentrations of H_2O_2. $^*P < 0.05$, compared with 0 μM PSP groups. (c) The effects of different concentrations of PSP on the cell viability affected by 200 μM H_2O_2. $^*P < 0.05$, compared with the control group.

was used to measure the expression level of IL-1β, COX2, and iNOS in the cells, which indicate the inflammatory state of the intervertebral disc. The result in Figure 5 showed that compared with the blank group, the model group rats maintaining the upright posture for a long time had a heightened expression of IL-1β, COX2, and iNOS ($P < 0.05$). Subsequently, we administered PSP intragastrically to rats with the degeneration of intervertebral disc for 1 month and found that PSP could effectively alleviate the inflammation caused by long-term upright posture. Accordingly, compared with the model group, the expression level of IL-1β, COX2, and iNOS in the PSP treatment group was significantly downregulated as shown in Figure 5 ($P < 0.05$).

3.5. Effect of PSP on Collagen Synthesis and Catabolism in Rats with Degeneration of the Intervertebral Disc. The mRNA expression level of Col2α1 and Col10α1 type collagen, as well as the expression level of Col2α1 degrading enzyme MMP3, was determined via qPCR. We found that the upright posture induced the downregulation of Col2α1 and upregulation of Col10α1 as well as MMP3 ($P < 0.05$), while PSP pretreatment completely restored the decrease of Col2α1 mRNA expression and downregulated the expression of MMP3 and Col10α1, as shown in Figure 6.

3.6. Effect of PSP on the Activity of NPCs in Rats with Degeneration of the Intervertebral Disc. NPCs were separated from rats with degeneration of intervertebral discs, and

cell viability was measured by CCK8 assay. The results showed that NPC activity in the model group was significantly lower than that in the blank group ($P < 0.05$) and PSP treatment effectively reversed the decrease of cell viability, as shown in Figure 7.

3.7. Effect of PSP on Oxidative Stress of NPCs in Rats with Degeneration of the Intervertebral Disc. NPCs were separated from rats with degeneration of intervertebral discs, the SOD activity and MDA content were measured according to the instruction of the kit, and the test results were then normalized. The result showed that the SOD activity in the NPCs in the model group was significantly lower than that in the blank group ($P < 0.05$) and the MDA content was significantly increased ($P < 0.05$). However, with the PSP treatment, the SOD activity was effectively increased ($P < 0.05$) and the content of MDA in the cells was decreased ($P < 0.05$), as shown in Figure 8.

4. Discussion

In recent years, significant progress has been made in the study of active polysaccharides [9, 10], among which Polygonatum sibiricum polysaccharide a health food has received extensive appreciation. Because of its rich biological activity, many studies have explored its role in osteoporosis, tumors, and other diseases [11]. Angiogenesis and inflammation in the pathological state of intervertebral disc degeneration
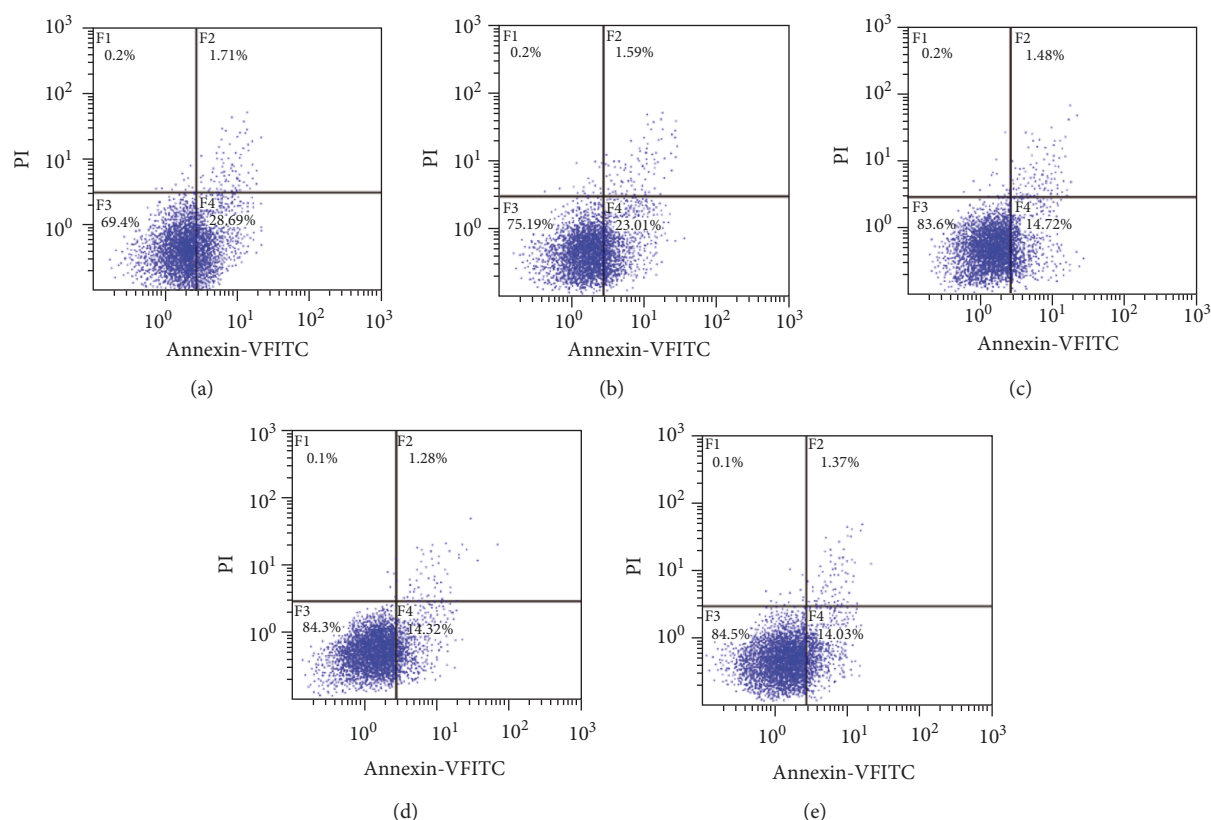
(a)

(b)

(c)

(d)

(e)

FIGURE 3: Flow cytometry was used to detect the effect of PSP on apoptosis induced by 200 μM H_2O_2. (a) Apoptosis rate in the control group: 30.4%. (b) Apoptosis rate (24.6%) under the treatment of 0.625 mg/L PSP. (c) Apoptosis rate (16.2%) under the treatment of 1.250 mg/L PSP. (d) Apoptosis rate (15.4%) under the treatment of 2.5 mg/L PSP. (e) Apoptosis rate (15.6%) under the treatment of 5 mg/L PSP.
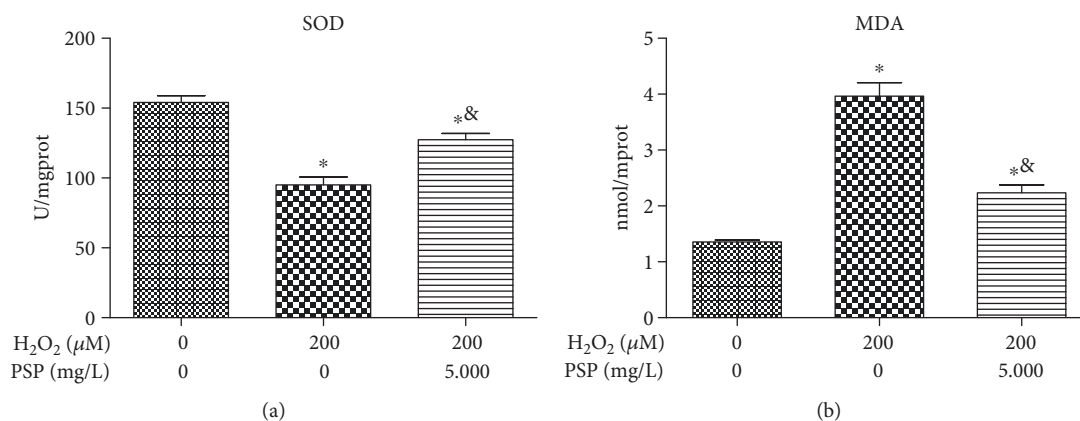

(a)

(b)

FIGURE 4: Protective effect of PSP on oxidative stress in rat NPCs. (a) Detection of the intracellular reducing substance SOD. (b) Detection of intracellular oxidation product MDA. $^*P < 0.05$, compared with the blank group. $^\&P < 0.05$, compared with the H_2O_2 induction group.

aggravate the oxidative stress of NPCs, promote the progression of IVDD, and form a vicious circle [12]. Under pathological conditions, excessive reactive oxygen species and inflammation were often generated which, in turn, could induce apoptosis of NPCs and were considered to be key targets for the treatment of IVDD [13]. We demonstrated that H_2O_2 could induce higher levels of MDA in NPCs and could increase NPC apoptosis in vitro but PSP treatment could alleviate this change. It has been reported that pretreatment of PSP significantly reduced $A\beta$(25-35)-induced PC12 cell death, increased Bax/bcl-2 ratio, inhibited mitochondrial dysfunction, and released cytochrome c to the cytosol. In addition, PSP significantly inhibited $A\beta$(25-35)-induced caspase-3 activation and enhanced phosphorylation of Akt in PC12 cells [1]. This line of evidence suggests that the protective effect of PSP may be related to the upregulation of the PI3K/Akt signaling pathway, which however needs further research and verification. Treatment of NPCs with
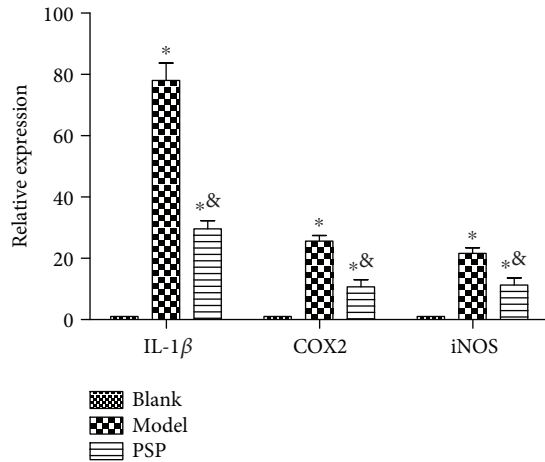
FIGURE 5: Protective effect of PSP on inflammation of rats with degeneration of the intervertebral disc. $^*P < 0.05$, compared with the blank group. $^\&P < 0.05$, compared with the model group.

FIGURE 6: Effect of PSP on the expression of Col2α1, Col10α1, and MMP3 in rats with degeneration of the intervertebral disc. $^*P < 0.05$, compared with the blank group. $^\&P < 0.05$, compared with the model group.

FIGURE 7: Effect of PSP on the activity of NPCs in rats with degeneration of the intervertebral disc.

FIGURE 8: Effect of PSP on oxidative stress in NPCs of rats with degeneration of the intervertebral disc. $^*P < 0.05$, compared with the blank group. $^\&P < 0.05$, compared with the model group.

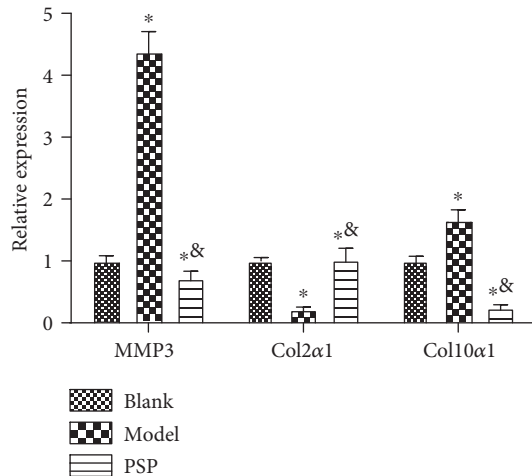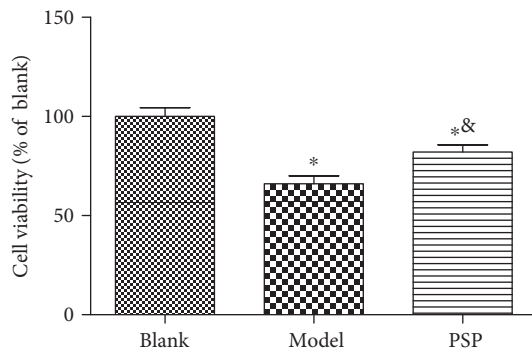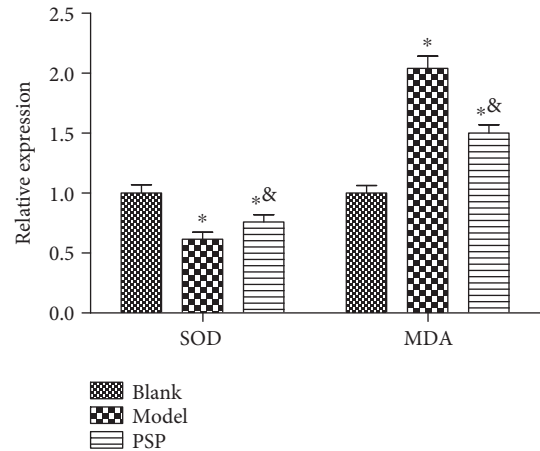PSP prior to H_2O_2 treatment can alleviate oxidative stress suggesting the antioxidant activity of PSP. PSP has the function of regulating the activity of the enzyme and the ability to chelate metal. We have shown a higher SOD content in the PSP treatment group compared with the model group. By constructing a rat model with intervertebral disc degeneration, it was further showed that PSP could effectively improve oxidative stress and mitigate apoptosis of NPCs during intervertebral disc degeneration.

Many studies have also shown that disc degeneration is typically accompanied by a certain degree of inflammation, and inflammation, in turn, promotes the development of the disease [14–16]. It has also been reported that PSP could reduce myocardial inflammatory injury in type I diabetes by inhibiting inflammatory response via the inhibitory effects on the expression of TLR4, MIF, and NF-κB [11]. Our in vivo studies have shown that PSP could inhibit the expression of inflammatory mediators in the intervertebral disc and reduce the expression of Col10α1, as well as increasing the content of Col2α1 in the intervertebral disc by inhibiting the expression of Col2α1 degrading enzyme MMP3.

5. Conclusion

Our in vitro and in vivo experiments confirmed that PSP is effective for the alleviation of oxidative stress and apoptosis in NPCs and lumbar disc degeneration caused by prolonged standing posture. Results from this study showed that PSP is a potential candidate for the treatment of IVDD-related diseases. Based on these findings, we firmly believe that PSP can play an effective role in inhibiting the degeneration of the intervertebral disc and is a promising drug for the treatment and prevention of disc degeneration.

Data Availability

The data used to support the findings of this study are available from the corresponding author upon request.

Conflicts of Interest

The authors declare that there are no conflicts of interest regarding the publication of this paper.

Authors' Contributions

Zhaohui Zhai and Zhaoxin Li contributed equally to this work. Also, Xiaosheng Lu and Zhonglei Ji contributed equally to this work.

Acknowledgments

References

[1] H. Zhang, Y. Cao, L. Chen et al., "A polysaccharide from Polygonatum sibiricum attenuates amyloid-β-induced neurotoxicity in PC12 cells," *Carbohydrate Polymers*, vol. 117, pp. 879–886, 2015.

[2] K. Yelithao, U. Surayot, J. H. Lee, and S. G. You, "RAW264.7 cell activating glucomannans extracted from rhizome of Polygonatum sibiricum," *Preventive Nutrition and Food Science*, vol. 21, no. 3, pp. 245–254, 2016.

[3] P. Zhao, C. Zhao, X. Li et al., "The genus Polygonatum: a review of ethnopharmacology, phytochemistry and pharmacology," *Journal of Ethnopharmacology*, vol. 214, pp. 274–291, 2018.

[4] Q. Zhu, X. Deng, S. B. Zhang et al., "Research progress in extraction technology, content determination and composition analysis of Polyonatum polysaccharides," *Central South Pharmacy*, vol. 15, pp. 1586–1590, 2017.

[5] N. Liu, Z. Dong, X. Zhu, H. Xu, and Z. Zhao, "Characterization and protective effect of Polygonatum sibiricum polysaccharide against cyclophosphamide-induced immunosuppression in Balb/c mice," *International Journal of Biological Macromolecules*, vol. 107, pp. 796–802, 2018.

[6] X. Zhao and J. Li, "Chemical constituents of the genus Polygonatum and their role in medicinal treatment," *Natural Product Communications*, vol. 10, no. 4, p. 1934578X1501000, 2015.

[7] I. Tegeder and J. Lotsch, "Current evidence for a modulation of low back pain by human genetic variants," *Journal of Cellular and Molecular Medicine*, vol. 13, no. 8B, pp. 1605–1619, 2009.

[8] A. Omair, M. Holden, B. A. Lie, O. Reikeras, and J. I. Brox, "Treatment outcome of chronic low back pain and radiographic lumbar disc degeneration are associated with inflammatory and matrix degrading gene variants: a prospective genetic association study," *BMC Musculoskeletal Disorders*, vol. 14, no. 1, 2013.

[9] K. Zhao, D. Li, W. Xu et al., "Targeted hydroxyethyl starch prodrug for inhibiting the growth and metastasis of prostate cancer," *Biomaterials*, vol. 116, pp. 82–94, 2017.

[10] S. Li, T. Zhang, W. Xu et al., "Sarcoma-targeting peptide-decorated polypeptide nanogel intracellularly delivers shikonin for upregulated osteosarcoma necroptosis and diminished pulmonary metastasis," *Theranostics*, vol. 8, no. 5, pp. 1361–1375, 2018.

[11] X. Cui, S. Wang, H. Cao et al., "A review: the bioactivities and pharmacological applications of Polygonatum sibiricum polysaccharides," *Molecules*, vol. 23, no. 5, p. 1170, 2018.

[12] S. Suzuki, N. Fujita, N. Hosogane et al., "Excessive reactive oxygen species are therapeutic targets for intervertebral disc degeneration," *Arthritis Research & Therapy*, vol. 17, no. 1, 2015.

[13] H. Chu, H. Yu, D. Ren, K. Zhu, and H. Huang, "Plumbagin exerts protective effects in nucleus pulposus cells by attenuating hydrogen peroxide-induced oxidative stress, inflammation and apoptosis through NF-κB and Nrf-2," *International Journal of Molecular Medicine*, vol. 37, no. 6, pp. 1669–1676, 2016.

[14] M. Molinos, C. R. Almeida, J. Caldeira, C. Cunha, R. M. Gonçalves, and M. A. Barbosa, "Inflammation in intervertebral disc degeneration and regeneration," *Journal of The Royal Society Interface*, vol. 12, no. 104, article 20141191, 2015.

[15] Y. Liu, Y. Qu, L. Liu et al., "PPAR-γ agonist pioglitazone protects against IL-17 induced intervertebral disc inflammation and degeneration via suppression of NF-κB signaling pathway," *International Immunopharmacology*, vol. 72, pp. 138–147, 2019.

[16] L. Shen, Y. Xiao, Q. Wu, L. Liu, C. Zhang, and X. Pan, "TLR4/NF-κB axis signaling pathway-dependent up-regulation of miR-625-5p contributes to human intervertebral disc degeneration by targeting COL1A1," *American Journal of Translational Research*, vol. 11, no. 3, pp. 1374–1388, 2019.

Research Article

Effect of Radix Hedysari Polysaccharide on Glioma by Cell Cycle Arrest and TNF-α Signaling Pathway Regulation

Xiaolong Du,[1,2] **Yujing Zhao,**[2] **Yongqian Ma,**[2] **Hongshun Xing,**[2] **and Xingang Li** ⓘ[1]

[1]*Qilu Hospital of Shandong University, China*
[2]*Weifang People's Hospital, China*

Correspondence should be addressed to Xingang Li; lixg@sdu.edu.cn

Objective. To investigate the possible development of radix hedysari polysaccharide as an antiglioma drug, we studied the effect of radix hedysari polysaccharide on glioma cells in vitro and the growth of glioma in nude mice and on the phagocytosis of macrophages in nude mice with glioma. *Methods.* The effect of radix hedysari polysaccharide on the growth of glioma was studied based on U251 cell line in vitro. The effect of radix hedysari polysaccharide on the growth of glioma was studied in vivo. The growth inhibition rate of radix hedysari polysaccharide on U251 cell line was determined by the MTT assay. The cell cycle of U251 was analyzed by flow cytometry. The expression of cytokines in U251 cells and tumor tissues was detected using PCR. The phagocytosis of macrophages in the serum of glioma nude mice was detected by Giemsa staining. TNF-α signaling pathway proteins in the serum of glioma nude mice were detected by ELISA. *Results.* Radix hedysari polysaccharide inhibited the growth of U251 cells, induced apoptosis in G1 phase by cell cycle arrest, and facilitated apoptosis in glioma mice by regulating cell cycle. Mice injected with radix hedysari polysaccharide showed delayed tumor growth and grew slowly. Radix hedysari polysaccharide enhanced the phagocytosis of macrophages in glioma nude mice. Radix hedysari polysaccharides could inhibit tumor development by regulating the immune function of tumor mice and affecting the TNF-α signaling pathway. *Conclusion.* Radix hedysari polysaccharide can effectively inhibit the growth of glioma and affect the TNF-α signaling pathway, thus playing an antiglioma role.

1. Introduction

Glioma is the most common and fatal primary central nervous system tumor in adults. Although the number of the therapeutic drugs for glioma is increasing, the therapeutic effect on glioma is still unsatisfactory. It was investigated that the survival time after a combined approach of surgical resection followed by chemoradiotherapy is short and the prognosis of patients with glioma is extremely poor [1]. Therefore, it is still urgent to seek for the excellent drug for the treatment of glioma. The primary task of developing new drugs is to explore the effect of drugs on proliferation and invasion of glioma and molecular mechanisms involved. Polysaccharides that widely exist in many plants are macromolecular substances with various biological activities, which have not only attracted extensive attention as excellent biological packaging materials but have also been widely used in enhancing immu-

nity, anticancer, and anti-inflammation [2–5]. It was reported that polysaccharides induced tumor cell cycle arrest by regulating cyclin E and D [3] or facilitated apoptosis in glioma cells by altering the Bax/Bcl-2-p53 axis [6]. Polysaccharides extracted from radix hedysari have attracted much attention due to their antitumor activity, immunomodulatory effects, and antioxidant properties [7], but there are few reports on the effects of radix hedysari polysaccharide on glioma.

In the occurrence and development of glioma, macrophages have two different characters, which perform functions of promoting growth and invasion of tumor or killing tumor cells in different microenvironments [8]. And it was reported that radix hedysari polysaccharide can significantly improve the phagocytosis of macrophages [9]. Tumor necrosis factor (TNF-α) is a key cytokine involved in inflammation, immunity, cellular homeostasis,

and tumor progression. TNF-α plays an essential role on the normal cell proliferation and function of macrophages, NK cells, T cells, B cells, and dendritic cells, and it is an important effector molecule for cell-mediated killing of some tumors [10]. Therefore, we proposed that radix hedysari polysaccharides can affect tumor growth and immune response through TNF-α signaling pathway. To explore the effect of radix hedysari polysaccharide on glioma, we studied the effects of radix hedysari polysaccharide on glioma cells in vitro and the growth of tumors in nude mice with glioma and on the phagocytosis of macrophages in nude mice with glioma.

2. Materials and Methods

The preparation of radix hedysari polysaccharide, referring to the preparation method of RHPs-4 by Dongfeng Wei, is as follows.

2.1. Cell Culture. In our studies, U251 cells were provided by the Cell Bank of Shanghai Institutes for Biological Sciences, CAS. U251 cells were cultured in DMEM containing 10% fetal bovine serum and 100 U/ml penicillin-streptomycin and were kept in a 37°C incubator with 5% CO_2.

2.2. Establishment of Glioma Model of Nude Mice. Twenty immunosuppressed nude mice (BALB/c-nu; 4-6 weeks old; 16-18 g) were provided by the Beijing Vital River Laboratory Animal Technology Co. Ltd. and randomly divided into 2 groups. Mice were kept in a pathogen-free environment. All animal experiments conformed to the international standards for the care and treatment of experimental animals. U251 cells (5*105) in logarithmic growth phase were taken for preparing cell suspension. The cell suspension was injected subcutaneously into the right tissue of nude mice to establish a xenograft model. Xenografted U251 glioma model of nude mice was randomly divided into the blank group and the RHPS group after inoculation. The mice were administered subcutaneously in the nape of the neck once a day for 24 consecutive days. The size of the xenografted tumor was measured with a caliper every 4 days during the 24-day observation period. The volume of the tumor was calculated according to the formula of volume = $L^* S^2/2$, and the growth curve of the tumor was drawn, where L is the longest tumor diameter and S is the shortest diameter of the two-dimensional tumor. The animals were sacrificed after observation, and the tumor weight was measured. Xenografted tumor tissue was taken and then prepared for cell suspension using a tissue homogenizer.

2.3. In Vitro Growth Inhibition Assay. The inhibitory effect of RHPS on human glioma cell line U251 or glioma in nude mice was studied by the MTT assay. Tumor cell suspension was prepared with cells (8×10^3 cells/well) seeded in 96-well plates. The different concentrations of RHPS or CPT were added, and cells were cultured for 48 hours at 37°C. Then, the culture medium was removed, and 0.5 mg/ml of MTT reagent 20 μl was added for incubation for 4 hours. The MTT reagent was discarded, and DMSO (150 μl/well)
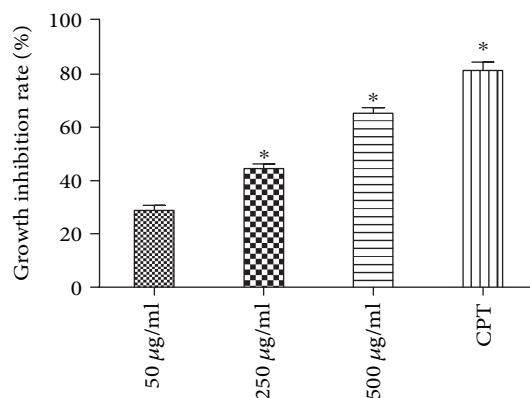

FIGURE 1: The growth inhibition of different concentrations of radix hedysari polysaccharide on U251 cells detected by the MTT assay. $^*P < 0.05$, comparing the 50 μg/ml RHPS experimental groups.

was added. The absorbance at 570 nm was measured by a spectrophotometer.

2.4. Cell Cycle Analysis. The effect of RHPS on cell cycle of U251 was detected using flow cytometry. U251 glioma cells (4×10^5) were incubated with RHPS (500 μg/ml) for 48 hours and then rinsed with PBS twice. Afterwards, the cells were fixed using 75% ethanol at 4°C overnight. Before flow cytometry analysis, the fixed cells were washed with PBS twice and stained with 50 μg/ml PI solution for 30 min at room temperature. The stained cells were transferred and flowed through a test tube with a 40 μm nylon mesh strainer for flow cytometry analysis.

2.5. Detection of Cytokine Expression. Expression levels of Bax, Bcl-2, caspase-3, and P53 mRNA were detected by RT-PCR. Sample cells or an appropriate amount of tumor tissues was collected, ground, and homogenized for subsequent RNA extraction. RNA extraction was carried out in accordance with the manufacturer's instructions. RNA concentration was quantitated by value of O.D before reverse transcription experiment, and the product cDNA was stored at -20°C. The PCR reactions were performed according to the instructions of the fluorescent quantitative PCR kit in which cDNA served as a template. Quantitative analysis was performed using 2-$\Delta\Delta$ct.

2.6. Western Blot Assay. We adopted western blot to detect the protein expression levels of cytokines Bax (Abcam, ab32503), Bcl-2 (Abcam, ab32124), caspase-3 (Abcam, ab13847), and p53 (Abcam, ab26). GAPDH (Abcam, ab181602) was used as an internal reference gene, and antibodies were used according to the product insert for Bax, Bcl-2, caspase-3, p53, E-cadherin, and GAPDH. Scanning imaging was performed using an imaging system (TANON, Tanon-5200), and the desired result has been achieved by resensing or shortening the photosensitizing time depending on the intensity of the band.

2.6.1. Secondary Antibody. Membranes incubated with primary antibody were washed three times with TBST for
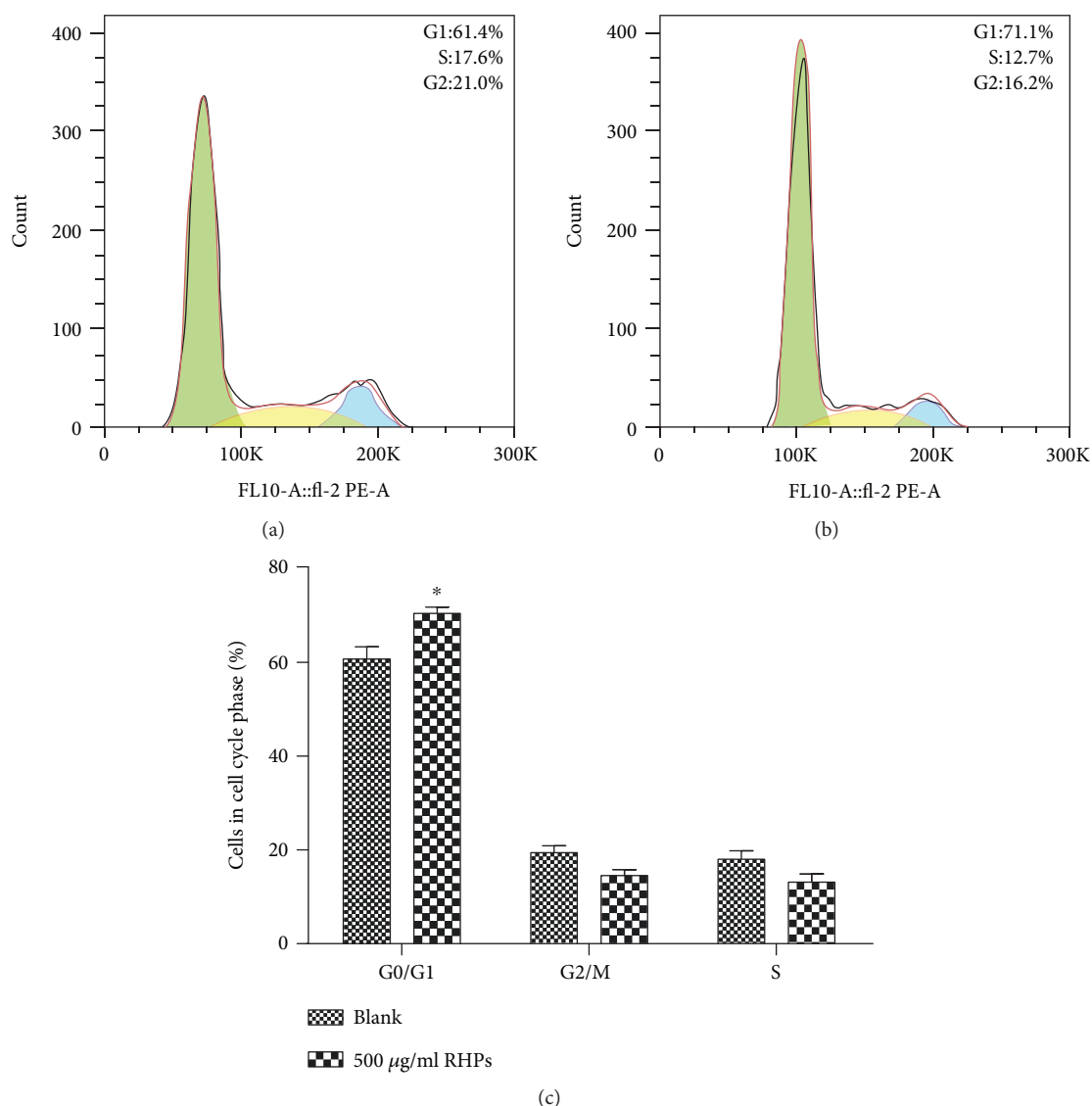
(a)

(b)

(c)

FIGURE 2: G1 arrest in glioma cells induced by radix hedysari polysaccharide. *$P < 0.05$, comparing the blank experimental groups.

5 min. The HRP-conjugated secondary antibody was subsequently diluted 1 : 1000 according to the amount and incubated with the membrane for 1 h at 37°C. They were washed three times with TBST for 5 min.

2.7. Macrophage Activity. Macrophage activity was detected by macrophage phagocytosis of chicken erythrocytes. Twenty-four hours after the last administration, the mice were intraperitoneally injected with 5% chicken red blood cell suspension 1 ml and sacrificed 1.5 hours later. The smear of rat peritoneal fluid was incubated at constant temperature of 37°C for 30 min, washed and dried, and then stained with Giemsa-Reiter solution for 15 min. Afterwards, it was washed and dried again with distilled water and observed under an oil immersion lens for counting cells. The phagocytic rate (number of macrophages that phagocytose chicken red blood cells/300 macrophages multiplied by 100%) and phagocytic index (total number of phagocytized chicken erythrocytes/300 macrophages) were calculated.

2.8. Detection of TNF-α Signaling Pathway. We further detected TNF-α, NF-KB P56, and caspase-3 in the serum of glioma nude mice by ELISA.

3. Results

3.1. Growth Inhibition Test of Radix Hedysari Polysaccharide on Glioma Cell Lines. The study set three groups: the blank control group, the RHPS experimental group (50 μg/ml, 250 μg/ml, and 500 μg/ml), and the camptothecin- (CPT-) positive control group. The growth inhibition rate of radix hedysari polysaccharide on glioma cell lines was determined by the MTT assay. As shown in Figure 1, the growth inhibition rate of radix hedysari polysaccharide on glioma cell lines showed dose dependency. The inhibition rate in the low-dose group was 29.5%, and the rate in the middle-dose group was 45.3%. The inhibition rate in the high-dose group was 66.0%, revealing that the growth of cells in the group was significantly suppressed compared with that of other groups
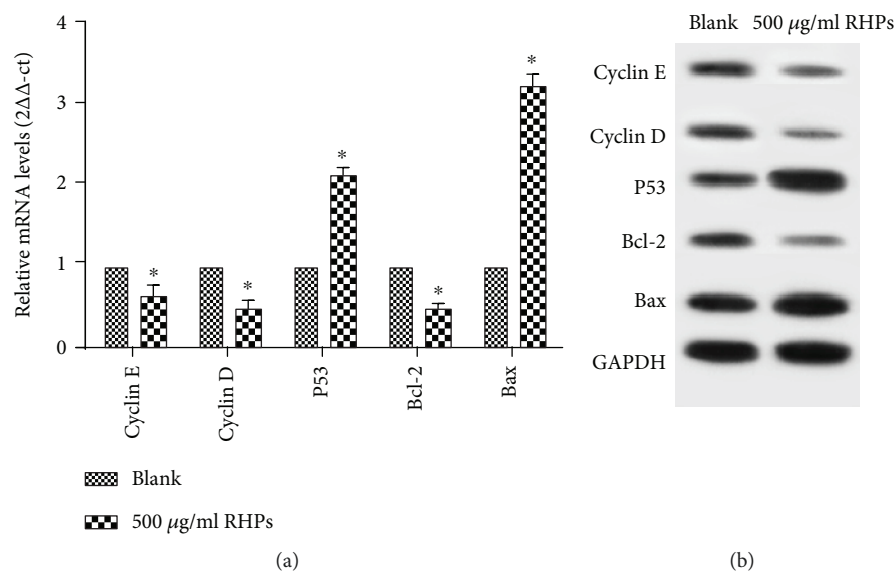
(a)

(b)

Figure 3: Effect of radix hedysari polysaccharide on cytokines in glioma cell lines. $^*P < 0.05$, comparing the blank experimental groups.

(Figure 1). These results indicated that radix hedysari polysaccharide obviously suppressed the growth of U251 cells and 500 μg/ml of radix hedysari polysaccharide had a better effect of inhibiting cell growth.

3.2. Effect of Radix Hedysari Polysaccharide on Cell Cycle of Glioma Cell Lines. In order to further explore the inhibitory effect of radix hedysari polysaccharide on U251 cells, we studied the changes in the cell cycle of U251 cells and analyzed their cell cycle distribution by flow cytometry. Figure 2 shows the effects of radix hedysari polysaccharide on the cell cycle of U251 cells (G1, S, and G2). As compared with the control group (the cell ratio in the G1 phase was 61.4%), the ratio of U251 cells in the G1 phase was significantly increased in the experimental group treated with 500 μg/ml of radix hedysari polysaccharide (the cell ratio in the G1 phase was 71.1%, $P < 0.05$). The results indicated that radix hedysari polysaccharide can suppress the growth of U251 cells and induce apoptosis in the G1 phase by cell cycle arrest (Figure 2).

3.3. Effect of Radix Hedysari Polysaccharide on Cytokines in Glioma Cell Lines. The cytokine expressions of the control group and the administration group treated with 500 μg/ml radix hedysari polysaccharide were detected by PCR. The results showed that the expression levels of P53 and Bax mRNA were significantly increased ($P < 0.05$), while the expression level of Bcl-2 mRNA was significantly decreased ($P < 0.05$), which indicated that radix hedysari polysaccharide induced the apoptosis of U251 cells by changing the expression of cytokine genes (see Figure 3). As compared with the control group, the expression levels of cyclin E and cyclin D in the administration group were significantly decreased ($P < 0.05$) (see Figure 3(a)) and the results of the western blot assay were consistent with those of the PCR assay (see Figure 3(b)), which further indicated that radix
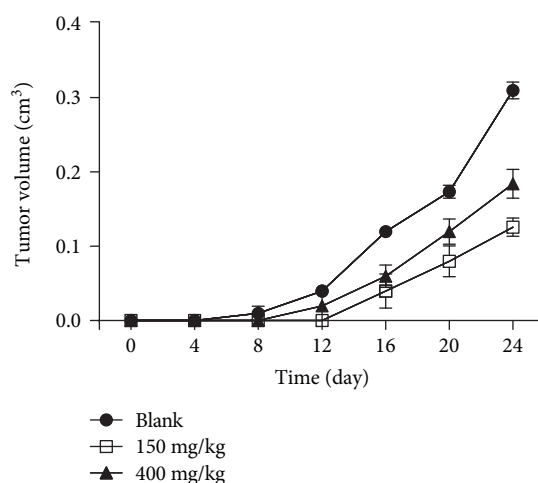

Figure 4: Effect of radix hedysari polysaccharide on the volume of tumor in nude mice with glioma.

hedysari polysaccharide induced apoptosis in the G1 phase through cell cycle arrest.

3.4. Effect of Radix Hedysari Polysaccharide on Mean Mass and Volume of Tumors in Nude Mice with Glioma. We have demonstrated that radix hedysari polysaccharide inhibited the proliferation of U251 cells in vitro by inducing G1 cell cycle arrest. The glioma model of nude mice was established to study the effect of radix hedysari polysaccharide on the growth of glioma in vivo. As shown in Figure 4, the mice injected with radix hedysari polysaccharide grew slowly and the progression of tumors in vivo was delayed. As compared with the high-dose group (400 mg/kg), the growth delay of the low-dose group (150 mg/kg) was significantly increased and the volume of tumor after 24 days of administration was significantly decreased ($P < 0.05$). After 24 days of
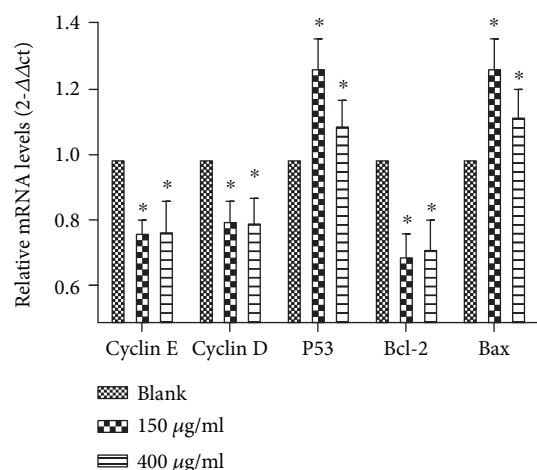
Figure 5: Effect of radix hedysari polysaccharide on cytokines in glioma tissues.

administration, the masses of the blank control group, the low-dose group, and the high-dose group were 0.32 ± 0.17 g, 0.13 ± 0.08 g, and 0.15 ± 0.05 g, respectively. The tumor mass of mice injected with radix hedysari polysaccharide was decreased significantly ($P < 0.05$), and the tumor mass of the low-dose group was decreased significantly ($P < 0.05$) compared with that of the high-dose group after 24 days of administration. These data suggested that radix hedysari polysaccharide can obviously inhibit tumorigenesis in nude mice.

3.5. Effect of Radix Hedysari Polysaccharide on Cytokines in Glioma Tissues. We examined the effect of radix hedysari polysaccharide on the changes in cytokine expression of tumor tissue cells by PCR. The results showed that the expression levels of P53 and Bax mRNA were significantly increased ($P < 0.05$), which was similar with the results in vitro, while the expression of Bcl-2 mRNA was significantly decreased ($P < 0.05$). The results indicated that the radix hedysari polysaccharide induced the apoptosis of tumor cells by changing the expression of cytokine genes in vivo (see Figure 5). As compared with the control group, the levels of cyclin E and cyclin D in tumor tissues of the administration group were significantly reduced ($P < 0.05$), indicating that the radix hedysari polysaccharide induced the apoptosis in mice with glioma by regulating the cell cycle (see Figure 5). The effect of radix hedysari polysaccharide on cytokine expression of tumor tissue cells was not dose dependent.

3.6. Effect of Radix Hedysari Polysaccharide on Phagocytosis of Macrophages in the Serum of Nude Mice with Glioma. Differentiation and development of glioma are closely related to the phagocytosis of macrophages. We detected the phagocytosis of macrophages in the serum of nude mice with glioma by Giemsa staining. The results showed that the phagocytic rate and index of the nude mice with glioma were significantly lower than those of the normal nude mice ($P < 0.05$), while the phagocytic rate and index of nude mice with glioma

significantly increased after administration of radix hedysari polysaccharide ($P < 0.05$). There were also remarkable differences between the high-dose group and the low-dose group (see Table 1). The results showed that radix hedysari polysaccharide enhanced the phagocytosis of macrophages in the nude mice with glioma.

3.7. Effect of Radix Hedysari Polysaccharide on TNF-α Signaling Pathway in Nude Mice with Glioma. As radix hedysari polysaccharide can enhance the phagocytosis of macrophages, we further detected such TNF-α signaling pathway proteins as TNF-α, NF-KB P56, and caspase-3 that are closely related to the macrophages in the serum of the nude mice with glioma by ELISA. The results showed that the expressions of TNF-α and caspase-3 in the nude mice with glioma were significantly lower than those in normal nude mice ($P < 0.05$), while the expression of NF-KB P56 was significantly overexpressed ($P < 0.05$). And this was obviously improved after the administration of radix hedysari polysaccharide. As compared with the nude mice with glioma, the expressions of TNF-α and caspase-3 in the serum were significantly elevated in the administration group ($P < 0.05$), and the highly expressed NF-KB P56 was significantly inhibited ($P < 0.05$) (see Table 2).

4. Discussion

Polysaccharides play an antitumor role by affecting tumor differentiation and apoptosis, changing intracellular signal transmission and immune regulation [11, 12]. This study found that radix hedysari polysaccharide inhibited the growth of U251 in vitro and arrested cells in the G1 phase, which is consistent with the results reported in other studies [13]. At present, there are many apoptosis-induced drugs, but their toxic and side effects are also serious [14]. As a macromolecular drug extracted from plants, radix hedysari polysaccharide has better effects in enhancing immunity, anticancer, and anti-inflammation and has less toxic and side effects, which therefore is a good candidate drug.

Studies have found that macrophages play an active role in the growth and invasion of glioma. However, as the main cells involved in the immune system, they can secrete TNF to induce apoptosis of tumor cells or directly engulf tumor cells under variable microenvironment [15]. The study found that phagocytosis of macrophages was significantly enhanced by the stimulation of radix hedysari polysaccharide. The link between inflammation and cancer has been well realized in the treatment of many cancers, and inflammation is considered the seventh characteristic of cancer. TNF-α is the main mediator of cancer-associated inflammation and is a factor that promotes tumor growth. The proinflammatory effect of TNF-α was mainly due to its ability to activate NF-κB, while its antitumor effect was due to the activation of caspase-3 and the induction of apoptosis. When exposed to TNF-α, NF-κB is activated and results in the expression of a variety of inflammation-related genes in almost every type of cell. However, the sustained activation of NF-κB is associated with several aspects of tumorigenesis, such as promoting tumor cell proliferation, preventing apoptosis of drug-

TABLE 1: Enhancement of phagocytosis of macrophages in nude mice with glioma by radix hedysari polysaccharide.

Group	Normal nude mice ($n = 6$)	Nude mice with glioma ($n = 6$)	150 μg/ml dose group ($n = 6$)	400 μg/ml dose group ($n = 6$)
Phagocytic rate	24.6 ± 1.5	22.1 ± 1.8	38.6 ± 2.3	36.9 ± 1.9
Phagocytic index	0.87 ± 0.02	0.77 ± 0.15	1.12 ± 0.17	0.99 ± 0.24

TABLE 2: Effect of radix hedysari polysaccharide on the TNF-α signaling pathway in nude mice with glioma.

Group	Normal nude mice ($n = 6$)	Nude mice with glioma ($n = 6$)	150 μg/ml dose group ($n = 6$)	400 μg/ml dose group ($n = 6$)
TNF-α (pg/ml)	16.65 ± 1.56	14.21 ± 1.57	21.69 ± 2.73	18.68 ± 1.09
NF-KB p65 (μg/ml)	27.69 ± 3.45	206.45 ± 15.12	69.16 ± 7.46	94.12 ± 11.14
Caspase-3 (μmol/l)	89.64 ± 11.44	80.69 ± 9.46	183.46 ± 13.56	126.67 ± 10.82

resistant cells, and increasing tumor angiogenesis and metastasis [16]. However, it was reported that local and repeated injections of large amounts of human recombinant TNF-α can induce hemorrhagic tumor necrosis in homologous and xenograft tumors. By contrast, low-dose chronic TNF-α had angiogenic activity and promoted tumor progression [17]. In this study, the low dose of radix hedysari polysaccharide could significantly increase the levels of TNF-α and caspase-3 in the serum of glioma nude mice and reduce the content of NF-κB. The results suggest that radix hedysari polysaccharide can regulate the immune function of tumor mice, affecting the TNF-α signaling pathway to inhibit tumor development.

Data Availability

All the data is available with the handwritten notebook documented in our lab.

Conflicts of Interest

The authors declare that there are no conflicts of interest regarding the publication of this paper.

Acknowledgments

References

[1] L. M. DeAngelis, "Brain tumors," *The New England Journal of Medicine*, vol. 344, no. 2, pp. 114–123, 2001.

[2] X.-R. Feng, J.-X. Ding, R. Gref, and X.-S. Chen, "Poly(β-cyclodextrin)-mediated polylactide-cholesterol stereocomplex micelles for controlled drug delivery," *Chinese Journal of Polymer Science*, vol. 35, no. 6, pp. 693–699, 2017.

[3] S. Li, T. Zhang, W. Xu et al., "Sarcoma-targeting peptide-decorated polypeptide nanogel intracellularly delivers shikonin for upregulated osteosarcoma necroptosis and diminished pulmonary metastasis," *Theranostics*, vol. 8, no. 5, pp. 1361–1375, 2018.

[4] J. Chen, J. Ding, W. Xu et al., "Receptor and microenvironment dual-recognizable nanogel for targeted chemotherapy of highly metastatic malignancy," *Nano Letters*, vol. 17, no. 7, pp. 4526–4533, 2017.

[5] K. Zhao, D. Li, W. Xu et al., "Targeted hydroxyethyl starch prodrug for inhibiting the growth and metastasis of prostate cancer," *Biomaterials*, vol. 116, pp. 82–94, 2017.

[6] S. Zhong, D. F. Ji, Y. G. Li, T. B. Lin, Z. Q. Lv, and H. P. Chen, "Activation of P27kip1-cyclin D1/E-CDK2 pathway by polysaccharide from *Phellinus linteus* leads to S-phase arrest in HT-29 cells," *Chemico-Biological Interactions*, vol. 206, no. 2, pp. 222–229, 2013.

[7] P. Sitarek, E. Skała, M. Toma et al., "A preliminary study of apoptosis induction in glioma cells via alteration of the Bax/Bcl-2-p53 axis by transformed and non-transformed root extracts of *Leonurus sibiricus* L.," *Tumor Biology*, vol. 37, no. 7, pp. 8753–8764, 2016.

[8] D. Wei, Y. Wei, W. Cheng, and L. Zhang, "Sulfated modification, characterization and antitumor activities of *Radix hedysari* polysaccharide," *International Journal of Biological Macromolecules*, vol. 51, no. 4, pp. 471–476, 2012.

[9] J. Xie, D. T. Wu, W. Z. Li et al., "Effects of polysaccharides in *Lycium barbarum* berries from different regions of China on macrophages function and their correlation to the glycosidic linkages," *Journal of Food Science*, vol. 82, no. 10, pp. 2411–2420, 2017.

[10] L. Pinton, E. Masetto, M. Vettore, and S. Solito, "The immune suppressive microenvironment of human gliomas depends on the accumulation of bone marrow-derived macrophages in the center of the lesion," *Journal for Immunotherapy of Cancer*, vol. 7, no. 1, p. 58, 2019.

[11] D. Li, W. G. Xu, P. Q. Li et al., "Self-targeted polysaccharide prodrug suppresses orthotopic hepatoma," *Molecular Pharmaceutics*, vol. 13, no. 12, pp. 4231–4235, 2016.

[12] L. Di, J. X. Ding, X. L. Zhuang, L. Chen, and X. S. Chen, "Drug binding rate regulates the properties of polysaccharide prodrugs," *Journal of Materials Chemistry B*, vol. 4, no. 30, pp. 5167–5177, 2016.

[13] P. W. Szlosarek and F. R. Balkwill, "Tumour necrosis factor alpha:a potential target for the therapy of solid tumours," *The Lancet Oncology*, vol. 4, no. 9, pp. 565–573, 2003.

[14] Y. L. Cheng, C. L. He, J. X. Ding, C. S. Xiao, X. L. Zhuang, and X. S. Chen, "Thermosensitive hydrogels based on polypeptides

for localized and sustained delivery of anticancer drugs," *Biomaterials*, vol. 34, no. 38, pp. 10338–10347, 2013.

[15] V. Haage, M. Semtner, R. O. Vidal, D. P. Hernandez, W. W. Pong, and Z. Chen, "Comprehensive gene expression meta-analysis identifies signature genes that distinguish microglia from peripheral monocytes/macrophages in health and glioma," *Acta Neuropathologica Communications*, vol. 7, no. 1, p. 20, 2019.

[16] A. Mantovani, P. Allavena, A. Sica, and F. Balkwill, "Cancer-related inflammation," *Nature*, vol. 454, no. 7203, pp. 436–444, 2008.

[17] A. Katsman, K. Umezawa, and B. Bonavida, "Chemosensitization and immunosensitization of resistant cancer cells to apoptosis and inhibition of metastasis by the specific NF-κB inhibitor DHMEQ," *Current Pharmaceutical Design*, vol. 15, no. 7, pp. 792–808, 2009.

Research Article

Nanoparticles Containing Hyaluronan Acid and Astragalus Polysaccharides for Treating Osteoarthritis

Gongbiao Lu,[1] **Lin Du,**[2] **Jishou Lu,**[1] **and Liuzhong Jin** ⬤[1]

[1]*Department of Spine Surgery, Jining No. 1 People's Hospital, Jining, Shandong 272011, China*
[2]*School of Nursing, Jining Medical University, Jining 272013, China*

Correspondence should be addressed to Liuzhong Jin; 13455580113@163.com

The pathogeny of osteoarthritis (OA) is very complicated and still is one of the difficulties in a treating procedure. Here, we constructed nanoparticles using hyaluronan acid (HA) and astragalus polysaccharides (APS) for OA therapy. We assessed OA biomarkers and IL-1β-induced matrix metalloproteinase (MMP) expressions. Nanoparticles of 100 nm showed high drug loading of 28.6% (w/w) and extended drug release of 59% over 1 month. Our results demonstrated that nano treatment significantly improved IL-1β-induced cell viability of chondrocytes. Induction of MMP-9, MMP-13, and TNF-α was alleviated by nanoparticles. Furthermore, nano elevated the expression of osteopontin (OPN) and attenuated inducible nitric oxide synthase (iNOS) protein. Our data indicated the protective role of HA and APS-capsuled nanoparticles in OA treatment.

1. Introduction

Polysaccharides not only are the main constituent of natural products and energy suppliers but also have exclusive and important biological activities. For example, it can improve the immunity and has obvious antioxidation and anticoagulation effects [1]. These bioactivities of polysaccharides are important for organisms, which have become the focus of many research disciplines. As reported, many traditional Chinese medicine polysaccharides used alone or combined with other traditional Chinese medicine polysaccharides can not only improve the local microcirculation but also reduce the microcirculation intraosseous pressure, scavenge oxygen free radicals, and inhibit synovitis and cartilage apoptosis and abnormal regulation of cytokines [2–5]. The pathological changes of the immune organs can improve the synovial lesion of the joint and effectively inhibit the inflammation. Therefore, the research on astragalus polysaccharides (APS) of traditional Chinese medicine may become one of the important directions of prevention and cure of OA.

Accumulated evidence has revealed the potential mechanism of prevention and treatment of OA by polysaccharide of traditional Chinese medicine [6]. To tackle the dilemma of rapid clearance of biologically active molecules from the lesion, nanoparticles were considered in this study. HA is also a type of biopolymer widely used in treating OA. However, injected HA is not a long-lasting treatment and remains uncertain because of the degradation [7]. Polypeptide micelles combined with antitumor drug and polyion complex have been documented [8, 9]. In addition, recently, HA has been used in drug delivery nanoparticles for targeting cell-surface glycoprotein 44- (CD44-) overexpressed solid tumors [10]. Considering that HA helps the elasticity of synovial fluid and binds to CD44 which is highly expressed in chondrocytes, we used HA as a drug carrier and fabricated HA-coated nanoparticle to target OA sites.

Thus, in the present study, we developed a novel drug delivery system composed of hyaluronan acid and astragalus polysaccharides. We subsequently evaluated the therapeutic effects of formulated HA and APS-capsuled nanoparticles on isolated human articular chondrocytes.

2. Materials and Methods

2.1. Synthesis of Nanoparticles. The nanoparticles formulated are comprised of two polymers: HA and APS. The

preparation of nanoparticles was performed as described previously [11]. We followed and modified the methods of Maudens et al. [12]. 1,2-Dilauroyl-sn-glycero-3-phosphoethanolamine (DLPE) and 1,2-dilauroyl-sn-glycero-3-glycerol (DLPG) were from Avanti Polar Lipids Inc. (Alabaster, AL, USA). HA obtained from Sigma-Aldrich (St. Louis, MO, USA) was diluted to 2 mg/mL in distilled water. APS and lipids (DLPE : DLPG mole ratio of 7 : 3) were dissolved in ethanol and mixed with HA. Nanoparticle solution was evaporated to dry overnight at room temperature in a Buchi Rotary Evaporator Vacuum System. Nanoparticle size was calculated by dynamic light scattering (DLS) using a BI-200SM size analyzer. The nanosuspensions were lyophilized and stored at 4°C for further use. The concentration of nano formulation includes 8% ethanol (96%), 92.8% HA (mL/mL), and 0.2% APS (g/mL).

2.2. In Vitro Drug Release.
Saline solution (0.9% (w/v) NaCl) and nano were saturated with the dexamethasone base (0.05, 0.50, and 2.50 mg mL^{-1}, respectively) at 20°C. Ten milliliters of each of the previous solutions was dialyzed (MWCO: 1000, Spectra/Por® membrane) against 400 mL of 0.9% (w/v) NaCl for 28 h at 37°C and 80 RPM. The polymer matrix was hydrolyzed by heating (121°C) to release the remaining content of dexamethasone, and DMSO was added (1 : 1, water : DMSO). The quantity of the drug released at each time point was quantified by reversed-phase UHPLC using a C18 Hypersil Gold column (50/2.1, 1.9 μm bead particle size, Thermo Scientific, Waltham, USA). The mobile phase consists of 0.1% (v/v) formic acid in water (A) and 0.1% (v/v) trifluoroacetic acid (TFA) in acetonitrile (B), and the following gradient elution sequence was applied at a flow rate of 400 μL min^{-1}: 30–95% A (0–3 min), 95–10% A (3–4 min), 10–30% A (4–4.5 min), and 30% A (4.5–5 min).

2.3. Isolation of Articular Chondrocytes.
OA model rabbits (New Zealand female rabbits, 8-month-old, 4.5 ± 0.5 kg) were created using the classic Hulth method as previously reported [2]. Synovial tissues were isolated from the knee joints of New Zealand white rabbits (female, average weight: 2.5 ± 0.5 kg) after being sacrificed with overdose of pentobarbital sodium (Sigma-Aldrich) under sterile conditions. The experimental protocol was approved by the Institution's Animal Care and Use Committee of Jining No. 1 People's Hospital. Cartilage was cut into small pieces and digested by 0.2% collagenase II (Gibco, Carlsbad, CA, USA) at 37°C for 12 h. After washing twice with PBS, the isolated synoviocytes were cultured in monolayers in culture medium composed of DMEM/F12 (Gibco) supplemented with 10% fetal bovine serum (FBS; Gibco, USA) and 1% antibiotics at 37°C with 5% CO_2.

2.4. Release of Nanoparticles.
Lyophilized nanoparticle powder (2 mg) was resuspended with 5 mL phosphate-buffered solution (PBS) and shaken at 100 r/min at 37°C. 500 μL of buffer was collected and measured at a predetermined time point. The amounts of releases were calculated as follows: accumulated released ration = APS amount in buffer/total APS amount × 100%. The encapsulation efficiency
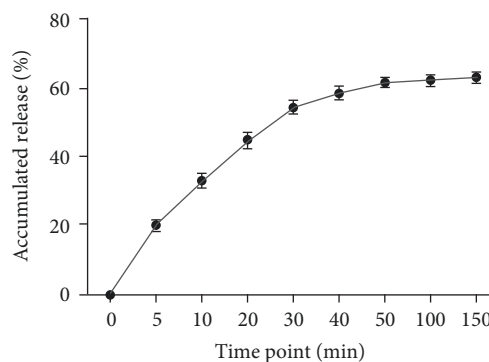

FIGURE 1: Release of nanoparticles in PBS (pH 7.4). Data are expressed as the mean ± standard deviation (SD) ($n = 4$). At least three independent experiments were conducted.

(EE) and loading efficiency (LE) were determined as previously reported [13]: drug loading = wt drug entrapped/wt microparticles × 100%.

2.5. Cytotoxicity Assays.
Cell proliferation was assayed using the Cell Counting Kit-8 (CCK-8; Dojindo, Japan). 100 L cell (2×10^6/well) suspension was prepared in a 96-well plate (37°C and 5% CO_2) for 24 hours. Various concentrations of nanoparticles (0.5, 5, 10, and 100 mg/L APS) or IL-1β (10 ng/mL) were added to each well at different concentrations and incubated for 24 hours. There were 6 groups in the present study: control (DMEM medium), IL-1β, IL-1β+0.5 mg/L APS, IL-1β+5 mg/L APS, IL-1β+10 mg/L APS, and IL-1β+100 mg/L APS. After incubation for 24 h, add 10 L CCK-8 solution to each well. Incubate the plates in the incubator for 1-4 hours. The absorbance at 450 nm was determined by a microplate analyzer (model 680; Bio-Rad, Hercules, CA, USA). Chondrocytes cultured without NMPs served as the control group.

2.6. Measurement of IL-1β, iNOS, OPN, and TNF-α.
Blood samples collected from rabbit were centrifuged at 1000 g for 15 min and 10 000 g for 10 min at 4°C. OPN, iNOS, and TNF-α were measured by ELISA (Hercules, CA, USA) according to the specifications of the manufacturer. Data were analyzed by Bio-Plex Manager software 6.1 to obtain concentrations.

2.7. Western Blot Analysis.
Proteins were extracted from the articular chondrocytes. After the concentrations of the proteins were evaluated, equal amounts of protein were electrophoresed on sodium dodecyl sulfate-polyacrylamide gel and transferred to polyvinylidene difluoride (PVDF) membranes. The membranes were blocked with 2% nonfat dry milk in Tris-buffered saline-0.05% Tween (pH 7.4) and incubated with anti-OPN and anti-iNOS antibodies (1 : 2000, Abcam) at 4°C overnight. The membrane was washed three times and incubated with horseradish peroxidase-conjugated secondary antibody (Abcam) at 37°C for 2 h. The protein bands were visualized by an enhanced chemiluminescence system, and GAPDH (Abcam) was used as an internal control to normalize.
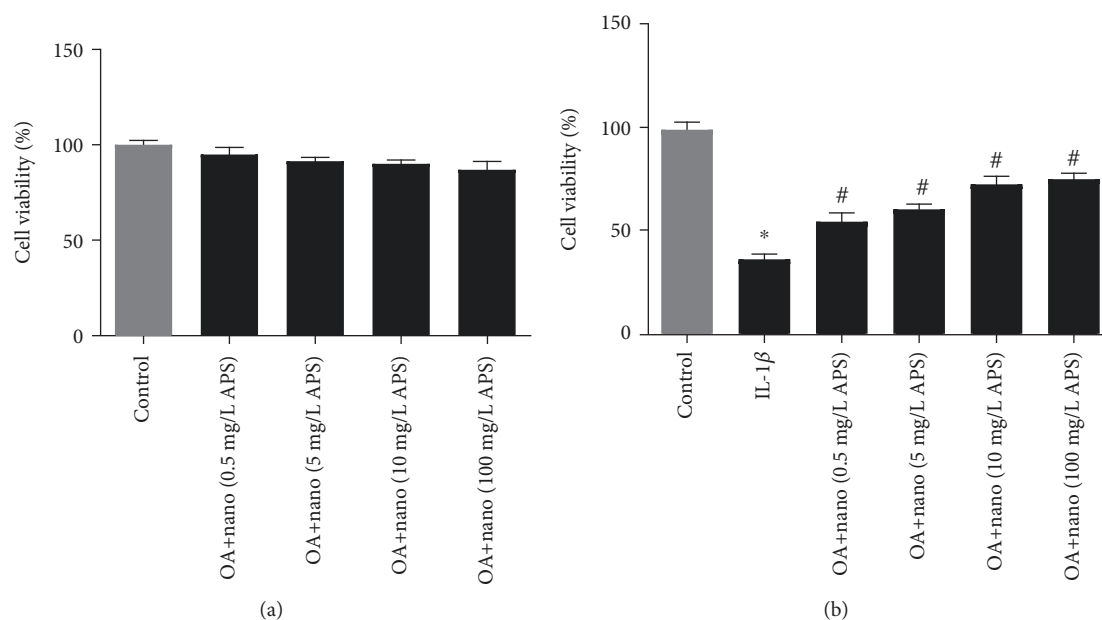
(a)

(b)

Figure 2: Nanoparticles attenuate the inhibitory effect on the cell viability induced by IL-1β. Cell viability of articular chondrocytes was evaluated using the CCK-8 assay. At least three independent experiments were conducted. (a) OA chondrocytes were treated with various concentrations of APS-loaded nanoparticles (0, 0.5, 5, 10, and 100 mg/L) for 24 h. (b) OA chondrocytes were treated with various concentrations of APS-loaded nanoparticles (0.5, 5, 10, and 100 mg/L) with IL-1β (10 ng/mL) for 24 h. *$P < 0.05$ compared with the control group, #$P < 0.05$ compared with the IL-1β group.

2.8. Statistical Analysis. All the continuous data were presented as the mean ± SD. All statistical analysis was performed using SPSS17.0. Unpaired Student's t-test was used for the comparisons between two different groups. $P < 0.05$ was considered significant.

3. Results

3.1. Basic Characteristics of APS-Loaded Nanoparticles. The nanoparticles have an average diameter of 110.6 ± 12.8 nm. The encapsulation efficiency was 32.4 ± 0.19%, and the loading efficiency was 75.0 ± 0.02%. The APS was released from nanoparticles in PBS (Figure 1). With the degradation of HA, the structure of nanoparticles was broken up and APS was released. In addition, nanoparticles of 100 nm showed high drug loading of 28.6% (w/w) and extended drug release of 59% over 1 month.

3.2. Cytotoxicity of Nanoparticles. We next examined the effect of nanoparticles on cell viability using the CCK-8 assay. As shown in Figure 2(a), treatment with nanoparticles caused slight decrease in cell viability. Also, we observed that when compared with the control group, IL-1β treatment remarkably decreased the cell viability of articular chondrocytes (Figure 2(b), $P < 0.05$). However, APS-capsuled nanoparticles sharply improved cell viability inducted by IL-1β in a dose-dependent manner. There is no significant difference between 10 and 100 mg/L APS; thus, 0.5-10 mg/L of APS was used in the following experiments.

3.3. The Production of MMP-9, MMP-13, and TNF-α. ELISA results showed that nano containing 0.5, 5, and 10 mg/L APS

significantly decreased the concentrations of MMP-9, MMP-13, and TNF-α, which was significantly elevated by IL-1β (Figure 3, $P < 0.05$). These results indicated that APS-loaded nano could reduce the levels of inflammation cytokines and matrix-degrading proteins, therefore protecting articular chondrocytes.

3.4. The Expression of OPN and iNOS. Then, we verified the effects of APS on OPN and iNOS in OA chondrocytes cultured with IL-1β. The data of the Western blot assay demonstrated that IL-1β significantly decreased the protein expression of OPN and increased the expression of iNOS, as compared with the control (Figure 4). However, APS-encapsuled nano markedly elevated IL-1β-induced OPN proteins and attenuated IL-1β-induced iNOS protein expression.

4. Discussion

All over the world, osteoarthritis is the most common joint disease, disturbing approximately 10% of men and 18% of women aged over 60, which was regarded as immortal cancer [14]. In general, there are various aspects in the pathogenesis process, including cytokines, apoptosis, and protease [15]. Current therapies are not effective or have unwanted side effects. Self-targetability has emerged as a new targeting strategy that has been used in breast tumor, orthotopic hepatoma, and other diseases [16, 17]. Recently, a body of evidence showed that polysaccharide drugs for OA are a promising approach in early and midterm treatment [18]. APS has been used in the treatment of OA in the past years. In this study, APS was chosen as a therapeutic agent
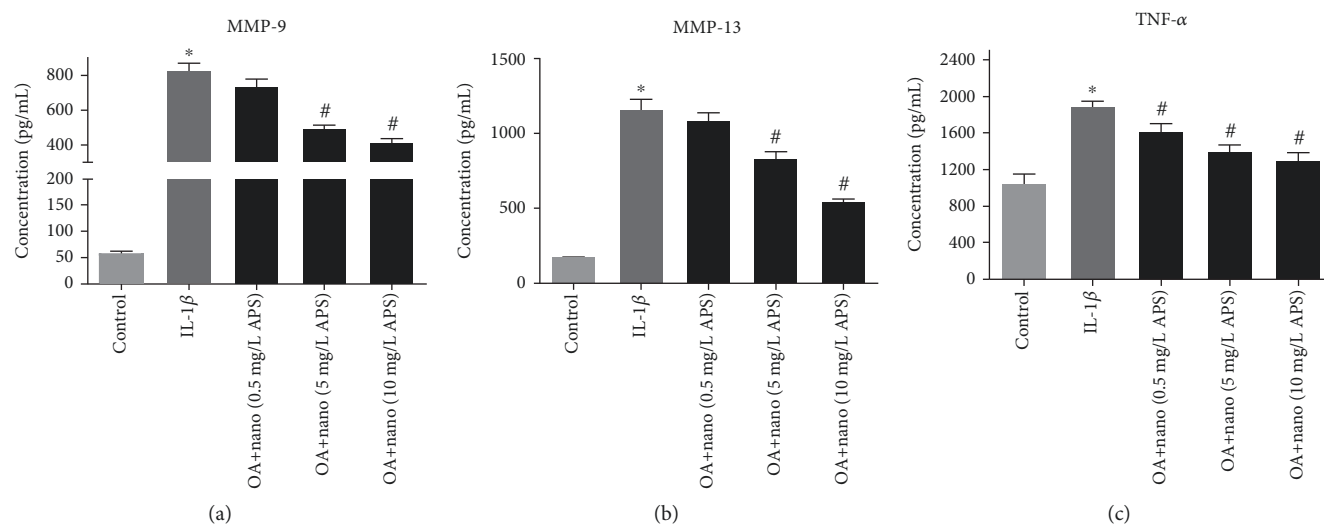
Figure 3: The levels of MMP-9, MMP-13, and TNF-α were determined using ELISA. The values are expressed as the mean ± standard deviation (SD). $^*P < 0.05$ compared with the control group; $^\#P < 0.05$ compared with the IL-1β group.
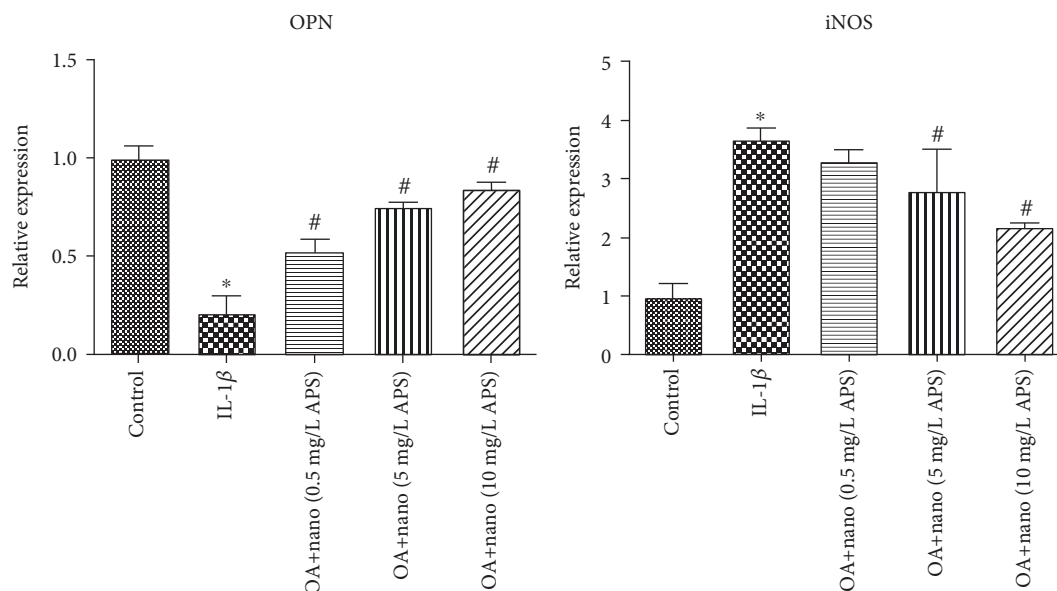

Figure 4: The protein levels of OPN and iNOS in articular chondrocytes. OA chondrocytes were pretreated with various concentrations of APS-loaded nanoparticles. $^*P < 0.05$ compared with the control group; $^\#P < 0.05$ compared with the IL-1β group. OPN: osteopontin.

because of the specific biological effect of polysaccharides. Hydrogels composed of natural polymers such as hyaluronic acid have been used in the delivery of biologies. Importantly, HA is capable of enhancing delivery efficiency for chondrocytes due to the fact that CD44 is the primary receptor for HA internalization, thus facilitating the access to chondrocytes in the joint. Due to the small size and large specific surface area, nanoparticles are considered to be a promising medicine [5, 19, 20]. In the present study, we first combined these two agents and encapsulated both APS and HA in the nano structure.

In our study, the APS-loaded nano were prepared successfully (the morphology of microspheres was not shown). The data of CCK-8 assays showed that various concentrations of nanoparticles presented low cytotoxicity and

improved the IL-1β-induced damage in chondrocytes. Based on the cytotoxicity data, we believed that the nano was safe and excellent.

It has been known that the MMP family is a vital biomarker related to articular cartilage degeneration [21]. MMPs are a big family including MMP-1, MMP-2, MMP-3, MMP-5, MMP-9, and MMP-13 [22]. Among these, MMP-9 and MMP-13 are well-studied in the role of OA. Elevation of MMP-9 and MMP-13 is responsible for cleaving extracellular matrix and the construction of chondrocytes [23–25]. Here, we found that our modified nano declined the elevation of MMP-9 and MMP-13 induced by IL-1β. Moreover, the nano had significantly decreased the expression of inflammatory factor TNF-α, indicating the anti-inflammation role of APS and HA combined nano.

OPN is known as a cytokine related to OA metabolism; it is noncollagen bone matrix glycoprotein that mediates varied kinds of biological behaviors and often presents in the cartilage and synovial fluid of patients with OA [26]. OPN is an inhibitor to inflammatory substances such as IL-1 and NO, thus inhibiting the inflammatory process in cartilage [27]. iNOS is an isoform of the NO synthase family of enzymes, which correlates with the development of toxicity [28]. Stimulation of IL-1β could increase the expression of iNOS in chondrocytes therefore promoting NO production [29]. We investigated the effect of nanosphere on the production of OPN and iNOS. Western blot analyses indicated that the nanosphere effectively attenuated the levels of OPN and iNOS, leading to suppression of the inflammatory process. These results suggested that the anti-inflammatory mechanism of nanosphere is due to the inhibition of key cytokines.

In summary, we provide a new microsphere of modified medicine that overcomes the quick degradation of drugs. We conclude that APS- and HA-loaded nano can effectively promote the survival of chondrocytes and protect chondrocytes by regulating the cytokines and proteinase.

Data Availability

All the data is available with the handwritten notebook documented in our lab.

Conflicts of Interest

The authors declare that they have no conflicts of interest.

Authors' Contributions

Gongbiao Lu and Lin Du contributed equally to this work.

References

[1] P. Rozi, A. Abuduwaili, P. Mutailifu et al., "Sequential extraction, characterization and antioxidant activity of polysaccharides from *Fritillaria pallidiflora* Schrenk," *International Journal of Biological Macromolecules*, vol. 131, pp. 97–106, 2019.

[2] J. N. Rogart, H. J. Barrach, and C. O. Chichester, "Articular collagen degradation in the Hulth-Telhag model of osteoarthritis," *Osteoarthritis and Cartilage*, vol. 7, no. 6, pp. 539–547, 1999.

[3] Z. Liang, Z. Yuan, J. Guo et al., "*Ganoderma lucidum* polysaccharides prevent palmitic acid-evoked apoptosis and autophagy in intestinal porcine epithelial cell line via restoration of mitochondrial function and regulation of MAPK and AMPK/Akt/mTOR signaling pathway," *International Journal of Molecular Sciences*, vol. 20, no. 3, p. 478, 2019.

[4] N. Yu, N. Song, C. Liu, and G. Yang, "The estrogen-like protective effect of Lycium barbarum polysaccharides in reducing oxidative stress on myocardial cells from ovariectomized rats," *Molecular Medicine Reports*, vol. 19, no. 3, pp. 2271–2278, 2019.

[5] L. J. Ke, G. Z. Gao, Y. Shen, J. W. Zhou, and P. F. Rao, "Encapsulation of aconitine in self-assembled licorice protein nanoparticles reduces the toxicity in vivo," *Nanoscale Research Letters*, vol. 10, no. 1, p. 449, 2015.

[6] Q. Chen, X. Shao, P. Ling, F. Liu, G. Han, and F. Wang, "Recent advances in polysaccharides for osteoarthritis therapy," *European Journal of Medicinal Chemistry*, vol. 139, pp. 926–935, 2017.

[7] A. Avenoso, A. D'Ascola, M. Scuruchi et al., "Hyaluronan in experimental injured/inflamed cartilage: in vivo studies," *Life Sciences*, vol. 193, pp. 132–140, 2018.

[8] W. Xu, J. Ding, and X. Chen, "Reduction-responsive polypeptide micelles for intracellular delivery of antineoplastic agent," *Biomacromolecules*, vol. 18, no. 10, pp. 3291–3301, 2017.

[9] J. Wang, W. Xu, H. Guo et al., "Selective intracellular drug delivery from pH-responsive polyion complex micelle for enhanced malignancy suppression in vivo," *Colloids and Surfaces B: Biointerfaces*, vol. 135, pp. 283–290, 2015.

[10] C. Yang, Y. He, H. Zhang et al., "Selective killing of breast cancer cells expressing activated CD44 using CD44 ligand-coated nanoparticles in vitro and in vivo," *Oncotarget*, vol. 6, no. 17, pp. 15283–15296, 2015.

[11] G. Bachar, K. Cohen, R. Hod et al., "Hyaluronan-grafted particle clusters loaded with mitomycin C as selective nanovectors for primary head and neck cancers," *Biomaterials*, vol. 32, no. 21, pp. 4840–4848, 2011.

[12] P. Maudens, S. Meyer, C. A. Seemayer, O. Jordan, and E. Allémann, "Self-assembled thermoresponsive nanostructures of hyaluronic acid conjugates for osteoarthritis therapy," *Nanoscale*, vol. 10, no. 4, pp. 1845–1854, 2018.

[13] Z. Chen, S. Deng, D. C. Yuan et al., "Novel nano-microspheres containing chitosan, hyaluronic acid, and chondroitin sulfate deliver growth and differentiation factor-5 plasmid for osteoarthritis gene therapy," *Journal of Zhejiang University-Science B*, vol. 19, no. 12, pp. 910–923, 2018.

[14] A. D. Woolf and B. Pfleger, "Burden of major musculoskeletal conditions," *Bulletin of the World Health Organization*, vol. 81, no. 9, pp. 646–656, 2003.

[15] D. Chen, J. Shen, W. Zhao et al., "Osteoarthritis: toward a comprehensive understanding of pathological mechanism," *Bone Research*, vol. 5, no. 1, article 16044, 2017.

[16] C. Yang, Y. Liu, Y. He et al., "The use of HA oligosaccharide-loaded nanoparticles to breach the endogenous hyaluronan glycocalyx for breast cancer therapy," *Biomaterials*, vol. 34, no. 28, pp. 6829–6838, 2013.

[17] D. Li, W. Xu, P. Li et al., "Self-targeted polysaccharide prodrug suppresses orthotopic hepatoma," *Molecular Pharmaceutics*, vol. 13, no. 12, pp. 4231–4235, 2016.

[18] M. M.-G. Sun, F. Beier, and M. A. Pest, "Recent developments in emerging therapeutic targets of osteoarthritis," *Current Opinion in Rheumatology*, vol. 29, no. 1, pp. 96–102, 2017.

[19] H. Guo, F. Li, W. Xu et al., "Mucoadhesive cationic polypeptide nanogel with enhanced penetration for efficient intravesical chemotherapy of bladder cancer," *Advanced Science*, vol. 5, no. 6, article 1800004, 2018.

[20] J. Wang, W. Xu, S. Li et al., "Polylactide-cholesterol stereocomplex micelle encapsulating chemotherapeutic agent for improved antitumor efficacy and safety," *Journal of Biomedical Nanotechnology*, vol. 14, no. 12, pp. 2102–2113, 2018.

[21] C. J. Malemud, "Matrix metalloproteinases and synovial joint pathology," *Progress in Molecular Biology and Translational Science*, vol. 148, pp. 305–325, 2017.

[22] N. Cui, M. Hu, and R. A. Khalil, "Biochemical and biological attributes of matrix metalloproteinases," *Progress in Molecular Biology and Translational Science*, vol. 147, pp. 1–73, 2017.

[23] A. Bahtiar, M. Nurazizah, T. Roselina, A. P. Tambunan, and A. Arsianti, "Ethanolic extracts of babandotan leaves (*Ageratum conyzoides* L.) prevents inflammation and proteoglycan degradation by inhibiting TNF-α and MMP-9 on osteoarthritis rats induced by monosodium iodoacetate," *Asian Pacific Journal of Tropical Medicine*, vol. 10, no. 3, pp. 270–277, 2017.

[24] H. Li, D. Wang, Y. Yuan, and J. Min, "New insights on the MMP-13 regulatory network in the pathogenesis of early osteoarthritis," *Arthritis Research & Therapy*, vol. 19, no. 1, p. 248, 2017.

[25] J. Song, E. H. Jin, D. Kim, K. Y. Kim, C. H. Chun, and E. J. Jin, "MicroRNA-222 regulates MMP-13 via targeting HDAC-4 during osteoarthritis pathogenesis," *BBA Clinical*, vol. 3, pp. 79–89, 2015.

[26] Z. Bai, X. H. Guo, C. Tang, S. T. Yue, L. Shi, and B. Qiang, "Effects of artesunate on the expressions of insulin-like growth factor-1, osteopontin and C-telopeptides of type II collagen in a rat model of osteoarthritis," *Pharmacology*, vol. 101, no. 1-2, pp. 1–8, 2018.

[27] M. G. Attur, M. N. Dave, S. Stuchin et al., "Osteopontin: an intrinsic inhibitor of inflammation in cartilage," *Arthritis & Rheumatism*, vol. 44, no. 3, pp. 578–584, 2001.

[28] Z. Kucuktag, B. Satar, S. Yetiser, Y. Hidir, and O. Gunhan, "Immunohistochemical investigation of inducible nitric oxide synthase, osteopontin, and calcium-sensing receptor in a myringosclerosis/tympanosclerosis model," *Otology & Neurotology*, vol. 35, no. 1, pp. e15–e23, 2014.

[29] Z. Ma, Y. Wang, T. Piao, and J. Liu, "Echinocystic acid inhibits IL-1β-induced COX-2 and iNOS expression in human osteoarthritis chondrocytes," *Inflammation*, vol. 39, no. 2, pp. 543–549, 2016.

Research Article

Effect of Porous Chitosan Microspheres Loaded with Platelet-Rich Plasma and Bone Marrow-Derived Mesenchymal Stem Cells on Regeneration of Tibia Defect

Qi Chen [1], **Ziru Zhao,** [2] **and Guoyong Yin** [3]

[1]*Department of Orthopedic, The Second Affiliated Hospital of Nanjing Medical University, Nanjing, 210011 Jiangsu, China*
[2]*Department of Orthopedic, Anting Hospital, JiaDing District, Shanghai, China*
[3]*Department of Orthopedic, The First Affiliated Hospital of Nanjing Medical University, Nanjing, 210000 Jiangsu, China*

Correspondence should be addressed to Guoyong Yin; guoyongyin888@sina.com

Objective. Repair of bone defects represents a grave clinical challenge because of the tremendous difficulties in the recovery of bone function and regeneration of bone loss. Therefore, we investigated the effects of platelet-rich plasma-loaded (PRP) porous chitosan microspheres (PCMs) on the differentiation of bone marrow-derived mesenchymal stem cells (BMSCs) and the proliferation and differentiation potential of BMSCs loaded by PCMs in vitro. We also established the model of bone defect repair in rat tibia to further explore the effects of PCMs loaded with PRP and BMSCs on bone regeneration. *Methods*. MTT assay was used to detect the proliferative ability of BMSCs after hypoxia/reoxygenation (H/R) treatment and the proliferative ability of BMSCs loaded by PCMs; polymerase chain reaction (PCR) was used to detect the expression of alkaline phosphatase (ALP), type I collagen (Col I), and type II collagen (Col II) in BMSCs after hypoxia and in BMSCs induced by PRP-loaded PCMs; PCR was used to detect the expression of Runt-associated transcription factor 2 (Runx2) and osteocalcin (OC) in the newly generated bone tissue; micro-CT scanning was applied to measure the bone mineral density and bone volume of the newly generated bone tissue in rats. *Results*. BMSCs still have the normal potential of proliferation and differentiation after H/R treatment. PCMs can provide a larger surface for the attachment of BMSCs, facilitating cell proliferation. Loaded by PCMs, PRP can be slowly released, effectively stimulating the differentiation of BMSCs. PCM/PRP/BMSC composites increased the expression levels of Runx2 and OC in the newly generated bone in rat tibia defect and the bone mineral density. Moreover, the composites improved the rate of regenerated bone volume. *Conclusion*. The application of PCM/PRP/BMSC composites is promising in the repair of tibia defects.

1. Introduction

Biomaterials such as hydrogels, including porous chitosan microsphere (PCM), and fiber sheets have drawn great attention as tissue engineering scaffolds in bone defect repair thanks to their good biocompatibility and biodegradability [1–3]. Of all biomaterials, chitosan microspheres are used as a typical biomedical material mainly in cell culture, drug carrier, and gene therapy. With a porous structure, PCMs can support cell adhesion and proliferation by incorporating platelet-rich plasma (PRP), which is rich in growth factors. Therefore, PCM has obvious advantages as a tissue engineering scaffold. PCMs prolong the half-life of growth factors and

maintain their activity and stability [4]. PCMs can not only load plasma but can also function as a cell carrier by increasing the diameter of the microspheres to induce cell aggregation [5]. By efficiently delivering growth factors and nutrients, PCMs facilitate the migration and adhesion of cells toward osteoblasts and also the proliferation and differentiation of cells into osteoblasts. With these remarkable properties, PCM has the clinical value of applying as a scaffold for bone tissue engineering [6]. PRP is similar to the normal blood in terms of the proportions of growth factors. Containing a variety of growth factors related to bone repair, PRP helps promote bone defect repair, such as growth/differentiation factor 5 (GDF-5), bone morphogenetic protein 2 (BMP-

2), and transforming growth factor $\beta1$ (TGF-$\beta1$). Increased levels of TGF-$\beta1$ and BMP-2 can improve osteogenesis [7, 8]. Bone marrow-derived mesenchymal stem cells (BMSCs) are multipotential stem cells that can differentiate into such cells as osteoblasts and chondrocytes. Therefore, BMSC-based therapies may improve the repair of bone defects [9, 10].

In this study, we explored the effects of PCM-PRP and PCM-BMSC composites on osteogenesis in vivo, demonstrating the cocktail effect of growth factors and BMSCs on bone formation in vivo and in vitro.

2. Materials and Methods

2.1. Preparation of Major Reagents and Cell Purchase. Chitosan-gelatin microspheres were prepared based on the method used by Song et al. [11]. Chitosan/β-glycerol phosphate solution (solution A) was prepared with chitosan solution (2.2% (v/v) acetic acid solution) and β-glycerol phosphate solution (50% (w/w) aqueous solution) in a v/v ratio of 5 : 1. Type I collagen solution (solution B) was prepared by adding 700 μl of type I collagen into the mixture of 30 μl of 0.1 mol/l sodium hydroxide solution and 100 ml of 10x D-Hanks. Solution A and solution B were mixed in a v/v ratio of 1 : 1 after filter sterilization. The mixed solution was gelled at 37°C for 15 minutes, froze in a -80°C refrigerator for 2 hours, and freeze-dried for 48 hours before 2.5% glutaraldehyde was added to crosslink proteins for 3 hours at room temperature. After that, PBS was used to wash the mixture twice and diluted ethanol was added to dehydrate the mixture to obtain chitosan-gelatin microspheres. PCM-PRP composites were prepared based on the method used by Deprés-Tremblay et al. [12]. The mice were decapitated to obtain blood samples, which were anticoagulated with 12.9 mM sodium citrate. The blood samples were then centrifuged at 160 g for 10 minutes using ACE E-Z PRPTM centrifuge. The supernatants and 1-2 mm of red blood cell pellets were taken and centrifuged at 400 g for 10 min at room temperature before 0.5 ml of materials at the bottom of the tube were resuspended to prepare PRP. PCMs were then mixed with PRP at a v/v ratio of 1 : 1 to obtain PCM-PRP composites. To prepare PCM-BMSC composites, we purchased a MC3T3-E1 cell line (ATCC, USA) as BMSCs. PCMs were incubated with 5×10^6 cells/ml of BMSC solution for 3 days to collect PCM/BMSC composites.

2.2. Animal Grouping and Modeling. A total of 20 male Wistar rats aged 4-8 weeks were divided into the Sham group, Model group, PRP/BMSC group, and PCM/PRP/BMSC group. The Sham group received sham surgery on the left tibia. The Model group received surgery to create a 3 mm diameter hole on the left tibia. The PRP/BMSC group received surgery to create a 3 mm diameter hole on the left tibia, and then, PRP and BMSCs were placed into the hole. For the PCM/PRP/BMSC group, PCM-PRP and PCM-BMSC composites (1 : 2, v/v) were implanted in the defect after a 3 mm diameter hole was made on the left tibia. Each of these implants contained approximately 10^4 BMSCs and 0.1 ml PRP. After 2 months and 4 months of treatment,

respectively, 5 rats were euthanized in each group, and the newly generated bone tissues at the site of bone defect were collected.

2.3. Expression of Cytokines Related to Osteogenesis. Alkaline phosphatase (ALP), type I collagen (Col I), and type II collagen (Col II) are key marker proteins during the differentiation of BMSCs into osteoblasts. Runt-associated transcription factor 2 (Runx2) and osteocalcin (OC) are key osteogenic genes for bone regeneration in bone defects [13]. Cells or tissue specimens were collected to extract RNA according to the instructions of the EASYspin Plus Bone Tissue RNA Kit. The mRNA expression levels of osteogenesis-related cytokines, including ALP, Col I, and Col II, and genes, including Runx2 and OC, were detected by quantitative real-time RT-PCR (qRT-PCR) using GAPDH as internal reference.

2.4. Measurement of Bone Mineral Density and Bone Volume. Tibiae were separated and scanned using micro-CT scanning. The bone mineral density and bone volume of newly generated bones were calculated.

2.5. Cell Proliferation. According to the MTT assay, 2×10^3 cells were seeded in a 96-well plate. MTT solution was prepared by adding MTT (Sigma; EMD Millipore) into phosphate-buffered saline. A total of 20 μg/l MTT solution was added to each well, and the cells were cultured for another 4 h, 8 h, and 16 h, respectively, before their viability was measured by the absorbance value (A) using a microplate reader at a wavelength of 490 nm.

2.6. Statistical Analysis. All data were processed using SPSS 20.0 software package. Measurement data were expressed as the mean ± standard deviation and compared using a t-test. A P value of <0.05 was considered to be statistically significant.

3. Results

3.1. Proliferation and Differentiation Potential of BMSCs after Hypoxia/Reaeration Treatment. To simulate the environment of chitosan microspheres prior to the sustained release of BMSCs, these stem cells were subjected to hypoxia/reoxygenation (H/R) treatment. The proliferative ability of BMSCs after H/R treatment was detected using the MTT. The results showed that there was no significant difference in MTT absorbance between H/R-treated cells and the control cells ($P > 0.05$), as shown in Figure 1. Studies have shown that the use of PRP can enhance the expression of osteogenic-related genes. After BMSCs were subjected to H/R treatment, PRP was used to induce cell differentiation for 7 days before the collection of total RNA. The intracellular expression levels of ALP, Col I, and osteopontin (OPN) were measured by qRT-PCR to evaluate the potential of cells differentiating into osteoblasts. The results showed that there were no significant differences in the expression levels of ALP, Col I, and OPN between H/R-treated BMSCs and PRP-induced BMSCs (all $P > 0.05$), as shown in Figure 2. This suggests that the
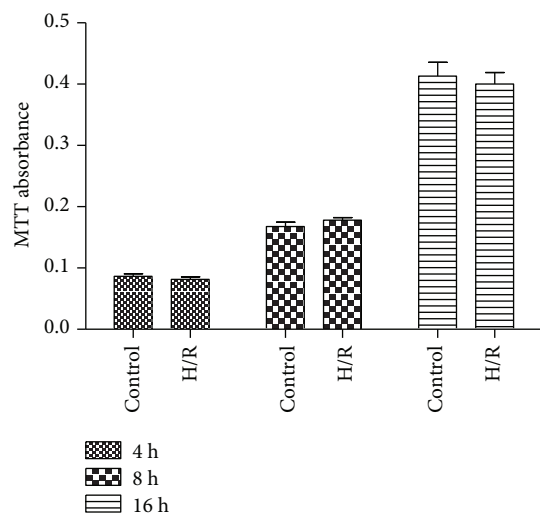
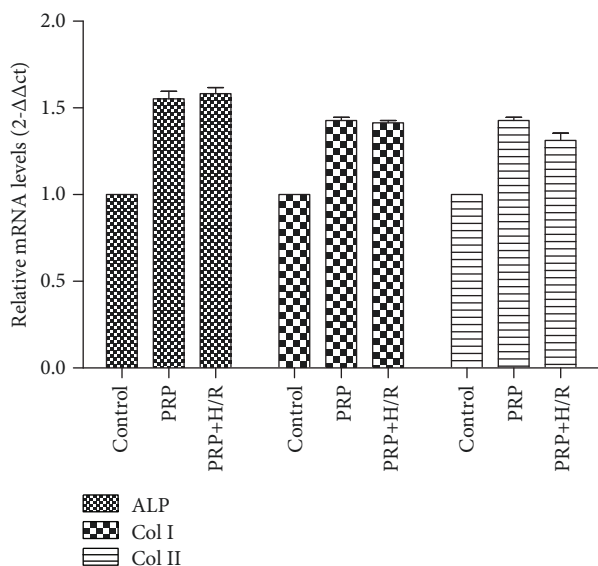Figure 1: Cell viability of BMSCs after H/R treatment.

Figure 2: Expression of ALP, Col I, and Col II in BMSCs after H/R treatment.

differentiation potential of BMSCs does not reduce when BMSCs are loaded by PCMs.

3.2. Cell Growth of PCM-BMSC Composites. BMSCs were cultured with PCMs for 3 days to prepare PCM/BMSC composites, and spherical particles were observed under the microscope. After the PCM/BMSC composites were cultured for another 7 days, only a fraction of irregular PCM residues was observed under the microscope. MTT assay was performed for PCM/BMSC composites. The results showed that the cell viability of BMSCs loaded by PCMs was higher ($P < 0.05$), and the results of MTT assay were shown in Figure 3. This suggests that before the degradation of PCMs, they can provide a larger surface for the attachment of BMSCs, facilitating cell proliferation.
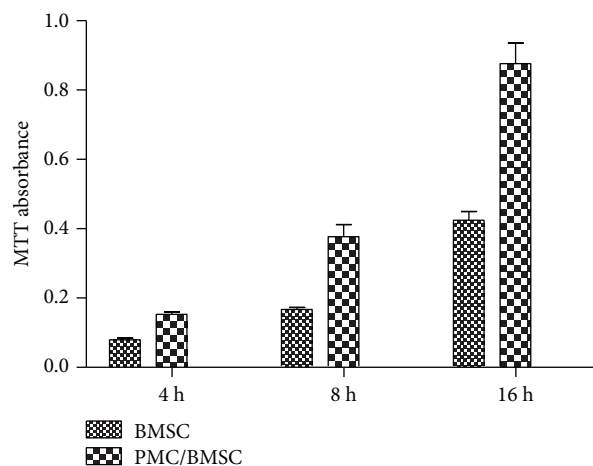

Figure 3: PCMs promote growth of BMSCs.

3.3. Effect of PCM/PRP Composites on Differentiation of BMSCs In Vitro. We first prepared PCM/PRP composites by incorporating PRP into PCMs. Total RNA was collected after in vitro induction of differentiation of BMSCs by PCM/PRP composites for 7 days. The intracellular expression levels of ALP, Col I, and OPN were detected by qRT-PCR. The results showed that the expression levels of ALP, Col I, and OPN in BMSCs induced by PCM/PRP composites were significantly increased compared with PRP-induced BMSCs ($P < 0.05$), as shown in Figure 4. This suggests that PCMs allow the sustained release of PRP, which is better in promoting the differentiation of BMSCs.

3.4. PCM/PRP/BMSC Composites Increased Bone Mineral Density in Rat Tibia Defect. We constructed a rat tibia defect model and used micro-CT scanning to detect the bone mineral density of the tibia defect. According to the results, the PRP/BMSC and PCM/PRP/BMSC groups had a significant increase in bone mineral density at 2 and 4 months after model establishment compared with the Model group ($P < 0.05$); the bone mineral density of the PCM/PRP/BMSC group was higher than that of the PRP/BMSC group ($P < 0.05$) and was closed to that of the Sham group ($P > 0.05$), as shown in Figure 5.

3.5. PCM/PRP/BMSC Composites Increased the Rate of Regenerated Bone Volume in Rat Tibia Defect. We used micro-CT scanning to detect the cortical bone thickness of the tibia defect, and the rate of regenerated bone volume is equal to the thickness of the regenerated cortical bone over the thickness of the cortical bone of the Model group. According to the results, the PRP/BMSC and PCM/PRP/BMSC groups had a significant increase in bone volume at 2 and 4 months after model establishment compared with the Model group ($P < 0.05$); the bone volume of the PCM/PRP/BMSC group was higher than that of the PRP/BMSC group ($P < 0.05$) and reached about 92.6% of that of the Sham group ($P > 0.05$), as shown in Figure 6.
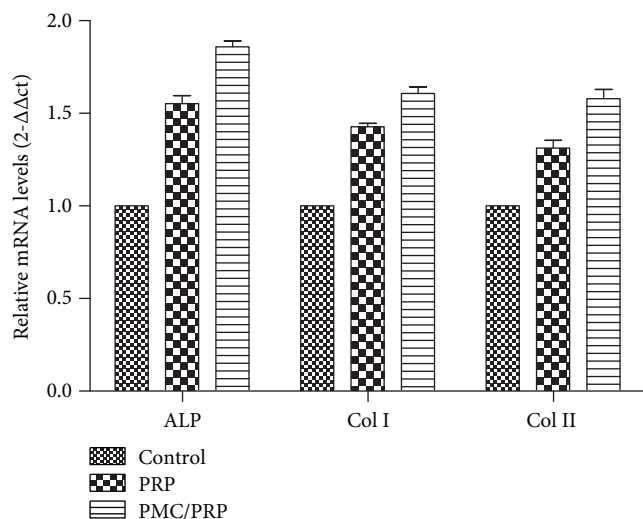
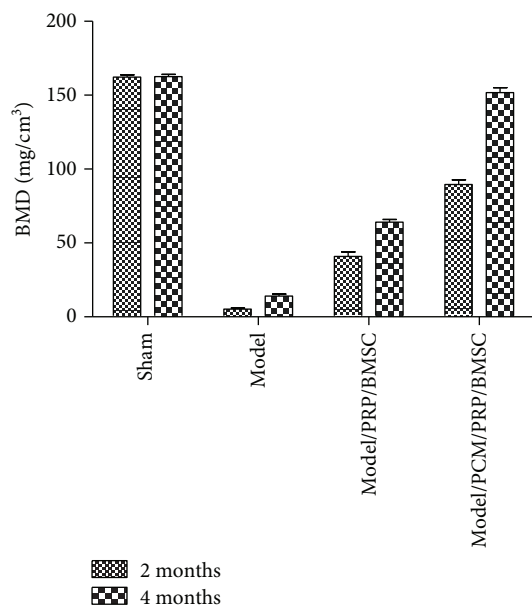Figure 4: Expression of ALP, Col I, and Col II in BMSCs induced by PCM/PRP composites in vitro.

Figure 5: PCM/PRP/BMSC composites increase bone mineral density in rat tibia defect.

3.6. PCM/PRP/BMSC Composites Increased the Expression of Runx2 and OC in Rat Tibia Defect. The regenerated tissue at the defect was collected 2 months after modeling to measure the expression of Runx2 and OC by PCR. The results showed that Runx2 and OC were expressed in the Model, PCM/PRP/BMSC, and PRP/BMSC groups ($P < 0.05$). The expression levels of Runx2 and OC in the PCM/PRP/BMSC group were higher than those of the PRP/BMSC group ($P < 0.05$), as shown in Figure 7.

4. Discussion

Biomaterials have received wide attention because of the properties like slowing drug release in tissues, inducing
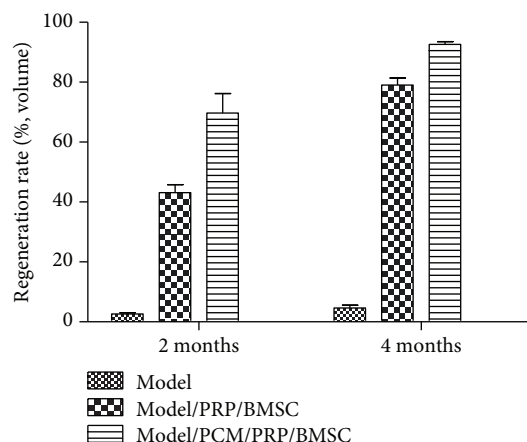

Figure 6: PCM/PRP/BMSC composites increase the rate of regenerated bone volume in rat tibia defect.
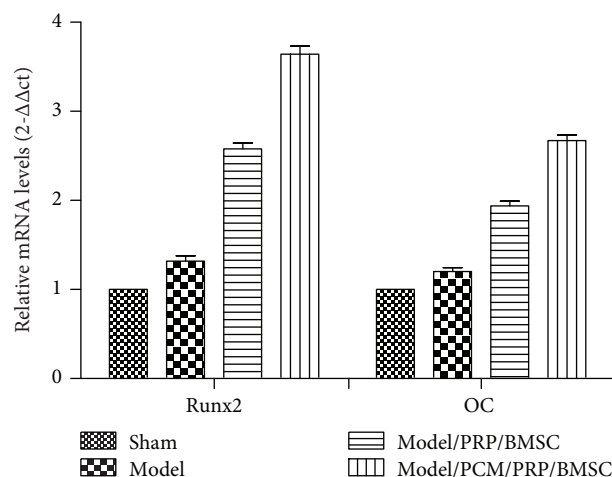

Figure 7: Expression of Runx2 and OC in rat tibia defect.

inflammatory responses, and recruiting immune cells or the capability of acting as scaffolds [14, 15]. Clinically, regeneration of bone defect is an intractable problem. The development of bone tissue engineering has a great significance for the regeneration of bone defects. However, due to the low bioactivity and poor hydrophilicity, the scaffold is not an ideal choice for the regeneration of bone defects. Therefore, biomaterials such as chitosan and gelatin are applied to bone defect regeneration and have received extensive attention [16]. PCM is a natural nontoxic biomaterial with good biocompatibility and biodegradability. This study used a combination of PCM-PRP and PCM-BMSC composites for the repair of rat tibia defects to evaluate their bone repair effects. We first proved that BMSCs in PCM-BMSC composites still have the ability of proliferation and differentiation and PCM-PRP composites are capable of inducing the differentiation of BMSCs. While BMSCs are capable of self-renewal and differentiation into osteoblasts, PRP is prominent in promoting osteogenesis, allowing it to induce the proliferation and differentiation of BMSCs into osteoblasts. Most of the endogenous cytokines peak at the early stage of bone fracture repair and are metabolized thereafter; moreover, part of the

endogenous cytokines, such as BMP-2, has to reach a certain concentration before they can promote osteogenesis [17]. After bone injury, exogenous cytokines can be supplied in an amount more sufficient than endogenous cytokines, but the direct use of exogenous cytokines is of limited effect due to the inactivation by enzymes in body fluids [18]. In addition, high dose of exogenous cytokines may also be counterproductive for it would promote osteoclastogenesis, thereby accelerating bone resorption and resulting in reduced bone mass at the injury site [19]. Therefore, an appropriate release of exogenous cytokines is an important factor for the induction of effective bone regeneration [20]. In this study, PCMs were used to load PRP and BMSC, respectively, which slowed down the release of PRP and BMSCs and improved the biological effect of PRP. In this study, we combined the advantages of BMSCs and PRP in bone regeneration after injury to optimize the treatment for bone defects in rat tibiae. Such a combination has produced satisfying results in tissue regeneration in some studies. Lian et al. found that the combination of BMSCs and PRP contributes to the repair and regeneration of diabetic wounds [21].

In conclusion, the use of PMC/PRP/BMSC composites benefits the repair of rat tibia defect. Its application is promising in the repair of tibia defects.

Data Availability

All the data are available in the handwritten notebook documented in our lab or available from the corresponding author upon request.

Conflicts of Interest

The authors declare no conflicts of interest.

Acknowledgments

References

[1] Y. Cheng, C. He, J. Ding, C. Xiao, X. Zhuang, and X. Chen, "Thermosensitive hydrogels based on polypeptides for localized and sustained delivery of anticancer drugs," *Biomaterials*, vol. 34, no. 38, pp. 10338–10347, 2013.

[2] J. Wu, K. Zhang, X. Yu, J. Ding, L. Cui, and J. Yin, "Hydration of hydrogels regulates vascularization *in vivo*," *Biomaterials Science*, vol. 5, no. 11, pp. 2251–2267, 2017.

[3] J. Zhang, T. Zheng, E. Alarçin et al., "Porous electrospun fibers with self-sealing functionality: an enabling strategy for trapping biomacromolecules," *Small*, vol. 13, no. 47, article 1701949, p. 13, 2017.

[4] S. Yu, X. Xu, J. Feng, M. Liu, and K. Hu, "Chitosan and chitosan coating nanoparticles for the treatment of brain disease," *International Journal of Pharmaceutics*, vol. 560, no. 14, pp. 282–293, 2019.

[5] R.-X. Shao, R.-F. Quan, T. Wang et al., "Effects of a bone graft substitute consisting of porous gradient HA/ZrO$_2$ and gela-tin/chitosan slow-release hydrogel containing BMP-2 and BMSCs on lumbar vertebral defect repair in rhesus monkey," *Journal of Tissue Engineering and Regenerative Medicine*, vol. 12, no. 3, pp. e1813–e1825, 2018.

[6] A. Ali and S. Ahmed, "A review on chitosan and its nanocomposites in drug delivery," *International Journal of Biological Macromolecules*, vol. 109, no. 1, pp. 273–286, 2018.

[7] D. Yang, S. Moon, and D.-W. Lee, "Surface modification of titanium with BMP-2/GDF-5 by a heparin linker and its efficacy as a dental implant," *International Journal of Molecular Sciences*, vol. 18, no. 1, p. 229, 2017.

[8] S. Kasagi and W. Chen, "TGF-beta1 on osteoimmunology and the bone component cells," *Cell & Bioscience*, vol. 3, no. 1, p. 4, 2013.

[9] D. Zou, Z. Zhang, D. Ye et al., "Repair of Critical-Sized Rat Calvarial Defects Using Genetically Engineered Bone Marrow-Derived Mesenchymal Stem Cells Overexpressing Hypoxia-Inducible Factor-1α," *Stem Cells*, vol. 29, no. 9, pp. 1380–1390, 2011.

[10] Y. Zhang, F. Wang, J. Chen, Z. Ning, and L. Yang, "Bone marrow-derived mesenchymal stem cells versus bone marrow nucleated cells in the treatment of chondral defects," *International Orthopaedics*, vol. 36, no. 5, pp. 1079–1086, 2012.

[11] K. Song, L. Li, X. Yan et al., "Characterization of human adipose tissue-derived stem cells in vitro culture and in vivo differentiation in a temperature-sensitive chitosan/β-glycerophosphate/collagen hybrid hydrogel," *Materials Science and Engineering*, vol. 70, Part 1, pp. 231–240, 2017.

[12] G. Deprés-Tremblay, A. Chevrier, N. Tran-Khanh, M. Nelea, and M. D. Buschmann, "Chitosan inhibits platelet-mediated clot retraction, increases platelet-derived growth factor release, and increases residence time and bioactivity of platelet-rich plasma *in vivo*," *Biomedical Materials*, vol. 13, no. 1, article 15005, p. 1, 2018.

[13] W. Q. Xu, J. X. Ding, C. X. Xiao, L. Y. Li, X. L. Zhuang, and X. S. Chen, "Versatile preparation of intracellular-acidity-sensitive oxime-linked polysaccharide-doxorubicin conjugate for malignancy therapeutic," *Biomaterials*, vol. 54, pp. 72–86, 2015.

[14] Y. Wang, Z. Jiang, W. Xu et al., "Chiral Polypeptide thermogels induce controlled inflammatory response as potential immunoadjuvants," *ACS Applied Materials & Interfaces*, vol. 11, no. 9, pp. 8725–8730, 2019.

[15] B. Zhu, W. Xu, J. Liu, J. Ding, and X. Chen, "Osteoinductive agents-incorporated three-dimensional biphasic polymer scaffold for synergistic bone regeneration," *ACS Applied Materials & Interfaces*, vol. 5, no. 2, pp. 986–995, 2018.

[16] J. H. Ye, Y. J. Xu, J. Gao et al., "Critical-size calvarial bone defects healing in a mouse model with silk scaffolds and SATB2-modified iPSCs," *Biomaterials*, vol. 32, no. 22, pp. 5065–5076, 2011.

[17] S. Pattnaik, S. Nethala, A. Tripathi, S. Saravanan, A. Moorthi, and N. Selvamurugan, "Chitosan scaffolds containing silicon dioxide and zirconia nano particles for bone tissue engineering," *International Journal of Biological Macromolecules*, vol. 49, no. 5, pp. 1167–1172, 2011.

[18] D. Lindhorst, F. Tavassol, C. von See et al., "Effects of VEGF loading on scaffold-confined vascularization," *Journal of Biomedical Materials Research Part A*, vol. 95, no. 3, pp. 783–792, 2010.

[19] F. Pati, B. Adhikari, and S. Dhara, "Collagen intermingled chitosan-tripolyphosphate nano/micro fibrous scaffolds for

tissue-engineering application," *Journal of Biomaterials Science. Polymer Edition*, vol. 23, no. 15, p. 16, 2012.

[20] B.-B. Seo, J.-T. Koh, and S.-C. Song, "Tuning physical properties and BMP-2 release rates of injectable hydrogel systems for an optimal bone regeneration effect," *Biomaterials*, vol. 122, pp. 91–104, 2017.

[21] Z. Lian, X. Yin, H. Li et al., "Synergistic effect of bone marrow-derived mesenchymal stem cells and platelet-rich plasma in streptozotocin-induced diabetic rats," *Annals of Dermatology*, vol. 26, no. 1, pp. 1–10, 2014.

Research Article

Effect of Codonopsis pilosula Polysaccharides on the Growth and Motility of Hepatocellular Carcinoma HepG2 Cells by Regulating β-Catenin/TCF4 Pathway

Yuan-yuan Zhang [iD],[1] **Ying-mei Zhang,**[1] **and Hai-yan Xu** [iD][2]

[1]*Department of Laboratory Medicine, The Affiliated Huaian No. 1 People's Hospital of Nanjing Medical University, Huai'an, Jiangsu 223300, China*
[2]*Department of Cardiology, The Affiliated Huaian No. 1 People's Hospital of Nanjing Medical University, Huai'an, Jiangsu 223300, China*

Correspondence should be addressed to Yuan-yuan Zhang; yuanyuanzhang1234@163.com

Objective. To study the effect of Codonopsis pilosula polysaccharide (CPP) on the growth and motility of HepG2 cells and its possible mechanism. *Methods.* Cells were randomly divided into Control group, CPP ($5\,\mu$M) group, CPP ($10\,\mu$M) group, and CPP ($20\,\mu$M) group. The proliferation, invasion, migration ability, and expression of proteins involved in the epithelial-mesenchymal transition (EMT) and signaling pathway of HepG2 cells were detected by CCK8 assay, BrdU staining, Transwell, Scratch test, and Western blot, respectively. *Results.* Codonopsis pilosula polysaccharide inhibited the proliferation of HepG2 cells cultured in vitro along with the expression level of Ki67 and PCNA protein ($P < 0.05$), decreased the number of invasive cells ($P < 0.05$), and reduced the scratch closure rate ($P < 0.05$). It also adjusted the expression of vascular endothelial growth factor (VEGF), E-cadherin, and N-cadherin ($P < 0.05$). Other than that, downregulation of β-catenin, TCF4, and c-Myc protein expression ($P < 0.05$) was observed as well. *Conclusion.* Codonopsis pilosula polysaccharide can inhibit the proliferation and motility of HepG2 cells cultured *in vitro*, and the underlying mechanism is proposed to be related to the inhibition of the β-catenin/TCF4 pathway.

1. Introduction

Hepatocellular carcinoma (HCC) is one of the leading causes of cancer-related mortality worldwide. The main driving factors associated with HCC include chronic infection of hepatitis B and chronic hepatitis C, alcoholic liver disease, and nonalcoholic fatty liver disease. Despite advances in new technologies of prevention, screening, diagnosis, and treatment of HCC, the morbidity and mortality rate of the disease continue to rise. About 600,000 people die of liver cancer every year worldwide. The treatments vary considering different tumor load and metastasis; moreover, the treatment for late-stage liver cancer is expensive and ineffective [1–3]. Therefore, it is necessary to expand researches regarding the treatment of HCC and identify more effective

therapeutic drugs. Codonopsis pilosula, also known as dangshen, belongs to the Campanulaceae family. The dried root from its subspecies dangshen, suhuadangshen, or chuandangshen, containing polysaccharides, saponins, sesquiterpenoids, polyphenols, terpenoids, alkaloids, volatile oil, and other ingredients, is commonly prepared for medical use. Codonopsis pilosula polysaccharide (CPP), one of active constituents in Codonopsis pilosula, has attracted extensive attention in the medical field due to its extensive physiological and biological activities. Previous studies have shown that Codonopsis pilosula polysaccharide has the effects of immunity enhancement, antivirus, liver protection, and neuroprotection [4–9]. It is worth noting that the polysaccharide from Codonopsis pilosula plays an important role in growth inhibition in various tumor cells such as breast cancer and

cervical cancer [10, 11]. At present, however, there are few reports on the effect of Codonopsis pilosula polysaccharide on human hepatoma HepG2 cells. Taken all these together, in this study, we studied the human hepatoma HepG2 cells cultured *in vitro* and explored the effect of Codonopsis pilosula polysaccharide on the proliferation and metastasis of hepatocarcinoma cells and its possible mechanism as well.

2. Materials and Methods

2.1. Reagents and Instruments. Dangshen polysaccharide (purity ≥98%) was purchased from China Food and Drug Administration Research Institute. DMEM cell culture medium, 0.25% trypsin, and fetal bovine serum were purchased from Gibco, USA. The CCK8 kit was purchased from Roche Group. Transwell chamber was purchased from Beijing Unicom Biotechnology Co. LTD. Monoclonal antibody and horseradish peroxidase-labeled secondary antibody were purchased from Abcam, UK. RIPA lysate was purchased from Sigma, USA. The BCA kit was purchased from Biyuntian Biotech. BrdU detection kits were purchased from Guangzhou Ruibo Biological Co. Ltd.

Both the electrophoresis apparatus and the semidry film transfer apparatus were purchased from Bole Corporation of the United States. The Gel View 6000 chemiluminescent gel imaging system was purchased from Guangzhou Yunxing Instrument Co. Ltd. The ordinary optical microscope was purchased from Olympus Corporation of Japan.

2.2. Cell Culture. The human liver cancer HepG2 cell line was purchased from FuHeng Cell Center, Shanghai, China. The cells were cultured in a DMEM medium containing 10% fetal bovine serum and 1% cyan-streptomycin at 37°C in a 5% CO_2 incubator and subcultured when the cell fusion rate reached 80%.

2.3. Experimental Methods

2.3.1. Cell Activity Was Detected by CCK8 Assay. The cells were seeded in a 96-well plate at a density of 4×10^4 cells/mL. After cell attachment, the cells were treated with different concentrations of CPP (0, 0.05, 0.1, 0.2, 0.5, 1, 2, 5, 10, 20, 50, 100, 200, and 400 μM) for 24 h, with 6 replicate wells per concentration. After 24 h, 10 μL of CCK8 reagent was added into each well and after incubation at 37°C for 4 h; the activity of each well was measured by an enzyme-labeling instrument. According to the test results, the CPP concentrations resulting in over 80% of cell activity were selected for subsequent experiments.

2.3.2. BrdU Staining for Cell Proliferation. The cells were seeded in a 6-well plate with 1 mL of cell suspension at the density of 2×10^6 cells/mL for each well. After cell attachment, the cells were incubated in a medium containing 0.4% FBS for 72 hours, each group containing 3 replicate wells. The cells were randomly divided into 4 groups: Control group, CPP (5 μM) group, CPP (10 μM) group, and CPP (20 μM) group. After the corresponding treatment of final concentration liquor, BrdU with final concentration of 0.03 μg/mL was added before another 40 minutes of

incubation. The culture medium was discarded, and the plate was washed three times with PBS, fixed with paraformaldehyde for 10 min, and cell proliferation assay was performed strictly according to the instructions. The number of BrdU-positive cells was counted under a microscope.

2.3.3. Transwell Detection of Cell Invasion Ability. The cells were seeded into the upper chamber of Matrigel-coated Transwell chambers at a density of 4×10^5 cells/mL, cultured in a medium containing no fetal bovine serum, while at the lower chamber, normal cell culture medium was added. After grouping according to Section 2.3.1 and further culture for 48 hours, the cells in the upper chamber were wiped with a sterile cotton swab, and the cells migrated to the lower chamber were stained with crystal violet. Five fields were randomly selected for each group for counting. There were 6 replicate wells in each group.

2.3.4. Cell Migration Ability Was Detected by Scratch Test. Cells were seeded in 12-well sterile plates at a density of 4×10^5 cells/mL. After attachment of cells to the wall, horizontal lines perpendicular to the marker were drawn by the 10 μL gun tip, and the plate was washed 3 times with PBS. After grouping according to Section 2.3.1 and drug administering, the plate was further cultured for 24 h. Wound closure rate = (initial width - measurement width)/initial width × 100%.

2.3.5. Western Blot Detection of Cell Proliferation, EMT, and Pathway Protein Expression. The total protein of each group was extracted with RIPA protein lysate on ice, and the concentration of proteins was measured and leveled by BCA kit for each group. Equal amount of proteins for each group was separated by 12% SDS-PAGE and transferred into a PVDF membrane. The membrane was then blocked with 5% skim milk for 2 h at room temperature. The blot was incubated in primary antibody overnight at 4°C. The next day, the primary antibody was discarded, and the buffer-washed PVDF blot was incubated in corresponding secondary antibody for 1 hour at room temperature. For imaging, ECL solution was added dropwise in the dark room for blot exposure and development. In this study, GAPDH was used as the internal reference.

2.4. Statistical Methods. All experimental data were statistically analyzed with statistical software SPSS 19.0. Differences between groups were tested by t, t-test, or one-way ANOVA. The experimental results were expressed as mean ± standard deviation. The difference was considered statistically significant at $P < 0.05$.

3. Results

3.1. Effect of CPP on the Proliferation of HepG2 Cells Cultured In Vitro. The effect of different concentrations of CPP on the survival rate of HepG2 cells was measured by CCK8 assay, as shown in Figure 1. As the CPP concentration reaches 50 μM and above, the survival rate of HepG2 cells remains less than 80%. It indicated that CPP concentration up to 50 μM has obvious cytotoxic effect on HepG2

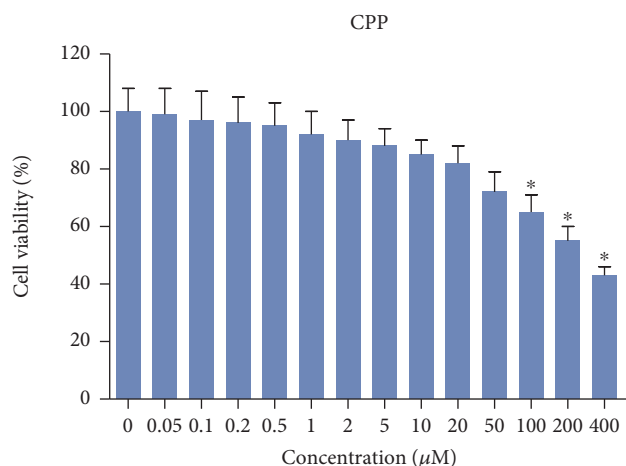FIGURE 1: Cell viability of HepG2 cells.

cells. Therefore, we selected 3 maximum concentrations of 5, 10, and $20\,\mu$M without a significant cytotoxicity for subsequent experiments.

The proliferation of cells was detected by BrdU staining. The results showed that the number of BrdU-positive cells in the CPP-treated groups was significantly lower than that in the Control group ($P < 0.05$, Figure 2(a)) and inversely proportional to the concentration of CPP. At the same time, the expression levels of proliferation-related proteins were further detected by Western blot. The results showed that the expression levels of Ki67 and PCNA proteins in CPP-treated cells were significantly lower than those in the Control group ($P < 0.05$, Figure 2(b)), and the differences were also CPP concentration-dependent.

3.2. Effect of CPP on the Invasive Ability of HepG2 Cells Cultured In Vitro. The cell invasive ability was determined by Transwell assay, and the results showed that, compared with the Control group, the CPP-treated groups showed significantly reduced number of invasive cells ($P < 0.05$, Figure 3); moreover, the number decreased with the increase of CPP treatment concentration.

3.3. Effect of CPP on the Migration Ability of HepG2 Cells Cultured In Vitro. The cell migration ability was tested by the scratch test. The results suggested that the wound closure rate of the CPP-treated groups was significantly lower than that of the Control group ($P < 0.05$, Figure 4) and was CPP concentration-dependent.

3.4. Effect of CPP on the Expression of EMT-Related Protein in HepG2 Cells Cultured In Vitro. The morphology of the cells in each group was observed under the microscope. The cells in the Control group were mostly ovoid in shape or nearly square with tight arrangement. While after CPP treatment, the cells gradually displayed long fusiform with loose arrangement.

Western blot results represented the expression level of EMT-related protein in cells. The results showed that the expression levels of VEGF and N-cadherin were significantly decreased in CPP-treated groups compared with the Control

group ($P < 0.05$, Figure 5). In contrary, the expression level of E-cadherin protein was significantly upregulated ($P < 0.05$, Figure 4) and was CPP concentration-dependent.

3.5. Effect of CPP on the Expression of Pathway Protein in HepG2 Cells Cultured In Vitro. The expression level of β-catenin, TCF4, and c-Myc proteins in CPP-treated cells was significantly lower than that in the Control group ($P < 0.05$, Figure 6) and was positively correlated with the CCP treatment concentration.

4. Discussion

Hepatocellular carcinoma is a primary liver cancer to which most liver cancers belong. As a malignant tumor originating from the liver epithelial or mesenchymal tissue, it is prone to vascular invasion and metastasis, which mainly develop in the portal vein or its branches, hepatic veins or its branches, and the inferior vena cava of the liver, and homotype clumping in the portal vein is the most common form of metastasis of hepatocellular carcinoma [2–12]. The etiology and exact molecular mechanism are still unclear, and it is currently considered to be a multifactor and multistep complex process. The treatment method is specialized for each individual and the comprehensive treatment depends on the different stages of the disease. The treatment types mainly include surgery, hepatic artery ligation, radiofrequency, freezing, laser, microwave, and chemotherapy. Many studies have shown that Codonopsis pilosula polysaccharides have a variety of biological functions, including cardiovascular and cerebrovascular protection, enhancing immunity and antitumor activities [4–11]. Based on all facts above, we studied human hepatoma HepG2 cells and further investigated the effect of Codonopsis pilosula polysaccharides on the proliferation and metastasis ability of hepatoma cells *in vitro* and its possible mechanism.

Firstly, the effect of Codonopsis pilosula polysaccharide on the proliferation of HepG2 cells *in vitro* was detected by BrdU staining. It was found that Codonopsis pilosula polysaccharide dose-dependently reduced the number of BrdU-positive cells in HepG2 cells. The effect of Codonopsis pilosula polysaccharides on the expression levels of proliferation-related proteins Ki67 and PCNA in hepatocellular carcinoma HepG2 cells was further examined by Western blot experiments. It was confirmed that Codonopsis pilosula polysaccharide dose-dependently inhibited the expression levels of proliferation proteins. These results complied with that of Xin et al.'s study on the effect of Codonopsis pilosula polysaccharide on ovarian cancer HO-8910 cells [11]. On the other hand, Bai et al.'s study [13] showed that the two water-soluble polysaccharides extracted from Codonopsis pilosula polysaccharide can inhibit the growth of HepG2 cells, and the underlying mechanism is related to cell cycle arrest induction and key protein expression inhibition.

In order to test the effect of Codonopsis pilosula polysaccharide on the motility of hepatocellular carcinoma HepG2 cells cultured in vitro, we performed a scratch test and a Transwell experiment, both of which demonstrated the

(a)

(b)

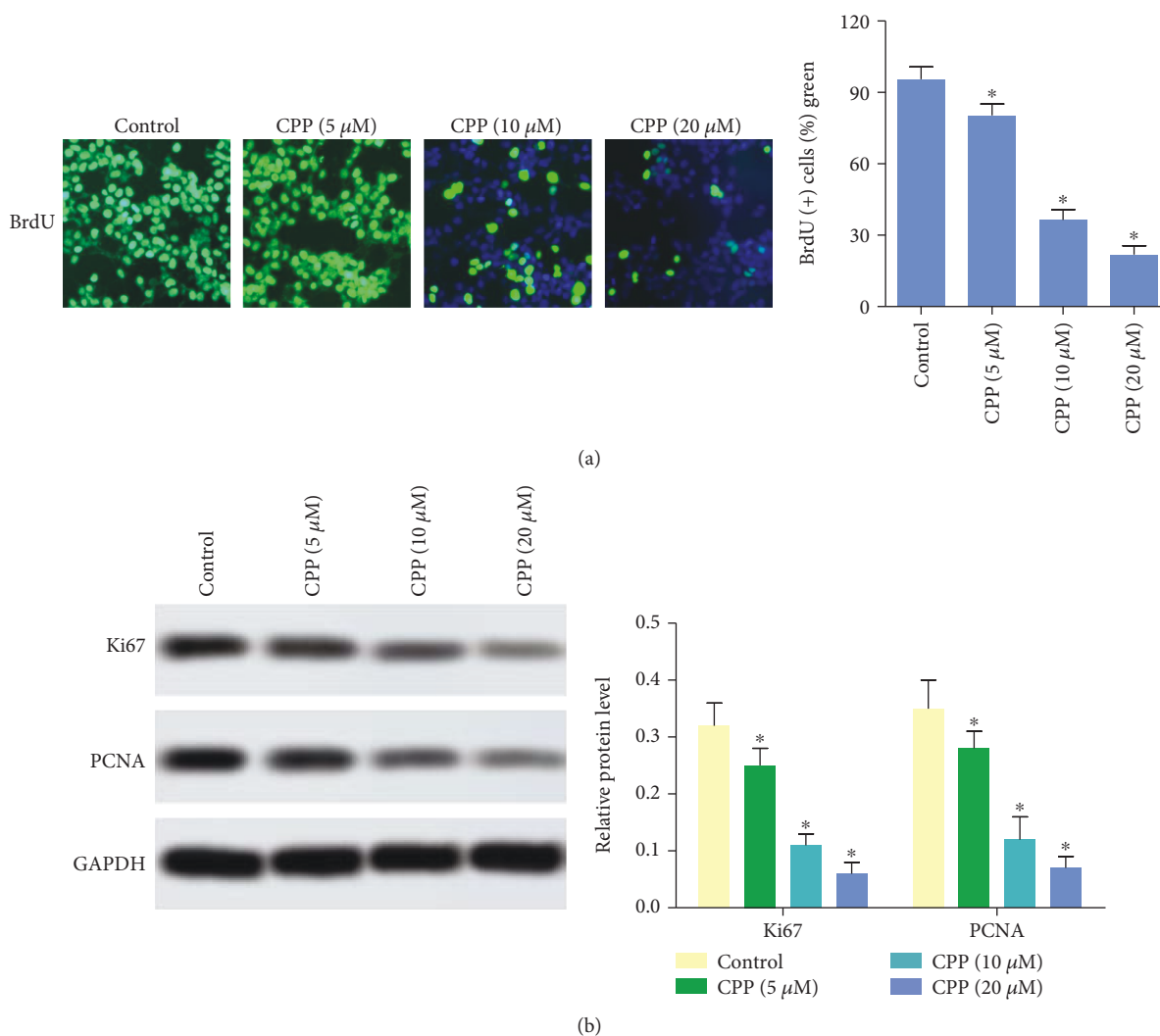FIGURE 2: Proliferation of HepG2 cells. (a) Cell proliferation detected by BrdU; (b) protein expression of Ki67 and PCNA was tested by Western blot. $^*P < 0.05$ versus Control group.
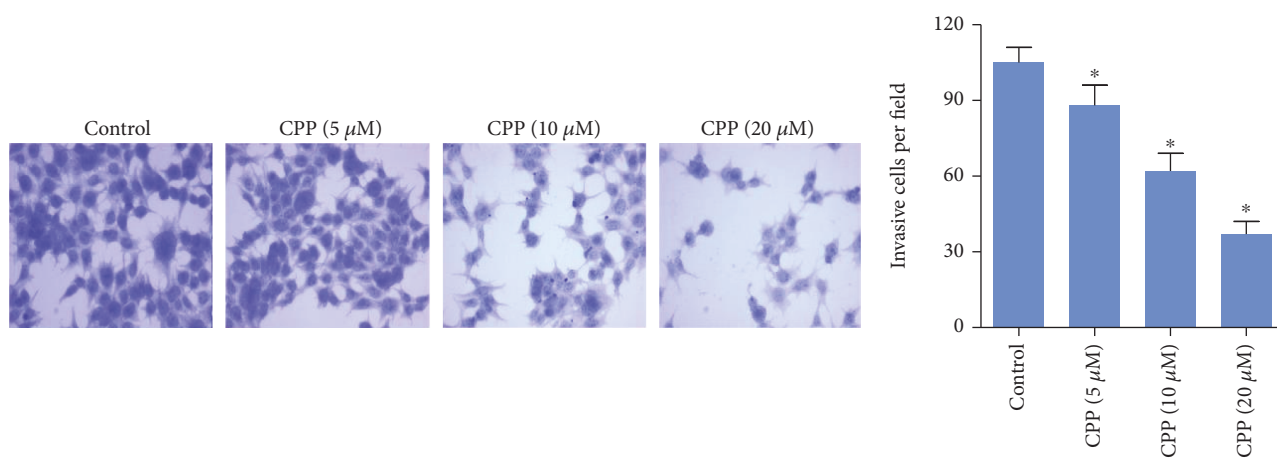

FIGURE 3: Invasion of HepG2 cells. $^*P < 0.05$ versus Control group.

FIGURE 4: Migration of HepG2 cells. $^*P < 0.05$ versus Control group.
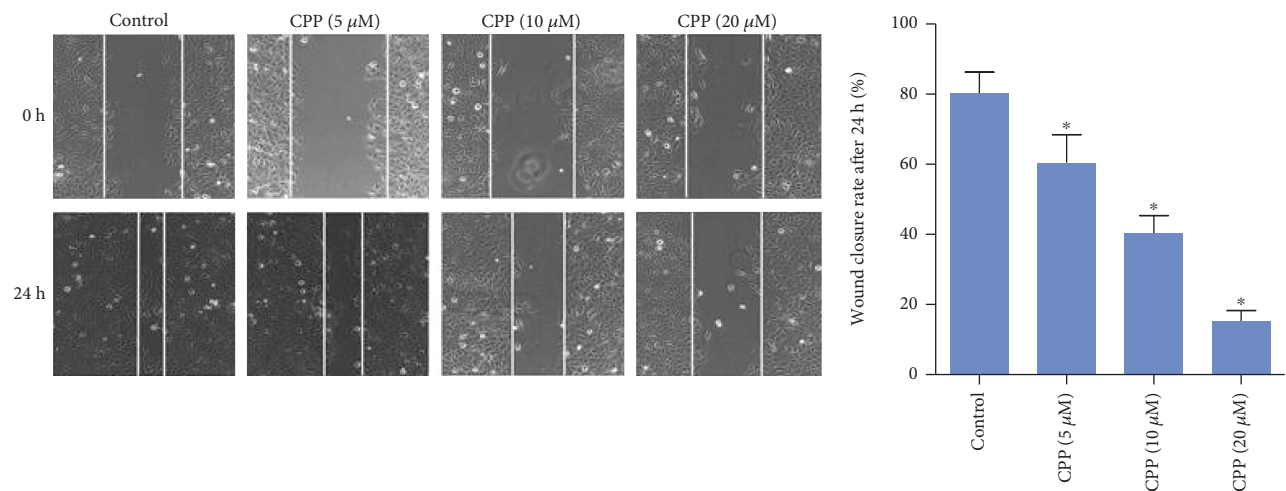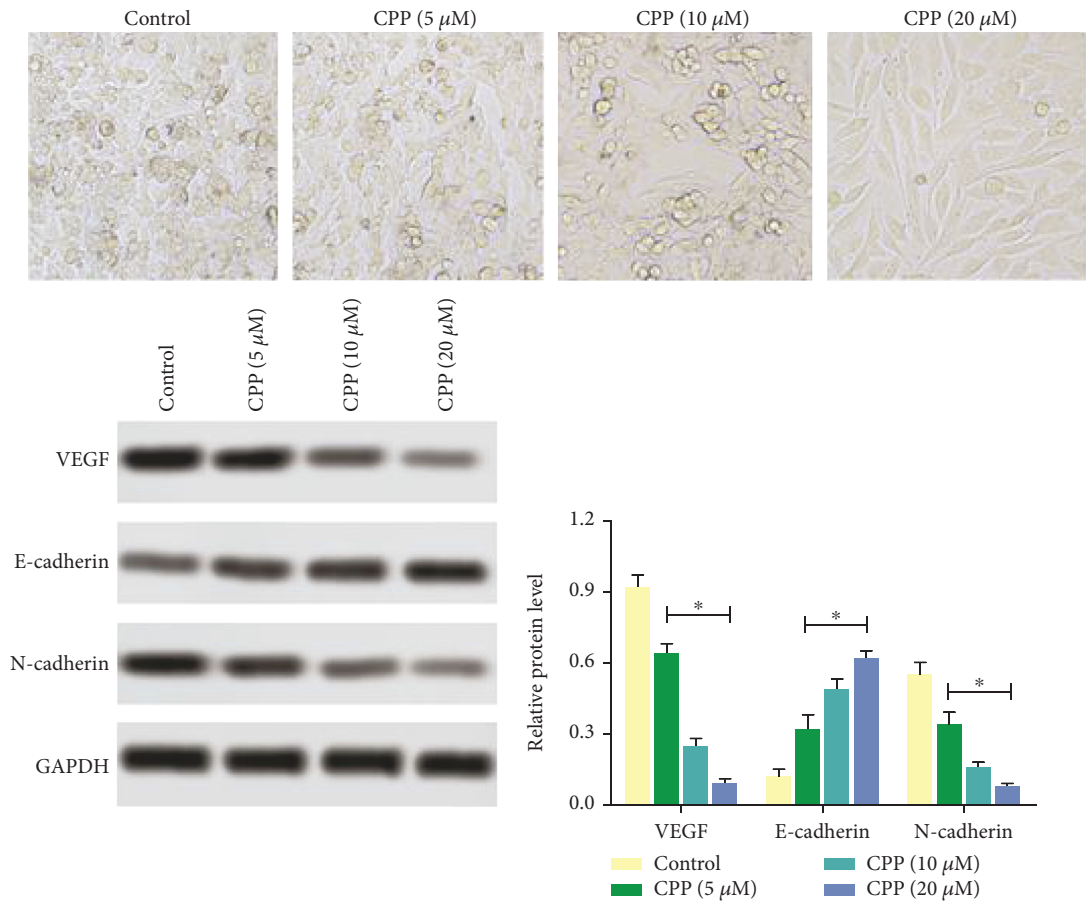

FIGURE 5: Expression of EMT-related protein in HepG2 cells. $^*P < 0.05$ versus Control group.

inhibitory effect of Codonopsis pilosula polysaccharide on the motility of HepG2 cells cultured *in vitro*. All these results are consistent with Bai et al.'s study [13].

Increased tumor cell migration capacity is the basis for tissue infiltration and distant metastasis. Epithelial

mesenchymal transition (EMT) is a process in which polarized epithelial cells lose epithelial properties and acquire interstitial properties, thus increasing cell metastasis and invasion; it is an important biological process that promotes tumor invasion and metastasis [14, 15]. E-cadherin, as an
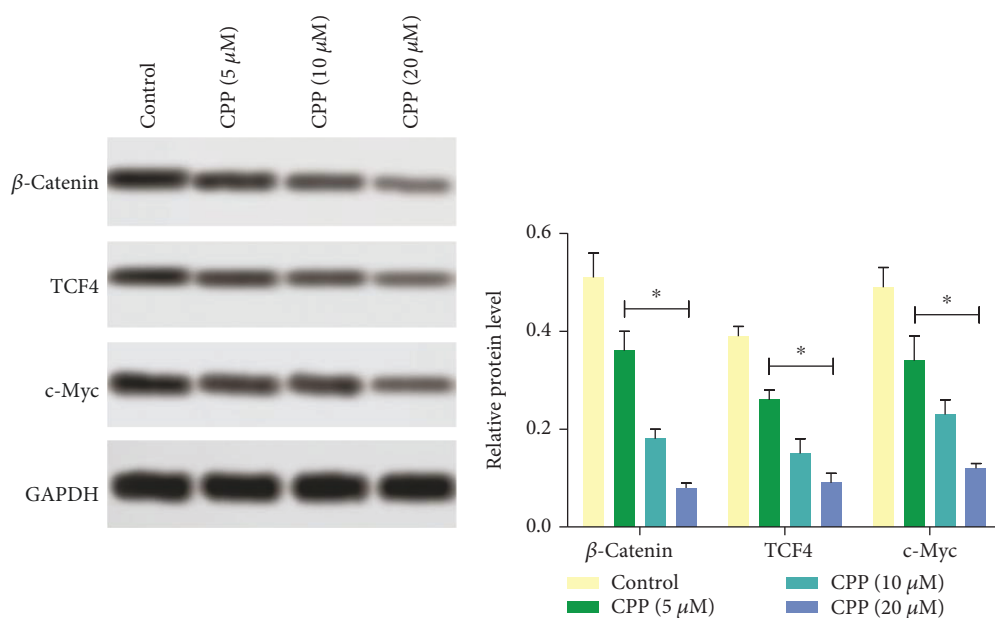
FIGURE 6: Expression of signaling pathway protein in HepG2 cells. $^*P < 0.05$ versus Control group.

important cell adhesion factor, participates in and mediates the adhesion between cells and is inextricably linked to the invasion and metastasis of various tumors. Its low expression or loss of expression plays a key role in epithelial mesenchymal transition [16]. Studies have shown that [17] overexpression of TCF4 in canine kidney epithelial cells can increase cell invasive ability, thereby accelerating the occurrence of tumor EMT, which can be represented by remarkable downregulation of epithelial marker protein E-cadherin and upregulation of the interstitial marker protein vimentin. To further explore the molecular mechanism of the effect of Codonopsis pilosula polysaccharide on the motility of hepatocellular carcinoma cells cultured *in vitro*, we performed Western blot and found that Codonopsis pilosula polysaccharide-treated cells showed higher expression of epithelial marker protein E-cadherin but lower expression of interstitial marker protein N-cadherin and migration marker protein VEGF. The results indicated that Codonopsis pilosula polysaccharide can inhibit the loss of polarity between human hepatoma HepG2 cells cultured *in vitro*, slow the development of stromal cells, and reduce the invasion and metastasis ability of cells, thus delaying the occurrence of EMT in HepG2 cells.

Wnt signaling pathway is involved in tumor formation. Upon activation, β-catenin translocates into the nucleus to competitively bind with TCF4 to form β-catenin/TCF4 complex. The complex then activates downstream transcription factors of TCF4, such as cycD and c-Myc, which ultimately leads to cell abnormalities, proliferation, and tumorigenesis [18, 19]. Studies have shown that abnormal activation of the TCF4 target gene by Wnt signaling can promote malignant transformation of colorectal cancer [20], and downregulation of the Wnt/β-catenin signaling pathway can inhibit epithelial-mesenchymal transition in nonsmall cell lung cancer [21]. Therefore, in order to investigate the

regulatory effect of concentration-dependent Codonopsis pilosula polysaccharide treatment on the signaling pathway β-catenin/TCF4 and its effect on human hepatoma HepG2 cells cultured *in vitro*, we performed series of experiments and found that the expression of β-catenin, TCF4, and the downstream C-Myc protein were significantly inhibited. These results indicated that Codonopsis pilosula polysaccharide can inhibit the proliferation, invasion, and EMT of human hepatoma HepG2 cells by downregulating the β-catenin/TCF4 signaling pathway.

In summary, this paper explored the role of Codonopsis pilosula polysaccharide in the proliferation, invasion, and interstitial transformation of human hepatoma HepG2 cells cultured *in vitro*, suggesting that the inhibition of Beta-catenin/Tcf4 protein expression by Codonopsis pilosula polysaccharide is related to the growth and metastasis of human hepatoma HepG2 cells cultured in vitro. This paper also provides experimental data for the role of Codonopsis pilosula polysaccharide in the occurrence and development of liver cancer, but there is still a lack of research on the effect of Codonopsis pilosula polysaccharide on cell growth and metastasis and its role in the growth of liver cancer cells in vivo in the presence of pathway inhibitor/activator.

Data Availability

The data used to support the findings of this study are available from the corresponding author upon request.

Conflicts of Interest

The authors declare that there is no conflict of interest regarding the publication of this paper.

Acknowledgments

References

[1] M. Sayiner, P. Golabi, and Z. M. Younossi, "Disease burden of hepatocellular carcinoma: a global perspective," *Digestive Diseases and Sciences*, vol. 64, no. 4, pp. 910–917, 2019.

[2] J. F. Jiang, Y. C. Lao, B. H. Yuan et al., "Treatment of hepatocellular carcinoma with portal vein tumor thrombus: advances and challenges," *Oncotarget*, vol. 8, no. 20, pp. 33911–33921, 2017.

[3] J. Balogh, D. Victor, E. H. Asham et al., "Hepatocellular carcinoma: a review," *Journal of Hepatocellular Carcinoma*, vol. 3, pp. 41–53, 2016.

[4] P. Zhang, L. Hu, R. Bai et al., "Structural characterization of a pectic polysaccharide from Codonopsis pilosula and its immunomodulatory activities in vivo and in vitro," *International Journal of Biological Macromolecules*, vol. 104, Pt A, pp. 1359–1369, 2017.

[5] C. Liu, J. Chen, E. Li et al., "Solomonseal polysaccharide and sulfated Codonopsis pilosula polysaccharide synergistically resist Newcastle disease virus," *PLoS One*, vol. 10, no. 2, article e0117916, 2015.

[6] C. Liu, J. Chen, E. Li et al., "The comparison of antioxidative and hepatoprotective activities of Codonopsis pilosula polysaccharide (CP) and sulfated CP," *International Immunopharmacology*, vol. 24, no. 2, pp. 299–305, 2015.

[7] X. Chu, X. J. Liu, J. M. Qiu, X. L. Zeng, and H. R. Bao, "Inhibitory effects of codonopsis pilosula polysaccharides on the deterioration of impaired phagocytosis of alveolar macrophage induced by fine particulate matter in chronic obstructive pulmonary disease mice," *Zhonghua Yi Xue Za Zhi*, vol. 96, no. 14, pp. 1134–1138, 2016.

[8] X. Chu, X. J. Liu, J. M. Qiu, X. L. Zeng, H. R. Bao, and J. Shu, "Effects of Astragalus and Codonopsis pilosula polysaccharides on alveolar macrophage phagocytosis and inflammation in chronic obstructive pulmonary disease mice exposed to PM2.5," *Environmental Toxicology and Pharmacology*, vol. 48, pp. 76–84, 2016.

[9] Q. Zhang, Y. Xia, H. Luo et al., "Codonopsis pilosula polysaccharide attenuates tau hyperphosphorylation and cognitive impairments in hTau infected mice," *Frontiers in Molecular Neuroscience*, vol. 11, p. 437, 2018.

[10] M. Chen, Y. Li, Z. Liu et al., "Exopolysaccharides from a Codonopsis pilosula endophyte activate macrophages and inhibit cancer cell proliferation and migration," *Thoracic Cancer*, vol. 9, no. 5, pp. 630–639, 2018.

[11] T. Xin, F. Zhang, Q. Jiang et al., "The inhibitory effect of a polysaccharide from Codonopsis pilosula on tumor growth and metastasis in vitro," *International Journal of Biological Macromolecules*, vol. 51, no. 5, pp. 788–793, 2012.

[12] B. H. Yuan, W. P. Yuan, R. H. Li et al., "Propensity score-based comparison of hepatic resection and transarterial chemoembolization for patients with advanced hepatocellular carcinoma," *Tumour Biology*, vol. 37, no. 2, pp. 2435–2441, 2016.

[13] R. Bai, W. Li, Y. Li et al., "Cytotoxicity of two water-soluble polysaccharides from Codonopsis pilosula Nannf. var. modesta (Nannf.) L.T.Shen against human hepatocellular carcinoma HepG2 cells and its mechanism," *International Journal of Biological Macromolecules*, vol. 120, pp. 1544–1550, 2018.

[14] J. Li, R. Yang, Y. Dong, M. Chen, Y. Wang, and G. Wang, "Knockdown of FOXO3a induces epithelial-mesenchymal transition and promotes metastasis of pancreatic ductal adenocarcinoma by activation of the β-catenin/TCF4 pathway through SPRY2," *Journal of Experimental & Clinical Cancer Research*, vol. 38, no. 1, p. 38, 2019.

[15] L. Przybyla, J. M. Muncie, and V. M. Weaver, "Mechanical control of epithelial-to-mesenchymal transitions in development and cancer," *Annual Review of Cell and Developmental Biology*, vol. 32, no. 1, pp. 527–554, 2016.

[16] C. Xiangming, S. Hokita, K. Nuruki et al., "The expression of cadherin-catenin complex in association with the clinicopathologic features of early gastric cancer," *Surgery Today*, vol. 28, no. 6, pp. 587–594, 1998.

[17] V. R. Sobrado, G. Moreno-Bueno, E. Cubillo et al., "The class I bHLH factors E2-2A and E2-2B regulate EMT," *Journal of Cell Science*, vol. 122, no. 7, pp. 1014–1024, 2009.

[18] T. Valenta, G. Hausmann, and K. Basler, "The many faces and functions of β-catenin," *The EMBO Journal*, vol. 31, no. 12, pp. 2714–2736, 2012.

[19] A. S. Arboatti, F. Lambertucci, M. G. Sedlmeier et al., "Diethylnitrosamine enhances hepatic tumorigenic pathways in mice fed with high fat diet (Hfd)," *Chemico-Biological Interactions*, vol. 303, pp. 70–78, 2019.

[20] Y. Yao, J. Zuo, and Y. Wei, "Targeting of TRX2 by miR-330-3p in melanoma inhibits proliferation," *Biomedicine & Pharmacotherapy*, vol. 107, pp. 1020–1029, 2018.

[21] J. Cai, L. Fang, Y. Huang et al., "Simultaneous overactivation of Wnt/β-catenin and TGFβ signalling by miR-128-3p confers chemoresistance-associated metastasis in NSCLC," *Nature Communications*, vol. 8, p. 15870, 2017.